# Journal of Turbomachinery

Published Quarterly by ASME

VOLUME 126 • NUMBER 4 • OCTOBER 2004





**Transactions of the ASME, Journal of Turbomachinery** (ISSN 0889-504X) is published quarterly (Jan., Apr., July, Oct.) by The American Society of Mechanical Engineers, Three Park Avenue, New York, NY 10016. Periodicals postage paid at New York, NY and additional mailing offices. POSTMASTER: Send address changes to Transactions of the ASME, Journal of Turbomachinery, c/o THE AMERICAN SOCIETY OF MECHANICAL ENGINEERS, 22 Law Drive, Box 2300, Fairfield, NJ 07007-2300.
**CHANGES OF ADDRESS** must be received at Society headquarters seven weeks before they are to be effective. Please send old label and new address.
**STATEMENT from By-Laws**. The Society shall not be responsible for statements or opinions advanced in papers or ... printed in its publications (B7.1, Par. 3).



**INDEXED** by Applied Mechanics Reviews and Engineering Information, Inc. Canadian Goods & Services Tax Registration #126148048


## TECHNICAL PAPERS




(**Contents continued on inside back cover**)



This journal is printed on acid-free paper, which exceeds the ANSI Z39.48-1992 specification for permanence of paper and library materials. ♾™
♻ 85% recycled content, including 10% post-consumer fibers.

Journal of Turbomachinery Volume 126, Number 4 OCTOBER 2004



## TECHNICAL BRIEF



## ANNOUNCEMENTS AND SPECIAL NOTES

# The Impact of Forward Swept Rotors on Tip Clearance Flows in Subsonic Axial Compressors

**G. Scott McNulty**

**John J. Decker**

**Brent F. Beacher**
Mem. ASME

GE Aircraft Engines,
One Neumann Way, MD A411,
Cincinnati, OH 45215

**S. Arif Khalid**
Mem. ASME
Streamline, Inc.,
Indianapolis, IN

*This paper presents an experimental and analytical study of the impact of forward swept rotors on tip-limited, low-speed, multistage axial compressors. Two different configurations were examined, one with strong tip-clearance flows and the other with more moderate levels. Evaluations were done at multiple rotor tip clearances to assess differences in clearance sensitivity. Compared to conventionally stacked radial rotors, the forward swept blades demonstrated improvements in stall margin, efficiency and clearance sensitivity. The benefits were more pronounced for the configuration with stronger tip-clearance flows. Detailed flow measurements and three-dimensional viscous CFD analyses were used to investigate the responsible flow mechanisms. Forward sweep causes a spanwise redistribution of flow toward the blade tip and reduces the tip loading in terms of static pressure coefficient. This results in reduced tip-clearance flow blockage, a shallower (more axial) vortex trajectory and a smaller region of reversed flow in the clearance gap.* [DOI: 10.1115/1.1773852]

## Introduction

One of the more significant design trends in recent years is the use of aerodynamic sweep to improve the performance and stability of transonic compressor blades. The experimental and analytical studies of single and multistage fans by Wadia et al. [1,2] demonstrated significant improvements in stall margin and efficiency associated with forward sweep. Reduced shock/boundary layer interaction and less accumulation of centrifuged blade boundary layer fluid at the tip for the forward swept blade were identified as the primary responsible flow mechanisms. However, it is less clear from the open literature what impact aerodynamic sweep has on subsonic blades, such as those found in the middle to rear stages of multistage axial compressors.

One notable difference between transonic fans and core compressors is the relative impact rotor tip-clearance flows have on performance and stall margin. Many military and commercial fans operate with rotor tip clearances that are a small percentage of annulus height (typically less than 1%). Core compressor blades, on the other hand, generally have larger clearances in relation to their size, especially in the rear stages of high pressure ratio machines. This leads to the tip-clearance flow being a larger source of loss and blockage. Add this to the fact that clearances can open significantly above their design values during ''real world'' operation due to such factors as deterioration, casing ovalization and thermal mismatching of rotating and stationary structures during engine transients. Thus, how well the compressor tolerates open clearances determines how robustly it operates in service. The work presented in this paper addresses the question of how forward sweep impacts the tip-clearance flow of subsonic core compressor blades.

Most of the recently published work on aerodynamic sweep has focused on transonic blades with much less information being available on its use for subsonic flows. One notable attempt to exploit sweep in a single-stage low-speed compressor was by Yamaguchi et al. [3]. In this work forward sweep was introduced by simply restacking the sections of a radial blade without redesigning the sections to account for the spanwise redistribution of flow due to sweep. An improvement in stage efficiency of 1.0% was measured with the swept rotor, but with reduced stall margin. Detailed hot-wire measurements showed that sweep improved the flow near the rotor tip, but weakened the hub. No discussion of the stall mechanism was given, leaving open the possibility of a hub stall to explain the reduced stall margin.

Another attempt to utilize sweep in a low-speed compressor was by Inoue et al. [4], also using a single stage but with an upstream stage simulated using an IGV and stator. Forward sweep was introduced by extending the rotor leading-edge upstream near the tip and hub, resulting in a local chord increase of 20% since the trailing-edge was fixed. Although not purely a sweep effect, it is interesting that the rotor with a forward swept leading-edge yielded a 0.7% improvement in stage peak efficiency along with a 6.4% increase in stall margin. Detailed hot-wire surveys near stall showed a reduction in blockage near the casing for the swept blade. Test data and CFD analyses indicated that stall was initiated near the rotor tip.

Based on its successful application in transonic fans, GE Aircraft Engines began investigating the application of forward sweep in core compressors. This paper presents the results of an experimental and analytical evaluation of the impact of forward swept rotors on tip-limited, low-speed, multistage axial compressors. The configurations examined are representative of subsonic rear stages in modern aircraft engine high pressure ratio compressors. To the best of the authors' knowledge this work is unique to the open literature for the following reasons:

- Forward sweep was evaluated on two different compressor configurations, one with strong rotor tip-leakage flows and the other with more moderate levels.
- Forward sweep was evaluated at multiple rotor tip clearances to assess changes in clearance sensitivity.
- Flow mechanisms are proposed for how forward sweep affects the rotor tip-leakage flow based on interpretations of detailed test data and CFD analyses.

## Rotor Designs

This test program was conducted in the GE Low-Speed Research Compressor (LSRC) facility to determine the impact of forward swept rotors on stable operating range, performance and tip-clearance sensitivity. Two different configurations were designed and tested with each being a low-speed model of the rear stages of a high-speed compressor. **Table 1** summarizes the rel-

Contributed by the International Gas Turbine Institute and presented at the International Gas Turbine and Aeroengine Congress and Exhibition, Atlanta, GA, June 16–19, 2003. Manuscript received by the IGTI December 2002; final revision March 2003. Paper No. 2003-GT-38837. Review Chair: H. R. Simmons.

  

**Table 1 Compressor design parameters**

| | Config. 1 (radial/swept) | Config. 2 (radial/swept) |
|---|---|---|
| Rotor tip stagger (deg) | 60.6/54.4 | 52.4/49.7 |
| Rotor tip solidity | 1.35 | 1.22 |
| Rotor aspect ratio | 0.99 | 1.04 |
| Flow coef., $\Phi$ | 0.47 | 0.46 |
| Pressure coef., $\psi'$ | 0.78 | 0.59 |
| Rotor D-factor (pitch) | 0.47 | 0.41 |
| Rotor $C_P$ (pitch) | 0.52 | 0.45 |
| Tip clearance, $\varepsilon_R/C_t$ | 1.34% | 1.48% |
| Radius ratio | 0.85 | 0.85 |

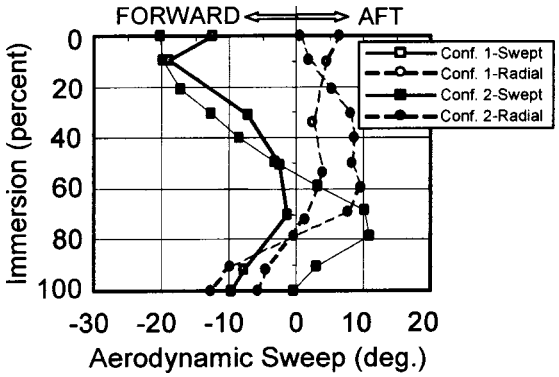


**Fig. 1 Comparison of aerodynamic sweep distributions**

evant design parameters for each configuration. The rotors for configuration 1 have high tip stagger and solidity with relatively high aero loading in terms of D-factor and static pressure coefficient, $C_P$. It will be shown that the performance and stability of configuration 1 are strongly influenced by the rotor tip-clearance flow. The rotors for configuration 2 have lower tip stagger, solidity and loading with more moderate tip-leakage flows.

All the airfoils used in this study were designed in the late 1990s with the same design and analysis techniques currently in use at GE Aircraft Engines. Unlike the sweep and dihedral studies of Gallimore et al. [5,6], the baseline airfoils in this study are modern three-dimensional designs with no known regions of separated flow at their design points. The stators incorporate design features such as bow and chord scalloping for reduced losses and improved off-design behavior. The performance of the baseline designs should be considered current state of the art for each configuration's respective duty. Thus, any performance improvements due to the introduction of sweep are primarily the result of changes in the rotor tip-clearance flow.

The airfoils were designed as isolated blade rows using a three-dimensional viscous computational fluid dynamics (CFD) code, [7], with boundary conditions supplied by a sophisticated throughflow analysis. The throughflow analysis includes models for secondary flow and spanwise mixing in addition to detailed semi-empirical loss and blockage correlations. It has well represented the axisymmetric-averaged flow of many multistage compressors even near endwalls where viscous effects dominate. The CFD analysis was heavily relied upon to guide detailed design decisions, especially regarding their impact on the tip-leakage flow. Both codes are proprietary to GE.

The baseline rotors are conventionally stacked and hereafter referred to as *radial* because of their low sweep levels. Forward sweep is implemented through a combination of axial and tangential stacking of the blade sections. For configuration 2, an additional constraint of limiting the axial position of the tip was imposed to satisfy axial clearance requirements with the upstream vane, a restriction likely to be present when retrofitting forward swept blades into legacy engines. **Figure 1** shows the resulting leading-edge aerodynamic sweep distributions calculated using the method of Smith and Yeh [8]. Although not shown, the trailing-edge sweep follows similar trends. For both configurations approximately 20 deg of forward sweep was introduced into the blade tip. A photograph of the forward swept and radial rotor of configuration 1 is shown in **Fig. 2**.

For each configuration the forward swept blade was designed to pump the same design flow and pressure rise as the radial blade and to match its exit total pressure profile. Differences in stator inlet swirl angle and velocity profiles were minimized so that the same stator could be used. The rotors for both configurations were designed with front-loaded velocity distributions typical of modern controlled diffusion airfoils. The spanwise chord distributions were held similar between the swept and radial blades.

One fundamental effect of forward sweep on subsonic rotors (i.e. not at unique incidence) is that it tends to alter the spanwise flow distribution by pulling more flow toward the tip. The meanlines of the swept rotors were altered in response to this flow shift by opening the tip and closing the remaining sections to maintain similar incidence along the span and to match the exit total pressure profile of the radial rotor. This is the reason for the reduced tip stagger of the forward swept rotors as shown in **Table 1**. The meanlines of the swept rotors were further tuned to maintain similar surface pressure distributions as the radial blades. For example, CFD analyses of preliminary swept rotor designs predicted more rear-loaded surface pressure distributions locally near the tip (consistent with the analytical predictions of Smith and Yeh [8]). The tip sections were redesigned with more camber in the front and less in the rear to match the surface pressure distributions of the radial rotors. This was done to maintain similar chordwise tip leakage flow distributions to assess the effects of sweep in a more aerodynamically equivalent manner.

**Figure 3** illustrates another effect of forward sweep which is a reduction in static pressure coefficient near the blade tip. These values are calculated using the previously mentioned throughflow analysis with detailed representations of each blade's geometry, including sweep and dihedral distributions. The reduced tip loading is a result of the spanwise flow shift in conjunction with radial equilibrium giving similar static pressure rise but with higher inlet dynamic pressure. Since both configurations are predicted to be tip limited, the reduced loading near the tip should have a beneficial impact on stable flow range. Similar to the findings of Wadia et al. [1], the swept rotors have better balanced spanwise loading distributions than the radial rotors which should allow them to use more of the loading capability of the entire blade before being limited by the tip. Subsequent CFD analyses will show the beneficial effects that reduced tip loading has on tip-leakage flow blockage. The hub loadings for configuration 1 were high enough

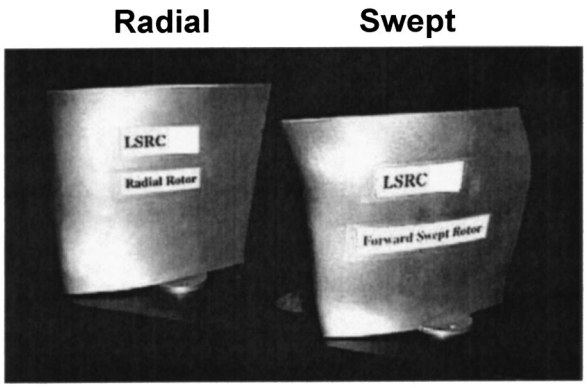


**Fig. 2 Configuration 1 radial and forward swept rotors**

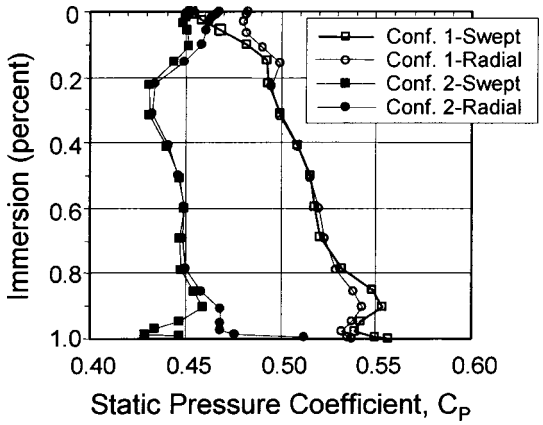


**Fig. 3 Comparison of design point static pressure coefficient distributions**

to be a concern at nominal tip clearance, so special attention was focused on the hub design of the swept rotor to mitigate predicted flow weaknesses.

For configuration 1, a preliminary high-speed rotor was designed to anticipate any potential mechanical difficulties associated with forward sweep. These studies indicated that the max thickness of the swept blade should be increased by 1.5% of chord in the hub with no change to the tip, linearly distributed. The low-speed swept rotor was thickened by this amount to factor in this realism. It should be mentioned that the LSRC design of configuration 1 was done before there was much forward swept rotor design experience at GE Aircraft Engines for core compressors. Current blade design techniques usually permit moderate amounts of forward sweep to be introduced with few mechanical penalties. For configuration 2, both blades were designed with the same leading-edge, trailing-edge, and max thicknesses.

## Test Facility

GE's Low-Speed Research Compressor (LSRC) is a test facility that duplicates the essential features of high-speed compressor flows in a low speed machine. The LSRC is set up with four identical stages with the objective of creating a repeating stage environment. Its large size permits detailed flow measurements not traditionally available in high-speed compressors. The LSRC is also relatively inexpensive to operate. This allows an experimental evaluation of various detailed blade design features, rotor (or stator) clearance levels and casing treatments which may not be practical in a high-speed test. This facility is described in more detail in Wisler [9,10].

**Instrumentation and Measurement Accuracy.** Standard performance data consists of measurements of airflow, rotating speed, power input to the compressor, and pressure rise across each blade row. Airflow is measured using a calibrated inlet bellmouth. Rotating speed is controlled up to 1200 rpm to produce the desired Reynolds number. Power input is determined by a calibrated strain-gage torque sensor that is mounted on the drive shaft. Pressure rise is obtained from static taps on the casing and hub. For some configurations more detailed flow measurements are taken using airfoil surface static taps, single-element Kiel probes, wool tuft probes, total pressure rakes, and hot-film anemometry probes. These detailed measurements are typically taken on the third stage.

High resolution pressure transducers, accurate to $+/-0.010$ percent of the full scale values of either 1 or 2 psi (0.068 or 0.136 bar), are used to record steady-state static and total pressures for determining both overall compressor performance and the static pressures along the casing and airfoil surfaces. Frequent calibrations are conducted. A strain-gauge torque meter, accurate to $+/-0.07\%$ of measured torque, is used to deduce shaft work input to quantify compressor efficiency. Overall measurement accuracy is as follows: flow coefficient and pressure coefficient are accurate to within $+/-0.15\%$ and efficiency to within $+/-0.25\%$.

Standard performance data is presented in terms of normalized pressures and stage characteristics that can be related to the high-speed compressor. The stage characteristics are described by the flow coefficient, pressure coefficient, work coefficient, and torque efficiency.

## Test Results

The overriding test objective was to determine the impact of forward swept rotors on stable operating range, performance and tip-clearance sensitivity in support of high-speed compressor designs. In some situations this resulted in tests where only overall performance data were taken, rather than the complete set of detailed measurements, due to schedule and cost considerations.

Both configurations were tested at nominal (design intent) and open clearance levels. The open clearance tests provide an important evaluation of the compressor at clearances that will be encountered during "real world" operation due to such factors as deterioration or engine transients. In fact, many aircraft engine compressors must tolerate clearances even larger than those tested here. For the swept rotor of configuration 1 the clearance was increased using the traditional LSRC method of shimming the casing above the rotors radially outward. This lead to steps in the casing flowpath, which were corrected for in the performance results. The efficiency correction for this case was estimated to be 1.2%. For the remaining tests (configuration 1 radial rotor and entire configuration 2) an improved method was developed in which the rotor tips were nominally machined to achieve the open clearances. The clearance was then reduced to the nominal level by attaching plastic blade extensions (created using stereo lithography) to the tip. No performance corrections were necessary for this improved method.

During the testing of configuration 1 the design flow coefficient of the high-speed compressor's rear stages was changed. Because of schedule considerations the low-speed airfoils were simply restaggered open from their original design settings, rather than redesigning them, to achieve the new flow. This resulted in higher rotor incidence and lower stator incidence than is normal design practice. This reduced the efficiency potential of the restaggered configuration somewhat and resulted in peak efficiency being closer to the stall line than normally desired. Only the results for the restaggered airfoils are presented for configuration 1.

**Stage Characteristics.** **Figure 4** presents the measured stage characteristics for configuration 1 at both nominal and open rotor tip clearances. Reference lines are drawn connecting operating points obtained at a given exit throttle area. These lines approximate constant values of throttle coefficient which is a useful measure of stable operating range at low speeds, analogous to stall margin for high-speed compressors. The lowest flow points on the characteristics are not stabilized but rather are extrapolated using the last stable throttle position during the transient closure to stall.

The pressure coefficient characteristics at nominal clearance in **Fig. 4** show the forward swept and radial rotors pumping similar flow and pressure rise as intended. Both rotors achieve a similar peak pressure rise but the swept rotor throttles 28% farther than the radial rotor before stalling. The swept rotor achieves this throttle range extension entirely through flow roll back with no improvement in peak pressure rise. The rotor surface static pressure data in **Fig. 5** indicate that between throttle setting 16 and 13 a flow weakness develops in the hub of the swept rotor that grows into a large corner separation at throttles 10 and beyond. By throttle 7 the separation has grown so large that signs of weakness are evident at midspan. The positive slope of the pressure characteristic is due to the increasing loss and blockage of this hub separation as the rotor is throttled beyond peak pressure. This behavior was not intended and confounds the nominal clearance

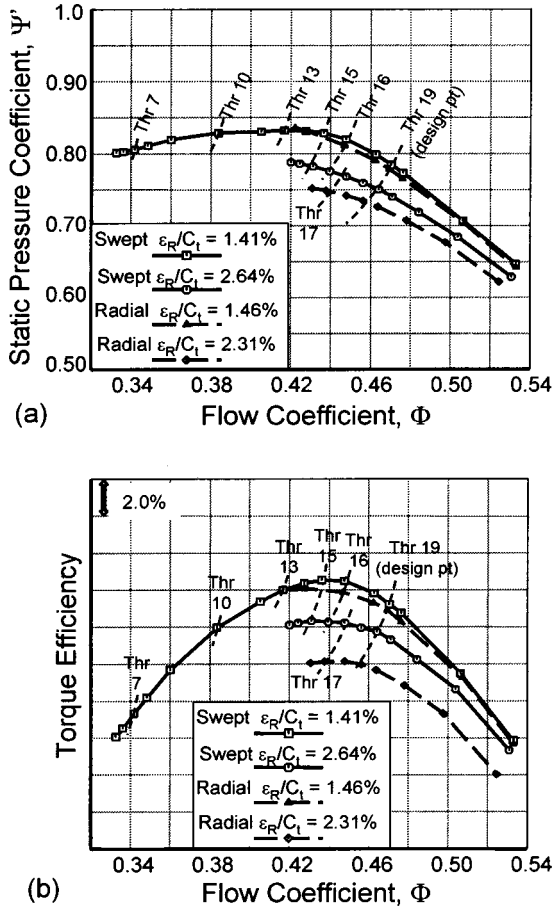


**Fig. 4 Characteristics data for configuration 1 at nominal and open clearance levels: (*a*) static pressure coefficient and (*b*) torque efficiency**

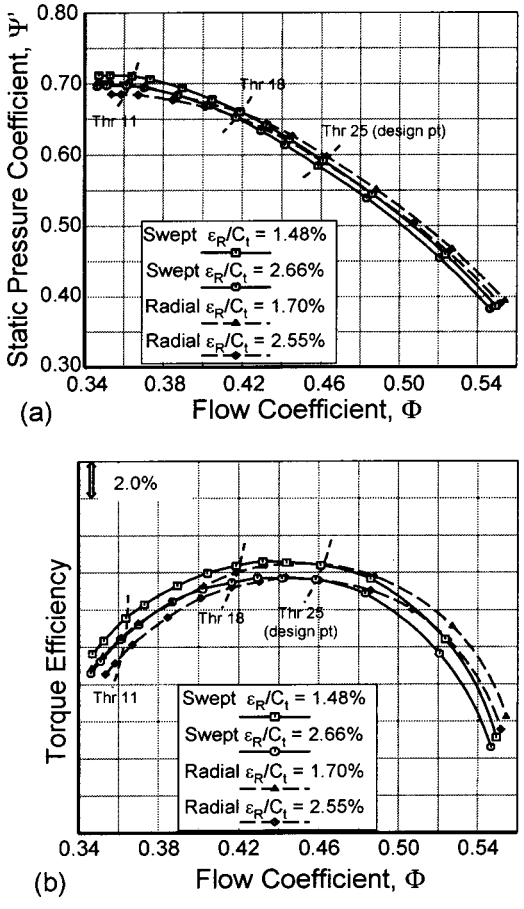


**Fig. 6 Characteristics data for configuration 2 at nominal and open clearance levels: (*a*) static pressure coefficient and (*b*) torque efficiency**

results because the resulting spanwise redistribution of flow prevents the tip from initiating stall where it otherwise would have. At open clearances the swept rotor does not exhibit this hub weakness.

At open clearance the differences between the radial and swept rotor characteristics are amplified. Along the design point throttle line the flow pumping of the swept rotor is reduced by about half as much as the radial rotor's relative to their values at nominal clearance. The swept rotor demonstrated 5% more throttle margin than the radial with more flow range and higher peak pressure rise. The fact that the swept rotor at open clearance stalls at almost the same flow as the radial rotor at nominal clearance also attests to the beneficial influence sweep is having on the flow near the blade tip.

The efficiency characteristics at nominal clearance in **Fig. 4** show that the swept rotor achieved 0.4% higher peak efficiency than the radial rotor. At open clearance the swept rotor has significantly higher performance over the entire flow range with 2.1% higher peak efficiency. Thus the stage characteristics data for configuration 1 demonstrate the significant benefits of forward sweep on stable operating range and performance, especially at open clearance levels.

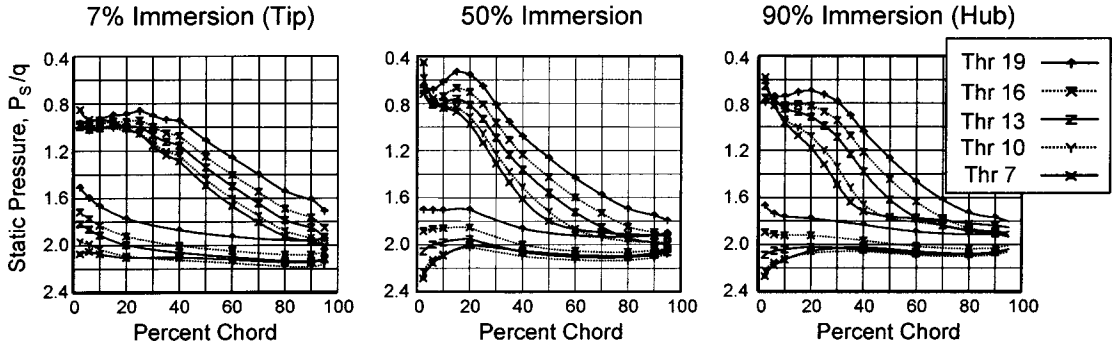


**Fig. 5 Configuration 1 forward swept rotor surface static pressure data at various throttle settings at nominal clearance**

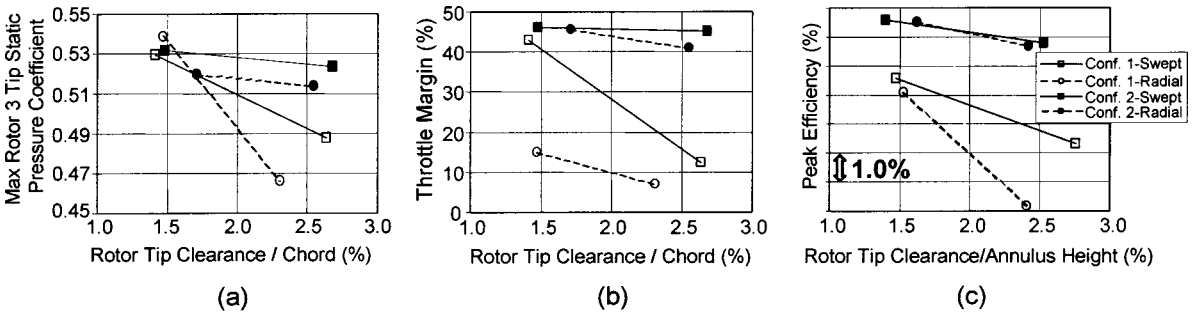


**Fig. 7 Measured rotor tip-clearance sensitivities: (*a*) maximum tip static pressure coefficient, (*b*) throttle margin, and (*c*) peak efficiency**

**Figure 6** presents the measured stage characteristics for configuration 2. Although these results are less dramatic than those of configuration 1, there are still meaningful differences. At nominal clearance the swept rotor has only 0.5% more throttle margin than the radial blade, but attains 3% higher peak pressure rise. At open clearance the swept rotor demonstrated 4% more throttle range with a corresponding 2.5% increase in stall pressure rise. At both clearance levels, the pressure characteristics of the swept rotor are steeper as throttled toward stall.

The efficiency characteristics do not show significant differences in design point performance at either clearance level. The forward swept rotor has better performance (up to 1.0%) when throttled above the design point and lower performance when unthrottled. At first glance these differences appear similar to what would be expected if the swept rotor was designed with lower incidence than the radial blade. However, rotor surface pressures verify that both rotors have similar incidence and loading distributions as intended. A plausible explanation for this trend is related to the fact that as the rotor is throttled the increased loading (especially near the leading-edge) significantly strengthens the tip-leakage flow. At conditions with strong clearance flow the rotor responds favorably to forward sweep, similar to configuration 1 which has strong clearance flow even at its design point. Conversely, at unthrottled conditions this data implies that forward sweep may be detrimental to the performance of rotors with mild tip-clearance flows.

**Tip-Clearance Sensitivity.** The standard performance data are presented in a different format in **Fig. 7** to better quantify differences in clearance sensitivity. Loading parameters are plotted versus clearance/chord and efficiency versus clearance/annulus height. This allows so-called *clearance derivatives* to be compared between the swept and radial blades as well as between the two configurations. Differences between the two configurations in absolute performance, or loading capability, are not relevant to this discussion and can be explained by differences in airfoil geometry and vector diagrams, [11,12]. This figure clearly shows how much more sensitive configuration 1 is to tip clearance than configuration 2.

**Figure 7**(***a***) presents the maximum rotor 3 tip static pressure coefficient as a measure of tip loading capability. The max rotor tip loading usually occurs near stall, but for the swept rotor of configuration 1 at nominal clearance it occurs near throttle 10. This data shows that the swept rotors for both configurations demonstrate a higher tip loading capability at a given clearance level with the exception being configuration 1 at nominal clearance where the higher hub loss and blockage reduced the static pressure rise over the entire span. The swept rotor for configuration 1 achieved 4.7% higher tip loading than the radial rotor at open clearance, even with a slightly larger clearance. The swept rotor for configuration 2 achieved approximately 2.0% higher tip loading than the radial rotor at both clearance levels. The swept rotor for configuration 1 demonstrated a 60% reduction in clearance sensitivity, whereas for configuration 2 there was little effect on its already low sensitivity. These results indicate that forward sweep notably improved tip loading capability at a given clearance level and significantly reduced its sensitivity to open clearances for the configuration with strong clearance flows.

**Figure 7**(***b***) presents throttle margin as a measure of stable operating range. Somewhat surprisingly, the data shows that the throttle margin for the swept rotor of configuration 1 is more sensitive to clearance than the radial rotor even though its absolute level is much higher. This is caused by the swept rotor's hub weakness at tight clearances, which gives it significantly more throttle margin via flow roll back, and thus should not be considered a true sweep effect. The large reduction in throttle margin at open clearances is an important reason why hub weaknesses should not be intentionally used to achieve the objective stall line for tip-limited blades. This sometimes used design ''crutch'' increases the compressor's clearance sensitivity, leading to poor deterioration characteristics. For configuration 2, the swept rotor demonstrated reduced clearance sensitivity with its throttle margin almost constant for the two clearances tested.

The sensitivity of peak efficiency to clearance is shown in **Fig. 7**(***c***). For configuration 1, the clearance derivative of the swept rotor is less than half that of the radial rotor. The magnitude of the swept rotor's derivative is somewhat uncertain due to the previously mentioned 1.2% efficiency correction at open clearance. However, subsequent clearance derivative test results in the tip region of the high-speed compressor rear stages were consistent with the low-speed derivative. For configuration 2, the swept rotor appears slightly less sensitive, but the differences are small enough to be inconclusive considering measurement accuracy. Thus, in terms of peak performance, forward sweep significantly reduced the clearance sensitivity of the configuration with strong tip-leakage flow and had a small effect on the configuration with more moderate levels.

**Rotor Surface Pressures.** The following section presents only a small fraction of the total rotor surface static pressure data taken. Configuration 1 was chosen because it is more sensitive to sweep and clearance changes. For configuration 1, surface pressure measurements were taken for both rotors (and stators) at each clearance with the exception of the radial rotor at nominal clearance. Static pressures are nondimensionalized by the tip speed dynamic pressure and plotted on an inverted scale to mimic the isentropic surface velocity distribution.

**Figure 8** compares the swept and radial rotors at open clearance near the tip and hub at the design point and near stall. At the design point the similarity of the surface velocity distributions is confirmed, indicating the radial flow distribution is consistent with pre-test predictions that guided the meanline modifications for the swept blade. The data show the swept rotor doing more diffusion which is presumably due to reduced tip-leakage flow blockage which is sensed over the entire blade. The near stall data show the higher incidence and loading achieved by the forward swept blade

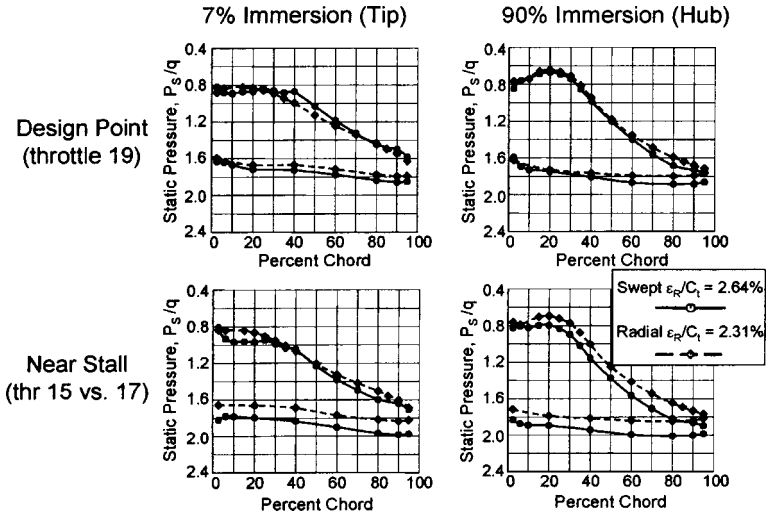


**Fig. 8 Comparison of forward swept and radial rotor surface static pressure data for configuration 1 at open clearances**

consistent with the pressure characteristics data. It is interesting that even near stall, the rotor (and stator) surface loadings do not indicate any significant boundary layer weakness. This data is consistent with pre-test CFD analyses predicting that stall is initiated by the flow in the tip-clearance region with relatively healthy boundary layers on the rest of the blade.

**Figure 9** illustrates the effect of tip clearance level on the surface pressure distributions of the forward swept rotor. At the design point, the blade diffuses more with tighter clearance, especially near the tip. The higher diffusion near the hub verifies that the tip-leakage related blockage affects the static pressure rise of the entire blade. At open clearance, the rotor has higher incidence near the tip and lower near the hub, reflecting the spanwise flow shift out of the tip due to the increased tip-leakage flow blockage. The data at peak pressure coefficient (throttle 13 for the nominal clearance) shows the much higher static pressure rise achieved with the nominal clearance. Note the similarity of the incidence near the tip even though the peak pressure for the nominal clearance is at a much lower flow coefficient. The data near the hub shows the higher incidence and loading at nominal clearance which weakens the boundary layer, eventually causing it to separate. At open clearance, the hub boundary-layer remains healthy up to the point where the tip stalls.

## CFD Analyses

Detailed CFD analyses were used to improve the understanding and interpretation of the test results. A large body of pre and post-test CFD analyses were performed on both configurations, but only select results from configuration 1 are presented here.

**Comparisons to Data.** Due to the availability of detailed flow measurements for the swept rotor of configuration 1 at nominal clearance, significant post-test analyses were performed on this case at throttles 16 (near peak efficiency) and 10 (part way to stall). First, a throughflow analysis was performed using loss, blockage and deviation adders to match the detailed flow measurements (hot-film velocities and flow angles, casing pressures, and total pressure traverses). This so-called ''data-match'' provided accurate, empirically derived boundary conditions (i.e., pro-

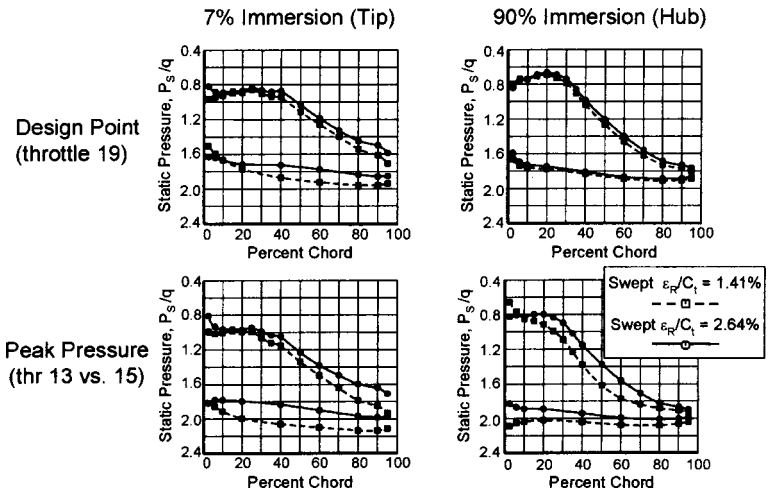


**Fig. 9 Comparison of surface static pressure data at nominal and open clearances for the forward swept rotor of configuration 1**

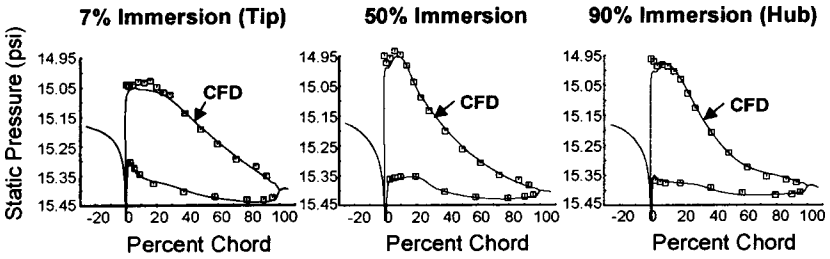


**Fig. 10 Comparison of surface static pressure data to CFD analysis for configuration 1 forward swept rotor at throttle 16 with nominal clearance**

files of inlet $P_T$, $T_T$ and absolute flow angles and exit static pressure) for the isolated blade row CFD analyses of rotor 3 and stator 3.

**Figure 10** compares the results of the swept rotor CFD analysis to the rotor 3 surface static pressure data at throttle 16. The spanwise incidence distribution compares well, indicating the analysis was run to the correct overall flow and accurately predicts the spanwise flow distribution. The excellent match of the entire surface distribution indicates an accurate prediction of the overall pressure rise and detailed diffusion gradients. **Figure 11** compares the CFD analysis to the measured rotor 3 inlet and exit radial profiles of relative flow angle, axial velocity and total pressure at throttle 16 (the radial rotor analysis is shown for reference). These results also indicate the CFD analysis does an excellent job capturing spanwise flow details. A similar quality agreement was obtained at throttle 10, including the prediction of the hub corner separation, using the same data-matching and CFD analysis techniques. These comparisons verify the accuracy of the CFD analysis in terms of both the boundary conditions and predicted flow details. It is reassuring that the analysis and independent flow measurements give such consistent results.

**Swept and Radial Rotor Comparisons.** A similar data-match was not available for the radial rotor at nominal clearance because detailed measurements were not taken. However, a CFD analysis of the radial rotor was performed at throttle 16 using the same boundary conditions as the forward swept blade. This should be a good approximation considering both rotors pump approximately the same flow with similar radial profiles at nominal clearance. This analysis provides a meaningful and consistent basis for evaluating the impact of forward sweep on the flow details.

Radial profiles are compared at rotor 3 inlet and exit in **Fig. 11**. For the swept rotor the analysis shows a significant spanwise flow redistribution toward the tip as expected from design analyses. The higher flow near the tip gives a lower inlet relative flow angle and requires a more open trailing edge metal angle to achieve the same total pressure profile. This is the reason the swept blades were designed with lower tip stagger. The predicted flow shift toward the tip is also consistent with earlier interpretations of the rotor surface pressure data.

**Figure 12**(***a***) compares axial velocity contours at the rotor trailing-edge. The low velocity fluid near the casing extending across the passage is associated with the tip-leakage flow. This figure clearly shows the tip-leakage flow being a large source of blockage even at design intent clearance levels. Qualitative comparisons of velocity contours show that the forward swept rotor has lower tip-leakage flow blockage. It will be shown that this reduction in tip-leakage blockage is believed to be due to the lower tip static pressure coefficient of the swept rotor. Near the hub, the swept rotor is predicted to have a weaker suction surface boundary layer which is consistent with previously mentioned test results.

Loss coefficient contours at the trailing-edge are presented in **Fig. 12**(***b***). The high loss fluid near the casing extending across the passage is also associated with the tip-leakage flow. By comparing

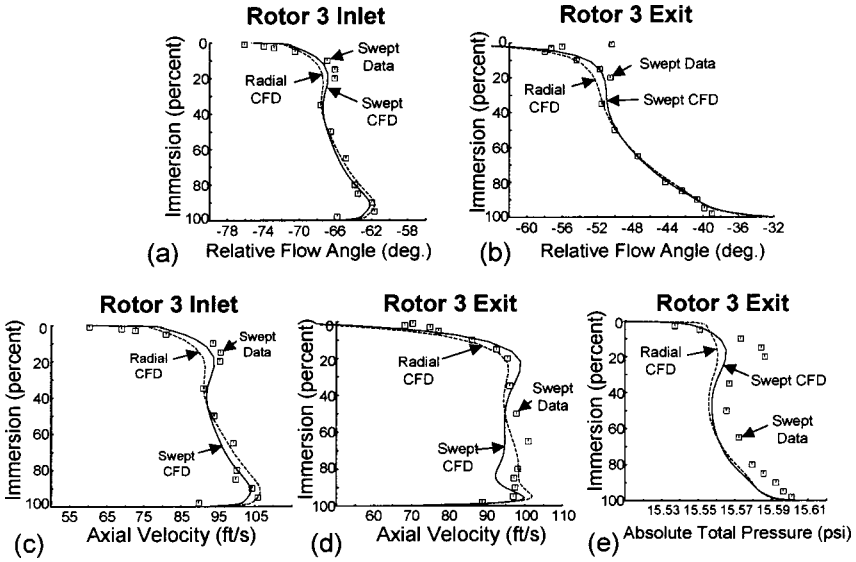


**Fig. 11 Comparison of flow measurements to CFD analysis for configuration 1 swept rotor at throttle 16 with nominal clearance: (*a*) inlet relative flow angle, (*b*) exit relative flow angle, (*c*) inlet axial velocity, (*d*) exit axial velocity, (*e*) exit absolute total pressure. (Radial rotor CFD shown for reference.)**

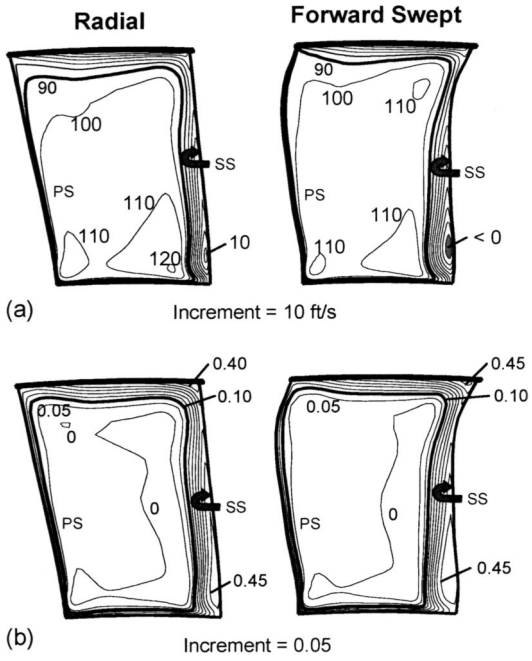


**Fig. 12 Comparison of rotor trailing-edge contours for configuration 1 CFD analyses at throttle 16 with nominal clearance: (*a*) axial velocity (*ft/s*), (*b*) loss coefficient.**

the 0.10 contour, the forward swept blade is seen to have lower loss in the pressure surface corner near the casing. However, in the suction surface corner the swept blade has a higher loss coefficient, possibly due to the acute angle between blade suction surface and the casing. Near the hub, the swept blade has higher losses due to the weaker boundary layer caused by the higher hub loading.

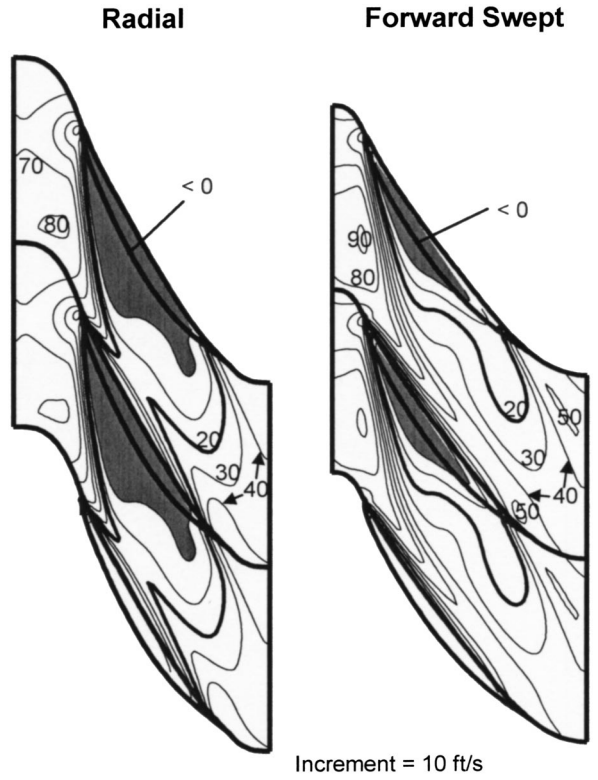


**Fig. 13 Comparison of blade-to-blade axial velocity contours at mid-clearance gap for configuration 1 CFD analyses at throttle 16 with nominal clearance**

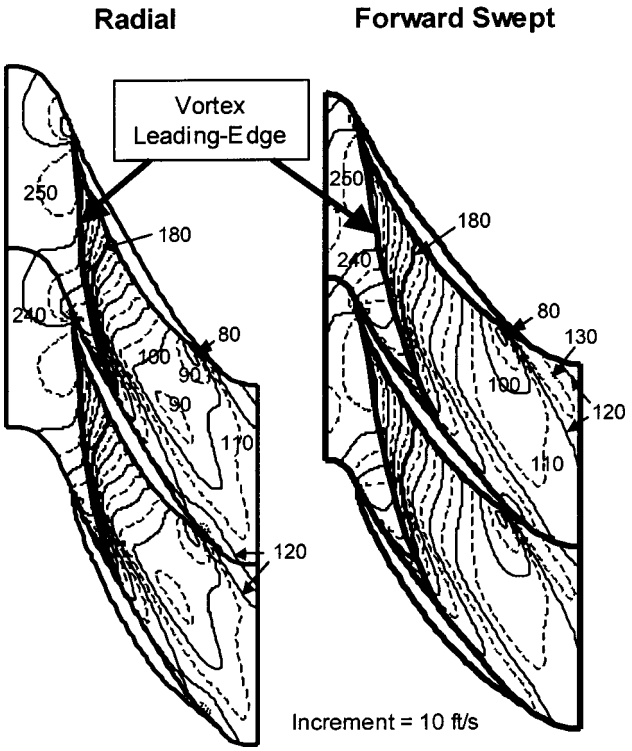


**Fig. 14 Comparison of blade-to-blade relative velocity contours at blade tip for configuration 1 CFD analyses at throttle 16 with nominal clearance**

Blade-to-blade contours near the blade tip are compared in **Figs. 13** and **14**. Axial velocity contours at mid-clearance gap are shown in **Fig. 13** with regions of reverse flow shaded and the rotor tip section shown for reference. Relative velocity contours at the rotor tip are shown in **Fig. 14** with a line drawn to highlight the vortex leading-edge. Before discussing differences, some common features of the tip-leakage flows are discussed. First, notice that much of the leakage flow exits the clearance gap into the passage with a negative axial velocity component. This is caused by the combination of high tip stagger and high lift for these blades. This upstream direction of leakage flow is detrimental to the rotor's aerodynamic stability, as it resists the incoming casing boundary layer fluid. Another common feature is the significant amount of low velocity tip-leakage fluid that intersects the pressure surface of the adjacent blade. The leakage flow originating from this low relative total pressure region has already leaked across the previous blade and will leak across again but with a lower streamwise velocity component. This phenomena has been referred to as ''double-leakage,'' [13], and it leads to increased mixing loss because of the larger velocity difference between the leakage and freestream flows. A proprietary GE semi-empirical tip-clearance model estimates that the tip-leakage related loss for the radial rotor of configuration 1 is doubled due to this phenomena. It is also thought to increase the sensitivity of the rotor to increased clearances. Unfortunately many rotors in modern aircraft compressors suffer from double-leakage by varying amounts depending on tip stagger, solidity, clearance, and loading levels.

Significant differences in the tip-leakage flow are also apparent in **Figs. 13** and **14**. The forward swept blade has a much smaller reverse flow region with less penetration into the blade passage. The increased flow into the tip, with corresponding higher relative total pressure, increases the streamwise momentum of the leakage

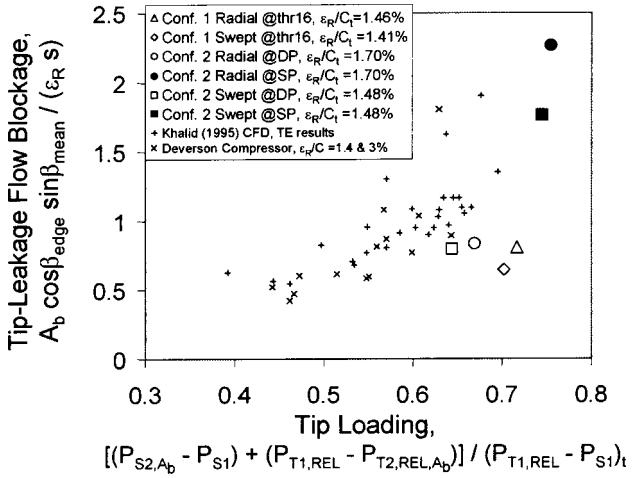


**Fig. 15 Comparison of nondimensional tip-leakage flow blockage versus tip loading parameter using the method of Khalid [15,16]**

flow, thereby reducing its negative axial component. Also notice that downstream of the vortex leading-edge the swept rotor's leakage flow has higher velocity levels. The tip-leakage blockage of the swept rotor is concentrated more rearward in the passage and farther away from the pressure surface of the adjacent blade.

## Discussion of Flow Mechanisms

This section describes the relevant flow mechanisms associated with forward sweep as interpreted from test data and CFD results. Unless otherwise noted, these mechanisms are believed to be general in nature, with the degree of effect increasing as the tip-leakage flow strengthens.

Detailed flow measurements and CFD analyses show that forward sweep pulls more flow toward the blade tip. One consequence of this flow shift is a higher relative total pressure near the casing which increases the streamwise momentum of the leakage flow. For high stagger, highly loaded blades, this reduces the negative axial component of the leakage flow and the size of the reverse flow region in the clearance gap. This also leads to a shallower (more axial) vortex trajectory.

Another important effect of forward sweep is the reduction in tip-leakage flow blockage. This is believed to be a result of the reduced tip loading, in terms of static pressure coefficient. The work of Khalid et al. [14] clearly links the amount of tip-leakage flow blockage to the streamwise static pressure rise through the passage, as well as other parameters. **Figure 15** presents the normalized tip-leakage flow blockage versus a tip loading parameter calculated from CFD analyses using the method of Khalid [15]. For reference, the CFD results used to establish this correlation are shown as well as the Whittle Laboratory Deverson compressor data taken and reduced by Khalsa [16]. This correlation is not believed to be universal, but rather a meaningful cause and effect relationship for a particular type of blade.

The previously presented CFD analyses for configuration 1 at throttle 16 are shown in this figure in addition to pre-test CFD predictions of configuration 2 at the design point and near stall conditions with nominal clearance. For configuration 1, the forward swept blade shows a 20% reduction in tip blockage for a relatively modest decrease in tip loading. This may be due to its nominally high loadings in conjunction with its large amount of double-leakage. For configuration 2, the swept rotor shows only a slight reduction in tip blockage at the design point. At the higher loadings near the stall line, the tip blockage increases dramatically from its design point values. At this condition the unloading of the tip provided by forward sweep is extremely beneficial because of the nearly asymptotic behavior of tip blockage at high loadings.

The changes in tip-leakage flow associated with forward sweep should be beneficial for aerodynamic stability. Similar to the findings of Adamcyzk et al. [17] numerical stall occurred in the CFD analyses when the tip-leakage flow spilled upstream of the leading-edge of the adjacent blade. This was the predicted stall mechanism for both configurations. As alluded to earlier, rotor surface static pressure data and the open clearance test results are consistent with this stall mechanism for both configurations. It is straightforward to understand why the swept rotor's shallower vortex trajectory, reduced tip blockage and smaller region of reversed flow improves the stable operating range and tip loading capability for blades that stall due to this tip-clearance flow related mechanism.

It is impossible to generalize how forward sweep impacts performance for all blade types, but this doesn't prevent some discussion of this subject. For some rotors, such as configuration 1, the large amount of double-leakage has a significant adverse affect on tip-leakage related loss. The forward swept rotor's shallower vortex trajectory and higher velocity levels downstream of the vortex leading-edge should reduce the amount of loss associated with double-leakage. Another potential loss mechanism is the extra mixing loss that occurs as the low velocity vortex core fluid is diffused by the streamwise pressure gradient. For highly loaded blades, this loss source may be large enough such that the reduced static pressure coefficient near the tip due to sweep is beneficial. However, for lightly loaded blades with little or no double-leakage, forward sweep may actually increase tip-leakage losses by pulling more flow into a high loss region of the blade with little benefit to the underlying loss mechanisms.

It is also important to consider that blockage developing in the rotor can have implications for the downstream stator performance. Rotor tip blockage affects the spanwise distribution of flow and tangential velocity entering the stator. If the rotor tip blockage is significantly higher than anticipated in the design, then this may appreciably alter the stator incidence distribution. Near the design point this is likely to have a detrimental effect on performance since the stator will be operating at higher incidence near the casing and lower incidence over the rest of the span. A forward swept rotor should also be beneficial in this situation because it reduces the magnitude of the spanwise flow redistribution. This interaction is particularly important to consider for cases with strong clearance flows operating at large clearances, such as configuration 1. Unfortunately, there were insufficient detailed measurements to accurately split out the loss between the rotor and stator. Inaccuracies in the CFD analyses at large clearances for configuration 1 also prevented a reliable estimate of the magnitude of this effect.

## Summary and Conclusions

The results of a detailed experimental and analytical evaluation of the impact of forward sweep on subsonic rotors representative of those in the rear stages of modern aircraft engine high pressure ratio compressors were presented. Evaluations were done on two different configurations, one with strong tip-leakage flows and the other with more moderate levels. Sweep was introduced in an aerodynamically equivalent manner and tested at multiple rotor tip clearances to assess changes in clearance sensitivity.

For the configuration with strong clearance flows, forward sweep demonstrated both improved performance and loading capability at a given clearance and reduced the clearance sensitivity of both these metrics by over 50%. For the configuration with moderate clearance flows, forward sweep provided notable improvements in loading capability and throttle margin at a given clearance and reduced the clearance sensitivity of throttle margin. In terms of peak performance, sweep had a small favorable impact on the baseline efficiency level and its clearance sensitivity. Thus the test results for both configurations were promising.

The improved loading capability of the forward swept blades is attributed to the spanwise shift of flow toward the tip and a re-

duced tip static pressure coefficient. In terms of flow details, CFD analyses show forward sweep providing reduced tip-leakage flow blockage, a shallower vortex trajectory and a smaller region of reversed flow in the clearance gap. These effects are thought to be beneficial for tip-limited rotors with stall initiated by a tip-clearance flow related mechanism.

The improved performance demonstrated by forward sweep for rotors with strong clearance flows is also attributed to the aforementioned changes in tip-leakage flow. The shallower vortex trajectory and reduced blockage is believed to reduce the mixing losses associated with so-called double-leakage. Also the lower tip static pressure coefficient reduces the mixing loss of the vortex core as it is diffused through the blade passage.


## Acknowledgments

The authors would like to especially acknowledge Mr. Peter Szucs of GE Aircraft Engines for his support, enthusiasm and technical guidance into the use of forward sweep technology. We would like to thank Dr. Roy Smith for his help in interrogating the test data. We also need to acknowledge Mr. Don Menner, Mr. Bill Groll and Dr. Hyoun-Woo Shin of GE's Aero Research Lab for their excellent support in obtaining the data. We are also grateful to GE's management for giving us permission to publish these results.


## Nomenclature

$A$ = annulus area
$A_b$ = blocked area due to tip-leakage flow
$C$ = chord length
$C_P$ = static pressure coefficient $= \Delta P_S/(P_{T1,\mathrm{REL}} - P_{S1})$
$D$-factor = diffusion factor $= 1 - W_2/W_1 + \Delta(RV_\theta)/(2\sigma_M R_M W_1)$
$h$ = annulus height
Immersion = $(R_t - R)/(R_t - R_h)$
$k$ = throttle coefficient $= \Phi/\sqrt{\Psi'}$
$\dot{m}$ = air flow
$P_{IN}$, $T_{IN}$ = compressor inlet pressure and temperature
$P_S$ = static pressure
$P_T$ = total pressure
$q$ = tip speed dynamic pressure $= 1/2\rho_{\mathrm{ref}} U_t^2$
$R$ = radius
$S$ = blade spacing
$T$ = stage torque
$TM$ = % throttle margin $= [(k_{DP}/k_{SP}) - 1] \times 100$
$U$ = rotor blade speed
$V$ = absolute velocity
$W$ = relative velocity
$\beta$ = relative flow angle
$\varepsilon$ = tip clearance
$\eta$ = torque efficiency $= \Psi'/\Psi$
$\overline{\rho}$ = compressor average density
$\rho_{\mathrm{ref}}$ = compressor bellmouth density
$\sigma$ = solidity $= C/S$
$\Phi$ = flow coefficient $= \dot{m}/\overline{\rho} A U_t$
$\Psi$ = work coefficient $= T/1/2\,\overline{\rho} U_t^2 \Phi R_t A$
$\Psi'$ = compressor pressure coefficient $C_p T_{IN}/1/2\,U_t^2[(\Delta P/P_{IN} + 1)^{Y-1/Y} - 1]$
$\omega$ = loss coefficient, $\Delta P_{T,\mathrm{REL}}/(P_{T1,\mathrm{REL}} - P_{S1})$

### Subscripts

$A_b$ = averaged over tip-leakage blockage region
edge = edge of velocity defect region
$h$ = hub
$M$ = mean or average
$R$ = rotor
REL = relative
$t$ = rotor tip
$DP$ = design point
$SP$ = stall point
$\theta$ = tangential component
1 = blade row inlet
2 = blade row trailing-edge

## References


[1] Wadia, A. R., Szucs, P. N., and Crall, D. W., 1998, "Inner Workings of Aerodynamic Sweep," ASME J. Turbomach., **120**, pp. 671–682.
[2] Wadia, A. R., Szucs, P. N., Crall, D. W., and Rabe, D. C., 2002, "Forward Swept Rotor Studies in Multistage Fans With Inlet Distortion," ASME Paper No. GT-2002-30326.
[3] Yamaguchi, N., Tominaga, T., Hattori, S., and Mitsuhashi, T., 1991, "Secondary-Loss Reduction by Forward-Skewing of Axial Compressor Rotor Blading," presented at Yokohama International Gas Turbine Conference.
[4] Inoue, M., Kuroumaru, M., Furukawa, M., Kinoue, Y., Tanino, T., Maeda, S., and Okuno, K., 1997, "Controlled-Endwall-Flow Blading for Multistage Axial Compressor Rotor," ASME Paper No. 97-GT-248.
[5] Gallimore, S. J., Bolger, J. J., Cumpsty, N. A., Taylor, M. J., Wright, P. I., and Place, J. M. M., 2002, "The Use of Sweep and Dihedral in Multistage Axial Flow Compressor Blading—Part I: University Research and Methods Development," ASME J. Turbomach., **124**, pp. 521–532.
[6] Gallimore, S. J., Bolger, J. J., Cumpsty, N. A., Taylor, M. J., Wright, P. I., and Place, J. M. M., 2002, "The Use of Sweep and Dihedral in Multistage Axial Flow Compressor Blading—Part II: Low and High-Speed Designs and Test Verification," ASME J. Turbomach., **124**, pp. 533–541.
[7] Holmes, D. G., Mitchell, B. E., and Lorence, C. B., 1997, "Three-Dimensional Linearized Navier-Stokes Calculations for Flutter and Forced Response," Proceedings of 8th International Symposium on Unsteady Aerodynamics and Aeroelasticity of Turbomachinery (ISUAAT), Stockholm, Sweden.
[8] Smith, L. H., and Yeh, H., 1963, "Sweep and Dihedral Effects in Axial Flow Turbomachinery," ASME J. Basic Eng., **85**, pp. 401–416.
[9] Wisler, D. C., 1985, "Loss Reduction in Axial Flow Compressors Through Low-Speed Model Testing," ASME J. Eng. Gas Turbines Power, **107**, pp. 354–363.
[10] Wisler, D. C., Halstead, D. E., and Beacher, B. F., 1999, "Improving Compressor and Turbine Performance Through Cost Effective Low-Speed Testing," ISABE99-7073, 14th International Symposium on Air Breathing Engines, Sept., Florence, Italy.
[11] Koch, C. C., 1981, "The Stall Pressure-Rise Capability of Axial Compressors," ASME J. Eng. Gas Turbines Power, **103**, pp. 645–656.
[12] Koch, C. C., and Smith, L. H., 1976, "Loss Sources and Magnitudes in Axial-Flow Compressors," ASME J. Eng. Gas Turbines Power, **98**(3), pp. 411–424.
[13] Sirakov, B. T., and Tan, C. S., 2002, "Effect of Upstream Unsteady Flow on Rotor Tip Leakage Flow," ASME Paper No. 02-GT-358.
[14] Khalid, S. A., Khalsa, A. S., Waitz, I. A., Tan, C. S., Greitzer, E. M., Cumpsty, N. A., Adamcyzk, J. J., and Marble, F. E., 1999, "Endwall Blockage in Axial Compressors," ASME J. Turbomach., **121**, pp. 499–509.
[15] Khalid, S. A., 1995, "The Effects of Tip Clearance on Axial Compressor Pressure Rise," Internal Gas Turbine Lab Report, Massachusetts Institute of Technology, Cambridge, MA.
[16] Khalsa, A. S., 1994, personal communication, reduced data taken at the Whittle Laboratory, Cambridge University.
[17] Adamczyk, J. J., Celestina, M. L., and Greitzer, E. M., 1993, "The Role of Tip Clearance in High-Speed Fan Stall," ASME J. Turbomach., **115**, pp. 28–39.

# Influence of Surface Roughness on Three-Dimensional Separation in Axial Compressors

**Semiu A. Gbadebo**

**Tom P. Hynes**

Whittle Laboratory,
University of Cambridge,
Cambridge, United Kingdom

**Nicholas A. Cumpsty**

Rolls-Royce Plc,
Derby, United Kingdom

*Surface roughness on a stator blade was found to have a major effect on the three-dimensional (3D) separation at the hub of a single-stage low-speed axial compressor. The change in the separation with roughness worsened performance of the stage. A preliminary study was carried out to ascertain which part of the stator suction surface and at what operating condition the flow is most sensitive to roughness. The results show that stage performance is extremely sensitive to surface roughness around the leading edge and peak-suction regions, particularly for flow rates corresponding to design and lower values. Surface flow visualization and exit loss measurements show that the size of the separation, in terms of spanwise and chordwise extent, is increased with roughness present. Roughness produced the large 3D separation at design flow coefficient that is found for smooth blades nearer to stall. A simple model to simulate the effect of roughness was developed and, when included in a 3D Navier–Stokes calculation method, was shown to give good qualitative agreement with measurements.* [DOI: 10.1115/1.1791281]

## Introduction

Almost all treatments of boundary layer effects, including the effect of surface roughness, have been two-dimensional in their approach. This is most obvious in the use of linear cascades but it also applies to consideration of losses around mid-span, away from the ''complicating'' effects of the endwalls. The emphasis in this paper is on 3D effects, including 3D separation, found where the suction surface meets the hub of a shrouded stator. Work reported by Gbadebo, Cumpsty, and Hynes [1] shows how widespread 3D separation is, and how much it affects performance. The surprising aspect of the present paper is the importance of surface roughness to the size of these 3D effects.

Most of the work carried out on the effect of rotor surface roughness on performance has been concerned with profile loss, an essentially two-dimensional view. An example is the work of Suder et al. [2], who carried out a detailed study on the effect of adding roughness and thickness to a transonic compressor rotor. They used different rough and smooth coating configurations, which were tested for a range of chordwise coating extents. Measurements were performed both at part and full speed. Their results showed that a rough coating over the front 10% of blade chord resulted in about 70% of the performance degradation caused by full-chord roughness coverage. About 9% loss in pressure ratio across the rotor near design mass flow was also reported for the rough coatings. Bammert and Woelk [3] also carried out measurements on a 3-stage axial compressor with smooth and emery-grain roughened blades. They observed that the overall efficiency reduced between 6% and 13% over the range of different roughness grades considered and there was a maximum reduction of 30% in the overall pressure ratio.

From a numerical approach, Boyle [4] used a quasi-3D Navier–Stokes analysis to predict the change in turbine efficiency due to change in blade surface roughness and incidence. The effect of roughness was determined using a mixing length turbulence model of Cebeci and Chang [5], in which the original mixing length (for a smooth blade) was augmented to account for the roughness height. A similar method was employed by Suder et al. [2]. Although the numerical results yielded the correct trend of performance deterioration, the impact of surface roughness on the performance was underpredicted.

The issue of whether or not distributed surface roughness alters three-dimensional (3D) separations, which contribute to performance deterioration, has not previously been investigated. The conventional two-dimensional view that surface roughness triggers transition and promotes turbulence, which will suppress flow reversal and hence two-dimensional separation, may not be applicable to three-dimensional flows. Three-dimensional separation does not need flow reversal as a condition for its occurrence (Chang [6]). However, boundary layer thickening, characteristic of rough surfaces due to an increased skin-friction coefficient, may also increase the size of separations in three-dimensional flows under adverse pressure gradients. In this light, the influence of surface roughness on 3D separation in a compressor stator and the consequent effect on stage performance, have been studied both experimentally and numerically. These were carried out in a single-stage low-speed axial compressor. Tests performed include oil-flow visualization to examine the pattern of 3D separation on the suction surface and a 3-hole probe area traverse downstream of the stator to measure losses and deviation. The effect of roughness on loading redistribution (shown using measurements made of surface static pressures) and on the measured stage characteristic is also presented. A simple model to simulate the effect of roughness was incorporated into a 3D Navier–Stokes calculation and the results are compared with the experiments.

## Experimental Faciltiy and Procedure

The experiments were performed on a large-scale single-stage low-speed facility, the Deverson compressor, in the Whittle laboratory of the University of Cambridge. A detailed description of the rig arrangement can be found in Place [7] as well as in Bolger [8]. The stage tested consists of radially stacked modern controlled-diffusion airfoils (CDA) with a rotor tip clearance of about 1.15% chord and a sealed stator hub. Preceding the stage is a row of inlet guide vanes (IGV) which produce the required amount of swirl into the rotor. Also incorporated are turbulence generators in the freestream, upstream of the IGV, and devices on the hub and casing to create endwall boundary layers similar to an embedded stage in a multistage compressor. The rig is equipped with an auxiliary fan that allows the mass flow rate to be varied

Contributed by the International Gas Turbine Institute (IGTI) of THE AMERICAN SOCIETY OF MECHANICAL ENGINEERS for publication in the ASME JOURNAL OF TURBOMACHINERY. Paper presented at the International Gas Turbine and Aeroengine Congress and Exhibition, Vienna, Austria, June 13–17, 2004, Paper No. 2004-GT-53619. Manuscript received by IGTI, October 1, 2003; final revision, March 1, 2004. IGTI Review Chair: A. J. Strazisar.

  

**Table 1 Deverson compressor stage parameters**

| | $\phi$ | $\Delta H_0/U^2$ | $\mathrm{Re}_{(\mathrm{chord})}$ |
|---|---|---|---|
| | 0.51 | 0.45 | $2.7\times10^5$ |
| | Rotor | | Stator |
| Profile | CDA | | CDA |
| Chord (m) | 0.1215 | | 0.1215 |
| $s/c$ | 0.6954 | | 0.7192 |
| $h/c$ | 1.25 | | 1.25 |
| Camber (deg.) | 31.0 | | 31.0 |
| Stagger (deg.) | 35.4 | | 34.4 |
| No. of blades | 51 | | 49 |
| Hub radius (m) | 0.6096 | | 0.6096 |
| Casing radius (m) | 0.762 | | 0.762 |

independently of the rotor speed. A brief summary of the stage geometric and design parameters at mid-height is given in Table 1.

The roughness height for the stators of the low-speed compressor rig was chosen by scaling roughness measurements obtained from Rolls-Royce on a modern turbofan engine after a long period of airline operation. The center-line average roughness ($k_{\mathrm{CLA}}$) is typically about 60–80 micro-inches (1.53–2.03 $\mu$m). A roughness scaling factor for the rig was obtained by matching the engine Reynolds number at take-off, based on the relative velocity and roughness height, to that of the research rig. The corresponding roughness value for the rig was calculated to be about 25 $\mu$m, which from the Koch and Smith's [9] correlation corresponds to an equivalent sand roughness of approximately 160 $\mu$m. Artificial roughness in the form of distributed patches of sand roughness was achieved using strips of ASTM150 emery paper. The roughness strip was cut into lengths covering 50% and 100% span and of width about 20% chord. Although in real engines the surface roughness is usually not uniform, it was thought that simple tests with uniform roughness will be useful in exploring the significance of surface roughness itself [10].

A strip of emery paper secured on the stator blade using double sided tape increased the blade thickness by 0.3 mm, which is about 3.5% increase in blade thickness at the hub and 2.2% at the casing. This also resulted in a step at the edges of the strip. In order to separate any effect due to thickness from the effect due to roughness, tests were performed by covering the leading edge/peak-suction region with smooth strips of thin cardboard of similar thickness to that of the emery paper. This configuration is referred to as a ''stepped'' blade row.

An area traverse was performed downstream of the stator with a pneumatic probe to assess the influence of roughness on performance. The uncertainty in the yaw angle measurement was estimated to be $\pm0.6$ deg. The uncertainty of total pressure was $\pm1.0\%$ of dynamic head and the measurement of the dynamic head was correct within $\pm5$ Pa. The area traverses were carried out at four operating flow coefficients ($\phi$=0.45, 0.51, 0.55, and 0.57). The performance was evaluated by calculating the mass averaged exit total pressure rise coefficient, made nondimensional by dynamic pressure based on the mid-height blade speed ($1/2\,\rho U_m^2$).

## Numerical Procedure

A numerical simulation of patch and full roughness on the blade surfaces, similar to the experiment, is implemented with roughness modeled mainly in terms of its effect on skin-friction as well as on turbulent mixing. Rough surfaces are known to develop considerably larger skin friction coefficients under turbulent flows when compared to smooth surfaces. In addition, roughness usually causes the velocity gradient near the wall to be less steep and the boundary layer thicker compared with hydraulically smooth surfaces (Schlichting [10] and White [11]). The roughness effect is therefore modeled as a shift in the wall functions ($u^+$ and $y^+$). With average roughness height denoted as $k$, the velocity distribution taking account of roughness can be written as

$$u^+ = A\ln y^+ + B - \Delta_B(k^+), \tag{1}$$

where

$$u^+ = \frac{u}{u^*} = f(y^+, k^+),$$

$$y^+ = \frac{yu^*}{\nu} \quad \text{and} \quad k^+ = \frac{ku^*}{\nu}$$

with

$$u^* = \sqrt{\tau_w/\rho} = \text{friction velocity}$$

$A$ is the well known Von Karman constant, $B$ is the original wall law intercept, and $\Delta_B(k^+)$ is the profile shift parameter due to surface roughness (White [11]). The second and the third term on the right-hand side of Eq. (1) now constitute the new wall-law intercept, with the third term causing a downward shift in the intercept. Following a fit for $\Delta_B(k^+)$ for sand grain roughness given by White [11] as

$$\Delta_{B_{\mathrm{sandgrain}}} = A\ln(1+0.3k^+) \tag{2}$$

and substituting for constants $A$ and $B$, ($A=0.4$ and $B=5.24$), Eq. (1) can be expressed in terms of the wall skin friction $\tau_w/(1/2\rho u^2)$ and the average roughness height $k$ as

$$u^+ = \left(\frac{\tau_w}{\rho u^2}\right)^{-(1/2)} = 1.25\ln\left(\frac{\tau_w}{\rho u^2}\right) + 2.5\ln(\mathrm{Re}) + 5.24 - 2.5\ln\left[1+0.3\,\mathrm{Re}\left(\frac{k}{y}\right)\left(\frac{\tau_w}{\rho u^2}\right)^{1/2}\right] \tag{3}$$

In Eq. (3), $k^+ = ku^*/\nu$ has been replaced by $\mathrm{Re}(k/y)(\tau_w/\rho u^2)^{1/2}$ and $\mathrm{Re}=yu/\nu$ is the Reynolds number based on the perpendicular distance $y$ from the wall.

The average roughness height is assumed to be uniform and also to cover both transitional and fully rough regimes. Equation (3) is solved iteratively to obtain the wall skin friction explicitly in terms of Re for various values of $(k/y)$, similar to the approach of Denton [12] for a smooth wall. The model was incorporated into the original code, which is a fully three-dimensional multi-stage turbomachinery Reynolds-averaged Navier–Stokes solver of Denton [13]. The calculations are performed using a control volume formulation on an ''H'' type mesh. Shear stress is modeled using a thin shear approximation to the Navier–Stokes equation and an eddy viscosity mixing length is used for turbulence modeling. The turbulence model therefore enables the contribution of surface roughness to turbulent mixing to be taken care of by augmenting the originally specified mixing length for the smooth surface by the average roughness height. Further detail of the modeling procedure can be found in Gbadebo [14]. The stage calculations were carried out using a grid distribution of $41\times226\times63$ in the pitchwise, streamwise and spanwise directions respectively with a total of nine spanwise mesh points used in the rotor tip clearance space.

## Results and Discussion

**Performance of a *Single* Roughened Stator.** Initial tests were carried out on a *single* roughened stator with the roughness strip located at 3 different parts of the blade; leading edge to peak-suction, around mid-chord and towards the trailing edge. This was to establish on which part of the stator suction surface, and under which operating condition, is the flow most sensitive to roughness. A diagram showing the stator blade with the roughness strip at different locations tested is presented in Fig. 1. It was found that the performance at flow coefficients near the design point ($\phi$=0.51), is particularly sensitive to roughness over the leading edge to peak-suction region. This corresponds to configurations *a* and *c* in Fig. 1, where the roughness strip covers both full span and the first half of the blade from the hub.

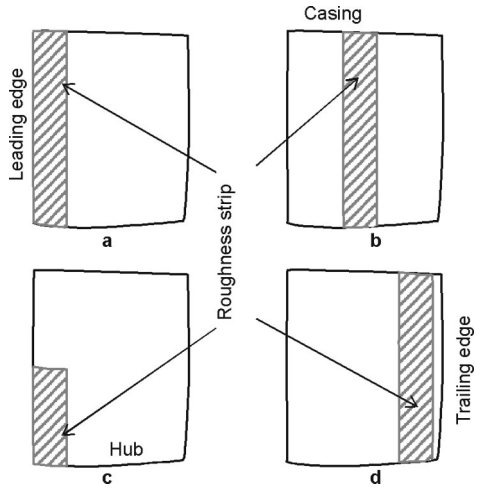


**Fig. 1 Schematic diagram of stator blade with roughness (a) full strip (leading edge to peak-suction); (b) full strip (mid-chord); (c) 50% span from hub (leading edge to peak-suction); (d) full strip (near trailing edge)**

This effect can be seen in the contours of stage total pressure rise coefficients, measured by traversing behind the smooth blade and single roughened blade with full-span strip plotted in Fig. 2. (The traverse result for the half strip of roughness near leading edge is qualitatively the same as that of the full strip and is not presented.) As can be seen from Fig. 2, the roughness results in significant loss of total pressure rise notably in the hub corner region with a marked increase in the size of the separated region. The experiments with roughness patches near the mid-chord position and rearward (near the trailing edge) (configurations *b* and *d* in Fig. 1) indicated conclusively that roughness in these regions had negligible effect and, for brevity, the results are not shown. The overall mass-averaged exit pressure rise coefficient was found

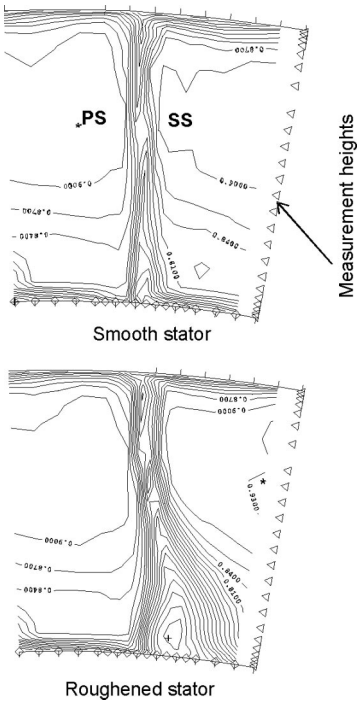


**Fig. 2 Contours of total pressure rise coefficient at the exit of a smooth and single stator roughened around leading edge/peak-suction at design point, $\phi$=0.51 (contour interval=0.03)**

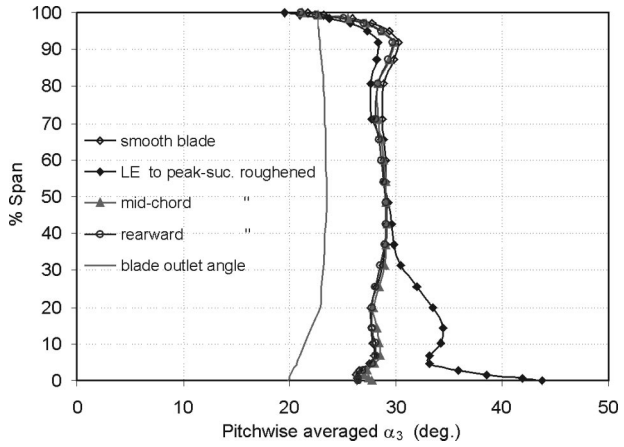


**Fig. 3 Influence of location of roughness strip on stator exit flow angles at design point, $\phi$=0.51**

to drop by about 5% when the blade was operated at the design flow rate, with the roughness element element located around the leading edge/peak-suction.

The radial profile of the exit flow angles at design point for different locations of the roughness element is shown in Fig. 3. It is apparent from the figure that the deviation towards the hub increases considerably when the blade is roughened around peak-suction and is virtually insensitive to roughness at other locations. Surface and hubwall flow visualization at the design operating point of this test blade show separation on the suction surface/hub corner for the smooth blade and for the roughened blade, Fig. 4. With roughness over the leading edge to peak-suction region, a larger 3D separation on the suction surface and hubwall is appar-

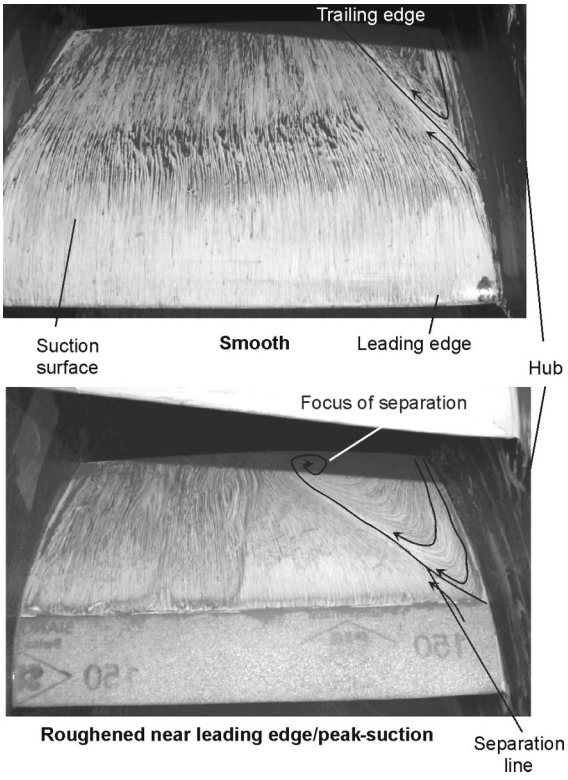


**Fig. 4 Suction surface flow visualization on smooth and roughened stator around leading edge/peak-suction at design point, $\phi$=0.51**

ent and the increased size of the separated region is clearly the cause of the extra loss and deviation when compared with a smooth blade.

The roughness element near the leading edge is at the most sensitive location in the blade passage because the boundary layer in this region is very thin. The ratio of average roughness height to the boundary layer thickness ($k/\delta$) may be significant enough to induce earlier transition, while at the same time introducing considerable frictional drag into the flow. In the presence of the passage adverse pressure gradient this can lead to premature thickening of the boundary layer. The compressor stage is of 51% reaction at mid-height and the requirement of the stator to remove much of the swirl out of the upstream rotor implies that the static pressure rise across the stator is highest at the hub (Cumpsty [15]). The combination of these factors is believed to provoke the large 3D separation observed and consequent loss of performance. With roughness downstream of the suction peak it is presumed that the roughness (chosen to model that measured on blades which has been in airline service) is too small to penetrate beyond the viscous sublayer, so the surface appears to be hydraulically smooth.

The single roughened blade gave a quick means to assess effects but the additional blockage caused by separations increased in size by surface roughness was able to influence the behavior in neighboring passages, as presented in Gbadebo [14]. The increased blockage caused by increased separation on the suction surface of the roughened blade causes the upstream flow to be diverted away from this blocked passage. This increases the incidence onto the blades on one side and decreases it for those on the other side. As a result, four or five succeeding passages on one side of the single roughened blade also exhibited increased separation due to these incidence changes.

**Smooth, Stepped, and Roughened Blade-Row Performance** Following the above observations, tests were carried out at the design flow coefficient with all the stator blades in the row roughened with full-span strip around the leading edge (covering from about 5% chord on the pressure surface over to the peak-suction, which is about 20% chord from the leading edge on the suction-surface). The emery strip was carried around onto the pressure surface to avoid blade-to-blade irregularities in the most sensitive region of the flow. The pattern of flow visualization on the suction surface of roughened and stepped (thickness but no roughness) blade-rows showed a larger separation region for the roughened case. The suction surface separation line for the roughened blade-row started at a distance of about 20% chord from the leading edge, extended diagonally from the hub towards the mid-span to wind into a focus near the trailing edge like that on the single roughened blade. A discussion of this type of pattern can be found in Gbadebo, Cumpsty, and Hynes [1]. The separation line for the stepped stator started at a distance of about 35% chord from the leading edge at the hub and terminated at the trailing edge at about 25% span from the endwall, which closely resembles the pattern on the smooth blade.

Figure 5 compares contours of stage total pressure rise coefficient for smooth and roughened blade rows at different operating flow coefficients. Similar to the observation for a single roughened stator, it is evident from the figure that the performance is very sensitive to roughness around the design point, $\phi=0.51$, and virtually insensitive to roughness at much higher flow coefficients. This may be because of the reduced overall static pressure rise at high flow coefficients. In addition, at high flow coefficient the flow approaches the blade at negative incidence so the stagnation point is moved to the suction side of the leading edge and the flow may be less affected by the roughness because of the reduced suction-peak. For the smooth blade-row, the wake around mid-span at design point and at higher flow coefficients can be seen to be comparatively thin and nearly two dimensional. The mid-height wake momentum thickness for the roughened blade-row, at the design point, is about 40% higher than that of the smooth blade-row.

The roughness has a marked effect for all flow coefficients with small or positive incidence. However the biggest difference between smooth and rough was close to the design incidence because for this the roughness was sufficient to alter the flow pattern to have the large 3D separation that only occurred for the smooth blade at lower flow rates.

Figure 6 shows the contours of stage pressure rise coefficient for the stepped blade-row at design point ($\phi=0.51$). By comparing this figure with the corresponding ones for smooth and roughened blade-rows, Fig. 5, it is clear that the thickness/step has a negligible contribution to wake thickening and virtually no effect on three-dimensional hub corner blockage. Consequently the loss of performance within the blade-row can be attributed to the surface roughness itself.

The radial distribution of pitchwise mass-averaged stage exit total pressure rise coefficient, axial velocity and swirl angle are plotted for the smooth, stepped and roughened blade rows in Figs. 7, 8, and 9. Also presented in each case is the profile for the preliminary single-roughened blade, which can be seen to be indicative of the trend but not quite correct in magnitude. Again the thickness/step formation seems to have negligible influence on the distributions of loss and axial velocity. From the pitchwise-averaged exit axial velocities, it is apparent that surface roughness over the leading edge and peak-suction significantly increases the loss, reduces the axial velocity and increases deviation from the hub to about 30% span.

Figure 10 compares the surface static pressure distributions for the blades roughened between the leading edge/peak-suction with that of the smooth blades. (The stepped blades showed the same distribution as smooth blades almost within experimental scatter.) The comparison is at design operating point at 20%, 50%, and 80% span, respectively, for which stator incidence was about 0.0 deg, $-2.0$ deg, and $-2.5$ deg, respectively. There is evidence of loading redistribution caused by surface roughness in these distributions; at all three spanwise locations, the influence of the roughness causes an overall lowering of static pressure on the pressure and suction surfaces of the entire blade-row with a net reduction in the average static pressure rise. This is mainly because of the extra blockage at the hub, which increases the axial velocity in the mid-span and the upper half of the passage, as depicted in Fig. 8. Near the hub (20% span) of the roughened blade row, the pressure distribution around the leading edge suggests an increase in the effective incidence onto the airfoil and an increased loading (i.e., larger difference between the suction and pressure surfaces). Although at 20% span the flow is separated, there is still static pressure rise over the rear of the blade.

The total-to-total and total-to-static stage characteristics plotted in Fig. 11 clearly show the degradation of stage performance caused by surface roughness, which is most apparent between the design operating point, $\phi=0.51$, and stall. The characteristic for the stepped blade-row are virtually identical to that of the smooth stage at all operating points except very close to the design point and are omitted for clarity. At high flow coefficients, corresponding to a negative incidence and reduced loading, the effect of roughness seems to be insignificant, and the curves collapse.

**Numerical Results.** The numerical ''roughness'' is applied to cover the leading edge to the peak suction of the airfoil, as for the experiments. Figure 12 shows the predicted streamlines on the suction surface for the smooth and roughened blades at design flow coefficient, $\phi=0.51$. The smooth blade displays a small separated region with a pattern very similar to the oil-flow pattern observed experimentally. However, a closer look at the computed streamlines in the trailing edge/casing region shows that the streamlines turn more perpendicular to the casing but not in the oil-flow pattern in Fig. 4. It is not clear which aspect of the flow physics, not captured by the CFD, is responsible for this.

For the roughened airfoil, the comparatively large separated region agrees reasonably well with experiment. The separation line can be seen to emanate from a saddle point on the suction

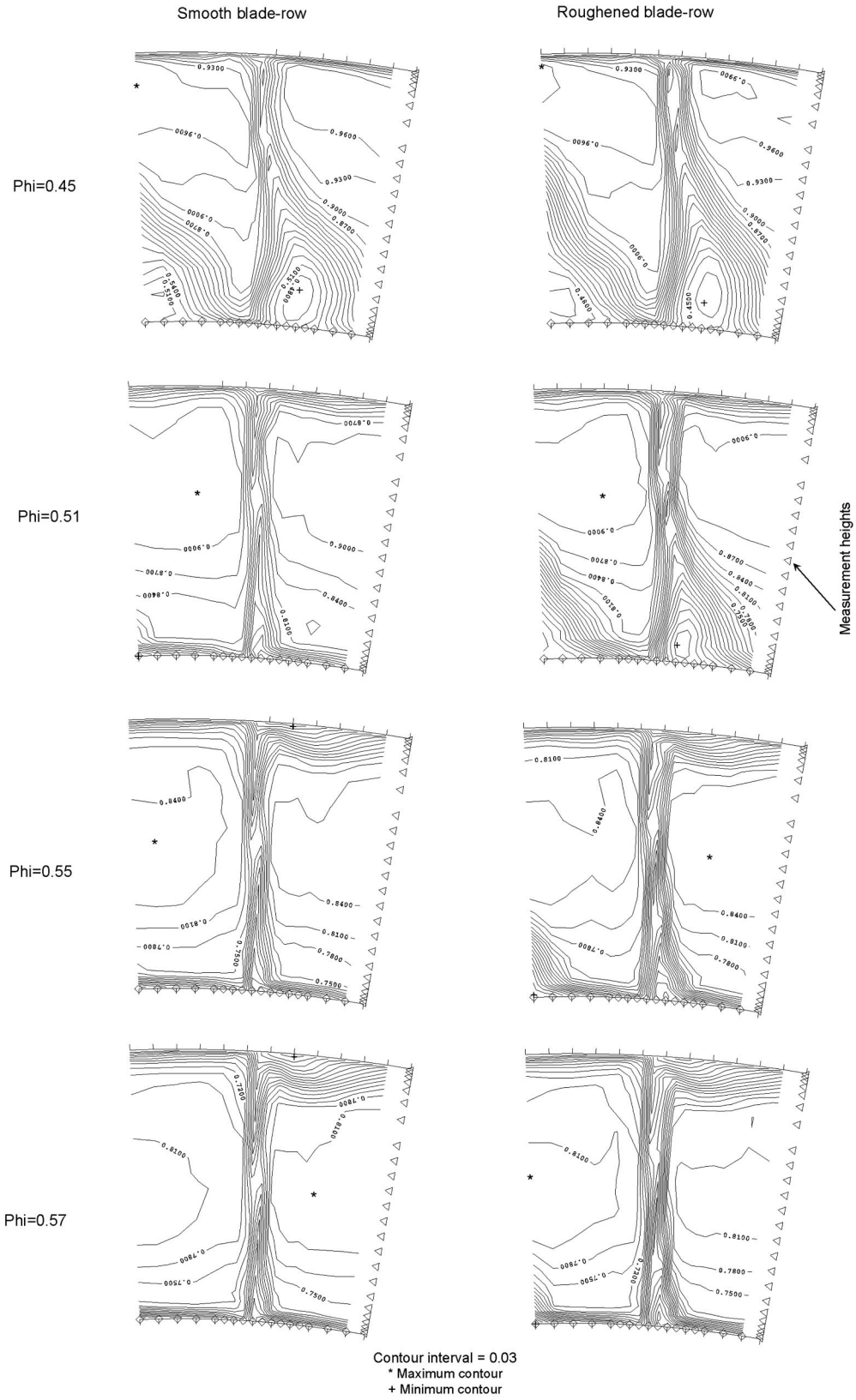


**Fig. 5 Contours of stage total pressure rise coefficients for smooth and roughened blade-rows at different flow coefficients. (Roughness from LE to peak-suction.)**

surface/endwall corner at a similar location to that in the oil flow visualization and winds into a focus near the trailing edge.

The predicted stator exit contours of total pressure rise are shown in Fig. 13 for smooth and rough blades at design flow coefficient, $\phi=0.51$. This shows a large increase in hub losses associated with growth in the 3D separations induced by surface roughness. The calculation also shows a significant wake thickening due to roughness when compared with the smooth blade.

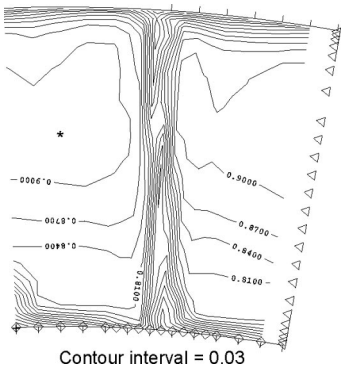


**Fig. 6 Contours of stage exit total pressure rise coefficient for stepped blade-row at design point, $\phi$=0.51. (Roughness from LE to peak-suction.)**

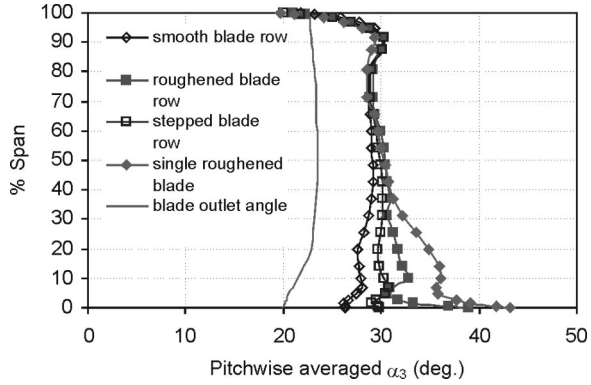


**Fig. 9 Radial profiles of pitchwise mass-averaged exit flow angles for smooth, stepped and roughened blade-rows and single roughened blade at design point, $\phi$=0.51. (Roughness from LE to peak-suction.)**

However the predicted change in loss is not as high as measured: the measured overall mass-averaged total pressure rise coefficient reduced by about 5.4% with roughness while the calculated value reduced by about 2.4%. Table 2 compares the measured and calculated values of the overall mass-averaged total pressure rise coefficient at the design point.

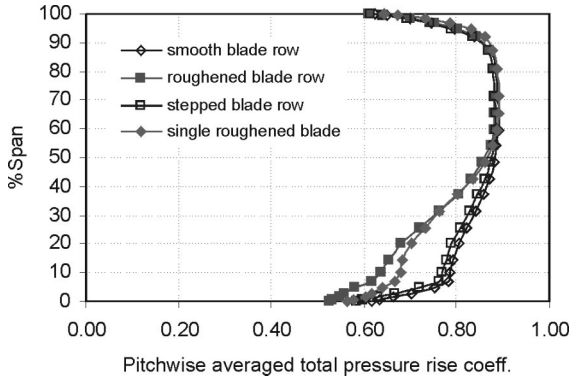


**Fig. 7 Radial profiles of pitchwise mass-averaged stage total pressure rise coefficients for smooth, stepped and roughened blade-rows and single roughened blade at design point, $\phi$=0.51. (Roughness from LE to peak-suction.)**

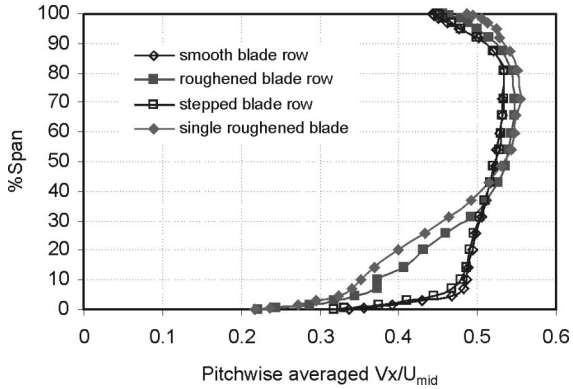


**Fig. 8 Radial profiles of pitchwise area-averaged axial velocities for smooth, stepped and roughened blade-rows together with single roughened blade at design point, $\phi$=0.51. (Roughness from LE to peak-suction.)**

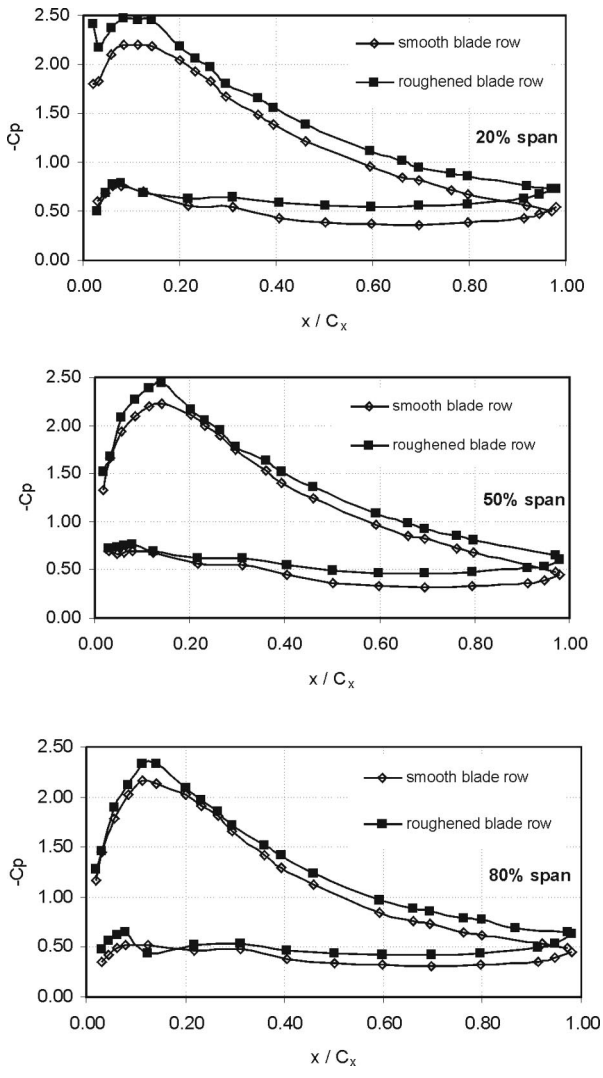


**Fig. 10 Comparison of surface static pressure distribution at different spanwise locations of smooth and roughened blade-rows at design point, $\phi$=0.51. (Roughness from LE to peak-suction.)**

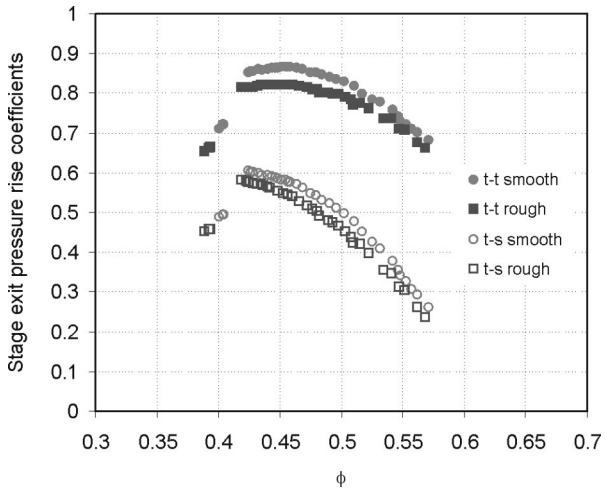


**Fig. 11 Comparison of total-to-total and total-to-static stage pressure rise characteristics for smooth and roughened blade-rows. (Roughness from LE to peak-suction.)**

The measured and predicted variation of the mass-averaged total pressure rise coefficient as a function of flow coefficient is plotted in Fig. 14 for smooth and roughened blades. The measurements are for single roughened blade as well as for the entire roughened blade-row. The calculation with roughness can be seen to capture the trend of measurements although the effect is underestimated, especially below the design point ($\phi$=0.51). As can be seen in Fig. 14, the experimental value of the average total pressure rise coefficient for the single roughened blade at $\phi$=0.45, is higher than that of the smooth blade. At this flow coefficient, the flow for the smooth blade has a large separated region and the roughness in the single passage may have other effects on the flow in this near-stall condition such that it is possible it makes the separation smaller. The discrepancy between calculated and measured pressure rise as stall is approached is perhaps to be expected because of the increased difficulty of modeling the flow in this regime.

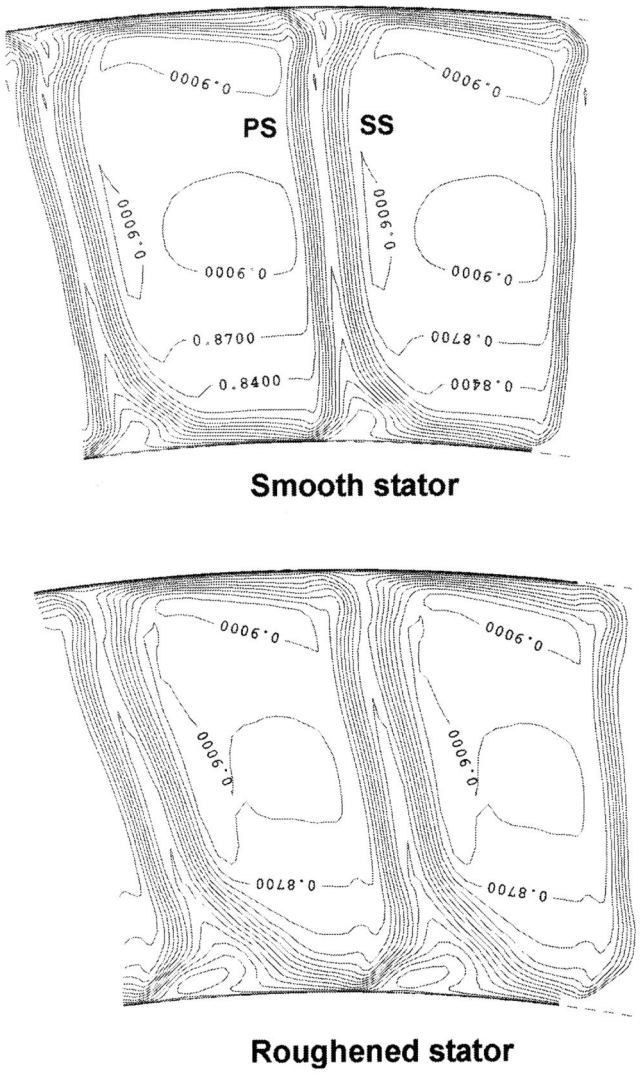


**Fig. 13 Predicted contours of exit total pressure rise coefficients for smooth and roughened stator blade at design point, $\phi$=0.51. (Roughness from LE to peak suction.)**

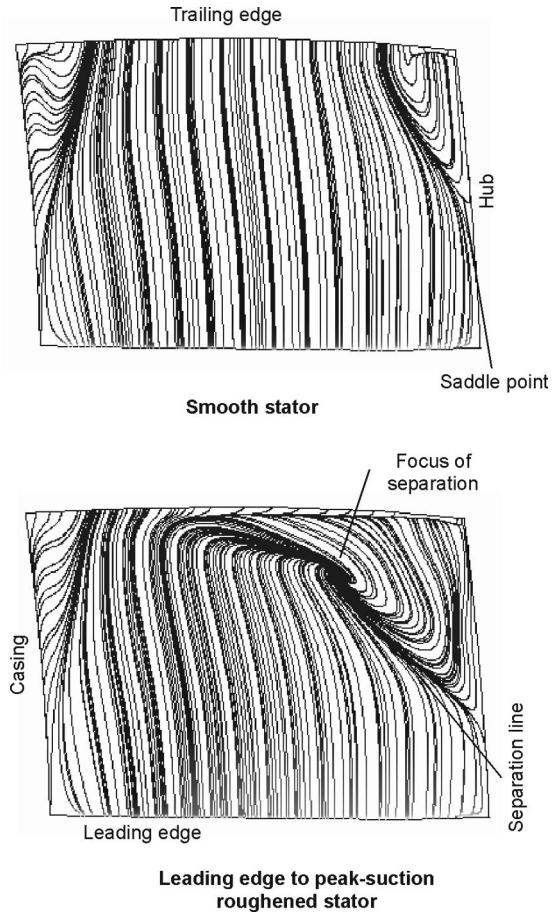


**Fig. 12 Numerical suction surface streamlines for smooth and roughened stator at design point, $\phi$=0.51**

**Table 2 Comparison of measured and calculated overall mass-averaged total pressure rise coefficient for smooth and roughened blade-rows at design point, $\phi$=0.51**

| | Smooth | Rough |
|---|---|---|
| Measured | 0.842 | 0.796 |
| Calculated | 0.841 | 0.821 |

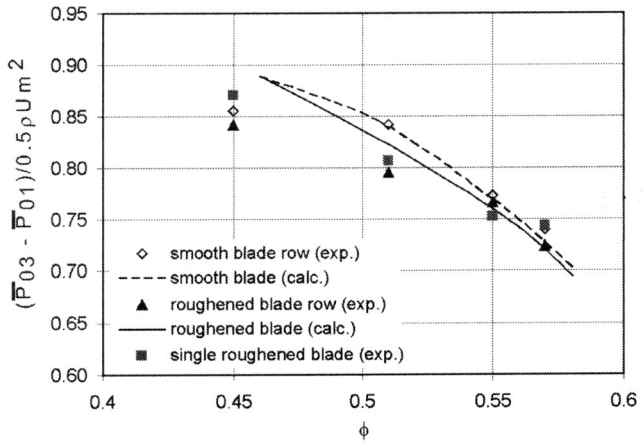


**Fig. 14 Comparison of measured and calculated mass-averaged stage exit total pressure rise coefficients at different operating points for smooth and roughened stator blade. (Roughness from LE to peak suction.)**

## Conclusions

The following conclusions can be drawn from this study:

(1) The experiments described in this paper have shown that surface roughness, typical of that which is likely to form during engine operating lifetime, can lead to a significant reduction in performance due to its effect on 3D separation.
(2) For the stator used in these experiments, roughness induced a large hub corner separation at the design flow coefficient, giving high loss, increased blockage and deviation. The portion of the blade affected extended from the hub to about 30% span.
(3) When tested as part of a stage, the 3D separation induced by roughness caused a significant loss in stage stagnation pressure rise over a wide range of flow.
(4) The blockage induced by the separation is responsible for a significant radial movement of flow, with a consequent radial redistribution of loading and change of effective incidence.
(5) In contrast to the strong effect on performance when applied between the leading edge and suction peak, roughness applied downstream of suction peak had negligible effect.
(6) A simple model for the effect of roughness on wall shear stress has been developed, suitable for use with RANS calculation methods. Calculations performed with this roughness model show that the effects of patch roughness on blade surfaces are reasonably well modelled.
(7) The predicted streamline pattern on the suction surface and on the hub wall show that the increase in the size of the 3D separation induced by roughness is reasonably well captured, as are the overall results for pressure rise. The extra losses and the increase in thickness of the boundary layer and separated region are underpredicted.
(8) Although only the stator blades were roughened in this study, it is also appropriate to carry out experiments on roughened rotor blades as well as on both stators and endwalls. This perhaps can be considered as a future work.

## Acknowledgments

This work was supported by Rolls-Royce Plc, the Applied Research Program of the Ministry of Defense, the Department of Trade and Industry Aeronautic Research Program and QinetiQ Ltd. The authors are very grateful for this and for their permission to publish. In particular, the many fruitful discussions with Dr. John Bolger of Rolls-Royce Plc have been appreciated. The authors would also like to thank Professor J. D. Denton of the Whittle Laboratory, University of Cambridge for the use of his CFD code, into which the roughness model was incorporated. The opinions expressed here are those of the authors and not necessarily those of Rolls-Royce plc or any other organization.

## Nomenclature

$c$ = chord
$C_p$ = pressure coefficient $(P-\bar{\bar{P}}_{02})/(1/2\rho V_2^2)$
$h$ = blade height (span), height from surface
$k$ = roughness height
$i$ = incidence
LE = leading edge
$P$ = pressure
PS = pressure surface/side
$r$ = radius
Re = Reynolds number
$s$ = blade pitch
SS = suction surface/side
$t$ = blade thickness
$u$ = local velocity
$U$ = blade speed
$V$ = absolute velocity
$x$ = axial distance
$y$ = perpendicular distance

### Greek Symbols

$\alpha$ = absolute flow angle
$\beta$ = blade (metal) angle
$\delta$ = boundary layer thickness
$\Delta$ = change across the stage
$\phi$ = flow coefficient $(Vx/U)$
$\nu$ = kinematic viscosity
$\rho$ = density
$\tau_w$ = wall shear stress

### Subscripts

0 = stagnation
1 = rotor inlet
2 = stator inlet
3 = stator exit
abs = absolute
calc = calculated values
CLA = center-line average
exp = experiment
mid, m = mid-height
h = hub
s = static
x = axial

### Superscript

$\bar{\bar{}}$ = passage averaged

## References

[1] Gbadebo, S. A., Cumpsty, N. A., and Hynes, T. P., 2004, Three-dimensional Separations in Axial Compressors, ASME Paper GT-2004-53617.
[2] Suder, K. L., Chima, R. V., Strazisar, A. J., and Roberts, W. B., 1994, Effect of Adding Roughness and Thickness to a Transonic Axial Compressor Rotor, ASME Paper 94-GT-339.
[3] Bammert, K., and Woelk, G. U., 1980, "Influence of the Blading Surface Roughness on the Aerodynamic Behavior and Characteristic of an Axial Compressor," ASME J. Eng. Gas Turbines Power, **102**, pp. 579–583.
[4] Boyle, R. J., 1994, "Prediction of Surface Roughness and Incidence Effects on Turbine Performance," ASME J. Turbomach., **116**, pp. 745–751.
[5] Cebeci, T., and Chang, K. C., 1978, "Calculation of Incompressible Rough-Wall Boundary-Layer Flows," AIAA J., **16**, pp. 730–735.
[6] Chang, P. K., 1970, *Separation of Flow, Interdisciplinary and Advanced Topics in Science and Engineering*, Vol. 3, Pergamon Press.
[7] Place, J. M. M., 1997, "Three-Dimensional Flow in Axial Compressors," Ph.D. thesis, University of Cambridge, United Kingdom.

[8] Bolger, J. J., 1999, ''Three-Dimensional Design of Compressor Blades,'' Ph.D. thesis, University of Cambridge, United Kingdom.
[9] Koch, C. C., and Smith, L. H., 1976, ''Loss Sources and Magnitudes in Axial Flow Compressors,'' ASME J. Eng. Gas Turbines Power, **98**, pp. 411–424.
[10] Schlichting, H., 1979, *Boundary Layer Theory*, McGraw–Hill, New York.
[11] White, F. M., 1991, *Viscous Fluid Flow*, McGraw–Hill, New York.
[12] Denton, J. D., 1992, ''Calculation of Three-Dimensional Viscous Flows Through Multistage Turbomachines,'' ASME J. Turbomach., **114**, pp. 18–26.
[13] Denton, J. D., 1999, ''Multistage Turbomachinery Flow Calculation Program-MULTIP,'' Whittle Laboratory, University of Cambridge, United Kingdom.
[14] Gbadebo, S. A., 2003, ''Three-Dimensional Separations in Compressors,'' Ph.D. thesis, University of Cambridge, United Kingdom.
[15] Cumpsty, N. A., 1989, *Compressor Aerodynamics*, Longman Scientific and Technical.

# Potential and Viscous Interactions for a Multi-Blade-Row Compressor

**Yu-Tai Lee**
Naval Surface Warfare Center,
Carderock Division,
West Bethesda, MD 20817
e-mail: LeeYT@nswccd.navy.mil

**JinZhang Feng**[1]
The Pennsylvania State University,
University Park, PA 16802
e-mail: fengji@pweh.com

*A computationally efficient time-accurate vortex method for unsteady incompressible flows through multiple blade row systems is presented. The method represents the boundary surfaces using vortex systems. A local coordinate system is assigned to each independently moving blade row. Blade shed vorticity is determined from two generating mechanisms and convected using the Euler equation. The first mechanism of vorticity generation is a potential mechanism from a nonlinear unsteady pressure-type Kutta condition applied at the blade trailing edges. The second mechanism is a viscous mechanism from a viscous wake vorticity (VWV) model implemented to simulate the viscous shear layers on the blade pressure and suction sides. Two different two-blade-row compressor systems, a rotor/stator (R/S) system and a stator/rotor (S/R) system, were used to investigate the interaction forces on each blade row. Computational results of the potential and viscous interaction forces are presented and compared to measurements. The comparison suggests that the viscous wake interaction accounts for 25–30% of the peak loading for an axial spacing of 10% chord length between the blade rows. The efficient computational method is particularly attractive for blade indexing study. Therefore a three-blade-row rotor/stator/rotor (R1/S/R2) compressor system is used to demonstrate the indexing calculations between the two rotor positions. Resultant forces on each blade row are presented for ten rotor indexing positions and three axial gap sizes for the gaps between R1 and S and between S and R2. The unsteady peak-to-peak force can reach 10–15% of inflow dynamic head for the gap spacing investigated. The minimum-to-maximum variation of the unsteady force can account for 40–50% of averaged unsteady force.* [DOI: 10.1115/1.1740778]

## Introduction

Blade-row interaction in turbomachinery is important because it generates unsteady forces on the blades and causes blade fatigue and interaction noise. In order to reduce these drawbacks it is desirable to investigate the blade-row interaction at an early stage of the design phase.

Many researchers in the past have undertaken experimental and/or computational investigations on rotor/stator interaction. Among the computational approaches, [1–5], Navier-Stokes and Euler solution methods with and without turbulence closures have been used to describe the unsteady flow phenomena between the blade rows. In addition, forced response due to blade/wake interaction has been investigated theoretically by Goldstein and Atassi [6] and Goldstein [7]. Experimental studies, [8–12], of the forced response provide wake/blade interaction contributed from potential effect and shed vortical wake. More recent studies, [13–14], use more advanced analysis tools and experimental data for analyzing wake and foil interaction. Valkov and Tan [15] use computational method to study the control of the shed viscous wake on the downstream stator. Blade-row clocking was investigated by indexing either the stator rows including IGV and nozzle, [13,16], or the rotor rows, [17].

Although recent advances in CFD methodologies for turbomachinery applications have been extraordinary, usage of these advanced tools for fully unsteady multiple blade-row calculations at an early design stage is still uncommon due to the time and effort required for correctly setting up the calculations. Certainly, a quick and efficient but still reasonably accurate approach for investigating the unsteady nature of the blade design is very desirable if unsteady loading is to be incorporated at the design stage.

This paper presents a computationally efficient method for analyzing unsteady forces in a multiple blade-row turbomachinery system. The current work adapts previous developments, [18,19], which account for the unsteady potential interactions in multiple blade-row turbomachinery. A viscous wake vorticity (VWV) model is developed and implemented along with the previously developed inviscid shed vorticity model to account for strong unsteady viscous blade-row interaction. The advantages of the current approach are (1) it does not require the generation of computational volume grids as required by Navier-Stokes/Euler solvers; (2) no numerical diffusion exists in the shed vorticity wake system; (3) no interpolation error exists in the blade-row grid interfaces; and (4) the numerical matrix system of unknowns is an order of magnitude smaller than that required by Navier-Stokes solvers.

Hsu and Wo's measurements, [17], on a low-speed compressor are used to validate the current VWV model on two-blade-row configurations including a rotor/stator (R/S) and a stator/rotor (S/R) system. A three-blade-row configuration is further investigated to demonstrate the potential of the current prediction scheme for blade-row indexing on a rotor/stator/rotor (R1/S/R2) system.

## The Vortex Computational Method

The vortex method includes the determination of blade surface vortices, the shed vorticity from the blade trailing edges, and the shed vorticity from shear layers on both sides of the blades. The blade surface vortices and trailing-edge shed vorticity are of an inviscid nature and the shed vorticity from the shear layers is of a viscous nature.

**Blade Surface Vortex System.** The blade surfaces are repre-

[1]Currently with United Technologies–Pratt & Whitney, East Hardford, CT.

Contributed by the International Gas Turbine Institute and presented at the International Gas Turbine and Aeroengine Congress and Exhibition, Atlanta, GA, June 16–19, 2003. Manuscript received by the IGTI December 2002; final revision March 2003. Paper No. 2003-GT-38560. Review Chair: H. R. Simmons.

  

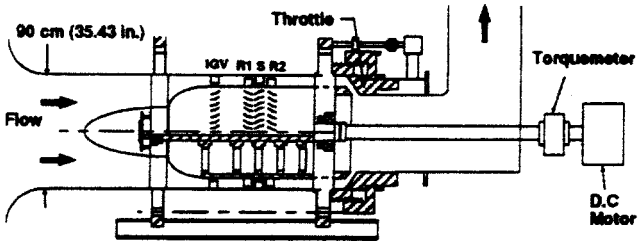


**Fig. 1 Schematics of the compressor tested by Hsu and Wo (1997)**

sented by vortex elements. The strengths $\vec{\xi}_b$ of these vortex elements are represented by the following integral equation.

$$\vec{u}(p,t)=\nabla\int_{\delta\Omega}u_nGds-\nabla\times\left[\int_{\delta\Omega}\vec{\xi}_bGds+\int_{\Omega}\vec{\xi}Gdv\right] \quad (1)$$

where $\vec{u}$ is the velocity at a field point $p$ and time $t$, and $G$ is the Green's function. The surface integrals are performed on the boundary surface $\delta\Omega$ for the surface normal velocity $u_n$ and $\vec{\xi}_b$. The volume integral over the flow domain $\Omega$ is for the shed vorticity $\vec{\xi}$ which, after its generation at the blade trailing edges, convects downstream according to the Euler equation:

$$\frac{\partial\vec{\xi}}{\partial t}+\vec{u}\cdot\nabla\vec{\xi}=0. \quad (2)$$

Equation (1) has a flow tangency boundary condition on the blade surfaces $\delta\Omega$ given by

$$u_n=\vec{u}_b\cdot\vec{n}. \quad (3)$$

$\vec{u}_b$ is the velocity on the blade surface and $\vec{n}$ is the unit surface normal vector on $\delta\Omega$. For the present work, the blade surface vortex strength is represented by a linear function for each discretized surface element. Equations (1) and (3) can be solved with a Kutta condition for the surface vorticity $\vec{\xi}_b$. The number of unknowns to be solved corresponds only to the number of surface elements.

**Blade Shed Vorticity System-Potential Effect.** The shed vorticity strengths $\vec{\xi}$ from the blade trailing edges can be determined from Kelvin's theorem which requires that the total circulation of the fluid at any instant be conserved. This condition is transformed to

$$\int_{\delta\Omega}\vec{\xi}_bds+\int_{\Omega}\vec{\xi}dv=\text{constant}. \quad (4)$$

The shed vorticity $\vec{\xi}$ in Eq. (4) contains the vorticity from the potential effect and the viscous effect. The numerical implementation of Eq. (4) with the system of equations for $\vec{\xi}_b$ as described in Eqs. (1) and (3) is presented in Lee et al. [19] along with a cascade extension, where the shed vorticity from the potential effect, $\vec{\xi}_{\text{pot}}$, is calculated.

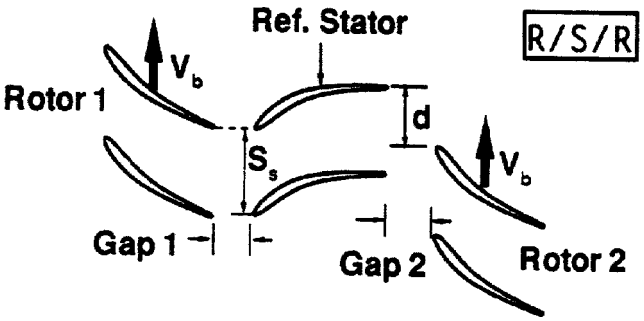


**Fig. 2 Definition for Gap 1, Gap 2, and indexing *d*/*S***

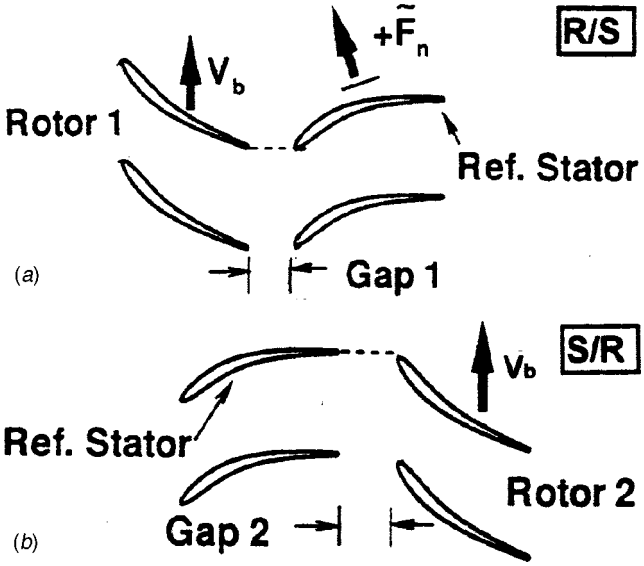


**Fig. 3 Configurations of R/S and S/R with the definition of the stator force**

**Blade Shed Vorticity System-Viscous Effect.** The viscous shear layers on both sides of the blades are also modeled in the present analysis. The additional vorticity generated from the viscous layers is related to the viscous boundary layers at the blade trailing edges.

$$\vec{\xi}_{\text{vis}}=\nabla\times\vec{V} \quad (5)$$

For a two-dimensional blade cross-section, Eq. (5) can be simplified as $\gamma=-\partial U(x,y)/\partial y$, where $U(x,y)$ is the blade wake defect velocity or the combined velocity profile from the two boundary layers on the blade pressure and suction sides. This viscous vorticity is only generated in a wake location close to the blade

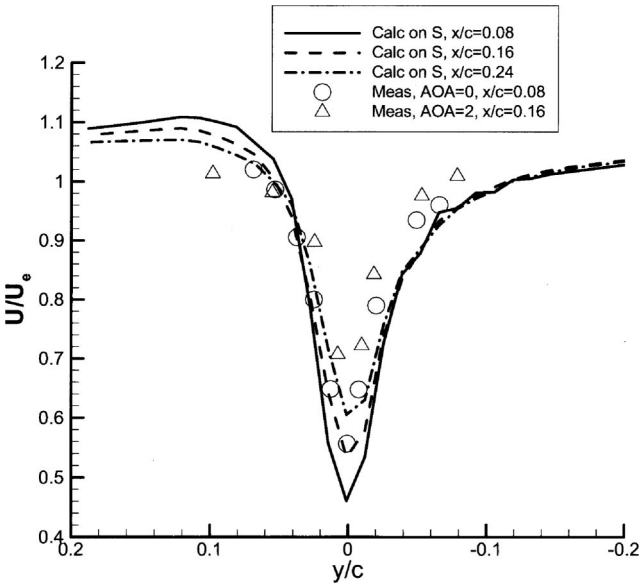


**Fig. 4 Comparison of blade wake velocities with the viscous wake vorticity (VWV) model**

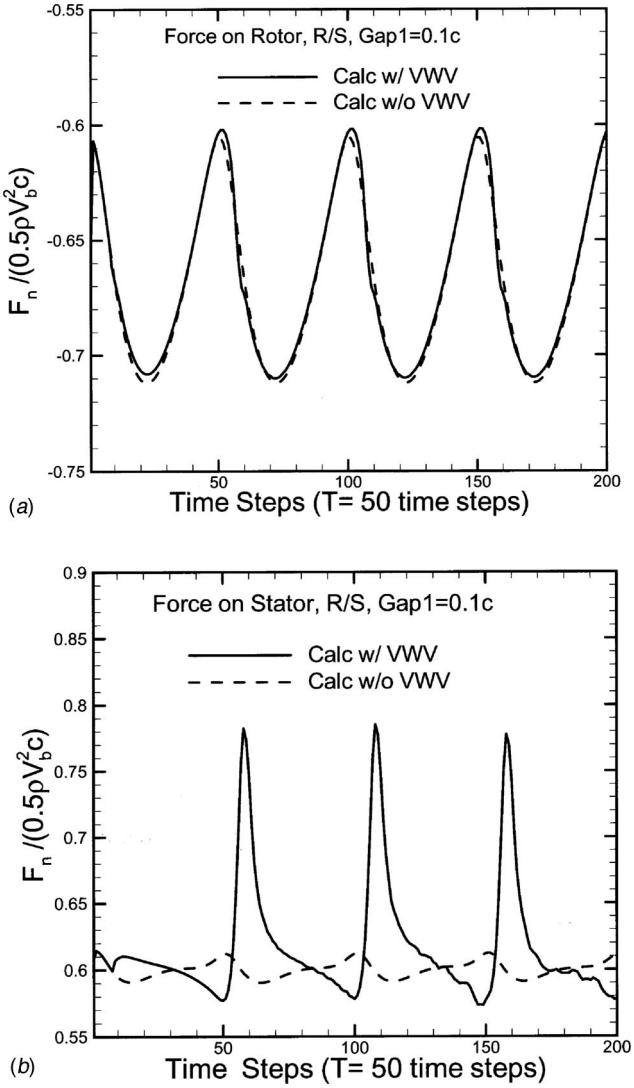


**Fig. 5 Normal forces on (*a*) the rotor; and (*b*) the stator for the R/S configuration with Gap1=0.1c**

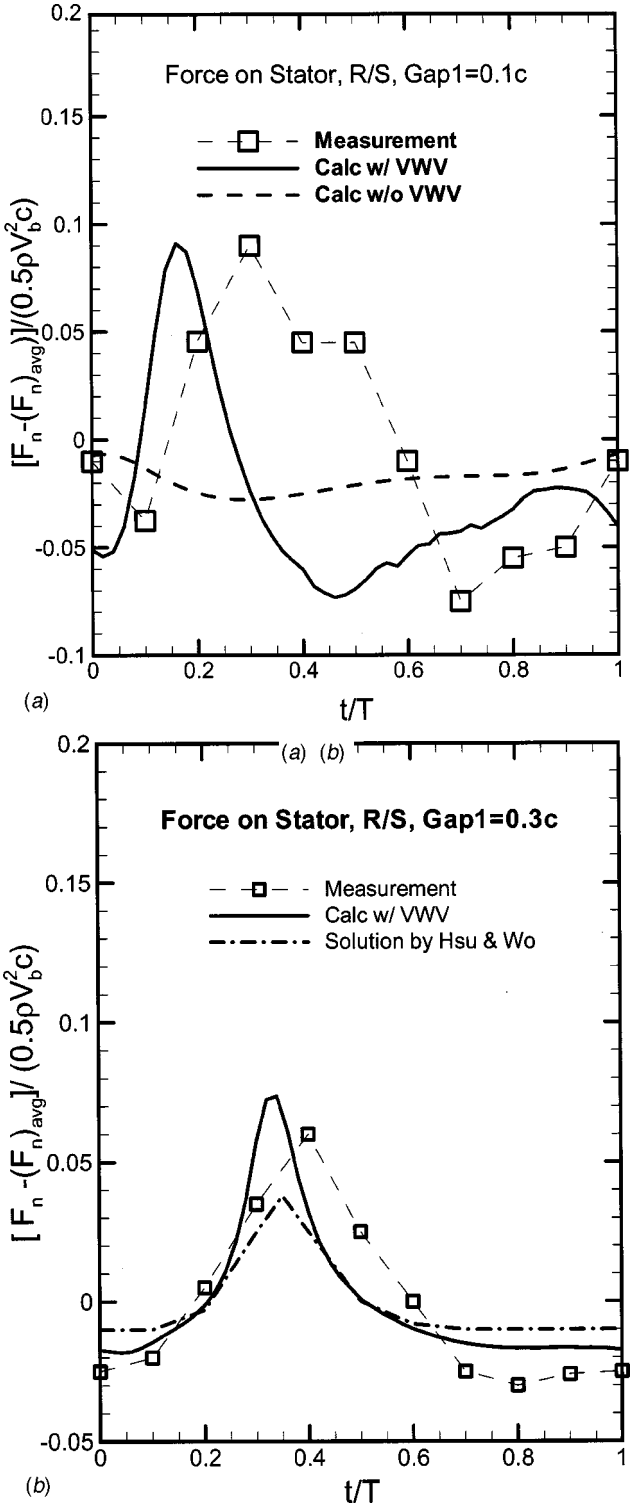


**Fig. 6 Comparison of unsteady forces on the stator under R/S configuration with Gap 1 of (*a*) 0.1c; and (*b*) 0.3c**

trailing edge and convected downstream with the blade wake while maintaining its strength. The wake defect velocity is formulated as

$$U(x,y)=U_e\left[1-\frac{U_e-U_c}{U_e}e^{-6(y/\delta)^2}\right] \tag{6}$$

where $U_e$ is the boundary layer edge velocity, $U_c$ the wake centerline velocity, and $\delta$ the wake shear layer thickness measured from the wake centerline. $\delta$ can be different for the upper and lower surfaces if the shear layers are asymmetric. The viscous shed vorticity is therefore represented as

$$\gamma=-\frac{12y}{\delta}D(U_e-U_c)e^{-6(y/\delta)^2}. \tag{7}$$

The damping factor $D$ in Eq. (7) is defined based on Raj and Lakshminarayana [20] as

$$D=1.25\sqrt{\frac{C_d}{(x/c+0.02)^{1-m}}} \tag{8}$$

where $c$ is the blade chord, $m$ relates to the pressure gradient at the trailing edge, and $C_d$ is the blade drag coefficient.

The viscous wake vorticity (VWV) obtained from Eqs. (5) through (8) is added to the shed vorticity obtained from the potential effect as

$$\vec{\xi}=\vec{\xi}_{\text{pot}}+\vec{\xi}_{\text{vis}}. \tag{9}$$

This total vorticity is applied in Eq. (4) to produce the total shed vorticity from the trailing edges.

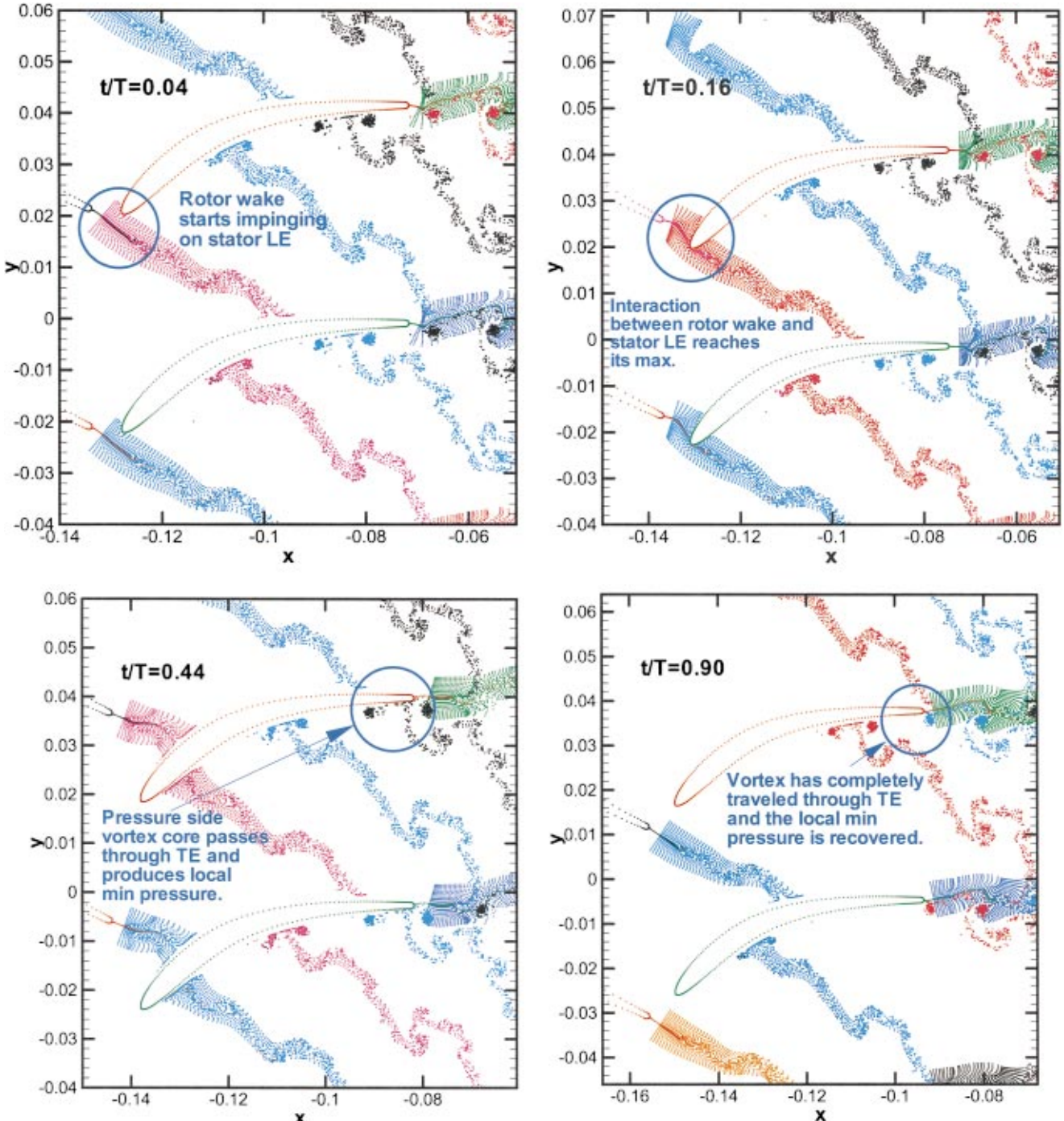


**Fig. 7 Patterns of vortex field for *t*/*T* at (*a*) 0.04; (*b*) 0.16; (*c*) 0.44; and (*d*) 0.90**

## Description of the Compressor and Test Data

The large-scale low-speed modern compressor used in this study was designed and tested by Hsu and Wo [17]. The compressor, as shown in **Fig. 1**, consists of three blade rows and an IGV far upstream for inflow conditioning. The compressor was designed to allow variable axial gaps, as shown in **Fig. 2**, between the first rotor and the stator (named Gap1) and between the stator and the second rotor (names Gap2). All blades have the same chord length *c* of 6 cm. The blade counts for rotors and stators are 58 and 60, respectively. The blade hub-to-tip ratio is 0.8 and the solidity ranges from 1.37 to 1.42. The comparisons between the predictions and the measurements are made at a near-design loading with a flow coefficient of 0.6 and a reduced frequency of 7.16. The test Mach number is 0.078 and the Reynolds number is $1.92\times10^5$ based on the rotor relative velocity and chord length.

The test data include unsteady pressures and forces acting on the stator for the rotor/stator (R/S), stator/rotor (S/R), and rotor/stator/rotor (R/S/R) test configurations as shown in **Figs. 2** and **3**. For the R/S configuration, the second rotor was removed. For the S/R configuration, the first rotor was installed two chord-length upstream of the stator. The forces presented in this paper are forces normal to the blade chord and normalized by the inflow dynamic pressure head.

## Compressor Predictions

This paper includes studies of blade interactions for two and three blade rows with the intention of understanding the physics of blade-row interaction and investigating the robustness of the present prediction scheme. First, the viscous wake vorticity (VWV) model is validated using a calculation on the stator alone. Then, blade interaction in the two-blade-row configurations, i.e., R/S and S/R, are examined. Finally, the three-blade-row configuration, i.e., R/S/R, is used to explore the indexing of two rotor blade rows, which produces the unsteady effect on all three blade rows. Since the blade count between the rotor and the stator is 58/60, all the calculations presented in this paper assume the rotors have the same pitch as the stator. All calculations were performed at midspan, where the experimental data were taken.

**Validation of the Viscous Wake Vorticity (VWV) Model** The implementation of the VWV model starts around $x/c=0.03$ in the blade near wake, where $(U_e-U_c)/U_e\approx 0.85$. For the controlled diffusion blades used by Hsu and Wo [17], it is estimated that $m\approx 0.12$, $C_d=0.02$ and $\delta/c\approx 0.07$ at a condition near to the experimental condition. Computed stator wake velocities based on the current VWV model at three axial locations are shown in **Fig. 4**. These velocity distributions are compared to measurements by Raj and Lakshminarayana [20] for a cascade similar to the present compressor. The wake velocity characteristics between the present compressor and the cascade used by Raj and Lakshminarayana [20] seem to be similar.

**Rotor-Stator (R/S) Calculation.** For the two-blade-row R/S configuration, two different sizes of Gap 1 (10% and 30% chord) were examined. The calculations converge in seven periods, i.e., about 350 time steps, to approach to a periodic condition. **Figure 5** demonstrates the normal forces acting on the rotor and the stator from the last 200 time steps for Gap1 = 0.1c. The results shown are based on the calculations with and without shedding the viscous wake vorticity (VWV). The VWV model has no impact on the upstream rotor, but it has a profound effect on the downstream stator. The peak force on the stator with the VWV model is about 30% larger than that without the VWV model.

**Figure 6** shows the unsteady forces on the stator for one complete period at both gap sizes. The unsteady force shown is the difference between the instantaneous force and the mean force. The present predictions with and without the VWV model are compared to the measurements for both gaps and also to the Navier Stokes solution obtained by Hsu and Wo [17]. The current calculations with the VWV model, when compared to the measured force, predict the magnitude of the peak force well, but the phase of the peak force is lagged. Note that the period $T$ for the present compressor covers 6° of tangential angle. However, the predicted phase of the peak force for Gap1 = 0.3c agrees well with Hsu and Wo's solution. The near peak force from the measurements persists for a longer time than that predicted by both the current method and by Hsu and Wo [17]. However, the differences between the peak phases in **Figs. 6**(***a***) and **6**(***b***) for the predictions and the measurments correspond to the times for the vorticity traveling an extra distance (0.2c) for the larger spacing. This difference is $0.18T$ for the prediction and $0.1T$ for the experiment from **Fig. 6** as compared to $0.17T$ estimated from the measured rotor exit flow angle when the stator blades cutting through the rotor mean wake. From the sparseness of the measured points for a complete $T$ in **Fig. 6** and the above comparison, the uncertainity of the measured peaks could reach to $\pm 0.1T$.

**Figure 7** shows the rotor shed vorticity interacting with the stator blades and their shed vorticity for the Gap1 = 0.1c case at the instants of $t/T=0.04$, 0.16, 0.44, and 0.90. Note that **Fig. 7** shows only the locations of all the generated and convected vorticity at four instants. The predicted instantaneous pressure distributions on the downstream stator blade associated with these four instants are plotted in **Fig. 8**. The integrated forces from these pressure profiles was given previously in **Fig. 6**(***a***). The rotor

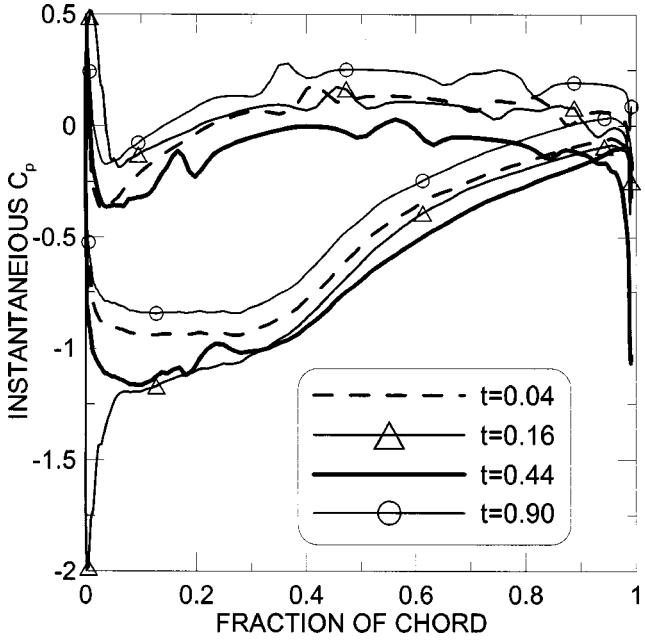


**Fig. 8 Instantaneous pressure distributions around the stator blade at four instants shown in Fig. 7**

blade trailing edges shown in **Fig. 7** move in the positive y direction. Each blade of the rotor and stator rows sheds both the potential ($\vec{\xi}_{\text{pot}}$) and the viscous ($\vec{\xi}_{\text{vis}}$) vorticity. These vorticity are convected based on Eq. (2). The maximum stator force occurring at $t/T=0.16$ (**Fig. 6**(***a***)) corresponds to the core of the rotor shed vorticity impinging on the leading edges of the stator blades as shown in **Fig. 7**(***b***). This rotor wake/stator leading edge interaction causes the effective flow incidence angle on the stator blade to change drastically and produces the leading-edge pressure peaks seen in **Fig. 8**. The minimum stator force occurring at $t/T=0.44$ (**Fig. 6**(***a***)) when the instantaneous pressure on the pressure side reaches a minimum shown in **Fig. 8**. This happens as the pressure-side vorticity moves off of the trailing edge and produces lower pressure on the pressure side than on the suction side. This negative effect on the stator normal force generation is gradually released after the pressure-side vorticity travels into the stator wake. The stator force reaches its second peak at $t/T=0.9$ (**Fig. 6**(***a***)) when the convected rotor wake sweeps past the stator trailing edge shown in **Fig. 7**(***d***).

**Stator-Rotor (S/R) Calculation.** The S/R configuration required a more elaborate analysis than the R/S configuration. As indicated earlier, the stator force was measured with the first rotor installed two chord lengths upstream of the stator. Hsu and Wo [17] assumed the rotor was far enough upstream to have a minimum effect on the stator. In order to test the validity of this assumption, two simulations of the S/R configuration were performed: one using only the stator and the second rotor (here, called the S/R case), and another using the experimental configuration with the first rotor located two chord lengths upstream of the stator (called the R/S/R-G1 = 2c case). In both cases, Gap2 = 0.1c and predictions were made both with and without the VWV model.

**Figure 9** shows the predicted normal forces acting on the stator and the rotor for the S/R case (no upstream rotor). The prediction results are similar to the prediction for the R/S configuration. The predicted force on the first blade row (stator) is not affected by the VWV model. The VWV model, however, has significant impact on the second blade row (rotor). The minimum rotor force is 25% lower than the average force obtained without the VWV model. **Figure 10** compares predicted forces of the unsteady component

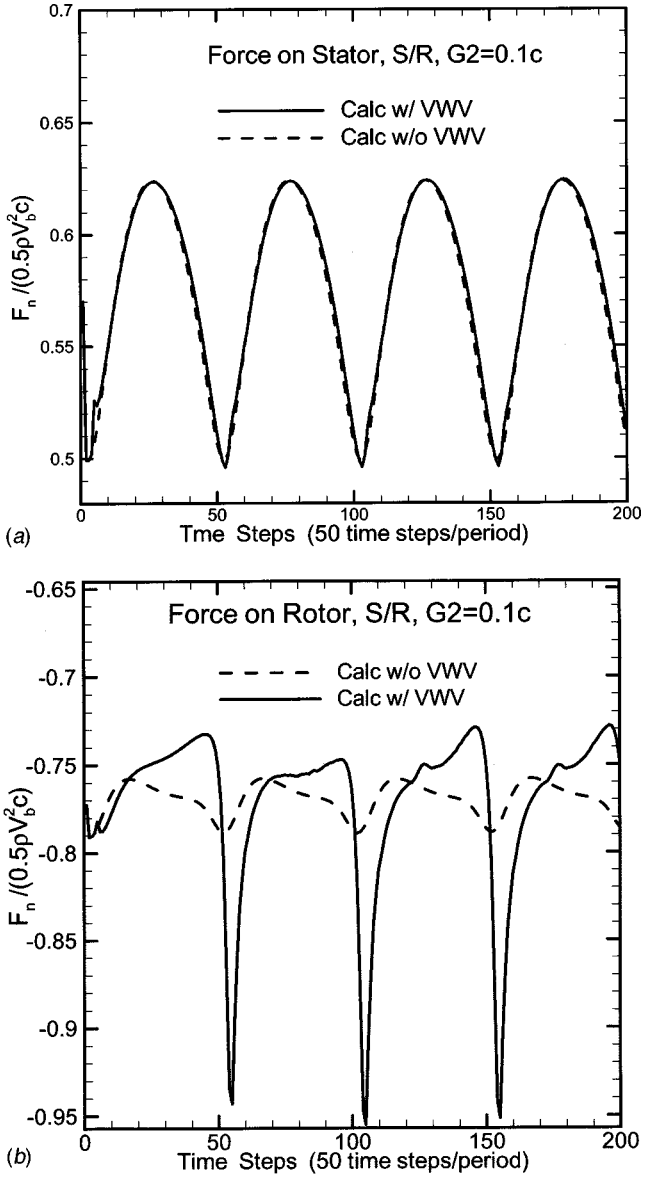


**Fig. 9 Normal forces on (*a*) the stator; and (*b*) the rotor for the S/R configuration with Gap2 = 0.1c**

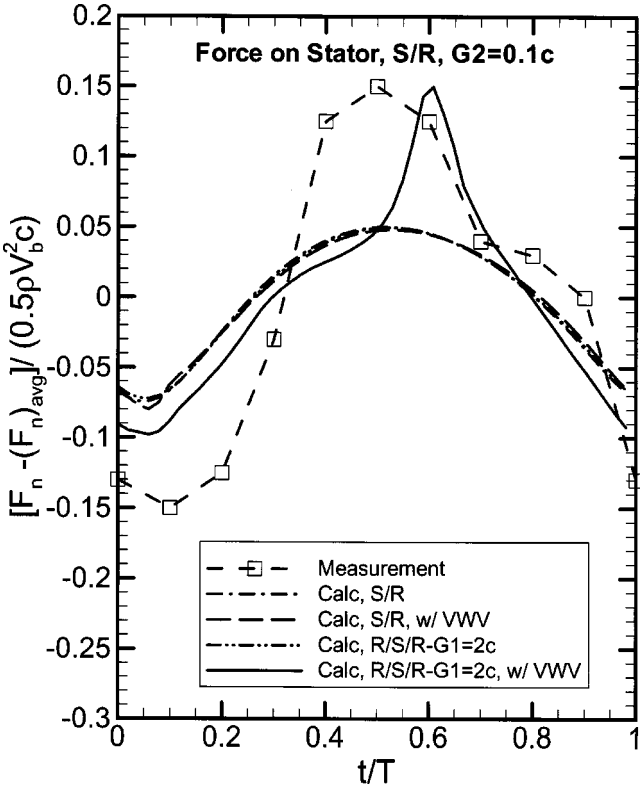


**Fig. 10 Comparison of unsteady forces on the stator under S/R configuration with Gap1 = 0.1c**

on the stator from the S/R case, the R/S/R-G1 = 2c case, and the measurements. Results from the R/S/R-G1 = 2c case agree much better with the measurements than those from the S/R case, particularly the peak-to-peak value. This suggests that the unsteady influence of the upstream rotor, although it is two chord lengths away, still exists.

**Rotor-Stator-Rotor (R1/S/R2) Calculation.** Calculations for the three-blade-row (R1/S/R2) configuration with various values for Gap1 and Gap2 were used to investigate the indexing between two rotors. The rotor indexing is represented by the parameter $d/S_s$ shown in **Fig. 2**.

First, a calculation was performed with Gap1 = Gap2 = 0.1c and $d/S_s = 0$. **Figure 11** compares the measured time-averaged pressure distributions on the stator with the predicted distributions with and without the VWV model. Although the current predictions overpredict the trailing-edge pressure, the loading curve from the measurement is similar to the predicted loading curves. The negligible difference between the two predicted curves demonstrates that the wake interaction with both potential and viscous effects has a minimum effect on the predicted mean pressures.

**Figures 12** and **13** show the impact of rotor indexing on the forces acting on the first rotor (R1), the stator (S) and the second rotor (R2). **Figure 12** shows the average force acting on each blade (average over one rotor period) as a function of indexing. Note that forces acting on R1 and R2 are opposite to those acting on S. **Figure 13** shows the difference between the minimum and maximum forces acting on each blade during the rotor period in response to the rotor indexing conditions shown in **Fig. 12**. **Figures 12**(*a*) and **13**(*a*) demonstrate the predicted forces for a con-

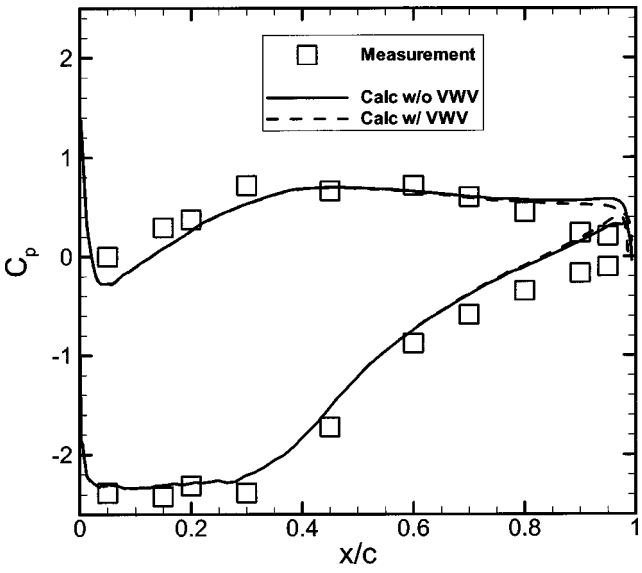


**Fig. 11 Averaged pressure distributions on the stator under R1/S/R2 with Gap1 = Gap2 = 0.1c and $d/S_s = 0$**

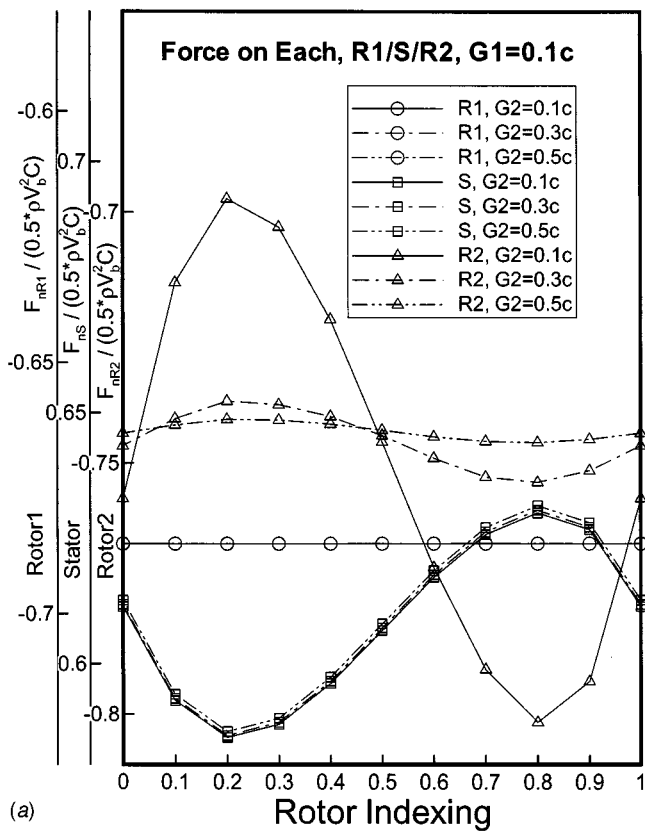


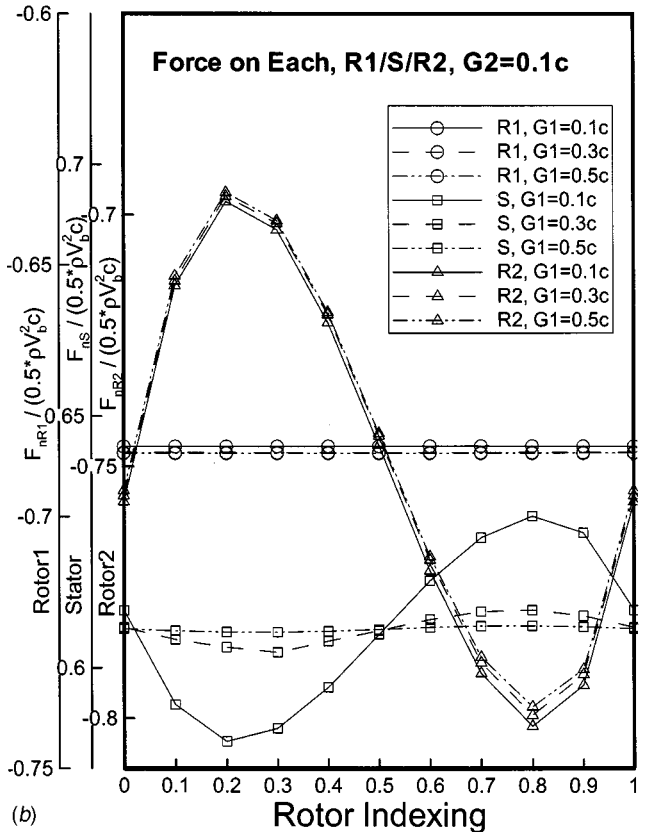


**Fig. 12 Averaged normal forces on R1, S, and R2 for the rotor indexing with (*a*) Gap1=0.1c; and (*b*) Gap2=0.1c**

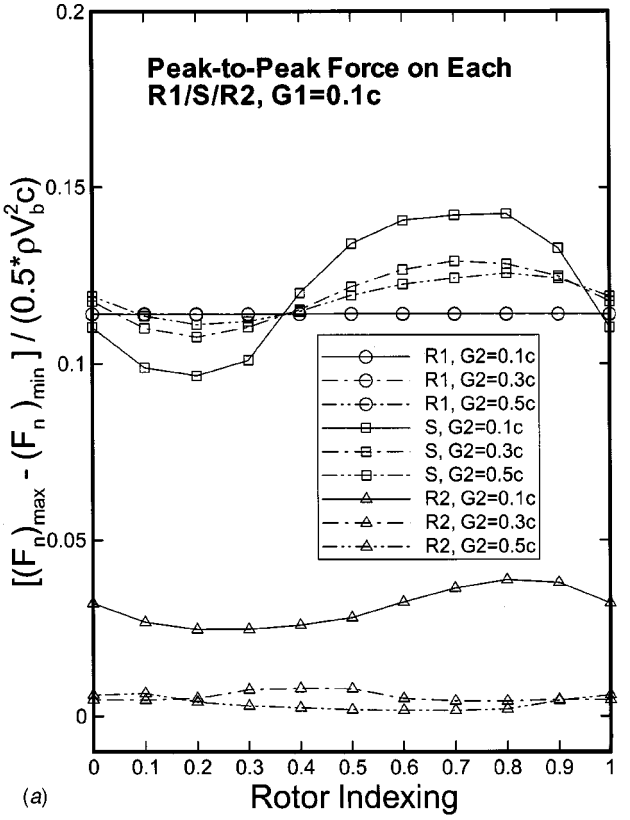


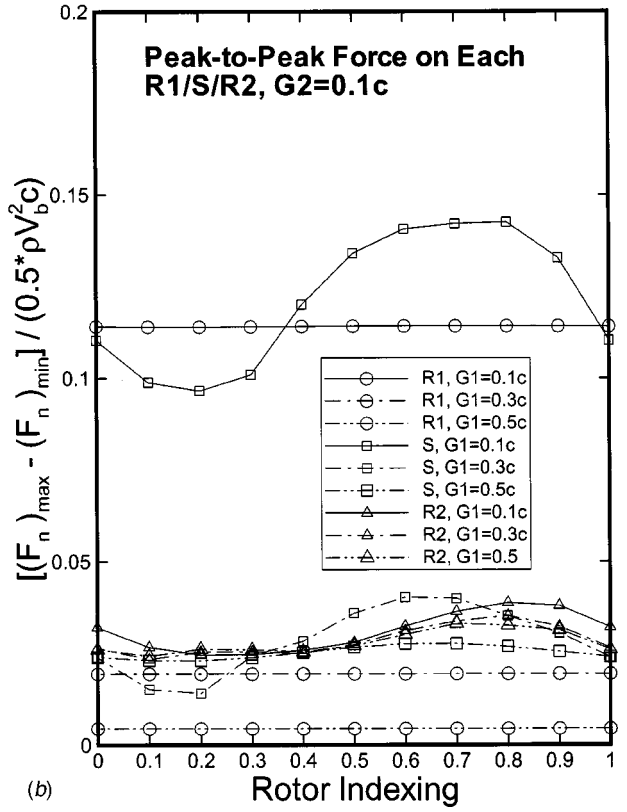


**Fig. 13 Instantaneous minimum-to-maximum normal forces on R1, S, and R2 for rotor indexing with (*a*) Gap1=0.1c; (*b*) Gap2=0.1c**

stant Gap1 size of 0.1c and a varying Gap2 size of 0.1c, 0.3c or 0.5c. **Figures 12(*b*)** and **13(*b*)** show the similar results for a constant Gap2 size of 0.1c and a varying Gap1 size of 0.1c, 0.3c or 0.5c. All calculations use the VWV model. These solutions were obtained using computational CPUs of two orders of magnitude less than those obtained from solving the unsteady Reynolds-averaged Navier-Stokes equations.

The unsteady force on R1 is affected by the changes of Gap1 (**Figs. 12(*b*)** and **13(*b*)**), but the changes in Gap2 and the rotor indexing have no effect on R1 (**Figs. 12(*a*)** and **13(*a*)**. Both the unsteady peak-to-peak (**Fig. 13(*b*)**) and average (**Fig. 12(*b*)**) forces on S vary with Gap1. As Gap1 increases from 0.1c to 0.5c, the peak-to-peak variation of the average stator force in response to the rotor indexing decreases from 0.05 to nearly zero (**Fig. 12(*b*)**). With Gap1 constant, the variation of Gap2 has a minimum effect on the stator average force (**Fig. 12(*a*)**) although the peak-to-peak unsteady force still varies with the change of Gap2 (**Fig. 13(*a*)**). Overall, the unsteady peak-to-peak force on R1 and S amounts to 10–15% of inflow dynamic head for Gap1 = 0.1c. For the larger values of Gap1 and all values of Gap2 investigated, the unsteady forces on all three blade rows are below 5% of the inflow dynamic head. However, the variation of unsteady peak-to-peak forces acting on S at G1 = 0.1c between the minimum and the maximum due to the rotor indexing accounts for 42% of the averaged unsteady peak-to-peak force (**Fig. 13**). Both **Figs. 12(*a*)** and **12(*b*)** indicate the average stator force is minimum at $d/S_S = 0.2$ and maximum at $d/S_S = 0.8$. This phenomenon agrees with the stator unsteady peak-to-peak forces shown in **Figs. 13(*a*)** and **13(*b*)** and is similar to the experimental finding of Hsu and Wo [17]. The average force on R2 varies with changes in Gap2 (**Fig. 12(*a*)**), but not with changes in Gap1 (**Fig. 12(*b*)**). Although the variation of unsteady peak-to-peak force on R2 due to rotor indexing is less than 5% (**Fig. 13**), the variation of unsteady force acting on R2 at G2 = 0.1c accounts for 50% of the averaged unsteady force. Also the force on R2 is similar to that on S and has a minimum force at $d/S_S = 0.2$ and a maximum force at $d/S_S = 0.8$.

## Conclusions

An efficient time-accurate vortex calculation method for multiple-blade-row turbomachinery is developed and validated for predictions of flow-induced unsteady forces on blades due to blade-row interaction. The blade shed vorticity is convected based on a Lagrangian tracking method. The current viscous wake vorticity (VWV) model is validated for flow fields near design operation. The computational method developed does not need complex volume grids, which many other CFD approaches depend on. The current solution does not have problems associated with numerical wake diffusion and blade-row interface interpolation. The computations presented for the current low-speed compressor suggest the following conclusions:

- The current VWV model accounts for 30% of the stator maximum force for the rotor/stator (R/S) configuration and 25% of the rotor minimum force for the stator/rotor (S/R) configuration.
- Vorticity impinging on the blade leading edges produces leading-edge suction and pressure peaks and a maximum instantaneous loading on the blades. On the other hand, vorticity leaving the pressure-surface trailing edges produces an opposite effect and therefore a minimum loading.
- The present method predicts the magnitude of the instantaneous forces well. However, for the two Gap1 sizes in the R/S configuration, the phases of both the current predictions and Hsu and Wo's Navier Stokes solution are off by 10% to 15% of the blade pitch. This difference may be attributed to the measurement uncertainty of the peak unsteady force.
- The S/R calculations show that unsteady blade-row interactions exist even for axial blade row spacing of up to two chord lengths.
- Changes in Gap1 of the R1/S/R2 configuration have a large effect on the instantaneous forces on both R1 and S, but on the average force on S only. Similarly changes in Gap2 have a big influence on the instantaneous forces on both S and R2, but the average force on R2 only.
- The unsteady peak-to-peak force accounts for 10–15% of inflow dynamic head for R1 and S with Gap1 = 0.1c of the R1/S/R2 configuration. This unsteady force reduces to a maximum of only 5% on all blades for larger values of Gap1 and all values of Gap2 studied.
- The rotor indexing on the rotor/stator/rotor (R1/S/R2) configuration has no effect on R1. Both S and R2 have a minimum unsteady and average force at a rotor indexing of $d/S_S = 0.2$, and a maximum at $d/S_S = 0.8$. The minmum-to-maximum variation of unsteady peak-to-peak forces on S or R2 at either G1 = 0.1c or G2 = 0.1c can account for 40–50% of the averaged unsteady peak-to-peak force. This feature is confirmed through Hsu and Wo's measurement. In addition, the unsteady viscous effect has a little effect on the blade mean pressure distribution.


## Acknowledgments

This work was sponsored by the Office of Naval Research (Program Element PE602121) under the Machinery Systems Task and the Hydroacoustics Task. The program monitors are LCDR F. Novak and Dr. L. Patrick Purtell. The authors are indebted to Prof. A. Wo for providing the compressor data. This work was initiated when Dr. J. Feng was employed at the Pennsylvania State University. Mr. J. D. Chen of the Pennsylvania State University contributed in the initial stage of the work presented here.


## Nomenclature

AOA = angle of attack
$b$ = blade
$c$ = blade chord
$C_d$ = blade drag coefficient used in Eq. (8), [20]
$C_p$ = static pressure coefficient, (pressure-reference pressure)/$0.5\rho V_b^2$
$D$ = damping factor, defined in Eq. (8)
$F_n$ = force normal to blade chord, defined in Fig. 3
G1,G2 = gap1 and gap2, defined in Fig. 3
$G$ = Green's function used in Eq. (1)
$m$ = parameter related to trailing-edge pressure gradient, used in Eq. (8), [20]
$\vec{n}$ = unit surface normal vector
$s$ = surface integration, used in Eq. (1)
$S_S$ = blade pitch
$t$ = time
$T$ = period
$\vec{u}$ = velocity vector
$\vec{u}_b, V_b$ = blade moving velocity
$u_n$ = velocity normal to surface
$U$ = wake velocity
$U_c$ = wake centerline velocity
$U_e$ = boundary layer edge velocity
$v$ = volume integration, defined in Eq. (1)
VWV = viscous wake vorticity
$\vec{V}$ = velocity associated with VWV
$x$ = axial coordinate
$y$ = local coordinate normal to streamline direction
$\delta$ = wake thickness
$\delta\Omega$ = blade boundary surface
$\Omega$ = volumetric flow domain
$\gamma$ = third component of $\vec{\xi}$, defined in Eq. (7)
$\rho$ = density

$\vec{\xi}$ = shed vorticity
$\vec{\xi}_b$ = blade surface vorticity
$\vec{\xi}_{\text{pot}}$ = shed vorticity due to potential effect
$\vec{\xi}_{\text{vis}}$ = shed vorticity due to viscous effect

## References


[1] Rai, M. M., 1987, ''Navier-Stokes Simulations of Rotor/Stator Interaction Using Patched and Overlaid Grids,'' J. Propul. Power, **3**(5), pp. 387–396.
[2] Rai, K. V., and Delaney, R. A., 1992, ''Investigation of Unsteady Flow Through a Transonic Turbine Stage, Part I, Analysis,'' AIAA Paper No. 90-2408.
[3] Giles, M., and Haimes, R., 1993, ''Validation of a Numerical Method for Unsteady Flow Calculation,'' ASME J. Turbomach., **115**, pp. 110–117.
[4] Ho, Y. H., and Lakshminarayana, B., 1996, ''Computational Modeling of Three-Dimensional Flow Through a Turbine Rotor Cascade With Strong Secondary Flows,'' ASME J. Turbomach., **118**, pp. 250–261.
[5] Arnone, A., and Pacciani, R., 1996, ''Rotor-Stator Interaction Analysis Using the Navier-Stokes Equations and a Multigrid Method,'' ASME J. Turbomach., **118**, pp. 679–689.
[6] Goldstein, M. E., and Atassi, H., 1976, ''A Complete Second-Order Theory for the Unsteady Flow About an Aiorfoil due to Periodic Gust,'' J. Fluid Mech., **74**, Part 4, pp. 741–765.
[7] Goldstein, M. E., 1978, ''Unsteady Vortical and Entropic Distortions of Potential Flows Round Arbitrary Obstacles,'' J. Fluid Mech., **89**, Part 3, pp. 433–468.
[8] Gallus, H. E., Groillus, H., and Lambertz, J., 1982, ''The Influence of Blade Number Ratio and Blade Row Spacing on Axial-Flow Compressor Stator Dynamic Load and Stage Sound Pressure Level,'' ASME J. Eng. Power, **104**, pp. 633–644.
[9] Henderson, G., and Fleeter, S., 1993, ''Forcing Function Effects on Unsteady Aerodynamic Gust Response: Part 1—Forcing Function,'' ASME J. Turbomach., **115**, pp. 741–750.
[10] Henderson, G., and Fleeter, S., 1993, ''Forcing Function Effects on Unsteady Aerodynamic Gust Response: Part 2—Low Solidity Airfoil Row Response,'' ASME J. Turbomach., **115**, pp. 751–761.
[11] Feiereisen, J. M., Montgomery, M. D., and Fleeter, S., 1994, ''Unsteady Aerodynamic Forcing Functions: A Comparison Between Linear Theory and Experiment,'' ASME Paper 93-GT-141.
[12] Weaver, M. M., and Fleeter, S., 1994, ''Turbine Rotor Generated Forcing Functions for Flow Induced Vibrations,'' ASME Paper 94-GT-328.
[13] Manwaring, S. R., and Wisler, D. C., 1993, ''Unsteady Aerodynamics and Gust Response in Compressors and Turbines,'' ASME J. Turbomach., **115**, pp. 724–740.
[14] Chung, M. H., and Wo, A. M., 1997, ''Navier-Stokes and Potential Calculations of Axial Spacing Effect on Vortical and Potential Disturbance and Gust Response in an Axial Compressor,'' ASME J. Turbomach., **119**, pp. 472–481.
[15] Valkov, T., and Tan, C. S., 1995, ''Control of The Unsteady Flow In A Stator Blade Row Interacting With Upstream Moving Wakes,'' ASME J. Turbomach., **117**, pp. 97–105.
[16] Capece, V. R., and Fleeter, S., 1989, ''Experimental Investigation of Multistage Interaction Guest Aerodynamics,'' ASME J. Turbomach., **111**, pp. 409–417.
[17] Hsu, S. T., and Wo, A. M., 1998, ''Reduction of Unsteady Blade Loading by Beneficial Use of Vortical and Potential Disturbances in an Axial Compressor with Rotor Clocking,'' ASME J. Turbomach., **120**, pp. 705–713.
[18] Lee, Y. T., Bein, T. W., Feng, J., and Merkle, C. L., 1993, ''Unsteady Rotor Dynamics in Cascade,'' ASME J. Turbomach., **115**, pp. 85–93.
[19] Lee, Y. T., Feng, J., and Merkle, C. L., 1994, ''Time-Dependent Inviscid Flow Analysis of Rotor-Stator System,'' *Proceedings of the Sixth International Conference on Numerical Ship Hydrodynamics*, Washington, DC.
[20] Raj, R., and Lakshminarayana, B., 1973, ''Characteristics of the Wake Behind a Cascade of Airfoils,'' J. Fluid Mech., **61**, Part 4, pp. 707–730.

# Detailed Flow Study of Mach Number 1.6 High Transonic Flow With a Shock Wave in a Pressure Ratio 11 Centrifugal Compressor Impeller

**Hirotaka Higashimori**
Mitsubishi Heavy Industries, Ltd., Nagasaki R&D Center, 5-717-1 Fukahori-Machi, Nagasaki 851-0392, Japan

**Kiyoshi Hasagawa**
Mitsubishi Heavy Industries, Ltd., Nagoya Guidance & Propulsion Systems Works, 1200 Higashi-Tanaka, Komaki, Aichi 485-8561,Japan

**Kunio Sumida**

**Tooru Suita**

Mitsubishi Heavy Industries, Ltd., Nagasaki R&D Center, 5-717-1 Fukahori-Machi, Nagasaki 851-0392, Japan

*Requirements for aeronautical gas turbine engines for helicopters include small size, low weight, high output, and low fuel consumption. In order to achieve these requirements, development work has been carried out on high efficiency and high pressure ratio compressors. As a result, we have developed a single stage centrifugal compressor with a pressure ratio of 11 for a 1000 shp class gas turbine. The centrifugal compressor is a high transonic compressor with an inlet Mach number of about 1.6. In high inlet Mach number compressors, the flow distortion due to the shock wave and the shock boundary layer interaction must have a large effect on the flow in the inducer. In order to ensure the reliability of aerodynamic design technology, the actual supersonic flow phenomena with a shock wave must be ascertained using measurement and Computational Fluid Dynamics (CFD). This report presents the measured results of the high transonic flow at the impeller inlet using Laser Doppler Velocimeter (LDV) and verification of CFD, with respect to the high transonic flow velocity distribution, pressure distribution, and shock boundary layer interaction at the inducer. The impeller inlet tangential velocity is about 460 m/s and the relative Mach number reaches about 1.6. Using a LDV, about 500 m/s relative velocity was measured preceding a steep deceleration of velocity. The following steep deceleration of velocity at the middle of blade pitch clarified the cause as being the pressure rise of a shock wave, through comparison with CFD as well as comparison with the pressure distribution measured using a high frequency pressure transducer. Furthermore, a reverse flow is measured in the vicinity of casing surface. It was clarified by comparison with CFD that the reverse flow is caused by the shock-boundary layer interaction. Generally CFD shows good agreement with the measured velocity distribution at the inducer and splitter inlet, except in the vicinity of the casing surface.* [DOI: 10.1115/1.1791645]

## Introduction

Extensive research has been carried out regarding the internal flow of high pressure ratio centrifugal compressors applied to small gas turbines and industrial compressors. In particular, the actual flow measurement using laser velocimeters and the Computational Fluid Dynamics (CFD) verification have been carried out with respect to the shock wave in the impeller inlet portion, as well as the low energy region in the vicinity of the shroud casing, wake, and jet at the impeller outlet.

Regarding the impeller outlet flow pattern, the jet and wake of a radial impeller with a pressure ratio of 2.1 were measured using Laser 2 Focus Velocimeter (L2F) by D. Eckardt [1]. Smoothing of the jet and wake in a backswept impeller with a pressure ratio of 4 was measured using L2F by H. Krain [2], and estimation using a three-dimensional (3D) viscous code was carried out by C. Hah [3]. Regarding the impeller inlet transonic flow, the pressure distribution of the shock wave in the inducer of a radial impeller with a pressure ratio of 10 was measured by Y. Senoo et al. [4], and flow patterns were measured using L2F by H. Hayami et al. [5]. Furthermore, the transonic flow of a backswept impeller with a pressure ratio 6.1 having a Mach number 1.3 with a shock wave was measured by H. Krain et al. [6,7], and estimation using a 3D viscous code was carried out by C. Hah and H. Krain [8].

The present authors also investigated the internal flow of centrifugal compressors, measuring the actual flow in certain impellers and verifying CFD in order to improve centrifugal compressor performance for small gas turbines and turbochargers. (LDV) measurement and CFD verification have been conducted for ''a subsonic impeller'' [9,10], and LDV measurement, pressure distribution measurement, and CFD verifications were carried out for ''a low transonic impeller'' [11].

Here, we report on ''the high transonic flow of a Mach number of about 1.6 at the inducer'' of a centrifugal compressor having a pressure ratio of 11, for practical application in an aeronautical gas turbine.

## Test Facility

Figure 1 shows the test impeller. A double splitter type backswept impeller design was adopted to decrease blade loading and to increase the impeller choke flow rate. Figures 2, 3 and Table 1 show the high pressure ratio centrifugal compressor test facility, compressor characteristics, and compressor and impeller specifications respectively. The tangential velocity of the impeller outlet is about 680 m/s, the inlet tangential velocity is about 460 m/s, and the machine Mach number reaches about 1.35. The blade tip clearance is about 0.2 mm. The impeller outlet absolute velocity is supersonic, and the Mach number is about 1.2. A radial channel

Contributed by the International Gas Turbine Institute (IGTI) of THE AMERICAN SOCIETY OF MECHANICAL ENGINEERS for publication in the ASME JOURNAL OF TURBOMACHINERY. Paper presented at the International Gas Turbine and Aeroengine Congress and Exhibition, Vienna, Austria, June 13-17, 2004, Paper No. 2004-GT-53435. Manuscript received by IGTI, October 1, 2003; final revision, March 1, 2004. IGTI Review Chair: A. J. Strazisar.

  

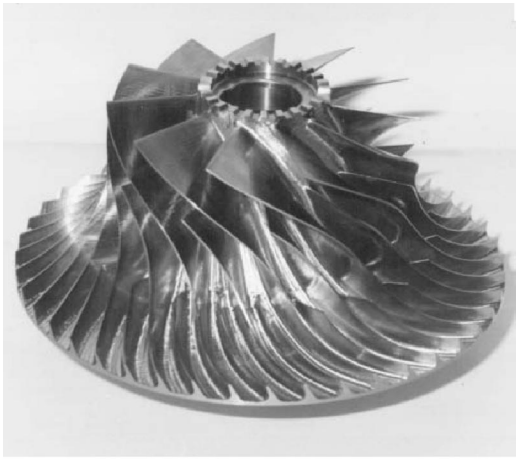

**Fig. 1 High transonic impeller**

diffuser is attached. A passage downstream of the diffuser is configured in the axial direction, with an axial vane diffuser and a corrector as shown in Fig. 2.

Regarding the compressor characteristics, the pressure ratio is 11 at a mass flow rate of 3.3 kg/s. The point just below the choke flow rate is the point of maximum efficiency. Both impeller efficiency and diffuser pressure recovery reach their maximum at this point, and LDV measurement was conducted at this operating point.

Table 2 shows specifications of the LDV system. The two component velocities are measured using a two color system. All of the effective data detected by LDV can be processed using a system that records LDV measurement data and the phase of revolution. The LDV measurement results shown in Figs. 5 and 8–10 are the average values of data detected in each section, corresponding to 1/80 of the blade pitch. The detected data number for each point is about 1000.

Table 3 shows the specifications of the pressure transducer. The sampling rate is 1 MHz, and 106 data points per pitch can be obtained. The pressure wave shown in Fig. 10 is the instantaneous data of two pitches, and the wave pattern is nearly the same for every pitch at the operating point. As the measured pressure data with 1 MHz sampling oscillate alternately, the mean values of the next 2 points are expressed. Considering that the natural frequency of the pressure transducer is 600 kHz, the resolution of pressure data is finer than 1/10 of the blade pitch. The absolute value of the pressure wave shown in the figure is composed of the fluctuation component detected by the pressure transducer and data from the static pressure tap.

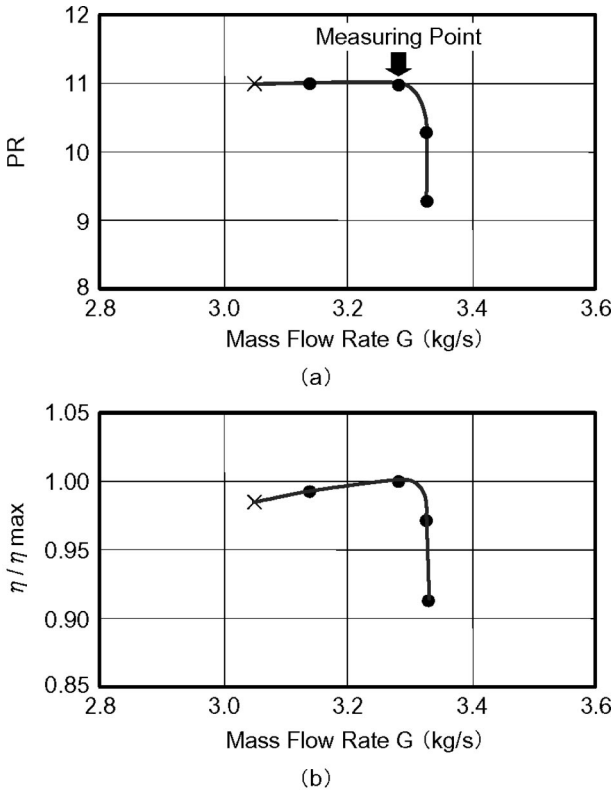


**Fig. 3 Compressor characteristics: (a) pressure ratio, (b) efficiency ratio maximum efficiency**

Figure 4 shows the arrangement of the LDV and pressure transducer measuring sections. LDV measurement was conducted for three Sections II, III, and IV. Section II is positioned so that the center of the throat can be measured, so as to determine the existence of the shock wave. Section III is positioned where the results of the shock-boundary layer interaction on the suction surface can be measured. Section IV is placed downstream from the first splitter leading edge so as to ascertain the low energy region

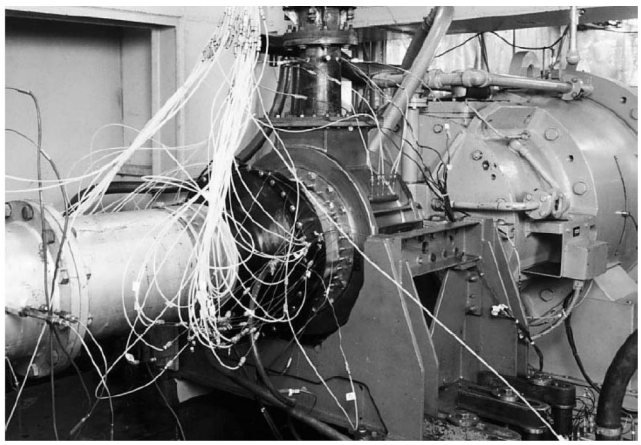

**Fig. 2 High pressure ratio compressor test facility**

Table 1 Specification of compressor and impeller

| | |
|---|---|
| Pressure Ratio | 11 |
| Mass Flow Ratio | 3.3 kg/s |
| Peripheral Velocity | 680m/s approx. |
| Blade Number | 11+11+22 (Double Splitter) |
| Inlet Diameter | 168 mm |

Table 2 Specification of LDV

| | |
|---|---|
| Focal Length | 600 mm |
| Signal Processor | BSA<br>2 Color, 4 Beam |
| Laser Power | 5 W Argon Laser |

Table 3 Specification of pressure transducer

| | |
|---|---|
| Pressure Transducer | $f_0$ = 600kHz<br>$\Delta P$ = 350kPa(FS)<br>Diameter = 1.52mm(3.2% pitch) |
| Amplifier | f = 1MHz |
| Data Recorder | f = 1MHz ( $\Delta t = 1\,\mu s$) |

extending on the shroud casing. The pitch of the pressure transducer is set to 4 mm in order to display the throat pressure distribution with five sections.

## Results of LDV Measurement

Figure 5 shows a three-dimensional image of the relative velocity on the three sections. A value of about 500 m/s was measured on the suction side near casing in Sec. II. At 6 mm from the casing surface, deceleration considered to be due to the shock wave is observed at the middle of the blade pitch. The measurement location 6 mm from casing is about 90% of the span. The relative velocity distortion expands at the position of the shock wave at 3 mm from the casing. In contrast to the fact that the slight influence of the shock wave remains even at 10 mm from casing, the relative velocity shows a potential type distribution in which deceleration occurs continuously from the suction surface toward the pressure surface.

In Sec. III, 3 mm from the casing, distortion of the velocity distribution estimated by the influence of the upstream distortion is seen. Figure 6(*b*) shows the Mach number contour in the vicinity of the casing in the inducer. The boundary layer on the suction surface tends to thicken because of shock boundary layer interaction on the suction surface, but this tendency cannot be seen in the measured velocity distribution. Regarding Sec. IV, the obvious distortion known as the ''low energy region'' at the corner of the casing and suction surface is also not detected. A detailed comparison between the LDV and CFD results is shown below.

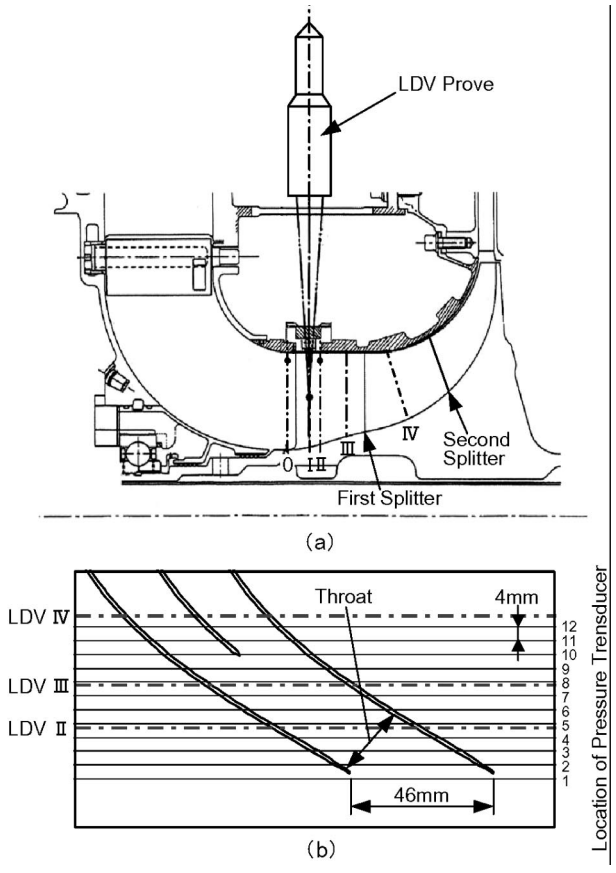


**Fig. 4 Cross section of compressor and location of LDV and pressure transducer: (a) LDV measuring section, (b) Pressure transducer and LDV window arrangement**

## Results of CFD

Figure 6 shows a computational grid and the relative Mach number contours of the two-stream surface about 3 and 1.5 mm from the casing. The numerical method is a modified Dawes's BtoB3D code for a double splitter impeller. The grid size is 60 $\times$133$\times$35 with 279 300 nodes. The clearance is about 0.3% of the blade height at the leading edge, and is expressed using four meshes. The upstream Mach number of the impeller leading edge is about 1.6. The oblique shock appears from the leading edge toward the suction side, and the passage shock appears across the throat.

Figure 7 shows the Mach number contour on each of the LDV measuring sections. In Sec. II, a high Mach number of about 1.5 appears at the corner of the suction side and casing. The Mach number decreases steeply toward the pitch of about 0.4, increases slightly and then decreases toward the pressure surface. The Mach number following the steep decrease appears to be about 1. Thus, the steep decrease of the Mach number seems to be an oblique shock wave. In Secs. III and IV, the boundary layer thickness increases at the suction side and casing corner, developing into the low energy region in Sec. IV.

## Comparison Between LDV and CFD

**A Section II.** Figure 8 shows a comparison between the LDV measurement results and the CFD results for Sec. II. The relative velocity is composed of the meridional velocity and the tangential velocity. The solid line corresponds to CFD, while the dotted line indicates the LDV results.

Regarding the velocity distribution at 6 mm from the casing, the relative velocity measured by LDV between 0.08 to 0.35 of the abscissa shows good agreement with the CFD results. Even in the vicinity of the suction surface, the deceleration of the relative velocity also shows good agreement. Steep deceleration of the relative velocity is seen at around 0.4 of the abscissa. Figure 6(*c*) shows the Mach number contour of CFD at about 1.5 mm from the casing Referring to Fig. 6(*c*), because Sec. II crosses with the shock wave in the position of 0.4 pitch, this deceleration is due to the shock wave. As for the CFD result referred to in Fig. 6(*a*), the velocity slope of the shock wave is not steep because the calculation mesh interval is coarse over part of the shock wave.

Regarding the velocity distribution at 3 mm from the casing, a large reverse flow region occurs at about 0.4 on the abscissa. Although the absolute value of this reverse flow velocity is about $-270$ m/s, the accuracy of this value is doubtful considering the measurement capability of the system. Considering both sides of the reverse flow, the velocity decelerates from 0.2 toward 0.4 and reaches a negative value on one side, while the velocity also decelerates from 0.7 toward 0.4 and reaches a negative value on the other side as well. As the velocity range of both sides of the reverse flow is within the measurement capability, the occurrence of the reverse flow is definite.

Regarding the meridional velocity at 6 mm from the casing, the velocity difference between LDV and CFD seems to be the effect of the reverse flow in the vicinity of the casing.

Referring to Fig. 6(*c*), the location where the reverse flow occurs is the intersection between the blade tip leakage flow and the shock wave, and it is considered that the reverse flow is caused by the interaction of these two factors.

However, CFD was incapable of estimating the large reverse flow in the vicinity of the casing measured by LDV. It is under-

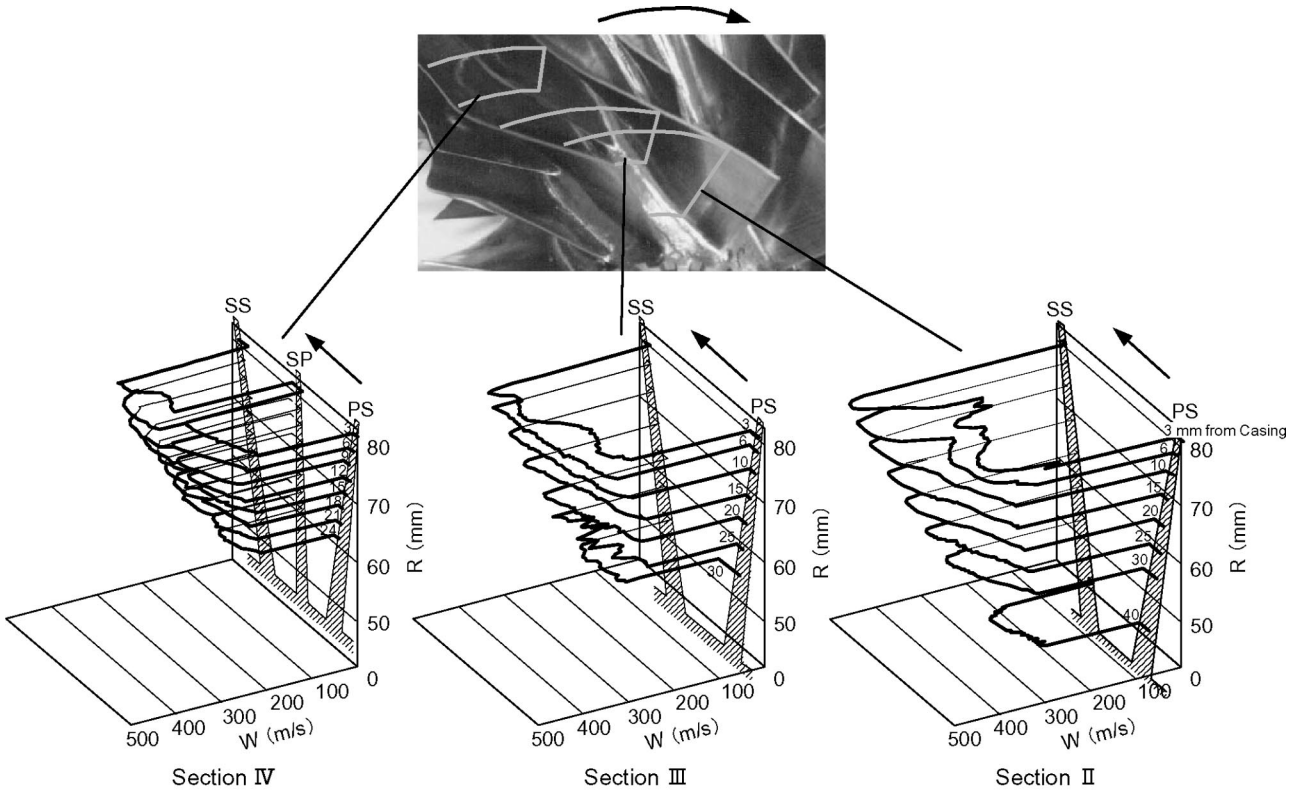


**Fig. 5 Relative velocity distribution**

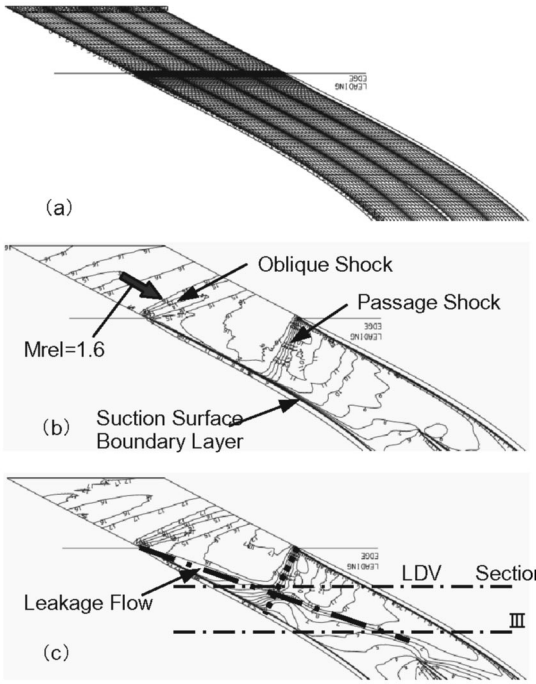


**Fig. 6 Computational grid and Mach number contour: (a) computational grid, (b) Mach number on a stream surface about 3 mm from casing, and (c) Mach number on a stream surface about 1.5 mm from casing**

stood, however, that CFD is able to estimate flow distribution with good accuracy in most of the flow range, except just after the shock wave. The reason why CFD fails to estimate the reverse flow was not clarified in the work reported here. The turbulence modeling, mesh arrangement, and clearance treatment are issues to be considered.

Regarding LDV measurement capability in the vicinity of the blade surface, and referring to Fig. 8(*a*), although the distance of the absolute measurement point from the suction surface is not clear, the relative velocity deceleration toward the suction surface can be observed at every location from the casing. These data shown in Figs. 8–10 are worth discussing in terms of the suction surface boundary layer. The boundary layer thickness in Sec. II estimated using CFD is about the same as that corresponding to LDV measurement.

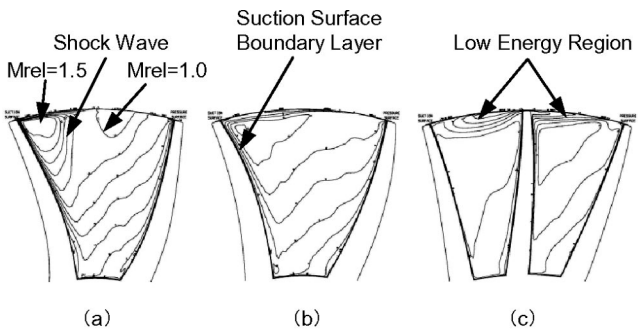


**Fig. 7 Mach number contour on each LDV measuring sections: (a) Section II, (b) Section III, (c) Section IV**

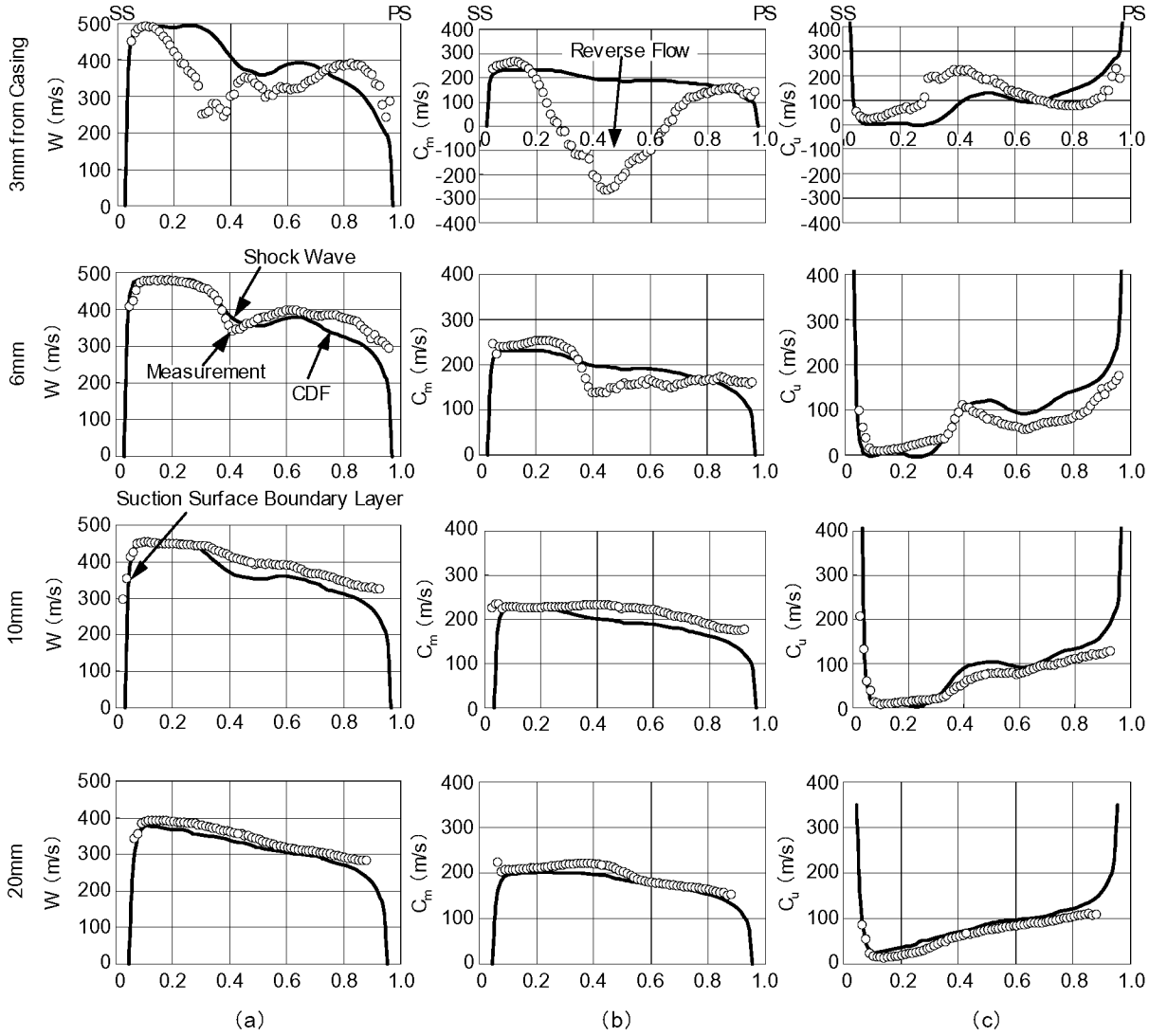


**Fig. 8 Comparison between LDV and CFD: (a) relative velocity, (b) meridional velocity, (c) tangential velocity**

**B Section III.** Figure 9 shows a comparison between the LDV measurement results and the CFD results for Sec. III. The velocity distribution at 3 mm from the casing shows substantial distortion in the middle of the pitch. This is considered to represent the influence of the upstream reverse flow.

Referring to Fig. 6(*b*) showing the Mach number contour about 3 mm from casing, the shock wave across the throat reaches the suction surface, and the suction surface boundary layer thickness increases due to interaction with the shock boundary layer. The effect appears on the relative velocity distributions at both 3 and 6 mm from the casing in Fig. 9(*a*). Despite the CFD estimation, the measured data in the vicinity of the suction surface at both 3 and 6 mm from the casing do not indicate boundary layer thickening. This shows that the shock boundary layer interaction does not affect the suction surface boundary layer in comparison to the casing boundary layer.

**C Section IV.** Figure 10 shows a comparison between the LDV measurement results and the CFD results for Section IV. According to CFD, the velocity at 3 mm from the casing shows a large low energy region, especially in the suction side passage and on the splitter blade suction surface. Even at 6 mm from the casing, CFD shows a low energy region in the suction side passage. On the other hand, although the measuring results indicate a small low velocity region at about 0.3 pitch of the suction side passage, an obvious low energy region was not measured. It was therefore understood that CFD tends to overestimate the low energy region.

## Results of Pressure Measurement

Figure 11 shows the instantaneous pressure oscillation of two pitches. The blade pressure surface and the suction surface are shown as a red line and a blue line respectively. Each figure includes the pressure data of the relevant section (red line with blue dots), preceding section (blue line), and interpolated two sections (green line; 1/3 from preceding section, red line; 2/3 from preceding section).

In segment No. 1, it is found that there is a peak just in front of the leading edge, and it must be the detached shock. This shock wave propagates to segments Nos. 2 and 3, and the highest pressure is obtained in segment No. 3. The pressure decreases at downstream of this shock wave in segments Nos. 3 and 4, with the pressure rising rapidly once again in the vicinity of the pressure surface in segment No. 4. This pressure decrease downstream from the shock wave corresponds to the slight increase in the Mach number in Fig. 7(*a*) and the relative velocity increase in Fig. 8(*a*) 6 mm from the casing. The pressure increase in the vicinity of the pressure surface of segment No. 4 overlaps with the pressure increase toward the pressure side from the suction side in

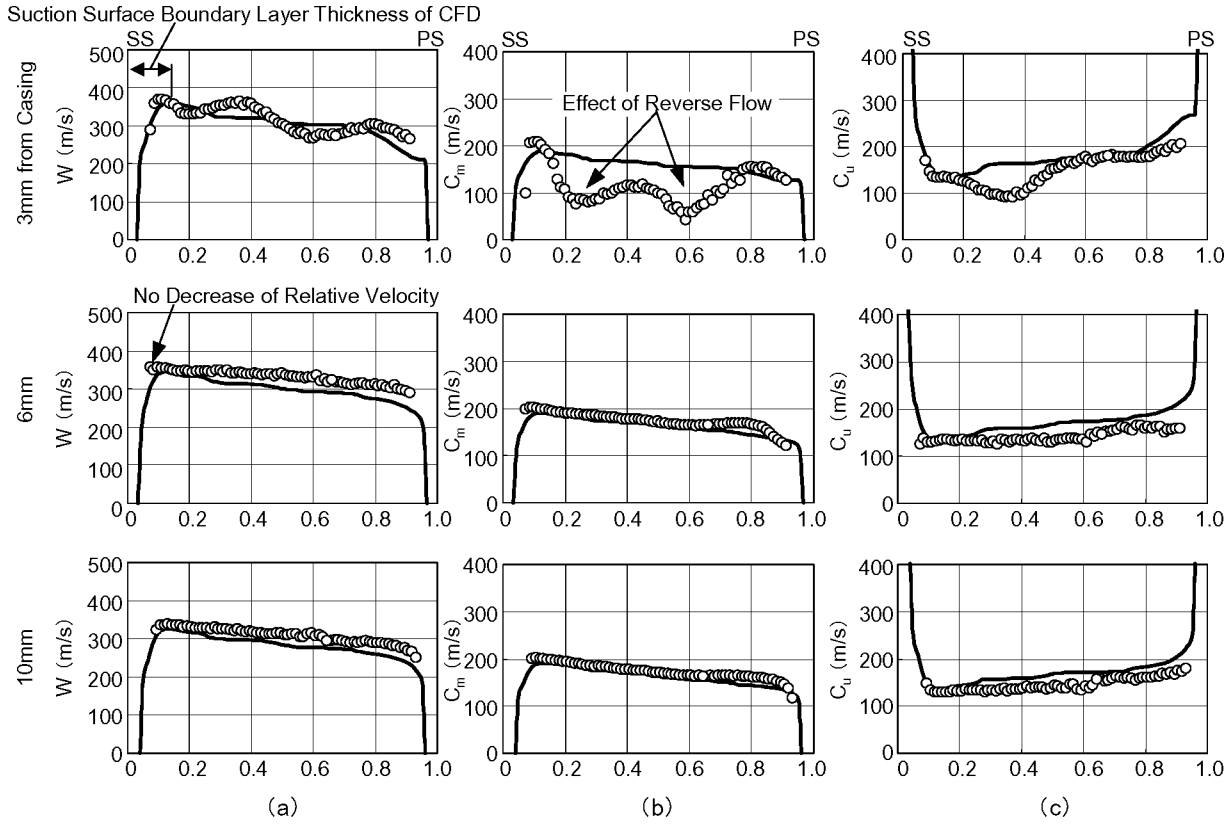


**Fig. 9 Comparison between LDV and CFD: (a) relative velocity, (b) meridional velocity, (c) tangential velocity**

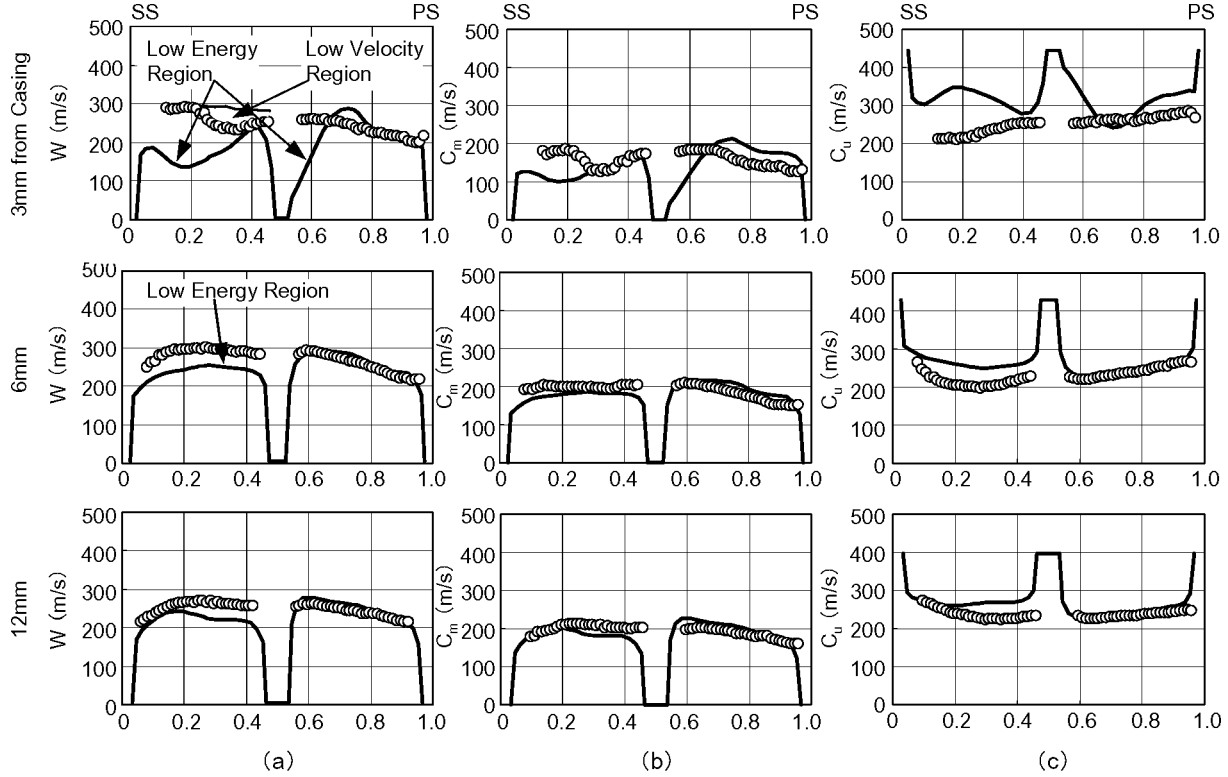


**Fig. 10 Comparison between LDV and CFD: (a) relative velocity, (b) meridional velocity, (c) tangential velocity**

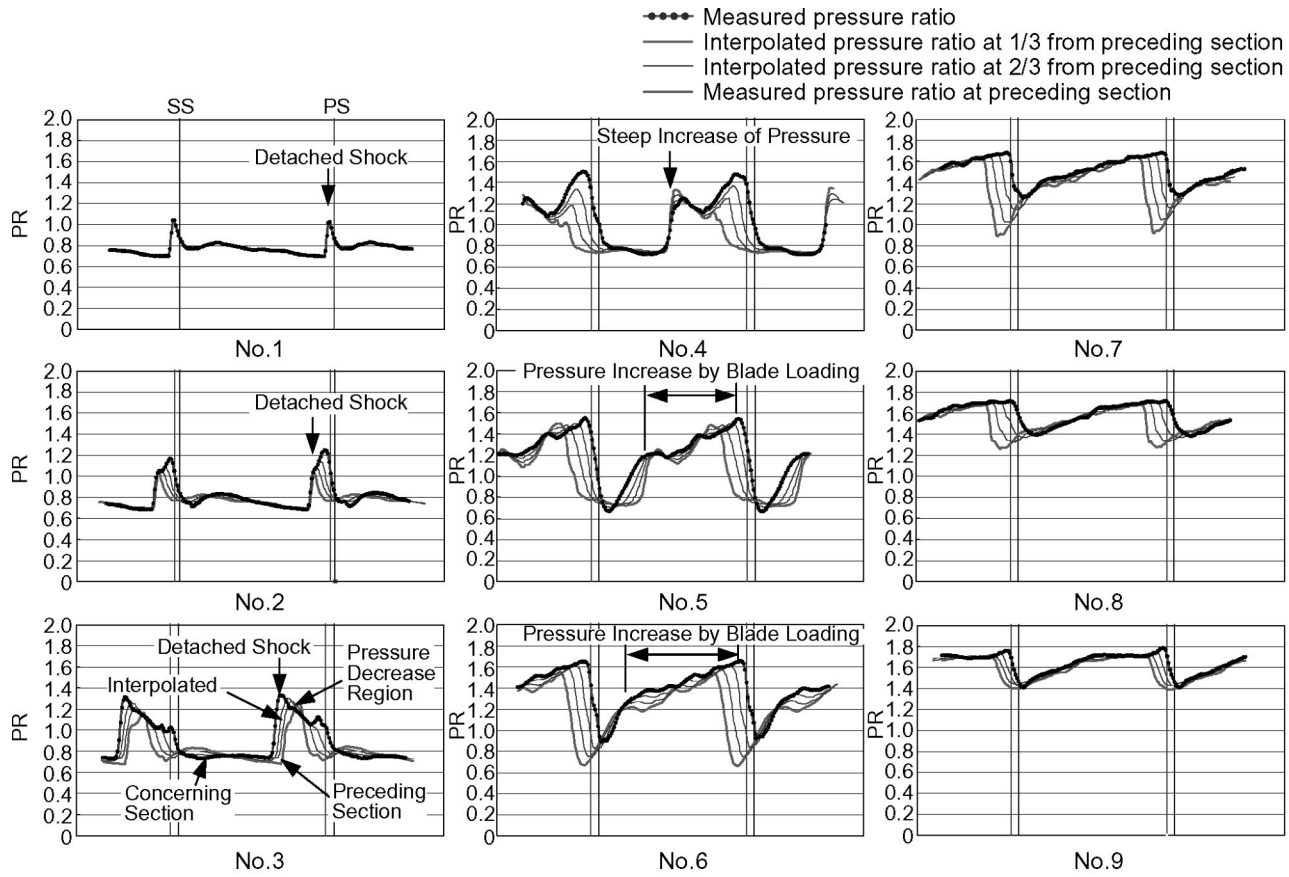


**Fig. 11 Instantanius pressure distribution between main blades**

segment No. 5. Thus, the mechanism of pressure increase in the vicinity of the pressure surface of segment No. 4 differs from the shock wave.

It is found that the pressure increase from about 1/3 pitch to the pressure surface of segment No. 5 is caused by the blade loading in the subsonic flow region. Referring the pressure distribution of segment No. 6, nearly the same pressure slope as segment No. 5 appears from about 1/5 pitch to the pressure surface. The following two segments, Nos. 7 and 8, also show the same slope. In segment No. 9, the pressure slope from the middle to the pressure surface becomes flat. This is why the first splitter leading edge extends to segment No. 10. The lower pressure on the suction surface of the first splitter affects the pressure slope of segment No. 9.

Figure 12 shows a three-dimensional image of the pressure distribution. The detached shock occurs just in front of the leading edge and this progresses to an oblique shock wave reaching the suction surface. The peak pressure shown as the yellow value in the oblique shock wave on the pressure side then appears. Downstream of the peak pressure, after the pressure decrease region

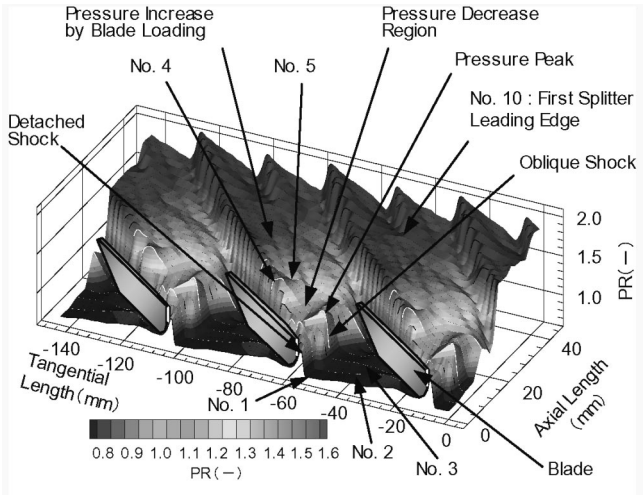


**Fig. 12 Pressure contour in the inducer**

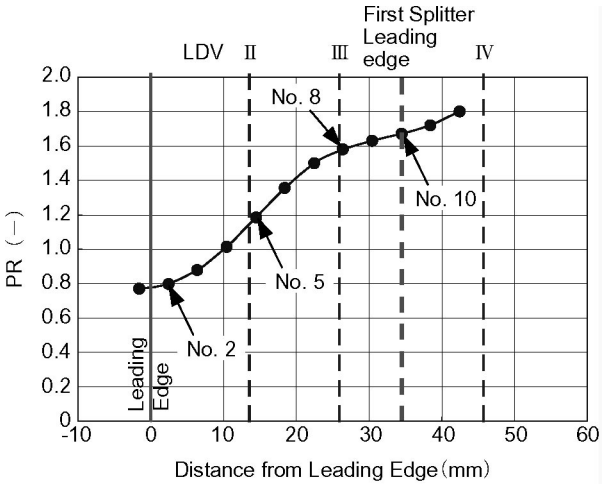


**Fig. 13 Static pressure increase in the inducer**

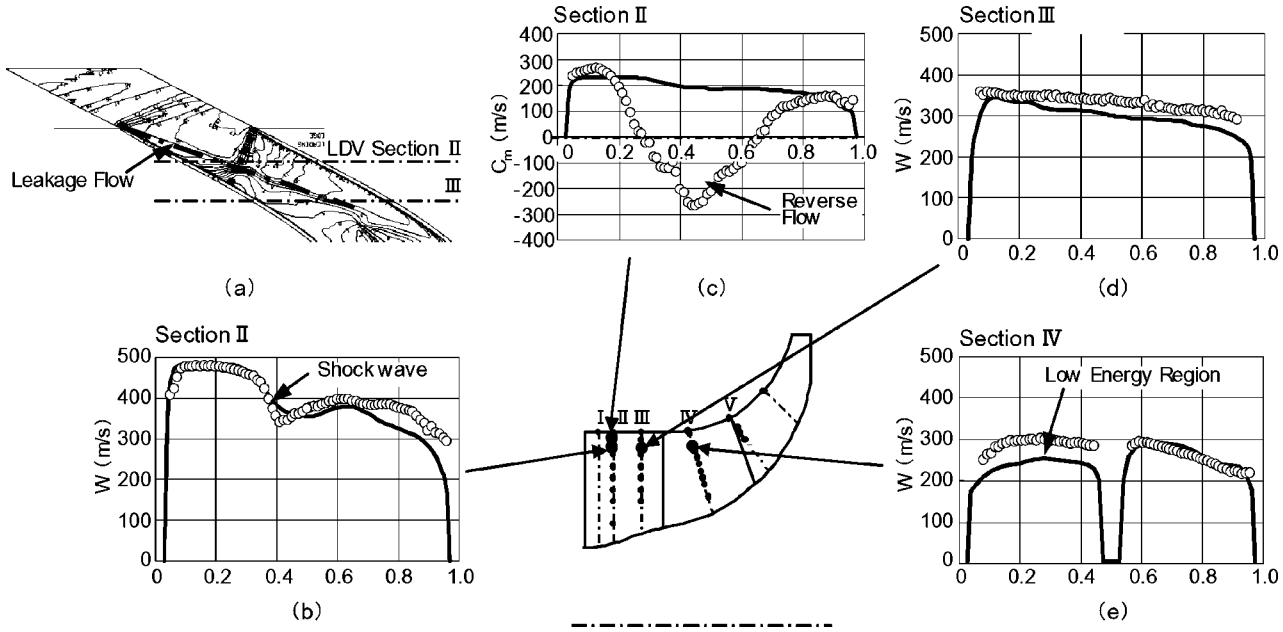


**Fig. 14 Summary of notable points: (a) CFD in the vicinity of shroud casing, (b) relative velocity distribution and shock wave at Sec. II, 6 mm from casing, (c) meridional velocity distribution in the vicinity of shroud casing, (d) relative velocity distribution at Sec. III, 6 mm from casing, (e) relative velocity distribution with splitter at Sec. IV, 6 mm from casing**

appears, the pressure increase is connected to the pressure increase caused by the blade loading in segment No. 5. The single slope between the blades in segment No. 5 is divided into two slopes downstream from the first splitter leading edge in segment No. 10.

Figure 13 shows the static pressure increase along the inducer casing. Although it seems as if the pressure increase from segments Nos. 2 to 8 due to the shock wave from segments Nos. 2 to 8, it is found that the shock wave causes the pressure increase from segments Nos. 2 through 5 through oblique shock and that the blade loading is responsible for the pressure increase from segments Nos. 5 to 8.

## Conclusions

The authors of the study reported here conducted detailed investigation of a high transonic impeller having Mach number about 1.6, using LDV and pressure transducers with respect to a centrifugal compressor with a high pressure ratio of 11. CFD verification was conducted using the measured results.

1. In the inducer portion, deceleration caused by the oblique shock wave was found in the middle of the throat. Reverse flow occurred in the vicinity of the casing caused by the interaction of the blade tip leakage flow and the shock wave.
2. Referring to CFD, although the shock wave measured in Sec. II should have reached the suction surface, thickening of the boundary layer was not found in Sec. III located downstream from the intersection.
3. In the splitter portion, a small low-velocity region in the vicinity of the shroud casing at about 0.3 pitches of the suction side passage was observed, but an obvious low velocity region estimated using CFD was not measured.
4. Although the CFD applied was unable to estimate the large reverse flow in the vicinity of the casing in the inducer portion, it is nevertheless understood that CFD is capable of estimating flow distribution with good accuracy in most of the flow range.
5. The static pressure increase in the inducer is caused by the oblique shock in the leading half, and by blade loading in the latter half.


## Acknowledgment

The authors would like to thank Dr. Y. Sugiyama, former Director of Third Research Center, Technical Research and Development Institute, Japan Defense Agency for all his help and instructive comments on the measurement and understanding of the phenomena involved in this study.


## Nomenclature

$C$ = Absolute velocity, m/s
$C_m$ = Meridional velocity, m/s
$C_u$ = Tangential velocity, m/s
$G$ = Mass flow rate, kg/s
Mrel = Relative Mach number
PR = Pressure ratio
$P_s$ = Static pressure
$U$ = Peripheral velocity, m/s
$W$ = Relative velocity, m/s
PS = Pressure surface
SP = Splitter blade
SS = Suction surface
Hub = Hub surface
Shroud = Shroud surface

## References


[1] Eckardt, D., 1976, ''Detailed Flow Investigations With in a High-Speed Centrifugal Compressor Impeller,'' ASME J. Fluids Eng., **98**, pp. 390–402.
[2] Krain, H., 1988, ''Swirling Impeller Flow,'' ASME J. Turbomach., **110**, pp. 122–128.
[3] Hah, C., and Krain, H., 1990, ''Secondary Flows and Vortex Motion in a High-Efficiency Backswept Impeller at Design and Off-Design Conditions,'' ASME J. Turbomach., **112**, pp. 7–13.
[4] Senoo, Y., Hayami, H., Kinoshita, Y., and Yamasaki, H., 1978, ''Experimental Study on Flow in a Supersonic Centrifugal Impeller,'' ASME paper no. 78-GT-2, 1978.
[5] Hayami, H., Senoo, Y., and Ueki, H., 1985, ''Flow in the Inducer of a Centrifugal Compressure Measured With a Laser Velocimeter,'' ASME J. Eng. Gas Turbines Power, **107**, pp. 534–540.
[6] Krain, H., Hoffmann, B., and Pak, H., 1995, ''Aerodynamics of a Centrifugal

Compressor Impeller With Transonic Inlet Conditions,'' ASME paper no. 95-GT-79.
[7] Krain, H., Karpinski, G., and Beversdorff, M., 2001, ''Flow Analysis in a Transonic Centrifugal Compressor Rotor Using 3-Component Laser Velocimetry,'' ASME paper no. 2001-GT-0315.
[8] Hah, C., and Krain, H., 1999, ''Analysis of Transonic Flow Fields Inside a High Pressure Ratio Centrifugal Compressor at Design and Off Design Conditions,'' ASME paper no. 99-GT-446.
[9] Higashimori, H., Matsuo, E., and Noda, M., 1987, ''Flow Study in Radial Impellers Using a Laser Velocimeter,'' 87-Tokyo-IGTC-2.
[10] Higashimori, H., Ibaraki, S., and Mikogami, T., 1998, ''Flow Study on A Centrifugal Compressor Impeller for Turbocharger,'' 22nd CIMAC 10-03 Copenhagen, pp. 1007–1015.
[11] Ibaraki, S., Higashimori, H., and Matsuo, T., 2001, ''Flow Investigation of a Transonic Centrifugal Compressor for Turbocharger,'' 23nd CIMAC, Hamburg, pp. 339–346.

# Advanced High-Turning Compressor Airfoils for Low Reynolds Number Condition—Part II: Experimental and Numerical Analysis

**Heinz-Adolf Schreiber**

**Wolfgang Steinert**

German Aerospace Center (DLR),
Institute of Propulsion Technology,
D-51170 Köln, Germany

**Toyotaka Sonoda**

**Toshiyuki Arima**
Honda R&D Company,
Wako Research Center,
Saitama 351-0193, Japan

*Part I of this paper describes the design and optimization of two high turning subsonic compressor cascades operating as an outlet guide vane (OGV) behind a single stage low pressure turbine at low Reynolds number condition ($Re=1.3\times10^5$). In the numerical optimization algorithm, the design point and off-design performance has been considered in an objective function to achieve a wide low loss incidence range. The objective of the present paper is to examine some of the characteristics describing the new airfoils as well as to prove the reliability of the design process and the applied flow solver. Some aerodynamic characteristics for the two new airfoils and a conventional controlled diffusion airfoil (CDA), have been extensively investigated in the cascade wind tunnel of DLR Cologne. For an inlet Mach number of 0.6 the effect of Reynolds number and incidence angle on each airfoil performance is discussed, based on experimental and numerical results. For an interpretation of the airfoil boundary layer behavior, results of some boundary layer calculations are compared to oil flow visualization pictures. The design goal of an increased low loss incidence range at low Reynolds number condition could be confirmed without having a negative effect on the high Reynolds number region.*
[DOI: 10.1115/1.1737781]

## Introduction

This paper contributes to modern design techniques and design considerations for improved turbomachinery blade elements. The present design is aimed at highly loaded, high turning cascades that operate as an exit guide vane in a wide Reynolds number range and especially at very low Reynolds number conditions.

Several publications on cascade investigations at low Reynolds numbers can be found in the literature ($Re<5\times10^5$, e.g., [1–3]) but little has been reported on how to design blade sections which operate at relatively low Reynolds numbers, for example in aero engine compressors at very high altitude cruise or in exit guide vanes behind turbine rotors. At Reynolds numbers below $2\times10^5$ profile aerodynamics become very critical and losses can increase considerably due to extended laminar and turbulent boundary layer separations. There exists a lot of experience on low Reynolds number wing section designs, e.g., [4,5], but this is of limited value for turbomachinery applications.

Therefore, a project was initiated to develop a modern numerical tool that allows automatic designs for turbomachinery blading suitable for a wide range of applications including the design of low Reynolds number airfoils. In Part I of this paper, [6], the design procedures for high turning exit guide vane cascades are described. Starting from a conventional controlled diffusion airfoil, two new highly loaded airfoils have been designed by employing two different optimization strategies. In the design process itself parametric profile generators, a Navier-Stokes flow solver, an Evolution Strategy (ES), [7], as well as a multi–objective genetic algorithm (MOGA), [8], are coupled to find cascades with superior performance, not only for the design incidence but also for off design flow angles.

Contributed by the International Gas Turbine Institute and presented at the International Gas Turbine and Aeroengine Congress and Exhibition, Atlanta, GA, June 16–19, 2003. Manuscript received by the IGTI December 2002; final revision March 2003. Paper No. 2003-GT-38477. Review Chair: H. R. Simmons.

The profiles and cascade geometry obtained after the numerical optimization process achieved considerably lower losses and a wider operating range compared to the baseline design.

Although the optimization tools do not have any understanding of the fluid-dynamical processes like the experienced aerodynamicist, they can be a valuable additional tool, since they operate unbiasedly on the design space.

The outcome of the two numerical optimizations employing ES and MOGA proved that these modern strategies can be quite successful and even applicable to very complex fluid-mechanical problems—like low Reynolds profile aerodynamics.

The aim of this second part of the paper is to validate the design process that was described in the first part, to assess the Honda Navier-Stokes blade to blade solver HSTAR, [9], that was employed, and to interpret why the optimized airfoils have a superior performance compared to the baseline airfoil. For flow analysis the HSTAR solver employes a $k$-$\omega$ turbulence model together with a newly implemented modified transition model according to Wilcox [10] and Drela [11].

Interpretation of the experimental results is additionally supported by comparing some typical blade Mach number distributions to the results of the viscous/inviscid blade to blade flow solver MISES of Drela and Youngren [11,12]. In particular, the blade surface boundary layer behavior of the three investigated blades is discussed with the help of simulated integral boundary layer distributions and some oil flow visualization pictures of the blade suction sides. Although all three cascades have been designed for the same flow turning, their geometry, profile Mach number distributions, and boundary layer development look quite different. Therefore, the detailed interpretation of the obtained results becomes rather difficult.

## Baseline and Optimized Cascades

The cascades were designed to operate as a midsection in an outlet guide vane (OGV) behind the last turbine rotor of a small

  

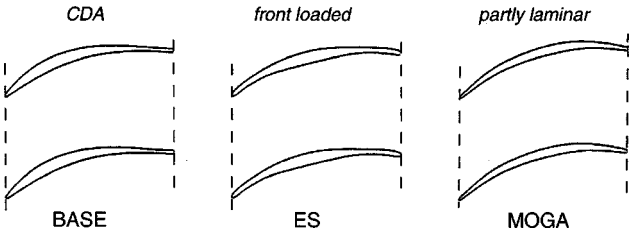


**Fig. 1 Geometry of cascades**

aero engine. The exit guide vane had to be designed for two-dimensional flow conditions with an inlet Mach number of 0.6 and a flow turning of about 43 deg. Especially due to the two-dimensional conditions (AVDR=1.0), the cascade is aerodynamically highly loaded and has to perform a strong diffusion down to an exit Mach number of 0.39. For the design incidence angle the diffusion factor is calculated to be approximately 0.53. Depending on flight conditions the blade chord Reynolds number varies from $1\times10^6$ for ground conditions to about 100,000 at high altitude cruise. In a first step a baseline cascade was designed by "hand" following the so-called controlled diffusion concept (CDA). Its suction-side Mach number distribution has a maximum at around 20% of the chord length followed by a fairly steep pressure gradient which progressively is reduced toward the trailing edge to prevent turbulent separation. This cascade, designated OGV-BASE, was designed for the high Reynolds number condition and tested in the entire relevant Reynolds number range. The calculated and measured design Mach number distribution and corresponding aerodynamic data are shown in **Fig. 1** (left). The performance was acceptable for the high Reynolds numbers but losses increased dramatically below Re=200,000 (see **Fig. 2**).

In order to improve the performance also in the low Reynolds number regime, two different optimization techniques (ES and MOGA) were applied; the principle of both methods is described in Part I. Again, the two-dimensional flow condition was assumed, the same velocity triangles as well as identical blade solidity. Because of the planned experimental validation, the freestream turbulence level during the numerical optimization was set to a value similar to the one present in the cascade windtunnel. After optimization the numerical results showed considerably lower losses in the whole Reynolds number range for both cascades although their geometry and thus the design blade Mach number distributions look quite different. **Figures 3** and **4** provide the cascade geometry and **Table 1** the design parameters.

The blade thickness in the ES optimization was prescribed; probably because of this, the OGV-ES blade looks like a "Flamingo" wing section, with maximum blade thickness concentrated at midchord location. The design blade Mach number distribution, shown in **Figs. 5** (center) and **6** (right), has its maximum at the leading edge close to $M=1.0$ followed by a steep pressure increase that successively is relaxed toward the rear. Previously Rhoden [1] found in his early low-speed experiments, that this triangular velocity distribution seems to be advantageous for the

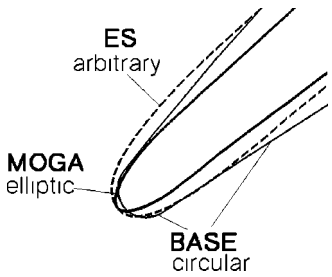


**Fig. 2 Comparison of leading edge geometry**

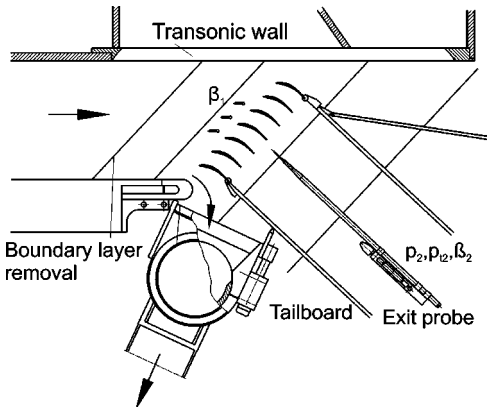


**Fig. 3 Test section of DLR facility**

low Reynolds number conditions, because this front loaded type of distribution tends to promote early transition without too strong laminar separations. Furthermore, the gradient of the pressure increase and the loading of the turbulent boundary layer on the rear suction side can be kept low.

The MOGA optimization produced a blade with a different blade pressure distribution, an obviously interesting alternative to the extreme front loaded design of the OGV-ES blade. MOGA came out with a slightly lower velocity peak at the leading edge, a very weak re-acceleration between 10% and 22% of chord and a moderate deceleration around midchord, forming a thin laminar separation bubble. Further along the chord an increased pressure gradient on the turbulent boundary layer is finally necessary to meet the flow turning requirement. In order to achieve low losses also at off-design incidences, the maximum blade thickness was reduced to 5.1%. The leading edge was designed elliptically to avoid the detrimental effects of the blunt circular leading edge of the OGV-BASE profile.

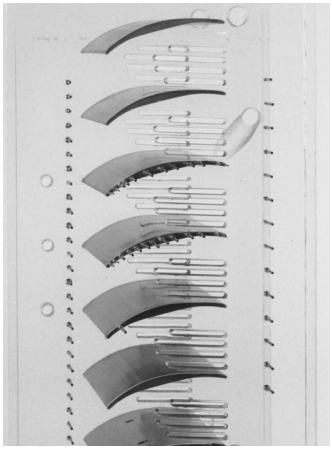

**Fig. 4 Test model of OGV-ES cascade**

**Table 1 Cascade design parameters and results**

| | OGV-BASE | OGV-ES | OGV-MOGA |
|---|---|---|---|
| $M_1$ | 0.6 | 0.6 | 0.6 |
| $\beta_1$ | 133 deg | 133 deg | 133 deg |
| $\Delta\beta$ | 43 deg | 44 deg | 44 deg |
| AVDR | 1.0 | 1.0 | 1.0 |
| $D_f$ | 0.53 | 0.537 | 0.537 |
| LE | circular | arbitrary | elliptic |
| $s/c$ | 0.577 | 0.577 | 0.577 |
| $t/c$ | 0.067 | 0.068 | 0.051 |

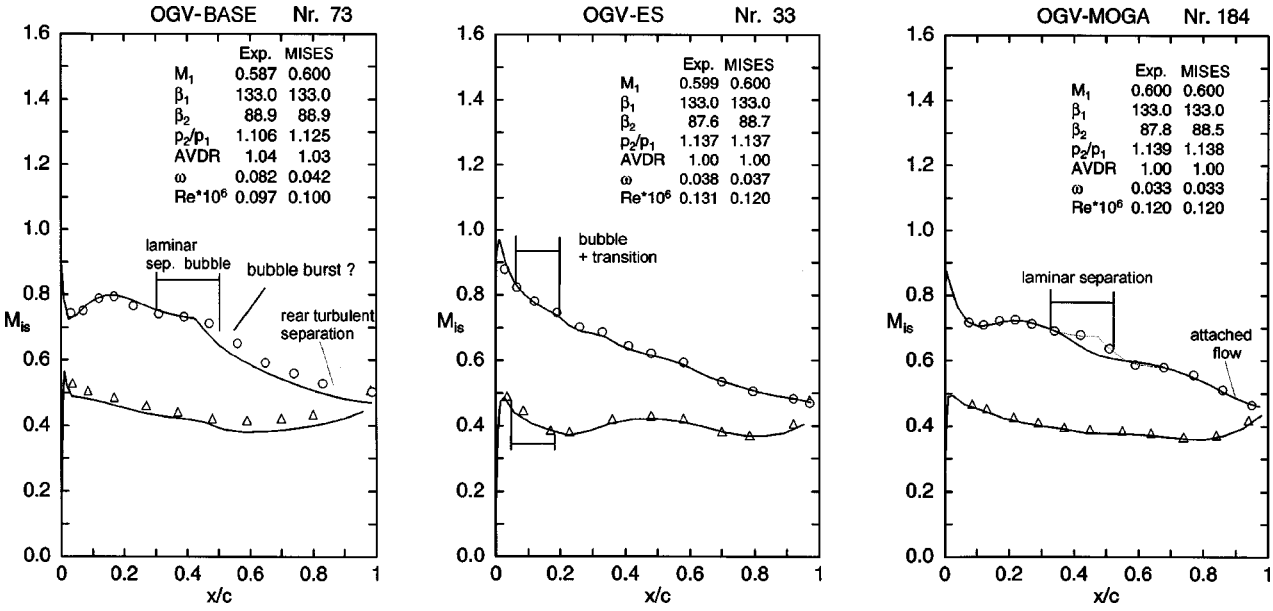


**Fig. 5 Profile Mach number distributions at design incidence and Re≈120,000, experiment (symbol) and MISES simulation**

## Test Facility and Experimental Approach

The experiments were performed in the transonic cascade tunnel of the DLR Cologne. This tunnel is a closed loop, continuously running facility with a variable nozzle, an upper transonic wall, and a variable test section height. The air supply system enables an inlet Mach number range from 0.2 to 1.4 and a Mach number independent variation of the Reynolds number from about $1\times10^5$ to $3\times10^6$. Tunnel sidewall boundary layers ahead of the cascade are removed through protruding slots. Within the blade pack aft of the minimum pressure region endwall boundary layers were controlled by suction through chordwise slots [13] to obtain practically two-dimensional flow condition around midspan region (AVDR=1.0). Tailboards combined with throttles are used to control inlet and exit boundary conditions. For the present tests seven blades with 65 mm chord and 168 mm blade span were installed in the test section, with the center blades instrumented on the pressure and suction side. A cross-sectional view of the test section and a photograph of the cascade model are shown in **Figs. 3** and **4**.

In order to obtain tests at low Reynolds numbers, the closed loop system of the facility must be evacuated by additional sets of radial compressors. By adjusting the total pressure between 1.1 and 0.1 bar blade chord Reynolds numbers were achieved between about 900,000 and 100,000. The cascades were tested at inlet Mach numbers of 0.5, 0.6, and 0.7 in the entire possible incidence range. In this paper, results for the inlet Mach number of 0.6 are discussed. The inlet flow angle is measured with probes at the same gap-wise locations for three consecutive blade channels. Inlet total temperature is about 305 K and the freestream turbulence level around 0.6%.

Prior to the tests each individual test point has been precalculated using the blade to blade code MISES 2.4. The theoretical profile Mach number distribution, displayed real time with the test data served as a goal for the experimental distribution. By doing so, the measurement accuracy, especially for the inlet flow angle could be improved considerably.

## Validation of Design and Discussion

The tests on the baseline cascade were performed in a first step and the results used to assess the blade to blade solver employed. Some results, especially the validation of the newly implemented transition model, are presented in Part I of this paper. This transition model enabled the Navier-Stokes solver to readily simulate the extension of the midchord laminar separation bubble which is particularly important for the low Reynolds number conditions.

The experimental results, especially those of the optimized blades, confirmed the design goals, in particular the design point profile Mach number distributions shown in **Figs. 5, 6**, and **7**. The off design Mach number distributions, not shown here, were met reasonably well too. Additionally, the main experimental performance data for all three cascades are summarized in **Table 2**. Here, the total pressure losses at the design incidence and the minimum losses are provided for the high and low Reynolds number conditions. For the high Reynolds numbers, losses at design incidence could be reduced from roughly 3.4% down to 2.6 or 3.2% for the ES and MOGA blade, respectively. The minimum losses are 2.2% and 2.0%, however, at negative incidences. A dramatic loss reduction was achieved for the low Reynolds number at which both new cascades showed only 3.7% and 3.3% losses compared to 8.4–10% of the OGV-BASE cascade (see **Fig. 8** (right)). In addition, the working range could be increased considerably toward the negative as well as the positive incidence.

In the following, some aerodynamic features of all three blades, the profile Mach number distributions, the incidence characteristics and the Reynolds number dependencies are discussed. In addition to the Navier-Stokes results some simulations of the profile Mach number distributions and the boundary layer parameters, using the viscous/inviscid flow solver MISES, [11,12] help to interpret the results obtained.

**High Reynolds Number.** The baseline cascade near its design incidence operated with a highly loaded suction side boundary layer, although it was designed following the controlled diffusion concept. Marginal increase in incidence caused rear unstable separation with a sudden loss rise; see **Fig. 8** (left) and the blade Mach number distribution of a corresponding test point in **Fig. 9** (left). Therefore, minimum losses were not obtained near design but near $\beta_1=130$ deg ($i=-3$ deg). The optimized blades overcame the problem of too strong suction side loading by reducing the gradient of the pressure increase along the whole surface. All three profile Mach number distributions are shown in **Fig. 9** and a direct comparison of the relevant suction side Mach numbers is given in **Fig. 10** (top-left). To discuss blade and boundary layer loading, plots in **Fig. 10** also provide a comparison of the simulated boundary layer displacement—and momentum thickness—

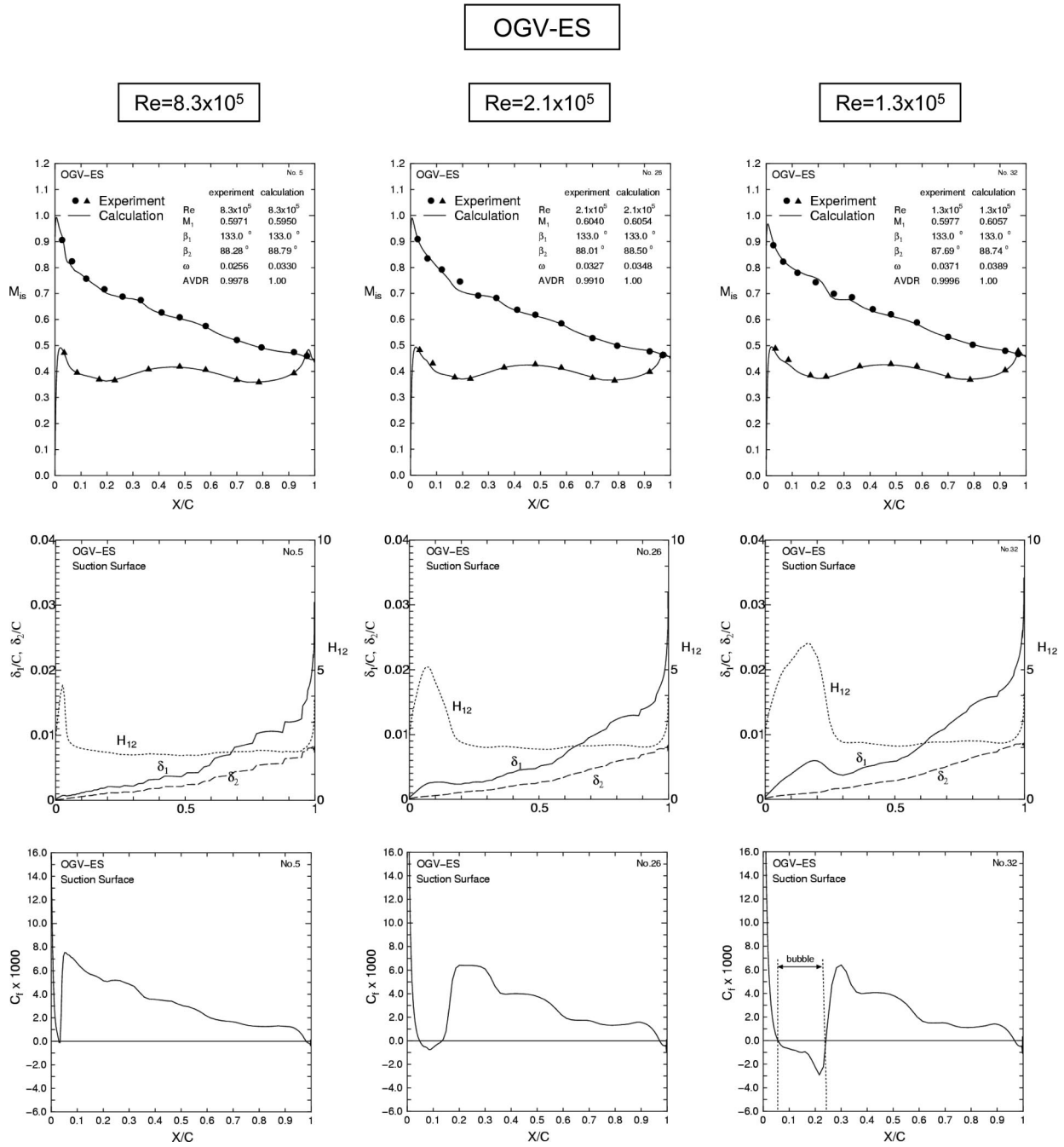


**Fig. 6 Effects of Reynolds number on profile Mach number distribution and suction side boundary layer development. Experiment and HSTAR simulation, optimized cascade OGV-ES, $M_1=0.6$, $i=0$ deg.**

the form factor $H_{12i}$, and the skin friction coefficient $C_f$. In the plot that shows the boundary layer thickness, it is clearly visible that the ES as well as the MOGA blade both have thinner displacement and momentum thickness and therefore lower losses compared to the baseline cascade. The development of the OGV-BASE form factor $H_{12i}$ (solid line) clearly indicates that the suction side boundary layer tends toward the separation criterion of approximately $H_{12\text{sep}}=2.5$ relatively early, a value above which separation of a turbulent boundary layer could be expected. The ES cascade clearly stays away from separation and the MOGA blade slightly tends toward separation at the very end. Effectively, in the experiments the MOGA blade boundary layer separates from the rear suction side, clearly visible in the experimental distribution of **Fig. 9** (right), but the losses still remain relatively low.

At this high Reynolds number, boundary layer transition is observed for all three blades just after the velocity peak at the leading edge and the rest of the suction side remains turbulent. The transition process occurs within a short laminar separation bubble that forms right behind the LE and turbulent re-attachment occurs due to an intensive entrainment process along the rear part of the bubble. This local separation considerably alters the LE pressure distribution in relation to pure inviscid or turbulent flows—as it is illustrated in **Fig. 11**—and alters the state of the boundary layer from the beginning.

The LE geometry of the three blades are very different (see **Fig. 2**), the base line LE is circular and the two optimized blades have an arbitrary and elliptic geometry. Therefore, the extension of the LE bubble and the status of the boundary layer after re-attachment

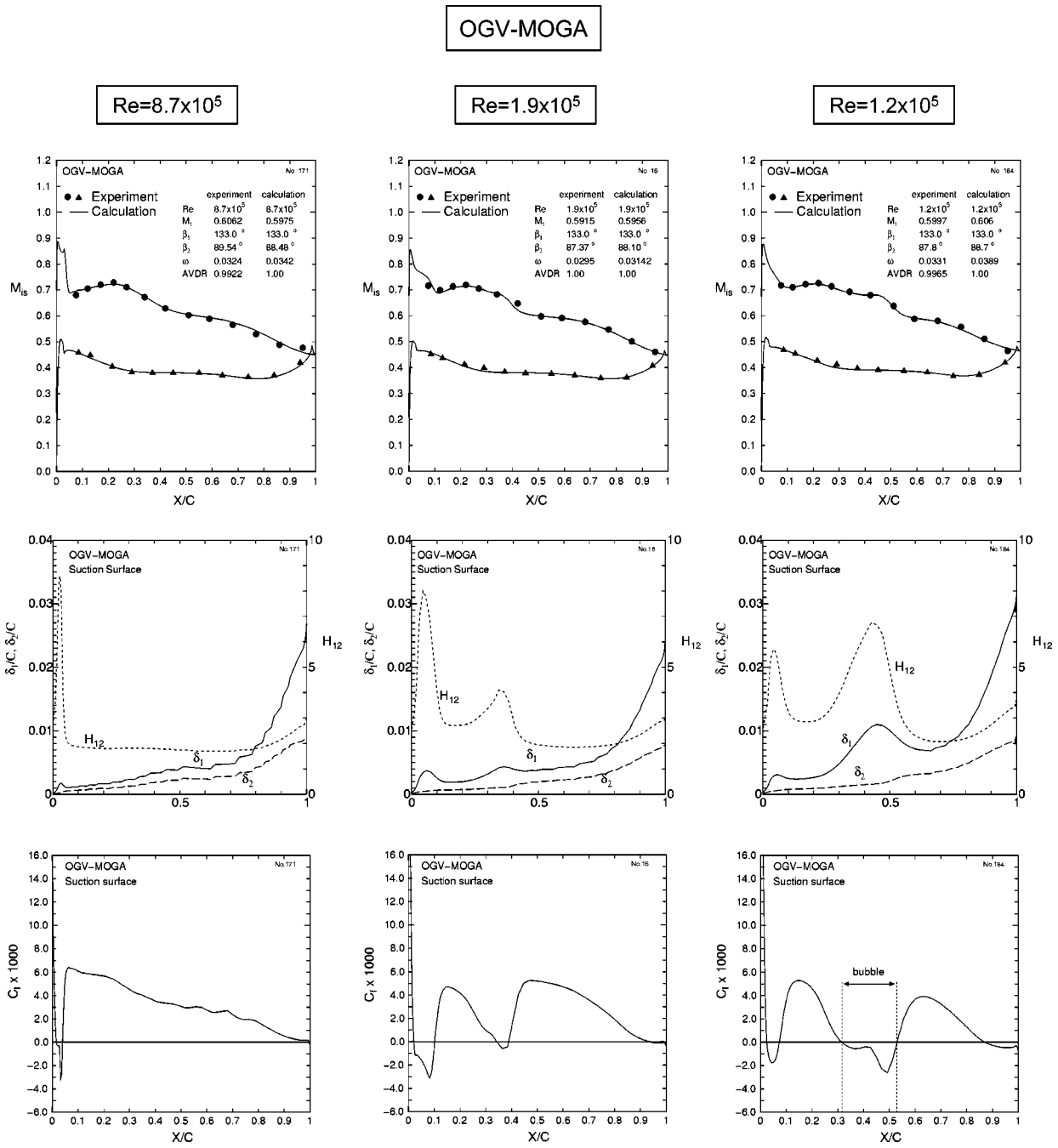


**Fig. 7 Effect of Reynolds number on profile Mach number distribution and suction side boundary layer development. Experimental and HSTAR simulation, optimized cascade OGV-MOGA, $M_1=0.6$, $i=0$ deg.**

**Table 2 Experimental losses, flow turning and incidence range at high and low Reynolds number**

| | OGV-BASE | OGV-ES | OGV-MOGA |
|---|---|---|---|
| Re | $0.87\times10^6$ | $0.85\times10^6$ | $0.85\times10^6$ |
| $\omega$% (i=0°) | 3.4 (AVDR=1.035) | 2.6 | 3.2 |
| $\omega_{min}$ % | 2.26 (i=−3 deg) | 2.2 (i=−4 deg) | 2.0 (i=−4 deg) |
| $\Delta\beta$ ($i=0°$) | 43 deg | 44 deg | 44 deg |
| $\Delta i$ ($\omega=2\omega_{min}$) | 7–8 deg | 13 deg | 12 deg |
| Re | $0.10\times10^6$ | $0.13\times10^6$ | $0.12\times10^6$ |
| $\omega$ % | 8.4–10 | 3.7 | 3.3 |
| $\omega_{min}$ % | 8.4 ($i=0$ deg) | 3.7 ($i=0$ deg) | 3.1 ($i=-2$ deg) |

are quite different too. A zoom of the local skinfriction coefficients, shown in **Fig. 10** (bottom right), clearly indicates the different extensions of the LE bubbles. The most pronounced and concentrated velocity peak with an intensive LE separation is found on the BASE blade, even if the LE Mach number levels of the ES and MOGA blade are slightly higher. Not the absolute height of the pressure or Mach number peak is relevant, rather its local pressure gradient. Therefore, the baseline blade starts with the most critical boundary layer being disturbed from the beginning resulting in a higher risk of a rear turbulent separation with additional losses. The ES blade with the arbitrary LE geometry obviously is doing the best job; MISES (Fig. 10) as well as the HSTAR simulations in **Fig. 6** (left) both indicate no LE separa-

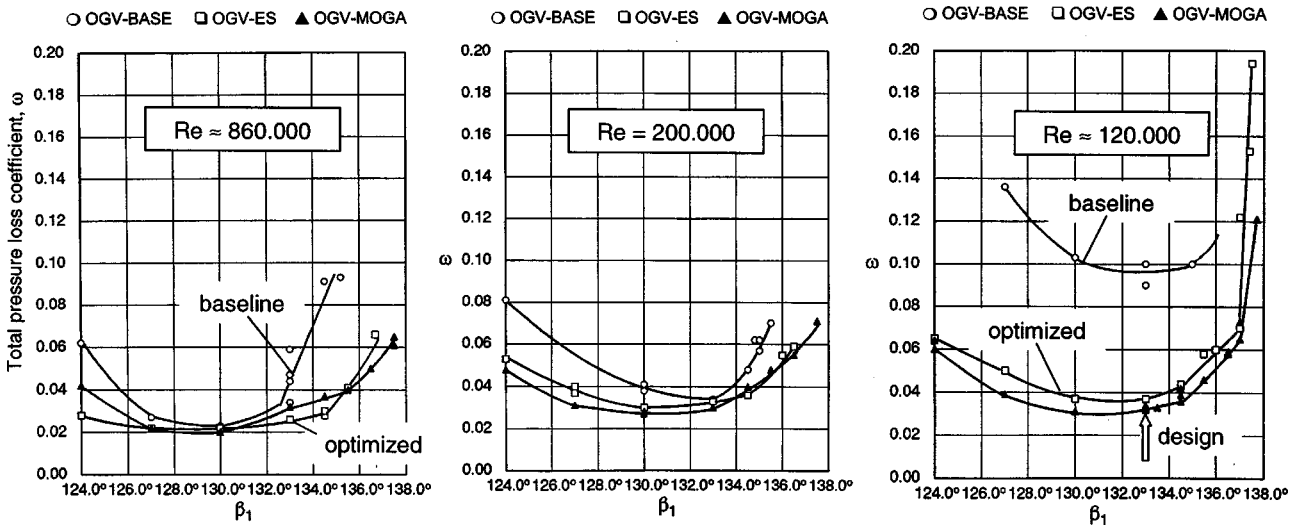


**Fig. 8 Experimental loss-incidence characteristics at three different Reynolds numbers, $m_1$=0.6, $\beta_{1design}$=133 deg ($i$=0 deg)**

tion, just transition, although oil flow pictures of a high Reynolds number test suggest a short bubble downstream of about 3% of chord.

In the present MISES as well as HSTAR simulations this LE peak is reasonably well simulated, but still some discrepancies between experimental losses and simulated losses are observed (see **Fig. 9**). However, Sanz and Platzer [14] found that none of their investigated transition models predicted the leading edge bubble very well, although their computational grid allowed $y^+$ values of the order of 1. In this context, it is suspected that with uncertainties coming from the simulation of the leading edge bubble, the boundary layer immediately behind the leading edge and further downstream may not be simulated correctly. This is more problematic especially if the rear part of the suction-side boundary layer is highly loaded and close to separation. The situation is worse if blades have circular leading edges at which the velocity peak is more pronounced with even more intensive local separations (Walraevens and Cumpsty, [15]).

The LE separation extends considerably if the Reynolds number is reduced, and it is more likely that the blade-to-blade solvers fail in simulating those local LE and severe rear separations. An example is given in test 73, **Fig. 5** (left), for which the agreement between MISES simulation and experiment is rather poor. The HSTAR simulation shows better performance both with respect to the resolution of the front peak as well as to the overall total pressure losses for the design incidence condition as shown in Fig. 14 (right) of Part I of the paper and in **Figs. 6** and **7** of the present paper. At off-design, nevertheless, some discrepancies still remain.

**Low Reynolds Number.** In spite of the more extended LE bubbles at the low Reynolds number, the suction side boundary layer along the front of the BASE and MOGA blade becomes laminar again and a midchord separation bubble develops. At this low Reynolds number. the BASE blade boundary layer fully separates from the suction side and losses increase to about 8–10%

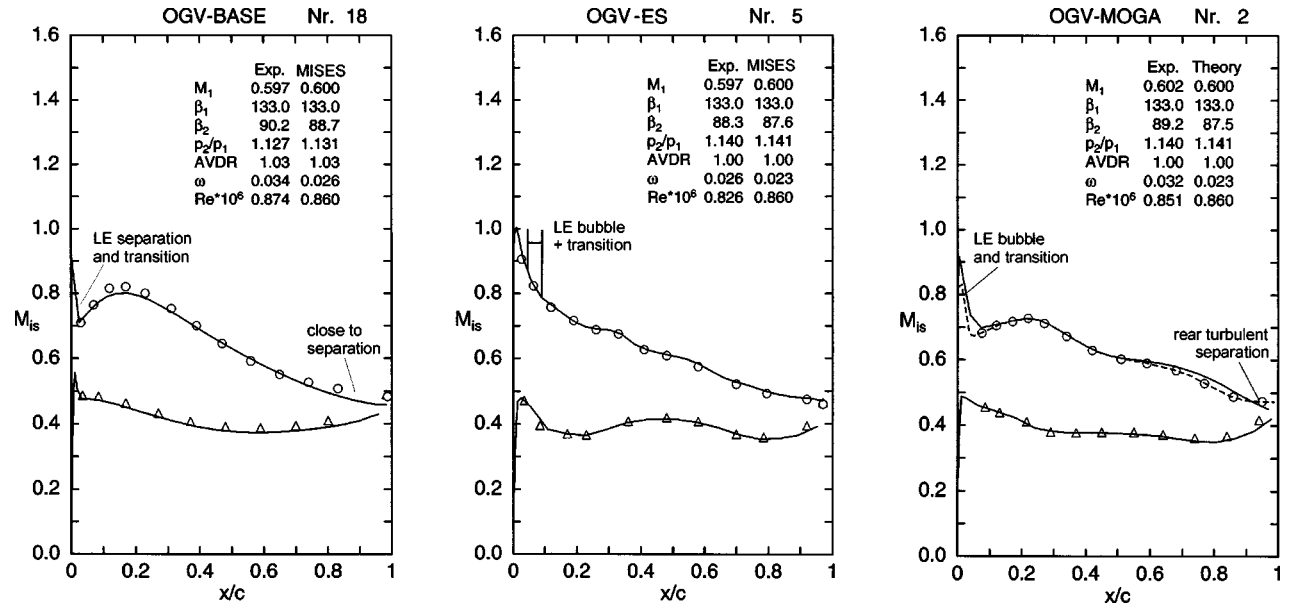


**Fig. 9 Profile Mach number distributions at design incidence and Re=860,000, experiment (symbol), and MISES simulation**

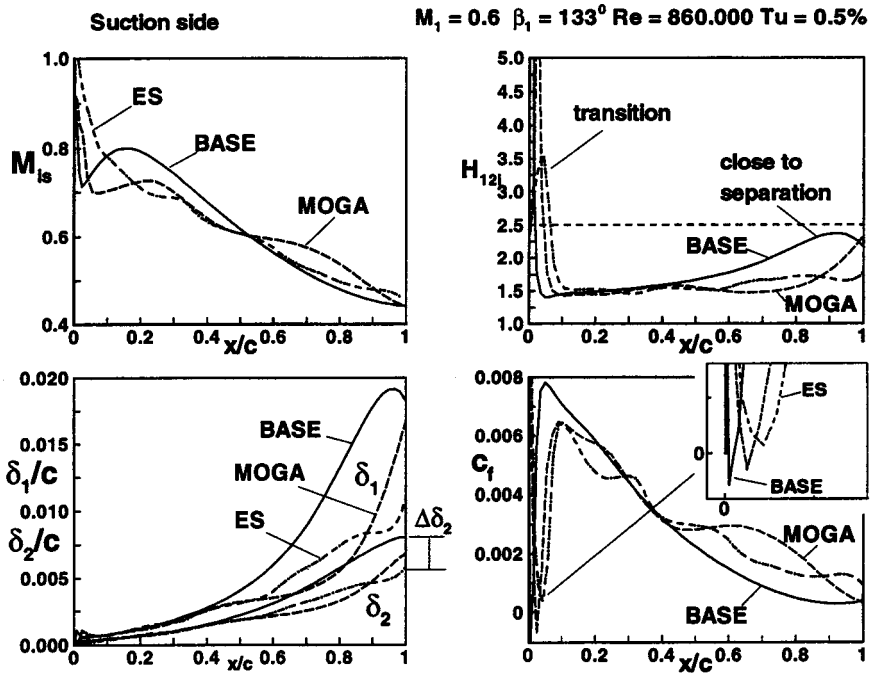


**Fig. 10 Discussion of suction side boundary layer parameters at Re=860,000 (MISES simulation)**

(**Fig. 5** (left)). In contrast, both optimized blades show losses of only 3.3 to 3.7% at Reynolds numbers around 120,000.

Due to the reduced adverse pressure gradient on the MOGA blade its midchord bubble is less pronounced and produces lower losses. Furthermore, the flow entrainment process during reattachment at the rear part of this bubble introduces new turbulent energy into the rear suction side boundary layer so that trailing edge separation is suppressed, which is visible in **Fig. 5** (right). From **Fig. 5** we realize that MISES, which was run with a free stream turbulence level of 0.5%, slightly underpredicts the extension of the midchord bubbles whereas HSTAR with the newly implemented transition model meets the bubble extensions reasonably well, as can be seen in **Figs. 6** and **7** as well as in Fig. 15 of Part I of the paper.

The front loaded ES blade design shows a more extended but thin bubble downstream at approximately 6% of chord with transition completed near 22%. The experimental and the simulated form factors, both do not indicate any rear turbulent separation, see **Figs. 5** (center) and **6**.

**Incidence Characteristics.** **Figure 8** provides the experimental total pressure losses for the entire investigated incidence range for Reynolds numbers around 8.6, 2.0, and $1-1.2\times10^5$. All three figures clearly show the essential advantage of the optimized blades: lower design point losses as well as a more wide incidence range. It is clearly visible in **Figs. 8** and **12** that the location of minimum losses is shifted from negative incidences ($i=-3-4$ deg) toward the design incidence ($\beta_1=133$ deg) if the Reynolds number is reduced (see also **Table 2**). At Re=200,000 the baseline cascade still has reasonably low losses, but for Re $\leqslant$130,000 the blade separates and losses increase considerably.

Both optimized blades achieved their design goal and losses remain low in the entire Reynolds number range. It is difficult to decide, which of the two cascades is superior: At the high Reynolds number and at the design incidence ($\beta_1=133$ deg) the MOGA blade separates slightly, but it seems to be marginally better over the entire incidence range at low Reynolds numbers.

**Navier-Stokes Analysis.** The experimentally observed loss-incidence characteristics are reproduced by the HSTAR solver reasonably well at least for the low Reynolds number conditions, as can be seen in **Fig. 13**. Also the high Reynolds number tests (**Fig. 14**) at $i=0$ deg were met, but the losses in the negative and positive incidence range differ considerably. This is true especially for the baseline cascade that showed an unstable suction side separation beyond $\beta_1=133$ deg in the experiments. However, the numerically simulated losses seem to be too high, not because of boundary layer separation, but rather due to high ''numerical losses'' within the entire flow field. There are probably

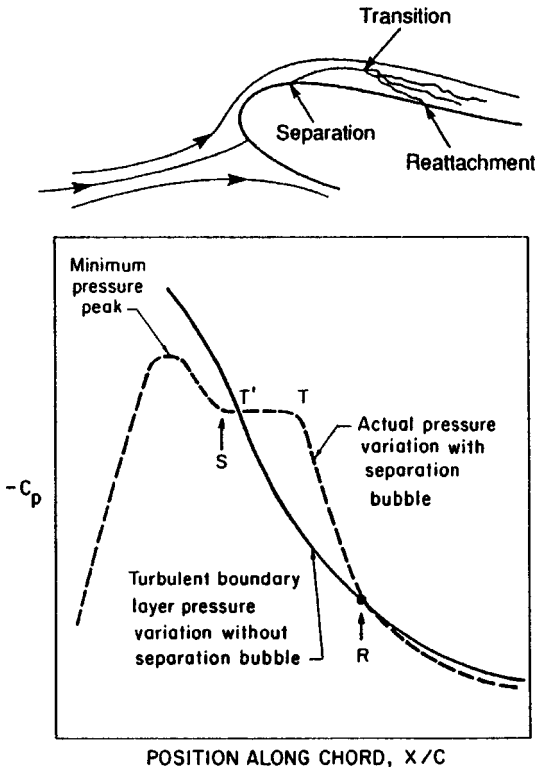


**Fig. 11 Principle of LE separation (Mueller [5])**

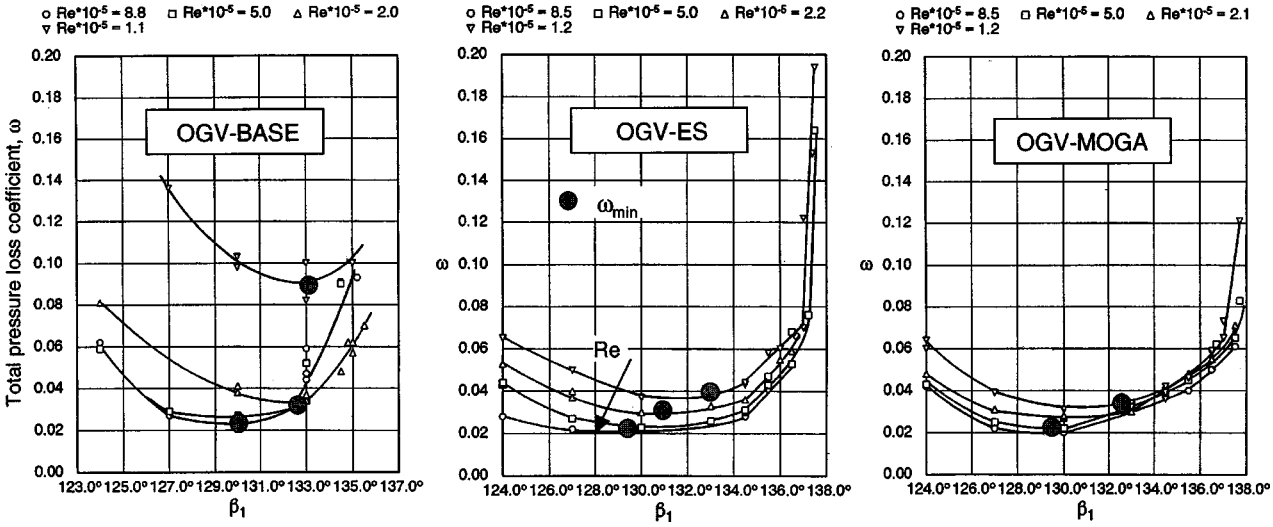


**Fig. 12 Influence of the Reynolds number on the loss-incidence characteristics, $M_1=0.6$**

several reasons for the discrepancy between the experimental losses and the numerical ones, and it is beyond the scope of this paper to investigate all of these. However, according to the assessment of different turbulence models (Chien's low Re $k$-$\varepsilon$ and low Re $k$-$\omega$) with the same numerical platform (computational grid and flow solver), there seems to be a general tendency that the losses from the k-$\omega$ turbulence model without the viscous modifications near the wall are high for the attached flow (not shown here). This may be caused by the overestimation of the turbulent energy due to the absence of a damping function in the $k$-$\omega$ model and/or due to the overproduction of turbulence, as pointed out by Michelassi et al. [16] for their calculations near the leading edge of turbine blades. Regardless of this disadvantage, the reason why we adopted the $k$-$\omega$ model without the viscous modifications, [10], for all calculations in this work is because this model is suitable for the introduction of the intermittency-based transition model and shows relatively better results than the others for the entire low Reynolds number condition.

**Reynolds Number Characteristics.** From **Fig. 12** that shows the experimental loss incidence characteristics of all three cascades, plots were derived to display the loss ~ Reynolds number dependency at three characteristic incidences. For all incidence angles it is clearly visible that the optimized blades ES and MOGA are superior to the baseline cascade in the entire Reynolds number range, whereby most improvements were achieved for Reynolds numbers below 200,000. As can be seen from **Fig. 12**, minimum losses are measured around $i=-3-4$ deg for all cascades in the high Reynolds number regime. The corresponding plot of the Reynolds number characteristics at this minimum loss incidence ($i=-3$ deg in **Fig. 15** (left)) clearly reveals the classical tendency with a marginal loss rise between 9 to $5\times10^5$, but an intensive loss increase below a certain "critical" Reynolds number, pronounced especially for the baseline cascade. For all three incidence angles shown in **Fig. 15**, a distinct "critical" Reynolds number for the optimized blades could not be recognized, at least not until the Reynolds numbers approach values of $1.0-1.2\times10^5$.

It is worth mentioning that the MOGA blade losses seem to be more or less independent of the Reynolds number, a slightly strange behavior. But this can be explained by the observation that the MOGA blade starts to separate at the high Reynolds number condition and not at the low Reynolds numbers, as was explained

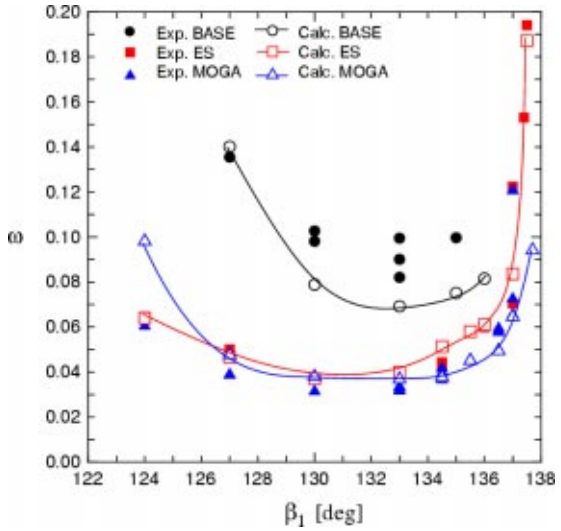


**Fig. 13 Incidence characteristic at the low Reynolds number, HSTAR simulation and experiment, Re≈1.0–1.2×10^5**

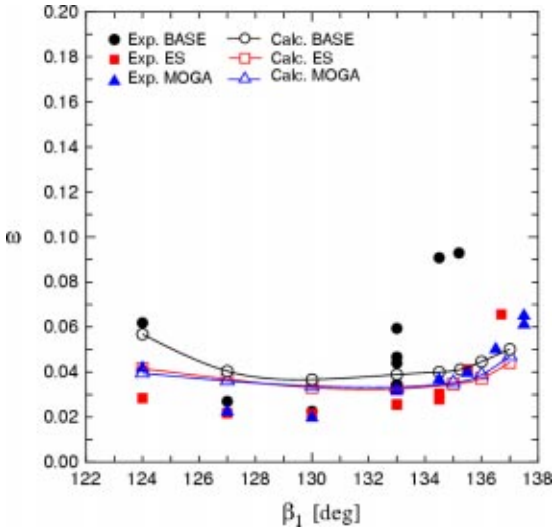


**Fig. 14 Incidence characteristic at high Reynolds number, HSTAR simulation and experiment, Re≈8.6×10^5**

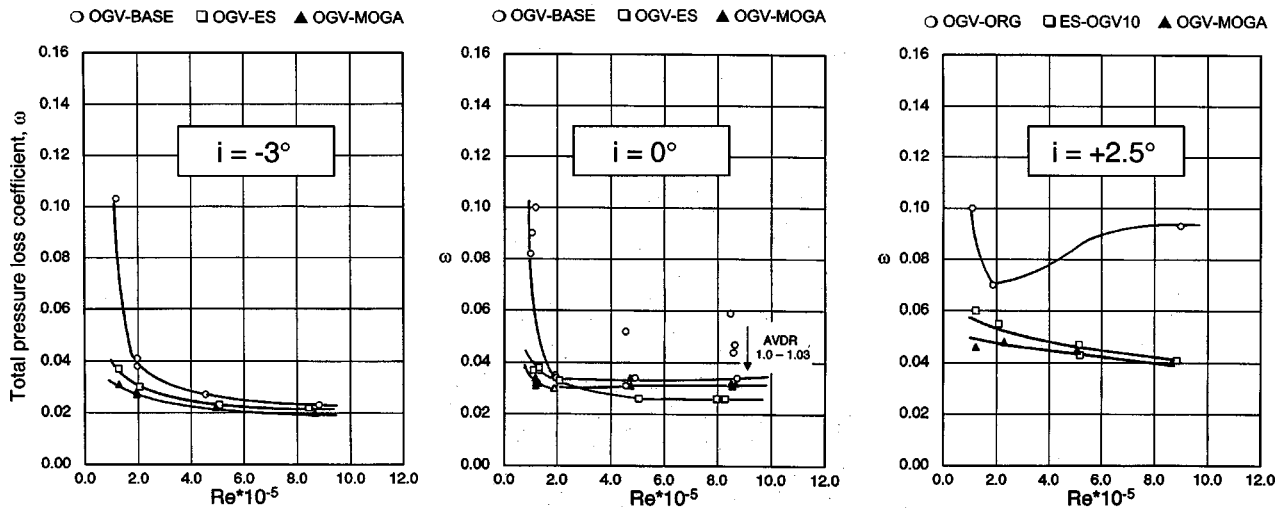


**Fig. 15 Effect of the Reynolds number on experimental losses at three incidence angles, $M_1=0.6$**

already in the previous section. A similar effect, i.e., that losses are relatively reduced when the Reynolds number decreases, can be observed with the baseline cascade for $i=0$ and $+2.5$ deg. Around the Reynolds number of 200,000, there seems to be a loss minimum. It is presumed that for these conditions the turbulent flow entrainment process at the rear part of the laminar separation bubble has a positive effect on the turbulent boundary layer; as a result the rear (turbulent) boundary layer separation is suppressed or reduced.

## Oil Flow Visualization

Oil flow visualization tests have been performed for conditions at high and low Reynolds numbers to study the blade surface boundary layer development. Our focus is the blade suction side at the low Reynolds number condition, the results of which are discussed below. The interpretation of the oil flow pictures is supported by the results of corresponding boundary layer calculations from the viscous/inviscid solver MISES. The calculations were performed at the experimental Reynolds number, but the freestream turbulence level was adjusted in such a way that the extension of the simulated laminar separation bubble is approximately in accordance with the extension observed in the experiment.

Particularly delicate was the interpretation of the tests for the baseline cascade (BASE) because it showed an unstable midchord laminar separation bubble. **Figure 16** provides results for the BASE cascade at design incidence and at a Reynolds number of 190,000, conditions under which the losses of this blade are still on a relatively low level of 3.7–4%. The oil streak lines indicate laminar flow until 29–30% and an unstable midchord separation bubble or rather a bubble that disappeared intermittently with an onset of intermittent rear turbulent separation. It is assumed that in the experiment, the local separation bubble behind the circular LE partly induces a destabilization of the shear layer and triggers the suction-side boundary layer to become turbulent. In this situation, the bubble disappeared but the rear suction side boundary layer separated. With the help of MISES these two observed situations, a laminar midchord bubble and a rear turbulent separation, could be simulated either by assuming a very low turbulence level of 0.05%, by which the experimental bubble length was met, or with a turbulence level of 0.5%, to obtain rear turbulent separation. The

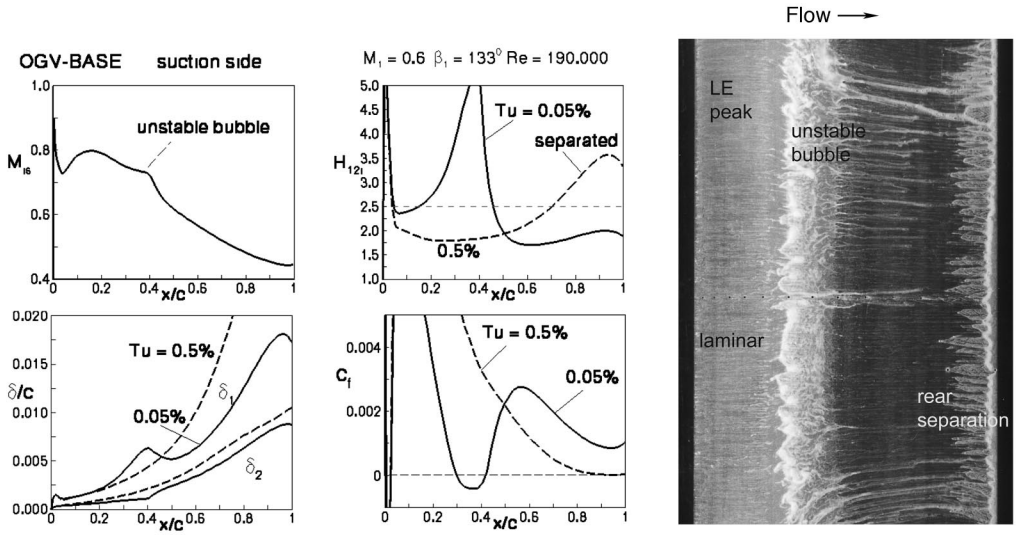


**Fig. 16 MISES suction side boundary layer parameters of OGV-BASE for $Tu=0.05$ and 0.5% and oil flow picture at $i=0$ deg and Re≈190,000**

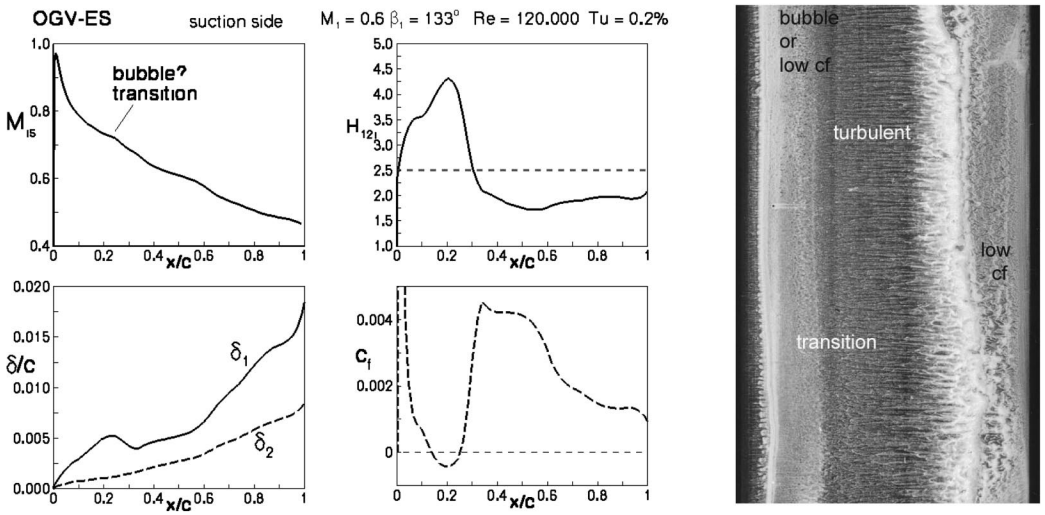


**Fig. 17 MISES suction-side boundary layer parameters of OGV-ES blade and oil flow picture at $i=0$ deg and Re≈120,000**

simulated form factors $H_{12i}$ and the $C_f$ distributions clearly reflect these two intermittently appearing situations, which seem to exist in parallel.

Oil streak lines and corresponding MISES boundary layer parameters for the two optimized blades are provided in **Figs. 17** and **18** for a Reynolds number around 120,000. The extremely front-loaded profile OGV-ES with its arbitrary leading edge starts with a flat laminar separation not immediately behind the LE but at approximately 6% of chord. From the oil picture it is difficult to decide whether there really is separation or just a transitional boundary layer with very low skin friction $C_f$. Downstream of about 22% the suction side is turbulent and there is no indication of a rear turbulent separation. The total pressure losses of this test achieve 3.8%. The corresponding MISES simulation required a turbulence level of 0.2% to approximate the low skin-friction region that is found on the front portion.

Behind the velocity peak of the MOGA blade, there is a short bubble (see the negative $C_f$ values in **Fig. 18**), but the suction-side boundary layer remains laminar until it separates in a bubble at 31% and re-attaches at 53%. As the blade surface curvature underneath the bubble and the amount of adverse pressure gradient behind the separation point is relatively low, the bubble height and the resulting losses remain low too, [17]. However, toward the trailing edge the skin friction coefficient tends to zero, as a result of which the rear part of the oil is not moved ϑ. Overall total pressure losses at this low Reynolds number test are measured to be around 3.4%.

## Conclusions

Two numerically optimized exit guide vane cascades designed for low Reynolds number conditions were tested and the results compared to a baseline cascade with controlled diffusion blades. Both the experimental and numerical results confirmed that the two different optimization methods were able to reduce the total pressure losses at design incidence and to increase the low loss incidence range in the positive direction by about 2–3 deg. Although the two optimized cascades show a considerably different geometry and loading distribution, losses at $\mathrm{Re}=1.0-1.2\times10^5$ could be reduced by about 60%. The superior performance in relation to the baseline CDA cascade was achieved because

a. the airfoils were designed with a more front-loaded pressure distribution and a reduced adverse pressure gradient along the suction side,

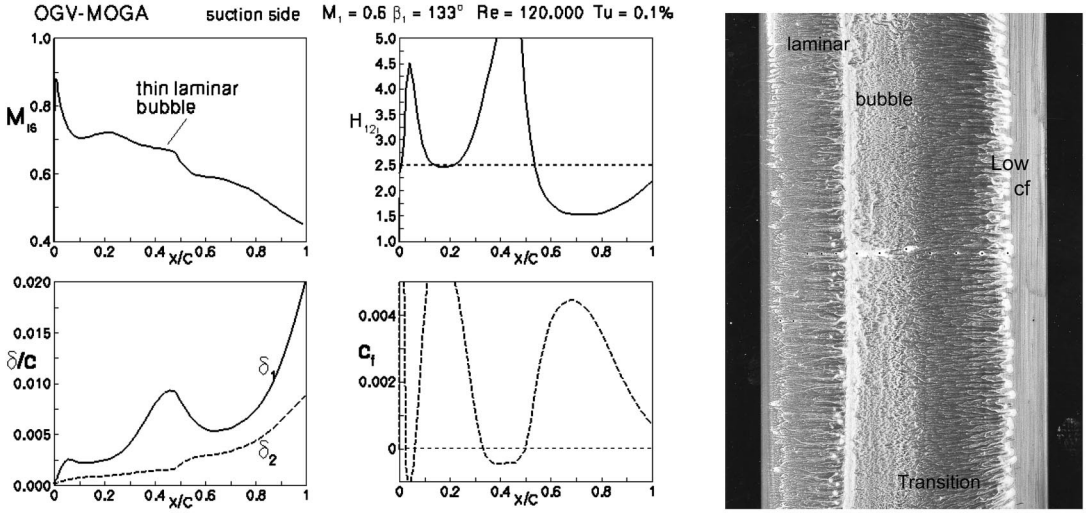


**Fig. 18 MISES suction side boundary layer parameters of OGV-MOGA blade and oil flow picture at $i=0$ deg and Re≈120,000**

b. the LE geometry was modified to avoid a concentrated LE peak with an intensive local separation,
c. in the region of a laminar separation bubble the surface curvature was reduced.

For blade chord Reynolds numbers well below 200,000 it seems to be advantageous to design the airfoils with a fairly steep adverse pressure gradient immediately at the front part in order to promote early transition to prevent the tendency for large laminar separations and the risk of bubble burst. The second obtained alternative, that has a slightly reduced front peak, still operates with laminar flow and a midchord separation bubble, but due to a reduced surface curvature underneath the bubble, its thickness and drag could be reduced considerably.

The Navier-Stokes solver embedded in the optimization process and employed for flow analysis allowed an excellent resolution of the low Reynolds number airfoil aerodynamics with LE bubble and midchord separation. Due to the implemented transition model, the low Reynolds number incidence characteristic was simulated reasonably well. At the same time, some improvements are still necessary to obtain better off-design characteristics especially at higher Reynolds numbers.

The authors are aware that in real turbomachinery environments the high turbulence level can alter the laminar separation behavior considerably, but some blade-to-blade calculations with a turbulence level of 5% revealed that even under the low Reynolds number conditions ($\mathrm{Re}=1.2\times10^5$) the present optimized blades both showed about 50% lower design point losses in relation to the baseline CDA blade.

This work demonstrated the intrinsic advantage of using automated blade optimizations even for complex low Reynolds number aerodynamics. The ability of the present design tools may still be limited, but they offer an essential advantage for the future. After further slight improvements, for example implementation of more problem oriented objective functions, these tools can be embedded in modern automated design processes for turbomachines and it will be possible to achieve new innovative configurations that could not be found by even very experienced design engineers.

## Nomenclature

AVDR = axial velocity density ratio $=(\rho_2 w_2 \sin\beta_2)/(\rho_1 w_1 \sin\beta_1)$
$D_f$ = diffusion factor $=1-w_2/w_1+(w_2/w_1{}^{*}\cos\beta_2\text{-}\cos\beta_1)s/2c$
$c$ = chord length
$C_f$ = friction coefficient $=2\tau_w/(\rho w^2)$
$H_{12}$ = shape factor $=\delta_1/\delta_2$ (index $i$ when incompressible)
$i$ = incidence angle $=\beta_1-\beta_{1\,\mathrm{design}}$
M = Mach number
$p$ = pressure
Re = Reynolds number based on chord length
$s$ = blade spacing
$w$ = velocity
$x$ = chordwise coordinate
$\beta$ = flow angle with respect to cascade front
$\delta_1$ = boundary layer displacement thickness
$\delta_2$ = boundary layer momentum thickness
$\rho$ = density
$\omega$ = total pressure loss coefficient: $\omega=(p_{t1}-p_t)/(p_{t1}-p_1)$

### Subscripts

1 = inlet plane, far upstream
2 = exit plane, far downstream
$is$ = is isentropic entity
$LE$ = leading edge
$TE$ = trailing edge

## References


[1] Rhoden, H. G., 1952, ''Effects of Reynolds Number on the Flow of Air Through a Cascade of Compressor Blades,'' ARC, R&M No. 2919.
[2] Roberts, W. B., 1975, ''The Effect of Reynolds Number and Laminar Separation on Axial Cascade Performance,'' ASME J. Eng. Gas Turbines Power, **97**, pp. 261–274.
[3] Roberts, W. B., 1979, ''Axial Compressor Blade Optimization in a Low Reynolds Number Regime,'' AIAA J., **17**(12), pp. 1361–1367.
[4] Selig, M. S., Gopalarathan, A., Giuere, P., and Lyon, C. A., 2001, ''Systematic Airfoil Design Studies at Low Reynolds Numbers,'' in *Fixed and Flapping Aerodynamics for Micro Air Vehicle Applications*, Prog. Astronaut. Aeronaut., **195**, pp. 143–167.
[5] Mueller, T. J., 1985, ''Low Reynolds Number Vehicles,'' AGARDograph No. 288, AGARD-AG-288.
[6] Sonoda, T., Yamaguchi, Y., Arima, T., Olhofer, M., Sendhoff, B., and Schreiber, H. A., 2003, ''Advanced High Turning Compressor Airfoils For Low Reynolds Number Condition, Part 1: Design and Optimization,'' ASME Paper GT-2003-38458.
[7] Olhofer, M., Arima, T., Sonoda, T., Fischer, M., and Sendhoff, B., 2001, ''Aerodynamic Shape Optimization Using Evolution Strategies,'' *Optimization in Industry III*, Springer-Verlag, New York.
[8] Yamaguchi, Y., and Arima, T., 2000, ''Multi-Objective Optimization for the Transonic Compressor Stator Blade,'' AIAA Paper 2000-4909.
[9] Arima, T., Sonoda, T., Shiratori, M., Tamura, A., and Kikuchi, K., 1999, ''A Numerical Investigation of Transonic Axial Compressor Rotor Flow Using a Low Reynolds number $k$-$\varepsilon$ Turbulence Model,'' ASME J. Turbomach., **121**(1), pp. 44–58.
[10] Wilcox, D. C., 1988, ''Reassessment of the Scale-Determining Equation for Advanced Turbulence Models,'' AIAA J., **26**(11), pp. 1299–1310.
[11] Drela, M., and Youngren, H., 1991, ''Viscous/Inviscid Method for Preliminary Design of Transonic Cascades,'' AIAA Paper 91-2364.
[12] Drela, M., 1995, ''Implementation of Modified Abu-Ghannam Shaw Transition Criterion,'' *MISES User's Guide*, M.I.T., Computational Aerospace Science Lab., Cambridge, MA.
[13] Steinert, W., Eisenberg, B., and Starken, B., 1991, ''Design and Testing of a Controlled Diffusion Airfoil Cascade for Industrial Axial Flow Compressor Application,'' ASME J. Turbomach., **113**(4), pp. 583–590.
[14] Sanz, W., and Platzer, M. F., 1997, ''On the Calculation of Laminar Separation Bubbles Using Different Transition Models,'' ASME Paper 97-GT-453.
[15] Walraevens, R. E., and Cumpsty, N. A., 1995, ''Leading Edge Separation Bubbles on Turbomachine Blades,'' ASME J. Turbomach., **117**, pp. 115–125.
[16] Michelassi, V., Rodi, W., and Gieß, P.-A., 1998, ''Experimental and Numerical Investigation of Boundary-Layer and Wake Development in a Transonic Turbine Cascade,'' Aerosp. Sci. Technol., (**3**), pp. 191–204.
[17] Eppler, R., 1990, *Airfoil Design and Data*, Springer-Verlag, Berlin.

# Unsteady Boundary Layer Development Due to Wake Passing Effects on a Highly Loaded Linear Compressor Cascade

**Lothar Hilgenfeld**

**Michael Pfitzner**

Institut fuer Strahlantriebe,
Universitaet der Bundswehr Muenchen,
Werner-Heisenberg-Weg 39,
85579 Neubiberg, Germany

*The effects of wake passing on boundary layer development on a highly loaded linear compressor cascade were investigated in detail on the suction side of a compressor blade. The experiments were performed in the High Speed Cascade Wind Tunnel of the Institut fuer Strahlantriebe at Mach and Reynolds numbers representative for real turbomachinery conditions. The experimental data were acquired using different measurement techniques, such as fast-response Kulite sensors, hot-film array and hot-wire measurements. The incoming wakes clearly influence the unsteady boundary layer development. Early forced transition in the boundary layer is followed in time by calmed regions. Large pressure fluctuations detectable in the ensemble averaged Kulite data reveal the existence of coherent structures in the boundary layer. Distinct velocity variations inside the boundary layer are amplified when approaching the blade surface. The time–mean momentum thickness values are reduced compared to the steady ones and therefore clarify the potential for a loss reduction due to wake passing effects.* [DOI: 10.1115/1.1791290]

## Introduction

The periodic disturbances caused by wake shedding of upstream blade rows and their downstream migration are a major source of unsteadiness in turbomachines. This inherently unsteady flow plays a significant role in the loss generation process of axial turbomachinery blades. The boundary layer transition on the profile from laminar to turbulent and the subsequent growth of the boundary layer thickness are the main source of loss generation and significantly affected by the unsteadiness of the flow.

Over the past years many experimental investigations on the influence of wake passing on the boundary layer development are reported in the literature. Fundamental studies along flat plates were performed, e.g., by Pfeil and Herbst [1], Pfeil et al. [2] and Orth [3]. Mayle [4] gives an excellent overview of the fundamental transition modes relevant in turbomachines. The transition process is influenced by several factors like the freestream turbulence, the pressure gradient and the strength of the incoming wakes. An increase in wake passing frequency has the same effect as a higher free stream turbulence level (Schobeiri et al. [5]). Due to the periodic wake passing, a combination of several transition modes can occur resulting in a multimode transition process. The maybe most comprehensive basic research work on the boundary layer development on compressor and turbine blades due to wake passing effects were carried out by Halstead et al. [6]. They clarify the fundamental effects regarding to wake passing like the early onset of transition in the wake-induced path, the suppression of a laminar separation bubble and the existence of a calmed region. The calmed region partially suppress laminar separation due to its higher shear stress level and delays the onset of transition in regions where under steady inflow conditions the flow is fully turbulent. Thus the profile losses can be reduced.

Measurements of the blade row interactions in axial compressors were carried out, e.g., by Walker et al. [7] and Mailach and Vogeler [8]. Recent hot-wire measurements within the boundary layer on the blade surface of a multi-stage axial compressor were performed by Shin et al. [9]. However, most of the boundary layer investigations were conducted in low speed wind tunnel flows or low speed research compressors. Only few investigations are available for compressible, high-speed compressor flow, see, for example, Teusch et al. [11,10].

Considering these effects in current aerodynamic design methods, reliable transition and turbulence models in unsteady CFD codes, which consider the effects of wake passing, are necessary. Nevertheless numerical code validation has still to be performed based on experimental test cases. Hence, one objective of the present investigation is to provide a detailed unsteady database for numerical code validation. The present work contributes to this objective as part of a joint research effort on unsteady flows in turbomachines. An overview of the complete project and its scope is given by Hourmouziadis [12]. For this reason experimental investigations focusing on unsteady boundary layer development due to wake passing have been performed on a highly loaded linear compressor cascade at Mach and Reynolds numbers representative for real turbomachinery conditions.

## Experimental Setup

**Compressor Cascade.** The measurements were performed on a large scale compressor cascade called V103-220 consisting of three NACA 65 blades which represent the mid-span of the hub section of a stator blade in a highly loaded axial compressor. Only the center blade is used for the measurements. To achieve a higher resolution of the boundary layer effects, a blade chord length of $l = 220$ mm was chosen. The design conditions with an inlet Mach number of $Ma_1 = 0.67$ and a Reynolds number based on the blade

Contributed by the International Gas Turbine Institute (IGTI) of THE AMERICAN SOCIETY OF MECHANICAL ENGINEERS for publication in the ASME JOURNAL OF TURBOMACHINERY. Paper presented at the International Gas Turbine and Aeroengine Congress and Exhibition, Vienna, Austria, June 13–17, 2004, Paper No. 2004-GT-53186. Manuscript received by IGTI, October 1, 2003; final revision, March 1, 2004. IGTI Review Chair: A. J. Strazisar.

  

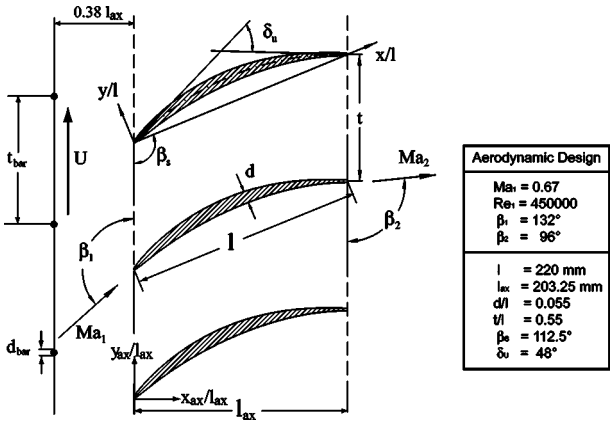


**Fig. 1 Compressor cascade V103-220**

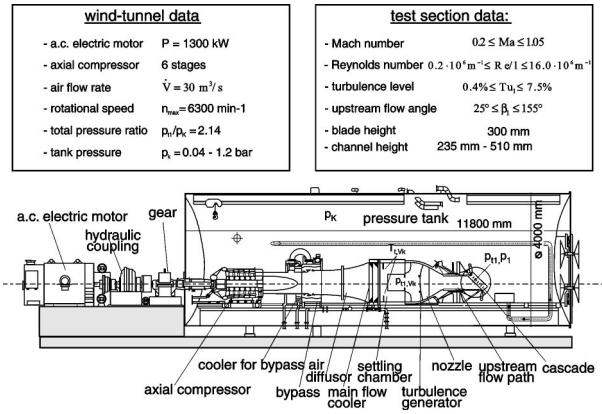


**Fig. 3 High speed cascade wind tunnel**

chord length of $Re_1=450{,}000$ lead to a fully subsonic cascade flow. The geometrical data of the cascade, the definitions of angles and distances and the design conditions are displayed in Fig. 1. The measurements have been performed at Reynolds numbers of 450,000 and 700,000.

**The Wake Generator.** The periodically unsteady flow caused by the relative motion of rotor and stator rows and its influence on the compressor cascade is simulated by a moving bar type wake generator with a bar diameter of $d_{bar}=2$ mm. Acton and Fottner [13] explain this so-called EIZ (Erzeuger Instationaerer Zustroemung; see Fig. 2) and its constructional principles in more detail. The cylindrical steel bars create a far wake very similar to the one produced by an actual airfoil (Pfeil and Eifler [14]). Preliminary tests showed that the wakes shed by bars of 2 mm diameter are representative for the wakes of the V103 profile geometry regarding the wake width. The distance ratio between the bars and the cascade inlet plane is about $x_{ax}/l_{ax}=0.38$. Two different bar pitches of 40 mm and 120 mm were used, resulting in a bar spacing to blade pitch ratio $t_{bar}$/t of 1/3 and 1, respectively. The belt mechanism drives the bars with speeds of up to 40 m/s. For the present investigation Strouhal numbers based on the chord length and the axial inlet velocity between 0.22 and 1.32 are generated for the investigated test cases.

It should be noted that the maximum bar speed together with the axial velocities is still too slow to produce a Strouhal number and inlet velocity triangle representative for modern compressors. The wakes in the rig enter the cascade passage almost parallel to the blades, whereas the data acquired with this setup cannot be transferred directly to real turbomachines. The measurements should be considered as basic investigations of the unsteady multimode transition process. Since the main purpose of the experimental investigations is to provide a database for numerical flow solvers, the angle of the incoming wakes is not essential for the validation of transition modeling in unsteady Navier–Stokes codes.

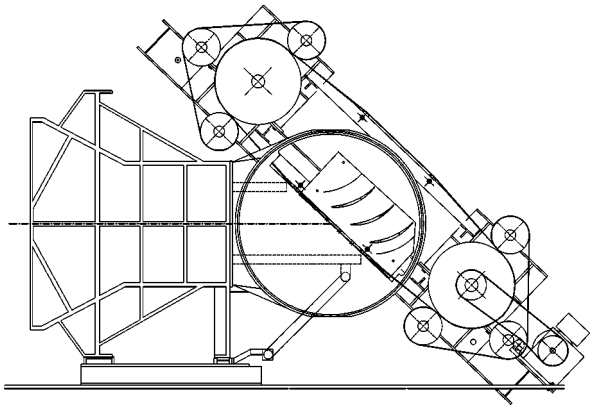

**Fig. 2 Wake generator (EIZ) with installed compressor cascade**

**Test Facility.** The experiments were carried out in the High Speed Cascade Wind Tunnel of the Institut fuer Strahlantriebe of the Universitaet der Bundeswehr Muenchen. The wind tunnel is an open-loop test facility located inside an evacuable pressure tank (Fig. 3). Mach and Reynolds number in the test section can be varied independently by lowering the pressure level inside the tank and keeping the total temperature constant by means of an extensive cooling set-up, therefore allowing to simulate real turbomachinery conditions (Sturm and Fottner [15]). All tests were performed with a constant total temperature of 303 K. The turbulence intensity in the test section is adjusted by fitting a turbulence grid upstream of the nozzle.

**Measuring Techniques.** The experimental data acquired provide time-averaged as well as time-resolved information regarding the boundary layer development on the suction side of a compressor blade.

The time-averaged loading of the compressor blade was measured by means of static pressure tappings on both the suction and the pressure side at the mid-span connected to a Scanivalve system. These pneumatic data were recorded via computer control and represent mean values. The time-resolved compressor profile loading was determined from a total of 10 Kulite fast-response pressure sensors embedded into the suction side of the center blade. Prior the measurement, each Kulite sensor is calibrated inside the pressure tank.

To document the unsteady inflow conditions, triple hot-wire measurements were taken upstream of the cascade inlet at a midspan at about $x_{ax}/l_{ax}=-0.16$. The probe employed in the present investigation consists of three sensing tungsten wires of 5 $\mu$m diameter with a measuring volume of approximately 1 mm in diameter. A single hot-wire anemometer system was used to analyze the boundary layer in the turbulent part of the compressor blade suction side. After passing an anti-aliasing filter, the anemometer output signals are digitized with a sampling frequency of 60 kHz and stored together with other peripheral data. A detailed description of the measuring system and the evaluation procedure of the velocity vector is given in Wolff [16]. The relative error of the hot-wire velocity is estimated to be less than 5%; the absolute angle deviation of the 3D system is less than 1 deg.

Surface mounted hot-film sensors are used to measure the qualitative distribution of unsteadiness and the quasi wall shear stress on the suction side. The entire length of the suction surface

is covered with a total of 56 gauges[1] at the midspan with their spacing varying between 2.5 and 5 mm. The sensors consist of a 0.4 mm thin nickel film applied by vapor deposition process onto a polyamide substrate. They were operated by a constant-temperature anemometer system in sets of 12 sensors and logged simultaneously at a sampling frequency of 50 kHz.

As shown, e.g., by Hodson [17], the boundary layer characteristics can be derived directly from the anemometer output and do not necessarily require an extensive calibration procedure. The quasi-wall shear stress QWSS is determined by the output voltage $E$ and the output voltage under zero flow conditions $E_0$ according to Eq. (1)

$$\mathrm{QWSS} = \mathrm{constant} \cdot \tau_w^{1/3} = \frac{E^2 - E_0^2}{E_0^2}. \tag{1}$$

A once-per-revolution trigger mechanism ensured that the wake passing effects were studied for wakes produced by identical bars. Processing of the raw data was done using the well-established PLEAT technique (**P**hase **L**ocked **E**nsemble **A**veraging **T**echnique, Lakshminarayana et al. [18]) in order to separate random and periodic signals. The time-dependent signal b is composed of a periodic component $\tilde{b}$ and the turbulent component $b'$ according to Eq. (2)

$$b = \tilde{b} + b' \quad \text{with} \quad \tilde{b}(t) = \frac{1}{N}\sum_{i=1}^{N} b_i(t) \tag{2}$$

$$\mathrm{RMS}(t) = \sqrt{\frac{1}{N}\sum_{i=1}^{N} [b_i(t) - \tilde{b}(t)]^2} \tag{3}$$

$$\mathrm{Skewness(t)} = \frac{\frac{1}{N}\Sigma_{i=1}^{N}[b_i(t) - \tilde{b}(t)]^3}{\left(\frac{1}{N}\Sigma_{i=1}^{N}[b_i(t) - \tilde{b}(t)]^2\right)^{3/2}} \tag{4}$$

A total of 300 ensembles was logged with each run and evaluated for quasi-wall shear stress, random unsteadiness RMS, Eq. (3), and skewness, Eq. (4), where the variable $b$ represents the anemometer output voltage. To be able to compare the hot-film sensors, the resulting RMS values were normalized with the anemometer voltage at zero flow, thereby eliminating the influence of manufacturing differences between the gauges.

## Results

**Inflow Conditions.** To provide a comprehensive unsteady data set for numerical modeling of wake passing, the inflow conditions for the cascade have to be investigated in detail. The ensemble averaged results at design inlet flow conditions, a bar pitch of 40 mm ($t_{\mathrm{bar}}/t = 1/3$) and a bar speed of 20 m/s ($\mathrm{Sr}_1 = 0.66$) are shown as an example in Fig. 4, where the normalized inflow velocity, the turbulence level Tu based on the local flow velocity and the inflow angle $\beta_1$ are plotted for four bar passing periods $t/T$.

The velocity deficit in the wake reaches about 12% of the inflow velocity. The turbulence level rises from about 6% background level to 9.5% in the bar wake and correlates with the velocity during the wake passing period. Compared to steady inflow conditions with a freestream turbulence intensity of 3.5%, the overall turbulence intensity in the unsteady case is substantial larger. The reduction in flow velocity also affects the velocity triangle and results in a periodic increase of the inflow angle of about $\Delta\beta = 2$ deg during every wake passing. Note that the absolute value of the inlet flow angle diverges from the geometric flow angle that should result from the installation. This is due to the loss of mass flow through the gaps at the upper and lower end of the cascade, which are required to be able to move the bars upstream of the cascade inlet plane. The wake width can be easily extracted from the figure.

[1]Only 33 gauges are used during the present investigation.

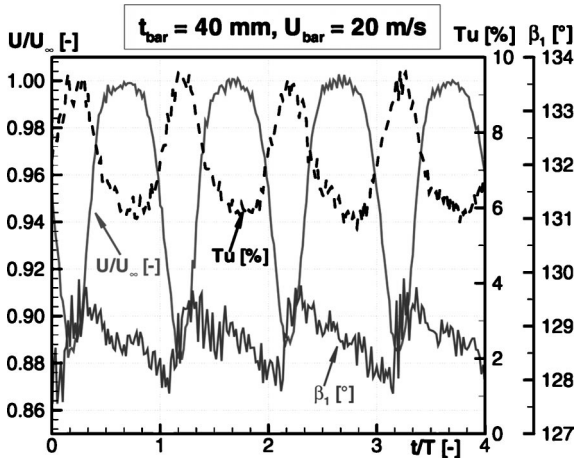


**Fig. 4 Unsteady inflow conditions; design inlet conditions**

**Unsteady Pressure Measurements.** The measurements were performed at different inlet Mach and Reynolds numbers in conjunction with two bar pitches and velocities. To get an impression of the cascade flow at design conditions with an inlet Mach number of $\mathrm{Ma}_1 = 0.67$ and an inlet Reynolds number of $\mathrm{Re}_1 = 450.000$, the mean blade loading in terms of the isentropic profile Mach number distribution is plotted in Fig. 5. Both steady and unsteady inflow conditions, measured with conventional static pressure tappings technique and fast-response Kulite sensors, are shown. The unsteady runs are performed at $t_{\mathrm{bar}}/t = 1/3$ ($t_{\mathrm{bar}} = 40$ mm) and $t_{\mathrm{bar}}/t = 1$ ($t_{\mathrm{bar}} = 120$ mm) at bar speeds of $u_{\mathrm{bar}} = 20$ m/s, resulting in Strouhal numbers of $\mathrm{Sr}_1 = 0.66$ and $\mathrm{Sr}_1 = 0.22$, respectively, based on axial inlet velocity.

The differences compared to the steady inflow case are due to a change of the inlet flow angle due to the moving bars. The mean Kulite data (filled symbols) show an excellent agreement with the values obtained from the static pressure tappings. At unsteady inlet flow conditions, the separation bubble on the suction side starting at about $x_{\mathrm{ax}}/l_{\mathrm{ax}} = 0.40$, is somewhat reduced compared to the steady case due to the time averaging of the periodically attached flow.

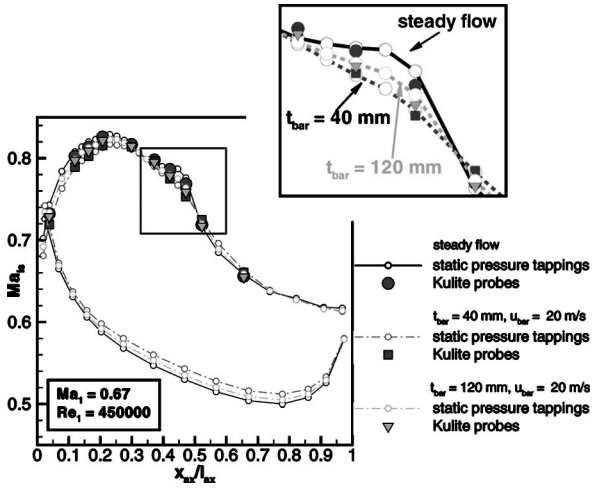


**Fig. 5 Isentropic profile Mach number distribution at design inlet conditions**

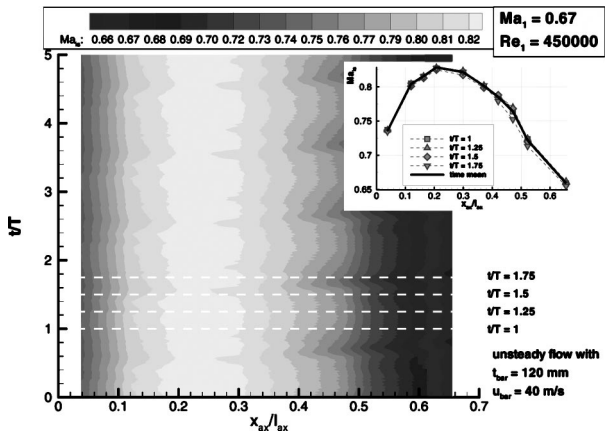


**Fig. 6 Contour of unsteady isentropic profile Mach number**

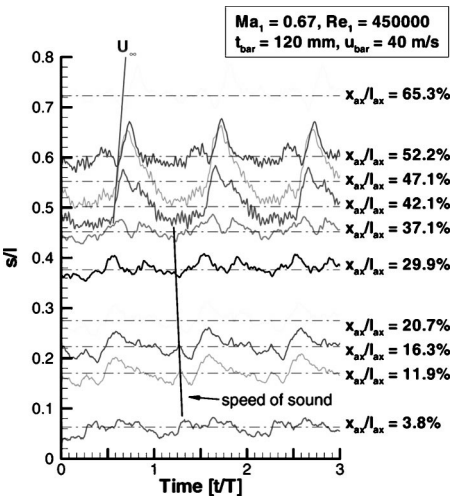


**Fig. 8 Ensemble averaged pressure traces, bar pitch=120 mm, bar speed=40 m/s ($t_{bar}/t=1$, $Sr_1=0.44$)**

As an example of the ensemble averaged unsteady surface pressures measured on the suction side, the isentropic profile Mach number distribution obtained from the Kulite data is given in Fig. 6 for a bar pitch of 120 mm ($t_{bar}/t=1$) and a bar speed of 40 m/s ($Sr_1=0.44$). In this space–time contour plot, nondimensionalized wake passing time $t/T$ along the ordinate is plotted over the nondimensionalized axial chord length along the abscissa. The detailed view shows the profile Mach number at four different time steps during one wake passing period. Near the leading edge there are only small differences from the mean value, but the passing wake leads to a periodical reduction of the separation bubble. Starting in the region of the separated flow at about $x_{ax}/l_{ax}=0.40$, large amplitude pressure oscillations with high frequency occurs. To get more information about these pressure oscillations, a detailed look at the time traces is needed. A selection of typical raw Kulite signals together with the ensemble averaged ones are shown in Fig. 7 for one sensor at $x_{ax}/l_{ax}=0.65$.

The large pressure fluctuations are visible in the raw signal. Although the ensemble averaging process reduces random fluctuations, the large amplitude and high frequency fluctuations are sustained in the average traces. This is an indication that these fluctuations are generated by deterministic coherent structures in the flow. The period is approximately 35% of the bar passing period. The entire ensemble averaged pressure traces measured on the suction side are shown in Fig. 8, which represent the same data as in Fig. 6. The magnitude of the pressure fluctuations, here indicated as solid lines, are arbitrary but congruent along the surface location, which is indicated as dash–dotted lines.

Also drawn in Fig. 8 are two lines representing the trajectory of the freestream velocity $U_\infty$ and the speed of sound. The origin of the high fluctuations is located in the region of the separated laminar flow at about 42% axial chord length. The onset of the following downstream fluctuations are concordant with the freestream trajectory, thus they are controlled by the passing wake. On the other side, the fluctuations prior to the laminar separation bubble propagate upstream with the speed of sound and are therefore triggered by an acoustic mechanism.

Large amplitude pressure fluctuations due to coherent structures are observed by Stieger [19] performing unsteady pressure measurements on the suction surface of a turbine blade. He showed, that the coherent structures are rollup vortices formed in the boundary layer as the wake passes and occur by an inviscid Kelvin–Helmholtz mechanism, therefore the fluctuations do not evolve purely from the periodic turbulent disturbances linked with the wake.

Figure 9 displays the pressure fluctuations obtained for the same inflow conditions but with half the bar speed of $u_{bar}=20$ m/s and bar pitches of 120 mm ($t_{bar}/t=1$) and 40 mm

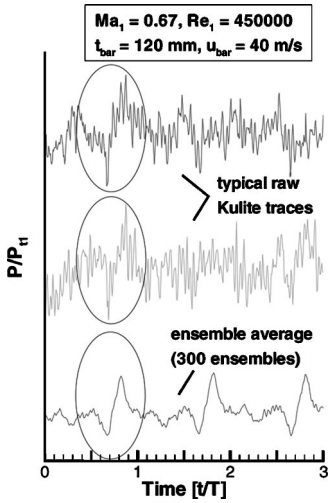


**Fig. 7 Unsteady pressure signals at $x_{ax}/l_{ax}=0.65$**

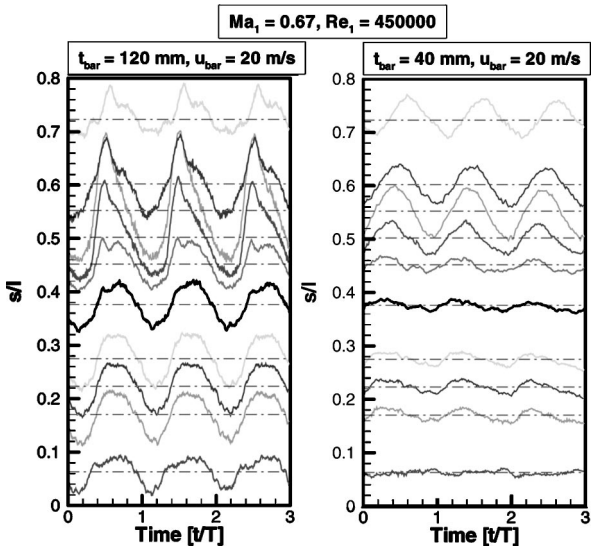


**Fig. 9 Ensemble averaged pressure traces, bar speed=20 m/s**

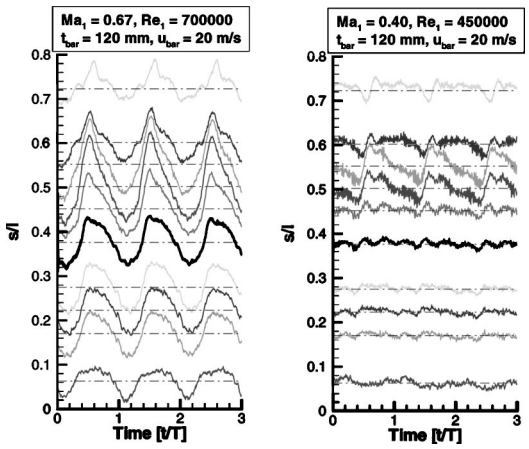


**Fig. 10 Ensemble averaged pressure traces, bar pitch=120 mm ($t_{bar}/t=1$), bar speed=20 m/s**

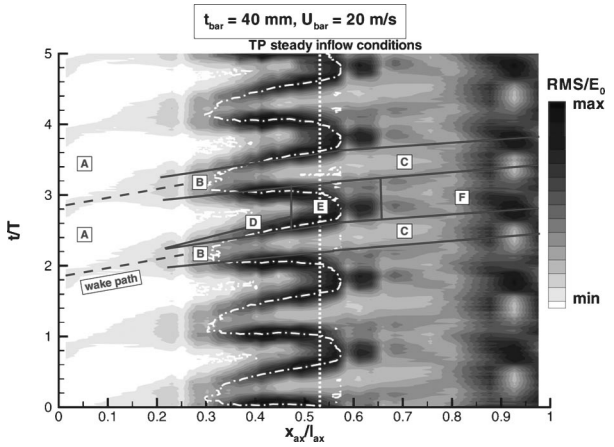


**Fig. 11 Ensemble averaged RMS values, $Ma_1=0.67$, $Re_1=450{,}000$, $t_{bar}=40$ mm, $u_{bar}=20$ m/s ($t_{bar}/t=1/3$, $Sr_1=0.66$)**

($t_{bar}/t=1/3$). The pattern of the pressure fluctuations in the separated flow region in case of the bar pitch 120 mm is comparable to the latter case but the amplitudes are increased. Different oscillation patterns arise in the front part of the suction side, where no characteristic high frequency fluctuations as seen, e.g., in Fig. 7 are detectable. The oscillations are nearly sinusoidal with similar negative and positive amplitudes. The period corresponds to the bar passing period. The appearance of these oscillations in the ensemble averaged values points again at the existence of coherent structures in the boundary layer. In case of the lower bar pitch 40 mm, large sinusoidal oscillations with nearly same amplitude start at about $x_{ax}/l_{ax}=0.42$ up to the last Kulite sensor position. The pattern of the pressure oscillations in the separated flow region strongly depends on the frequency of the bars in terms of the bar pitch and bar speed.

Changing the inlet Mach or Reynolds number results in a similar oscillation pattern as could be seen in Fig. 10 for an increased Reynolds number of $Re_1=700{,}000$ (left side, constant inlet Mach number $Ma_1=0.67$) and for a decreased Mach number of $Ma_1=0.40$ (right side, constant inlet Reynolds number $Re_1=450{,}000$). However, the amplitudes of the fluctuations are reduced in case of the lower Mach number and only small pressure variations are observable prior to the separation.

**Surface-Mounted Hot-Film Measurements.** The effects of the wake passing on the boundary layer transition on the suction side will be considered in the following section. The state of the boundary layer will be identified using the parameters quasi wall shear stress (QWSS) and the root mean square (RMS). The results of the hot-film measurements in terms of space–time diagrams of ensemble averaged normalized RMS values and ensemble averaged QWSS are shown in the following figures. The data are mapped only qualitatively; dark regions indicate maximum and light areas minimum values. To identify the movement of the transition point, the dash–dotted white lines within the RMS diagrams, representing zero skewness, are used. The transition point under steady inflow conditions is shown as a dotted vertical line. To illustrate the wake-induced transition process, different regions representative for various boundary layer states are marked in the figures similar to Halstead et al. [6].

The flow development takes place along a wake-induced path and a path between two wakes. Following the wake path in Fig. 11, a wake-induced transitional flow regime (B) emerges, where early transition is forced as can be seen in the RMS values and the white zero skewness line. The migration of the transition point covers about 27% of the surface length. The path between two wakes remains still laminar (A). The transitional region (B) is followed in time by a stable calmed region (D) with decreasing RMS values. The calmed region is able to delay the onset of transition in the path between two wakes (E). The transition point moves periodically downstream in the region influenced by calming effects (D) as compared with steady inflow conditions. The regions (C) and (F) are turbulent up to the trailing edge, but the boundary layer properties change in time as could be seen in the next chapter.

The wake-induced transitional region (B) exhibits a double peak of high RMS values. Mailach and Vogeler [8] pointed out that this double peak is a response of the boundary layer due to the increased turbulence of the incoming wake. The wake generated by the bars can generally be described as a von Karman vortex street with shedded vortices. Due to the short axial gap between the bar plane and the cascade inlet plane, the vortices are not mixed out as they enter the cascade inlet plane as shown in the single hot-wire measurements of Teusch et al. [10]. As a possible consequence of the larger measuring volume of the current used triple hot-wire probe, the present measurements (Fig. 4) do not show any double peaks in the turbulence distribution upstream the cascade inlet. However, the wake width in the RMS diagrams corresponds to the results of the triple hot-wire measurements displayed in Fig. 4.

Closer insight can be obtained by looking at one single sensor during wake passing, as shown, for example, in Fig. 12 for the axial location $x_{ax}/l_{ax}=0.40$. Note that the origin of the nondimensional time on the abscissa represents the start of the measurement and do not necessarily coincide with the wake impact on the boundary layer at this specific sensor location. Due to the high reduced frequency in case of the bar pitch of 40 mm

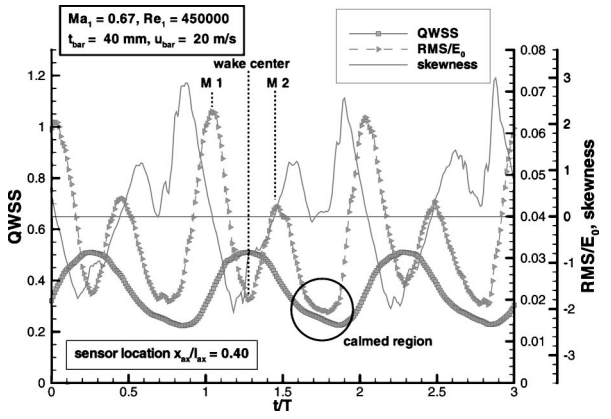


**Fig. 12 Ensemble averaged values at single sensor location $x_{ax}/l_{ax}=0.40$, $Ma_1=0.67$, $Re_1=450{,}000$, $t_{bar}=40$ mm, $u_{bar}=20$ m/s ($t_{bar}/t=1/3$, $Sr_1=0.66$)**

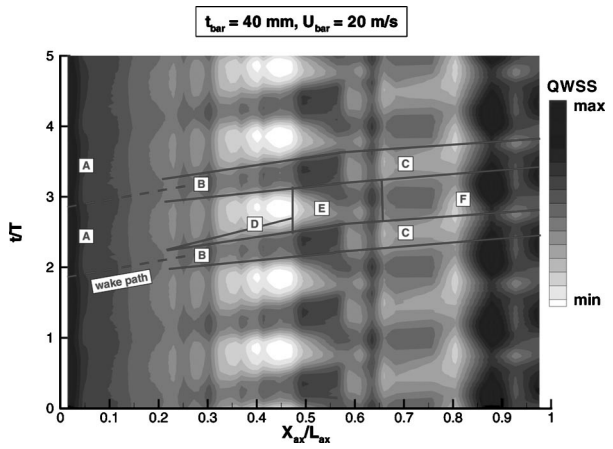


**Fig. 13 Ensemble averaged QWSS values, $Ma_1=0.67$, $Re_1=450{,}000$, $t_{bar}=40$ mm, $u_{bar}=20$ m/s ($t_{bar}/t=1/3$, $Sr_1=0.66$)**

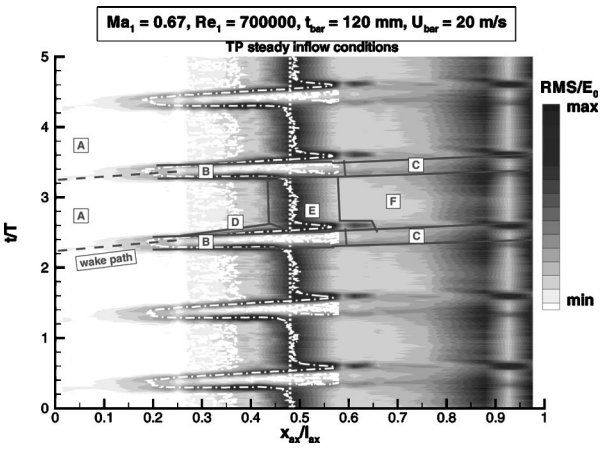


**Fig. 15 Ensemble averaged RMS values, $Ma_1=0.67$, $Re_1=700{,}000$, $t_{bar}=120$ mm, $u_{bar}=20$ m/s ($t_{bar}/t=1$, $Sr_1=0.22$)**

($Sr_1=0.66$), no distinct regions of undisturbed laminar boundary layer flow exist. The wall shear stress increases after the impact of the wake due to the increased turbulence inside the wake. The maximum fluctuations marked as M1 and M2 occur at temporally uniformly distributed parts of the laminar and turbulent boundary layer with an intermittency of $\gamma=0.5$. Between the points M1 and M2, the turbulent part in the boundary layer outweighs with an intermittency of $0.5<\gamma<1$, indicated by the minimum RMS value and the maximum of the QWSS value at the center of the wake. Then the wall shear stress decreases. Subsequent to the wake influence, the wall shear stress is still decreasing for a short time while the fluctuations remain at a low level. This is according to Halstead et al. [6] the indication of the calmed region. The calmed region is interrupted by the appearance of the next wake.

The space–time diagram of quasi wall shear stress on the suction side surface (Fig. 13) allows identifying the location and extent of the laminar separation bubble characterized by minimum values in the QWSS distribution. Every wake passing, the transitional flow regime (B) prevents the formation of a separation bubble and transition takes place via bypass mode. The calmed region also suppresses the laminar separation.

In case of the high bar pitch 120 mm ($t_{bar}/t=1$) shown in Fig. 14, a region of undisturbed transition similar to the steady case exists, where a laminar separation bubble develops between two wakes. The migration of the transition point covers about 27% of the surface length. There is only a small delay of the transition onset downstream due to the calming effects of the calmed region. The influence of the Reynolds number to the transition process is displayed in Fig. 15 for an inlet Reynolds number $Re_1=700{,}000$. The bar pitch is still 120 mm. Following the wake-induced path, the downstream migration of the transition point is more obvious. The periodical migration process covers about 35% of the surface length. With increasing Reynolds number, the effect of the calmed region is therefore amplified.

**Boundary Layer Traverses.** To get detailed information on the change of characteristic boundary layer parameters during the wake passing, single hot-wire traverses have been performed in the turbulent part of the boundary layer. All the traverses have been performed at a bar speed of 20 m/s. Figure 16 shows the ensemble averaged normalized velocities across the boundary layer at design inlet conditions and a bar pitch of 40 mm for one axial position $x_{ax}/l_{ax}=0.65$. The wall–normal distance $\eta/l$ along the ordinate is plotted over a nondimensionalized bar passing period $t/T$. The wake path can be identified in the freestream due to its velocity deficit.

The large velocity oscillations inside the boundary layer exhibit a pattern similar to the pressure traces in Fig. 9 (right side). The oscillations are amplified across the boundary layer, but slightly damped when approaching the blade surface. Similar results for the velocity distribution can be found in Chakka and Schobeiri [20]. In case of the higher bar pitch 120 mm ($t_{bar}/t=1$). which is shown in Fig. 17, the typical pattern of the large amplitude and

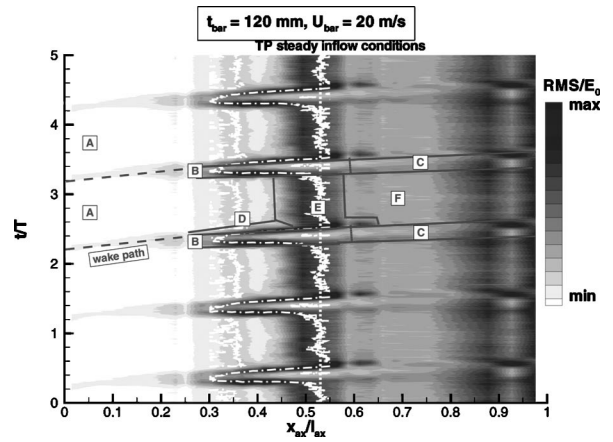


**Fig. 14 Ensemble averaged RMS values, $Ma_1=0.67$, $Re_1=450{,}000$, $t_{bar}=120$ mm, $u_{bar}=20$ m/s ($t_{bar}/t=1$, $Sr_1=0.22$)**

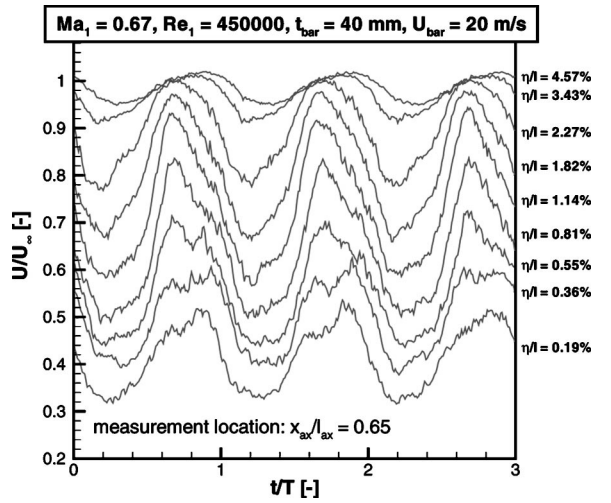


**Fig. 16 Ensemble averaged velocity, $Ma_1=0.67$, $Re_1=450{,}000$, $t_{bar}=40$ mm, $u_{bar}=20$ m/s ($t_{bar}/t=1/3$, $Sr_1=0.66$)**

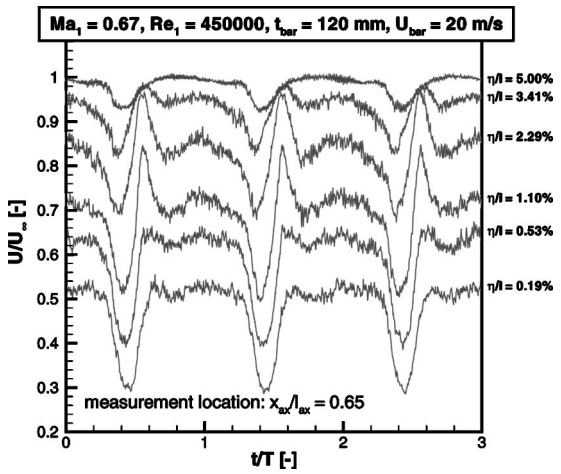


**Fig. 17 Ensemble averaged velocity, $Ma_1=0.67$, $Re_1=450{,}000$, $t_{bar}=120$ mm, $u_{bar}=20$ m/s ($t_{bar}/t=1$, $Sr_1=0.22$)**

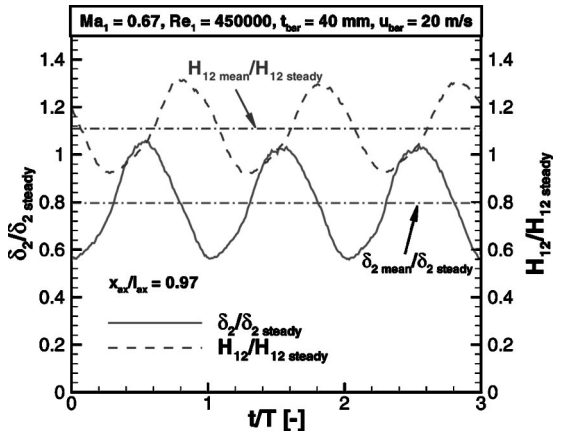


**Fig. 18 Momentum thickness and shape factor at $x_{ax}/l_{ax}=0.97$, $Ma_1=0.67$, $Re_1=450{,}000$, $t_{bar}=40$ mm, $u_{bar}=20$ m/s ($t_{bar}/t=1/3$, $Sr_1=0.66$)**

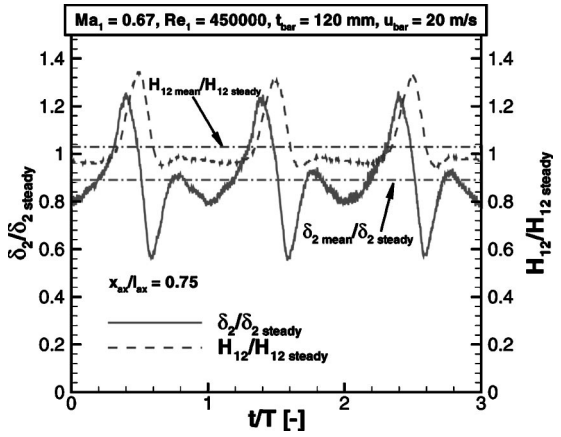


**Fig. 19 Momentum thickness and shape factor at $x_{ax}/l_{ax}=0.75$, $Ma_1=0.67$, $Re_1=450{,}000$, $t_{bar}=120$ mm, $u_{bar}=20$ m/s ($t_{bar}/t=1$, $Sr_1=0.22$)**

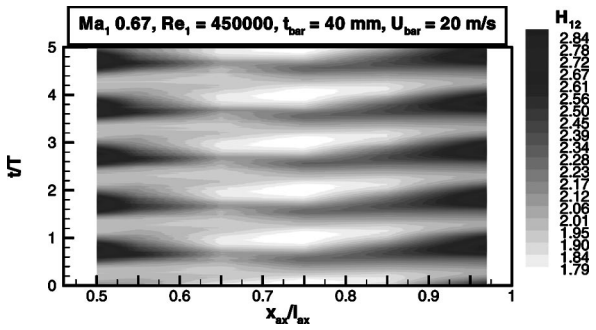


**Fig. 20 Ensemble averaged shape factors, $Ma_1=0.67$, $Re_1=450{,}000$, $t_{bar}=40$ mm, $u_{bar}=20$ m/s ($t_{bar}/t=1/3$, $Sr_1=0.44$)**

high frequency oscillations already identified in the Kulite signals (see, e.g., Fig. 7) are obvious. The period of this fluctuation is about 40% of the bar passing period. These patterns, and therefore the underlying coherent structures, emerge within the boundary layer, whereas in the freestream and near the wall only the wake-typical velocity deficit appears.

Figures 18 and 19 display the corresponding integral boundary layer parameters momentum thickness $\delta_2$ and shape factor $H_{12}$ obtained near the trailing edge at $x_{ax}/l_{ax}=0.97$ and $x_{ax}/l_{ax}=0.75$,[2] respectively, both normalized with their values from steady inflow conditions. In case of the low bar pitch 40 mm, the oscillations about the mean values are again sinusoidal. During one wake passing, the momentum thickness varies between plus 5% and minus 45% compared to the steady case, while the time–mean momentum thickness shows a decrease of about 20%. As the momentum thickness at the trailing edge is regarded as a measure for the profile losses, a substantial loss reduction compared to the steady case is estimated. The time–mean shape factor value shows an increase of about 11%.

There is only a moderate increase of the time-mean shape factor of about 3% in case of the bar pitch 120 mm ($t_{bar}/t=1$). The time–mean momentum thickness is reduced at about 11% compared to the steady inflow case. In contrast to the case at low bar pitch, the momentum thickness temporarily increases up to 25% during the high peak fluctuations.

The space–time diagram of the ensemble averaged shape factors is given in Fig. 20 for the low bar pitch of 40 mm ($t_{bar}/t=1/3$). The alternation of high shape factors in the region of about $x_{ax}/l_{ax}=0.50$ representing separated flow and low values representing attached flow is clearly visible.

## Conclusions

Detailed experimental investigations were performed on a highly loaded linear compressor cascade focusing on unsteady boundary layer development due to wake passing effects. Cylindrical bars moving parallel to the cascade inlet plane simulate the periodically unsteady flow caused by the relative motion of rotor and stator rows. The experimental data were acquired using different measurement techniques, such as fast-response Kulite sensors, hot-film array and hot-wire measurements. The experiments were carried out using two different bar pitches of the wake generator. In case of the high bar pitch of 120 mm ($t_{bar}/t=1$), the passing wakes lead to a periodical change of the blade loading. Large amplitude pressure oscillations with high frequency due to deterministic coherent structures in the boundary layer start in the region of the separated flow. They trigger the upstream pressure fluctuations by an acoustic mechanism as they propagate upstream with the local speed of sound. The reduction in flow velocity also affects the velocity triangle and results in a periodic increase of

[2]At the present, no data are available for the high bar pitch of 120 mm beyond $x_{ax}/l_{ax}=0.75$.

the inflow angle of about $\Delta\beta=2$ deg during every wake passing. The overall background turbulence level is significant larger compared to steady inflow conditions. Surface mounted hot-film sensors are used to measure the qualitative distribution of unsteadiness and the quasi wall shear stress along the suction side over time. For both bar pitches, the separation bubble is periodically reduced, but still existent. The migration of the transition point covers up to one third of the surface length. The RMS values in the wake-induced transitional region exhibit a double peak as a response of the boundary layer to the structure of the incoming wakes. To get detailed information on the change of characteristic boundary layer parameters during wake passing, single hot-wire traverses have been performed in the turbulent part of the boundary layer. Large velocity oscillations inside the boundary layer occur, which are amplified across the boundary layer. The time-mean momentum thickness values at unsteady inflow conditions are significantly reduced compared to the steady ones and therefore clarify the potential for a loss reduction due to wake passing effects.

The measurements are also intended as a contribution to the validation process of unsteady Navier–Stokes codes.

## Acknowledgments

The authors wish to acknowledge the support of the Deutsche Forschungsgemeinschaft (DFG) for the research program partly reported in this paper. The work was performed within the joint project ''Periodical Unsteady Flow in Turbomachines.''

## Nomenclature

$E$ [V] = anemometer output voltage
M1, M2 [-] = RMS maxima within the wake-induced path
Ma [-] = Mach number
$N$ [-] = number of ensembles
QWSS [-] = quasi wall shear stress
Re [-] = Reynolds number
RMS [-] = root mean square
Sr [-] = Strouhal number
T [s] = bar passing period
Tu [%] = turbulence intensity
$b$ [V] = general time-dependent signal
$b'$ [-] = turbulent component of signal
$\tilde{b}$ [-] = period component of signal
$d_{\mathrm{bar}}$ [m] = bar diameter
$l$ [m] = blade chord length
$t$ [s] = time
$t$ [m] = blade pitch
$t_{\mathrm{bar}}$ [m] = bar spacing
$u$ [m/s] = velocity
$x$ [m] = chordwise position
$\beta$ [°] = flow angle
$\gamma$ [-] = intermittency
$\tau_w$ [N/m$^2$] = wall shear stress

### Subscripts

0 = zero flow conditions
1 = cascade inlet plane
2 = cascade exit plane
ax = axial distance
$i$ = time index

## References

[1] Pfeil, H., and Herbst, R., 1979, ''Transition Procedure of Instationary Boundary Layers,'' ASME Paper No. 79-GT-128.
[2] Pfeil, H., Herbst, R., and Schröder, T., 1983, ''Investigation of the Laminar-Turbulent Transition of Boundary Layers Disturbed by Wakes,'' ASME J. Eng. Power, **105**, pp. 130–137.
[3] Orth, U., 1993, ''Unsteady Boundary Layer Transition in Flow Periodically Disturbed by Wakes,'' ASME J. Turbomach., **115**, pp. 707–713.
[4] Mayle, R. E., 1991, ''The Role of Laminar–Turbulent Transition in Gas Turbine Engines,'' ASME J. Turbomach., **113**, pp. 509–537.
[5] Schobeiri, M. T., Read, K., and Lewalle, J., 1995, ''Effect of Unsteady Wake Passing Frequency on Boundary Layer Transition: Experimental Investigation and Wavelet Analysis,'' ASME Paper No. 95-GT-437.
[6] Halstead, D. E., Wisler, D. C., Okiishi, T. H., Walker, G. J., Hodson, H. P., and Shin, H.-W., 1997, ''Boundary Layer Development in Axial Compressors and Turbines: Part 1–4,'' ASME J. Turbomach., **119**, pp. 114–127, pp. 426–444, pp. 225–237, pp. 128–139.
[7] Walker, G. J., Hughes, J. D., and Solomon, W. J., 1999, ''Periodic Transition On An Axial Compressor Stator: Incidence and Clocking Effects: Part I-Experimental Data,'' ASME J. Turbomach., **121**, pp. 398–407.
[8] Mailach, R., and Vogeler, K., 2003, ''Aerodynamic Blade Row Interaction in an Axial Compressor. Part I: Unsteady Boundary Layer Development,'' ASME Paper No. GT2003-38765.
[9] Shin, Y. H., Elder, R. L., and Bennet, I., 2003, ''Boundary Layer Measurement on the Blade Surface of a Multi-Stage Axial Flow Compressor,'' ASME Paper No. GT2003-38183.
[10] Teusch, R., Swoboda, M., and Fottner, L., 1999, ''Experimental Investigation of Wake-Induced Transition in a Linear Compressor Cascade With Controlled Diffusion Blading,'' ISABE Paper No. 99-7057.
[11] Teusch, R., Brunner, S., and Fottner, L., 2000, ''The Influence of Multimode Transition Initiated by Periodic Wakes on the Profile Loss of a Linear Compressor Cascade,'' ASME Paper No. 2000-GT-271.
[12] Hourmouziadis, J., 2000, ''Das DFG-Verbundvorhaben Periodisch Instationaere Stroemungen in Turbomaschinen,'' DGLR Paper No. JT2000-030.
[13] Acton, P., and Fottner, L., 1996, ''The Generation of Instationary Flow Conditions in the High-Speed Cascade Wind Tunnel,'' 13th Symp. on Meas. Techn. for Transonic and Supersonic Flows in Cascades and Turbomachines.
[14] Pfeil, H., and Eifler, J., 1976, ''Turbulenzverhaeltnisse Hinter Rotierenden Zylindergittern,'' Forschung Ingenieurwesen, **42**, pp. 27–32.
[15] Sturm, W., and Fottner, L., 1985, ''The High-Speed Cascade Wind Tunnel of the German Armed Forces University Munich,'' 8th Symp. on Meas. Techn. for Transonic and Supersonic Flows in Cascades and Turbomachines, Genoa.
[16] Wolff, S., Brunner, S., and Fottner, L., 2000, ''The Use of Hot-Wire Anemometry to Investigate Unsteady Wake-Induced Boundary-Layer Development on a High-Lift LP Turbine Cascade,'' ASME J. Turbomach., **122**, pp. 644–650.
[17] Hodson, H. P., Huntsman, I., and Steele, A. B., 1994, ''An Investigation of Boundary Layer Development in a Multistage LP Turbine,'' ASME J. Turbomach., **116**, pp. 375–383.
[18] Lakshminarayana, B., and Poncet, A., 1974, ''A Method of Measuring Three-Dimensional Rotating Wakes Behind Turbomachines,'' J. Fluids Eng., **96**, pp. 87–91.
[19] Stieger, R. D., 2002, ''The Effects of Wakes on Separating Boundary Layers in Low Pressure Turbines,'' Ph.D. thesis, Cambridge University.
[20] Chakka, P., and Schobeiri, M. T., 1999, ''Modeling Unsteady Boundary Layer Transition on a Curved Plate Under Periodic Unsteady Flow Conditions: Aerodynamic and Heat Transfer Investigations,'' ASME J. Turbomach., **121**, pp. 88–97.

# Surge Avoidance in Gas Compression Systems

**R. Kurz**

**R. C. White**

Solar Turbines Incorporated,
9330 Skypark Court,
San Diego, CA 92123

*The phenomenon of compressor surge and its prevention have drawn significant attention in the literature. An important aspect of surge avoidance lies in the design of the compressor station and, in particular, the piping upstream and downstream of the compressor. Most anti-surge systems are perfectly capable of avoiding surge during normal operating conditions. However, unplanned emergency shutdowns present a significant challenge, and surge avoidance in these cases depends to a large degree on the station layout. In this paper, data from a compressor that surged during an emergency shutdown are presented. The data are analyzed to determine the effects of surge and the rate of deceleration. A model to simulate shutdown events is developed and used to develop simpler rules that help with proper sizing of upstream and downstream piping systems, as well as the necessary control elements. The compression system is analyzed, thus verifying the model and the simplifications.* [DOI: 10.1115/1.1777577]

## Introduction

In light of recent attempts to increase the stability margin of a compressor by active (Epstein et al. [1] and Blanchini et al. [2]) or passive means (Arnulfi et al. [3]), or by increasing the accuracy of determining the surge margin (McKee and Deffenbaugh [4]), it is often overlooked that meaningful gains can be made by better understanding the interaction between the compressor, the anti-surge devices (control system, valves) and the station piping layout (coolers, scrubbers, check valves). This study focuses on centrifugal compressors driven by two-shaft gas turbines (**Fig. 1).**

The possible operating points of a centrifugal gas compressor are limited by maximum and minimum operating speed, maximum available power, choke flow, and stability (surge) limit (**Fig. 2**). Surge, which is the flow reversal within the compressor, accompanied by high fluctuating load on the compressor bearings, has to be avoided to protect the compressor. The usual method for surge avoidance (''anti-surge-control'') consists of a recycle loop that can be activated by a fast acting valve (''anti-surge valve'') when the control system detects that the compressor approaches its surge limit. Typical control systems use suction and discharge pressure and temperature, together with the inlet flow into the compressor as input to calculate the relative distance (''surge margin'') of the present operating point to the predicted or measured surge line of the compressor (**Fig. 2**). The surge margin is defined by

$$SM = \left. \frac{Q_{op} - Q_{\text{surge}}}{Q_{op}} \right|_{N=\text{const}} . \qquad (1)$$

If the surge margin reaches a preset value (often 10%), the anti-surge valve starts to open, thereby reducing the pressure ratio of the compressor and increasing the flow through the compressor. The situation is complicated by the fact that the surge valve also has to be capable of precisely controlling low. Additionally, some manufacturers place limits on how far into choke (or overload) they allow their compressors to operate.

A very critical situation arises upon emergency shutdown (ESD). Here, the fuel supply to the gas turbine driver is cut off instantly, thus letting the power turbine and the driven compressor coast down on their own inertia[1]. Because the head-making capability of the compressor is reduced by the square of its running speed, while the pressure ratio across the machine is imposed by the upstream and downstream piping system, the compressor would surge if the surge valve cannot provide fast relief of the pressure. The deceleration of the compressor as a result of inertia and dissipation are decisive factors. The speed at which the pressure can be relieved of the pressure not only depends on the reaction time of the valve, but also on the time constants imposed by the piping system. The transient behavior of the piping system depends largely on the volumes of gas enclosed by the various components of the piping system, which may include, besides the piping itself, various scrubbers, knockout drums, and coolers. The system boundaries for this study are the first downstream check valve, while the upstream boundary may be either a check valve or an infinite plenum (at constant pressure, **Fig. 3**).

The requirements of the anti-surge system for such situations as ESD or other massive system disturbances are distinctly different from the usual process control case. The former is a massive, fast

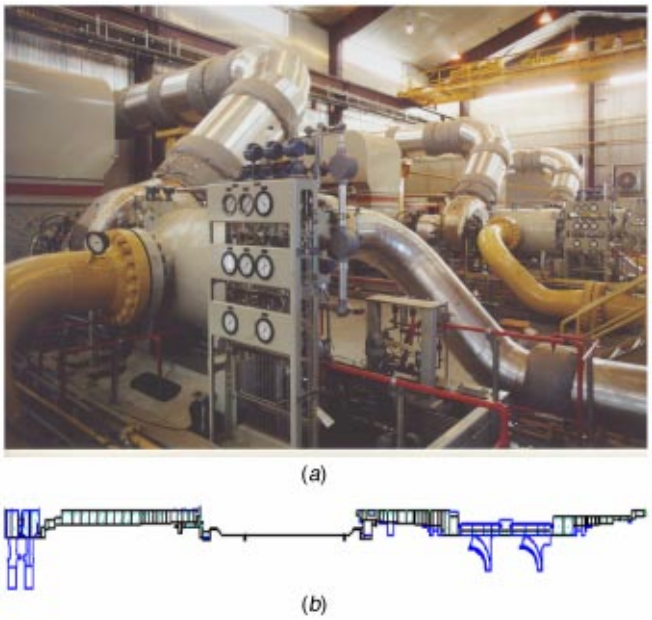


**Fig. 1 Compressor station and rotor system consisting of power turbine, coupling, and compressor rotor**

Contributed by the Turbomachinery Division of THE AMERICAN SOCIETY OF MECHANICAL ENGINEERS for publication in the JOURNAL OF TURBOMACHINERY. Manuscript received by the Turbomachinery Division, May 21, 2004; revised manuscript received, May 27, 2004. Editor: D. Wisler.

[1]Some installations maintain fuel flow to the turbine for 1 to 2 seconds while the recycle valve opens. However, this can generate a safety hazard.

  

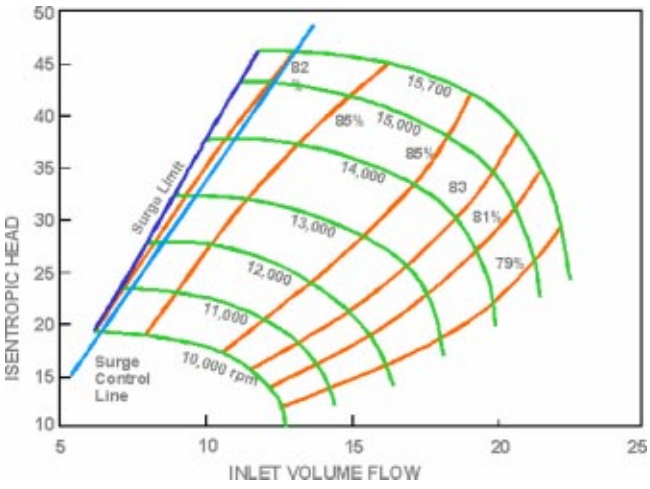


**Fig. 2 Typical compressor map**

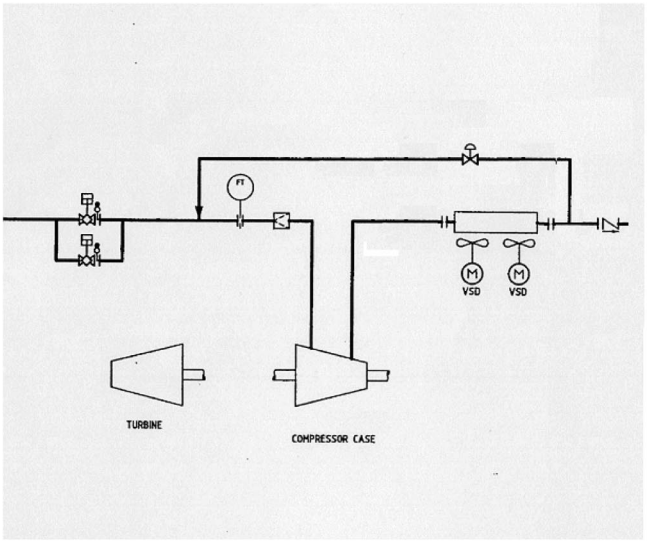


(*a*)

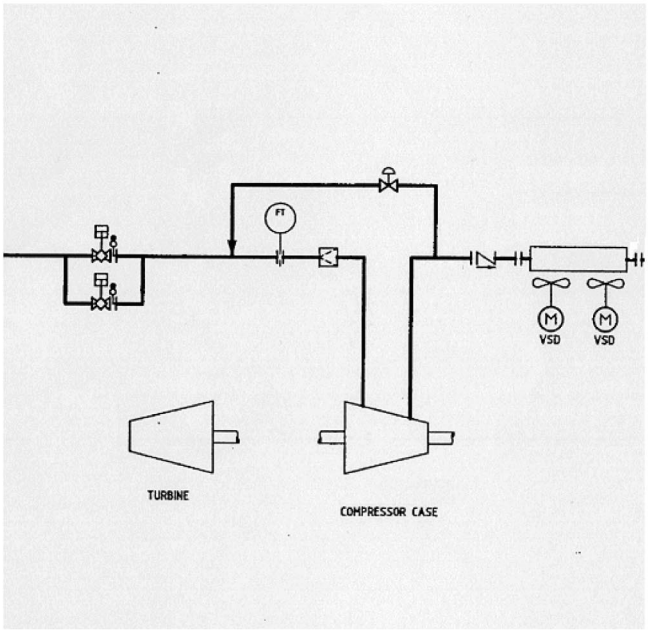


(*b*)

**Fig. 3 Anti-surge and recycle system; (*a*) cooled recycle, (*b*) hot recycle**

change in conditions that first and foremost requires fast system reaction. This requires, among others, extremely fast opening valves with sufficiently large flow areas. The latter requires the capability to precisely control slow changes in the process, such that no oscillations occur, which can be accomplished with precisely positioned valves.

## Surge Phenomenon

**Figure 4**, [5], shows the head versus flow characteristic of a typical centrifugal compressor, including the areas of unstable operation. At flows lower than the stability point, the compressor initially shows a reduced capability to generate head with reduced flow, until it experiences reverse flow, that is, the gas now flows from the discharge to the suction side. Once flow reversal occurs, the amount of flow depends on the pressure ratio across the compressor, since in this situation the compressors acts more or less like an orifice. The flow reversal means that the pressure downstream of the compressor is gradually reduced. The speed of pressure reduction depends largely on the size of the volume downstream of the compressor. Once the pressure is reduced sufficiently, the compressor will recover and flow gas again from the suction to the discharge side. Unless action is taken, the events repeat again. Ongoing surge can damage thrust bearings (due to the massive change of thrust loads), seals, and eventually overheat the compressor. Details of the energy transfer from the compressor into the gas are described in [6].

## Modeling the Piping Surge Control Interaction

Design of the piping and valves, together with the selection and the placement of instruments will significantly affect the performance of an anti-surge control system. This is a major issue during the planning stage because the correction of design flaws can be very costly once the equipment is in operation. Typical configurations for recycle systems are outlined in **Fig. 3**. In its simplest form, the system includes a flow-measuring element in the compressor suction, instruments to measure pressures and temperatures at suction and discharge, the compressor, an after-cooler and a discharge check valve, as well as a recycle line with a control valve, connected upstream of the discharge check valve and compressor flow-measuring device.

The control system monitors the compressor operating parameters, compares them to the surge limit, and opens the recycle valve as necessary to maintain the flow through the compressor at a desired margin from surge. In the event of an ESD, where the fuel to the gas turbine is shut off instantly, the surge valve opens immediately, essentially at the same time the fuel valve is closing.

In a simple system, the boundaries for the gas volume ($V$) on the discharge side are established by the discharge check valve, compressor, and recycle valve. The volume on the suction side is usually orders of magnitude larger than the discharge volume and,

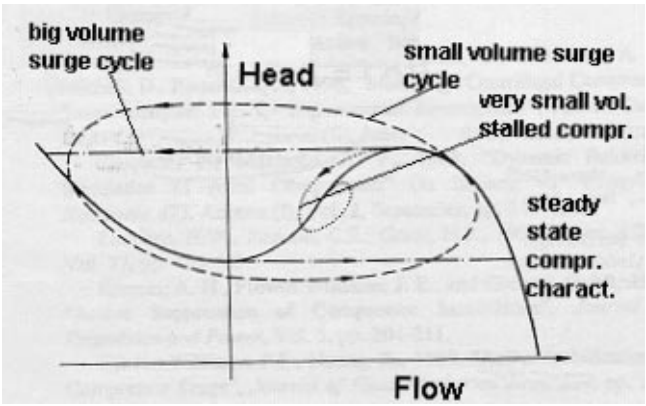


**Fig. 4 Simplified surge cycles, [5]**

therefore, can be considered infinite. Thus, for the following considerations, the suction pressure remains constant. In a surge avoidance system, a certain amount of the valve's flow capacity will be consumed to recycle the flow through the compressor. Only the remaining capacity is available for de-pressurizing the discharge volume.

The worst-case scenario for a surge control system is an ESD, particularly if the compressor is already operating close to surge when the engine shutdown occurs[2]. With the initiation of shutdown, the compressor will decelerate rapidly under the influence of the fluid forces counteracted by the inertia of the rotor system. A 30% loss in speed equates to approximately a loss in head of 50%. The valve must, therefore, reduce the pressure across the compressor by about half in the same time as the compressor loses 30% of its speed. This speed loss is very rapid.

The larger the volumes are in the system, the longer it will take to equalize the pressures. Obviously, the larger the valve, the better its potential to avoid surge. However, the larger the valve, the poorer its controllability at partial recycle. The faster the valve can be opened, the more flow can pass through it. There are, however, limits to the valve opening speed, dictated by the need to control intermediate positions of the valve, as well as by practical limits to the power of the actuator. The situation may be improved by using a valve that is only boosted to open, thus combining high opening speed for surge avoidance with the capability to avoid oscillations by slow closing.

If the discharge volume is too large and the recycle valve cannot be designed to avoid surge, a short recycle loop (hot recycle valve) may be considered, where the recycle loop does not include the aftercooler.

While the behavior of the piping system can thus be predicted quite accurately, the question about the rate of deceleration for the compressor remains. It is possible to calculate the power consumption for a number of potential steady-state operating points. The operating points are imposed by the pressure in the discharge volume, which dictates the head of the compressor. For a given speed, this determines the flow that the compressor feeds into the discharge.

In a simple system as described above, mass and momentum balance have to be maintained (Sentz [7] and Wachter and Rohne [5]). The valve can be described by its flow as a function of the pressure differential, with $p_v$ the pressure just upstream of the valve

$$Q_v = \sqrt{\frac{1}{K_v}(p_v - p_1)} \tag{2}$$

unless the flow across the valve is choked, thus

$$Q_v = C\sqrt{\frac{p_v}{\rho_v}} \tag{3}$$

while mass and energy balance yield

$$\frac{dp_v}{dt} = \frac{k}{V}\left[p_2 Q - p_v Q_v - \frac{k-1}{k} H_{\text{cooler}}\right] \tag{4}$$

and the momentum balance

$$\frac{d(p_2 Q)}{dt} = \frac{p_2 - p_v}{L}\left[ART_2 - \frac{p_2 Q^2}{A p_v}\right] \tag{5}$$

where $p_2$ is a function of the compressor operating point, expressed by

$$\frac{p_2}{p_1} = \left[1 + \frac{k-1}{k}\cdot\frac{h(Q,N)\cdot SG}{287\cdot ZT_1}\right]^{k/k-1} \qquad \frac{h}{N^2} = \alpha\left(\frac{Q}{N}\right)^2 + \beta\frac{Q}{N} + \gamma. \tag{6}$$

[2]Similar considerations are to be made for the trip of an electric motor driver. The main difference is the different inertia of the motor (and the gearbox).

The above relationship can be used for any positive flow. If the compressor exhibits reverse flow, it can be modeled as an orifice with

$$Q = -\sqrt{\frac{1}{K_{v,\text{compr}}}(p_2 - p_1)} \tag{7}$$

where $K_{v,\text{compr}}$ describes the flow resistance of the compressor against the reverse flow. It should be noted that this somewhat crude formulation suffices for the present study because we want to determine whether the compressor will go into surge at ESD or not. The post-surge behavior is, thus, not important and is only introduced to keep the numerical model stable.

The behavior of the compressor during ESD is governed by two effects. The inertia of the system consisting of the compressor, coupling and power turbine (and gearbox where applicable) is counteracted by the torque ($T$) transferred into the fluid by the compressor (mechanical losses are neglected). The balance of forces thus yields

$$T = -2\pi\cdot J\cdot\frac{dN}{dt}. \tag{8}$$

Knowing the inertia ($J$) of the system and measuring the speed variation with time during rundown yields the torque and, thus, the power transferred to the gas

$$P = T\cdot N\cdot 2\pi = -(2\pi)^2\cdot J\cdot N\cdot\frac{dN}{dt}. \tag{9}$$

If the rundown would follow through similar operating points, then $P\sim N^3$, which would lead to a rundown behavior of

$$\frac{dN}{dt} = \frac{k}{J}\frac{N^2}{(2\pi)^2} \rightarrow \int N^{-2}dN = \frac{k}{J(2\pi)^2}\int dt + c \rightarrow$$

$$N(t) = -\frac{1}{-\frac{k}{J(2\pi)^2}t - \frac{1}{N_{t=0}}}. \tag{10}$$

Regarding the proportionality factor ($k$) for power and speed, this factor is fairly constant, no matter where on the operating map the rundown event starts. Thus, the rate of deceleration, which is approximately determined by the inertia and the proportionality factor, is fairly independent of the operating point of the compressor when the shutdown occurred; i.e., the time constant ($dN/dt(t=0)$) for the rundown event is proportional to $k/J$. However, the higher the surge margin is at the moment of the trip, the more head increase can be achieved by the compressor at constant speed.

From this complete model, some simplifications can be derived, based on the type of questions that need to be answered. Obviously, for relatively short pipes, with limited volume (such as the systems desired for recycle lines), the pressure at the valve and the pressure at compressor discharge will not be considerably different. For situations like this, the heat transfer can also be neglected. The set of equations then is reduced to

$$\frac{dp_2}{dt} = \frac{k\cdot p_2}{V}[Q - Q_v]. \tag{11}$$

This means that the discharge pressure change depends on the capability of the valve to release flow at a higher rate than the flow coming from the compressor. It also shows that the pressure reduction for a given valve will be slower for larger pipe volumes ($V$).

The model described above, which contains and accounts for all physical features of the discharge system, can be simplified even further to determine whether the combination of discharge volume and valve size can prevent the compressor from surge during an ESD. Thus, it allows the two important design parameters to be easily varied to avoid surge during ESD. The surge valve size and

opening speed can be increased for a given discharge volume or the maximum allowable discharge volume for a given configuration of valves and compressor characteristic can be limited. The second method, which has the advantage of being more transparent for the station design, is used here.

The simplified model calculates the maximum discharge volume where the head across the compressor can be reduced by half in one second, based on the assumption that this reflects the speed decay during an ESD as outlined above. Therefore, the lengthy calculation of the instant compressor speed is replaced by a fixed, presumed to be known, deceleration rate. The assumption is made that the power turbine and compressor will lose about 25% speed in the first second of deceleration. This is, for example, confirmed by data from Bakken et al. [8], where the gas turbine driven configurations lost about 20 to 25% speed in the first second, while the electric motor driven configuration lost 30% speed in the first second. As a result of the loss of 25% speed, the head the compressor can produce at the surge line is about 56% lower than at the initial speed, if the fan law is applied. A further assumption is made about the operating point to be the design point at the instant of the ESD.

Any ESD is initiated by the control system. As a result of various delays in the system (fuel valve to shut completely, hot pressurized gas supply to the power turbine seizes, opening time of the recycle valve), ESD data show that the surge control valve reaches full open and the beginning of deceleration of the power turbine/compressor are considered to happen simultaneously. This is the starting time ($T_0$) for the model.

Usually, the suction volume (no check valve) is more than three orders of magnitude greater than the discharge volume and is therefore considered at a constant pressure. The general idea is now to consider only the mass flow into the piping volume (from the compressor) and the mass flow leaving this volume through the recycle valve. Since the gas mass in the piping volume determines the density and, thus, the pressure in the gas, we can for any instant see whether the head required to deliver gas at the pressure in the pipe volume exceeds the maximum head that the compressor can produce at this instant. Only if the compressor is always capable of making more head than required can surge be avoided.

A further conceptual simplification can be made by splitting the flow coefficient of the recycle valve ($c_v$) into a part that is necessary to release the flow at the steady-state operating point of the compressor ($c_{v,ss}$) and the part that is actually available to reduce the pressure in the piping volume ($c_{v,\text{avail}}$).

The first stream and, thus, $c_{v,ss}$ of the valve necessary to cover it are known. Also known is the $c_v$ rating of the valve. Thus, the flow portion that can effectively reduce the backpressure is the determined by the difference:

$$c_{v,\text{avail}} = c_v - c_{v,ss}\,. \tag{12}$$

The model is run at constant temperature. Most of the compressor systems modeled contain aftercoolers. The thermal capacity of the cooler and the piping are much larger than the thermal capacity of the gas; thus, the gas temperature changes are negligible within the first second.

The rate of flow through the valve is calculated with the standard ISA method, [9][3]:

$$Q_{\text{std}} = 1360 \cdot F_p \cdot c_v \cdot Y \cdot \left[\frac{dp}{p_2} \cdot \frac{1}{SG \cdot T_2 \cdot Z_2}\right]^{0.5} \tag{13}$$

The compressibility is calculated with the Redlich-Kwong equation of state. The flow calculated above in each step of the iteration is then subtracted from the gas contained in the discharge and a new pressure in the pipe volume is calculated. Depending on whether the system has achieved a reduction of head of at least 50% in the first second, the volume of the system is either increased or reduced by a small margin. Thus, the calculation yields the maximum allowable piping volume for the set parameters that will not cause surge at ESD.

[3]Qstd is the standard flow. $Fp$ is the piping geometry factor. It is usually not known and can be assumed to be 1. The pressure is assumed to be constant in the entire pipe volume. It is thus the same just upstream of the valve and at the discharge pressure of the compressor.

**Table 1 Problem definition (full model)**

| | |
|---|---|
| $P1$ | 4938 kPa |
| $P2$ | 6100 kPa |
| $V$ | 21 $m^3$ |
| $L$ | 42 m |
| $SG$ | 0.59 |
| $T1$ | 305 K |
| $J$ | 34.593 kg $m^2$ |
| Recycle valve $Kv$ | N/A |

## Validation

The system used to validate the complete model is outlined in **Fig. 3** and **Table 1**. Reduced compressor characteristics are given in **Fig. 5**.

Data were available for a situation where the recycle valve failed to open at a shutdown situation. The complete model was run against the data and the results are shown in **Fig. 6**. The model predicts initially a faster deceleration than indicated by the test data. This is likely due to some residual power provided by the power turbine even after the fuel supply is shut off. Since the purpose of the calculations will be to determine the capability of a recycle system to avoid surge, this deviation is acceptable. The onset of surge is predicted quite accurately. Interestingly enough,

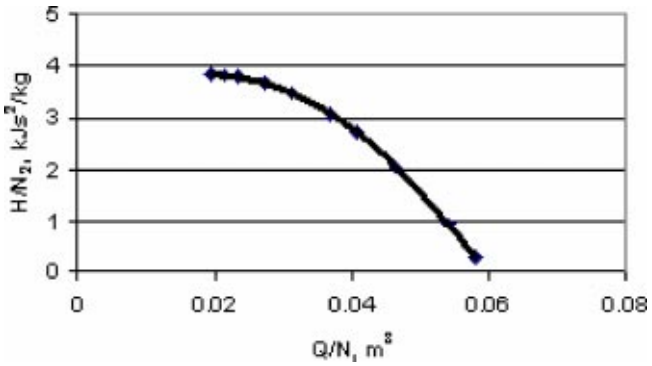


**Fig. 5 Compressor characteristics**

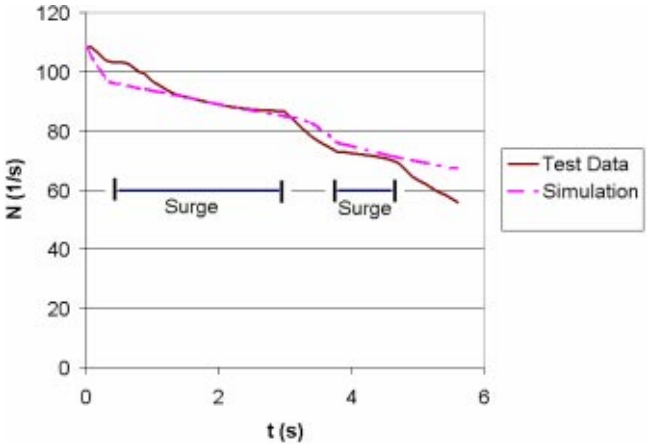


**Fig. 6 Emergency shutdown against closed recycle valve. Test data versus simulation with complete model. Time spans in surge based on vibration data from test flow and reverse flow.**

**Table 2 Problem definition (reduced model)**

| | |
|---|---|
| $P1$ | 5900 kPa |
| $P2$ | 8900 kPa |
| $V$ | 21 $m^3$ |
| $L$ | 42 m |
| $SG$ | 0.59 |
| $T1$ | 305 K |
| $J$ | 34.593 kg $m^2$ |
| Recycle valve $Kv$ | 30000 |

even the post-surge behavior is captured quite well, despite the fact that no particular effort was made to optimize the compressor characteristics for operating points at lower than surge.

Both data and model show the characteristic flattening of the speed line in surge, largely due to the fact that the impeller absorbs less power in these situations. The presence of surge in the data was determined by the analysis of vibration data taken at the compressor bearings.

Next, the complete model is used to simulate the recycle system defined in **Table 2**, using the same compressor as before, with the compressor characteristics as shown in **Fig. 5**.

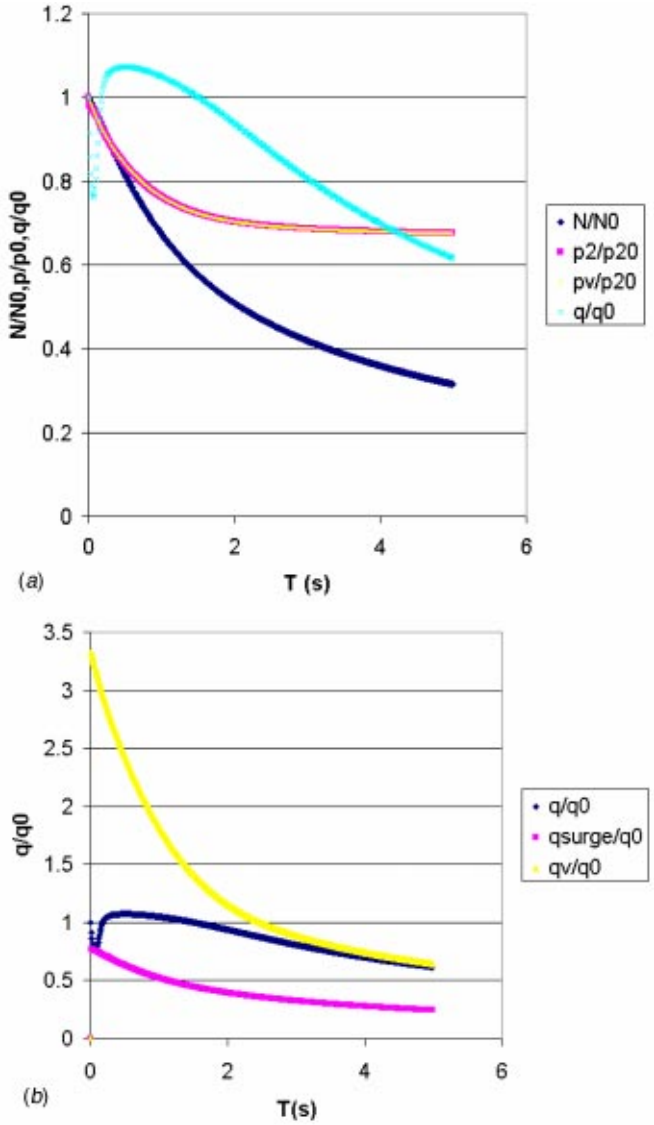


**Fig. 7 Emergency shutdown with recycle valve opening; (*a*) speed and pressures versus time, (*b*) flow versus time**

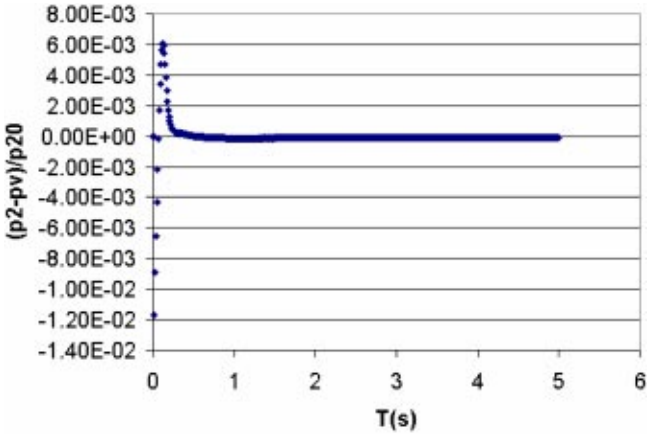


**Fig. 8 Relative difference between discharge pressure and valve pressure**

The results are shown in **Fig. 7**. With the parameters selected, the compressor barely avoids surge at 0.1 second and coasts down with a comfortable surge margin thereafter. A high surge margin is seen by some compressor designers as undesirable. Besides the realistic reduction in speed of about 30% in the first second, the data also show that the pressure at the compressor discharge ($p_2$) and the pressure upstream of the valve ($p_v$) are almost identical, thus confirming the assumptions for the simpler models (**Fig. 8**).

The simplified system is used for the same conditions, first with a prescribed speed reduction and second with the calculated speed reduction as in the full model, and shows very similar results compared to the complete model (**Fig. 9**). The method described can easily be expanded to situations where a relatively small suction volume leads to a fast increase in suction pressure. In the system simulated, test data did not indicate this pressure increase; i.e., the assumption of a large suction volume was valid.

## Conclusions

A model to simulate shutdown events was developed and used to define simpler rules that help with proper sizing of upstream and downstream piping systems, as well as the necessary control elements. The compression system is analyzed, thus verifying the model and the simplifications. The model coincides well with the data, particularly with regards to proper prediction of surge events. The inaccuracies and limitations inherent in the current model are only problematic if the entire rundown process needs to be described. The goal in this paper, to determine whether a system will surge during ESD situations, can be achieved with either version of the simulation.

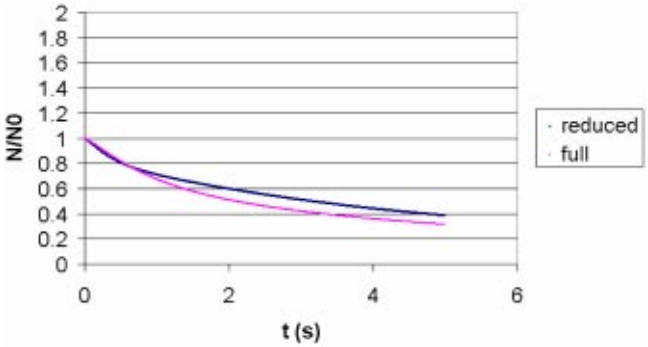


**Fig. 9 Comparison between full and reduced model**

## Acknowledgments

The authors would like to acknowledge the contributions of Daryl D. Legrand and Roland Kaiser, both with Solar Turbines Incorporated, who provided the referenced data.

## Nomenclature

$A$ = flow area
$c_v$ = flow coefficient
$C$ = compressible valve coefficient
$F_p$ = piping geometry factor
$h$ = head
$H_{\text{cooler}}$ = gas cooler heat transfer (W)
$J$ = inertia
$k$ = isentropic exponent
$k$ = constant
$K_v$ = valve coefficient
$L$ = pipe length
$N$ = speed (1/s)
$p$ = pressure
$Q$ = volumetric flow
$SG$ = specific gravity
$SM$ = surge margin (%)
$T$ = temperature
$t$ = time
$V$ = volume
$Y$ = coefficient
$Z$ = compressibility factor
$\alpha,\beta,\gamma$ = constants
$\rho$ = density

### Subscripts

avail = available
compr = compressor
$op$ = operating point
surge = at surge
std = at standard conditions
$ss$ = steady state
$v$ = valve
1 = compressor inlet
2 = compressor discharge

## References

[1] Epstein, A. H., Ffowcs Williams, J. E., and Greitzer, E. M., 1994, ''Active Suppression of Compressor Instabilities,'' Paper No. AIAA-86-1994.
[2] Blanchini, F., Giannatasio, P., Micheli, D., and Pinamonti, P., 2001, ''Experimental Evaluation of a High-Gain Control for Compressor Surge Suppression,'' ASME Paper No. 2001-GT-0570.
[3] Arnulfi, G. L., Giannatasio, P., Micheli, D., and Pinamonti, P., 2000, ''An Innovative Control of Surge in Industrial Compression Systems,'' ASME Paper No. 2000-GT-352.
[4] McKee, R. J., and Deffenbaugh, D., 2003, ''Factors that Affect Surge Precursors in Centrifugal Compressors,'' Proc. GMRC Gas Machinery Conference, Salt Lake City, UT.
[5] Wachter, J., and Rohne, K. H., 1984, ''Centrifugal Compressor Surge Behavior,'' ASME Paper No. 84-GT-91.
[6] Ribi, B., and Gyarmathy, G., 1997, ''Energy Input of a Centrifugal Stage into the Attached Piping System During Mild Surge,'' ASME Paper No. 97-GT-84.
[7] Sentz, R. H., 1980, ''The Analysis of Surge,'' Texas A&M Turbomachinery Symposium.
[8] Bakken, L. E., Bjorge, T., Bradley, T. M., and Smith, N., 2002, ''Validation of Compressor Transient Behavior,'' ASME Paper No. GT-2002-30279.
[9] ANSI/ISA S75.01, 1995, ''Flow Equations for Sizing Control Valves.''

# Rotor-Stator Interactions in a Four-Stage Low-Speed Axial Compressor—Part I: Unsteady Profile Pressures and the Effect of Clocking

**Ronald Mailach**
e-mail: mailach@tus.mw.tu-dresden.de

**Konrad Vogeler**
e-mail: kvogeler@tus.mw.tu-dresden.de

Dresden University of Technology,
Institute for Fluid Mechanics,
01062 Dresden, Germany

*This two-part paper presents detailed experimental investigations of unsteady aerodynamic blade row interactions in the four-stage Low-Speed Research Compressor of Dresden. In part I of the paper the unsteady profile pressure distributions for the nominal setup of the compressor are discussed. Furthermore, the effect of blade row clocking on the unsteady profile pressures is investigated. Part II deals with the unsteady aerodynamic blade forces, which are calculated from the measured profile pressure distributions. The unsteady pressure distributions were analyzed in the first, a middle and the last compressor stage both on the rotor and stator blades. The measurements were carried out on pressure side and suction side at midspan. Several operating points were investigated. A complex behavior of the unsteady profile pressures can be observed, resulting from the superimposed influences of the wakes and the potential effects of several up- and downstream blade rows of the four-stage compressor. The profile pressure changes nearly simultaneously along the blade chord if a disturbance arrives at the leading edge or the trailing edge of the blade. Thus the unsteady profile pressure distribution is nearly independent of the convective wake propagation within the blade passage. A phase shift of the reaction of the blade to the disturbance on the pressure and suction side is observed. In addition, clocking investigations were carried out to distinguish between the different periodic influences from the surrounding blade rows. For this reason the unsteady profile pressure distribution on rotor 3 was measured, while stators 1–4 were separately traversed stepwise in the circumferential direction. Thus the wake and potential effects of the up- and downstream blade rows on the unsteady profile pressure could clearly be distinguished and quantified.* [DOI: 10.1115/1.1791641]

## 1 Introduction

The flow in turbomachines is highly unsteady and turbulent. The rotor and stator blades, moving relative to each other, aerodynamically interact because of the viscous wakes and the potential effects of the blades. Due to these aerodynamic interactions the pressure distribution on the blades changes considerably in time. For this reason unsteady aerodynamic blade forces and moments are generated. Other sources stimulating unsteady blade forces are struts and inlet distortions, for instance. Critical blade vibrations are excited if the frequency of the aerodynamic stimulation matches the natural frequencies of the blades. This can lead to a reduction of fatigue life or even a destruction of the blading. This is the reason why unsteady effects due to periodic blade row interactions should be considered during the design process. For this purpose it is necessary to improve the knowledge of the aerodynamic response of the unsteady profile pressure distributions as well as the excitation mechanism and the expected magnitude of the blade forces.

Early analytical studies into the propagation of wakes through blade rows, the unsteady pressure response and the excitation of unsteady blade forces were performed by Kemp and Sears [1], Meyer [2] and Lefcort [3].

Contributed by the International Gas Turbine Institute (IGTI) of THE AMERICAN SOCIETY OF MECHANICAL ENGINEERS for publication in the ASME JOURNAL OF TURBOMACHINERY. Paper presented at the International Gas Turbine and Aeroengine Congress and Exhibition, Vienna, Austria, June 13–17, 2004, Paper No. 2004-GT-53098. Manuscript received by IGTI, October 1, 2003; final revision, March 1, 2004. IGTI Review Chair: A. J. Strazisar.

Within recent years a number of experimental and numerical investigations associated with the blade row interaction in turbomachines have been carried out. Experimental data on unsteady blade row interactions and aerodynamic forces in cascades are available from Grollius [4]. Hodson [5] reported about the wake motion and the wake-generated unsteadiness in a large-scale low-speed turbine.

The time-resolved pressure field on the rotor blades in high pressure turbine stages was investigated by Denos et al. [6], Laumert et al. [7], Valenti et al. [8] and Miller et al. [9].

Pieper [10] investigated the unsteady pressures on the blades of a single stage compressor with inlet guide vane (IGV). Sanders and Fleeter [11] considered the unsteady response of the stator blades in a single stage compressor to incoming wakes. Durali and Kerrebrock [12] performed experiments on the unsteady pressure distribution in a single stage transonic compressor and provided results on the unsteady blade forces due to the incoming wakes.

Much computational effort has been done in recent years to improve the understanding of blade row interactions in turbomachines. A detailed insight into this problem is provided by the numerical investigations of Korakianitis [13], Manwaring and Wisler [14], Valkov and Tan [15], Arnone and Pacciani [16], Fan and Lakshminarayana [17] as well as by Lee and Feng [18].

In previous publications of the authors several aspects of the rotor-stator interactions were discussed for the first stage of the Dresden Low-Speed Research Compressor (LSRC). Some results on the unsteady profile pressures and the unsteady aerodynamic blade forces are already provided for the first stage rotor and stator blades (Mailach et al. [19]). First results for the unsteady

  

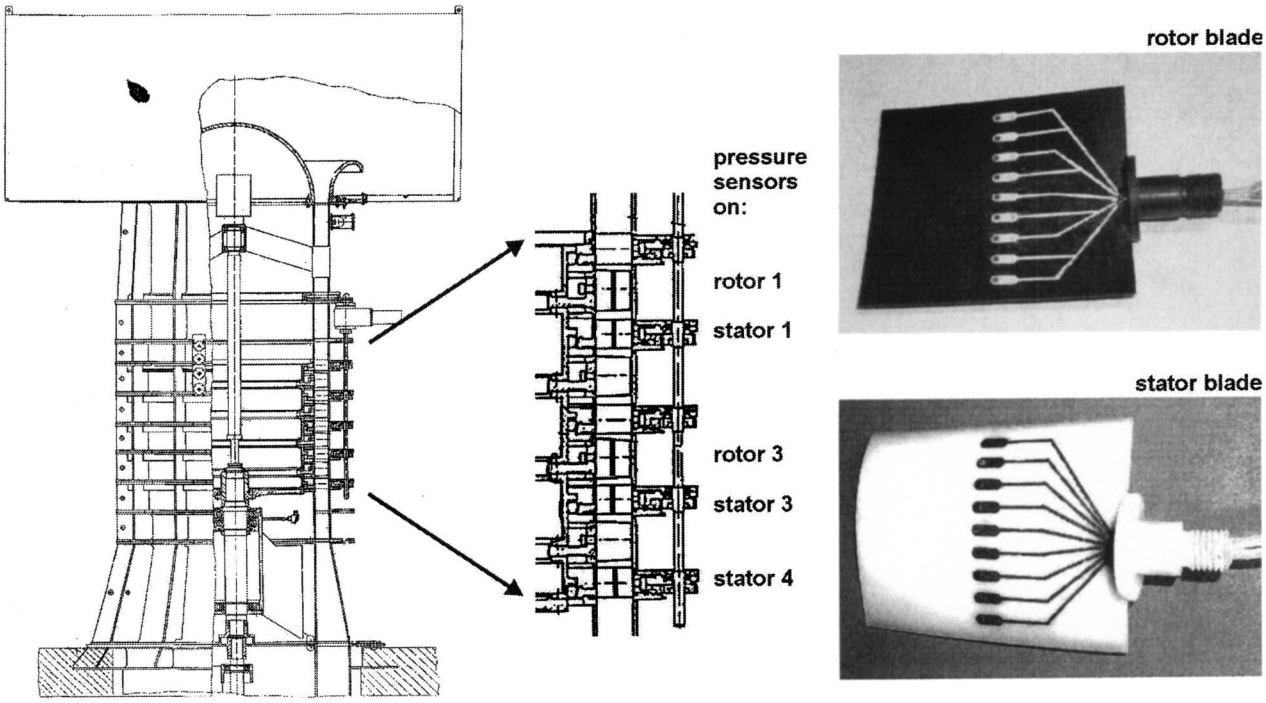


**Fig. 1 Sectional drawing of Dresden LSRC, rotor and stator blades with piezoresistive pressure transducers on PS and SS**

aerodynamic blade forces during rotating stall are also discussed there. Furthermore the unsteady boundary layer development on stator 1 is discussed and compared to the unsteady profile pressures (Mailach and Vogeler [20,21]).

The experiments described in these papers have been continued for several blade rows throughout the four-stage compressor. In the present two-part paper results for the unsteady profile pressures and the unsteady aerodynamic forces on the blades of the first stage (rotor 1, stator 1), a middle stage (rotor 3, stator 3) as well as for the last blade row (stator 4) of the Dresden LSRC are provided. In part I of the paper the unsteady response of the profile pressures on wakes and potential effects is discussed for these blade rows. Results are shown for design point and an operating point near the stability limit. In part II of the paper the algorithm to calculate the unsteady aerodynamic blade forces on the basis of the experimental data is presented [22]. Results for the time traces and frequency contents of the unsteady blade forces are provided for several blade rows and operating conditions. The aim of this two-part paper is to deliver a detailed insight into the complex physics of blade row interactions in multistage turbomachinery.

## 2 Experimental Setup

The experiments were performed in the low-speed research compressor of Dresden University of Technology (Dresden LSRC). The compressor consists of four identical stages, which are preceded by an inlet guide vane row. Figure 1 shows a sectional drawing of the compressor, a cut-out of the blading section and the instrumented blades.

The blading of the compressor was developed on the basis of the profiles of a middle stage of a high-pressure compressor of a gas turbine. Detailed descriptions of the compressor are given by Sauer et al. [23], Müller et al. [24] and Boos et al. [25]. Table 1 gives a summary of the main design parameters.

The rotor blade rows of all stages are identical. The stator blade rows are identical as well. For this reason a single rotor blade and a single stator blade were equipped with piezoresistive pressure transducers and mounted step by step in all compressor stages to be investigated (Fig. 1). In addition, the time-averaged profile pressures are measured using pneumatic pressure taps.

The unsteady pressures on the stator blade were acquired using time-resolving piezoresistive miniature pressure transducers (*Kulite LQ47*). The sensors are equally distributed along the midspan (MS) as well on the pressure side (PS) and the suction side (SS) of a single rotor blade and a single stator blade, respectively (Fig. 1). On both blades the sensors are positioned from 10% to 90% chord with steps of 10% chord. To minimize the influence on the flow the sensors and the wires were fitted into the blade surfaces. The positions near the leading edge and the trailing edge could not be equipped with pressure transducers without noticeably disturbing the flow.

The signals from the transducers were amplified 125 times. This was done using a separate miniature amplifier for each sen-

**Table 1 Design parameters of Dresden LSRC**

| IGV + 4 identical stages | |
|---|---|
| Reynolds number, rotor inlet, MS, DP (related to rotor chord length) | $5.7 \cdot 10^5$ |
| Mach number, rotor inlet, MS, DP | 0.22 |
| Design speed | 1000 rpm |
| Mass flow, DP | 25.35 kg/s |
| Mean flow coefficient, DP | 0.553 |
| Enthalpy coefficient $\Psi$is, DP | 0.794 |
| Hub diameter | 1260 mm |
| Hub to tip ratio | 0.84 |
| Axial gaps between all blade rows, MS | 32 mm |

| | IGV | rotor | stator |
|---|---|---|---|
| Blade number | 51 | 63 | 83 |
| Chord length, MS | 80 mm | 110 mm | 89 mm |
| Stagger angle, MS (vs. circumference) | 82.8° | 49.3° | 64.0° |
| Solidity, MS | 0.941 | 1.597 | 1.709 |
| Lieblein diffusion factor, third stage, MS, DP | - | 0.458 | 0.427 |

MS: midspan
DP: design point

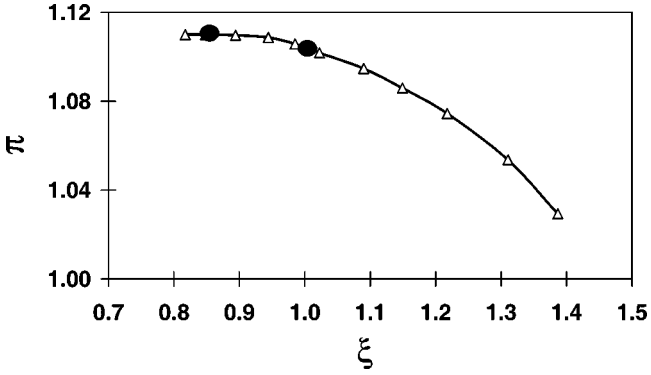


**Fig. 2 Compressor map of Dresden LSRC, design speed**

sor. For the measurements on the rotor blades the amplifier card was mounted within the rotor. The amplified signals are transmitted via slip rings into the stationary system.

The signals were recorded using a VXI data acquisition system of Hewlett-Packard. The sampling rate for the measurements was 51.2 kHz while the blade passing frequency (BPF) is 1.05 kHz for the rotor blades and 1.38 kHz for the stator blades at design conditions.

The steady pressure distributions on the stator and rotor blades were determined using pneumatic pressure taps. They are positioned at midspan between 2.5% and 95.0% of chord both on PS and SS of the rotor and stator blades. Pressure measurement systems from *Scanivalve* were applied to transform the pneumatic pressures to electrical voltages in the fixed and rotating frames of reference.

Furthermore, the flow field in the axial gaps up- and downstream the considered blade rows was investigated with a pneumatic five-hole probe and a single hot wire.

Different operating points were investigated for design speed including the design point and an operating point near the stability limit. The two main points of interest are the design point ($\xi = 1.00$) and an operating point near stability limit with 85% of reduced mass flow ($\xi = 0.85$) at design speed ($\zeta = 1.0$). These points are highlighted in the compressor map (Fig. 2).

The rotor blade numbers (63) and the stator blade numbers (83) are identical for all stages. For the investigations with the nominal setup of the compressor (without clocking) the rotor blades and the stator blades are at the same circumferential positions in each stage, respectively. Results with clocking of the blade rows are presented in Sec. 7 in this part of the paper only. The clocking setup is described there.

## 3 Data Postprocessing

The zero point drift of the piezoresistive pressure sensors during the experiments is not negligible. To improve the precision of the results the pressure $p(t)$ was determined by adding the time-averaged pressure from the pressure taps $\overline{p}$ and the unsteady part of the pressure $\tilde{p}(t)$, measured with the piezoresistive pressure transducers for each time step

$$p(t) = \overline{p} + \tilde{p}(t) \tag{1}$$

The time-averaged root mean square (rms) value includes information about both periodic and stochastic pressure fluctuations

$$\overline{\text{rms}} = \sqrt{\frac{1}{N}\sum_{i=0}^{N-1}(p_i(t) - \overline{p})^2} \tag{2}$$

For averaging the pressure with respect to the moving blades (rotor or stator blade, depending on frame of reference) the data

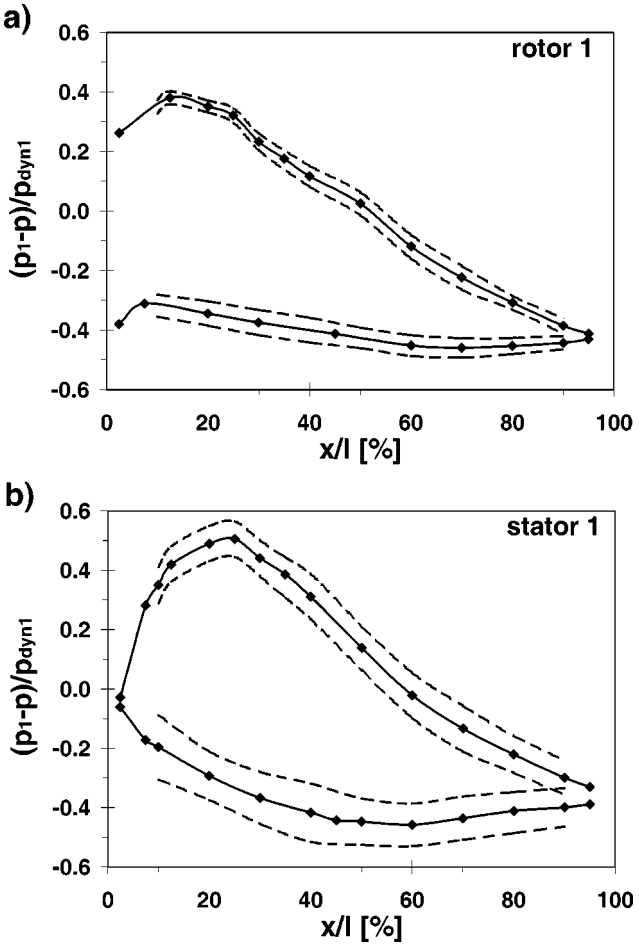


**Fig. 3 Pressure distribution on the rotor and stator blades of the first stage, MS, design speed, design point ($\xi = 1.00$, $\zeta = 1.0$)**

were ensemble averaged using a 1/revolution signal. Using this method, periodic and stochastic fluctuations can be separated. This was done with the equation

$$\langle p(t) \rangle = \frac{1}{M}\sum_{j=0}^{M-1} p_j(t) \tag{3}$$

The parameter $p_j(t)$ is the instantaneous pressure at a given relative position to a point of reference, which is a moving blade in this case. The value $\langle p(t) \rangle$ is the resulting ensemble-averaged value at this position. In our case the number of time traces per ensemble was $M = 250$. By averaging with a 1/revolution signal the results are referred to individual, identical blades. Thus information about small differences of the influence of the different blades on the flow field can be obtained.

The ensemble-averaged rms value reveals information about the stochastic pressure fluctuations. It is calculated as follows:

$$\langle \text{rms}(t) \rangle = \sqrt{\frac{1}{M}\sum_{j=0}^{M-1}(p_j(t) - \langle p(t) \rangle)^2} \tag{4}$$

## 4 Time-Averaged Pressure Distribution on Rotor and Stator Blades

As a first result Fig. 3 exemplarily shows the steady pressure distribution at midspan of the rotor and stator blades of the first stage for the design point ($\xi = 1.00$, $\zeta = 1.0$). In addition, the sta-

tistical fluctuations around the steady distribution are represented as dashed lines. In this case the pressure coefficient is calculated from the time-averaged values $\overline{p} \pm \overline{rms}$.

On the SS of the rotor blades an acceleration of the flow can be observed between leading edge and 10% of chord length, where the minimum pressure is reached [Fig. 3(*a*)]. Behind this point the flow is decelerating. On the PS the flow decelerates between 7% and 70% of chord. Downstream that position the flow slightly accelerates.

The aerodynamic loading of stator 1 is higher than that of rotor 1 [Fig. 3(*b*)]. On the SS of the stator blades an acceleration of the flow can be observed between leading edge and 25% of chord length, where the minimum pressure is reached. Behind this point the flow is decelerating. The strongest adverse pressure gradient occurs between 40% and 50% of chord length; after that point it decreases. On the PS of the stator blades the flow decelerates between the leading edge and 60% chord and slightly accelerates between 60% chord and trailing edge.

The fluctuations around the mean pressure distribution are relatively small for rotor 1. For stator 1 clearly stronger fluctuations can be observed. In both cases maximum pressure fluctuations on PS and SS can be found in regions with stronger deceleration of the flow. This is near the leading edge on PS and around 50% chord on SS. However, the fluctuations on the PS are somewhat larger than on SS.

For operating points towards the stability limit the mean loading increases. The fluctuations around this mean value increase as well due to the stronger periodic influence of the wakes and the potential effects (no figure).

## 5 Unsteady Pressure Distribution on the Stator Blades

In this section results of the unsteady profile pressure distribution will be discussed for all blade rows investigated. The results for the design point of the compressor ($\xi = 1.00$, $\zeta = 1.0$) will be discussed in detail. Additional results for an operating point near the stability limit ($\xi = 0.85$, $\zeta = 1.0$) will be shown for stator 1 only. The presented results are in ensemble-averaged form (excepting the frequency spectra and results derived from them, Figs. 6, 14, 20). In all cases the fluctuating part of the pressure $\tilde{p}$ is shown. It is ensured by comparisons of the time-resolved and ensemble-averaged data, that due to the averaging no information concerning the periodic blade passing signals is lost.

### 5.1 Stator 1

*Design Point.* The stator blade row of the first stage is located between the upstream rotor 1 and the downstream rotor 2 with identical blade numbers. This is why the unsteady pressure distribution is affected by both the viscous wakes and the potential effect of the upstream blade row and the potential effect of the downstream blade rows. Following results on the unsteady pressure distributions on PS and SS of the blades of stator 1 will be discussed for the design point.

Figures 4(*a*) and 4(*b*) show the unsteady pressure distributions at midspan on PS and SS in space-time ($s$-$t$) diagrams. The abscissa shows the dimensionless chord length. The time, which is shown as ordinate, is related to the blade passing period of the rotor blades $t_{\text{rotor}}$. The ensemble-averaged unsteady part of the pressure is shown as grayscale.

Figure 4 shows the unsteady response of the stator pressure distribution to the influences of the up- and downstream rotor blade rows. The maximum profile pressure fluctuations are about $\pm 12\%$ of the dynamic head of the incoming flow. The highest pressure fluctuations on PS and SS along the blade surface can be observed in the regions with decelerated flow. This is in the front part of the blade on the PS and behind 30% chord on the SS.

Generally, two different forms of wake influences on the unsteady profile pressures can be distinguished: this is on the one hand the wake effect, propagating with the speed of sound, and on the other hand the wake effect propagating with the convective

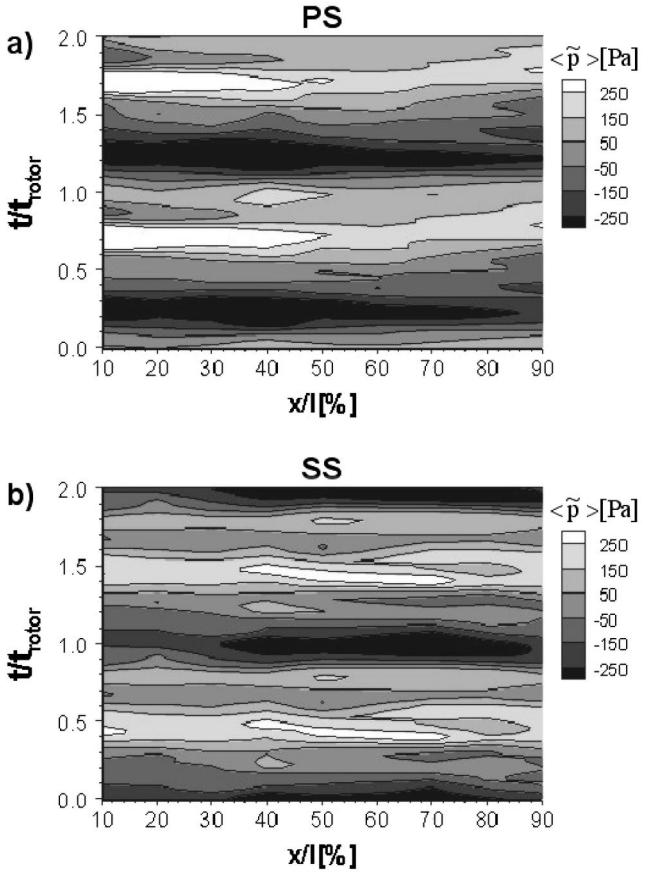


**Fig. 4 Unsteady pressure distribution on PS and SS of stator 1, MS, design point ($\xi = 1.00$, $\zeta = 1.0$)**

speed. In some cases in the literature the first effect is observed to be the dominant one (Durali and Kerrebrock [12], Sanders and Fleeter [11]). However, in other cases the convective propagating wake effect is predominant, as described by Hodson [5].

Durali and Kerrebrock [12] conclude that the chordwise pressure distribution is substantially determined by the change of the blade circulation due to the passing blades. Generally the circulation of a blade changes if the inlet or outlet flow conditions of the blade vary. Thus the circulation as well as the profile pressure distribution of the considered stator blade changes for every passing rotor blade of the up- and downstream blade rows. If a rotor wake impinges the leading edge of the considered stator blade the circulation of this blade varies due to the changing incidence angle and velocity. Because of this the wake influence propagates along the blade surface towards the trailing edge as a pressure wave with the velocity of sound.

In our case on stator 1 (as well as on the other blade rows discussed later) the periodic pressure signals due to the wakes of the rotor blades propagate along the blade surface with a velocity well above the convective speed (Fig. 4). As a result a nearly instantaneous change of the pressure along the PS and SS blade surface appears. Thus the surface pressure is independent of the wake propagation within the stator passages. This corresponds to the results of Durali and Kerrebrock [12] in a transonic compressor, for instance. Therefore no fundamental differences of the response of the unsteady profile pressure on incoming wakes in low- and high-speed machines are expected. (The path of the wake propagation would appear as an inclined line in the $s$-$t$-diagrams, e.g. Fig. 4. Within the stator blade passages the rotor wakes need a time period of about $t/t_{\text{rotor}} \approx 1.5$ on the SS and 1.9 on the PS to propagate from the leading edge to the trailing edge.)

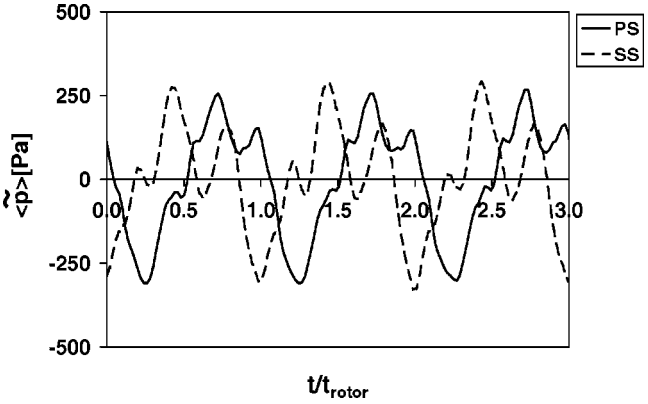


**Fig. 5 Unsteady pressure on PS and SS of stator 1, MS, 50% chord, design point ($\xi=1.00$, $\zeta=1.0$)**

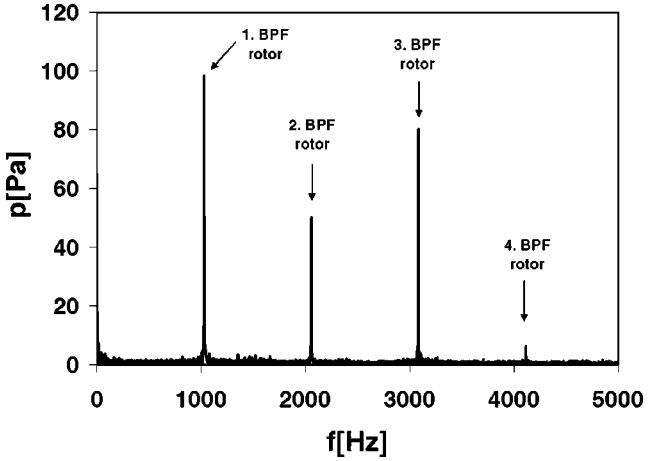


**Fig. 6 Frequency spectrum of pressure on stator 1, SS, MS, 50% chord, design point ($\xi=1.00$, $\zeta=1.0$)**

Since the potential effects of the downstream rotor blades propagate upstream with the velocity of sound the pressure along the surface responds to this rotor-periodic influence again nearly instantaneously in time (Fig. 4). Because of the identical blade numbers of the up- and downstream rotor blade rows and the fast propagation of the pressure fluctuations along the blade surface, the influence of the wakes and the potential effect of the downstream blade row cannot clearly be distinguished. It will be shown later for other blade rows and by means of the clocking investigations, that both the wakes of upstream blades and the potential flow field of downstream blades have a considerable effect on the unsteady pressure distribution.

In the data published by Sanders and Fleeter [11] and Durali and Kerrebrock [12] it can be seen that more than one peak can appear due to the passing of a wake only. In contrast to that Stadtmüller and Fottner [26] observed a single wave-like pressure variation on the blade surface as a result of a passing wake.

Also in our data several pressure peaks can be observed during one passing period at a given position of the blade (Fig. 4). This becomes more obvious in Fig. 5, which explicitly shows the results for the midchord position on PS and SS. The appearance of several peaks within one blade passing period is mainly caused by the interaction of periodic influences from up- and downstream for this embedded blade row. The time difference of the arrival of the incoming wakes at the leading edge and the potential flow field of downstream blade rows at the trailing edge of the considered stator blade determine the amplitude and shape of the resulting unsteady pressure. This is verified by the clocking investigations, discussed in Sec. 7.

The shape of the pressure development in time is comparable on both sides of the blade. The variation of the pressure signal for the subsequent passing rotor blades is negligible. A phase shift of the unsteady pressure of $\phi\approx 90-120$ deg can be observed between PS and SS of the blade (Figs. 4 and 5). (The exact value of the phase shift depends on which typical point is considered, e.g., pressure maximum/minimum or zero passing.) Figure 5 clearly shows for the midchord positions, that this phase shift is constant in time. This is because of the same blade numbers of the up- and downstream moving blade rows. The pressure on the SS reacts earlier on the periodic influences due to the wakes and the potential effect of the surrounding rotor blade rows.

In contrast to our results, Sanders and Fleeter [11] observed a phase shift of 180 deg between PS and SS as a response to the incoming wakes. Also in the data published by Durali and Kerrebrock [12] a clear phase shift between PS and SS on incoming wakes can be seen, but the amount of it is not specified. To the knowledge of the authors, up to now no detailed data on the unsteady profile pressure response on both the blade PS and SS of multistage compressors were available in literature.

The different peaks, which are superimposed on a fundamentally wave-like variation of the pressure, are reflected as higher harmonics in the frequency spectrum, Fig. 6. In the frequency spectrum the 1. BPF dominates, which is due to the wave-like pressure variation for one rotor blade passing. Within the group of higher harmonics the third BPF has the highest amplitudes, because three more or less distinct peaks are superimposed on the wave-like pressure traces for one rotor blade passing, visible in Fig. 5.

*Operating Point Near the Stability Limit.* The unsteady part of the pressure distribution at midspan of the considered blade rows does not change significantly when approaching the stability limit of the compressor. As an example, the behavior on stator 1 will be discussed for an operating point near the stability limit of the compressor (Fig. 7).

As for the design point, the pressure reacts nearly instantaneously in time along the blade surface due to the influence of wakes and potential effects of the rotor blades. The amplitudes are somewhat higher than for the design point (compare Fig. 4). Again several peaks are superimposed on a basically wave-like pressure variation during blade passing. These several pressure maxima are less significant compared to the design point. This seems to be an effect which appears due to the broadening of the wakes when approaching the stability limit of the compressor.

Again comparable pressure traces with a phase shift can be seen for the same chordwise position on PS and SS (Fig. 8). This phase shift is somewhat reduced compared to the design point, but in the same order of magnitude ($\phi\approx 60-90$ deg). As discussed for rotor 1 (Sec. 6.1), the time distance of the arrival of the disturbances from up- and downstream at the considered blade is responsible for the amount of this phase shift.

On the other blade rows, considered following, the same fundamental changes like for stator 1 can be observed when throttling the compressor. These are the slightly increasing amplitudes of the unsteady pressure, a somewhat changing phase shift of pressure traces between PS and SS and smoothed, more wave-like pressure traces. For this reason the unsteady profile pressure distributions for operating points near the stability limit will not be discussed separately for these blade rows.

**5.2 Stator 3.** Figure 9 shows the unsteady profile pressure distribution on stator 3 for design point (sensor at 10% chord on PS was defect). The main features of these time-resolved distributions are comparable to those of stator 1. As discussed, the unsteady pressure distributions depend on the superposition of the influences of up- and downstream blade rows. Also for stator 3 the number of the up- and downstream rotor blades is identical.

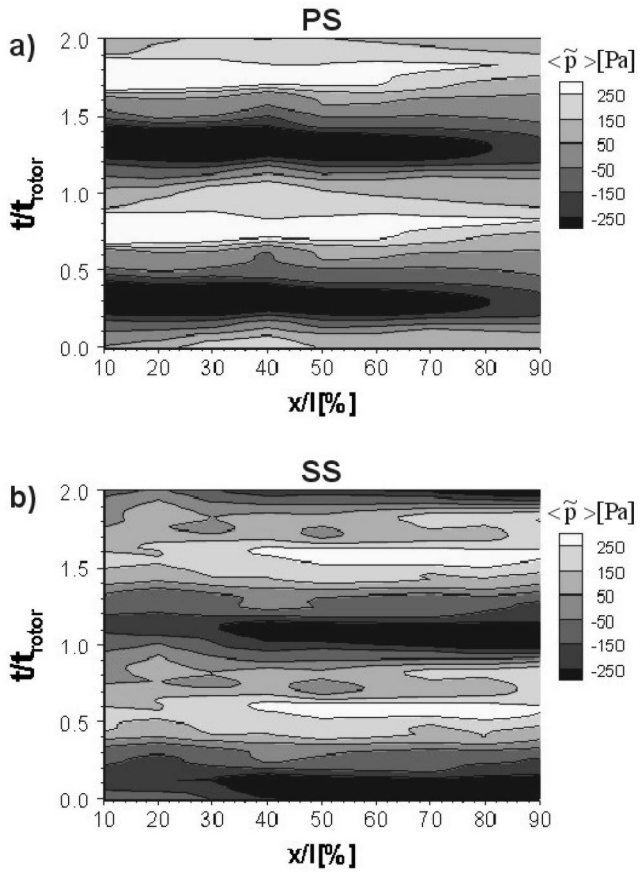


**Fig. 7 Unsteady pressure distribution on PS and SS of stator 1, MS, operating point near stability limit ($\xi$=0.85, $\zeta$=1.0)**

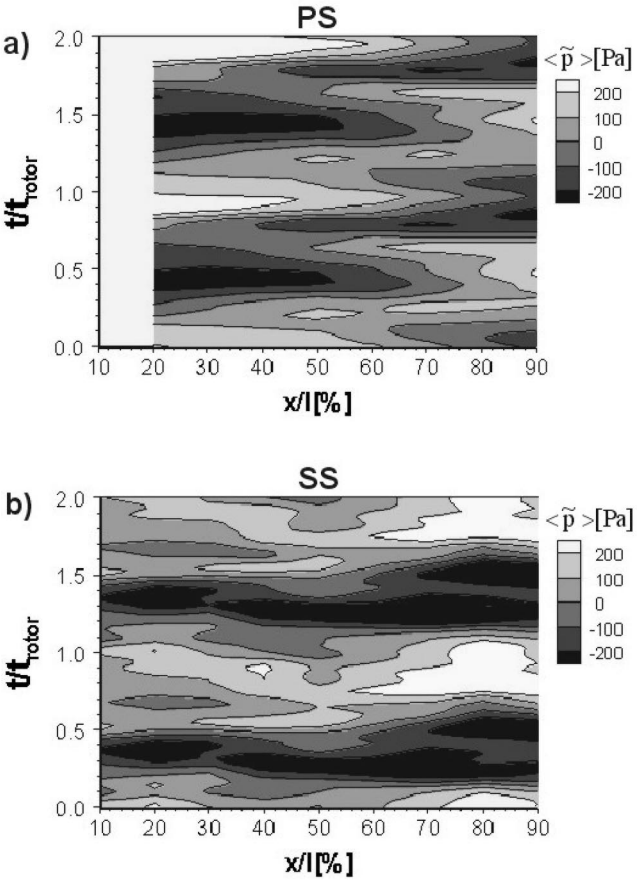


**Fig. 9 Unsteady pressure distribution on PS and SS of stator 3, MS, design point ($\xi$=1.00, $\zeta$=1.0)**

The unsteady pressure amplitudes of stator 3 are somewhat lower than for stator 1, but in the same order of magnitude. These changes are due to the comparatively small differences of the flow angle and velocity between the first and third stage. As a result of it the time difference between the arrival of the wake at the stator leading edge and the potential effect of the downstream rotor blades at the stator trailing edge changes. Hence, due to the superposition of these influences, the amplitude and shape of the final unsteady pressure traces change as well.

For stator 3 a distinction between the wake effect of the upstream rotor 3 (which is strongest near the leading edge of the considered blade) and the potential effect of the downstream rotor 4 (with higher amplitudes near the trailing edge of the considered blade) seems to be possible, especially on the PS of the blade (Fig. 9).

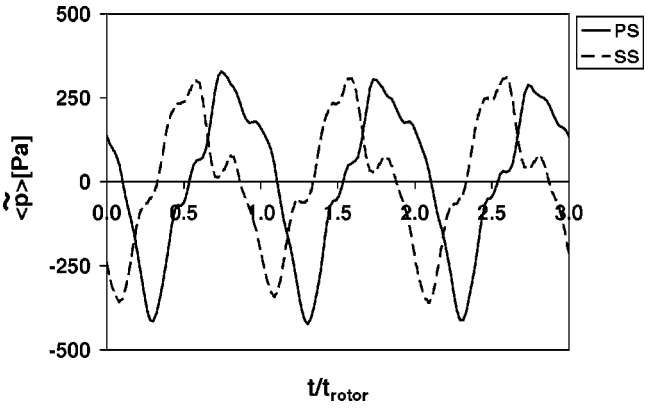


**Fig. 8 Unsteady pressure on PS and SS of stator 1, MS, 50% chord, operating point near stability limit ($\xi$=0.85, $\xi$=1.0)**

**5.3 Stator 4.** The investigations on stator 4, which is the last blade row of the compressor, were performed to obtain information of the behavior on a blade, which is influenced by upstream blade rows only. For the other blade rows investigated, a superimposed influence of the wakes and the potential effects of downstream blades appears. These periodic influences cannot clearly be distinguished in most cases because of the nearly instantaneous response of the unsteady pressures along the blade surface.

From Fig. 10 it clearly follows that there is a strong wake effect on the unsteady profile pressure distribution. Also in the case of the wake influence only, a nearly instantaneous change of the pressure along the blade surface appears. In the results a very fast downstream propagation of the wake influences can be observed (Fig. 10). As for other blade rows, several peaks appear for a single blade passing (clearly visible on SS, rear part of blade). Certainly the strongest influence is due to the wakes of the upstream rotor 4. However, it will be shown with the clocking investigations in Sec. 7 that the influence of previous blade rows is not negligible. The influences of the wakes and the potential field propagate through several compressor stages. Probably one of the pressure peaks of the unsteady pressure distribution in Fig. 10 is attributed to the wake influence of the previous rotor 3.

The ensemble-averaged rms values of the stator 4 pressure distribution show that the convective wake propagation in the passage can be tracked along a path of increased stochastic pressure

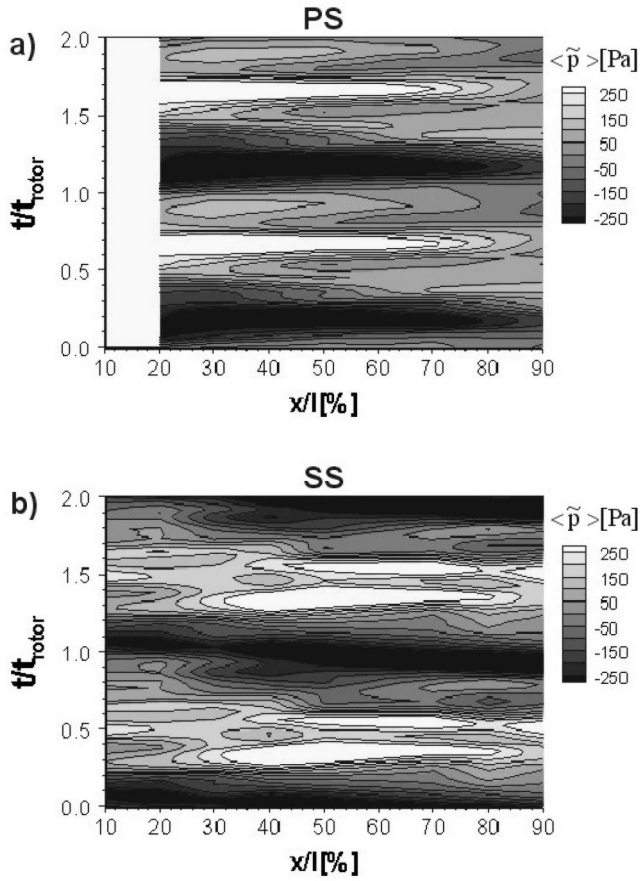


**Fig. 10 Unsteady pressure distribution on PS and SS of stator 4, MS, design point ($\xi=1.00$, $\zeta=1.0$)**

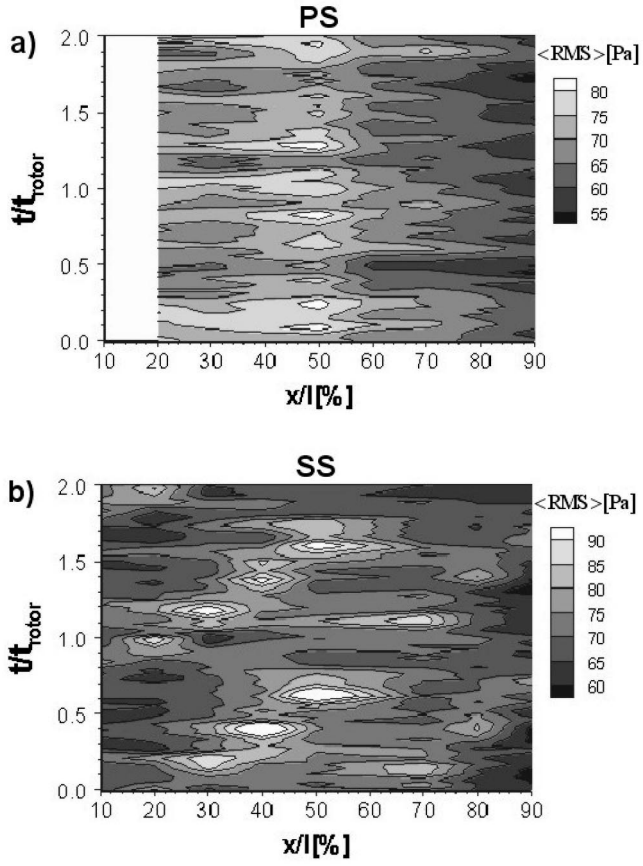


**Fig. 11 Unsteady pressure distribution (rms values) on PS and SS of stator 4, MS, design point ($\xi=1.00$, $\zeta=1.0$)**

fluctuations in several cases (Fig. 11, see also Ref. [21]). For stator 4 this is visible at the SS for the design point. For operating points near the stability limit of the compressor the basic fluctuation level on the SS increases and masks the path of the convective wake propagation. On the PS no signs for the convective propagating wakes could be detected, although the mean rms values are somewhat lower than on the SS. For both the PS and SS, higher pressure fluctuations appear in regions of decelerated flow, Fig. 11.

These results show that the unsteady pressure distribution on the blades is not completely independent from the convective wake propagation in the passage. However, the ensemble-averaged pressure does not indicate it.

## 6 Unsteady Pressure Distribution on the Rotor Blades

**6.1 Rotor 1.** The rotor blade row of the first stage is preceded by the inlet guide vane row (IGV) with 51 blades and followed by a stator blade row with 83 blades. These blade rows move relative to the considered rotor blades.

The pressure on PS and SS reacts both on the incoming wakes of the IGV and the upstream propagating potential effect of the downstream stator blade row (Fig. 12, design point). Because of the different blade numbers their effects on the pressure distribution on the rotor blades can be distinguished. The time scale $t$ in the $s$-$t$ diagrams in Fig. 12 is related to the passing time of two subsequent blades of the downstream stator blade row $t_{\text{stator}}$.

The maximum profile pressure fluctuations are about $\pm 6\%$ of the dynamic head of the incoming flow for design point (Fig. 12). The unsteady pressure distribution is dominated by the potential effect of the stator blades. This is the case on PS and SS of the rotor blades independent from the operating point. It can be seen that the pressure wave due to the potential flow field of the downstream stator blades propagates very fast upstream along the rotor blade surface. So the pressure along the whole blade chord changes nearly instantaneously.

The wakes of the IGV play only a secondary role. This is due to the fact that the IGV in fact consists of turbine blades used for adjusting the inlet flow angle of the first stage rotor blades. While the velocity deficit of the rotor and stator wakes is typically in the range of 40% of the free-stream velocity in the Dresden LSRC (Mailach and Vogeler [20]), it is relatively small at 20% for the IGV wakes. Consequently, the influence on the unsteady pressure distribution of the following rotor 1 blades is small as well. The IGV influence is only visible if it coincides with that of the stator blades. This is, for instance, if on the considered rotor blade the pressure maximum due to an IGV wake coincides with that due to a stator blade. In this case the resulting unsteady pressure amplitude increases. Otherwise, if the pressure field of the IGV and stator are out of phase, the resulting amplitudes decrease. In Fig. 12 one can see both on the PS and SS the different amplitudes due to passing of the first and second stator blade. This is due to the modulation of the stator potential effect with the IGV wake effect which appears due to the different blade numbers of these blade rows.

Figure 13 shows the pressure traces on PS and SS of rotor 1 for a longer period of time. The time scales are referred to the passing time of the downstream stator blades and the IGV, respectively. One can clearly see the dominating influence of the stator potential effect as well as the changing amplitude and shape of the pressure fluctuations versus time. This is clearly different to the behavior on stator 1 (Fig. 5), which is embedded into up- and downstream moving blade rows with equal blade numbers.

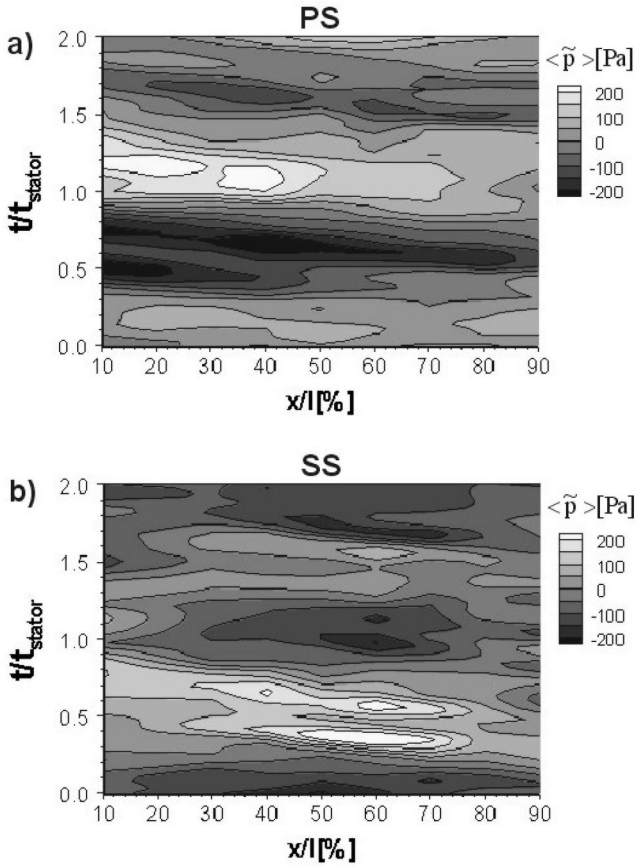


**Fig. 12 Unsteady pressure distribution on PS and SS of rotor 1, MS, design point ($\xi=1.00$, $\zeta=1.0$)**

Between the signals on PS and SS of the rotor blades a phase shift can be observed. This phase shift is changing in time between about 90–180 deg. This is caused by the superimposed influence the IGV and the stator blades. Due to the different blade numbers of IGV and stator 1 the time difference between the arrival of the IGV wakes at the leading edge and the potential effect of the downstream stator blades at the trailing edge of the rotor blades changes in time. This is the reason why the phase difference of the pressure on PS and SS of the rotor blade varies in time.

A variety of different peaks appears in the frequency spectrum of rotor 1, Fig. 14. As identified in the previous results, the largest

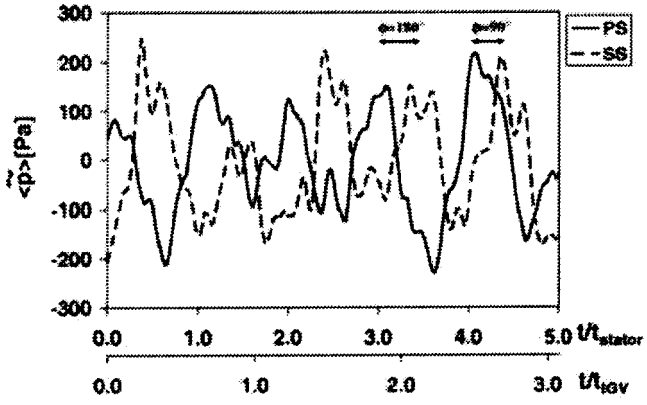


**Fig. 13 Unsteady pressure on PS and SS of rotor 1, MS, 50% chord, design point ($\xi=1.0$, $\zeta=1.0$)**

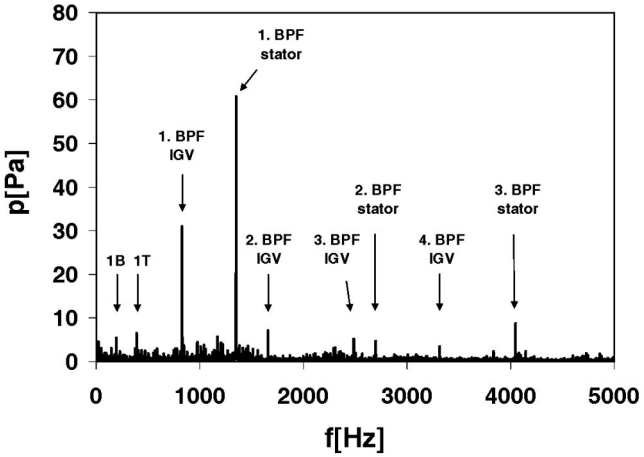


**Fig. 14 Frequency spectrum of pressure on rotor 1, SS, MS, 50% chord, design point ($\xi=1.00$, $\zeta=1.0$)**

influence on the unsteady pressure distribution is due to the potential effect of the downstream stator 1 (1. BPF stator). The amplitude due to the weak IGV wake (1. BPF IGV) is only 50% than that of the stator potential effect. Some higher BPFs of the stator and IGV appear with small influence only. The natural frequencies of the blade are clearly below the BPFs of IGV and stator. The first bending mode (1B) appears at 200 Hz while the first torsion mode (1T) is visible at 440 Hz.

For operating points towards the stability limit the periodic influence of the potential flow field on the pressure fluctuations increases (no picture shown). This is due to the increasing pressure difference over the blade rows of the compressor. Independent from the operating point, smaller pressure fluctuations appear due to the IGV wakes.

**6.2 Rotor 3.** Clear differences, however, can be seen between rotor 1 and rotor 3 (Fig. 15, design point). One reason for this is the increased wake effect of stator 2 compared to the IGV. In fact, rotor 3 has equal stator blade numbers up- and downstream, which is not the case for rotor 1.

The fundamental characteristics of the unsteady pressure distribution on rotor 3 are comparable to that of other blade rows. Also in this case the wake and potential effects of the surrounding blade rows are responsible for the periodic changes of the pressure. The different influences propagate as pressure waves along the blade surface. The fluctuation amplitudes on rotor 3 are comparable to the other blade rows.

A variation of the amplitudes for subsequent passing stator blades appears because of the IGV wake influence, which is still existent in the third stage (Fig. 15).

## 7 Influence of Clocking on the Unsteady Profile Pressure Distribution

As shown above, the influences of wakes and upstream propagating potential effects on the unsteady profile pressure distribution of a considered blade cannot clearly be separated in most cases for the nominal setup of the compressor (excepting on rotor 1). To distinguish between the different periodic influences the stator blade rows were individually shifted stepwise in circumferential direction. This method is known as clocking or indexing. In our case we did not investigate the possible advantages concerning the efficiency of the compressor, which are known from literature (Reinmöller et al. [27], Arnone et al. [28]). However, we used this method to distinguish the influences of the individual blade rows on the profile pressure distribution of a selected blade row. For this reason rotor 3 was chosen.

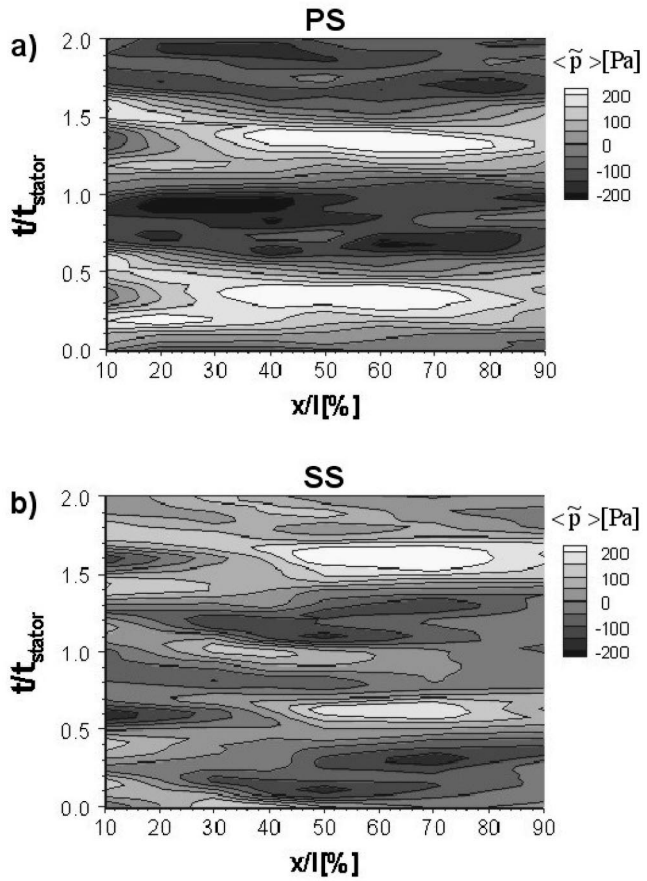


**Fig. 15 Unsteady pressure distribution on PS and SS of rotor 3, MS, design point ($\xi$=1.00, $\zeta$=1.0)**

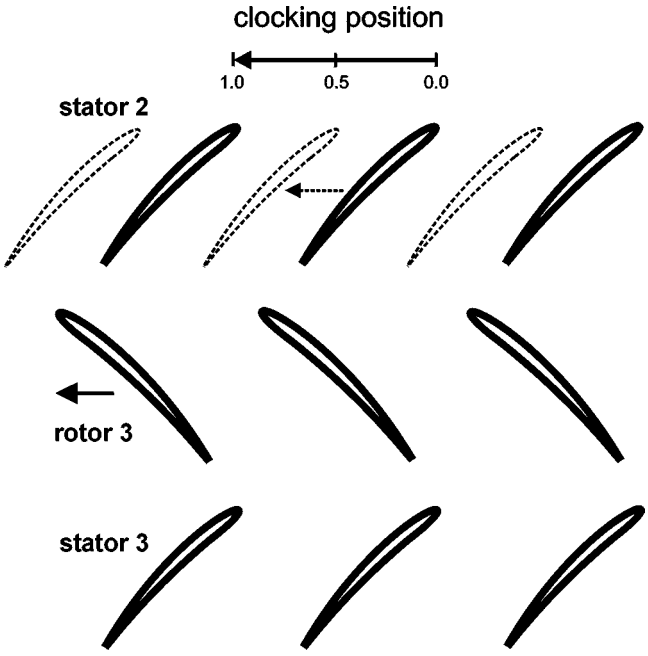


**Fig. 16 Blade section with clocking positions of stator 2; IGV, stator 1, 3 and 4 at fixed positions**

The effect of clocking on the unsteady profile pressures and blade forces was experimentally investigated by Hsu and Wo [29] and numerically by Cizmas and Dorney [30]. They observed a remarkable influence due to blade row clocking on the unsteady pressure amplitudes.

In our four-stage compressor each single stator blade row was shifted separately. The selected stator blade row was traversed one blade pitch in circumferential direction in steps of 10% of the stator blade pitch. As an example a schematic of one clocking configuration is given in Fig. 16. In this case stator 2 is traversed stepwise while the other stator blade rows and the IGV remain at fixed positions. Thus the changes of the unsteady pressure distributions on the investigated rotor 3 are caused by the stepwise shifted wakes of stator 2 for this clocking configuration.

Typical results are shown for the individual clocking of stator 2 (Fig. 17) and stator 3 (Fig. 18). The influence of the stepwise traversed blade row is highlighted by a dashed line. The impact of the fixed blade rows appears at constant points of time for all clocking positions. This is marked with arrows in the figures.

If the influences of different blade rows appear at the same time at the considered position on the blade (rotor 3, SS, 50% chord) they superimpose each other and the unsteady pressure amplitude increases. This can be observed for the stator 2 clocking configuration at the points A and B, Fig. 17. At point A the wake of the shifted stator 2 and the potential effect of stator 4 superimpose each other (Fig. 17, clocking position: 0.8, 1.8 . . . ). At point B the wake of stator 2 is responsible for a pressure maximum, which appears at nearly the same time as the potential effect of stator 3 and the wake effect of stator 1 (Fig. 17, clocking position: 0.7, 1.7 . . . ). For these clocking constellations the unsteady pressure fluctuations at the considered rotor 3 are clearly higher than for the nominal setup of the compressor. If the pressure maxima of the fixed blade rows and the pressure minimum of the clocked blade row coincides, the pressure fluctuations amplitude decreases (point C, Fig. 17, clocking position 0.3, 1.3 . . . ).

From Fig. 17 also follows, that the influence of the stator 2 appears at $t/t_{stator}=0.55$ (1.55) for the nominal setup of the compressor without clocking (intersection of dashed line and abscissa).

The second exemplary result is for the clocking of stator 3, which influences the rotor 3 pressure distribution by its potential effect (Fig. 18). Also in this case an increase of the overall amplitudes can be observed, if the influences of the different blade rows coincide and superimpose (Fig. 18, points A and B). The amplitude increase at point B is comparatively small, because stator 1

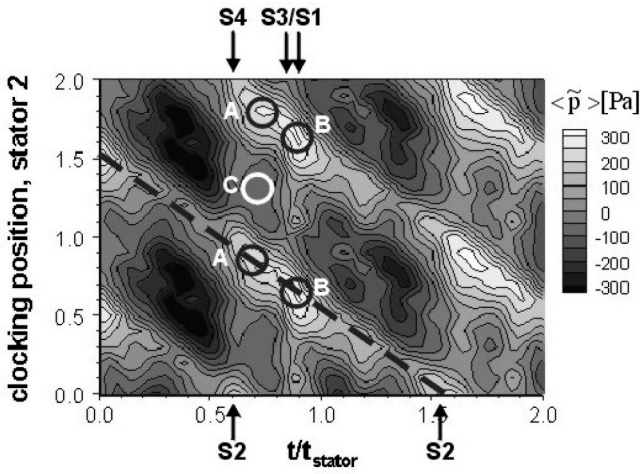


**Fig. 17 Ensemble-averaged pressure on rotor 3 depending on clocking position of the upstream stator 2 (stator 1, 3 and 4 at fixed positions), SS, MS, 50% chord, design point ($\xi$=1.00, $\zeta$=1.0)**

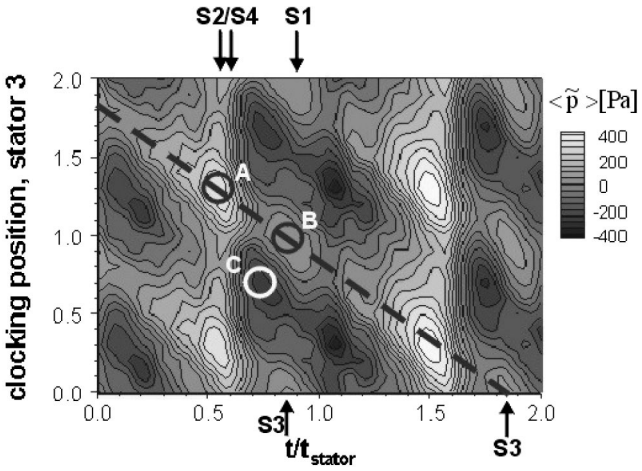


**Fig. 18 Ensemble-averaged pressure on rotor 3 depending on clocking position of the downstream stator 3 (stator 1, 2 and 4 at fixed positions), SS, MS, 50% chord, design point ($\xi$=1.00, $\zeta$=1.0)**

has only a slight influence on the pressure distribution on rotor 3. The influence of stator 3 for the zero-clocking configuration can be identified at $t/t_{stator}=0.85$ (1.85).

Further on the clocking of stator 1 and 4 was analyzed the same way. The results are summarized in Figs. 19 and 20. Figure 19 shows for comparison a time trace without clocking, e.g., for the nominal setup of the compressor (as shown in Fig. 15, midchord position on SS). This is also identical to the time traces for the zero-clocking position in Figs. 17 and 18. The different influences of the four stator blade rows, which could be identified with the clocking investigations, are marked with arrows. The wake of stator 2 is mainly responsible for the first peak, which is superimposed on the basically wave-like pressure pattern. At about the same time the potential effect of stator 4 could be identified with lower amplitudes. The second peak is due to the strong potential effect of stator 3 and the comparatively small wake influence of stator 1.

It has been shown by means of Figs. 17 and 18 that the unsteady pressure amplitudes depend on the relative positions of the stator blade rows to each other. The following Fig. 20 summarizes the dependency of the unsteady pressure amplitudes on the clocking position of the individual blade rows. It shows the pressure

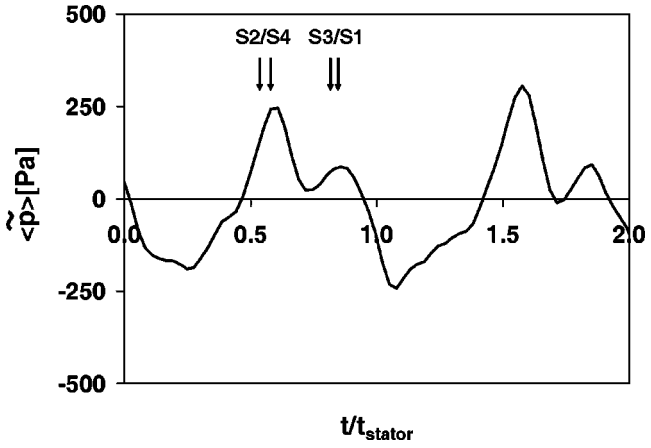


**Fig. 19 Classification of the influences of stator 1–4 on unsteady pressure on rotor 3, SS, MS, 50% chord, design point ($\xi$=1.00, $\zeta$=1.0)**

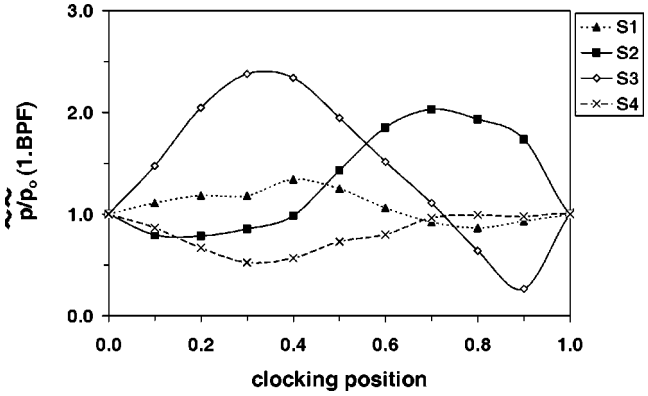


**Fig. 20 Variation of first harmonic of pressure on rotor 3, SS, MS, 50% chord, depending on clocking position of individually clocked stator 1–4, design point ($\xi$=1.00, $\zeta$=1.0)**

fluctuations for the first harmonic of the passing stator blades (1. BPF from the pressure spectra). These values are related to the amplitude for the zero-clocking position $p_0$.

As expected, the relative positions of stator 2 and stator 3, which are up- and downstream of the considered rotor 3, are of most relevance on its unsteady pressure distribution. For the clocking of the downstream stator 3 the maximum pressure fluctuation is nearly 2.5 times the value for the zero clocking (Fig. 20, S3). It appears at the clocking position of 0.3, where the superposition with the wakes of stator 2 and the potential effect of stator 4 takes place (compare Fig. 18, point A). This results in the enormous increase of the pressure fluctuations. A strong effect on the excited blade vibrations is expected for this constellation. The minimum unsteady pressure of rotor 3 appears at the stator 3 clocking position of 0.9, where the pressure fluctuation amplitudes are only 25% of that for the zero-clocking position.

For the clocking of the upstream stator 2 the maximum pressure fluctuations are comparatively strong as for stator 3 (Fig. 20, S2). The maximum magnification is about 2.0 times the value for the zero clocking. It appears if the wake effect of stator 2 coincides with the influence of the fixed blade rows, especially stator 3 (clocking position: 0.7, compare Fig. 17, B).

The clocking of the stator 1 and stator 4, which are further up- and downstream, respectively, also causes remarkable, but less drastic changes of the unsteady pressure distribution of rotor 3 if they are traversed in circumferential direction (Fig. 20, S1, S4).

It should not be forgotten, however, that the variation of the amplitudes at a considered clocking position is not due to the shifted stator blade row alone, but always because of the superposition with the wake and potential effects of the other stator blade rows.

The clocking of stator 1–4 also has a strong influence on the pressure distributions of the other rotor blade rows. This effect cannot be considered here. To find an optimum clocking configuration concerning the unsteady pressure distributions for the whole compressor, the other rotor blade rows have to be included in the investigations.

## 8 Conclusions

In this two-part paper experimental investigations of unsteady aerodynamic blade row interactions throughout the four-stage Low-Speed Research Compressor of Dresden are presented. In part I of the paper the unsteady profile pressure distributions for nominal setup of the compressor are discussed in detail. Results are shown for the first, a middle and the last compressor stage both on the rotor and stator blades. The design point and an operating point near stability limit are considered.

A very complex behavior of the unsteady profile pressures can be observed in this multistage machine. Both the wakes from

upstream and the potential flow field of downstream blade rows affect the unsteady profile pressure distribution. The amplitude and shape of the time traces of the unsteady profile pressures strongly depend on the aerodynamic interaction of several upstream and downstream blade rows. Hence the unsteady blade pressures are a function of several geometrical parameters (blading, axial gap, blade numbers, clocking of blade rows, etc.) and aerodynamic parameters (flow angles, loading, etc.) of the machine. The different periodic wake and potential influences superimpose to a resulting time-dependent pressure pattern.

The profile pressure changes nearly simultaneously along the blade chord if a wake or potential effect arrive at the leading edge or the trailing edge of the blade, respectively. This can be explained by a change of the circulation of the considered blade for every passing blade of up- and downstream blade rows. Another point is that the pressure waves associated with the wakes and potential effects propagate with the speed of sound. Thus the unsteady profile pressure distribution is nearly independent of the convective wake propagation within the blade passage.

Between pressure side and suction side of the blade a phase shift of the response to the disturbances can be observed. For the different blade rows this phase shift is between 60 and 180 deg. This parameter is dependent on several geometric and aerodynamic parameters and changes with the operating point of the compressor.

For embedded blade rows with equal counts of up- and downstream moving blades, the wakes and the potential effect from up- and downstream cannot be separated for the nominal experimental setup because of the fast pressure changes along the chord. To distinguish between the different periodic influences from the surrounding blade rows clocking investigations were carried out in addition. For this reason the unsteady profile pressure distribution on rotor 3 was measured, while stator 1–4 were separately traversed stepwise in circumferential direction. As a result the influences of the up- and downstream blade rows on the unsteady profile pressure could clearly be separated. Furthermore, it is shown hereby that the superposition of wakes of upstream blade rows and the potential effect of downstream blade rows dominantly affects the amplitudes of the unsteady pressure on a considered blade. The incoming wakes and the potential effects of the downstream blades have a comparatively strong effect. Another result, important under the aspect of blade vibration in multistage compressors, is that blade rows located several stages up- or downstream also have an ascertainable effect on the unsteady pressure distributions of a considered blade.

In part II the unsteady aerodynamic forces acting on the rotor and stator blades of the compressor are calculated from the experimental data discussed in this part of the paper.

## Acknowledgments

The work reported in this paper was performed within the project: ''Unsteady Forces and Boundary Layer Behavior on the Blades of a Low-Speed Axial Compressor'' which is part of the joint project: ''Periodical Unsteady Flow in Turbomachines'' funded by the DFG (German Research Society). Information on this project can be found at http://www.turboflow.tu-berlin.de. The permission for publication is gratefully acknowledged.

## Nomenclature

$\langle\ \rangle$ = ensemble-averaged value
$-$ = mean value
$f$ = frequency [Hz]
$h$ = enthalpy [J/kg]
$l$ = chord length [m]
$M,N$ = number of time steps
$p$ = pressure [Pa]
$\tilde{p}$ = fluctuating part of pressure [Pa]
rms = root mean square of pressure [Pa]
$t$ = time [s]
$u$ = rotor speed [m/s]
$x$ = chordwise position [m]
$\zeta$ = reduced speed/reduced design speed
$\xi$ = reduced mass flow/reduced design mass flow
$\pi$ = total pressure ratio of compressor
$\phi$ = phase shift [deg]
$\Psi_{is}$ = enthalpy coefficient, $\Psi is = \Delta h_{is}/u_{MS}^2$

### Subscripts

0 = zero-clocking position
1 = measurement plane in the middle of axial gap upstream of the considered blade row
dyn = dynamic
$i,j$ = indices for time traces

### Abbreviations

BPF = blade passing frequency
DP = design point
LSRC = low-speed research compressor
IGV = inlet guide vane
MS = midspan
PS = pressure side
SS = suction side
S1-S4 = stator 1-4

## References

[1] Kemp, N. H., and Sears, W. R., 1955, ''The Unsteady Forces Due to Viscous Wakes in Turbomachines,'' J. Aeronaut. Sci., **22**(7), pp. 478–483.
[2] Meyer, R. X., 1958, ''The Effect of Wakes on the Transient Pressure and Velocity Distributions in Turbomachines,'' Trans. ASME, **80**, pp. 1544–1552.
[3] Lefcort, M. D., 1965, ''An Investigation Into Unsteady Blade Forces in Turbomachines,'' ASME J. Eng. Power, **87**, pp. 345–354.
[4] Grollius, H.-W., 1981, ''Experimentelle Untersuchung von Rotor-Nachlaufdellen und deren Auswirkungen auf die dynamische Belastung axialer Verdichter- und Turbinengitter,'' PhD thesis, RWTH Aachen, Germany.
[5] Hodson, H. P., 1985, ''Measurements of Wake-Generated Unsteadiness in the Rotor Passages of Axial Flow Turbines,'' ASME J. Eng. Gas Turbines Power, **107**, pp. 467–476.
[6] Denos, R., Arts, T., Paniagua, G., Michelassi, V., and Martelli, F., 2001, ''Investigation of the Unsteady Rotor Aerodynamics in a Transonic Turbine Stage,'' ASME J. Turbomach., **123**, pp. 81–89.
[7] Laumert, B., Martensson, H., and Fransson, T. H., 2002, ''Investigation of Unsteady Blade Excitation Mechanisms in a Transonic Turbine Stage, Part I: Phenomenological Identification and Classification, Part II: Analytical Description and Quantification,'' ASME J. Turbomach., **124**, pp. 410–428.
[8] Valenti, E., Halama, J., Denos, R., and Arts, T., 2002, ''Investigation of the 3D Unsteady Rotor Pressure Field in a HP Turbine Stage,'' ASME paper no. GT-2002-30365.
[9] Miller, R. J., Moss, R. W., Ainsworth, R. W., and Harvey, N. W., 2003, ''Wake, Shock, and Potential Flow Field Interactions in a 1.5 Stage Turbine, Part I: Vane-Rotor and Rotor Vane Interactions, Part II: Vane-Vane Interaction and Discussion of Results,'' ASME J. Turbomach., **125**, pp. 33–47.
[10] Pieper, S. J., 1995, ''Erfassung instationärer Strömungsvorgänge in einem hochtourigen invers ausgelegten einstufigen Axialverdichter mit Vorleitrad,'' PhD thesis, RWTH Aachen, Germany.
[11] Sanders, A. J., and Fleeter, S., 2001, ''Multi-Blade Row Interactions in a Transonic Axial Compressor, Part II: Rotor Wake Forcing Function & Stator Unsteady Aerodynamic Response,'' ASME paper no. 2001-GT-0269.
[12] Durali, M., and Kerrebrock, J. L., 1998, ''Stator Performance and Unsteady Loading in Transonic Compressor Stages,'' ASME J. Turbomach., **120**, pp. 224–232.
[13] Korakianitis, T., 1993, ''On the Propagation of Viscous Wakes and Potential Flow in Axial-Turbine Cascades,'' ASME J. Turbomach., **115**, pp. 118–127.
[14] Manwaring, S. R., and Wisler, D. C., 1993, ''Unsteady Aerodynamics and Gust Response in Compressors and Turbines,'' ASME J. Turbomach., **115**, pp. 724–740.
[15] Valkov, T., and Tan, C. S., 1995, ''Control of the Unsteady Flow in a Stator Blade Row Interacting With Upstream Moving Wakes,'' ASME J. Turbomach., **117**, pp. 97–105.
[16] Arnone, A., and Pacciani, R., 1996, ''Rotor-Stator Interaction Analysis Using the Navier-Stokes Equations and a Multigrid Method,'' ASME J. Turbomach., **118**, pp. 679–689.
[17] Fan, S., and Lakshminarayana, B., 1996, ''Time-Accurate Euler Simulation of Interaction of Nozzle Wake and Secondary Flow With Rotor Blade in an Axial Turbine Stage Using Nonreflecting Boundary Conditions,'' ASME J. Turbomach., **118**, pp. 663–678.
[18] Lee, Y., and Feng, J., 2003, ''Potential and Viscous Interactions for a Multi-Blade-Row Compressor,'' ASME paper no. GT-2003-38560.
[19] Mailach, R., Müller, L., and Vogeler, K., 2003, ''Experimental Investigation of

Unsteady Forces on Rotor and Stator Blades of an Axial Compressor,'' in *Proceedings of the Fifth European Conference on Turbomachinery—Fluid Dynamics and Thermodynamics*, Stastny, M., Sieverding, C. H., and Bois, G. Eds., March 18–21, Prague, Czech Republic, pp. 221–223.
[20] Mailach, R., and Vogeler, K., 2004, ''Aerodynamic Blade Row Interaction in an Axial Compressor, Part I: Unsteady Boundary Layer Development,'' ASME J. Turbomach., **126**, pp. 35–44.
[21] Mailach, R., and Vogeler, K., 2004, ''Aerodynamic Blade Row Interaction in an Axial Compressor, Part II: Unsteady Profile Pressure Distribution and Blade Forces,'' ASME J. Turbomach., **126**, pp. 45–51.
[22] Mailach, R., and Vogeler, K., 2004, ''Rotor-Stator Interactions in a Four-Stage Low-Speed Axial Compressor, Part II: Unsteady Aerodynamic Forces of Rotor and Stator Blades,'' **126**, pp. 518–525.
[23] Sauer, H., Bernstein, W., Bernhard, H., Biesinger, T., Boos, P., and Möckel, H., 1996, ''Konstruktion, Fertigung und Aufbau eines Verdichterprüfstandes und Aufnahme des Versuchsbetriebes an einem Niedergeschwindigkeits-Axialverdichter in Dresden,'' Abschlußbericht zum BMBF-Vorhaben 0326758A, Dresden, Germany.
[24] Müller, R., Mailach, R., and Lehmann, I., 1997, ''The Design and Construction of a Four-Stage Low-Speed Research Compressor,'' in *Proceedings of the IMP '97 Conference on Modelling and Design in Fluid-Flow Machinery*, Badur, J., Bilicki, Z., Mikielewicz, J., and Sliwicki E., Eds., Nov. 18–21, Gdansk, Poland, pp. 523–531.
[25] Boos, P., Möckel, H., Henne, J. M., and Selmeier, R., 1998, ''Flow Measurement in a Multistage Large Scale Low Speed Axial Flow Research Compressor,'' ASME paper no. 98-GT-432.
[26] Stadtmüller, P., and Fottner, L., 2000, ''Fast Response Pressure Transducers for the Investigation of Wake-Induced Transition on a Highly Loaded LP Turbine,'' *Proceedings of the XVth Bi-Annual Symposium on Measuring Techniques in Transonic and Supersonic Flows in Cascades and Turbomachines*, 21–22 September, Firenze, Italy.
[27] Reinmöller, U., Stephan, B., Schmidt, S., and Niehuis, R., 2001, ''Clocking Effects in a 1.5 Stage Axial Turbine—Steady and Unsteady Experimental Investigations Supported by Numerical Simulations,'' ASME paper no. 2001-GT-0304.
[28] Arnone, A., Marconcini, M., Pacciani, R., Schipani, C., and Spano, E., 2002, ''Numerical Investigation of Airfoil Clocking in a Three-Stage Low-Pressure Turbine,'' ASME J. Turbomach., **124**, pp. 61–68.
[29] Hsu, S. T., and Wo, A. M., 1998, ''Reduction of Unsteady Blade Loading by Beneficial Use of Vortical and Potential Disturbances in an Axial Compressor with Rotor Clocking,'' ASME J. Turbomach., **120**, pp. 705–713.
[30] Cizmas, P. G. A., and Dorney, D. J., 2000, ''The Influence of Clocking on Unsteady Forces of Compressor and Turbine Blades,'' Int. J. Turbo & Jet Engines, **17**(2), pp. 133–142.

# Rotor-Stator Interactions in a Four-Stage Low-Speed Axial Compressor—Part II: Unsteady Aerodynamic Forces of Rotor and Stator Blades

**Ronald Mailach**
e-mail: mailach@tus.mw.tu-dresden.de

**Lutz Müller**
e-mail: lmueller@tus.mw.tu-dresden.de

**Konrad Vogeler**
e-mail: kvogeler@tus.mw.tu-dresden.de

Dresden University of Technology,
Institute for Fluid Mechanics,
01062 Dresden, Germany

*This two-part paper presents detailed experimental investigations of unsteady aerodynamic blade row interactions in the four-stage low-speed research compressor of Dresden. In Part I of the paper the unsteady profile pressure distributions for the nominal setup of the compressor are discussed. Furthermore the effect of blade row clocking on the unsteady profile pressures is investigated. Part II deals with the unsteady aerodynamic blade forces, which are determined from the measured profile pressure distributions. A method to calculate the aerodynamic blade forces on the basis of the experimental data is presented. The resulting aerodynamic blade forces are discussed for the rotor and stator blade rows of the first stage and the third stage of the compressor. Different operating points between design point and stability limit of the compressor were chosen to investigate the influence of loading on the aerodynamic force excitation. The time traces and the frequency contents of the unsteady aerodynamic blade force are discussed. Strong periodic influences of the incoming wakes and of potential effects of downstream blade rows can be observed. The amplitude and shape of the unsteady aerodynamic blade force depend on the interaction of the superimposed influences of the blade rows.*
[DOI: 10.1115/1.1791642]

## 1 Introduction

The flow in turbomachines is highly unsteady and turbulent. The rotor and stator blades, moving relative to each other, aerodynamically interact because of the viscous wakes and the potential effects of the blades. Due to these aerodynamic interactions the pressure distributions on the blades changes considerably in time. For this reason unsteady aerodynamic blade forces and moments are generated. Critical blade vibrations are excited if the frequency of the aerodynamic stimulation matches the natural frequencies of the blades. This can lead to a reduction of fatigue life or even a destruction of the blading. This is the reason why unsteady effects due to periodic blade row interactions should be considered during the design process. For this purpose it is necessary to improve the knowledge of the aerodynamic response of the unsteady profile pressure distributions as well as the excitation mechanism and the expected magnitude of the blade forces.

A literature survey on the research about blade row interaction is given in Part I of the paper [1]. Early analytical studies into the excitation of unsteady blade forces were performed by Kemp and Sears [2], Meyer [3], and Lefcort [4].

Only limited experimental data about the unsteady aerodynamic blade forces in turbomachinery are available. Experiments on the aerodynamic blade forces in cascades were performed by Grollius [5]. Manwaring and Fleeter [6] analyzed the aerodynamic response of the rotor blades to inlet distortions in an axial research compressor. Durali and Kerrebrock [7] investigated the unsteady pressure distribution in a single stage transonic compressor and provided results on the unsteady aerodynamic blade force due to the incoming wakes. The force on the rotor blades of a transonic turbine stage, which is determined by the shock sweeping, was analyzed by Denos et al. [8].

Numerical investigations concerning the effect of wakes and the potential flow field on the excitation of unsteady blade forces of a turbine cascade were conducted by Korakianitis [9].

Hsu and Wo [10] investigated rotor-stator interactions in a 1 1/2 stage large-scale low-speed compressor. In a recent publication Lee and Feng [11] presented numerical results for the same compressor. The authors considered the effect of wakes and potential effects on the unsteady blade loading and the excited aerodynamic blade forces. Moreover they discussed the influence of rotor clocking on the unsteady force excitation. Numerical results of the clocking influence on unsteady turbine blade forces are presented by Cizmas and Dorney [12].

In previous publications of the authors' results on the unsteady aerodynamic blade forces of the rotor and stator blades of the first stage of the Dresden low-speed research compressor (LSRC) for several operating points as well as for rotating stall are discussed (Mailach et al. [13], Mailach and Vogeler [14]). The unsteady blade forces are influenced by the wakes as well as by potential effects of the surrounding blade rows.

The aim of this two-part paper is to provide a detailed insight into the complex physics of blade row interactions in multistage turbomachinery. In Part I of this paper experimental investigations of the steady and unsteady profile pressure distributions in the four-stage Dresden LSRC are presented [1]. Based on these data the aerodynamically excited forces on several blade rows of the four-stage compressor are determined. Results for different operating points will be discussed. So a comprehensive data base on aerodynamic blade forces in a multistage compressor is provided.

Contributed by the International Gas Turbine Institute (IGTI) of THE AMERICAN SOCIETY OF MECHANICAL ENGINEERS for publication in the ASME JOURNAL OF TURBOMACHINERY. Paper presented at the International Gas Turbine and Aeroengine Congress and Exhibition, Vienna, Austria, June 13–17, 2004, Paper No. 2004-GT-53099. Manuscript received by IGTI, October 1, 2003; final revision, March 1, 2004. IGTI Review Chair: A. J. Strazisar.

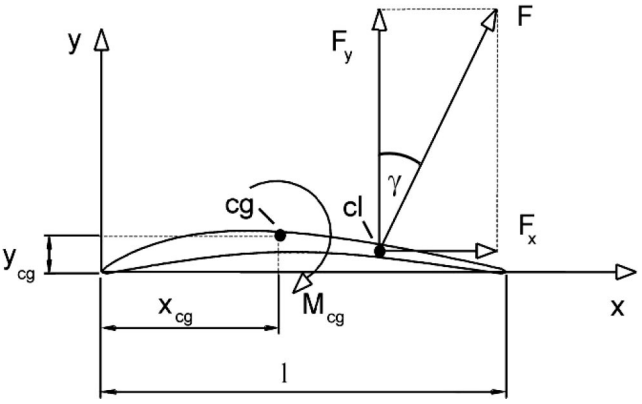


**Fig. 1 Forces in blade coordinate system**

## 2 Experimental Setup and Calculation of Unsteady Aerodynamic Blade Forces

The experimental investigations were performed in the four-stage low-speed research compressor of Dresden University of Technology, Dresden, Germany (Dresden LSRC). Information about the compressor, the experimental setup and the data post-processing are given in part I of the paper [1]. The unsteady aerodynamic blade forces, discussed in Part II, were calculated from the unsteady rotor and stator pressure distributions, which are available for the midspan positions on pressure side (PS) and suction side (SS). Results of the unsteady forces for the first stage (rotor 1/stator 1) and a middle stage (rotor 3/stator 3) of the compressor will be presented. Five operating points were investigated in each case. The results discussed in this part of the paper are for the nominal setup of the compressor. The investigation of the unsteady pressures on stator 4 and for clocked blade rows in part I was of particular interest for improving the physical understanding of the blade row interactions and will not be discussed in this part of the paper. The algorithm for calculating the pressure forces, which will be described following, was implemented into a computer program by Müller [15].

Since the piezoresistive pressure transducers were arranged at the pressure side (PS) and suction side (SS) of a single rotor and stator blade, respectively, it is possible to consider the pressure distribution and hence the aerodynamic blade forces in a time-resolved manner as well as in ensemble-averaged form. Excepting the results in Sec. 3, which show time-averaged results, all results are calculated from the ensemble-averaged pressures. There is no loss of information due to the ensemble-averaging concerning the periodic part of the signals due to the passing blades. This has been tested by comparing the ensemble-averaged and time-resolved results for the blade forces.

As in Grollius [5] the force components are referred to the blade coordinate system (Fig. 1). The components of the force $F$ are those acting along the blade chord direction ($F_x$) and perpendicular to that ($F_y$). The moment $M_{cg}$ is referred to the center of gravity (cg) of the blade.

Using our experimental configuration the aerodynamic blade force acting at midspan of the blade is calculated. The components of the aerodynamic blade force as well as the moment are determined by integrating the pressure along PS and SS of the blade surface with respect to the blade contour [Eqs. (1)–(3)]. The contribution of shear forces cannot be taken into account. The pressure force calculation is done for each individual time step of the measuring data. The blade height has to be taken into consideration to get a force which is linked to the whole blade surface. However, a spanwise variation of the unsteady aerodynamic force cannot be realized with the current experimental setup.

$$\langle F_x(t)\rangle = h \oint \langle p(t,x)\rangle \frac{dy}{dx} dx \tag{1}$$

$$\langle F_y(t)\rangle = -h \oint \langle p(t,x)\rangle dx \tag{2}$$

$$\langle M_{cg}(t)\rangle = -h \oint \langle p(t,x)\rangle \left( (y_{cg}-y)\frac{dy}{dx} + (x_{cg}-x) \right) dx \tag{3}$$

The resulting force $F$ and the angle $\gamma$ between $F$ and the direction normal to the chord were determined using trigonometric functions (Fig. 1).

The pressure taps, delivering time-averaged data, are arranged from 2.5% to 95.0% of chord on both sides of the blades. Time-resolved data are available from 10% to 90% chord. The pressure in the leading edge and the trailing edge region, where no measurements were possible, was extrapolated. The stagnation points are assumed to be at the leading and the trailing edge, respectively. This extrapolation toward the leading and trailing edge is particularly necessary for the calculation of $F_x$, acting in tangential direction of the blade. This is because of the fact that the largest portions of this force component in this direction are induced near the leading edge and the trailing edge.

As shown in Part I the amplitude variation of the unsteady part of the pressure along the blade surface is comparatively small. Moreover the pressure distribution changes nearly instantaneously along the blade surface due to wakes and potential effects. Hence the extrapolation of the steady and unsteady part of the pressure at the leading and trailing edge is a useful way to improve the accuracy of the results.

Because the excited aerodynamic forces are associated with the flow field up- and downstream the considered blade the force coefficient $c_F$ is a relevant parameter. The force coefficients of the rotor and stator blades are determined with the equation

$$\langle c_F(t)\rangle = \frac{\langle \mathrm{F}(t)\rangle}{\rho/2 \times \overline{\mathrm{v}}_\infty^2 \times A} \tag{4}$$

while $\overline{\mathrm{v}}_\infty$ is the vectorial average of the mean velocities of the incoming and outgoing flow of a considered blade row (absolute velocity for stator and relative velocity for rotor blades) and $A$ is the blade surface. The force coefficients of the force components $F_x$ and $F_y$ are calculated accordingly. The nondimensional moment in ensemble-averaged form is calculated with

$$\langle c_{\mathrm{M,cg}}(t)\rangle = \frac{\langle M_{cg}(t)\rangle}{\rho/2 \times \overline{\mathrm{v}}_\infty^2 \times A \times 1} \tag{5}$$

whereas 1 is the blade chord length.

Furthermore time-averaged results of these parameters are determined, which are discussed in Sec. 3.

## 3 Time-Averaged Aerodynamic Blade Forces

As a first result the time-averaged force coefficients of the rotor and stator blades of the first and third stage are shown in Fig. 2. The dimensional mean force values show only relatively small changes depending on the operating point. The aerodynamic force coefficients clearly change with the operating point because they are linked with the dynamic head of the flow and the flow turning (loading) of the blades. An increase of the force coefficient is observed for all blade rows if the operating point is shifted toward the stability limit of the compressor. For rotor 1 the aerodynamic force coefficient remains on a nearly constant level between $\xi$=1.00–0.90, for rotor 3 this is the case between $\xi$=0.95–0.90. The highest force coefficient within the whole operating range appears for the first stage stator blades due to the higher loading of this blade row (compare profile pressure distribution in Part I [1], Fig. 3). Somewhat lower values are observed for the rotor blades.

The mean values of the aerodynamic force coefficient, its components in the $x$- and $y$-directions, the moment around the center

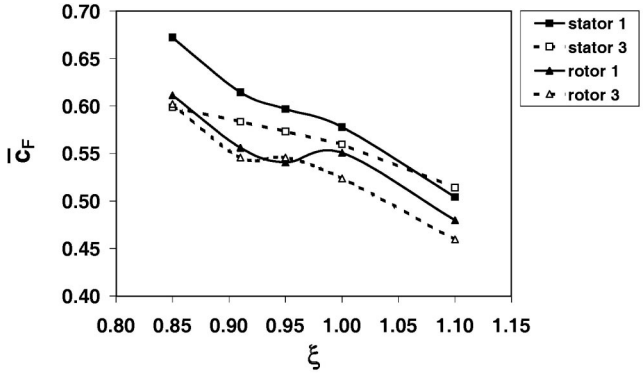


**Fig. 2 Time-averaged aerodynamic force coefficients of the rotor and stator blades of stage 1 and 3, design speed ($\zeta$=1.0)**

**Table 1 Time-averaged aerodynamic forces of the rotor and stator blades of stage 1 and 3, design speed ($\zeta$=1.0)**

| | $\xi$ | $\overline{c}_F$ | $\overline{c}_{F,y}$ | $\overline{c}_{F,x}$ | $\overline{c}_{M,cg}$ | $\overline{\gamma}$ [deg] |
|---|---|---|---|---|---|---|
| stator 1 | 1.00 | 0.58 | 0.57 | -0.04 | -0.26 | -4.1 |
| | 0.85 | 0.67 | 0.66 | -0.08 | 0.05 | -7.0 |
| stator 3 | 1.00 | 0.56 | 0.55 | -0.05 | -0.08 | -5.5 |
| | 0.85 | 0.60 | 0.59 | -0.08 | 0.24 | -8.5 |
| rotor 1 | 1.00 | 0.55 | 0.55 | -0.06 | 0.65 | -6.7 |
| | 0.85 | 0.62 | 0.61 | -0.10 | 1.10 | -9.3 |
| rotor 3 | 1.00 | 0.52 | 0.52 | -0.08 | 0.67 | -8.5 |
| | 0.85 | 0.60 | 0.59 | -0.10 | 1.06 | -10.0 |

of gravity and the angle $\gamma$ between $F$ and $F_y$ are given in Table 1 (definitions in Fig. 1). The results are for the design point ($\xi$ =1.00) and an operating point near stability limit with 85% mass flow ($\xi$=0.85) at design speed ($\zeta$=1.0).

The following tendencies are observed: As discussed with Fig. 2 the aerodynamic force coefficient increases towards the stability limit of the compressor (Table 1). For all operating points the amount of the force component normal to the blade chord (*y*-direction) is much larger than that into blade chord direction (*x*-direction). Therefore the amount of $\overline{c}_{F,y}$ is nearly identical to $\overline{c}_F$, while $\overline{c}_{F,x}$ is small. For this reason the mean angle $\overline{\gamma}$ for all operating points is comparatively small with about $-10$ deg $<\overline{\gamma}<-4$ deg. For all blade rows the absolute value increases by 2.5–3.0 deg if the operating point is shifted from design point towards the stability limit. The moment $\overline{c}_{M,cg}$ strongly depends on the blade curvature (location of center of gravity) as well as on the loading distribution of the blade. For the stator blades the center of lift is closer to the trailing edge of the blade than the center of gravity at design point. Therefore the moment $\overline{M}_{cg}$ as well as the moment coefficient $\overline{c}_{M,cg}$ are negative, using the definition in Fig. 1. Near the stability limit the maximum pressure difference between PS and SS of the blades and consequently the position of the center of lift are shifted toward the leading edge of the blade. This is why the moment becomes positive for stator 1 and 3 at $\xi$=0.85. For the rotor blades of stage 1 and 3 the moment is positive already for design point (c1 is upstream of cg). Toward the stability limit it increases due to the decreasing dynamic head and a larger distance between the centres of lift and gravity (Table 1, $\xi$=0.85).

## 4 Unsteady Aerodynamic Blade Forces on the Stator Blades

Following the ensemble-averaged time traces of the aerodynamic force and moment coefficient for several blade rows are represented. Generally the amplitudes of the force component $F_y$ acting normal to the blade chord are clearly larger than for those of $F_x$ which is directed in blade chord direction. Depending on the blade row and the operating point the amount of the mean value of $F_y$ is 5–15 times than $F_x$.

### A Stator 1

*1 Design Point.* Figure 3 shows the results for the aerodynamic force of stator 1 at design point ($\xi$=1.00, $\zeta$=1.0). These are the aerodynamic force coefficient of the resulting force and its components, the moment around the center of gravity and the angle of the force to the normal direction of the blade. The time base is related to the passing period of the rotor blades.

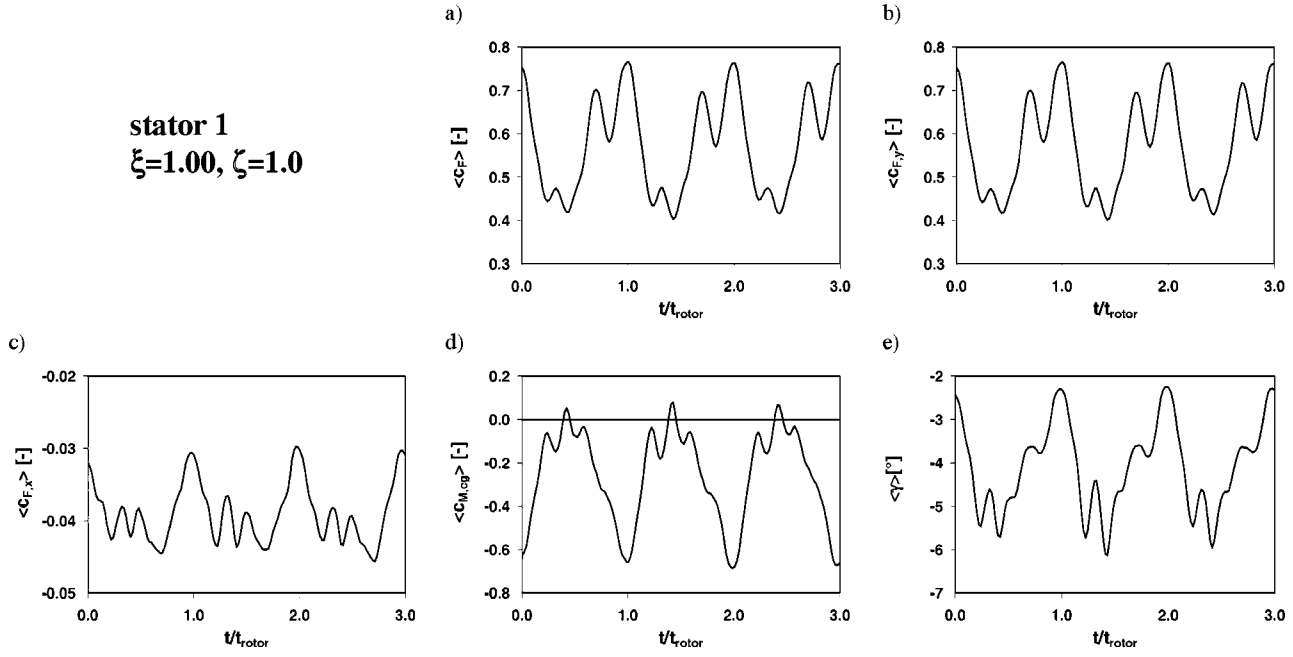


**Fig. 3 Unsteady aerodynamic force parameters of stator 1, design point ($\xi$=1.00, $\zeta$=1.0)**

As discussed in Part I [1] the unsteady pressures and consequently the force of the first stage stator blades are periodically influenced by the up- and downstream passing rotor blades. The rotor passing period is clearly visible for all depicted parameters of the blade force (Fig. 3). Several peaks appear during one blade passing period. These peaks are due to the superimposed influences of the upstream and the three downstream located rotor blade rows, affecting the unsteady pressure distribution of the considered stator blade [1]. The shapes of the time traces of the aerodynamic force $F$ and its dominating component $F_y$ are comparable to that of the pressure fluctuations (Figs. 3(*a*) and 3(*b*), compare to Figs. 4 and 5 in Ref. [1]). This is mainly due to the fact that the pressure changes nearly instantaneously along the blade chord due to the aerodynamic interaction of the blade rows. Certainly the phase shift of the pressure between PS and SS influences the shape of the resulting time-dependent force traces as well.

The amplitudes and shapes of $c_F$ and $c_{F,y}$ (as well as $F$ and $F_y$) are nearly identical. This is because of the small amplitudes of the force component $F_x$ ($c_{F,x}$), which is directed along the blade chord direction [Fig. 3(*c*)]. The mean value of $c_{F,y}$ is 15-times of $c_{F,x}$ for the design point ($\xi$=1.00) and nine-times of $c_{F,x}$ for the operating point near stability limit ($\xi$=0.85), respectively.

For the design point the maximum fluctuation amplitudes of the resulting aerodynamic force coefficient $c_F$ (and $c_{F,y}$) are about $\pm$30% of its mean value. Those of $c_{F,x}$ are somewhat lower but not relevant for the blade excitation because of its low absolute mean values.

High fluctuation amplitudes can be observed for the moment around the center of gravity of the blade because of its small mean value [Fig. 3(*d*)]. As discussed in Sec. 2 this parameter depends on the blade profile (relative position of center of lift and center of gravity to each other) and the loading. Due to the passing wakes and the potential effect of downstream moving blades the chordwise loading changes in time. For this reason the center of lift is shifted up- and downstream of the center of gravity of the blade. This strongly influences the amount of the moment acting on the blade. If the center of lift is located upstream the center of gravity the moment becomes positive. This can be observed only for short periods of time for stator 1 at design point [Fig. 3(*d*)].

The last considered parameter, depicted in Fig. 3(*e*), is the angle $\gamma$ between the directions of the force $F$ and the $y$-coordinate (defined in Fig. 1). For the design point the mean value is only $-4°$ because of the small contribution of the $F_x$ component. So the force $F$ is nearly directed normal to the blade chord. The fluctuations of $\gamma$ are about $\pm$2 deg.

Hsu and Wo [10] observed fluctuations of the blade force of up to $\pm$20% depending on their experimental setup. This value is confirmed by Lee and Feng [11]. The experiments of Grollius [5] showed fluctuations up to the same order of magnitude. Denos et al. [8] found force fluctuations of 29% in a transonic turbine stage for design point. However, the strongest fluctuations are induced by the shocks in this case.

To compare our results to further experiments in addition the force components in the axial-circumferential directions are calculated (not depicted). Comparable patterns and amplitudes as for the force $F$ can be observed for these components [Fig. 3(*a*)]. The maximum fluctuations, related to the mean value, are about $\pm$20% for the axial force component and $\pm$30% for the circumferential force component for design point. Hence they are in the same order of magnitude as observed for the values in the blade coordinate system, which is used throughout this paper. Comparable amplitudes for the axial and circumferential unsteady force fluctuations of 25% are reported by Durali and Kerrebrock [7] for a transonic compressor stage.

In the following for stator 1 ($\xi$=0.85), stator 3, rotor 1, and rotor 3 only figures of the time-resolved aerodynamic force coefficients will be shown (Secs. 4 and 5). The reason for this is that the $y$ component of the force coefficient is nearly identical to the force coefficient itself. The $x$ component of the force coefficient is nearly negligible for the blade excitation. Results will only be shown for the design point for the other blade rows. The tendential changes of the considered parameters when approaching the stability limit are comparable to those of stator 1, discussed below. The time-mean values for all blade rows are summarized in Table 1. More results on periodic changes for all blade rows and two operating points are discussed by means of the frequency contents in Sec. 4.

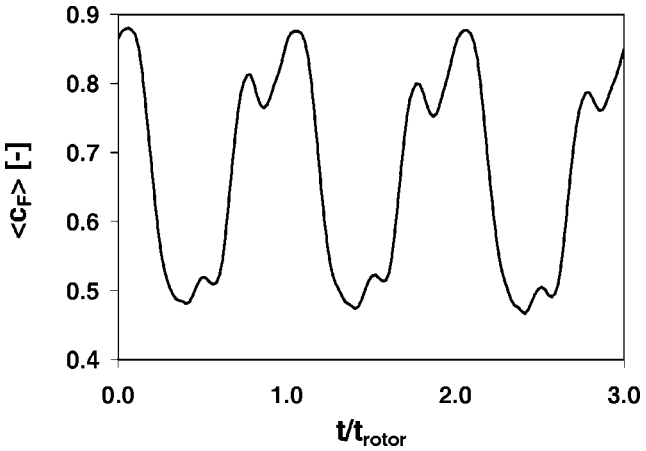


**Fig. 4 Unsteady aerodynamic force coefficient of stator 1, operating point near stability limit ($\xi$=0.85, $\zeta$=1.0)**

*2 Operating Point Near the Stability Limit.* The force coefficient for an operating point near the stability limit ($\xi$=0.85, $\zeta$=1.0) is shown in Fig. 4. The mean unsteady force coefficient is increased by 16% compared to the design point (Table 1). As for the design point the maximum fluctuations are about $\pm$30% (Fig. 4). The shape of the unsteady force and its components is determined by the time-resolved pressure and the phase shift of the pressure between PS and SS. As discussed in Part I [1] the time traces of the pressure are more wavelike for the operating point near stability limit. The superimposed peaks are weaker than for design point. This is reflected in the shape of the unsteady force pattern.

Due to the increasing blade incidence near the stability limit the mean position of the center of the lift is shifted upstream the center of gravity of the blades. Hence the moment acting around the center of gravity of the blade is positive most of the time (no Fig., compare Table 1).

Because of the increased amplitudes of the $F_x$ component the mean absolute value of the angle $\gamma$ as well as its fluctuations increase. Compared to the design point the mean absolute $\gamma$ is increased by 3 deg (Table 1). The maximum fluctuations for $\xi$=0.85 are $\pm$3 deg (no Fig.) and somewhat larger than for design point [Fig. 3(*e*)].

**B Stator 3.** Figures 5(*a*) and 5(*f*) show the unsteady aerodynamic force coefficients of stator 3, rotor 1, and rotor 3 for design point and an operating point near stability limit. First of all the results for stator 3 will be discussed.

The mean aerodynamic force coefficient for stator 3 at design point is in the same order of magnitude as for stator 1 [Fig. 5(*a*)], compare Fig. 3(*a*). Certainly the shape of the time-resolved force coefficient on stator 3 differs from that of stator 1. This is because of the differences in the unsteady profile pressure distributions, caused by the unsteady interactions of up- and downstream blade rows (discussed in Part I).

The maximum force fluctuations for stator 3 are $\pm$25% for design point [Fig. 5(*a*)]. These values are somewhat lower than for stator 1. This corresponds to lower fluctuation amplitudes of the unsteady profile pressure on stator 3 (Part I, Figs. 4 and 9).

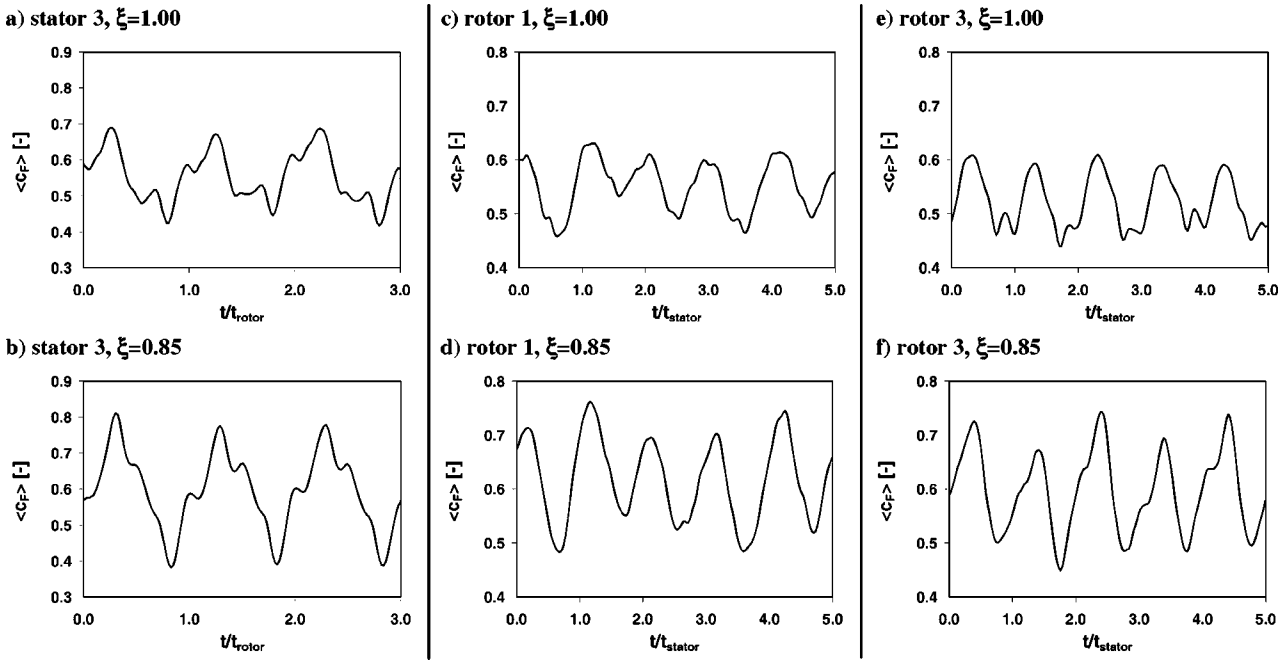


**Fig. 5 Unsteady aerodynamic force coefficients of different blade rows for design point ($\xi$=1.00) and an operating point near stability limit ($\xi$=0.85), design speed ($\zeta$=1.0)**

As for stator 1 the moment for stator 3 is comparatively low (Table 1). This is because the centers of gravity and lift are located at nearly the same position. This is the case for stator 1 as well as for stator 3 since they have the same blade profiles and a comparable loading distribution.

While the mean absolute value of $\gamma$ is increased to 5.5 deg (Table 1), the fluctuations are comparable to those of stator 1 ($\pm$2.5 deg, no Fig.).

For the considered operating point near stability limit the mean force coefficient slightly increases (Fig. 5(*b*), Table 1). The maximum deviations from this mean value increase to $\pm$35%. The shape of the time-dependent force coefficients for the two considered operating points differs somewhat from each other due to the changing flow conditions.

## 5 Unsteady Aerodynamic Blade Forces on the Rotor Blades

**A Rotor 1.** The timescale in Fig. 5(*c*) is related to the passing time of the stator blades. The figure shows the passing of five stator blades, which nearly corresponds to the passing of 3IGV's (83 stator blades, 51 IGV). The unsteady aerodynamic force on the rotor blades of the first stage is clearly dominated by the passing of the downstream stator blades (Fig. 5(*c*)). As discussed in Sec. VI A of Part I, the influence of the IGV wakes on the unsteady pressure distribution is only about 50% compared to that of the upstream propagating potential effect of the stator blades for design point (depending on the position on the blade).

In the same manner as for $c_F$ the force component $c_{F,y}$ shows the dominant influence of the stator blade passing (no Fig.). The time traces of the chordwise component $c_{F,x}$ ($F_x$) as well as the moment $c_{M,\mathrm{cg}}$ ($M_{\mathrm{cg}}$) are less periodic (Mailach et al. [13]). This may be an effect due to the nonexisting pressure transducers in the leading edge and trailing edge region of the rotor blade, necessitating an extrapolation of the pressure there (Sec. 2). However, the stator passing dominates also these time traces.

For the design point the maximum fluctuation amplitudes of the calculated force coefficient are $\pm$15% of its mean values (Fig. 5(*c*)). For the operating point near stability limit the maximum differences to the mean values increase to $\pm$22% (Fig. 5(*d*)). This is clearly below the values of the stator blades. For $\xi$=0.85 the mean force coefficient increases due to the higher loading (Table 1).

For both operating points the amplitudes at given points of time depend on the relative position of the incoming IGV wakes and the potential flow field of the stator blades to each other. As already visible in the time traces of the unsteady pressure the aerodynamic effects of these blade rows superimpose upon each other (Part I, Figs. 12–13). This results in a modification of the unsteady pressure and force amplitudes in time. The peak amplitudes of the aerodynamic force coefficient increase between $t/t_{\mathrm{stator}}$ = 0.5–1.5 and $t/t_{\mathrm{stator}}$ = 3.5–4.5, for instance [Figs. 5(*c*) and 5(*d*)]. The time between corresponds to three stator blade passings and nearly to the passing of 2 IGV's. This means that the increase of the resulting amplitudes of the aerodynamic blade force is due to the adding influence of the IGV wakes and the stator potential effects at the considered two periods of time.

**B Rotor 3.** The unsteady pressures and consequently the force on the rotor blades of the third stage are dominated by the passing of the up- and downstream stator blades with identical blade numbers [Figs. 5(*e*) and 5(*f*)]. Nevertheless also for this blade row of a middle compressor stage a modulation of the amplitudes and shape for the subsequent passing stator blades appears. This is caused by the influence of the IGV wakes. The IGV influence was observed to be comparatively small in the first stage. However, the IGV wakes travel through the first and second stage of the compressor without reducing their amplitudes significantly. This is best visible in the frequency spectra of the force coefficients, discussed in Sec. 6.

The time-mean value of the force coefficient of rotor 3 is comparable to that of rotor 1 for both considered operating points (Table 1). The maximum fluctuations of the aerodynamic force coefficient of rotor 3 are in the same order of magnitude than for rotor 1 ($\xi$=1.00: $\pm$15%, $\xi$=0.85: $\pm$25%).

## 6 Frequency Contents of the Aerodynamic Blade Forces

**A Design Point.** In the following the frequency contents of the aerodynamic blade forces will be discussed. A consideration of

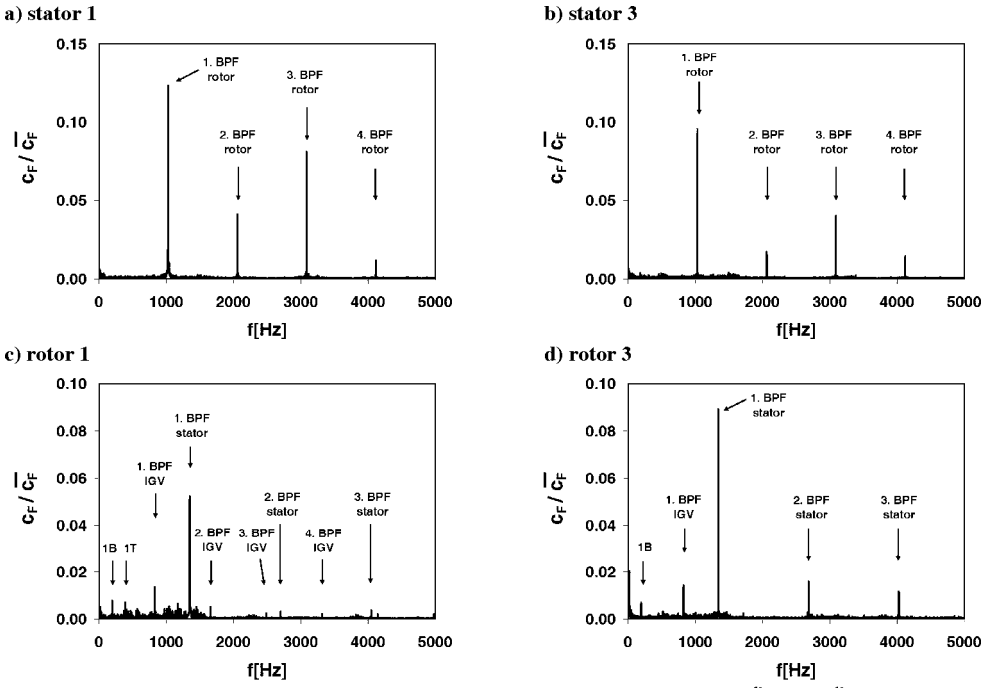


**Fig. 6 Frequency spectra of force coefficient, design point ($\xi$=1.00, $\zeta$=1.0)**

the periodic portions of the force is reasonable for an estimation of the excited blade vibrations and a comparison to the natural frequencies of the blades. In the frequency spectrum different periodic influences can clearly be separated from each other. The frequency spectra of the force coefficient for the different blade rows are shown in Figs. 6(*a*)–6(*d*) for the design point. The force coefficient is related to its mean value in each case.

In accordance to the previous findings the rotor blade passing frequency (BPF) and its higher harmonics dominates the frequency distribution of stator 1 [Fig. 6(*a*)]. (The 1. BPF is the product of the rotor speed and the number of the moving blades of a blade row.) The highest amplitude occurs for the 1. BPF (12%). The periodic parts for the 3. BPF are of stronger influence than that at the 2. BPF. This is due to the fact that three more or less distinct peaks appear during the passing period of the rotor blades [Fig. 3(*a*)]. Higher frequency components up to the 6. BPF can be observed with small amplitudes. The higher harmonics of the BPF, observed in the frequency spectrum, mainly appear due to the superimposed influence of the wake and potential effects of several rotor blade rows on the unsteady profile pressure of stator 1. Other discrete frequency components, which are not related to the rotor blade passing, do not appear.

The distribution of the amplitudes in the $c_F$-spectrum of stator 1 is comparable to that in the spectra of the unsteady pressure (Part I [1], Fig. 6). This is also the case for the other blade rows and operating points.

For stator 3 a comparable distribution of the different blade passing frequencies can be observed as for stator 1, whereby the amplitudes of the periodic influences are lower [Fig. 6(*b*)].

In the frequency spectrum of rotor 1 the blade passing frequencies of the IGV and the stator blade row, which move relative to the considered rotor blade row, can be observed [Fig. 6(*c*)]. The 1. BPF of the downstream stator blades, which appears due to the potential effect of these blades, dominates clearly. The fluctuation amplitudes due to the IGV wakes are only 25% of that of the stator blades potential effect. The influence of higher harmonics of the IGV and stator BPF's is negligible. The amplitudes of the natural frequencies of the blades, realized with the pressure transducers, are clearly below those of the BPF's of IGV and stator. The first bending mode (1B) appears at 200 Hz and the first torsion mode (1T) at 440 Hz. This behavior, observed for the force coefficient, is according to the results obtained for the unsteady pressure distributions [1]. The fluctuation amplitudes for the 1. BPF are clearly lower than those on the stator blades. This corresponds to the ensemble-averaged results discussed above.

The frequency spectrum of the force coefficient of rotor 3 is shown in Fig. 6(*d*). The amplitudes of the 1. BPF are clearly higher than for rotor 1. This can not be concluded from the ensemble-averaged results in Fig. 5. The differences in the periodic parts in the signals may appear due to the fact that for rotor 1 the noise level in the frequency range below 1.5 kHz is higher than for the other blade rows. In contrast to rotor 1 higher BPF's have a noticeable influence for rotor 3.

The IGV influence is clearly visible in the frequency spectrum of rotor 3. This clearly shows that the wake patterns travel through several blade rows in a multistage machine. The fluctuation amplitude for the 1. BPF of the IGV is about 15% of that for the 1. BPF of the stator blades. However, the periodic influence due to the IGV is nearly the same on rotor 1 and 3 for the design point. In both cases the fluctuations of the force coefficient caused by the IGV wakes is about 1.5% of the mean force.

**B Operating Point Near the Stability Limit.** Figures 7(*a*)–7(*d*) shows the frequency spectra of the force coefficients for an operating point near stability limit ($\xi$=0.85).

For stator 1 and stator 3 a clear increase of the amplitudes of the 1. BPF compared to the design point can be seen [Figs. 7(*a*) and 7(*b*)]. This is also visible in the ensemble-averaged results in Figs. 3–5. For both blade rows an increase of the amplitudes for $\xi$=0.85 was observed there, while the shape of the time-resolved force coefficient becomes more wavelike. Higher BPF's are of low influence for $\xi$=0.85 [Figs. 7(*a*) and 7(*b*)].

For rotors 1 and 3 the differences to the design point are comparatively small [Figs. 7(*c*) and 7(*d*)]. For rotor 1 only a slight increase is observed for the 1. BPF of the stator, while the influence of the IGV is clearly stronger than for design point. Now the IGV wake influence is 55% of the stator potential effect. The time-resolved interaction of these superimposed influences deter-

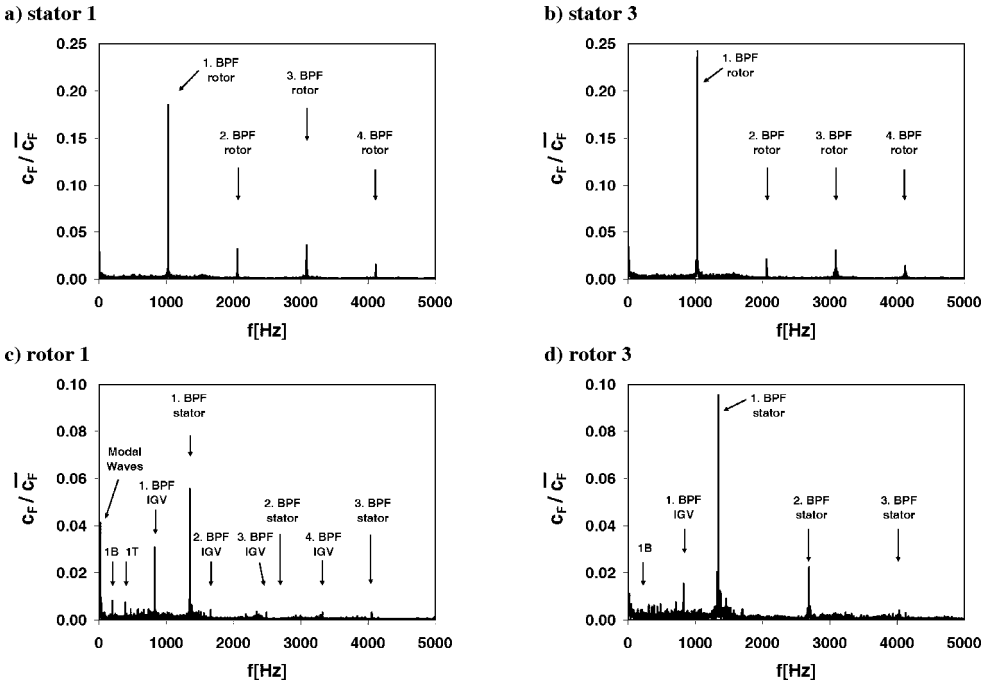


**Fig. 7 Frequency spectra of force coefficient, operating point near stability limit ($\xi$=0.85, $\zeta$=1.0)**

mines the amplitudes of the aerodynamic force coefficient. For the ensemble-averaged results an increase of the amplitudes of $c_F$ is observed [Figs. 5(*c*) and 5(*d*)].

An additional effect influencing the excited blade forces are modal waves, which appear for stable operating points near the stability limit of the compressor [Fig. 7(*c*), $f=22$ Hz]. Modal waves are a long-scale wavelike variation of the flow properties which can be directly responsible for rotating stall inception (Mailach [16]). The fluctuations of $c_F$ due to the modal waves are in the same order of magnitude as for the wake and potential effects. Due to the modal waves the fluctuations of $c_F$ due to the wakes and potential effects are increased or decreased in time. This depends on the fact, if the considered blade is located in a velocity minimum or maximum of the rotating modal waves at a given point of time. In the ensemble-averaged results the influence of the modal waves is averaged, since this disturbance is not synchronous with the rotor turning.

The spectrum of rotor 3 shows a comparatively small increase of both the 1. and 3. BPF's of the stator, while the influence of the IGV is about the same as for the design point [Fig. 7(*d*)]. This is in accordance to the ensemble-averaged results [Figs. 5(*e*) and 5(*f*)], which show an increase of the amplitudes for each blade passing, while the stator blade to blade amplitude are modulated due to the influence of the IGV wakes.

## 7 Conclusions

This two-part paper provides a detailed insight into the complex physics of blade row interactions in multistage turbomachinery. In Part I of the paper the unsteady profile pressure distributions of the blades of the four-stage low-speed research compressor of Dresden are presented. In Part II the unsteady aerodynamic blade forces are determined from the experimental data.

The unsteady aerodynamic blade forces are calculated for the rotor and stator blade rows of the first and third stages of the compressor. The design point and an operating point near the stability limit are discussed in detail. Time traces and frequency contents of the aerodynamic blade force are considered.

The wakes and potential effects of the surrounding blade rows are responsible for fluctuations of the unsteady profile pressures and consequently for unsteady changes of the aerodynamic blade forces. The amplitude and the time-resolved development of the blade force are determined by the superposition of wake and potential influences from up- and downstream. Depending on the blade row and the operating point the amplitudes of the unsteady forces are between 15% and 35% of the mean values.

In all cases the first blade passing frequencies of the up- and downstream blade rows dominate the spectra of the unsteady force of the considered blades. It is observed that wake and potential influences travel through several blade rows of the multistage machine and consequently influences the unsteady blade excitation. Higher harmonics of the first blade passing frequency mainly appear due to the superimposed influences of several upstream and downstream blade rows with identical blade numbers. The amplitudes of the harmonics of the blade passing frequencies, appearing due to the wake and potential influences, do not only depend on the intensity of the wake and potential influence itself, but on the interaction of them.

## Acknowledgments

The work reported in this paper was performed within the project: ''Unsteady Forces and Boundary Layer Behavior on the Blades of a Low-Speed Axial Compressor'' which is part of the joint project: ''Periodical Unsteady Flow in Turbomachines'' funded by the DFG (German Research Society). Information on this project can be found at http://www.turboflow.tu-berlin.de. The permission for publication is gratefully acknowledged.

## Nomenclature

$\langle\ \rangle$ = ensemble-averaged value
$\overline{\ }$ = mean value
$A$ = blade surface [m$^2$]
$c_F$ = aerodynamic force coefficient
$c_{M,cg}$ = moment coefficient, related to center of gravity
$f$ = frequency [Hz]
$F$ = aerodynamic force [N]
$h$ = blade height [m]
$l$ = chord length [m]
$M$ = moment [Nm]
$p$ = pressure [Pa]

$s$ = position along profile contour [m]
$t$ = time [s]
$v$ = velocity in absolute or relative frame of reference [m/s]
$v_\infty$ = vectorial average of the velocity of incoming and outgoing flow of a blade row [m/s]
$x$ = chordwise position [m]
$y$ = position perpendicular to chord [m]
$\alpha$ = angle between y-direction and the tangent at the profile contour [deg]
$\gamma$ = angle between resulting force and normal direction (Fig. 1) [deg]
$\zeta$ = reduced speed/reduced design speed
$\xi$ = reduced mass flow/reduced design mass flow
$\rho$ = density [kg/m$^3$]

**Subscripts**

$x$ = component in blade chord direction
$y$ = component perpendicular to the blade chord

**Abbreviations**

BPF = blade passing frequency
cg = center of gravity
cl = center of lift
LSRC = low-speed research compressor
IGV = inlet guide vane
PS = pressure side
SS = suction side

## References


[1] Mailach, R., and Vogeler, K., 2004, ''Rotor-Stator Interactions in a Four-Stage Low-Speed Axial Compressor, Part I: Unsteady Profile Pressures and the Effect of Clocking,'' ASME J. Turbomach., **126**, pp. 506–517.
[2] Kemp, N. H., and Sears, W. R., 1955, ''The Unsteady Forces Due to Viscous Wakes in Turbomachines,'' J. Aeronaut. Sci., **22**(7), pp. 478–483.
[3] Meyer, R. X., 1958, ''The Effect of Wakes on the Transient Pressure and Velocity Distributions in Turbomachines,'' Trans. ASME, **80**, pp. 1544–1552.
[4] Lefcort, M. D., 1965, ''An Investigation Into Unsteady Blade Forces in Turbomachines,'' ASME J. Eng. Power, **87**, pp. 345–354.
[5] Grollius, H.-W., 1981, ''Experimentelle Untersuchung von Rotor-Nachlaufdellen und deren Auswirkungen auf die dynamische Belastung axialer Verdichter- und Turbinen-gitter,'' PhD thesis, RWTH Aachen, Germany.
[6] Manwaring, S. R., and Fleeter, S., 1991, ''Forcing Function Effects on Rotor Periodic Aerodynamic Response,'' ASME J. Turbomach., **113**, pp. 312–319.
[7] Durali, M., and Kerrebrock, J. L., 1998, ''Stator Performance and Unsteady Loading in Transonic Compressor Stages,'' ASME J. Turbomach., **120**, pp. 224–232.
[8] Denos, R., Arts, T., Paniagua, G., Michelassi, V., and Martelli, F., 2001, ''Investigation of the Unsteady Rotor Aerodynamics in a Transonic Turbine Stage,'' ASME J. Turbomach., **123**, pp. 81–89.
[9] Korakianitis, T., 1993, ''On the Propagation of Viscous Wakes and Potential Flow in Axial-Turbine Cascades,'' ASME J. Turbomach., **115**, pp. 118–127.
[10] Hsu, S. T., and Wo, A. M., 1998, ''Reduction of Unsteady Blade Loading by Beneficial Use of Vortical and Potential Disturbances in an Axial Compressor With Rotor Clocking,'' ASME J. Turbomach., **120**, pp. 705–713.
[11] Lee, Y., and Feng, J., 2003, ''Potential and Viscous Interactions for a Multi-Blade-Row Compressor,'' ASME GT2003-38560.
[12] Cizmas, P. G. A., and Dorney, D. J., 2000, ''The Influence of Clocking on Unsteady Forces of Compressor and Turbine Blades,'' Int. J. Turbo Jet Eng., **17**(2), pp. 133–142.
[13] Mailach, R., Müller, L., and Vogeler, K., 2003, ''Experimental Investigation of Unsteady Forces on Rotor and Stator Blades of an Axial Compressor,'' *Proceedings of the 5th European Conference on Turbomachinery—Fluid Dynamics and Thermodynamics*, M. Stastny, C. H. Sieverding, and G. Bois, eds., March 18–21, Prague, Czech Republic, pp. 221–233.
[14] Mailach, R., and Vogeler, K., 2004, ''Aerodynamic Blade Row Interaction in an Axial Compressor, Part II: Unsteady Profile Pressure Distribution and Blade Forces,'' ASME J. Turbomach., **126**, pp. 45–51.
[15] Müller, L., 2002, ''Zeitaufgelöste Bestimmung von Schaufelkräften auf Verdichterschaufeln,'' Diploma thesis, TU Dresden, Germany.
[16] Mailach, R., 2001, ''Experimentelle Untersuchung von Strömungsinstabilitäten im Betriebsbereich zwischen Auslegungspunkt und Stabilitätsgrenze eines vierstufigen Niedergeschwindigkeits-Axialverdichters,'' PhD thesis, TU Dresden, ISBN 3-18-341007-9, Fortschritt-Berichte VDI, Reihe 7, Nr. 410, VDI-Verlag, Düsseldorf, Germany.

**Behnam H. Beheshti**[1]
School of Mechanical Engineering,
Sharif University of Technology,
Tehran, Iran

**Joao A. Teixeira**

**Paul C. Ivey**

Turbomachinery, Icing and Gas Turbine
Instrumentation Group,
School of Engineering,
Cranfield University,
United Kingdom

**Kaveh Ghorbanian**
School of Aerospace Engineering,
Sharif University of Technology,
Tehran, Iran

**Bijan Farhanieh**
School of Mechanical Engineering,
Sharif University of Technology,
Tehran, Iran

# Parametric Study of Tip Clearance—Casing Treatment on Performance and Stability of a Transonic Axial Compressor

*The control of tip leakage flow through the clearance gap between the moving and stationary components of rotating machines is still a high-leverage area for improvement of stability and performance of aircraft engines. Losses in the form of flow separation, stall, and reduced rotor work efficiency are results of the tip leakage vortex (TLV) generated by interaction of the main flow and the tip leakage jet induced by the blade pressure difference. The effects are more detrimental in transonic compressors due to the interaction of shock TLV. It has been previously shown that the use of slots and grooves in the casing over tip of the compressor blades, known as casing treatment, can substantially increase the stable flow range and therefore the safety of the system but generally with some efficiency penalties. This paper presents a numerical parametric study of tip clearance coupled with casing treatment for a transonic axial-flow compressor NASA Rotor 37. Compressor characteristics have been compared to the experimental results for smooth casing with a 0.356 mm tip clearance and show fairly good agreement. Casing treatments were found to be an effective means of reducing the negative effects of tip gap flow and vortex, resulting in improved performance and stability. The present work provides guidelines for improvement of steady-state performance of the transonic axial-flow compressors and improvement of the stable operating range of the system.* [DOI: 10.1115/1.1791643]

## Introduction

Rotating machines operate with a tip clearance often larger than aerodynamically desirable. This is basically due to changes of tip clearance gap with altering operating conditions as well as the manufacturing limitations. Tip clearance is known to be detrimental to the pressure rise, flow range, efficiency, and stability of axial compressors. Two features of tip clearance flow are the blockage, a fluid dynamic aspect and the loss which is a thermodynamic effect. For a low-speed compressor, Smith and Cumpsty [1] have shown a 23% drop in pressure rise and a 15% increase in flow coefficient at stall condition with an increase of the tip clearance from 1% to 6% of the blade chord. Wisler [2] reported a 1.5 point drop in peak efficiency when the tip clearance gap was doubled in a low-speed compressor.

Suder and Celestina [3] showed that the interaction of shock and the tip leakage vortex creates a large region of low-speed fluid immediately downstream of the interaction. The blockage can displace the flow throughout the endwall region which causes greater adverse pressure gradients. This can lead to flow separation and stall. Adamczyk et al. [4] studied the effects of tip clearance variation on stability of high speed fans. Results indicated that the fan flow range is strongly controlled by the shock-vortex interaction.

The use of slots and grooves in the shroud over the tip of the blade, known as casing treatment, is reported to substantially increase the stable flow range by improving the flow conditions near the tip and weakening the tip leakage vortex. Various forms of casing treatment have been successfully employed since 1970 [5–9].

In fans and compressors, casing treatments usually comprise circumferentially extending grooves which receive fluid at a fluid extraction site and discharge it into the flowpath where the migrated fluid is better able to advance against an adverse pressure gradient [7,8].

Another type of casing treatment, known as recirculating vaned passage casing treatment, incorporates a passageway to remove flow from the main flow stream at a judicious location downstream of the rotor blade leading edge (downstream of the trailing edge in some designs) and inject it at an appropriate location upstream of the point of removal. In order to return the flow at an increased axial velocity, a set of anti swirl vanes is sited through the passage. Recirculating casing treatments increase the temperature of the flow and degrade efficiency since they recirculate flow several times through the rotor endwall region. Furthermore, they are geometrically complex featuring an annular intake over the rear of the blade and an annular exhaust upstream of the rotor [9,10].

Although previous researches have uncovered many features of casing treatment design, the exact mechanisms are still not fully understood. Regarding the experimental and numerical studies in the literature, the parametric studies of casing treatment are few in number. Crook et al. [11] used a grooved endwall to numerically model NASA rotor 67. The suction of the low total pressure fluid at the rear of the blade and the suppression of the blockage in the core of the leakage vortex were identified as the main effects of the treatments.

Thompson et al. [12,13] investigated the effects of stepped tip gaps and clearance size on the performance of a transonic axial-flow compressor. Stepped tip gaps were found to be an effective means of reducing the effects of tip region blockage, resulting in improved pressure ratio, efficiency, and mass flow. Results indicated that an optimum paired combination of clearance level and stepped tip gap may exist but more research will be required to confirm the supposition.

Yang [14] studied numerically the effects of a self-recirculating

[1]Current address: Visiting Student—Turbomachinery, Icing and Gas Turbine Instrumentation Group, School of Engineering, Cranfield University, UK.

Contributed by the International Gas Turbine Institute (IGTI) of THE AMERICAN SOCIETY OF MECHANICAL ENGINEERS for publication in the ASME JOURNAL OF TURBOMACHINERY. Paper presented at the International Gas Turbine and Aeroengine Congress and Exhibition, Vienna, Austria, June 13–17, 2004, Paper No. 2004-GT-53390. Manuscript received by IGTI, October 1, 2003; final revision, March 1, 2004. IGTI Review Chair: A. J. Strazisar.

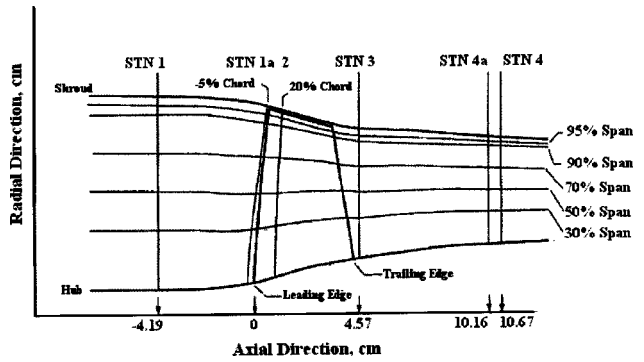


**Fig. 1 NASA Rotor 37 experimental and numerical reporting locations [3].**

**Table 1 Design values for NASA Rotor 37 [15]**

| | |
|---|---|
| Number of rotor blades | 36 |
| Tip solidity | 1.288 |
| Rotor inlet hub-to-tip diameter ratio | 0.7 |
| Rotor blade aspect ratio | 1.19 |
| Rotor tip relative inlet Mach number | 1.48 |
| Rotor hub relative inlet Mach number | 1.13 |
| Design tip clearance (mm) | 0.356 |
| Choking mass flow rate (Kg/s) | 20.93 |
| Design wheel speed (rad/s) | 1800 |
| Tip speed (m/s) | 454.136 |
| Reference temperature (k) | 288.15 |
| Reference pressure ($kN/m^2$) | 101.33 |
| Rotor total pressure ratio | 2.106 |
| Rotor polytropic efficiency | 0.889 |

casing treatment on the stall margin and performance of a transonic axial compressor. Due to a noncontiguous contact with the blade passage in the circumferential direction, an unsteady time-accurate coupling procedure was used to simulate the interaction between the casing treatment and the blade passage. The self-recirculating casing treatment was found to effectively extend the stall margin by weakening tip leakage flow but with a slight decrease of the overall efficiency near the design point. The unsteady simulations showed that the self-recirculating casing treatment can be beneficial to the overall efficiency near the stall operating condition.

This paper presents a numerical study of tip clearance size effects on the overall performance and stability of NASA Rotor 37, a well studied axial transonic compressor. The three-dimensional finite element based finite volume method solver CFX-TASCFLOW (VERSION 2.12) has been employed to numerically solve the steady state compressible Navier-Stokes equations. To validate the simulations, the compressor and efficiency maps, as well as some flow parameters at various locations (Fig. 1), have been compared to the experimental data for a 0.356 mm tip clearance (0.5% span). The validations indicate that the same model can be used for further studies including effects of tip clearance variation coupled with casing treatment.

For a better understanding of tip gap size effects on the flow features, the NASA Rotor 37 blade has also been studied for 1% and 1.5% span clearance heights with and without casing treatment.

The main objectives of this research can be summarized as follows:

1. To determine the effects of tip clearance size on the performance of transonic axial-flow compressors.
2. To identify the effectiveness of casing treatment at different tip gaps.
3. Expand the numerical data available in the open literature for a transonic axial-flow compressor including tip clearance coupled with casing treatment.

## 1 Numerical Details

NASA rotor 37 is an isolated axial flow compressor rotor which has been designed and initially tested at NASA Lewis Research Center. Representative values for this blade are given in Table 1 [15].

In order to deal with the different gap sizes as well as to easily cope with the variation in the axial and radial location of the casing treatment, as done in the previous work by the authors, regarding the effects of small scale casing treatment in axial transonic compressors [16], a structured two block grid is employed. The main block includes the whole blade and 0.156 mm of the tip clearance. The second block placed on the top of the first, includes the rest of the tip clearance and whole of the casing treatment. For the second segment, the mesh is designed so that the pitchwise grid lines have an axisymmetric orientation. The computational grid employed in the simulations is illustrated in Fig. 2. The H-type mesh topology is applied to the entire rotor blade passage. The main grid consists of 121 nodes in the streamwise, 43 nodes in spanwise, and 45 nodes in the blade-to-blade direction. Furthermore, 16 nodes with an approximately constant radial distance of 0.04 mm in the spanwise direction are used to describe the 1% span tip clearance gap. The overall mesh size used in the computation is 234,135 cells for the main passage and 87,120 cells for the casing treatment. The grid clustering was specified so as to ensure that it satisfies the $y^+$ wall coordinate while providing adequate description of local gradients of the flow.

The three-dimensional finite element based finite volume method solver CFX-TASCFLOW (V2.12) has been employed to numerically solve the steady state compressible Navier-Stokes equations. For turbulent compressible flows, where the density fluctuations are important, the direct application of Reynolds averaged Navier Stokes equations leads to the appearance of third-order moments including temperature and density fluctuations as well as velocity fluctuations. Therefore, the Favre-averaged Navier Stokes (FANS) procedure is used resulting in equations very similar to the Reynolds-averaged incompressible case. The mass weighted Favre splitting is applied to all variables except density and pressure which are split conventionally. The detailed FANS procedures are described by Anderson et al. [17] and Cebeci and Smith [18]. Averaged equations are then discretized by evaluating them at the center of each side known as integration point.

All the velocity and surface vector components are Cartesian and fluxes are determined at the integration points. The mass flows at the integration points are linearized using Newton-Raphson linearization.

To speed up the convergence to the correct nonlinear solution a continuity loop is used which is an iterative procedure that updates the mass flow coefficients. To terminate the continuity loop, a 3.0E-5 maximum error has been applied to all the variables. To achieve the near stall condition, a variable solution relaxation parameter is used to provide adequate convergence. All the numerical simulations are started at choked conditions and then marched toward the near stall point with gradual increase of the back pressure (average outlet pressure). The predicted near stall point is judged to be the last stable condition prior to the oscillation in flow parameters and divergence. In the present work a two-equation $\kappa$-$\varepsilon$ turbulence model is utilized. A scaleable wall function formulation enabling the employment of a lower value for $y^+$ is applied.

At solid boundaries, i.e., hub, blade, and casing surfaces, no slip and no heat transfer (adiabatic walls) conditions are imposed. Wall pressure is extrapolated from the pressure values of the interior cells. The hub is divided into rotating and stationary regions to more accurately model an actual compressor. At the inflow boundary, the total pressure ratio, and the flow angle are pre-

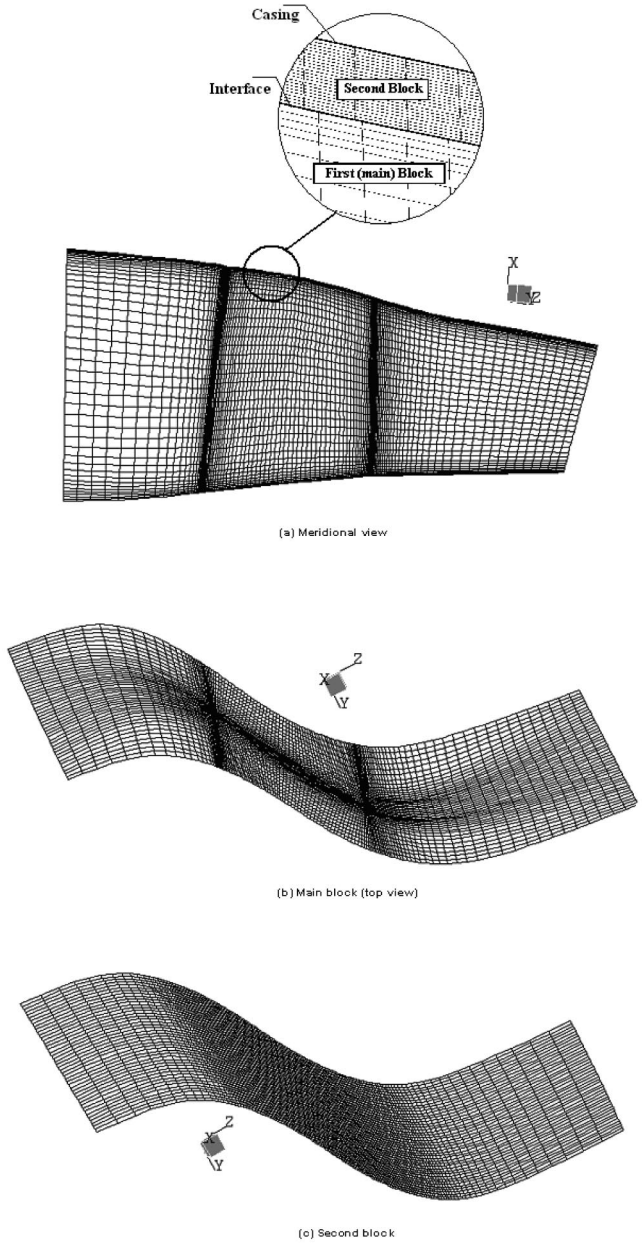


**Fig. 2 Computational grid for NASA Rotor 37. (*a*) Meridional view, (*b*) main block (top view), and (*c*) second block.**

scribed according to experimental data [3]. Total temperature is fixed (288 K) and turbulence intensity and energy-containing eddy length scale are specified as 3% and 0.03 m, respectively. At the outlet, average static pressure integrated over the entire outflow boundary surface is specified. For the periodic boundaries from blade passage to adjacent blade passage, periodic flow conditions are imposed.

## 2 Numerical Results

**2.1 Choked Mass Flow Validation.** To validate the simulations, a number of flow characteristics have been compared to the experimental data for NASA Rotor 37 with smooth casing and a small (0.356 mm≈0.5% span) tip clearance. The measuring locations are shown in Fig. 1.

Figure 3 shows a comparison of computed compressor and efficiency maps with experimental data. The computed and experimental mass flow rates have been normalized using the corresponding choked mass flow. The simulation overestimates the pressure ratio (about 2%) but the predicted efficiency is in good agreement with the experimental data. This discrepancy can be seen in many reports [19,20]. As indicated by Arnone et al. [21], the improvement in the prediction of the rotor total pressure is partially possible by doubling the number of grid points but was found not to be substantial for a mean overestimation of about 3%.

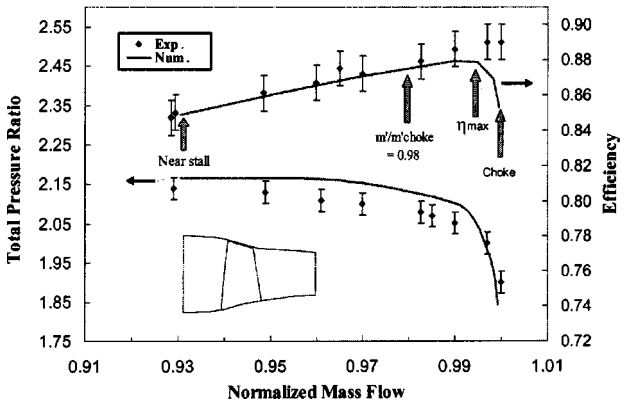


**Fig. 3 Pressure ratio and efficiency maps**

The spanwise distribution of total pressure at the passage exit, station 4, is displayed in Fig. 4 for the near stall condition which corresponds to the near stall conditions. It can be noticed that near the hub the simulation fails to predict the low-pressure region suggested by the measurements. This problem which has also been observed in nearly all of the predictions supplied to ASME, led NASA to make an important find known as hub corner stall which can be discussed as follows: The section of the hub wall upstream of the blade leading edge does not rotate and therefore the presence of a 0.75 mm axial gap in the hub annulus line before the rotor blade, can strongly affect the hub region flow [15].

Figure 5 presents a comparison of the spanwise distribution of total temperature ratio at the exit for 98% of choked mass flow (CMF). Results agree fairly well with the probe data measurements reported by Suder and Celestina [3].

The pitchwise averaged absolute flow angle distribution in spanwise direction for 98% of CMF is illustrated at station 4, in Fig. 6 and predictions are almost within the measuring uncertainties.

In Fig. 7, the relative Mach number for 98% CMF is plotted at

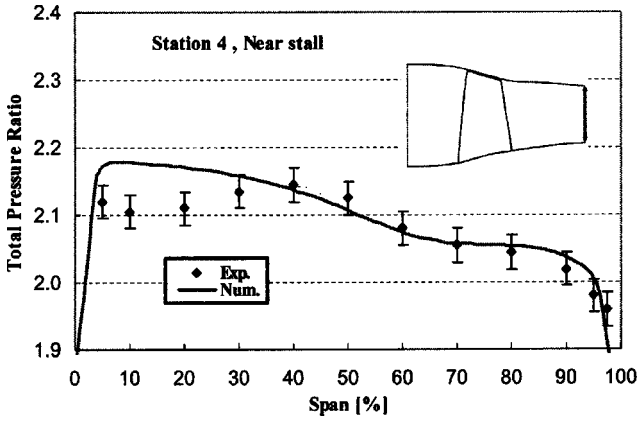


**Fig. 4 Spanwise distribution of total pressure at the passage exit (near stall condition)**

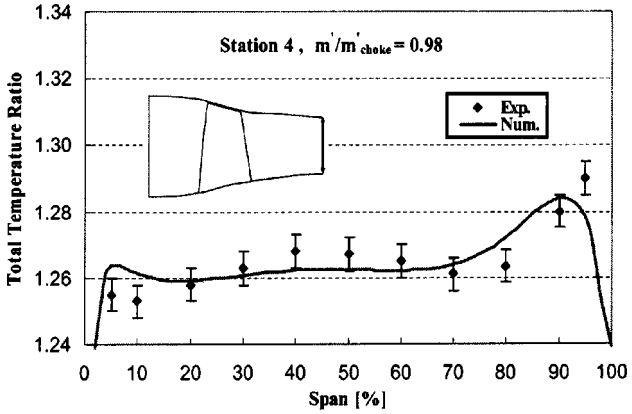


**Fig. 5 Spanwise distribution of total temperature at the passage exit**

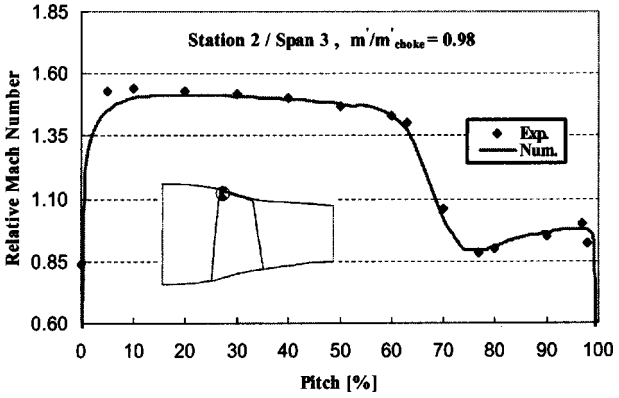


**Fig. 7 Pitchwise distribution of relative Mach number at 20% chord and 90% span**

20% chordwise and 90% spanwise locations (station 2 and span 3). Computations show an excellent prediction of the shock location.

The blade to blade computation of the wake Mach number at station 3 and 90% span is shown in Fig. 8 for 98% CMF. Although the position of the wake is well predicted and is in agreement with the experiments, its profile is slightly deeper in the computational results. This inaccuracy as suggested by Chima [20] can be explained as follows: The rapid mixing of the wake may be a result of unsteady vortex shedding after the blade trailing edge which can not be accurately modeled with the steady simulations and also a highly stretched grid could be used downstream of the blade trailing edge as a possible strategy to improve the predictions.

Finally, the interblade relative Mach number at 95% span and peak efficiency is compared with measured contours in Fig. 9. Agreement between calculation and experiments is good and the simulation can capture the details of shock wave precisely.

On the whole, the simulations for NASA Rotor 37 with a smooth casing and design tip clearance, shows very good agreement with the measurements and can predict the overall shape and quantity of flow characteristics reasonably well. This indicates that the same model can be used for further studies including effects of tip clearance with and without casing treatment. More validation results will be reported in the authors' future paper.

**2.2 Effects of Tip Clearance Size.** To predict the effects of clearance height on rotor performance and endwall flow structure, the same series of simulations are executed for a medium clearance of 0.775 mm (1% span) and a large clearance of 1.1 mm (1.5% span). To keep the NASA Rotor 37 blade design parameters unchanged, the compressor tip clearance is enlarged by increasing the shroud inner radius.

As shown in Fig. 10, the model with the small gap size leads to the highest pressure ratio. Efficiency also tends to decrease with increased clearance. The effect of tip clearance on operating range can be observed and the increased gap has detrimental effects on the operating margin.

The negative effects of tip clearance on pressure rise capability, stability, and efficiency are the results of two aspects of the tip clearance flow; blockage, which is a fluid dynamic effect, and loss, which is a thermodynamic effect.

In Fig. 11, the compressor peak efficiency and maximum pressure ratio are plotted versus relative tip clearance. The influence of different clearances is evident.

To study the compressor stability the stall margin (SM) is defined as follows [22]:

$$\mathrm{SM}=\left(\frac{\pi_{t-t,s}\times m_d'}{\pi_{t-t,d}\times m_s'}-1\right)\times 100$$

As shown in Fig. 12 when the clearance decreases the stall margin expands steeply.

To clarify the influence of tip gap size on the compressor operating range, Fig. 13 presents the flow range at different clearances. Increasing the clearance raises the choked mass flow despite the increased flow blockage. This is due to the enlarged shroud inner radius used to present the tip clearance increase. Whereas the choking line shows only slight changes, the influence at stall conditions is more remarkable.

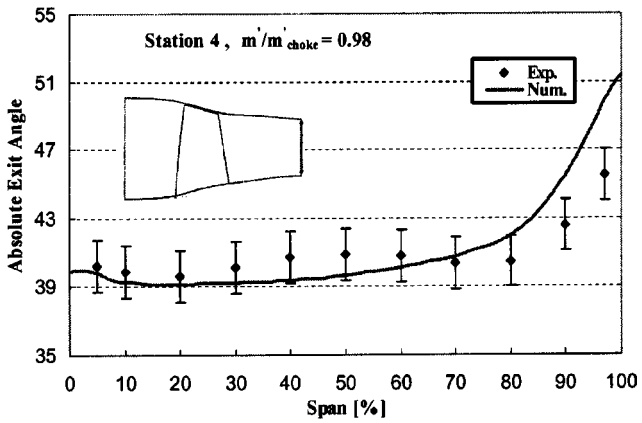


**Fig. 6 Spanwise distribution of exit angle**

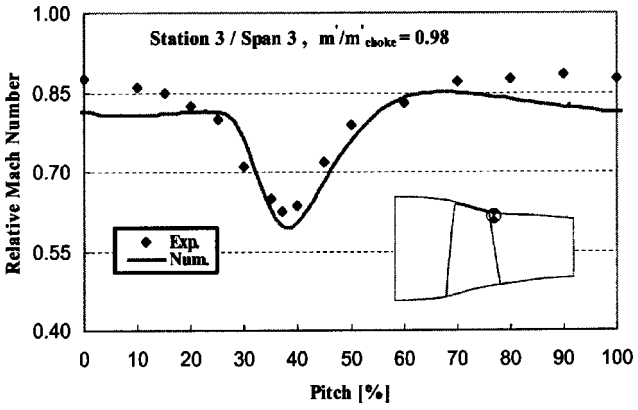


**Fig. 8 Pitchwise distribution of relative Mach number after blade trailing edge and 90% span**

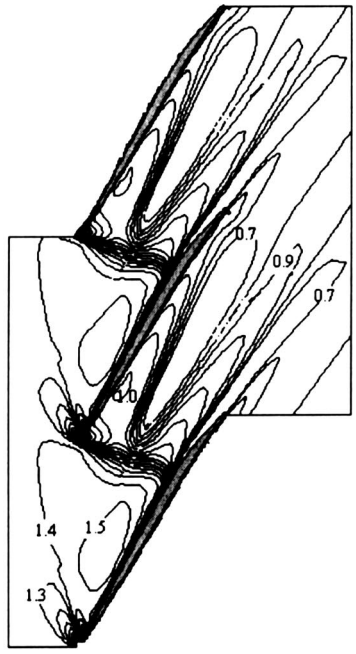


(a) Computations

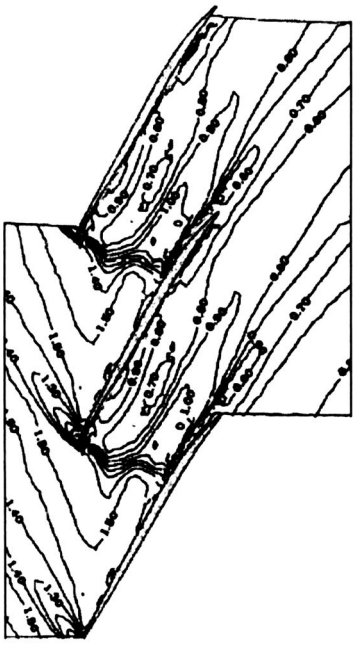

(b) Experiments [23]

**Fig. 9 Blade relative Mach number at 95% span and peak efficiency. (*a*) Computations and (*b*) experiments [23].**

In order to understand the physics that underpin the performance variations shown in Figs. 10–13, the results should be compared under the same reference state. In this paper, this is ensured by comparing the flows at the respective peak efficiency.

For the case of large tip gap as shown in Fig. 14(*c*), an extensive low-speed region is observed immediately downstream of where the shock and tip leakage vortex (TLV) interact. The pockets of low-speed fluid create blockage of flowfield area and deterioration of compressor performance. The low-speed region displaces the main flow and creates higher adverse pressure gradients which can lead to separation and stall. For the case with medium tip gap, Fig. 14(*b*), the flowfield in the rotor appears to be more stable and as seen in Fig. 14(*a*) for small tip gap no recirculation area associated with a reduction in speed occurs in the blade passage.

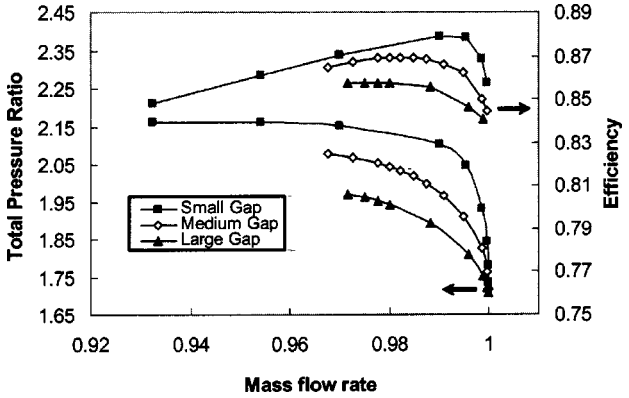


**Fig. 10 Effects of tip clearance size on compressor total pressure ratio and efficiency**

In addition, the strong interaction of shock-vortex at larger clearances creates curvature in the shock and therefore raises shock-induced growth of TLV.

The structure of TLV is influenced by the gap height. Figure 15(*a*) through Fig. 15(*c*) show the contour plots of the total pressure loss coefficient ($\omega$) at 25% chord. The maximum values cor-

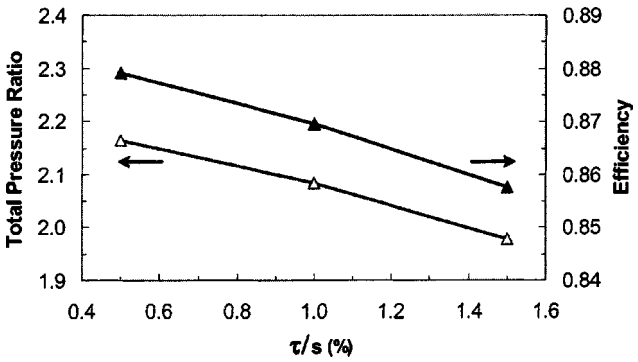


**Fig. 11 Effects of tip clearance size on compressor peak efficiency and total pressure ratio**

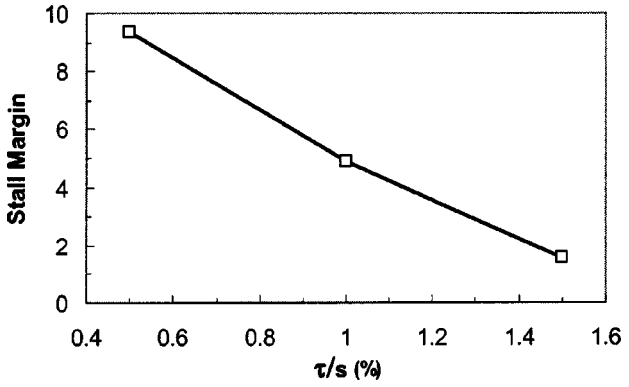


**Fig. 12 Effects of tip clearance size on compressor stall margin**

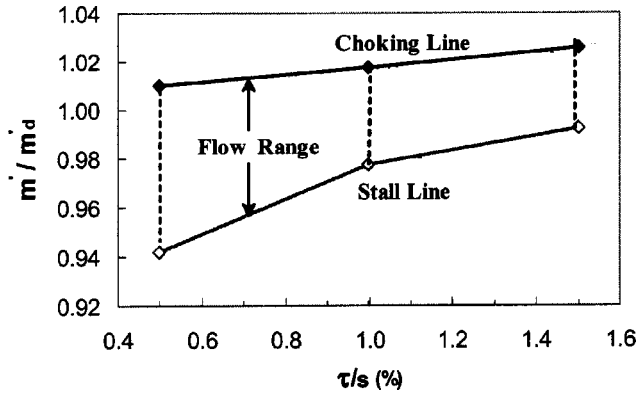


**Fig. 13 Effects of tip clearance size on compressor flow range**

respond to effects of the leakage vortex and as seen for small gap the vortex is less powerful, and less expanded and therefore induces less detrimental effects.

**2.3 Effects of Casing Treatment.** Circumferentially extended casing treatments, comprising groove(s) substantially per-

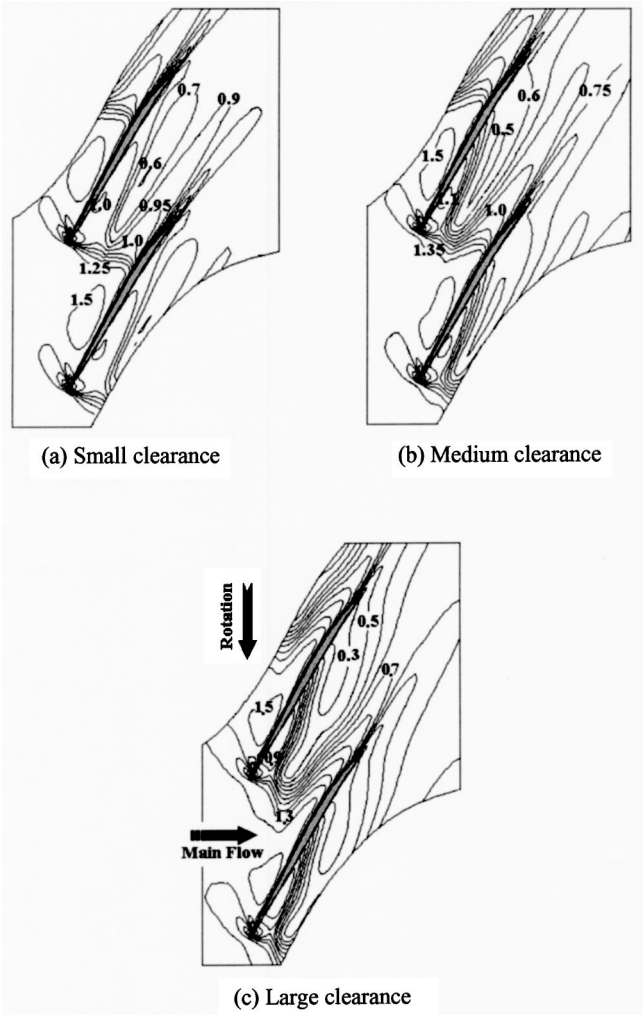


**Fig. 14 Relative Mach number at 95% span and peak efficiency. (*a*) Small clearance, (*b*) medium clearance, and (*c*) large clearance.**

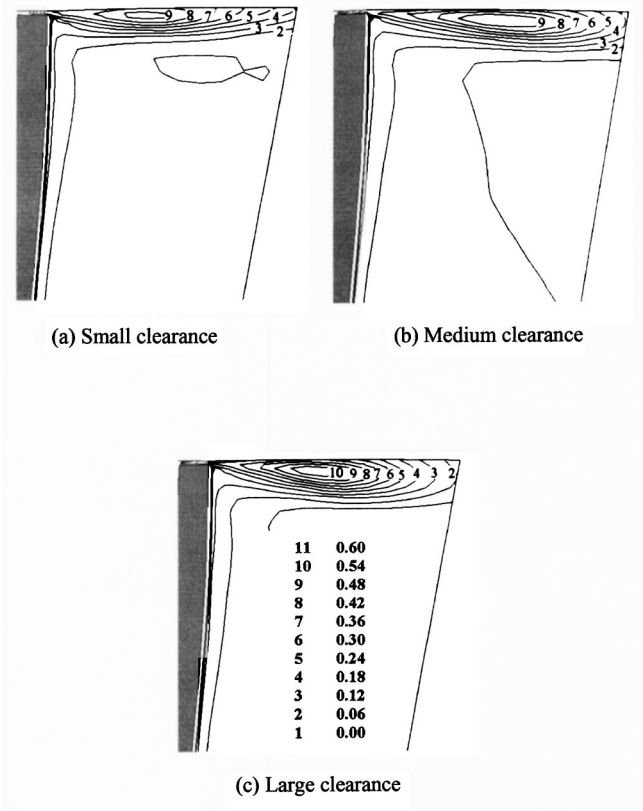


**Fig. 15 Contours of total pressure loss coefficient ($\omega$) at 25% chord and peak efficiency. (*a*) Small clearance, (*b*) medium clearance, and (*c*) large clearance.**

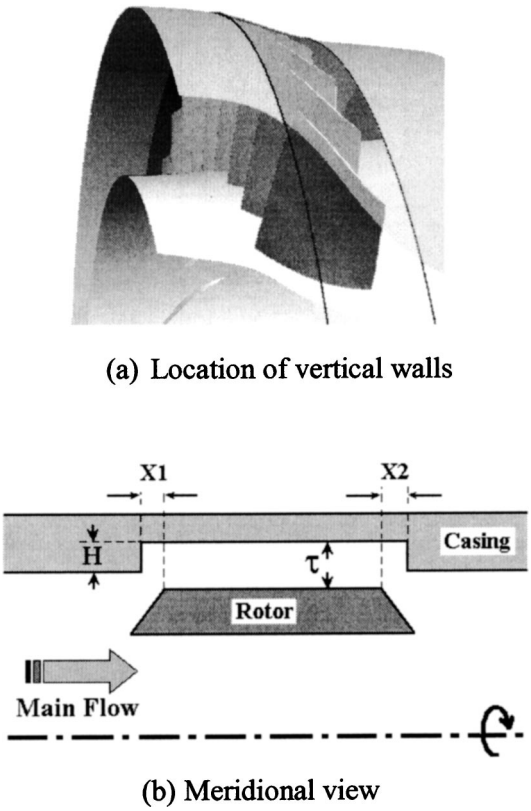


**Fig. 16 Casing treatment configuration. (*a*) Location of vertical walls and (*b*) meridional view.**

**Table 2 Geometric values for casing treatment**

| | $X_1$ (mm) | $X_2$ (mm) | $H$ (mm) | Tip clearance Size (mm) |
|---|---|---|---|---|
| Medium gap | 7.98 | 9.1 | 0.5 | 0.775 (1% span) |
| Large gap | 7.98 | 9.1 | 0.88 | 1.1 (1.5% span) |

pendicular to the main stream flow, are a well-known way to help designers enhance the compressor stability. The grooves can provide a means for fluid to exit the flowpath where the blade loading is severe and the local pressure is high, migrate circumferentially, and re-enter the flowpath at a location where the pressure is more moderate. The flow relocation is better able to contend with the adverse pressure gradient. This leads to stability improvement since the flow relocation helps to relieve the locally severe blade loading [7].

In addition to the effects mentioned, casing treatments degrade the compressor efficiency. Recirculating grooves recirculate flow several times through the tip region. This can raise the fluid temperature and degrade the efficiency. In circumferentially extended grooves, although no flow recirculation exists, the presence of sharp edges in the cavity region induces corner separation and

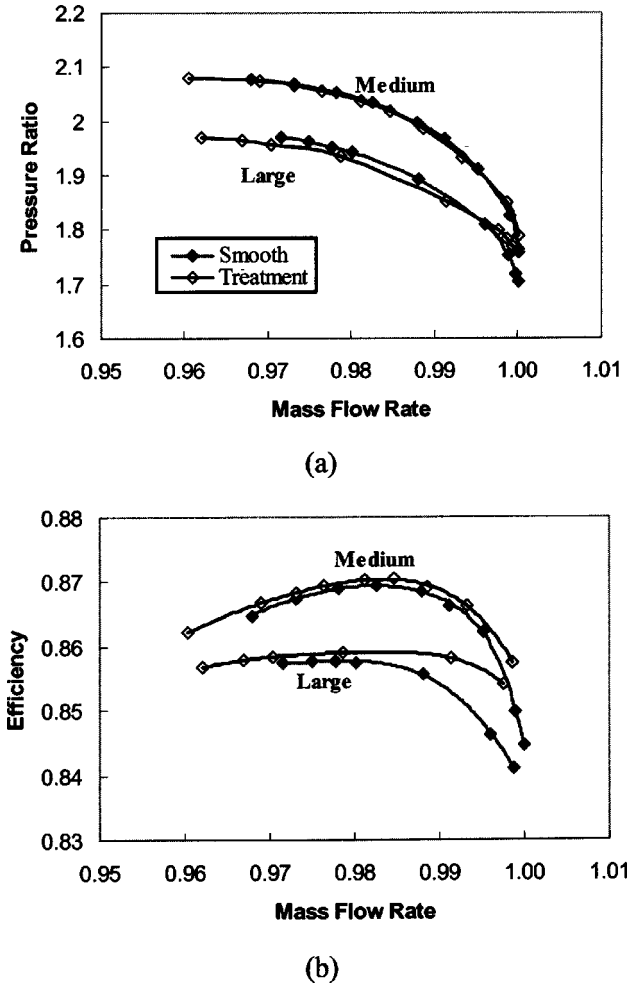


**Fig. 17 Effects of casing treatment on compressor efficiency map. (*a*) Compressor pressure ratio and (*b*) compressor efficiency.**

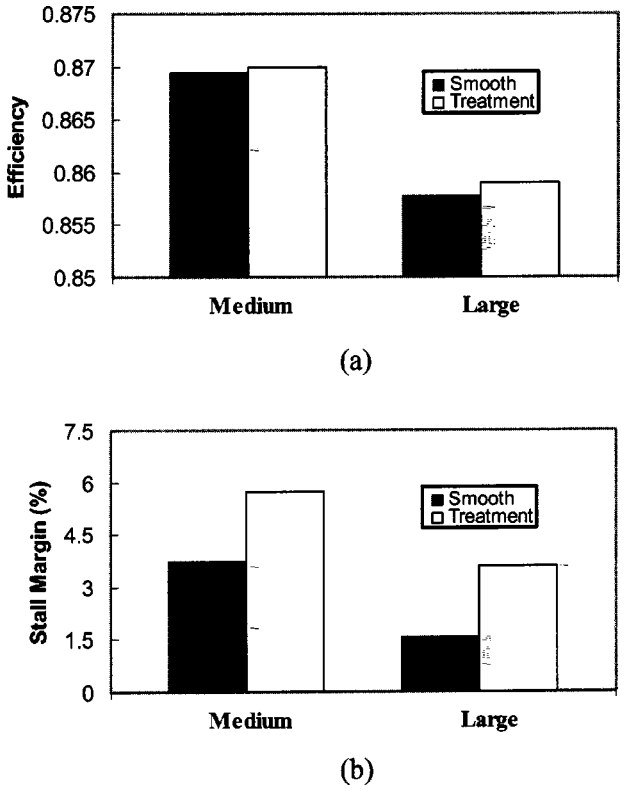


**Fig. 18 Effects of casing treatment on compressor performance and stability. (*a*) Compressor efficiency and (*b*) compressor stability.**

generates increased losses [10]. To investigate case dependency, an identical groove configuration has been applied to a medium (1% span) and a large tip gap (1.5% span).

The findings are then compared to the corresponding cases without treatment. Figure 16(*a*) shows the configuration of the groove in the compressor passage and Fig. 16(*b*) depicts the position of the casing treatment with respect to one of the compressor blade rotors. Table 2 gives the geometric values for the grooves.

The effects of casing treatment on rotor performance and efficiency are shown in Fig. 17 for both clearance sizes. The predicted characteristics are also provided for both cases with casing treatment and with untreated smooth wall. As seen in Fig. 17(*a*), the addition of casing treatment does not degrade significantly the total pressure ratio of the compressor.

Figure 17(*b*) shows the overall effects of casing treatment on the efficiency map. It can be observed that the application of the casing treatment is beneficial to the efficiency of the compressor. Increasing the casing diameter for the area surrounding the rotor blade while the clearance size is constant, can potentially reduce tip leakage flow through the endwall zone and improve the compressor efficiency. This can be due to a more complex path for the rotor upstream flow to navigate its way inside the gap region. The extension of the stall margin is also noteworthy.

To explore the influence of tip gap size on the effectiveness of the casing treatment, the efficiency and stall margin are shown in Figs. 18(*a*) and, 18(*b*). It is seen that for large tip gap the efficiency is improved more effectively. The stall margin extension appears similar for both gap sizes but a more careful comparison indicates that for the large gap the improvement ratio is 2.2 against 1.5 for the medium one. Thus, results imply that for the large gap the casing treatment can play a more significant role in compressor performance and stability improvement. This is basi-

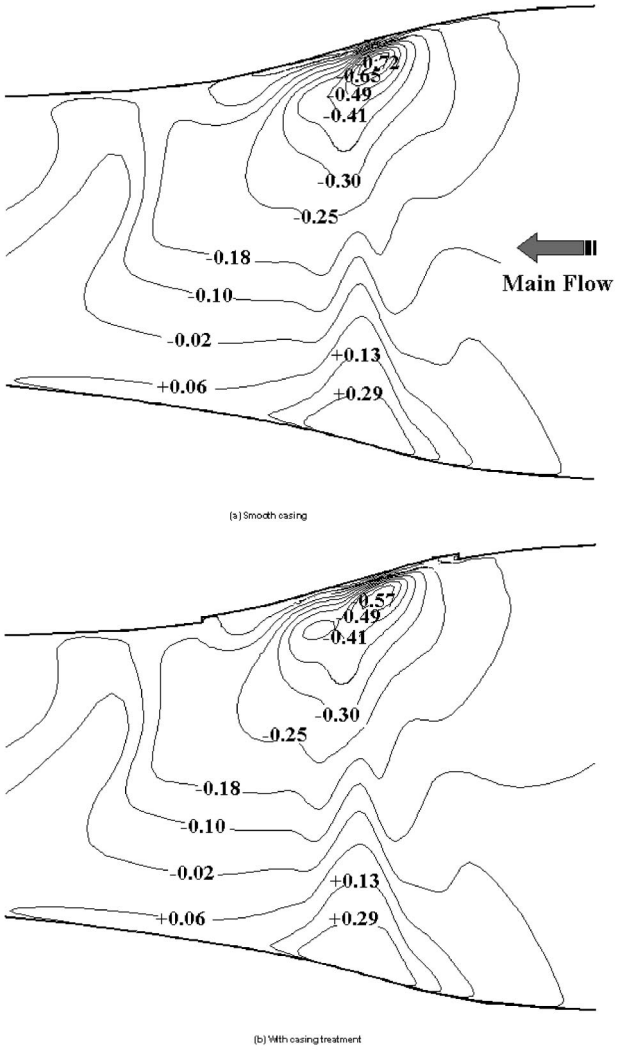


**Fig. 19 Meridional view of normalized axial velocity at peak efficiency for large tip gap. (*a*) Smooth casing and (*b*) with casing treatment.**

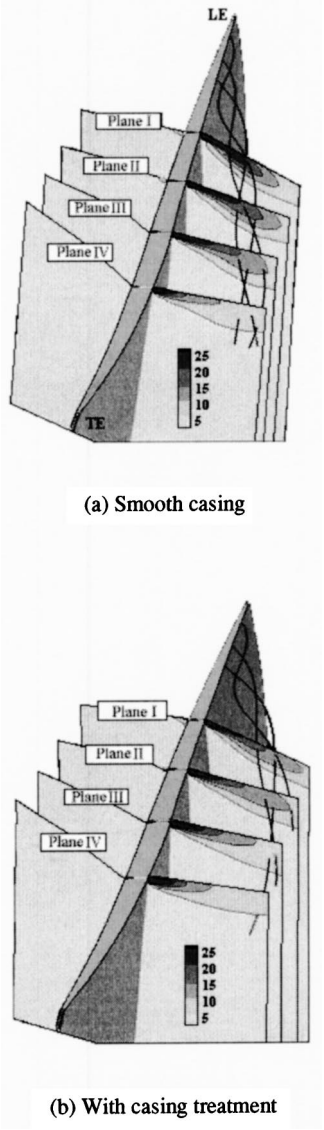


**Fig. 20 Tip leakage vortex normalized vorticity ($\xi_n$) at 34, 45, 60, and 75% chord for large tip gap. (*a*) Smooth casing and (*b*) with casing treatments.**

cally due to the better capability of circumferential grooves in controlling TLV which is more substantial for a large clearance.

In a similar way to what has been done for the untreated smooth casing with different clearances, the flow features are compared under the same reference state (design point). In Fig. 19(*a*), for the large clearance height, a low-speed region is observed for the case with smooth wall and this is thought to cause blockage of flowfield area and deterioration of compressor performance. For the case with casing treatment, Fig. 19(*b*), the flowfield in the rotor passage appears to be more stable and a much weaker recirculation area associated with a reduction in normalized axial velocity (normalized by the inlet mean axial velocity) occurs in the blade passage. Hence, Fig. 19 can help to illustrate the compressor stability and performance improvement. With the casing treatment, most of the low-energy fluid from the tip leakage flow is sucked into the treated region and thereby energizing the tip low-energy fluid at the aft part of the shock-vortex interaction.

Finally, in order to investigate the effects of casing treatment on TLV, the normal vorticity ($\xi_n$) in four positions (40, 50, 60, and 75% chord) which are nearly perpendicular to the blade surface are shown in Fig. 20 for both with and without treatment at the large tip gap. The normal vorticity of TLV decays in the axial direction for both cases. The plots of normal vorticity are useful in identifying the strength and location of the TLV in both cases. For smooth endwall, the core of TLV is detected as the region with the concentrated normal vorticity. For the treated endwall at 60 and 75% chord planes, strong changes can be observed in the TLV structure and the vortex core corresponds to lower values of vorticity. This implies the reduction of TLV intensity due to effects of the casing treatment. It can be seen that the casing treatment shows more evident degrading effects on TLV strength at the aft part of the passage.

## 3 Concluding Remarks

To understand the physical process associated with tip clearance and casing treatment, a numerical parametric study has been done for a transonic axial-flow compressor. A NASA Rotor 37 is investigated for both treated and untreated endwalls at different tip gap heights (0.5%; small, 1%; medium, and 1.5% span; large). The main conclusions are as follows:

1. Numerical calculations agree fairly well with experimental data.
2. Increasing the tip gap size has detrimental effects on the compressor performance and stability. This is basically due to the generation of an extensive low-speed region immediately downstream of shock-vortex interaction which is more evident for larger tip gap configurations because of formation of a stronger tip leakage vortex.
3. Circumferential casing treatment can be a successful means for reducing the effects of tip region blockage, resulting in noticeable improvement in efficiency and extended stall margin.
4. Endwall treatments are more efficient at large size of tip gap simply due to the better capability of circumferential grooves in controlling TLV which is more significant at a large clearance.

In closing, since the effectiveness of casing grooves is likely case dependent, further research efforts by the authors to determine more efficient configurations are in progress.


## Acknowledgments

The authors gratefully acknowledge the British Council and the Iranian Ministry of Science, Research and Technology for their financial support.


## Nomenclature Symbols

$H$ = casing treatment depth
$X_1, X_2$ = casing treatment axial locations
$m'$ = mass flow rate
$s$ = blade span
$x, y, z$ = Cartesian coordinates
$u, v, w$ = Cartesian velocity components
$y^+$ = nondimensional wall distance $= \Delta y \sqrt{\rho \tau_w}/\mu$
$\Delta y$ = distance from the wall
$\mu$ = dynamic viscosity
$\xi$ = total vorticity magnitude $= |\vec{\xi}| = (\xi_x^2 + \xi_y^2 + \xi_z^2)^{1/2}$
$\vec{\xi}$ = vorticity vector $= (\xi_x, \xi_y, \xi_z)$
$\xi_n$ = normalized vorticity $= |\vec{\xi}|/4\Omega$
$\xi_x$ = vorticity $x$-component $= (\partial w/\partial y - \partial v/\partial z)$
$\xi_y$ = vorticity $y$-component $= (\partial u/\partial z - \partial w/\partial x)$
$\xi_z$ = vorticity $z$-component $= (\partial v/\partial x - \partial u/\partial y)$
$\pi$ = pressure ratio
$\rho$ = density
$\tau$ = tip clearance size
$\tau_w$ = wall shear stress
$\omega$ = total pressure loss coefficient $= \pi_{t,\infty} - \pi_t / \pi_t$
$\Omega$ = blade rotational speed (rad/s)

### Subscripts

$d$ = design computation
$s$ = stall computation
$t$ = total value
$t$-$t$ = total to total
$\infty$ = far upstream

### Acronyms

CMF = choked mass flow
SM = stall margin in percentage
STN = station
TLF = tip leakage flow
TLV = tip leakage vortex

## References


[1] Smith, G. D. J., and Cumpsty, N. A., 1984, "Flow Phenomena in Compressor Casing Treatment," ASME J. Eng. Gas Turbines Power, **106**, pp. 532–541.
[2] Wisler, D. C., 1985, "Loss Reduction in Axial Flow Compressors through Low-Speed Model Testing," ASME J. Turbomach., **107**, pp. 354–363.
[3] Suder, K. L., and Celestina, M. L., 1996, "Experimental and Computational Investigation of the Tip Clearance Flow in a Transonic Axial Compressor Rotor," ASME J. Turbomach., **118**, pp. 218–229.
[4] Adamczyk, J. J., Celestina, M. L., and Greitzer, E. M., 1993, "The Role of Tip Clearance in High-Speed Fan stall," ASME J. Turbomach., **115**, pp. 28–39.
[5] Prince, D. C., Jr., Wisler, D. D. and Hivers, D. E., 1974, "Study of Casing treatment stall Margin Improvement," NASA CR-134552.
[6] Takata, H., and Tsukuda, Y., 1977, "Stall Margin Improvement by Casing Treatment—Its Mechanism and Effectiveness," ASME J. Eng. Power, **99**, pp. 121–133.
[7] Goto, A., and Katsumata, T., 1998, "Turbomachine," United State Patent Application, U.S. Serial No. 5,707,206, 1998.
[8] Barnett, M., Graf, M., Raw, J. A., Sharma, O., and Sprout, W. D., 2003, "Casing Treatment for a Fluid Compressor," United State Patent Application, U.S. Serial No. 6,619,909, 2003.
[9] Koff, C. S., Nikkanen, J. P., and Mazzawy, R. S., 1994, "Rotor Case Treatment," United State Patent Application, U.S. Serial No. 5,308,225, 1994.
[10] Suder, K. L., Hathaway, M. D., Thorp, S. A., Strazisar, A. J., and Bright, M. B., 2001, "Compressor Stability Enhancement Using Discrete Tip Injection," ASME J. Turbomach., **123**, pp. 14–23.
[11] Crook, A. J., Greitzer, E. M., Tan, C. S., and Adamczyk, J. J., 1993, "Numerical Simulation of Compressor Endwall and Casing Treatment Flow Phenomena," ASME J. Turbomach., **115**, pp. 501–511.
[12] Thompson, D. W., King, P. I., and Rabe, D. C., 1998, "Experimental Investigation of Stepped Tip Gap Effects on the Performance of a Transonic Axial-Flow Compressor Rotor," ASME J. Turbomach., **120**, pp. 477–486.
[13] Thompson, D. W., King, P. I., Hah, C., and Rabe, D. C., 1998, "Experimental and Computational Investigation of Stepped Tip Gap Effects on the Flowfield of a Transonic Axial-Flow Compressor Rotor," ASME paper no. 98-GT-90.
[14] Yang, H., 2003, "Unsteady Flow Simulation of a Transonic Compressor Coupled with Casing Treatment," The Eleventh Annual Conference of the CFD Society of Canada, May 2003, Vancouver, Canada.
[15] Dunham, J., 1998, "CFD Validation for Propulsion System Components," AGARD Advisory Report 355, ISBN 92-836-1075-X.
[16] Beheshti, B. H., Teixeira, J. A., Ivey, P. C., Farhanieh, B., and Ghorbanian, K., 2003, "Study of Small Scale Casing Treatment on the Performance of Axial Transonic Compressors," IMechE Conference, London, UK.
[17] Anderson, D. A., Tannehill, J. C., and Pletcher, R. H., 1984, "Computational Fluid Mechanics and Heat Transfer, Computational Methods in Mechanics and Thermal Sciences," Taylor and Francis, Bristol, PA.
[18] Cebeci, T., and Smith, A. M. O., 1974, "Anaylsis of Turbulent Boundary Layers," Academic Press, New York.
[19] Dalbert, P., and Wiss, D. H., 1995, "Numerical Transonic Flow Field Prediction for NASA Compressor Rotor 37," ASME paper no. 95-GT-326.
[20] Chima, R. V., 1996, "Calculation of Tip Clearance Effects in a Transonic Compressor Rotor," ASME paper no. 96-GT-114.
[21] Arnone, A., Carnevale, E., and Marconcini, M., 1997, "Grid Dependency Study for the NASA Rotor 37 Compressor Blade," ASME paper no. 97-GT-384.
[22] Weigl, H. J., Paduano, J. D., Frechette, J. D., Epstein, A. H., Greitzer, E. M., Bright, M. M., and Strazisar, A. J., 1998, "Active Stabilization of Rotating Stall and Surge in a Transonic Single-Stage Axial Compressor," ASME J. Turbomach., **120**, pp. 625–636.
[23] Suder, K. L., 1996, "Blockage Development in a Transonic, Axial Compressor Rotor," ASME paper no. 96-GT-394.

# The Transition Mechanism of Highly Loaded Low-Pressure Turbine Blades

**R. D. Stieger**[1]
**H. P. Hodson**

Whittle Laboratory,
Cambridge University,
Engineering Department,
Madingley Road,
Cambridge CB3 0DY, UK

*A detailed experimental investigation was conducted into the interaction of a convected wake and a separation bubble on the rear suction surface of a highly loaded low-pressure (LP) turbine blade. Boundary layer measurements, made with 2D LDA, revealed a new transition mechanism resulting from this interaction. Prior to the arrival of the wake, the boundary layer profiles in the separation region are inflexional. The perturbation of the separated shear layer caused by the convecting wake causes an inviscid Kelvin-Helmholtz rollup of the shear layer. This results in the breakdown of the laminar shear layer and a rapid wake-induced transition in the separated shear layer.* [DOI: 10.1115/1.1773850]

## Introduction

Historically, turbomachinery blading has been designed using a combination of steady cascade measurements and steady computational tools. These design procedures lead to design rules that limited boundary layer deceleration to avoid laminar separation and the associated loss penalties. Schulte and Hodson [1] showed that the periodic passing of turbulent wakes affected the separation bubble on a modern LP turbine blade and reported a reduction in profile loss due to wake passing for some flow conditions. Schulte and Hodson [2] subsequently explained this by presenting hot film measurements showing that turbulent spots induced by the wake upstream of the separation point prevented the boundary layer from separating. The calmed regions that follow the turbulent spots were also shown to be responsible for suppressing separation due to their full velocity profiles.

Loss reductions are intimately linked to the relative portions of the blade surface covered by laminar, turbulent, calmed, and separated flow. This is true for steady and unsteady flows. As the Reynolds number decreases, the steady flow losses rise due to the increased extent of separation. In the wake passing case, the separation is periodically suppressed by the turbulent and calmed flow. The flows associated with the turbulent and calmed periods produce less entropy than the steady separation and this leads to a reduction of loss in the time-mean. The loss reduction is thus also dependant on the reduced frequency and it is fortuitous that the reduced frequency in LP turbines is typically in the correct range for loss reductions.

Armed with this improved understanding of unsteady transition, the traditional steady flow design rules that limited boundary layer diffusion were challenged. A new generation of blade profiles was designed based on the extensive experimental work of Curtis et al. [3] and Howell et al. [4]. These ''high lift'' LP turbine blade profiles were reported to reduce the number of blades in the LP turbine by 20% (Cobley et al. [5]) thus reducing the cost of ownership by simultaneously reducing weight and manufacturing costs without an efficiency penalty. The pitch to chord ratio and Zweifel lift coefficient of these blades are approximately unity. The advent of ''Ultra High Lift'' blades reported by Haselbach et al. [6] lead to a further reduction in the number of blades of 11%. However, such increases in blade loading were only possible when accompanied by the extensive experimental validation of Brunner et al. [7] and Howell et al. [4,8].

Despite significant reductions in the number of blades, the fundamental transition mechanisms involved in reducing losses are not fully understood. Although the understanding of bypass transition has been greatly enhanced by the DNS calculations of Wu et al. [9] and the models of Johnson [10], the effects of separated boundary layers have not been adequately accounted for. The correlations of D'Ovidio et al. [11,12] have attempted to provide a workable solution but a lack of physical insight into the transition process resulting from the interaction of a convected wake and laminar separation remains a limiting factor.

In order to gain a better understanding of the wake boundary layer interaction a series of boundary layer traverses were performed using 2D LDA in a low-speed bar passing cascade. The results, presented here provide new insight into the wake-induced transition mechanisms found on LP turbine blades with inflexional boundary layer profiles associated with separation bubbles. The boundary layer state is investigated at four representative phases during the wake passing cycle and this identifies the coherent structures in the boundary layer to be rollup vortices embedded in the boundary layer. These vortices are shown to originate from the breakdown of the separated shear layer that is triggered by the passing wake. Finally, the transition mechanism is described schematically and a new picture of wake-induced transition is presented.

## Experimental Details

The measurements reported in this paper were performed on bar passing cascade facility at the Whittle laboratory of Cambridge University. The bar passing cascade, shown in **Fig. 1**, simulates the unsteady wake passing environment of a turbomachine by traversing bars across the inlet flow. No attempt is made to simulate the unsteady potential field of adjacent blade rows. The bars are held between two nylon belts that run on two sets pulleys. The pulley system is driven through a belt drive by a DC motor. The configuration of the bar passing cascade required that the top and bottom walls of the cascade be slotted to permit the passage of wake generator bars. These slots provide two additional passages to the flow and may result in a non-uniform inlet static pressure. In order to maintain inlet periodicity, an additional dummy passage was created on the suction side of the cascade. The throat of this dummy passage was then adjusted so that the periodicity of inlet static pressure was within 2.5% of the inlet dynamic head.

Details of the five-blade cascade of the T106 profile are presented in **Table 1**. Under steady inflow, this profile has a separation bubble over the rear of the suction surface. This is evident in the measured isentropic surface velocity distribution shown in **Fig. 2**.

[1]Current address: Rolls-Royce plc, Derby, UK.

Contributed by the International Gas Turbine Institute and presented at the International Gas Turbine and Aeroengine Congress and Exhibition, Atlanta, GA, June 16–19, 2003. Manuscript received by the IGTI December 2002; final revision March 2003. Paper No. 2003-GT-38304. Review Chair: H. R. Simmons.

  

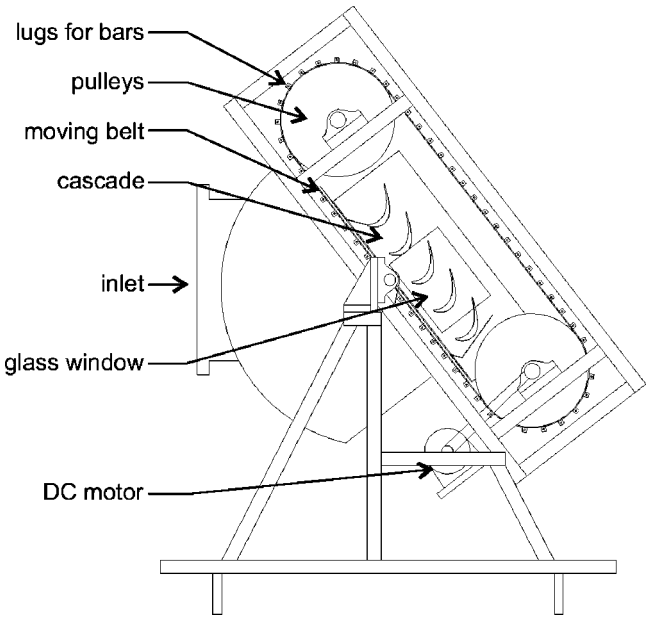


**Fig. 1 Bar passing cascade with T106 profile**

**Table 1 T106 bar passing cascade details**

| | | |
|---|---|---|
| Chord | (mm) | 198 |
| Blade stagger | (deg) | 59.3 |
| Cascade Pitch | (mm) | 158 |
| Span | (mm) | 375 |
| Inlet flow angle | (deg) | 37.7 |
| Design exit flow angle | (deg) | 63.2 |
| Bar diameter | (mm) | 2.05 |
| Axial distance: bars to LE | (mm) | 70 |
| Flow Coefficient ($\phi$) | | 0.83 |

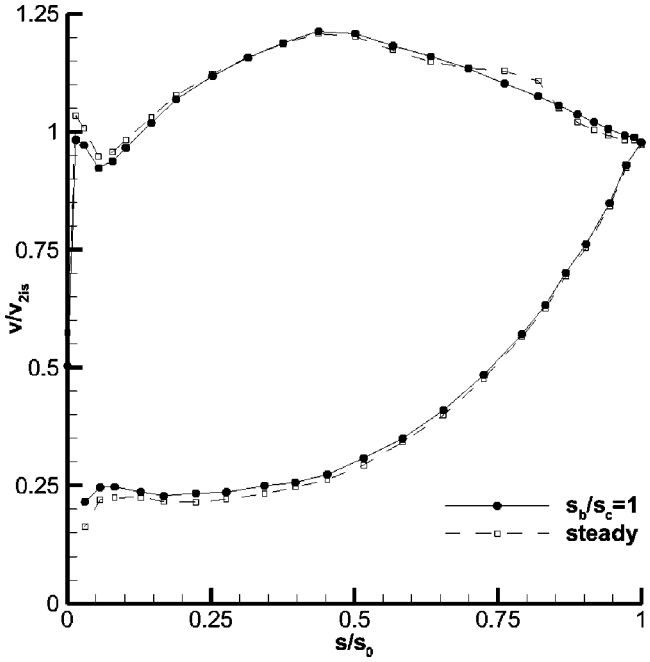


**Fig. 2 Isentropic surface velocity distribution measured on the T106 LP turbine cascade**

The unsteady wake-passing flow conditions were chosen to match those of a repeating stage of the T106 profile. The Reynolds number based on chord and time mean isentropic exit velocity of 12.6 m/s was $\mathrm{Re}=1.6\times10^5$. The flow coefficient was $\phi=0.83$. The bar pitch matched the cascade pitch so that $s_b/s_c=1$ ($f_r=0.68$). The bar diameter of 2.05 mm was chosen to match the loss of a representative turbine blade and the axial gap is representative of that found in LP turbines. The inlet flow angle was set to the design value of $\alpha_1=37.7$ deg.

The unsteady flow field was measured using a commercial two-dimensional LDA system. LDA was selected due to the absence of probe interference and directional ambiguity associated with more traditional thermal anemometry. Light was supplied by a 5W argon-ion laser. The transmitting optics consisted of a Dantec FibreFlow unit incorporating a color separator and Bragg cell. A two-dimensional probe was used with a 1.95 beam expender and a lens of 500 mm focal length. The optical configuration resulted in a measuring volume of $0.077\times0.076\times1.0116$ mm for the 514.5 nm beam and $0.073\times0.072\times0.963$ mm for the 488 nm beam. A backward scatter configuration was used and the receiving optics included a Dantec 55X35 color separator and two Dantec 9057X0081 photo-multiplier tubes. Dantec BSA signal processors were used to process the photo-multiplier outputs.

Seeding of the flow was by means of smoke generated by a Dantec SPT smoke generator using Shell Ondina oil. The smoke was injected into the constant area section of the wind tunnel through the trailing edge of a streamlined injector tube. The point of injection was approximately 3 m upstream of the test section and upstream of the honeycomb, contraction and final screens of the wind tunnel. The effect of the injector on the flow was thus immaterial. Phase Doppler anemometry measurements showed the characteristic size of the smoke particles used to be 1.5 $\mu$m. At each traverse point a maximum of $1\times10^5$ samples were collected in up to 60 seconds. This corresponded to a maximum of approximately 2500 wake passing cycles. Validated data rates typically varied from 1.5 to 5 kHz. Two component measurements were made with both processors acting as coincidence masters. Final coincidence filtering was performed by software to reject any samples not detected by both photo-multipliers within a 5 $\mu$s window corresponding to twice the sample record length.

Ensemble averaging of the LDA data was performed relative to a once per bar passing trigger. The wake passing period was divided into 128 time bins. Each coincident measurement was then assigned to a time bin according to its time relative to the trigger signal. The statistics of each time bin were then calculated with a residence time weighting to remove velocity bias as suggested by George [13].

A series of boundary layer traverses were performed on the suction surface of the central blade of the T106 LP turbine cascade. Each traverse was performed perpendicular to the local blade surface. The blade was painted matt black to minimize reflections from the intersecting laser beams except for a strip at midspan, which was left unpainted to avoid contamination of the static pressure tappings. For this reason the traverses were performed at 45% of the cascade span. Positioning of the measuring volume in the streamwise direction was performed manually. The location of the surface was then found by traversing the LDA probe towards the blade surface in steps of 0.05 mm while monitoring the photo-multiplier outputs. A peak in the photo-multiplier output indicates maximum light reflection, which occurs when the measuring volume intersects the wall. The wall was located with both the flow and rotating bars switched on. The first traverse point was 0.1 mm from the blade surface and the first 16 points were exponentially distributed within the boundary layer. The final 4 of the 20 traverse points were evenly spaced from the boundary layer edge to a point 16 mm from the blade surface. Twenty-five measurement locations were used in the streamwise direction. These were selected based on previous measurements.

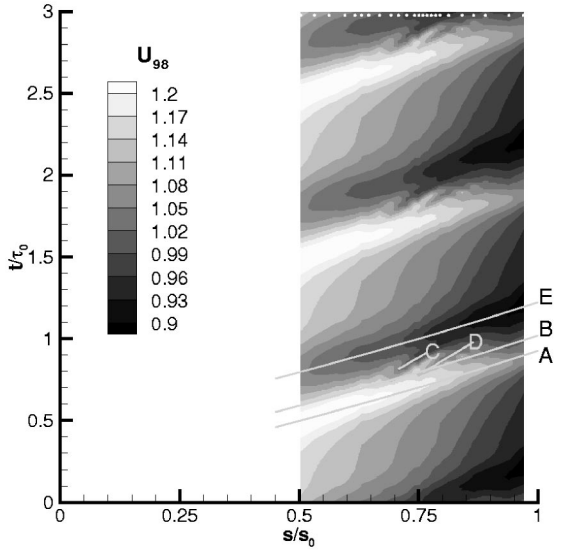


**Fig. 3 Space-time diagram of boundary layer edge velocity nondimensionalised by $V_{2is}$**

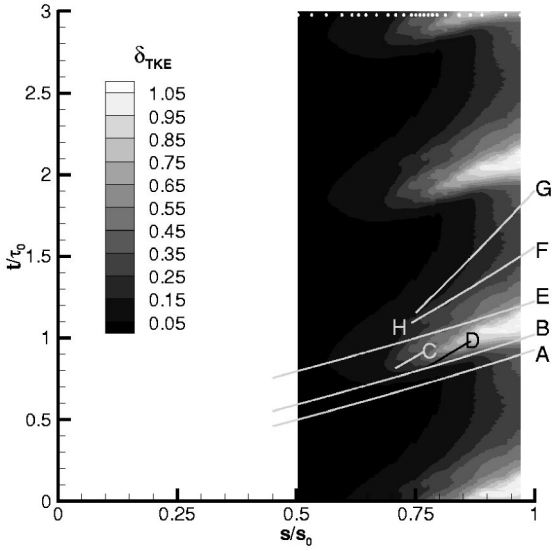


**Fig. 5 Space-time diagram of measured boundary layer TKE thickness**

## Results

The isentropic surface velocity distribution derived from static pressure measurements on the cascade under wake passing conditions is also shown in **Fig. 2**. It is apparent that in the time mean the wake passing suppresses the suction surface separation bubble. It is an unavoidable consequence of the experimental facility that the wake passing conditions introduce a small amount of incidence on the cascade as shown by the small differences between the steady and unsteady pressure distributions over the front of the blade. This incidence is small and has no significant impact on the blade surface boundary layers downstream of peak suction.

## A Space-Time View of the Measured Boundary Layer

The two-dimensional LDA boundary layer data are presented as S-T diagrams in **Figs. 3–5**. To aid visualization of the periodic unsteady process the data is copied onto three wake passing periods. The streamwise locations of the traverses are indicated by dots across the top of each of these figures.

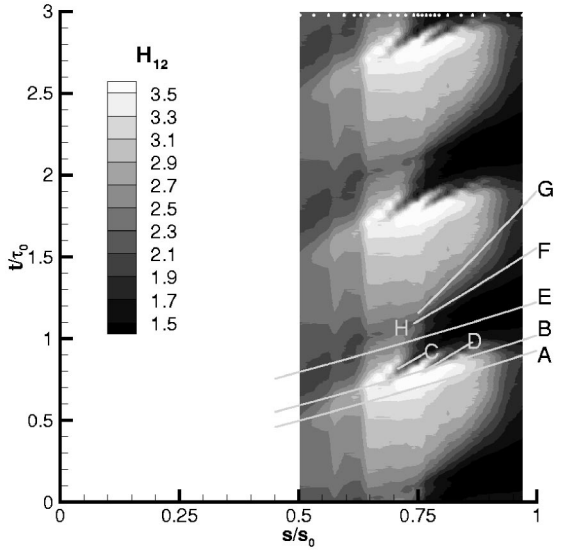


**Fig. 4 Space-time diagram of measured $H_{12}$**

**Boundary Layer Edge Velocity.** The boundary layer edge is defined as the wall normal distance where the velocity is 98% of the maximum velocity measured in the local ensemble-average profile. The velocity at this point is taken as the boundary layer edge velocity. Measurements of the boundary layer edge velocity are nondimensionalized by the isentropic exit velocity and plotted as an S-T diagram in **Fig. 3**. Three trajectory lines denoted *A*, *B*, and *E*, are drawn at the time average boundary layer edge velocity. Line *A* marks the peak velocity that results from kinematics of the approaching wake (see Meyer [14] and Hodson [15]) and line *E* marks the minimum velocity, which occurs after the negative jet of the wake has passed. Line *B* is placed half way between lines *A* and *E* and is the approximate path of the center of the wake.

Two further lines, labeled *C* and *D*, are drawn to mark two distinct structures originating along the wake center at $s/s_0 \approx 0.70$ and $s/s_0 \approx 0.77$. These perturbations to the boundary layer edge velocity have not previously been observed. They are attributed to the rollup vortices that form due to the interaction of the wake and separated shear layer. Further evidence of this will be presented later. These structures can be seen to follow trajectories slower than the local freestream, indeed, lines *C* and *D* are drawn with a trajectory of half the freestream velocity.

**Boundary Layer Shape Factor.** The integral parameters were calculated from the measured ensemble average velocity profiles and the shape factor was calculated from these. An S-T diagram of the shape factor, $H_{12}$, is shown in **Fig. 4** with the trajectory lines and labels copied from **Fig. 3**.

The wake path lies between lines *A* and *E*. Along line *A*, the outer part of the boundary layer is accelerated by the approaching wake. The increased velocity is not transmitted through the boundary layer instantaneously due to viscous effects. As a result the outer portion of the boundary layer accelerates more than the inner portion and the levels of $H_{12}$ are increased between lines *A* and *B* downstream of $s/s_0 = 0.60$.

Along line *B*, the separating flow indicated by high $H_{12}$ breaks down into wedge shaped regions originating at $s/s_0 \approx 0.70$ and at $s/s_0 \approx 0.77$. These structures, which follow trajectory lies *C* and *D*, were observed in **Fig. 3**, and are sites of rapid break down of the high $H_{12}$ flow to a turbulent boundary layer.

After the wake center has passed over the region of high $H_{12}$, a more typical wake-induced transition occurs at $s/s_0=0.75$ along trajectory $E$. This process, which lags behind the wake passing, may be a result of wake turbulence diffusing into the boundary layer and causing bypass transition. A characteristic wedge of turbulent boundary layer follows the wake-induced transition. The trailing edge of the wake induced turbulent strip is bound by line $F$, which is drawn at $0.5U$. The structures traced by trajectories $C$ and $D$ merge with the turbulent strip.

Line $G$ is drawn with a trajectory of $0.3U$. This marks the approximate trailing edge of the calmed region, which is characterized by slowly increasing levels of $H_{12}$ as the turbulent boundary layer relaxes back to the inflexional profiles of the separating boundary layer under a strong adverse pressure gradient. The calmed region controls the rear of the high $H_{12}$ region.

**TKE Thickness.** Due to practical constraints, the boundary layer state on turbomachinery blading is often inferred from measurements made with hot-film anemometers. The measurements are qualitative, however, as it is not the quasi-shear stress, but rather the random unsteadiness (ensemble average RMS), which is most useful in indicating the boundary layer state. D'Ovidio et al. [11,12] sought to recover the familiarity of using RMS as an indicator of boundary layer state while using all the data from hot wire boundary layer traverses. They adopted the Blackwelder parameter, which is an integral of the RMS fluctuations through the boundary layer nondimensionalised by the boundary layer edge velocity. A similar approach is adopted for the current measurements. The parameter $\delta_{\mathrm{TKE}}$ is defined as the integral of TKE through the boundary layer according to

$$\delta_{\mathrm{TKE}}=\frac{1}{U_{98}^2}\int_{y=0}^{\delta_{98}}\frac{1}{2}(\overline{u'^2}+\overline{v'^2})dy \tag{1}$$

An S-T diagram of $\delta_{\mathrm{TKE}}$ is shown in **Fig. 5** with the trajectory lines and labels from **Fig. 4** repeated. Upstream of $s/s_0=0.70$, $\delta_{\mathrm{TKE}}$ is low throughout the wake passing cycle. This indicates that the boundary layer in this region is laminar throughout the wake passing cycle and is not significantly affected by the passing wakes. Downstream of this, the wake-induced path is characterized by very high levels of $\delta_{\mathrm{TKE}}$, which originate along trajectory line $B$. The onset does not lag behind the wake and corresponds to the region where the structures $C$ and $D$ were observed in **Fig. 3** and **Fig. 4**.

A second strip of elevated $\delta_{\mathrm{TKE}}$ is seen to originate at label $H$. This strip lags behind the passing of the wake and is a result of a wake-induced bypass transition that occurs once the wake turbulence has diffused into the boundary layer. As in **Fig. 4**, the turbulent wedge may be identified by high levels of $\delta_{\mathrm{TKE}}$ between lines $E$ and $F$, while the calmed region between lines $F$ and $G$ is characterized by low levels of $\delta_{\mathrm{TKE}}$ that extend to the trailing edge.

At the traverse location closest to the trailing edge, four distinct levels of $\delta_{\mathrm{TKE}}$ are distinguishable. The highest levels occur between lines $B$ and $E$ and originate from the interaction of the wake and the inflexional profiles of the separating boundary layer. The next highest region of $\delta_{\mathrm{TKE}}$ occurs between lines $E$ and $F$ and results from the turbulent strip formed by the wake induced bypass transition. The lowest region of $\delta_{\mathrm{TKE}}$ occurs between lines $F$ and $G$. This region corresponds to the calmed region and shows that the calmed region persists to the trailing edge. Finally between $G$ and $A$ of the following cycle the level of $\delta_{\mathrm{TKE}}$ is again elevated due to the natural transition that occurs once the influence of the calmed region has passed. It is worthy of note that the peak levels of $\delta_{\mathrm{TKE}}$ arise in the region of the interaction of the wake and separating boundary layer.

## Unsteady Boundary Layer Development

Further details of the two-dimensional LDA boundary layer traverses are presented in **Figs. 6–9** as a series of snapshots of the boundary layer at illustrative phases through the wake passing cycle. At each of these phases, velocity vectors, perturbation velocity vectors and contour plots of vorticity describe the ensemble-averaged flow field. The perturbation velocity is the difference between the ensemble averaged and time-averaged velocity fields and the vorticity is calculated with velocities normalized by $V_{2is}$ and lengths normalized by $C$ according to

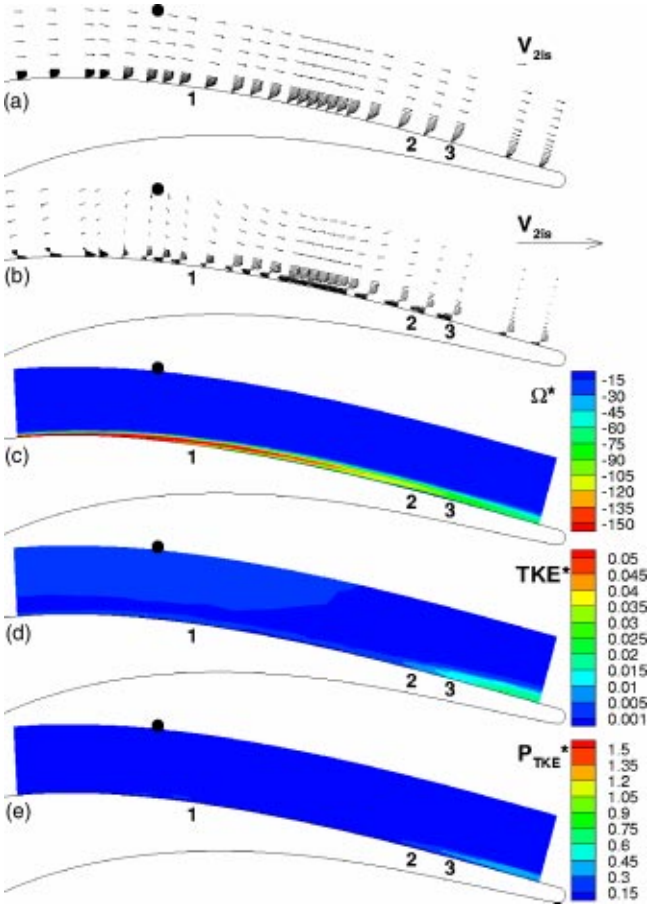


**Fig. 6 Boundary layer structure prior to the wake arrival. Vector plots of (*a*) ensemble average velocity and (*b*) perturbation velocity. Contour plots of nondimensional (*c*) vorticity, (*d*) turbulent kinetic energy, and (*e*) production of TKE. Re=1.6 $\times 10^5$, $s_b/s_c=1$.**

$$\Omega=\partial V/\partial x-\partial U/\partial y. \tag{2}$$

The $x$ coordinate is in the axial direction and positive downstream.

The turbulent kinetic energy (TKE) is calculated from the measured velocity variance components normalized by $V_{2is}^2$

$$\mathrm{TKE}=\frac{1}{2}(\overline{u'^2}+\overline{v'^2}) \tag{3}$$

and is presented as contour plots. The production of TKE ($P_{\mathrm{TKE}}$) is calculated from the normalized mean velocity gradients and the normalized measured Reynolds stresses

$$P_{\mathrm{TKE}}=-\overline{u'^2}\frac{\partial U}{\partial x}-\overline{v'^2}\frac{\partial V}{\partial y}-\overline{u'v'}\left(\frac{\partial U}{\partial y}+\frac{\partial V}{\partial x}\right). \tag{4}$$

**Boundary Layer State Before the Interaction of the Wake and Inflexional Profiles.** **Figure 6** shows the boundary layer prior to the interaction of the wake and separation bubble. The position of the centerline of the wake (trajectory line $B$ in the S-T diagrams) is marked by a dot and is evident form the perturbation

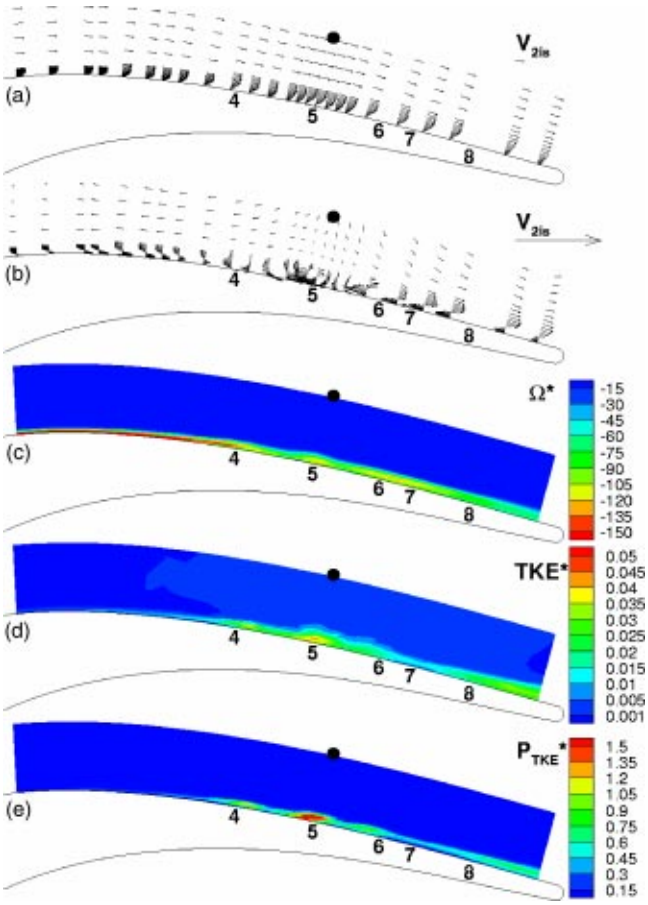


**Fig. 7 Boundary layer structure during the interaction of wake and separated shear layer. Re=1.6×10$^5$, $s_b/s_c$=1.**

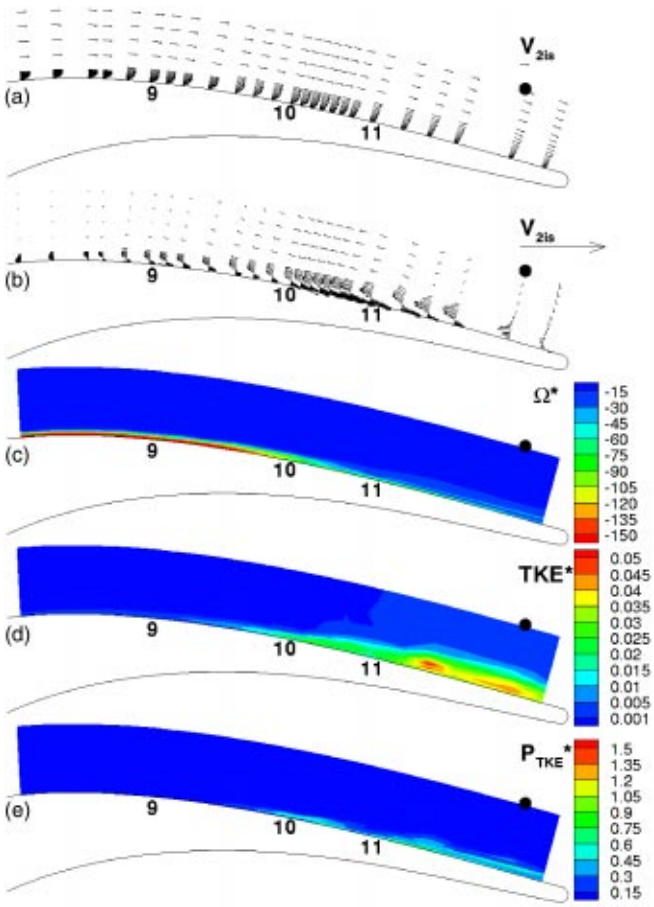


**Fig. 8 Boundary layer structure through the wake-induced turbulent strip. Re=1.6×10$^5$, $s_b/s_c$=1.**

velocity vectors of **Fig. 6**(***b***), which shows the wake as a jet impinging on the blade surface and splitting into two streams along the blade surface. At this phase, the wake is upstream of the steady separation point, which is labeled 1. Upstream of the separation point, the boundary layer is laminar and attached as seen by the profiles of the mean velocity vectors in **Fig. 6**(***a***). The highest levels of vorticity are found on the wall and the levels of TKE and $P_{TKE}$ are low. Downstream of 1 the boundary layer profiles become inflexional and the peak levels of vorticity are detached from the wall. A separated shear layer extends from 1 to 2. In the ensemble mean, this shear layer is not perturbed. This is confirmed by the smooth distribution of vorticity and the absence of wall normal components of the perturbation velocity vectors in this region. The separated shear layer reattaches downstream of 2. In this region, the velocity profiles become fuller and the levels of vorticity in the outer boundary layer reduce. Increased levels of TKE are also observed downstream of 2.

**Interaction of Wake With Separated Shear Layer.** The interaction of the wake and inflexional profiles of the separated shear layer is shown in **Fig. 7**. The wake is now located over the separated region with its center marked by a dot. The perturbation velocity vectors of **Fig. 7**(***b***) show that the wake passing over the separated shear layer has induced significant wall-normal velocity components.

Between 4 and 6 the velocity profiles alternate between being inflexional and very full. This rapid change with distance along the blade surface is attributed to the rollup of the separated shear layer, which is induced by the wake. The profiles are thus the superposition of a vortex on the boundary layer profile. Indeed, rollup vortices may be identified at 4 and 5 both in the perturbation velocity vectors of **Fig. 7**(***b***) and as localized regions of high vorticity embedded within the boundary layer in **Fig. 7**(***c***)**.**

The boundary layer edge can be inferred from the edge of the elevated vorticity region and the rollup vortices can be seen to thicken the boundary layer locally. The perturbation velocity vectors of **Fig. 7**(***b***) show significant wall normal velocities associated with the rollup vortices. The rollup vortex with its center at 5 may be identified in the perturbation velocity vectors. It is clear that the rollup vortex at 5 induces large local flow curvature. Indeed, the unsteady surface pressure measurements of Stieger et al. [16] indicate that there is a strong local pressure field associated with the streamline curvature of rollup vortices embedded in the boundary layer.

Downstream of the wake, between 6 and 8, the velocity profiles are inflexional and the vorticity contours again show a peak detached from the wall. This region has not yet been affected by the wake passing and there are no wall normal velocity components in the perturbation velocity vectors. The transition and reattachment of the inflexional profiles downstream of 8 occurs as for the previous phase shown in **Fig. 6**.

**Figure 7**(***d***) shows contours of TKE. The elevated turbulence associated with the wake can be seen to extend from 4 to the trailing edge and the boundary layer TKE is elevated throughout this region. Regions of high TKE are distinguishable at labels 4 and 5. The highest levels of TKE are located at 5, which is the newly formed rollup vortex. The reduced levels of TKE at 7 correspond to the undisturbed inflexional profiles downstream of the wake. Downstream of this, the elevated TKE is a result of the natural transition of the inflexional profiles.

The production of TKE, presented in **Fig. 7**(***e***), follows the

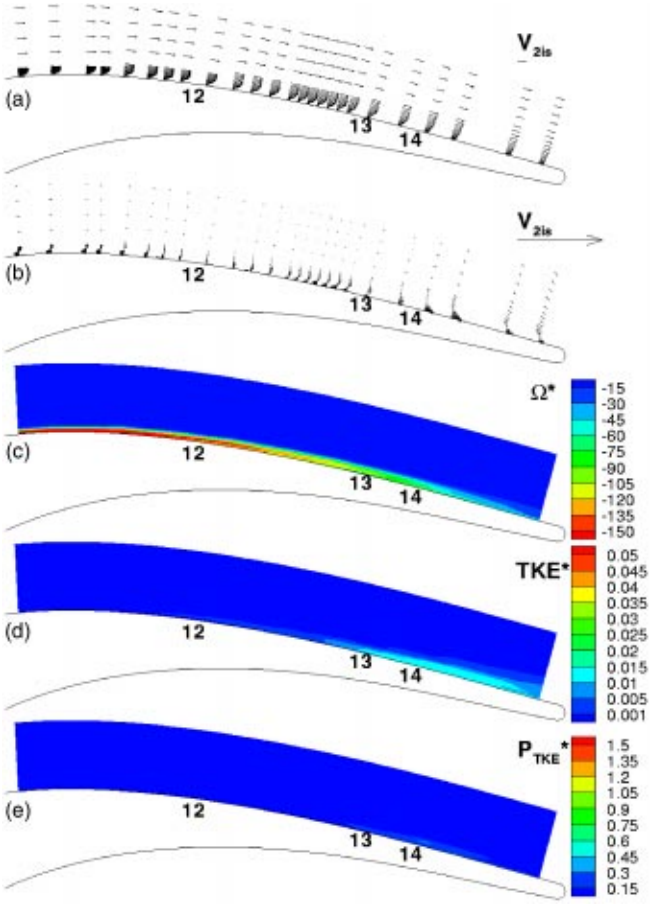


**Fig. 9 Boundary layer structure in the calmed region. Re=1.6 $\times 10^5$, $s_b/s_c=1$.**

distribution of TKE with elevated production at the center of the vortex. The peak levels of production are located at the center of the vortex at 5. The natural transition downstream of 8 is also associated with elevated levels of TKE production.

**Boundary Layer After Wake Interaction.** **Figure 8** shows the boundary layer state with the wake downstream of the separation region as indicated by the dot. Upstream of 9 the boundary layer profiles are laminar. Between 9 and 10 the boundary layer profiles have the shape of attached laminar profiles but the levels of TKE in this region are elevated as shown in **Fig. 8(*d*)**. This suggests that the profiles in this region are transitional.

Downstream of 10 the velocity profiles have a turbulent shape. However, the levels of TKE downstream of 11 are far higher than between 10 and 11. This is attributed to the breakdown of the rollup vortices. An isolated region of elevated TKE can be identified in **Fig. 8(*d*)** at 11. Although not evident in the vorticity contours due to the coarse spacing of the traverses in this region, this is attributed to a rollup vortex and is accompanied by elevated TKE production. The levels of production measured at the vortex center are lower than those of **Fig. 7**. The vortex is now further from the wall and so the boundary layer velocity gradients are smaller and this reduces the production of TKE at the vortex center. The reduced streamwise resolution of the measurements downstream of 11 causes streaks in the contours and this prevents the identification of rollup vortices downstream of this location.

The boundary layer between 10 and 11 is due to the wake-induced bypass transition and is characterized by elevated TKE together with elevated production and dissipation. The production in this region is of similar magnitude to that of the vortex centred at 11, however, the extent is smaller.

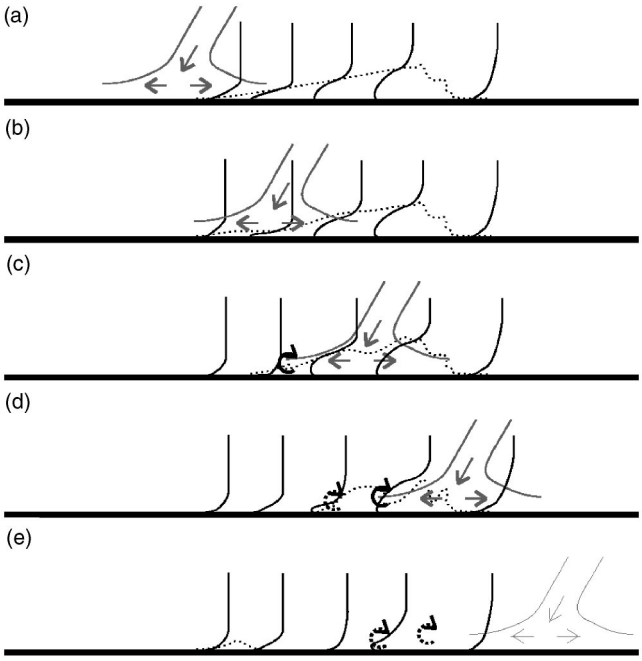


**Fig. 10 Sketch of rollup mechanism**

**Calmed Boundary Layer.** After the passage of the wake, the boundary layer starts to relax back to its pre-transitional state. The phase shown in **Fig. 9** is representative of this process.

Upstream of 12 the boundary layer is laminar and attached with low levels of TKE. Between 12 and 13, the boundary layer is laminar and in the upstream part of this region, the profiles are becoming inflexional. This is emphasised by the vorticity peak moving away from the wall. Over the rear portion of the region between 12 and 13 the boundary layer profiles are fuller and more like the calmed profiles that are observed between 13 and 14. The profiles between 12 and 13 describe the process whereby the calmed profiles become inflexional and begin to separate under the strong adverse pressure gradient.

The TKE is shown in **Fig. 9(*d*)**. The levels of TKE are observed to be low. The elevated region between 13 and 14 is due to the decaying boundary layer turbulence in the calmed region, while downstream of 14 the turbulence is due to the turbulent boundary layer.

The production of TKE is presented in **Fig. 9(*e*)** and the levels are very low throughout the measurement domain with only a small region of low magnitude production at 14. These low levels of TKE production point to the loss reducing mechanism associated with the calmed region.

## Mechanism of Wake-Induced Transition

Based on the observed interaction of a convected wake and the separated shear layer of the re-establishing separation bubble on the T106 LP turbine cascade, it is possible to describe the mechanism whereby boundary layer transition occurs on highly loaded LP turbine blades with laminar separation.

The process is illustrated schematically in **Fig. 10**. Schematic velocity profiles are shown at selected locations through the separation bubble and the dotted line indicates the separated shear layer. The wake is represented by a jet (negative jet) pointed towards the blade surface.

**Figure 10(*a*)** depicts the flow prior to the interaction of the wake and separated shear layer. The negative jet impinging on the blade splits into two streams, one pointed downstream which has the effect of accelerating the flow downstream of the approaching wake and one pointing upstream which retards the flow after the

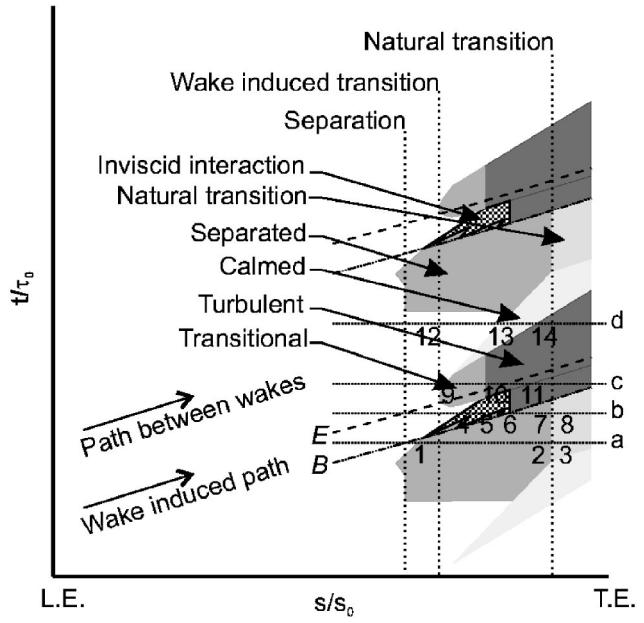


**Fig. 11 Schematic of the transition mechanism resulting from the interaction of a wake and separating boundary layer**

wake has passed. As the wake approaches the separation, the outer region of the boundary layer is accelerated. The inner region of the boundary layer responds more slowly than the freestream due to the fluid viscosity and as a result, the shear of the separation is intensified by the approaching wake.

As the wake convects over the separation, the wall normal component of the negative jet deforms the shear layer as shown in **Fig. 10**(***b***). The separated shear layer is naturally unstable and the perturbation of the wake triggers an inviscid Kelvin-Helmholtz rollup as shown in **Fig. 10**(***c***). The resulting rollup vortex convects at half the freestream velocity and so the wake, which convects with the freestream, moves ahead of the rollup and perturbs the separated shear layer further downstream. This results in the formation of further rollup vortices as shown in **Fig. 10**(***d***). The vortices formed by the inviscid rollup of the shear layer rapidly breakdown to turbulence thereby causing boundary layer transition. After the passing of the rollup vortices and the turbulent boundary layer, a calmed region is formed and once the influence of the calming has subsided the boundary layer begins to separate once again. This is shown in **Fig. 10**(***e***)**.**

## Schematic of Wake-Induced Transition

Based on measurements presented thus far and the mechanism described above, a schematic of the wake induced transition process involving the interaction of a wake and separating boundary layer may be drawn as in **Fig. 11**. The horizontal lines, labeled a–d, mark the phases shown in **Figs. 6** to **9**, respectively, and the numbers used to identify features in these figures are transferred to **Fig. 11**. The trajectory lines ***B*** and ***E*** are copied from previous S-T diagrams.

Following the description of Halstead et al. [17], two generic transition paths may be identified on the blade surface. The wake-induced path and the transition path between wakes are indicated in **Fig. 11.**

The wake-induced path differs from the traditional wake induced path for attached flow transition due to the interaction of the wake and separating boundary layer. The rollup of the separated shear layer into vortices that results from the interaction of the wake and inflexional profiles occurs by an inviscid mechanism. The diffusion of turbulence into the boundary layer is thus not a necessary precursor to the rollup of the shear layer and there is no time lag between the wake passing and the boundary layer response. The inviscid rollup is represented in **Fig. 11** by a series of wedges originating beneath the center of the wake at 4 and 5. The rollup vortices break down and a region of turbulent boundary layer follows the inviscid rollup process.

After the inviscid rollup of the shear layer, the wake turbulence diffuses into the boundary layer. This induces bypass transition in the attached boundary layer as described by Halstead et al. [17]. This bypass transition and the wake-induced transitional and turbulent strips occur along trajectory *E* of **Fig. 11**.

After the wake has passed, the stimulus for early transition is removed and the turbulent boundary layer upstream of the natural transition location relaxes to its pre-transition state. This is the transition path between wakes labeled in **Fig. 11**. This relaxation process results in the calmed region, which is characterized by full velocity profiles that resist separation. The calmed region spreads as it convects downstream due to the different propagation velocities for the trailing edge of turbulent spots and the trailing edge of the clamed region. After the influence of the calming has decayed, the boundary layer profiles become inflexional and begin to separate under the adverse pressure gradient. The leading edge of this region of inflexional profiles initially follows the trajectory of the trailing edge of the calmed region. Thereafter, the inflexional or separating flow undergoes transition. The calmed region and early stages of separation are characterized by low levels of dissipation as shown by Stieger [18] and this is the loss reducing mechanism exploited by high-lift LP turbine blade designs. Immediately prior to the arrival of the wake, the separation location is observed to move fractionally upstream. This is the influence of the negative jet, which alters the pressure gradient locally and is a precursor to the inviscid rollup occurring beneath the wake.

## Discussion

The transition mechanism described above is specific to conditions were wake-induced bypass transition does not dominate the attached boundary layer flow upstream of separation point. For the formation of the rollup vortices to occur the separated laminar shear layer is required. This means that the Reynolds number and freestream turbulence must be low to permit separation. Furthermore, the wake passing frequency must not be so high as to prevent the boundary layer from beginning to separate between wake passing events. The PIV measurements of Stieger et al. [16] identified rollup vortices embedded in the boundary layer. The preservation of these vortices in ensemble-averaged data is remarkable and emphasises the deterministic nature of the rollup mechanism resulting from the periodic wake passing. It is also notable that the flat plate boundary layer measurements of Stieger and Hodson [19] and the unsteady surface pressure measurements conducted by Stieger et al. [16] on this T106 cascade show that the natural transition occurring as the calmed region breaks down is also preserved through the ensemble average processing and is deterministic. The ensemble-averaging process does, however, remove the random unsteadiness and as a result the TKE levels are likely to be overestimated.

## Conclusions

The ensemble-average two-dimensional LDA measurements of the boundary layer on the T106 LP turbine cascade provide new insight into the wake-induced transition mechanism. The measurements show the separated shear layer associated with the inflexional profiles of the re-establishing separation bubble form rollup vortices beneath the passing wake. The vortices were formed by an inviscid Kelvin-Helmholtz mechanism. Due to the inviscid nature of the rollup mechanism, there was no delay between the wake passing and the boundary layer response. The rollup vortices were observed to breakdown into highly turbulent flow that convected along the blade surface.

The mechanism described above results when no wake induced turbulent spots are formed upstream of the separation location.

The turbulent wake then convects over the inflexional profiles of the separating boundary layer and the inviscid breakdown described above results.


## Acknowledgments

The first author would like to acknowledge the financial support of the ORS and a Peterhouse Research Studentship. The funding of EPSRC grant GR/L96660/01 is also gratefully acknowledged.


## Nomenclature

$C$ = chord
$f_r$ = reduced frequency $f_r = fC/U_b$
$H_{12}$ = shape factor $H_{12} = \delta^*/\theta$
$P_{\mathrm{TKE}}$ = normalized production of TKE
Re = Reynolds number
$s$ = surface distance
$s_0$ = surface length
$s_b$ = bar pitch
$s_c$ = cascade pitch
TKE = normalized turbulent kinetic energy
$\overline{u'^2}, \overline{v'^2}$ = normalized velocity variance components
$\overline{u'v'}$ = normalized Reynolds stress
$U_b$ = bar speed
$U_{98}$ = normalized boundary layer edge velocity
$U, V$ = normalized velocity components
$V_{x1}$ = axial inlet velocity
$V_{2is}$ = isentropic exit velocity
$x, y$ = normalized linear dimensions
$\delta^*$ = displacement thickness
$\delta_{\mathrm{TKE}}$ = TKE thickness
$\phi$ = flow coefficient $\phi = V_{x1}/U_b$
$\theta$ = momentum thickness
$\Omega$ = normalized vorticity

## References


[1] Schulte, V., and Hodson, H. P., 1994, ''Wake-Separation Bubble Interaction in Low Pressure Turbines,'' AIAA/SAE/ASME/ASEE 30th Joint Propulsion Conference and Exhibit, Indianapolis, IN.

[2] Schulte, V., and Hodson, H. P., 1998, ''Unsteady Wake-Induced Boundary Layer Transition in High Lift LP Turbines,'' ASME J. Turbomach., **120**, pp. 28–35.

[3] Curtis, E. M., Hodson, H. P., Banieghbal, M. R., Denton, J. D., and Howell, R. J., 1996, ''Development of Blade Profiles for Low Pressure Turbine Applications,'' ASME Paper 96-GT-358.

[4] Howell, R. J., Ramesh, O. N., Hodson, H. P., Harvey, N. W., and Schulte, V., 2000, ''High Lift and Aft Loaded Profiles for Low Pressure Turbines,'' ASME Paper 2000-GT-261.

[5] Cobley, K., Coleman, N., Siden, G., and Arndt, N., 1997, ''Design of New Three Stage Low Pressure Turbine for BMW Rolls-Royce BR715 Engine,'' ASME Paper 97-GT-419.

[6] Haselbach, F., Schiffer, H.-P., Horsman, M., Dressen, S., Harvey, N., and Read, S., 2001, ''The Application of Ultra High Lift Blading in the BR715 LP Turbine,'' ASME Paper 2001-GT-0436.

[7] Brunner, S., Fottner, L., and Schiffer, H.-P., 2000, ''Comparison of Two Highly Loaded Low Pressure Turbine Cascades Under the Influence of Wake-Induced Transition,'' ASME Paper 2000-GT-268.

[8] Howell, R. J., Hodson, H. P., Schulte, V., Schiffer, H.-P., Haselbach, F., and Harvey, N. W., 2001, ''Boundary Layer Development on the BR710 and BR715 LP Turbines—The Implementation of High Lift and Ultra High Lift Concepts,'' ASME Paper 2001-GT-0441.

[9] Wu, X., Jacobs, R. G., Hunt, J. C. R., and Durbin, P. A., 1999, ''Simulation of Boundary Layer Transition Induced by Periodically Passing Wakes,'' J. Fluid Mech., **398**, pp. 109–153.

[10] Johnson, M. W., 2002, ''Predicting Transition Without Empiricism or DNS,'' ASME Paper GT-2002-30238.

[11] D'Ovidio, A., Harkins, J. A., and Gostelow, J. P., 2001 a, ''Turbulent Spots in Strong Adverse Pressure Gradients: Part 1—Spot Behavior,'' ASME Paper 2001-GT-0194.

[12] D'Ovidio, A., Harkins, J. A., and Gostelow, J. P., 2001, ''Turbulent Spots in Strong Adverse Pressure Gradients: Part II—Spot Propagation and Spreading Rates,'' ASME Paper 2001-GT-0406.

[13] George, W. K., 1975, ''Limitations to Measuring Accuracy Inherent in the Laser-Doppler Signal,'' *Proc. LDA Symp.*, Copenhagen.

[14] Meyer, R. X., 1958, ''The Effects of Wakes on the Transient Pressure and Velocity Distributions in Turbomachines,'' ASME J. Basic Eng., Oct. pp. 1544–1552.

[15] Hodson, H. P., 1998, ''Bladerow Interactions In Low Pressure Turbines,'' *Blade Row Interference Effects Axial Turbomachinery Stages* (VKI Lecture Series No. 1998-02), Von Karman Institute, Feb. 9–12.

[16] Stieger, R. D., Hollis, D., and Hodson, H. P., 2003 ''Unsteady Surface Pressures due to Wake Induced Transition in a Laminar Separation Bubble on a LP Turbine Cascade,'' ASME Paper GT-2003-38303.

[17] Halstead, D. E., Wisler, D. C., Okiishi, T. H., Walker, G. J., Hodson, H. P., and Shin, H.-W., 1997, ''Boundary Layer Development in Axial Compressors and Turbines: Part 1—Composite Picture,'' ASME J. Turbomach., **119**, pp. 114–127.

[18] Stieger, R. D., 2002, ''The Effects of Wakes on Separating Boundary Layers in Low Pressure Turbines,'' Ph.D. thesis, University of Cambridge, Cambridge, UK.

[19] Stieger, R. D., and Hodson, H. P., 2003, ''Unsteady Dissipation Measurements on a Flat Plate Subject to Wake Passing,'' submitted to the 5th European Turbomachinery Conference, Prague.

# Unsteady Surface Pressures Due to Wake-Induced Transition in a Laminar Separation Bubble on a Low-Pressure Cascade

**R. D. Stieger**[1]
Whittle Laboratory,
Cambridge University,
Engineering Department,
Madingley Road,
Cambridge CB3 0DY, UK

**David Hollis**
Department of Aeronautical and Automotive Engineering,
Loughborough University,
Stewart Miller Building,
Leics LE 11 3TU, UK

**H. P. Hodson**
Whittle Laboratory,
Cambridge University,
Engineering Department,
Madingley Road,
Cambridge CB3 0DY, UK

*This paper presents unsteady surface pressures measured on the suction surface of a LP turbine cascade that was subject to wake passing from a moving bar wake generator. The surface pressures measured under the laminar boundary layer upstream of the steady flow separation point were found to respond to the wake passing as expected from the kinematics of wake convection. In the region where a separation bubble formed in steady flow, the arrival of the convecting wake produced high frequency, short wavelength, fluctuations in the ensemble-averaged blade surface pressure. The peak-to-peak magnitude was 30% of the exit dynamic head. The existence of fluctuations in the ensemble averaged pressure traces indicates that they are deterministic and that they are produced by coherent structures. The onset of the pressure fluctuations was found to lie beneath the convecting wake and the fluctuations were found to convect along the blade surface at half of the local freestream velocity. Measurements performed with the boundary layer tripped ahead of the separation point showed no oscillations in the ensemble average pressure traces indicating that a separating boundary layer is necessary for the generation of the pressure fluctuations. The coherent structures responsible for the large-amplitude pressure fluctuations were identified using PIV to be vortices embedded in the boundary layer. It is proposed that these vortices form in the boundary layer as the wake passes over the inflexional velocity profiles of the separating boundary layer and that the rollup of the separated shear layer occurs by an inviscid Kelvin-Helmholtz mechanism.*
[DOI: 10.1115/1.1773851]

## Introduction

The boundary layers of low-pressure (LP) turbine blades have received a great deal of attention due to the advent of high lift and ultra high lift LP turbines. The design of these turbines exploits unsteady transition phenomena, as described by Halstead et al. [1–4], to reduce component counts at little or no efficiency penalty. Much of the understanding of unsteady transition is based on attached flow bypass transition and excellent reviews by Mayle [5] and Walker [6] provide extensive correlations built to predict transition in attached boundary layers. However, LP turbines operate at low Reynolds numbers, typically in the range $0.9–2 \times 10^5$, this coupled with high levels of boundary layer diffusion lead to the formation of a separation bubble under steady flow. The effect of wake passing has been shown by Schulte and Hodson [7] to periodically suppress the separation bubble. However, the details of the unsteady transition mechanism in strong adverse pressure gradients and separating boundary layers remains poorly understood. The work of D'Ovidio et al. [8,9] has extended the useful range of transition correlations but has not provided fundamental insight into the transition mechanism resulting from the interaction of a wake and laminar separation.

A detailed investigation into the unsteady boundary layer development has been conducted on the T106 LP turbine cascade in a bar passing rig to simulate the unsteady LP turbine environment at low speed. In particular the unsteady suction surface pressure distribution has been measured together with hot wire boundary layer traverses and PIV. Large amplitude pressure fluctuations were measured and were identified as being associated with rollup vortices formed by the wake passing over the inflexional boundary layer.

## Experimental Facility and Techniques

The measurements reported in this paper were made on the T106 LP turbine profile in a bar passing cascade at the Whittle Laboratory. The rig, shown in **Fig. 1**, simulates the unsteady wake-passing environment of a LP turbine by traversing bars across the inlet flow. The wakes shed from these bars simulate the wakes of an upstream blade row in a multistage turbine. Details of the cascade are presented in **Table 1** and further details of the bar passing cascade facility can be found in Stieger [10]. Also shown in **Fig. 1** is the light sheet location used for PIV measurements.

In this study the unsteady blade surface pressures were measured at mid span of the T106 cascade using four Kulite XCS-062 pressure transducers fitted with B screens and yielding a maximum frequency response of approximately 20 kHz. The diameter of the Kulite is 1.6 mm, which corresponds to 0.6% of the suction surface length. The transducer was mounted in a brass sheath, which was screwed into the holes in the blade so that the transducer was flush with the surface as shown in **Fig. 2**. The suction surface of the central blade of the T106 cascade was instrumented at 21 streamwise locations along the suction surface at midspan. Brass plugs were made for each of the vacant transducer locations. These plugs were polished flush with the surface of the blade.

Fylde 492BBS bridges were used to power the Kulite transducers and the bridge outputs were fed into Fylde 254GA amplifiers with a gain of 1000. A National Instruments PCI-MIO-16E-1 A/D card was used to measure the amplifier outputs. Only the fluctuating pressure was measured by the Kulites. On-line calibration of the transducers, bridges and amplifiers was performed simulta-

[1]Current address: Rolls-Royce plc, Derby, UK.

Contributed by the International Gas Turbine Institute and presented at the International Gas Turbine and Aeroengine Congress and Exhibition, Atlanta, GA, June 16–19, 2003. Manuscript received by the IGTI Dec. 2002; final revision Mar. 2003. Paper No. 2003-GT-38303. Review Chair: H. R. Simmons.

  

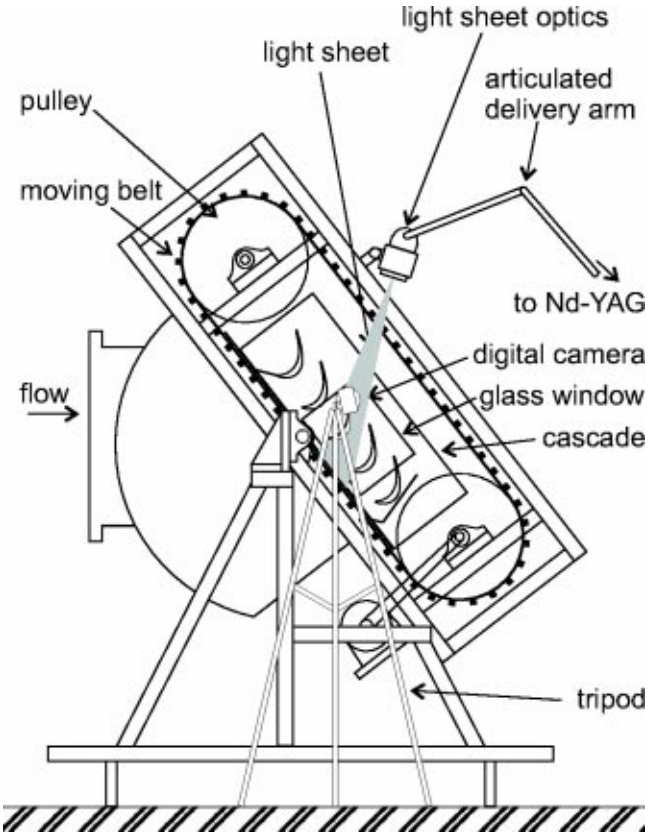


**Fig. 1 Bar passing cascade**

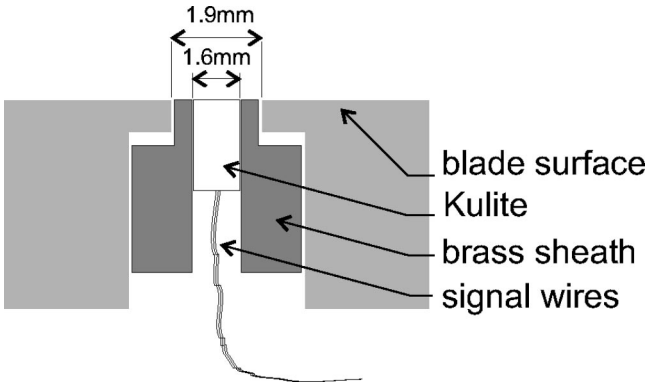


**Fig. 2 Mounting of pressure transducers to measure unsteady blade surface pressure**

neously using a Druck DPI520 as a pressure source. The system described above resulted in a sensitivity of approximately 500 Pa/V, with a discretization error of 0.05 Pa. Each measurement of the fluctuating pressure consisted of 256 ensembles of 4096 points logged at 10 KHz.

Pneumatic static pressure tapings, located at 25% span, were used to determine the mean pressure level at each of the Kulite locations. Oil and dye flow visualization showed that the static pressure tappings were within the two-dimensional flow region on the cascade.

The mean pressure level was measured using a Scanivalve DSA 3017 array with a $\pm 10$ in $H_2O$ range and 16-bit A/D. The discretization error on this measurement is thus 1.0 Pa which corresponds to 1.0% exit dynamic head at the nominal flow condition of Re $=1.6\times 10^5$. The voltage outputs of the Kulites were converted to pressure by a linear calibration, before ensemble averaging and adding the mean pressure measured by the DSA. The results were nondimensionalized by isentropic exit dynamic head to give the ensemble-averaged pressure coefficient.

PIV measurements were made using a commercial TSI PIV system. A pair of 50 mJ New Wave Nd-YAG lasers delivered light to the terminal optics via an articulated delivery arm. A 25.4 mm focal length negative cylindrical lens and a 500 mm focal length spherical lens were used to generate the light sheet that was between 0.5 mm and 1.5 mm thick on the blade surface.

**Table 1 T106 bar passing cascade details**

| | | |
|---|---|---|
| Chord | (mm) | 198 |
| Blade stagger | (deg) | 59.3 |
| Pitch | (mm) | 158 |
| Span | (mm) | 375 |
| Inlet flow angle | (deg) | 37.7 |
| Design exit flow angle | (deg) | 63.2 |
| Bar diameter | (mm) | 2.05 |
| Axial distance: bars to LE | (mm) | 70 |
| Flow coefficient ($\phi$) | | 0.83 |

A Kodak digital camera with 1024×1024 CCD array was used to acquire the images through a 105 mm Nikon lens providing a 19.0 mm square field of view. The inter frame delay was set to $\Delta t = 3$ ms, which gave particle displacements in the range 3 to 6 pixels. The maximum data rate of the PIV system was 15 Hz so it was not possible to capture a sequence of images within one bar passing cycle. A trigger signal generated by the bar passing was passed through a delay generator thereby allowing the PIV images to be acquired at selected phases relative to the bar passing trigger.

The flow was seeded with a mist of groundnut oil generated by a pair of TSI Six-Jet Atomisers. The seeding was introduced into plenum chamber of the wind tunnel approximately 3 m upstream of the bar passing cascade.

The acquired image pairs were processed using LaVision's DaVis V.6.03 software (LaVision [11]). An adaptive multipass technique was used with the initial cell size of 64×64 pixels decreasing to a final cell size of 16×16 pixels with a spatial resolution of 304 $\mu$m×304 $\mu$m. The final cells were overlapped by 50% effectively increasing the data yield and giving a vector grid spacing of 152 $\mu$m.

The arrangement of the light sheet and the camera is shown in **Fig. 1**. The position of the light sheet optic was chosen so that shadows from the returning bars of the wake generator were not present at the phases of interest. The light sheet optic was also positioned out of the main exit flow to minimize blockage. The camera was positioned to look parallel to the blade surface through the glass sidewall to minimize flare.

## Time Mean Surface Pressure Distribution

The surface distribution of static pressure coefficient, $C_p$, is shown in **Fig. 3** for four different configurations together with the envelope of unsteady pressures measured for the case $s_b/s_c = 1$. For steady inflow, the pressure distribution is shown for both the suction and pressure surfaces. Peak suction is located at $s/s_0 = 0.45$. A laminar separation bubble is evident over the rear portion of the suction surface with separation at $s/s_0 = 0.60$. The pressure plateau, typically associated with the laminar shear layer of a steady separation bubble, extends to $s/s_0 \approx 0.82$. At this location the pressure begins to recover as the separated shear layer undergoes transition and reattaches by $s/s_0 = 0.88$.

For both cases with incoming wakes, only the suction surface $C_p$ distribution is shown. For the case of $s_b/s_c = 1$ ($f_r = 0.68$) the time-mean surface pressure distribution shows no sign of the separation bubble. In the time-mean, the separation bubble has been suppressed by the wakes. For the case of $s_b/s_c = 2$ ($f_r = 0.34$), where the steady-state boundary layer has more opportunity to re-establish between wake passing events, the time average

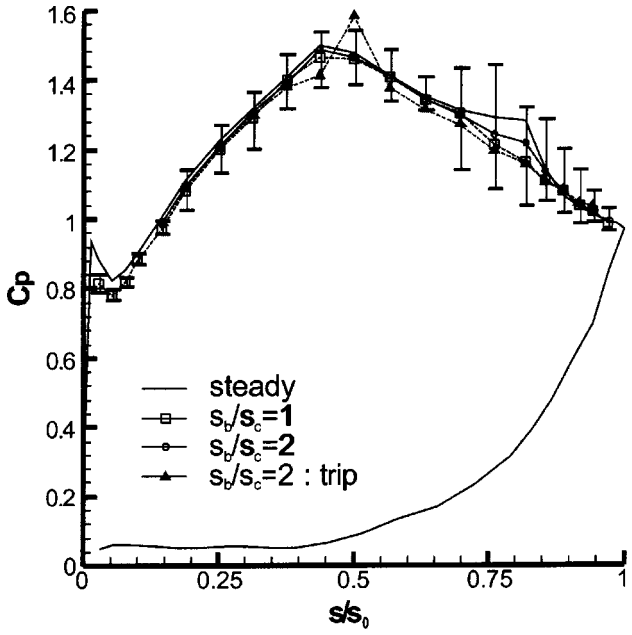


**Fig. 3 Pressure distribution measured on the T106 cascade at Re=1.6×10$^5$**

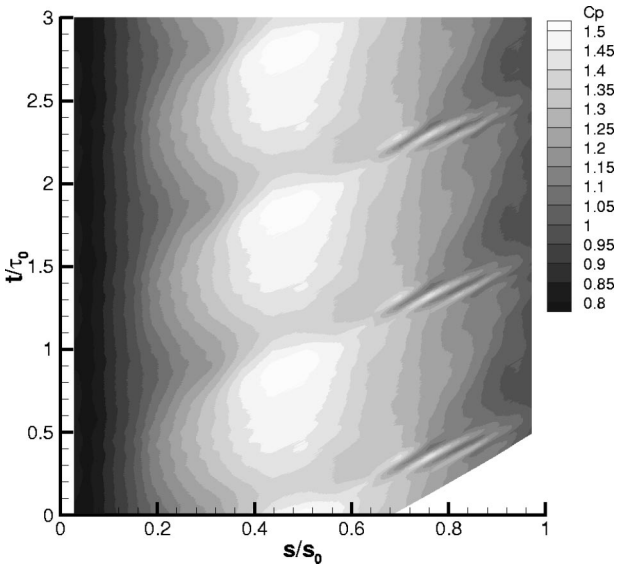


**Fig. 4 ST diagram of ensemble average $C_p$. Re=1.6×10$^5$, $s_b/s_c=1$.**

surface pressure distribution indicates the presence of a separation bubble. The separation and reattachment point for this case are indistinguishable from the case for steady inflow; however, the pressure plateau is not as prevalent as in the steady flow case. This is due to the pneumatic averaging of the measurement system. The flow is periodically attached by the presence of the passing wake. The final surface pressure distribution on **Fig. 3** is for the case of $s_b/s_c=2$ with the boundary layer tripped by a 0.056 mm diameter wire attached to the blade surface at $s/s_0\approx0.44$. The resulting turbulent boundary layer shows no signs of separation. The $C_p$ distribution is altered by the presence of the trip wire, with local deceleration and acceleration before and after the trip-wire.

Near the leading edge of the suction surface, the $C_p$ distributions differ for the steady inflow case and the cases with bar passing. The differences are due to an effective change in incidence of the incoming flow due to the bars of the wake generator turning the inlet flow. This alteration of the incidence is small and does not significantly alter the pressure distribution downstream of peak suction, which is the region of primary interest. Nor, as the later results will show, does it affect the boundary layer that enters this region.

## Ensemble-Average Suction Surface Pressures

The ensemble-averaged unsteady surface pressures measured on the suction surface for the case of $s_b/s_c=1$ are presented as contours of $C_p$ on an ST diagram in **Fig. 4**. The convection of the wake is evident and, upstream of the separation point, is explained in terms of the negative jet model of Meyer [12]. The negative jet, incident on the suction surface, causes the surface pressure to increase locally as the wake convects over the suction surface. The increase in surface pressure corresponds to the reduction in $C_p$ observed in **Fig. 4**. The nature of the pressure traces in the region where the wake passes the steady flow separation bubble is markedly different from upstream where the boundary layer is laminar and attached. The fact that these pressure fluctuations are evident in the ensemble-averaged pressure traces indicates that they are formed by deterministic coherent flow structures. As the wake arrives at the steady flow separation location, a series of large amplitude pressure oscillations arise. At $s/s_0=0.76$ the peak-to-peak amplitude of these pressure fluctuations is $\Delta C_p=0.3$. It should be noted that the contours of **Fig. 4** are drawn with the mesh aligned at half the mean flow velocity. This reduces the aliasing due to the contour algorithm that results from the temporal resolution being much finer than spatial resolution.

Ensemble-averaged pressure traces measured over the rear half of the suction surface, are shown in **Fig. 5**. This is a portion of the data shown in **Fig. 4**. Here, the dash-dot lines indicate the surface location of each Kulite while the solid lines are the ensemble-averaged traces of the measured surface pressure fluctuation. The vertical scale of the pressure traces is arbitrary but the same for all of the traces.

The line, labeled *A*, in **Fig. 5** is a trajectory line drawn at the freestream velocity. The onset of the large amplitude pressure oscillations in **Fig. 5**, fall along line A showing that the onset of the pressure oscillations is dictated by the wake convecting with the

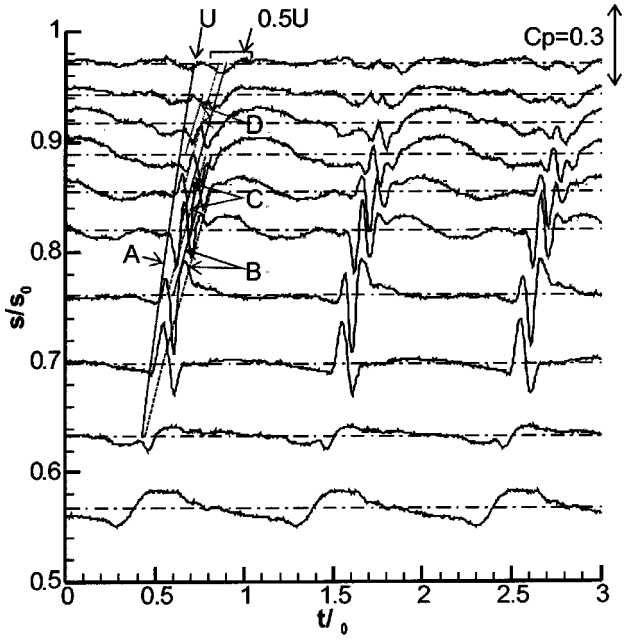


**Fig. 5 Ensemble-average pressure traces measured over the rear of the suction surface. Re=1.6×10$^5$, $s_b/s_c=1$.**

freestream. The onset of the pressure oscillations is thus not controlled by the convection of turbulent spots nor instability waves within the boundary layer as these phenomena convect slower than the freestream. It can also be deduced that the onset is not controlled by an acoustic mechanism as for a low Mach number flow these would travel ahead of the convecting wake.

The pressure fluctuations are observed to originate between the transducers located at $s/s_0=0.57$ and $s/s_0=0.63$. The amplitude of the fluctuations increases up to $s/s_0=0.70$ and thereafter remains approximately constant. The period of the oscillations is also constant downstream of $s/s_0=0.70$. The amplitude of the fluctuations reduces slightly downstream of $s/s_0=0.82$. This region corresponds to the pressure recovery region of the steady separation bubble and is typically associated with transition in a separation bubble. With increased levels of turbulence and turbulent mixing that results from transition, the ensemble-average pressure fluctuations decrease in amplitude.

The trajectory lines labeled *B* and *C* are drawn at half the local freestream velocity. These lines are positioned to trace the convection of the maxima and minima of the pressure fluctuations and show that the coherent structures responsible for the pressure fluctuations travel at half the freestream velocity.

The number of maxima and minima in the ensemble averaged pressure traces is not the same at every sensor location in **Fig. 5**. At $s/s_0=0.70$ there is only one maxima and one minima observed, however, at $s/s_0=0.82$ there are three sets of maxima and minima. The appearance of more than one coherent structure is due to the different trajectories of the onset and convection of the structures. Once formed the structures convect slower than the wake thus allowing the wake to generate new structures at points further downstream as it passes over the undisturbed inflexional profiles of the separating boundary layer.

By extending the trajectory lines *C* to intersect line *A*, the origin of line *C* is seen to be at $s/s_0\approx0.60$. However, by $s/s_0\approx0.86$ the feature occurring along line *C* disappears. The convection speed of *C* is lower than the convection speed of the leading edge of a turbulent spot. The disappearance of *C* is attributed to turbulent spots formed at an upstream location in the boundary layer overtaking the coherent structure. This turbulence destroys the coherence of structure *C*.

**The Effect of Bar Passing Frequency.** **Figure 6** shows the ensemble-averaged unsteady surface pressures for the identical flow condition in **Fig. 5**, but with double the bar spacing so that $s_b/s_c=2$ ($f_r=0.34$). Both the time axis and the scale of the pressure traces are identical to that of **Fig. 5**.

The pressure fluctuations are again observed as the wake passes over the region of the steady flow separation bubble. No change in the onset location is evident and the period of oscillation is the same as before. The period of the pressure fluctuations are thus independent of the wake passing frequency in the range relevant for LP turbines. The pattern of the pressure oscillations is also the same as for the higher bar passing frequency up to $s/s_0=0.86$ but their magnitude is larger for the lower bar passing frequency.

The lower bar passing frequency gives the boundary layer more time to re-establish steady-state conditions between the wake passing events. In this time a series of pressure oscillations, smaller in magnitude and of lower frequency arise downstream of $s/s_0=0.88$. The pattern of these pressure traces is different to those resulting from the wake-separation bubble interaction and are more nearly sinusoidal. The fact that these oscillations may be ensemble averaged is remarkable and indicates that they too are deterministic and caused by coherent structures in the re-establishing boundary layer. Based on Stieger and Hodson's [13] observations of Tollmien-Schlichting waves on a flat plate with identical pressure distribution, it is proposed that these oscillations in surface pressure are due to natural transition phenomena.

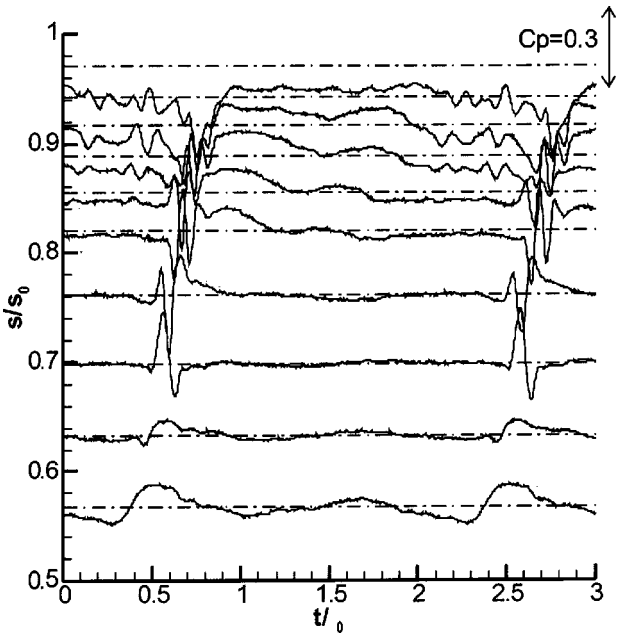


**Fig. 6 Ensemble-average pressure traces for Re=1.6×10$^5$, $s_b/s_c=2$**

**The Effect of a Boundary Layer Trip.** A trip wire was fixed to the surface of the blade to cause transition of the boundary layer so that downstream of the trip wire, the boundary layer is turbulent throughout the wake passing cycle suppressing the formation of a separation bubble. **Figure 7** shows ensemble averaged pressure traces for identical flow conditions to those presented in **Fig. 6**, but with a trip wire at $s/s_0=0.44$. Immediately obvious is the absence of the pressure fluctuations. The coherent structures responsible for the pressure fluctuations are thus only formed when the wake interacts with the separating boundary layer.

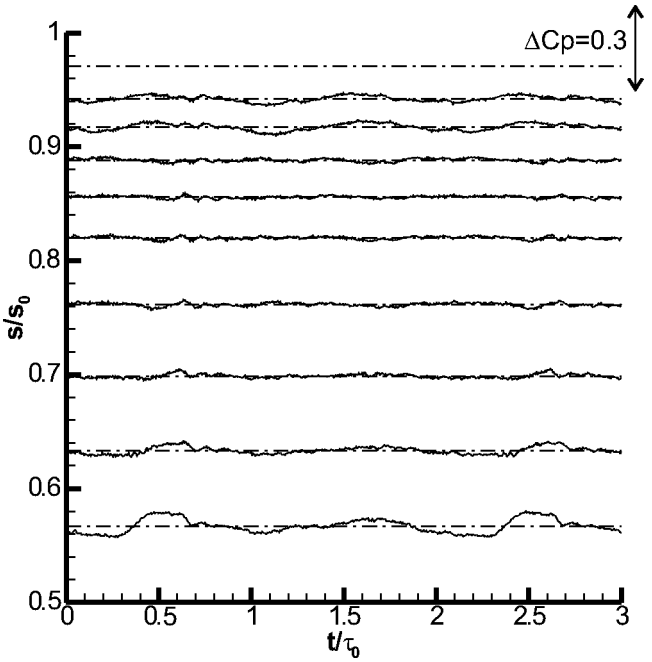


**Fig. 7 Ensemble-average traces—tripped boundary layer, Re =1.6×10$^5$, $s_b/s_c=2$**

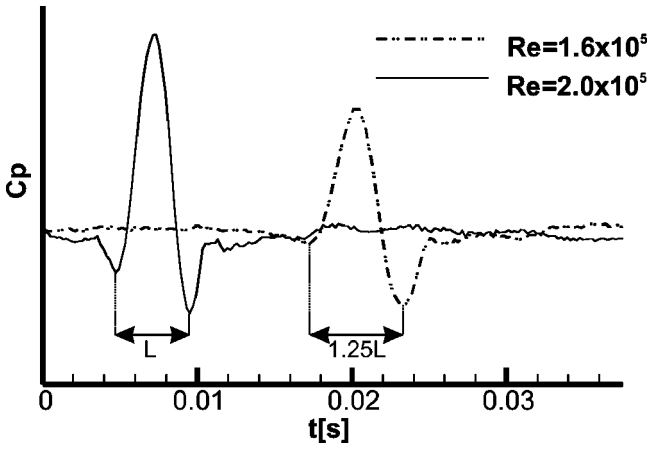


**Fig. 8 Effect of Reynolds number on the period of pressure oscillations at $s/s_0=0.70$**

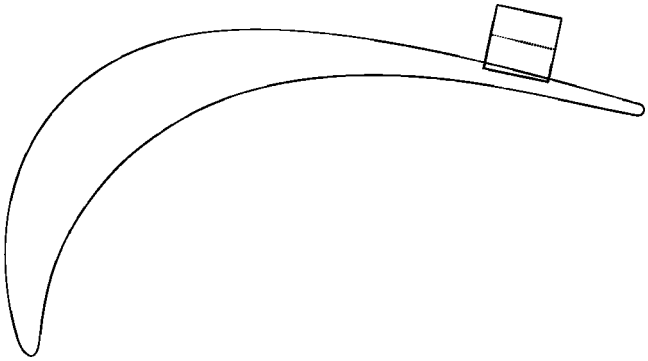

**Fig. 9 Location of PIV measurement on the T106 blade. The line dividing the field of view indicates the portion of the measurement shown below.**

**The Effect of Reynolds Number.** It was established above that the period of the large amplitude pressure fluctuations is independent of the bar passing frequency. However, the period of the pressure fluctuations is dependent on Reynolds number. The pressure traces at a Reynolds number of $\mathrm{Re}=1.6\times10^5$ and at a Reynolds number $\mathrm{Re}=2.0\times10^5$, are compared at $s/s_0=0.70$ in **Fig. 8** where the period of interest is shown on a dimensional time axis. It is apparent that the period of the pressure oscillations is not the same at the different Reynolds numbers. The time offset between the two sets of pressure traces is due to difference in the absolute time of the trigger used for the ensemble averaging of the different Reynolds number flow conditions. The period of oscillations at $s/s_0=0.70$ are approximately inversely proportional to the Reynolds number.

The convective time scale

$$\tau_{\mathrm{conv}} \propto \frac{C}{U} \tag{1}$$

and viscous diffusion time scale

$$\tau_{\mathrm{visc}} \propto \frac{\delta^{*2}}{\nu} \propto \frac{\left(\frac{x}{\sqrt{\mathrm{Re}_x}}\right)^2}{\nu} \propto \frac{x}{U} \tag{2}$$

are indistinguishable for a given velocity distribution as the ratio of local surface position to chord is constant. It is thus not possible to determine if the large pressure fluctuations are related to viscous or convective phenomena.

A correlation for the period of the disturbance with the maximum amplification rate in the Falkner-Skan velocity profiles over the whole range of pressure gradient parameter is given by Walker [14] as

$$\tau_{\mathrm{crit}} \propto \frac{1}{f_{\mathrm{crit}}} = \frac{\nu}{3.2\,\mathrm{Re}_{\delta^*}^{-3/2} U^2}. \tag{3}$$

This correlation was shown by Stieger and Hodson [13] to reasonably predict the frequency of Tollmien-Schlichting waves in similar unsteady flow conditions. The period of a viscous instability in a highly decelerated boundary layer is thus expected to vary nonlinearly with Reynolds number. The observed linear relationship between the period of the pressure fluctuations and Reynolds number demonstrates that a viscous stability mechanism is not responsible for the large-amplitude pressure fluctuation. Villermaux [15] showed that inviscid instability processes have a negligible Reynolds number dependence and so a pure inviscid instability mechanism is excluded.

## Visualization of the Instantaneous Flow Field Using PIV

PIV is essentially a quantitative flow visualisation technique whereby the correlation of two images of a seeded flow is used to determine the fluid velocity. In order to identify the structures responsible for the pressure fluctuations presented above PIV measurements were made over a small portion of the rear suction surface of the T106 cascade as shown in **Fig. 9**.

The results of a PIV measurement in the region between $s/s_0=0.8$ and $s/s_0=0.9$ at the phase $t/\tau_0=0.85$ are shown in **Fig. 10**. The instantaneous vector map is shown in the upper plot of **Fig. 10**. Two vortices are visible in the boundary layer. Instantaneous streamlines calculated from the vector map are shown in the lower plot of **Fig. 10** and confirm that the structures are vortices embedded in the boundary layer. A number of PIV measurements were made and not all showed identical features to the results of **Fig. 10**. The vortices were not always evident and their size and position varied.

The vorticity of the vortices is of the same sense as the boundary layer vorticity. The vortex centers are separated by approximately 5% of the suction surface length with their centres at ap-

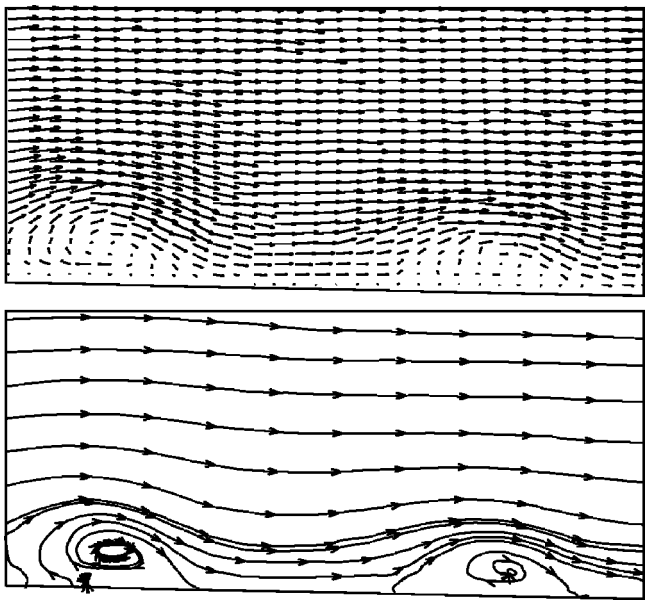

**Fig. 10 Instantaneous vector map and computed streamlines from PIV measurement over the rear suction surface at $t/\tau_0=0.85$. $\mathrm{Re}=1.6\times10^5$, $s_b/s_c=1$.**

proximately a third of the local time-average boundary layer thickness. It is argued below that these vortices are responsible for the measured pressure fluctuations.

### The Source of Pressure Fluctuations

Saathoff and Melbourne [16] conducted an investigation into the cause of large pressure fluctuations occurring near the leading edges of sharp-edged bluff bodies. A long two-dimensional rectangular prism was mounted in a wind tunnel and the surface pressure was measured under the separation bubble that formed at the leading edge. Flow visualization was performed with a laser light sheet and high-speed cine camera. The cine camera was used to simultaneously capture flow visualisation pictures and an oscilloscope output from the pressure transducers. The results showed that large surface pressure fluctuations were caused by vortices in close proximity to the surface of the model. The rollup of the separated shear layer, initiated by perturbations in the approaching flow, was identified as the source of these vortices.

Luton et al. [17] conducted a numerical investigation of the interaction of a convected spanwise vortex and a Blasius boundary layer. By solving the full Navier-Stokes equations, they showed a minimum in surface pressure to coincide with the location of the vortex center. The magnitude of the pressure fluctuations associated with the vortex was shown to depend on the distance of the vortex from the wall as well as the strength of vortex. They reported fluctuations as high as 55% of the dynamic head for one of the cases calculated.

The measurements presented here are thus confirmed by the literature and the vortices identified by the PIV flow visualization are responsible for the large amplitude pressure fluctuations measured on the surface of the T106 cascade.

### The Formation of Coherent Structures in Boundary Layers

The classical studies in boundary layer stability conducted by Schubauer and Skramstad [18] provided experimental evidence of coherent structures in boundary layers, in this case Tollmien-Schlichting waves evolving from disturbance generated by a vibrating ribbon. The development of a small square wave disturbance in a Blasius boundary layer was investigated experimentally by Gaster [20] In this case, the disturbance was found to develop into a downstream propagating wave packet. Gaster found that the initial structure of the wave packet was well predicted by tracking the development of the amplified wave numbers using linear stability theory. The linear instability mechanism associated with the boundary layer lead to the amplification of particular frequencies. The exponential amplification rate associated with these frequencies lead to the dominance of the most amplified mode. Such a selective amplification process acts as a filter that leads to a single mode becoming dominant and this leads to the formation of a coherent structure being formed in the boundary layer, in this case a traveling wave packet.

Watmuff [19] conducted a detailed hot-wire and flying cross wire measurements of the evolution of a periodically applied point disturbance in a boundary layer with a laminar separation bubble. Despite an initial region of decay, the disturbance was found to amplify after the separation point before developing into a three-dimensional rollup vortex loop embedded in the boundary layer. Furthermore, the vortex structure was discernable up to 20 boundary layer thicknesses downstream of the time mean reattachment point. The maximum amplitude of the disturbance was observed to follow the trajectory of the inflexion points in the velocity profile and contours of the measured spanwise vorticity, along the centreline of the disturbance, revealed a cat's eye pattern, characteristic of a Kelvin-Helmholtz breakdown of the shear layer. This evidence allowed Watmuff to conclude that the instability mechanism governing the amplification of the wave packet in a separation bubble is predominantly inviscid.

The work of Gaster [20] and Watmuff [19] shows that the selective amplification associated with boundary layer stability, both viscid and inviscid, provides a mechanism able to select and amplify particular disturbance frequencies that subsequently form coherent structures in the boundary layer. It is proposed that the deterministic coherent structures responsible for the measured pressure fluctuations, namely the rollup vortices identified by the PIV measurements are formed by the selective amplification of such an instability mechanism. By contrast to the measurements of Watmuff [19], the wake is a uniform two-dimensional disturbance and as a consequence it is expected that the rollup would initially be two-dimensional and uniform across the span of the blade in the bar passing cascade.

### The Mechanism of Surface Pressure Oscillations

An overview of the mechanism whereby pressure fluctuations are formed is presented in **Fig. 11**. The central plot shows the measured mean pressure distribution over the rear suction surface of the T106 LP turbine cascade for steady flow. Also shown is the hypothetical inviscid pressure distribution. Short portions of the ensemble averaged time traces of surface pressure are also shown for each measurement location. The lower plot shows a series of measured hot wire boundary layer profiles at different positions in the separation bubble corresponding to the boundary layer state just before the arrival of the wake. The dotted line, drawn by hand, passes approximately through the inflexion points of these boundary layer profiles. Just before the arrival of the wake, the laminar shear layer extends from the steady separation point to the end of the pressure plateau (from $s/s_0 \approx 0.60$ to $s/s_0 \approx 0.82$). The final set of profiles at $s/s_0 = 0.88$ does not have an inflexion point at any time during the wake passing cycle. This is representative of the reattached boundary layer after a separation bubble. This description of the profiles prior to the arrival of the wake agrees with what would be expected for a separation bubble within a steady flow and a free laminar shear layer exists before the arrival of the wake.

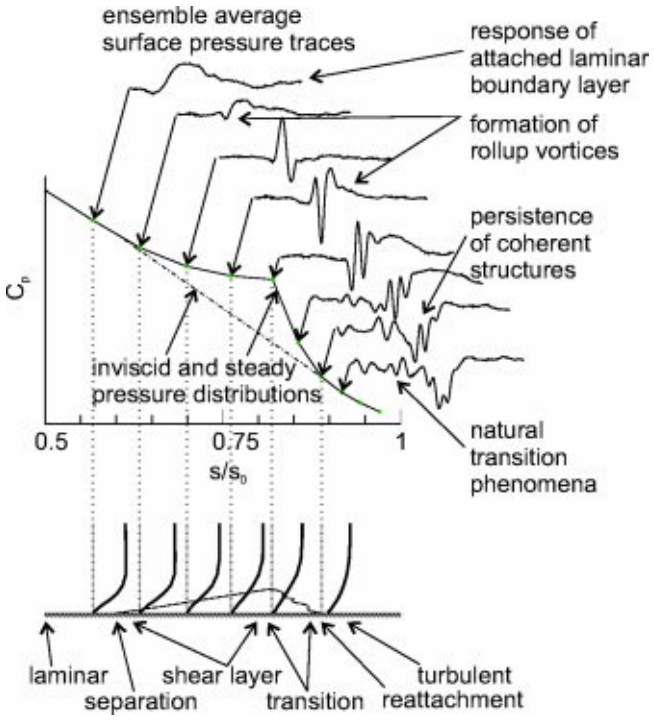


**Fig. 11 Schematic showing the evolution of pressure oscillations due to the interaction of the wake and separating boundary layer**

Between $s/s_0=0.63$ and $s/s_0=0.70$ the amplitude of the pressure fluctuations due to the wake passing rises significantly. Prior to the arrival of the wake, the boundary layer profiles are inflexional over this region of the blade surface. The intense amplification observed in this region is attributed to the instability mechanism resulting from the inflexional velocity profiles.

By $s/s_0=0.70$ the free shear layer has rolled up into a series of rollup vortices. The point disturbances in Watmuff's work were observed to grow laterally in the adverse pressure gradient and form vortex loops, however, for the case of wake passing, where the disturbance sources may be viewed as a two-dimensional strip of convecting wake fluid, the amplified disturbances would not break down into vortex loops, but rather a more two-dimensional spanwise rollup vortex. Rollup vortices formed in a shear layer convect at about the mean velocity of the shear layer, which would be approximately half the freestream velocity. The coherent structures responsible for the pressure fluctuations were previously identified to convect at half the freestream velocity. This further supports the argument that the coherent structures responsible for the large-amplitude surface pressure fluctuations are rollup vortices formed in the separated shear layer associated with the inflexional boundary layer velocity profiles.

The pressure fluctuations labeled 'natural transition phenomena' in **Fig. 11** are believed to be caused by Tollmien-Schlichting type waves. As would be expected, the pressure traces observed in this region have a different character to those associated with the rollup vortices.

## Conclusions

Measurements of the unsteady surface pressure on the T106 LP turbine cascade showed the laminar boundary layer upstream of the steady flow separation point to respond to the wake passing in an essentially inviscid manner. However, unexpected large amplitude fluctuations in surface pressure were measured as the wake convected over the region of the steady flow separation bubble. The pressure oscillations were suppressed when the boundary layer was tripped indicating that a separating laminar boundary layer was necessary for the development of the pressure oscillations. The pressure oscillations were found to be generated as the wake passed over the region covered by the separation bubble in the case of steady flow and to convect at half the local freestream velocity. The pressure oscillations were unaltered by a change in the bar passing frequency.

PIV measurements were used to identify vortices present in the boundary layer. It was confirmed by reference to literature that these vortices are responsible for the pressure oscillations.

In the ensemble-averaged measurements, the vortices appear as coherent and deterministic structures. Hot-wire boundary layer traverses confirmed the existence of inflexional velocity profiles prior to the arrival of the wake. It is proposed that the instability mechanism associated with the inflexional velocity profiles amplifies perturbations to the laminar shear layer caused by the wake passing. This amplification leads to the formation of rollup vortices embedded in the boundary layer and these rollup vortices are responsible for the large amplitude pressure fluctuations.

## Acknowledgments

The authors would like to thank John Black for providing access to the PIV equipment and for his help in setting up the PIV. The first author is also indebted to financial support provided by the ORS and the Peterhouse Research Studentship. The funding of EPSRC grant GR/L96660/01 is also gratefully acknowledged.

## Nomenclature

$C$ = chord
$Cp$ = pressure coefficient $Cp=(P_0-P)/(P_0-P_{2is})$
$f$ = bar passing frequency
$f_r$ = reduced frequency $f_r=fC/V_{2is}$
$P$ = local surface pressure
$P_0$ = total pressure
$P_{2is}$ = isentropic exit pressure
Re = Reynolds number $\mathrm{Re}=V_{2is}C/\nu$
$\mathrm{Re}_{\delta^*}$ = displacement thickness Reynolds number
$s$ = distance along blade surface
$s_0$ = suction surface length
$s_b$ = bar pitch
$s_c$ = cascade pitch
$t$ = time
$\tau_0$ = bar passing period
$U_b$ = bar speed
$V_{2is}$ = isentropic exit velocity
$V_{x1}$ = inlet axial velocity
$\delta^*$ = displacement thickness
$\phi$ = flow coefficient $\phi=V_{x1}/U_b$
$\nu$ = kinematic viscosity

## References

[1] Halstead, D. E., Wisler, D. C., Okiishi, T. H., Walker, G. J., Hodson, H. P., and Shin, H.-W., 1997, "Boundary Layer Development in Axial Compressors and Turbines: Part I—Composite Picture," ASME J. Turbomach., **119**, pp. 114–127.
[2] Halstead, D. E., Wisler, D. C., Okiishi, T. H., Walker, G. J., Hodson, H. P., and Shin, H.-W., 1997, "Boundary Layer Development in Axial Compressors and Turbines: Part II—Compressors," ASME J. Turbomach., **119**, pp. 114–127.
[3] Halstead, D. E., Wisler, D. C., Okiishi, T. H., Walker, G. J., Hodson, H. P., and Shin, H.-W., 1997, "Boundary Layer Development in Axial Compressors and Turbines: Part III—LP Turbines," ASME J. Turbomach., **119**, pp. 114–127.
[4] Halstead, D. E., Wisler, D. C., Okiishi, T. H., Walker, G. J., Hodson, H. P., and Shin, H.-W., 1997, "Boundary Layer Development in Axial Compressors and Turbines: Part IV—Computations and Analyses," ASME J. Turbomach., **119**, pp. 114–127.
[5] Mayle, R. E., 1991, "The Role of Laminar-Turbulent Transition in Gas Turbines Engines," ASME J. Turbomach., **113**, p. 509.
[6] Walker, G. J., 1993, "The Role of Laminar Turbulent Transition in Gas Turbine Engines: A Discussion," ASME J. Turbomach., **115**, pp. 207–217.
[7] Schulte, V., and Hodson, H. P., 1998, "Unsteady Wake-Induced Boundary Layer Transition in High Lift LP Turbines," ASME J. Turbomach., **120**, pp. 28–35.
[8] D'Ovidio, A., Harkins, J. A., and Gostelow, J. P., 2001, "Turbulent Spots in Strong Adverse Pressure Gradients: Part I—Spot Behavior," ASME Paper 2001-GT-0406.
[9] D'Ovidio, A., Harkins, J. A., and Gostelow, J. P., 2001, "Turbulent Spots in Strong Adverse Pressure Gradients: Part II—Spot Propagation and Spreading Rates," ASME Paper 2001-GT-0406.
[10] Stieger, R. D., 2002, "The Effects of Wakes on Separating Boundary Layers in Low Pressure Turbines," Ph.D. thesis, Cambridge University, Cambridge, UK.
[11] LaVision, 2001, "DaVis Flowmaster," v. 6.03, February 2001, LaVision GmbH, Anna-VandenHoeck-Ring 19, 37081 Goettingen, FRG.
[12] Meyer, R. X., 1958, "The Effects of Wakes on the Transient Pressure and Velocity Distributions in Turbomachines," ASME J. Basic Eng., Oct. pp. 1544–1552.
[13] Stieger, R. D., and Hodson, H. P., 2003, "Unsteady Dissipation Measurements on a Flat Plate Subject to Wake Passing," submitted to 5th European Turbomachinery Conference, Prague.
[14] Walker, G. J., 1989, "Transitional Flow in Axial Turbomachine Blading," AIAA J., **27**(5), pp. 595–602.
[15] Villermaux, E., 1998, "On the Role of Viscosity in Shear Instabilities," Phys. Fluids, **10**(2) pp. 368–373.
[16] Saathoff, P. J., and Melbourne, W. H., 1997, "Effects of Free-Stream Turbulence on Surface Pressure Fluctuations in a Separation Bubble," J. Fluid Mech., **337**, pp. 1–24.
[17] Luton, A., Ragab, S., and Telionis, D., 1995, "Interaction of Spanwise Vortices With a Boundary Layer," Phys. Fluids, **7**(11) pp. 2757–2765.
[18] Schubauer, G. B., and Skramstad, H. K., 1947, "Laminar Boundary-Layer Oscillations and Transition on a Flat Plate," NACA Report No. 909.
[19] Watmuff, J. H., 1999, "Evolution of a Wave Packet Into Vortex Loops in a Laminar Separation Bubble," J. Fluid Mech., **397**, pp. 119–169.
[20] Gaster, M., 1981, "On Transition to Turbulence in Boundary Layers," *Transition and Turbulence*, R. E. Meyer, ed., Academic Press, San Diego, CA.

**Claus H. Sieverding**
e-mail: sieverding@vki.ac.be

**Davide Ottolia**

**Carlo Bagnera**

**Andrea Comadoro**

**J.-F. Brouckaert**

von Karman Institute for Fluid Dynamics,
Chaussée de Waterloo 72,
B-1640 Rhode-Saint-Genèse, Belgium

**Jean-Michel Desse**
desse@onera.fr
ONERA, Institut de Mécanique des Fluides de Lille,
Boulevard Paul Painlevé 5,
F-59045 Lille Cedex, France

# Unsteady Turbine Blade Wake Characteristics

*The paper presents an experimental investigation of large coherent structures, commonly referred to as "von Karman vortex street," in the wake of a turbine blade at high subsonic Mach number ($M_{2,is}=0.79$) and high Reynolds number ($RE=2.8\times10^6$ and their effect on the steady and unsteady pressure and temperature distribution in the wake. Ultra short smoke visualizations and two interferometric measurement techniques, holographic interferometry and white light differential interferometry provide insight into the vortex formation and shedding process. In addition, the interferometric measurement provides quantitative information on the stream wise evolution of the minimum density associated with the vortices and on their lateral spreading. Wake traverses are performed with a four-head fork probe carrying a Kiel probe and a fast response Kulite pressure probe for pressure measurements and a thermocouple probe and a cold wire resistance probe for temperature measurements. The results confirm the observation of energy separation in the wake as found by other researchers. The experimental data are a unique source for the validation of unsteady Navier-Stokes codes.* [DOI: 10.1115/1.1737783]

## Introduction

The presence of large coherent structures in turbine blade wakes, known as von Karman vortices, has experimentally been put into evidence by many authors using various types of techniques like: smoke visualizations at low speed by Han and Cox [1]; ultra-short Schlieren photographs at medium subsonic and transonic Mach numbers by Lawaczeck and Heinemann [2], Heinemann and Bütefisch [3], Carscallen et al. [4], Cicatelli and Sieverding [5], and Cicatelli and Sieverding [6], interferometric density measurements by Desse [7], Sieverding et al. [8], and Sieverding et al. [9]; LDV measurements in a large-scale low-speed turbine cascade without and with trailing edge flow ejection by Ubaldi and Zunino [10], Ubaldi et al. [11], and Zunino et al. [12], and PIV measurements by Raffel et al. [13]. Cicatelli and Sieverding [6] and Sieverding et al. [9] are the first to provide detailed steady and unsteady measurements around the blade trailing edge and on the rear suction side of a large-scale turbine nozzle guide vane at medium and high subsonic downstream Mach numbers. Probably the most significant result of the latter publication is the observation of a change from the typical time-averaged isobaric base pressure region at low and medium outlet Mach numbers to a non-isobaric region at high subsonic Mach numbers.

Carscallen et al. [14] are the first to measure the effect of the trailing edge vortices on the unsteady pressure and temperature distributions in the wake of a transonic turbine blade. For this purpose the authors made use of a fast-response dual hot-film probe developed by Buttsworth and Jones [15]. The authors confirmed the existence of energy separation in the wake with cold spots up to $-15$ deg in the wake center and hot spots of $+8$ deg at the edges of the wake. Known as the Eckert-Weise effect, Eckert and Weise [16], the phenomenon of energy separation had been investigated hitherto mostly in the context of vortex shedding from cylinders although it has been observed in many other applications, see Eckert [17]. Kurosaka et al. [18] gave a very detailed analysis of this phenomenon related to the vortex street behind a cylinder. Ng et al. [19] measured it quantitatively with a fast response dual hot wire aspirating probe and found similar temperature fluctuations as Carscallen behind a cylinder for an upstream Mach number of 0.4 only.

The results presented in this paper are a further contribution to the quantitative determination of unsteady wake characteristics behind turbine blades. The paper is a followup of that by Sieverding et al. [9] which treated in detail with the effect of the vortex shedding on the unsteady blade pressure distribution and is equally based on the outcome of the European Research Project BRITE/EURAM CT96-0143 on ''Turbulence Modelling of Unsteady Flows in Axial Turbines.''

## Experimental Setup and General Flow Conditions

A detailed description of the experimental setup and flow conditions can be found in Sieverding et al. [9]. The main geometric and aerodynamic characteristics are repeated in **Tables 1 and 2** for completeness of the paper. A photograph of the test section is shown in **Fig. 1.**

**Two-Dimensionality.** Because of the low aspect ratio of $h/c=0.714$ boundary layer fences were set at 5% of the span on the blade suction side to limit the spanwise extension of secondary flows. As a result the secondary flow regions are reduced by 50% and occupy only 5 to 7% of the blade height on each side in Sieverding et al. [9].

**Periodicity.** The downstream Mach number distribution varied over 2 pitches by less than $+/-2\%$. The blade-to-blade surface Mach number variation of $\Delta M=0.027$ between the two central blades was judged satisfactory for such a small number of blades.

**Blade Velocity Distribution.** The blade surface velocity distribution is presented in the form of the isentropic Mach number distribution in function of the axial chord in **Fig. 2**. The design of the blade with a flat rear-suction surface results in a strong suction-side velocity peak at $x/c_{ax}=0.61$ with nearly sonic conditions followed by a constant Mach number plateau of $M_1=0.8$ up to the trailing edge circle where the flow undergoes a strong reacceleration before separating from the blade surface. On the pressure side the flow accelerates continuously from the leading edge to the trailing edge. The crossing of the pressure and suction-side curves near the trailing edge is typical for blades with straight rear-suction side.

Contributed by the International Gas Turbine Institute and presented at the International Gas Turbine and Aeroengine Congress and Exhibition, Atlanta, GA, June 16–19, 2003. Manuscript received by the IGTI December 2002; final revision March 2003. Paper No. 2003-GT-38934. Review Chair: H. R. Simmons.

  

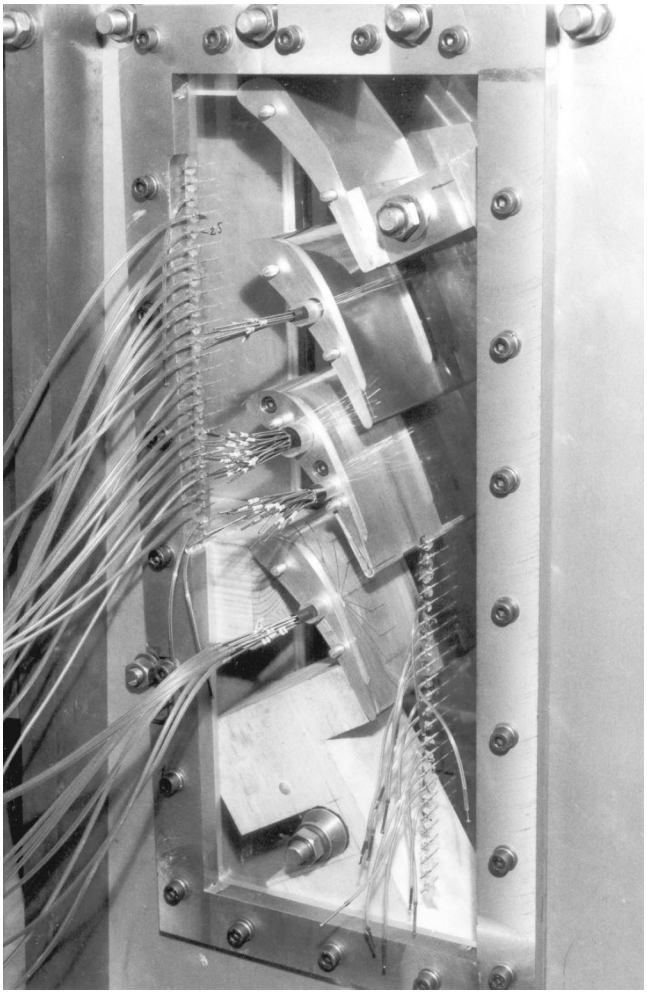

**Fig. 1 Photograph of test section**

Boundary layer profiles were measured with a flattened pitot probe of 0.25-mm probe head thickness at a distance equal to one trailing edge diameter upstream of the trailing edge circle. The uncertainty of the probe positioning is $+/-0.05$ mm.

The boundary layer profiles for nominal outlet flow conditions are presented in **Fig. 3**. The physical boundary layer thickness is about 2.2 mm on the suction side and 0.7 mm on the pressure sides. The compressible shape factor is, respectively, $H=1.31$ and 1.53 for the suction side and pressure sides. This is a clear indication for a turbulent state of the boundary layer on both sides before trailing edge separation.

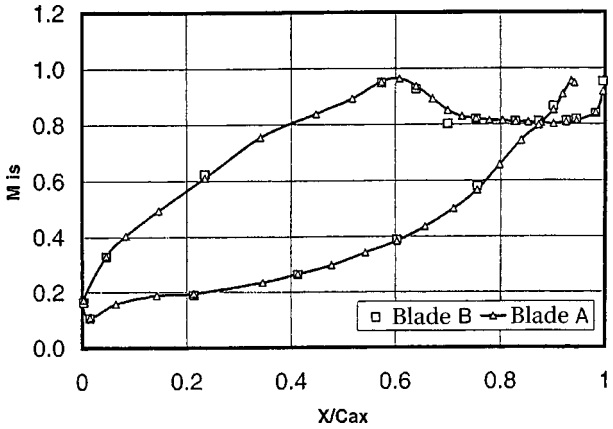


**Fig. 2 Blade Mach number distribution for $M_{2,is}=0.79$**

## Wake Flow Visualisations and Vortex Shedding Frequency

Contrary to the schlieren photographs presented by Sieverding et al. [9] the vortical structures in the wake are at present put into evidence through smoke visualizations, **Fig. 4**. The smoke is emitted from a tube in the upstream settling chamber and seeds only the flow close to the blade surfaces. The laser sheet is coming from the right side as indicated by the large arrow and illuminates the blade suction side at midspan. The pressure side lies in the shadow. A Nd:YAG laser produces the light sheet. The pictures are taken with a PCO video camera. The laser was triggered at a frequency rate of 8.2 Hz, while the maximum acquisition rate for the camera was 4.12 Hz. Given the low frequency of the laser and the camera the individual smoke visualizations in **Fig. 4** do not belong to the same vortex shedding cycle. They are taken at different time instances and are arranged in sequential order. Pictures 6 and 1 are the same. Fluctuations in the smoke density and the lateral spreading of the smoke affect somewhat the continuity in the flow patterns. The objective of the camera is aligned on the center of the circular quartz window, which results in a three-dimensional view of the trailing edge region.

Contrary to schlieren photographs which visualise density changes, smoke pictures show the instantaneous flow patterns and are therefore particularly well suited to show the vortical wake structures. The formation of the vortices and their gradual shedding is put clearly into evidence in **Fig. 4**. Picture 2 shows the start of the enrolment of the pressure side shear layer into a vortical motion. This vortex grows in pictures 3 and 4 and starts to move away from the trailing edge in picture 5 due to the appearance of the suction-side vortex and its entrainment effect of low momentum material from the opposite shear layer. This results in a cutoff of the vorticity supply to the vortex, the pressure-side vortex is shed off the trailing edge.

A close look on the vortex structures reveals that the distances between successive vortices are not equidistant. In fact the distance between a pressure-side vortex following a suction side vortex is always smaller than the distance between the latter and the next downstream pressure-side vortex. A possible reason is that the pressure-side vortex plays a dominant role and exerts an attraction on the suction-side vortex. Already Han and Cox [1] found the pressure vortex to be stronger then the suction-side vortex and attributed this to the blade circulation.

**Vortex Shedding Frequency.** The vortex shedding frequency is measured with a fast response pressure sensor positioned at $x/c_{ax}=0.933$ at the beginning of the pressure-side trailing edge circle. The Strouhal number is defined as

$$\mathrm{St}=(fD)/U \tag{1}$$

where $U$ is derived from the pitch averaged downstream cascade side wall pressure distribution taken at a trailing edge distance $x/c_{ax}=0.2$ and the upstream total pressure. The vortex shedding frequency at $M_{2,is}=0.79$ is 7.6 kHz and the corresponding Strouhal number amounts to $\mathrm{St}\cong 0.219$ which is typical for a turbulent state of the boundary layers on both suction and pressure side near the trailing edge.

## Unsteady Wake Density Fields

**Interferometric Measurement Techniques.** Holographic interferometry (VKI) and white light differential interferometry (ONERA) were used to investigate the variation of the unsteady density distribution in the wake. Details of the holographic technique are given in Sieverding et al. [8]. Information on the white

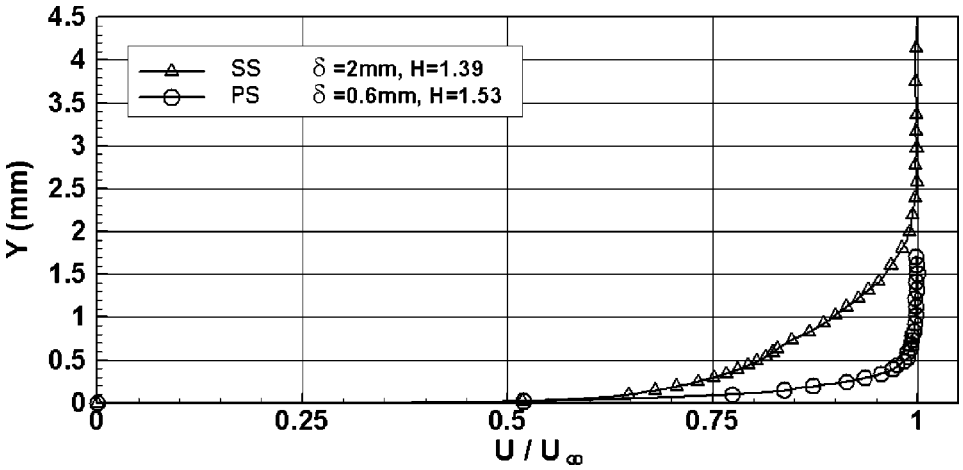


**Fig. 3 Boundary layer profiles at blade trailing edge**

light differential interferometry technique can be found in Desse [20,21]. The time instant for a give moment in a vortex shedding cycle will be defined by the phase angle $\varphi$. The phase angle is evaluated with respect to the pressure variation recorded with a pressure sensor positioned at $x/c_{ax}=0.933$ on the pressure side. The zero phase angle is defined by the time instant when the falling pressure crosses the mean pressure averaged over one vortex shedding cycle. **Figures 5** and **6** present typical interferograms with both techniques, taken at a phase angle of ~90 deg and of 0 deg for the holographic and white light interferometry, respectively.

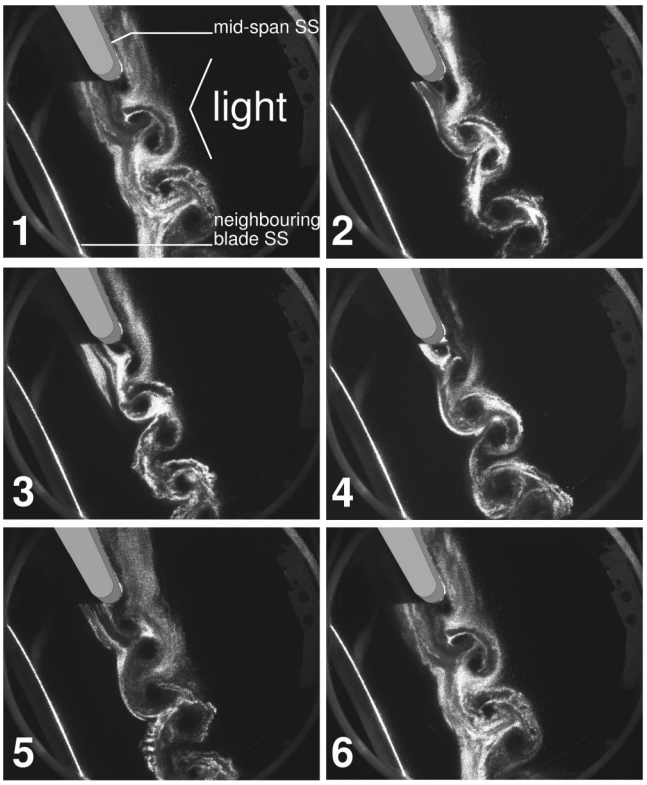


**Fig. 4 Smoke visualizations for different instances over one vortex shedding cycle at outlet Mach number $M_{2,is}=0.79$**

*Holographic Interferometry.* The interferograms obtained with holographic interferometry give only the relative density variations between two successive iso-density lines following the relation

$$\Delta\rho=\lambda/(k1). \tag{2}$$

With $\lambda$–wave length of laser light (Ruby laser $\lambda=6.94\times10^{-7}$ [m]), $k$–Gladestone constant ($2.25\times10^{-4}$ [m$^3$/kg]), and 1–tunnel width (0.1 m) the density variation becomes

$$\Delta\rho=0.030858\ [\mathrm{kg/m^3}]. \tag{3}$$

The reference density is evaluated from pressure measurements with the fast response needle static pressure probe positioned outside of the wake (see flow visualizations), assuming the total temperature to be constant outside the wake. Nondimensionalized by the upstream total density $\rho_0$ the relative density change between two successive density fringes is $\Delta\rho/\rho_{01}=0.0184$.

The interferogram in **Fig. 5** shows the suction side vortex at a phase angle $\varphi\sim90$ deg. The vortex is in its shedding phase. The suction-side shear layer is near its most outward position (see Sieverding et al. [9]). On the pressure side the density patterns point to the start of the formation of a new pressure side vortex. The pressure side vortex of the previous cycle is situated at a trailing edge distance $x/D=2$. The vortex is defined by ten fringes

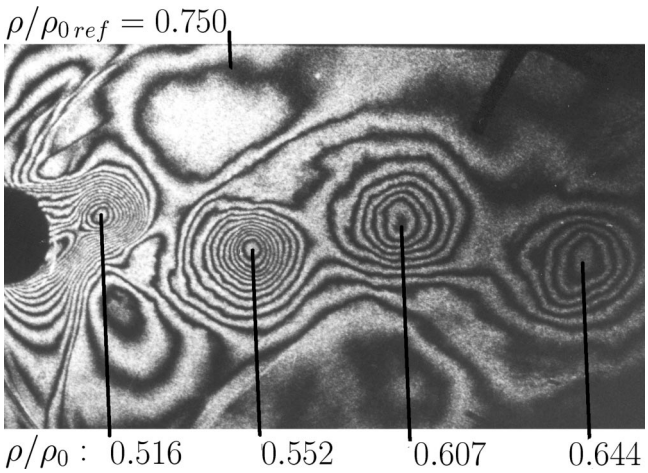


**Fig. 5 Example of holographic interferogram, phase angle $\varphi\sim90$ deg**

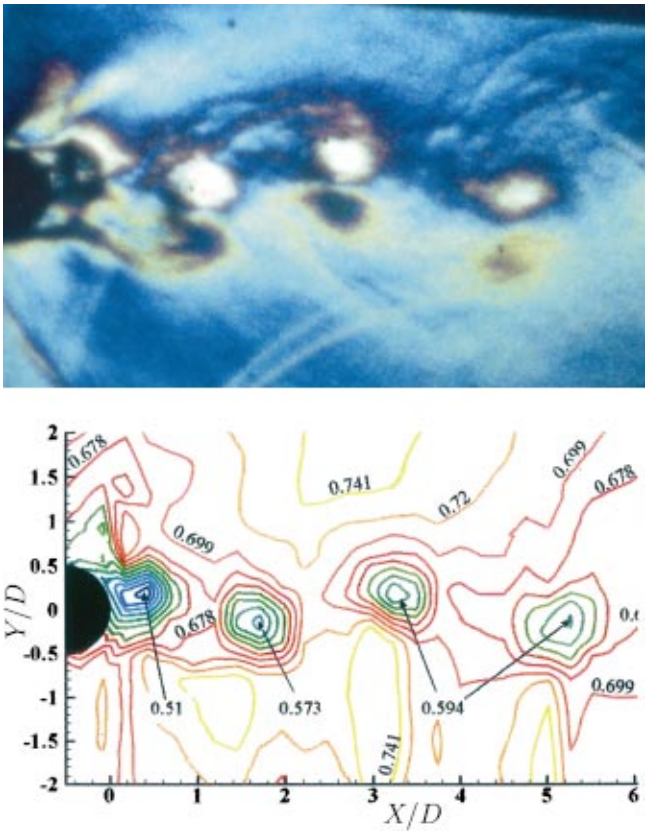


**Fig. 6 Example of white light differential interferogram with fringes set parallel to wake centerline and corresponding gas density field, phase angle $\varphi \sim 0$ deg**

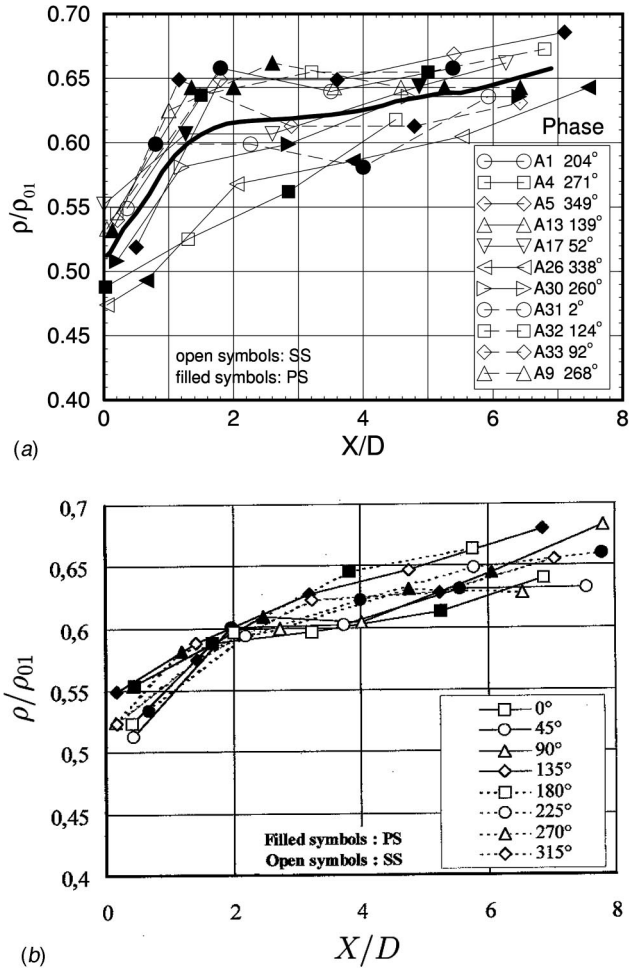


**Fig. 7 Evolution of vortex density minima with increasing downstream distance; (top) holographic interferometry, (bottom) white light differential interferometry**

which implies a total relative density change from the outside to the vortex center of $\Delta(\rho/\rho_{01}) = 0.184$. This is to be compared with an isentropic downstream static to total density ratio $\rho_s/\rho_{01} = 0.745$.

*White Light Differential Interferometry.* The technique of differential interferometry using a white light source and two Wollaston prisms, equipped with respectively a polarizer and an analyzer, allows obtaining color interference fringes in the field under observation. By orienting the two Wollaston prisms a set of either normal or parallel interference fringes to the flow can be obtained. Contrary to the holographic interferometry technique which visualizes iso-density contours with fixed density changes between the contours, the white light differential interferometry technique provides information on the continuous variation of the density gradient field. Due to the nature of the differential measurement technique, a data integration is necessary to obtain the refraction index in the direction normal to the interference fringes. The local density $\rho_\lambda$ is obtained via the determination of the local refractive index $n_1$, the refractive index and the density being related through the Gladstone constant,

$$n_1 - 1 = k(\rho_1/\rho s), \tag{4}$$

with: $k$–Gladstone constant [$m^3$/kg] and $\rho_s$ [kg/$m^3$]–gas density under standard condition.

As for the holographic interferometry the reference value for the gas density is given by a fast response needle static pressure probe positioned in the freestream on the suction side of the wake.

The white light differential interferograms are recorded by a CORDIN 350 high-speed rotating drum and rotating prism camera. The time exposure of the images recorded on the camera is 750 ns and the time interval between two successive frames is close to 28.5 $\mu$s. A maximum of 100 images can be recorded on the film, corresponding to about 25 periods of the phenomenon. With a vortex shedding frequency of ~7.6 kHz the camera records about four pictures per cycle. Each picture can then precisely be dated with respect to the simultaneous recorded pressure signal of a fast pressure sensor implemented on the blade pressure side at the beginning of the trailing edge circle at $x/c_{ax} = 0.933$.

**Figure 6** shows an interferogram at the phase angle $\varphi = 0$ deg. The interferogram is taken with the wollaston prisms oriented to set the interference fringes parallel to the blade wake, i.e., the picture visualizes mainly the gradients across the wake. Each vortex appears as a pair of white and dark dots, which reflects the density change through the vortex. At $\varphi = 0$ deg the suction side vortex is completely formed and will start its shedding phase while on the pressure side the vortex formation phase will start. The density in the vortex center on the suction side is as low as $\rho/\rho_{01} = 0.51$. The minimum density ratio of the vortex of the previous cycle positioned at $x/D = 3$ from the trailing edge has increased to 0.59.

**Streamwise Evolution of Density Minima and Lateral Displacement of Vortices.** Because of lack of space we shall focus our attention only on the evolution of the density minima of the vortex cores and their lateral spreading. This information provides insight into the dissipation of the vortex strength and is of prime importance for code validation.

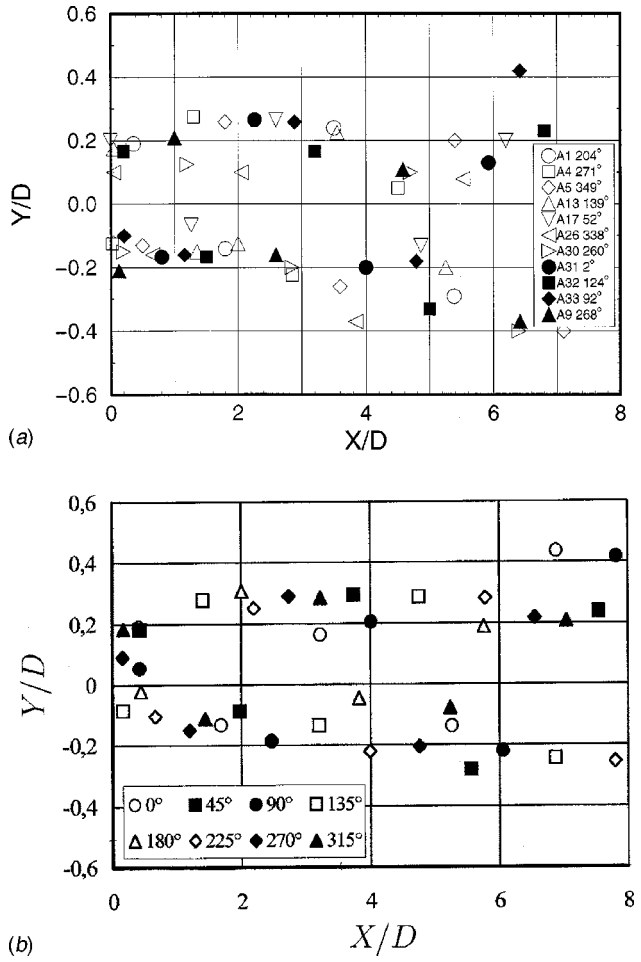


**Fig. 8 Lateral spreading of vortex minima with increasing downstream distance; (top) holographic interferometry, (bottom) white light differential interferometry**

**Figure 7** shows the variation of the vortex density minima nondimensionalized by the upstream total density, $\rho/\rho_0$, in function of the trailing edge distance $x/D$ ($D$-trailing edge diameter). **Figure 7** (top) shows the results obtained with holographic interferometry, **Fig. 7** (bottom) the results with white light interferometry.

The holographic data in **Fig. 7** (top) are derived from a total of 11 holograms taken at different phase angles. Open symbols correspond to vortices shed from the suction side, closed symbols to vortices from the pressure side. It is recalled that the pictures are taken randomly and do not belong to a single cycle.

The figure conveys the impression of rather poor measurements. The uncertainty in the determination of the vortex minima density is affected not only by errors associated with the measurement of the reference density (reference static pressure with needle probe) but also by the resolution of the measuring technique. The latter is of the order of the density difference between two successive iso-lines. The total uncertainty of the density measurements is evaluated as $\Delta(\rho/\rho_{01}) = +/-0.015$. Hence the largest differences in the wide band of experimental data are due to real variations in the flow properties between the various tests which were taken randomly over a period of several days. The continuous solid curve represents the mean variation of the minimum density averaged over all curves.

Nevertheless some general conclusions can be drawn:

- There are two distinct regions for the evolution of the vortex density minima: a very rapid linear density rise up to a distance of $x/D \cong 1.7$ followed by a much slower rise further downstream. The average density variation is nearly linear in both regions.
- There is no distinct difference between the minima of the pressure and suction side vortices. This is contrary to observations of some authors based on flow visualizations only, Han and Cox [1] and Cicatelli and Sieverding [5], who find that the suction side vortex is weaker than the pressure side vortex. Han and Cox attribute this to the blade circulation.
- The average minimum density ratio is about 0.52 at the trailing edge. At $x/D=7$ the minimum density has risen to 0.67. This is plausible if we compare it to the density of $\rho/\rho_{01} = 0.74$ corresponding to the nominal outlet Mach number of 0.79 in the downstream plane $x/c_{ax}=0.5$ equivalent to a trailing edge distance of $x/D \cong 15$ in streamwise direction.

The results obtained with white light interferometry are in broad agreement with those presented for the holographic interferometry except for a somewhat slower density rise in the near wake region, i.e., for $0 \leqslant x/D \leqslant 2$. The white light interferometry data also confirm that there is no difference in the intensity between the suction and pressure side vortices. Compared to the holographic data the scatter is much smaller. This is explained by the fact that the pictures are taken not randomly but over a total time period of only $\sim 3 \times 10^{-3}$ seconds with a continuously running camera. It may be assumed that the variation in the intensity of the vortex shedding over this period is much smaller than in case of randomly taken pictures. However, it is likely that repeating testing would result in a similar scatter as for the holographic interferometric tests.

**Figure 8** presents the downstream evolution of the lateral displacement of the pressure and suction side vortices with respect to the tangent to the mean camber line defined by $y/D=0$. Again the data set obtained with the white light interferometry technique appears to be more consistent. The evolution of the lateral displacement of the vortex centres with respect to the 0-line is not symmetric. In particular within the range of $x/D \leqslant 4$ the wake appears to be shifted to the suction side. The ratio between the streamwise distance of two successive vortices and the lateral distance between the pressure side and suction side vortices is about 6–7.

## Wake Flow Traverses

**Multihead Pressure/Temperature Fork Probe.** The measurement of the total pressure and temperature distribution in the wake was carried out using the probe in **Fig. 9**. The probe stem carries four different probe heads: for time averaged data a pneumatic Kiel type total pressure probe and a thermocouple probe, for fast response measurements a semi-conductor (Kulite) total pressure probe and a thin wire total temperature probe. The probe is a compromise between spatial resolution, angular sensitivity, frequency response, probe blockage effect and probe vibration. Each probe underwent extensive calibration tests. The insensitivity angle range for the two total pressure probes was found experimentally to be 15 deg and 25 deg, respectively, for the Kulite probe with a conical entrance of 20 deg and for the pneumatic Kiel-type probe. Note that the Kiel probe differs from the usual construction in as much as the ''Kiel effect'' operates only in pitchwise direction since the spanwise width of the flattened pitot tube is equal to the inner diameter of the surrounding cylinder. The influence of the recess of the Kulite probe pressure sensor from the probe mouth was evaluated on the basis of the theory of Bergh and Tijdeman [22], to about 40 kHz which was judged adequate for the wake shedding frequency of 7.5 kHz at the nominal outlet Mach number $M_{2,is}=0.79$. As regards the cold wire probe, numerical compensation is used to extend the naturally rather low frequency response of the 2 $\mu$m wire to much higher ranges (Dénos and Sieverding [23]). A frequency analysis of the probe output signal in the turbine blade wake showed apart from

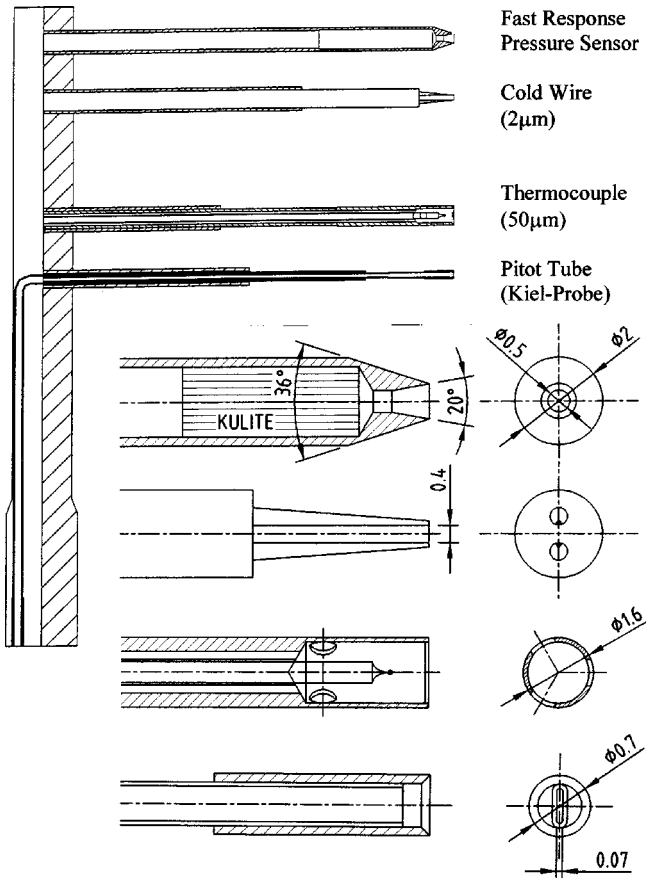


**Fig. 9 Multihead fork probe for mean and time accurate total pressure and temperature measurements**

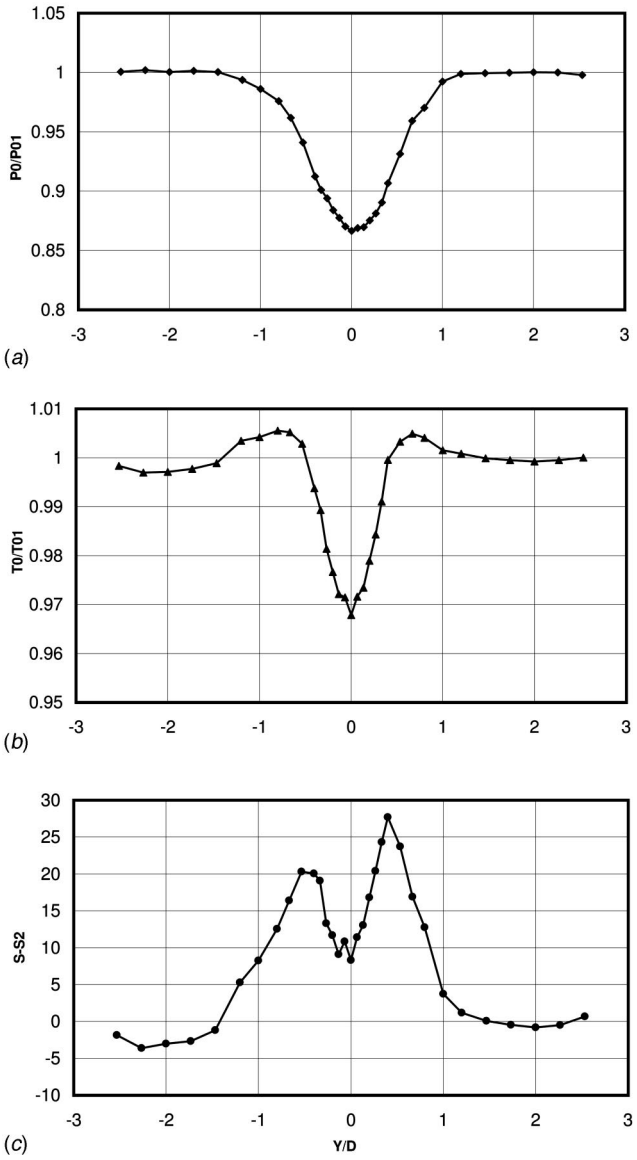


**Fig. 10 Steady-state total pressure, temperature, and entropy distribution through wake at trailing edge distance $x/D=2.5$**

the dominating frequency of 7.6 kHz very clearly the first harmonic and faintly also the second harmonic. This is clearly inadequate to reconstruct a square wave signal at the same frequency which would require a frequency response up to the tenth harmonic but in the present case the signal is nearly sinusoidal.

The wake traverse was performed at a trailing edge distance equal to $2.5\times D$ (trailing edge diameter) in direction of the tangent to the blade camber line. This tangent form an angle of 66 deg with respect to the axial direction and the traverse is made normal to this tangent. The probe presence did neither effect the pressure distribution around the trailing edge nor the downstream side-wall pressure distribution opposite the probe head.

**Steady-State Pressure and Temperature Measurements in Wake. Figure 10** presents the total pressure and total temperature distribution as measured with the Pitot tube and thermocouple probes, respectively, and the time-averaged entropy variation through the wake. Both the temperature and the pressure measurements were nondimensionalized with respect to the cascade inlet total temperature and pressure. With an error of 1 mbar in the pressure measurement and 1 deg in the temperature measurement, the error in the total pressure ratio amounts to ~0.1%, the error in the total temperature ratio to 0.3%.

The temperature distribution is characterized on the borders of the wake, between $y/D=1.5$ and 0.5 by temperature peaks in excess of the inlet total temperature while a strong minimum is recorded in the wake center. The temperature for $y/D>1.5$ should reach the freestream temperature, i.e., the total upstream temperature. This is clearly not the case for the left side (pressure side) of the wake. However, the lowest value of $T_0/T_{01}=.997$ at $y/D=-2$ corresponds to a temperature difference $-.85$, which is still within the measuring accuracy of 1 deg. Apart from these measurement errors in the range $|y/D|>1.5$, the deviations of the temperature from the freestream value are referred to in the literature as ''Eckert-Weise Effect,'' see Eckert [17] and Carscallen et al. [14], and are attributed to the presence of the very intense von Karman vortices in the wake. However, the mass integrated temperature value across the wake should be $T_{02}/T_{01}=1$. Because of the lack of information on the local velocity it is unfortunately not possible to perform this integration.

The entropy variation reflects the influence of the temperature variation. A drop of the temperature leads to a decrease in the entropy, see the entropy drop in the wake center, while a temperature rise contributes to a rise in the entropy, i.e., on the borders of the wake.

**Unsteady Temperature and Pressure Measurements in Wake.** The phase-lock averaging procedure for the unsteady measurements turned out to be a very difficult task. The main problem resides in the fact that the aspect of the pressure and temperature fluctuations vary strongly through the wake. The outer wake regions are dominated respectively by either the pres-

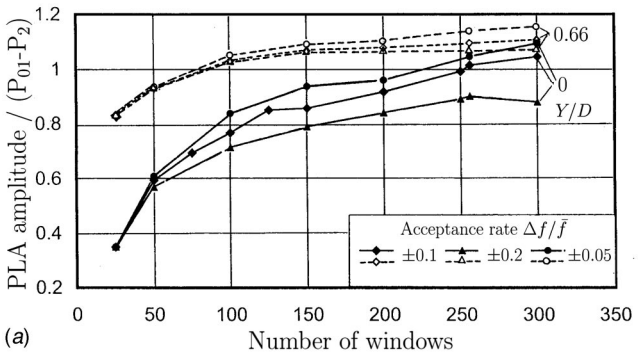


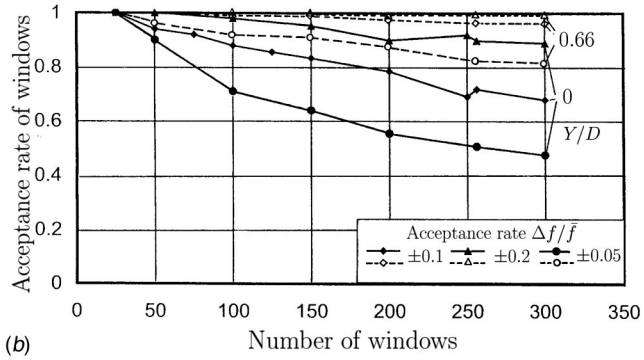


**Fig. 11 (top) Phase-lock averaged pressure amplitudes versus number of windows on wake centerline ($y/D=0$) and at $y/D=0.66$ (bottom), acceptance rate**

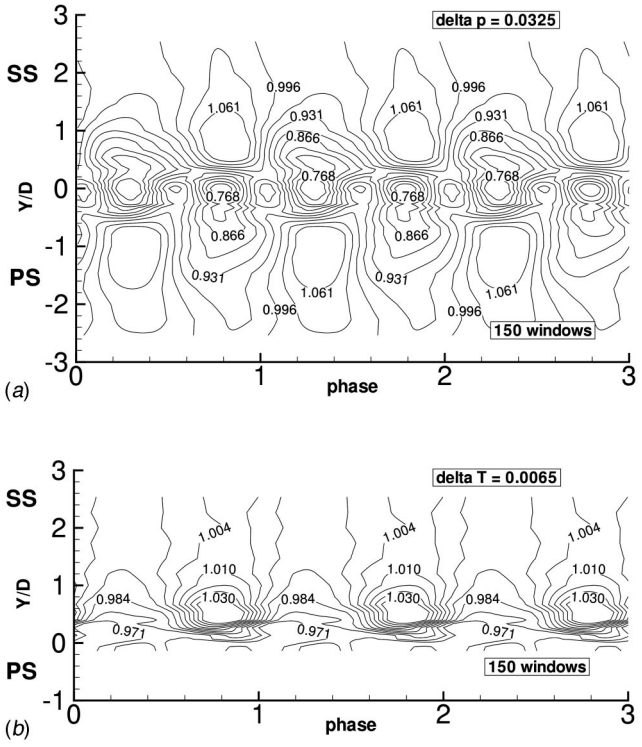


**Fig. 12 Wake total pressure and temperature fluctuations through wake at $x/D=2.5$**

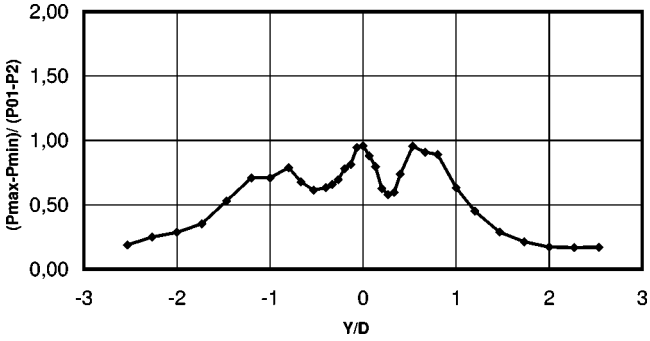


**Fig. 13 Variation of phase-lock averaged pressure amplitude through wake**

sure or suction side vortices while the wake inner regions are equally affected by the vortex shedding process from both blade sides. Hence the dominating frequency changes from ~7.5 kHz in the outer region to ~15 kHz in the wake center. The FFT analysis was used to determine the period for the phase lock averaging procedure of the signal. Windowing of the raw signal turned out to be an absolute necessity to avoid excessive amortisation of the signal amplitudes due to significant frequency variations. **Figure 11** (top) and **11** (bottom) shows the result of a systematic study of the effect of the number of windows on the phase-lock averaged amplitude for two positions in the wake, i.e., at $y/D=0.66$ and at $y/D=0$ (wake center). The amortization effect of a frequency change for a given data string diminishes of course with increasing number of windows. As an additional mean to reduce the effect of frequency variations on the phase lock averaged signal amplitude, a frequency variation acceptance rate was defined for each window. Phase lock averaged amplitudes in **Fig. 11** (top) are plotted for three different acceptance rates: $\Delta f/f=0.05$, 0.1 and 0.2. A $\Delta f/f=0.1$ means that all windows in which the frequency varies by more than 10% are rejected. The acceptance rate of the number of windows is presented in **Fig. 11** (bottom). The following results are based on a data analysis with 150 windows and a frequency variation acceptance rate of $\Delta f/f=10\%$. With 150 windows, each window contains about ten periodic events with a total of about 400 data points.

**Figure 12** (top) presents the total pressure fluctuations across the wake (at a trailing edge distance $x/D=2.5$) in function of time (phase). The fluctuations extend far beyond the time averaged wake width of $y/D\sim\pm1.5$. The time-averaged pressure amplitude variation through the wake is shown in **Fig. 13**. Maximum amplitudes of up to 90% of the downstream dynamic pressure are recorded. The amplitude variations show three pronounced peaks: in the wake center on the pressure side at $y/D=-1.0$ and on the suction side at $y/D=0.7$.

The phase-lock averaged temperature variations are presented in **Fig. 12** (bottom). As explained earlier, data were recorded for only half of the wake. The maximum and minimum temperature variations are $T_0/T_{01}=1.046$ and 0.96, respectively. With $T_{01}=280$ K the maximum total temperature variations amount to ~24 deg. Similar values were reported by Carscallen et al. [14].

## Conclusion

The experimental program presented in this paper has made use of a wide range of measurement techniques to contribute elucidating the unsteady turbine blade wake characteristics related to the presence of large coherent wake structures known as von Karman vortices. Smoke visualizations at high subsonic Mach numbers proved to be a remarkable tool and visualise better than schlieren photographs the interaction between the suction-side and pressure-side vortices in the far wake.

Two different interferometry techniques (the white light differential technique being a first application to tubomachinery blad-

**Table 1 VKI cascade characteristics**

| | |
|---|---|
| Chord length, $c$ | 140 mm |
| Axial chord length, $c_{ax}/c$ | 0.656 |
| Pitch to chord ratio, $g/c$ | 0.696 |
| Blade height, $h$ | 100 |
| Aspect ratio, $h/c$ | 0.714 |
| Trailing edge thickness to chord ratio, $D/c$ | 0.0531 |
| Trailing edge wedge angle, $\delta_{te}$ | 7.5 deg |
| Inlet angle $\alpha_1$ (from axial direction) | 0 deg |
| Gauging angle $\alpha_2$ (arc cos $o/g$) | 70.9 deg |
| Stagger angle $\gamma$ | 49.83 deg |
| Number of blades including end blades | 4 |

**Table 2 Overall flow conditions**

| | |
|---|---|
| Upstream total temperature, $T_{01}$ | 280 K |
| Upstream total pressure, $P_{01}$ | 1400 mbar |
| Upstream turbulent intensity $TU$ | 1% |
| Downstream isentropic Mach number $M_{2,is}$ | 0.79 |
| Reynolds number Re (Based on chord and downstream velocity) | $2.8\times10^6$ |

ings) were used and provided first quantitative results on the wake density field. They demonstrated in particular the different evolution of the density minima associated with the vortex cores in the near wake ($x/D<2$) and in the far wake ($x/D>2$).

A multihead fork probe for the measurement of the steady state and the time varying pressures and temperatures in the wake was developed. The thin wire fast response temperature probe head proved unfortunately too fragile to achieve a complete wake traverse. Nevertheless, the results confirm clearly the existence of hot spots on the borderline of the wake and cold spots near the wake center as already found by other researchers. This effect is known as energy separation effect. The unsteady total temperature distribution through the wake affects also the steady-state total temperature distribution through the wake with a total temperature near the center line considerable below the inlet total temperature and a higher value on the wake border. As regards the total pressure fluctuations, maximum pressure amplitudes equal to the downstream dynamic head are recorded. (See **Tables 1** and **2**).

## Acknowledgments

The above research was carried out under contract for the European Commission as part of the Industrial and Materials Technology Program (BRITE/EURAM III), project CT96-0143 on "Turbulence Modelling of Unsteady Flows in Axial Turbines." The authors wish to acknowledge their financial contribution.

## Nomenclature

$c$ = chord length (mm)
$D$ = trailing edge diameter (mm)
$g$ = pitch (mm)
$H$ = boundary layer shape factor
$h$ = blade height (mm)
$M$ = Mach number
$o$ = throat (mm)
$P$ = static pressure (mbar)
$P_{01}$ = upstream total pressure (mbar)
Re = Reynolds number based on chord and downstream velocity
$S$ = entropy
$s$ = stream line coordinate
St = Strouhal number based on trailing edge diameter and downstream velocity
$n$ = refractive index
$T_{01}$ = upstream total temperature (K)
$TU$ = turbulent intensity $\sqrt{\overline{u'^2}/u^2}$
$U$ = velocity (m/s)
$u'$ = fluctuating velocity
$x$ = coordinate
$y, Y$ = coordinate
$\delta$ = boundary layer thickness (mm)
$\delta_{te}$ = trailing edge wedge angle (deg)
$\zeta$ = kinetic energy loss coefficient
$\rho$ = density (kg/m$^3$)
$\gamma$ = stagger angle (resp. axial direction)

### Subscripts

$ax$ = axial
$is$ = isentropic
$o$ = total
1 = upstream
2 = downstream
$\infty$ = freestream

## References

[1] Han, L. S., and Cox, W. R., 1983, "A Visual Study of Turbine Blade Pressure Side Boundary Layer," ASME J. Eng. Gas Turbines Power, **105**, pp. 47–52.
[2] Lawaczeck, O., and Heineman, J., 1975, "von Karman Vortex Street in the Wake of Subsonic and Transonic Blades," *Unsteady Phenomena in Turbomachinery*, Paper 28, AGARD-CP-177.
[3] Heinemann, J., and Bütefisch, K. A., 1977, "Determination of the Vortex Shedding Frequency of Cascades With Different Trailing Edge Thicknesses," Paper 11, AGARD-CP-227.
[4] Carscallen, W. E., Feige, H. U., and Gostelow, J. P., 1996, "Transonic Turbine Vane Wake Flows," ASME Paper No. 96-GT-419.
[5] Cicatelli, G., and Sieverding, C. H., 1996, "A Review of the Research on Unsteady Turbine Blade Wake Characteristics," *Loss Mechanisms and Unsteady Flows in Turbomachines*, Paper 6, AGARD-CP-571.
[6] Cicatelli, G., and Sieverding, C. H., 1997, "The Effect of Vortex Shedding on the Unsteady Pressure Distribution Around the Trailing Edge of a Turbine Blade," ASME J. Turbomach., **119**, pp. 810–819.
[7] Desse, J. M., 1998, "Effect of Time Varying Wake Characteristics Behind Flat Plates," AIAA J., **36**(11), pp. 2036–2043.
[8] Sieverding, C. H., Cicatelli, G., Desse, J. M., Meinke, M., and Zunino, P., 1999, "Experimental and Numerical Investigation of Time Varying Wakes Behind Turbine Blades," *Notes on Numerical Fluid Mechanics*, **67**, Vieweg, Braunschweig/Wiesbaden.
[9] Sieverding, C. H., Richard, H., and Desse, J.-M., 2003, "Turbine Blade Trailing Edge Flow Characteristics at High Subsonic Outlet Mach Number," ASME J. Turbomach., **125**, pp. 298–309.
[10] Ubaldi, M., and Zunino, P., 1999, "An Experimental Study of the Unsteady Characteristics of the Turbulent Wake of a Turbine Blade," *4th International Symposium on Engineering Turbulence Modelling and Measurements*, Ajaccio.
[11] Ubaldi, M., Zunino, P., Cattanei, A., and Campora, U., 1999, "Effect of Trailing Edge Cooling on Turbine Wake Unsteady Flow Characteristics," *4th European Tubomachinery Conference*, London.
[12] Zunino, P., Ubaldi, M., Cattanei, A., and Campora, U., 2001, "An Experimental Investigation for the Interaction Between Trailing Edge Coolant Jet and Wake," *3rd European Tubomachinery Conference*, Firenze, Italy, pp. 283–294.
[13] Raffel, M., Höfer, F., Kost, C., and Kompenhans, J., 1996, "Experimental Aspects of PIV Measurements of Transonic Flow Fields at a Trailing Edge Model of a Turbine Blade," *8th International Symposium on Application of Laser Techniques to Fluid Mechanics*, Lisbon, Portugal.
[14] Carscallen, W. E., Currie, T. C., Hogg, S. I., and Gostelow, J. P., 1998, "Measurement and Computation of Energy Separation in Vortical Wake Flow of a Turbine Blade," ASME J. Turbomach., **121**, pp. 703–708.
[15] Buttsworth, D., and Jones, T. V., 1998, "A Fast Response Total Temperature Probe for Unsteady Compressible Flows," ASME J. Eng. Gas Turbines Power, **120**, pp. 694–701.
[16] Eckert, E. R. G., and Weise, W., 1943, "Messungder Temperaturverteilung auf der Oberfläche schnell angeströmter Körper," Forsch. Ing. Wesen, **13**, pp. 246–254.
[17] Eckert, E. R. G., 1986, "Energy Separation in Fluid Streams," Int. Commun. Heat Mass Transfer, **13**, pp. 127–143.

[18] Kurosaka, M., Gertz, J. B., Graham, J. E., Goodman, J. R., Sundaram, P., Riner, W. C., Kuroda, H., and Hankey, W. L., 1987, ''Energy Separation in aVortex Street,'' J. Fluid Mech., **178**, pp. 1–29.
[19] Ng, W. F., Chakrun, W. M., and Kurosaka, M., 1990, ''Time Resolved Measurements of Total Temperature and Pressure in the Vortex Street Behind a Cylinder,'' Phys. Fluids A, **2**(6), pp. 971–978.
[20] Desse, J. M., 1990, ''Instantaneous Density Measurement in Two-Dimensional Gas Flow by High Speed Differential Interferometry,'' Exp. Fluids, **9**(1/2), pp. 85–91.
[21] Desse, J. M., 1997, ''Recording and Processing of Interferograms by Spectral Characterization of the Interferometric Setup,'' Exp. Fluids, **23**(4), pp. 265–271.
[22] Bergh, H., and Tijdeman, H., 1965 ''Theoretical and Experimental Results for the Dynamic Response of Pressure Measuring Systems,'' NLR-TR-F. 238, 18 pgs.
[23] Dénos, R., and Sieverding, C. H., 1997, ''Assessment of the Cold Wire Resistance Thermometer for High Speed Turbomachinery Applications,'' ASME J. Turbomach., **119**, pp. 140–148.

# Active Flow Control Using Steady Blowing for a Low-Pressure Turbine Cascade

**Brian R. McAuliffe**

**Steen A. Sjolander**

Department of Mechanical and Aerospace Engineering,
Carleton University,
1125 Colonel By Drive,
Ottawa, ON K1S 5B6, Canada

*The paper presents mid-span measurements for a turbine cascade with active flow control. Steady blowing through an inclined plane wall jet has been used to control the separation characteristics of a high-lift low-pressure turbine airfoil at low Reynolds numbers. Measurements were made at design incidence for blowing ratios from approximately 0.25 to 2.0 (ratio of jet-to-local freestream velocity), for Reynolds numbers of 25,000 and 50,000 (based on axial chord and inlet velocity), and for freestream turbulence intensities of 0.4% and 4%. Detailed flow field measurements were made downstream of the cascade using a three-hole pressure probe, static pressure distributions were measured on the airfoil suction surface, and hot-wire measurements were made to characterize the interaction between the wall jet and boundary layer. The primary focus of the study is on the low-Reynolds number and low-freestream turbulence intensity cases, where the baseline airfoil stalls and high profile losses result. For low freestream turbulence (0.4%), the examined method of flow control was effective at preventing stall and reducing the profile losses. At a Reynolds number of 25,000, a blowing ratio greater than 1.0 was required to suppress stall. At a Reynolds number of 50,000, a closed separation bubble formed at a very low blowing ratio (0.25) resulting in a significant reduction in the profile loss. For high freestream turbulence intensity (4%), where the baseline airfoil has a closed separation bubble and low profile losses, blowing ratios below 1.0 resulted in a larger separation bubble and higher losses. The mechanism by which the wall jet affects the separation characteristics of the airfoil is examined through hot-wire traverse measurements in the vicinity of the slot.* [DOI: 10.1115/1.1791291]

## Introduction

Recent advancements in low-pressure turbine design have resulted in highly loaded airfoils that are subject to boundary layer separation. At low Reynolds numbers, typical of high altitude cruise conditions, the separated shear layer can fail to reattach to the surface resulting in increased losses and reduced flow turning (Hourmouziadis [1], Mayle [2]), which has a direct impact on stage efficiency and work output.

Transition plays an important role in the boundary layer development over the surfaces of low-pressure turbine airfoils. In many cases, transition occurs within a separated shear layer. Hatman and Wang [3] and Malkiel and Mayle [4] have examined the separated-flow transition process at low-freestream turbulence and have observed the amplification of Kelvin–Helmholtz (K–H) instabilities within the separated shear layer. This type of instability is typically associated with transition in free-shear flows such as jets, wakes, and mixing layers. Yaras ([5,6]) has examined the effects of freestream turbulence and pressure gradient history on separated-flow transition and has noted that both play an important role in both the onset and length of transition within the separated shear layer.

The low-pressure turbine airfoil considered in the current experiments is the Pak-B profile, which is an industry supplied research airfoil that has been the subject of many experimental studies. Mahallati et al. [7], Murawski and Vafai [8], and Dorney et al. [9] have investigated the performance of the Pak-B airfoil under various Reynolds numbers and freestream turbulence intensities in linear cascade experiments. Mahallati et al. [7] have shown that decreases in Reynolds number and turbulence intensity result in a delay of transition onset within the separated shear layer, and stall was observed at the lowest levels of Reynolds number and turbulence intensity examined. Stall resulted in a significant increase in the profile losses. Bons et al. ([10,11]) have shown that flow control can be used to prevent stall and reduce the losses of the Pak-B airfoil at low Reynolds numbers. Vortex generator jets were used by Bons et al. to promote transition and prevent separation of the suction surface boundary layer. The current study employs a different method of blowing flow control for the Pak-B airfoil.

In general, there are two methods of flow control, each characterized by the energy expenditure required by the flow control device. Passive flow control requires no auxiliary energy and no control loop. Active flow control requires energy expenditure and may use a control loop (Gad-el-Hak [12]). For active flow control there are two general control strategies. The first is known as ''predetermined'' control, in which steady or unsteady energy input is applied without regard to the state of the flow. The second is known as ''reactive'' control, in which a control loop is continually adjusted based on measurements of the flow, using either an open feedforward or a closed feedback control loop.

Although passive flow control devices require no energy input, these devices may be effective only at operating conditions where control is required, and may have a negative impact on performance at operating conditions where control is not required. This effect has been observed in the measurements of Volino [13] and Lake et al. [14], who both used trip wires to prevent stall of the Pak-B airfoil at low-Reynolds numbers. Although stall was prevented with the trip wires, losses at higher Reynolds numbers were significantly greater than their corresponding clean-blade cases. The benefit of active flow control is that the control device can be turned on only when needed. The current study evaluates a method of active flow control for separation control in a low-pressure turbine cascade, under steady inflow conditions. A pre-

Contributed by the International Gas Turbine Institute (IGTI) of THE AMERICAN SOCIETY OF MECHANICAL ENGINEERS for publication in the ASME JOURNAL OF TURBOMACHINERY. Paper presented at the International Gas Turbine and Aeroengine Congress and Exhibition, Vienna, Austria, June 13–17, 2004, Paper No. 2004-GT-53646. Manuscript received by IGTI, October 1, 2003; final revision, March 1, 2004. IGTI Review Chair: A. J. Strazisar.

  

determined control strategy is used for the present experiments, but the implementation of a reactive control loop might be desirable for practical use.

The current control strategy consists of localized fluid injection by means of an inclined plane wall jet, at a location upstream of the expected suction surface separation point. This blowing technique has been used by Fottner [15], Sturm et al. [16], and Culley et al. [17] for separation suppression on highly-loaded compressor blades. The wall jet supplies energy to the decelerating boundary layer downstream of the suction peak. This injected fluid can increase the momentum in the near-wall region of the boundary layer. The fuller boundary layer profile is then expected to resist stronger adverse pressure gradients and which may, therefore, delay or even suppress separation. For the current investigation in which a laminar boundary layer separates from the surface, the injected fluid is also expected to have an effect on the transition process.

**Table 1 Geometry of flow control cascade**

| Parameter | Value |
|---|---|
| True chord length, $C$ | 83.3 mm |
| Axial chord length, $C_x$ | 75.4 mm |
| Pitch, $S$ | 66.8 mm |
| Suction surface length, $SSL$ | 112.3 mm |
| Stagger angle, $\gamma$ | 25.5° |
| Aspect ratio, $AR$ | 2.4 |
| Inlet blade angle, $\beta_i$ | 35° |
| Exit blade angle, $\beta_o$ | 60° |
| Cascade solidity, $\sigma$ | 1.13 |
| Zweifel coefficient, $Z$ | 1.08 |
| Flow control slot location, $s_s$ | 0.52 SSL |
| Flow control slot width, $b$ | 0.3 mm |
| Flow control slot length, $h_s$ | 0.78 $h$ |
| Flow control slot inclination angle, $\theta$ | 38° |

## Experimental Apparatus and Procedures

**Test Section and Cascade.** All measurements were made in a variable-incidence linear cascade test section, which is shown in Fig. 1. The inlet to the test section has a rectangular cross-section 67.3 cm high and 20.0 cm wide. Two boundary layer bleed slots, one on each endwall, are located downstream of the inlet to reduce the thickness of the incoming boundary layers. The linear cascades are mounted on a turntable which allows incidence variations over a range of 60 deg. The turntable serves as the back endwall and a removable Plexiglas wall serves as the front endwall. Seven flow control devices are used to adjust the flow in and out of the cascade and are depicted in Fig. 1. The flaps and tailboards are used to adjust the inlet flow uniformity and outlet flow periodicity of the cascade, the bypass flaps control the mass flow rate through the cascade, and the floating wall is used to maintain a constant area flow channel entering the cascade. Two-axis traverse mechanisms are mounted to the backside of the turntable to allow movement of measurement probes across the blade span and pitch, both upstream and downstream of the cascade.

The cascade used for the present experiments consists of the Pratt & Whitney Pak-B profile. Details of the Pak-B cascade geometry are tabulated in Table 1. The cascade contains nine airfoils, the middle three of which include a slot through which air can be injected for flow control, as shown enlarged in Fig. 2. Pressurized air is supplied to the ''air supply pipe'' at both ends of the blade. There are 19 holes along the upstream side of the pipe, spaced approximately 1 cm apart, that discharge air into the blade plenum. The plenum serves as a settling chamber for the flow control slot which injects air into the blade passage at approximately 52% of the suction surface length (64% axial chord). This slot location is slightly upstream of the expected separation point. Ideally, the slot should span the full length of the airfoil to simulate two-dimensional flow, it should inject the flow tangent to the surface to minimize mixing losses due to the normal component of velocity, and it should have a small width to minimize the required secondary air supply. For manufacturing reasons the slot spans the middle 78% of the airfoil span, is inclined 38 deg from

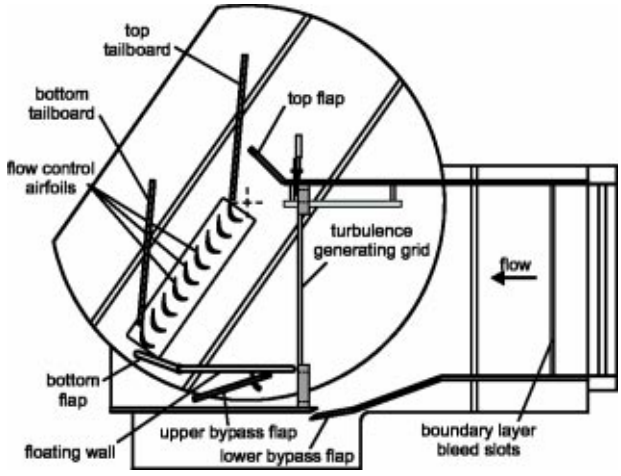


**Fig. 1 Schematic of test section.**

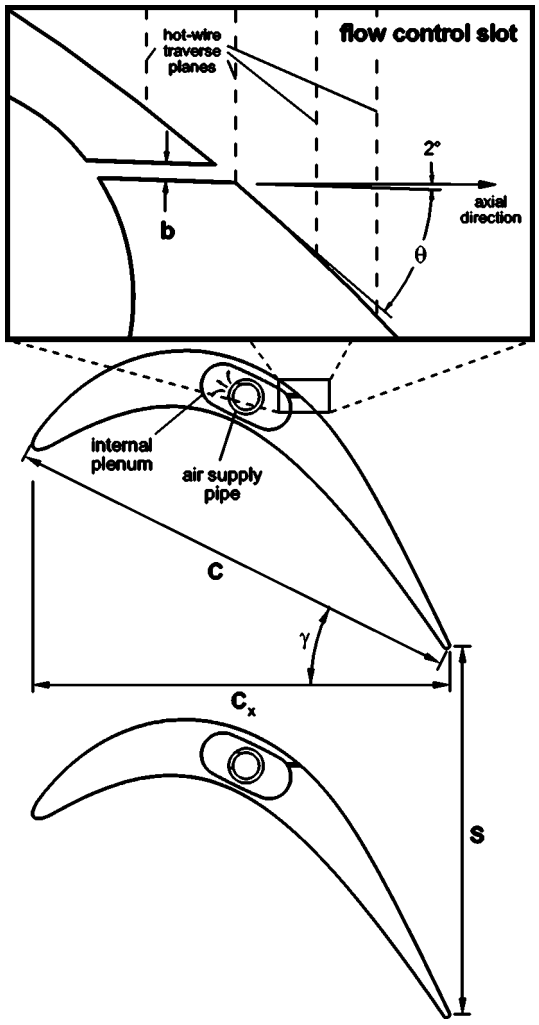


**Fig. 2 Geometry of blade and flow control arrangement**

**Table 2 Estimated uncertainties in three-hole pressure probe measurements**

| Reynolds Number, Re | 25,000 | 50,000 |
|---|---|---|
| Flow angle, $\delta\alpha$ | $\pm 0.9°$ | $\pm 0.3°$ |
| Dynamic pressure, $\delta q/q_{\text{ref}}$ | $\pm 0.006$ | $\pm 0.002$ |
| Total pressure, $\delta P_0/q_{\text{ref}}$ | $\pm 0.005$ | $\pm 0.001$ |

the surface, and has a width of 0.3 mm (0.3% of SSL). One static pressure tap is located inside the plenum near the turntable wall to adjust and monitor the jet blowing rate.

A distribution system was designed to deliver shop air to the flow control blades. Shop air first passes through a Schrader model 3533-1000 filter/water trap to remove any impurities or moisture from the flow, followed by a Schrader model 3566-2000 pressure regulator used to control the flow rate of air to the blades. A utility hose then delivers the air to a manifold. The manifold has six Swagelok model B-1RS6-A needle valves to adjust the flow rates to each blade. Tygon vinyl tubing connects the manifold valves to both ends of the flow control blades, through the turntable on the back side of the test section and through the Plexiglas wall on the front side.

The background turbulence level entering the test section is approximately 0.4%. To simulate the elevated levels of turbulence in a low-pressure turbine, passive turbulence generating grids are used in the test section. For the current study, a circular-rod woven mesh grid is located 35 cm upstream of the cascade middle blade leading edge, as shown in Fig. 1. This grid produces a freestream turbulence intensity (FSTI) at the cascade middle blade leading edge of 4% with an integral length scale ($\Lambda$) of 10% of the blade axial chord. The uncertainty in FSTI is estimated at $\pm 0.5\%$ and the uncertainty in $\Lambda$ is estimated at $\pm 4\%$ of the axial chord.

**Instrumentation and Data Acquisition.** Three types of measurements have been made during the present study, all at the mid-span of the cascade. The downstream measurements, from which mixed-out profile losses and deviation angles have been calculated, have been made with a three-hole pressure probe. The probe tip has a width of 2 mm and a thickness of 0.64 mm. The probe has been calibrated in increments of 0.5 deg over the required range of flow misalignment. Estimated uncertainties in the measured downstream flow angle, dynamic pressure and total pressure are tabulated in Table 2 for the two Reynolds numbers examined in the present experiments. The downstream three-hole probe measurements were made 0.5 axial chord lengths downstream of the three flow control airfoils, with 65 measurement points per blade pitch.

Surface static pressure measurements have been made over the suction surface of the cascade middle blade, with one pressure tap located upstream of the flow control slot and 13 pressure taps located downstream of the slot. The maximum uncertainty in the loading coefficient, $C_{\text{PL}}$, is estimated to be $\pm 0.20$ for the Reynolds number of 25,000 cases and $\pm 0.08$ for the Reynolds number of 50,000 cases.

Hot-wire traverse measurements have been made in the vicinity of the slot to characterize the effects of the injected fluid on the local boundary layer. The traverse locations for one set of measurements are shown in the enlarged section of Fig. 2. A Dantec type 55P01 normal hot-wire probe has been used with an A.A. Lab System AN-1003 constant-temperature anemometer. Calibration of the hot-wire probe was performed regularly and the uncertainties in mean velocity and turbulence intensity (RMS fluctuation level divided by mean velocity) are estimated to be below $\pm 5\%$ of the calculated value, except at low velocities ($<5$ m/s) where the uncertainties can be as high as $\pm 10\%$. All hot-wire measurements were sampled at 30 kHz with a 14 kHz low-pass filter for 0.55 seconds ($2^{14}$ samples), and were corrected for differences in flow temperature between the calibration and the wind tunnel measurements.

The downstream and surface pressure measurements have been made with Data Instruments linear differential pressure transducers, models DRAL501DN ($\pm 250$ Pa) and DRAL505DN ($\pm 1250$ Pa). Estimated uncertainties due to combined linearity, hysteresis and long-term stability are $\pm 0.5$ Pa for the DRAL501DN's and $\pm 2$ Pa for the DRAL505DN's. All pressure measurements were made at a sampling rate of 1 kHz and 20 seconds of data were collected for each measurement point (20,000 samples per point).

The data acquisition system used for the current experiments consists of a data acquisition board and a Windows-based software system. The data acquisition board is a United Electronic Industries (UEI) model PD2-MFS-8-800/14 PowerDAQ simultaneous sample-and-hold PCI card installed in a Pentium II powered personal computer. The board has eight 14-bit analog channels and has the ability to sample at 800 kHz. The software was developed in-house by Mahallati [18], and was designed to bring device setup, control, data acquisition, instrument calibration, and data reduction under one Windows-based environment.

**Data Reduction.** The loss measurements presented in this paper are expressed in terms of the mixed-out profile loss coefficient, $Y_m$, and represent the total pressure loss across the mid-span of the cascade. This loss includes surface shear layer losses, base-pressure losses, wake-mixing losses, and losses generated through mixing of the injected jet and the blade passage flow. The mixed-out profile loss coefficient is defined as

$$Y_m = \frac{\overline{P}_{0i} - P_{0m}}{q_m}, \tag{1}$$

where the mixed-out total pressure, $P_{0m}$, and the mixed-out dynamic pressure, $q_m$, are calculated by performing a constant-area mixing calculation of the downstream three-hole pressure probe measurements. The mixed-out flow angle, $\alpha_m$, is calculated from the mixed-out axial and tangential velocities. From the mixed-out flow angle, the mixed-out deviation angle, $\delta_m$, is obtained ($\delta_m = \beta_o - \alpha_m$). The inlet total pressure, $\overline{P}_{0i}$, is a net total pressure which takes into account the momentum of the injected jet. This net total pressure is calculated by mass-averaging the total pressures of the cascade inlet flow and the jet flow at the injection slot outlet plane. The losses defined using $\overline{P}_{0i}$ are called the ''corrected'' losses. The ''uncorrected'' losses, based on the cascade inlet plane total pressure only, $P_{0i}$, are presented in the loss plots but are not discussed in any detail. Although these ''uncorrected'' losses do not account for the momentum of the injected jet, they may be useful in a mean-line design procedure. As a note, when the jet momentum is approximately twice that of the local freestream, negative ''uncorrected'' losses have been observed. These negative losses indicate that the jet momentum is greater than the momentum losses incurred through viscous dissipation within the blade passage and downstream wake.

The profile loss coefficient data is presented in the form of a normalized profile loss coefficient, defined as

$$\overline{Y}_m = \frac{Y_m}{Y_{m\text{ref}}}, \tag{2}$$

where $Y_{m\text{ref}}$ is the profile loss coefficient for a particular baseline (non-flow control) Pak-B case.

One purpose of the current study is to examine the effectiveness of the active flow control device at reducing losses due to flow separation. An effectiveness coefficient is proposed, which represents the performance gain obtained using the flow control device in relation to the momentum input of the device. The performance gain of the flow control device is defined as the difference between the baseline airfoil total pressure loss, $\Delta P_0|_{\text{BAS}} = (q_m Y_m)_{\text{BAS}}$ and the flow control total pressure loss, $\Delta P_0|_{\text{AFC}}$

$=(q_m Y_m)_{\mathrm{AFC}}$. The momentum input of the flow control device is defined as the momentum flux rate through the outlet plane of the flow control slot, $\rho \overline{U_j^2} b$, where $\overline{U_j}$ is the mean velocity of the jet. The momentum flux rate calculated using the mean jet velocity is of similar magnitude to the actual momentum flux rate calculated by integrating the momentum flux across the jet injection plane. For the current measurements, the values obtained with this simplifying assumption are within $\pm 5\%$ of the actual momentum flux rate. The proposed effectiveness coefficient, $\zeta$, is defined as

$$\zeta = [(q_m Y_m)_{\mathrm{BAS}} - (q_m Y_m)_{\mathrm{AFC}}] \frac{S}{\rho \overline{U_j^2} b}, \tag{3}$$

where $S$ is the blade spacing. An effectiveness coefficient of this form allows a comparison with other injection-type flow control and cascade configurations.

## Experimental Results

**Operating Conditions.** Measurements are presented for two Reynolds numbers, based on axial chord and inlet velocity, of 25,000 and 50,000, at two freestream turbulence intensities (FSTI) of 0.4% and 4%, and at the design incidence. The blowing ratio, $B$, has been used as the characteristic jet velocity parameter, and is defined as

$$B = \frac{\rho_j U_{j\,\max}}{\rho_e U_e}, \tag{4}$$

where $U_{j\,\max}$ is the maximum velocity of the jet profile at the injection slot outlet plane, $U_e$ is the local freestream velocity, and $\rho_j$ and $\rho_e$ are the densities of the jet and freestream flows, respectively. The flow is assumed incompressible (maximum observed velocity of 45 m/s), and since the measured temperature difference between the jet and freestream flows was less than $2°-3°$C, the density ratio is assumed to be 1.0. The blowing ratio, as used in the current study, is then

$$B = \frac{U_{j\,\max}}{U_e}. \tag{5}$$

Prior to performing the detailed measurements, the jet blowing ratio was calibrated against the internal plenum pressure to allow correct adjustment during the experiments. This was accomplished by traversing the jet and local boundary layer with a hot-wire at the injection slot outlet plane. For the detailed experiments, the blowing ratio was varied between approximately 0.25 and 2.00 for the low-FSTI measurements and between approximately 0.25 and 1.25 for the high-FSTI measurements. Increments in the blowing ratio were approximately 0.25. At a blowing ratio of 2.00, the mass flow rate of the injected jet was approximately 1.3% of the blade passage inlet mass flow rate.

The baseline (nonflow control) airfoil measurements are presented in the paper by Mahallati et al. [7] and were made in the same test section with a cascade of nine solid airfoils. This baseline airfoil is stalled at Reynolds numbers of 25,000 and 50,000 with an FSTI of 0.4%. For the same Reynolds numbers at an FSTI of 4%, the airfoil does not stall but a separation bubble is present over the aft suction surface, resulting in acceptable profile losses for a low-pressure turbine operating under these conditions. Although flow control is not required at high FSTI, these conditions were examined to assess the effects of the inclined wall jet on a closed separation bubble.

### Blade Pressure Distribution and Mixed-Out Profile Losses

*Re=25,000, FSTI=0.4%.* The effects of the blowing ratio on the normalized profile loss for a Reynolds number of 25,000 and an FSTI of 0.4% are presented in Fig. 3. The suction surface static pressure distributions are also presented in Fig. 3 for selected levels of blowing ratio. The baseline airfoil is stalled at this Reynolds number and FSTI, which results in high profile losses. Stall is indicated by the large pressure plateau over the aft suction surface.

With flow control, the suction-surface flow remains stalled up to a blowing ratio of approximately 1.00. At a blowing ratio of

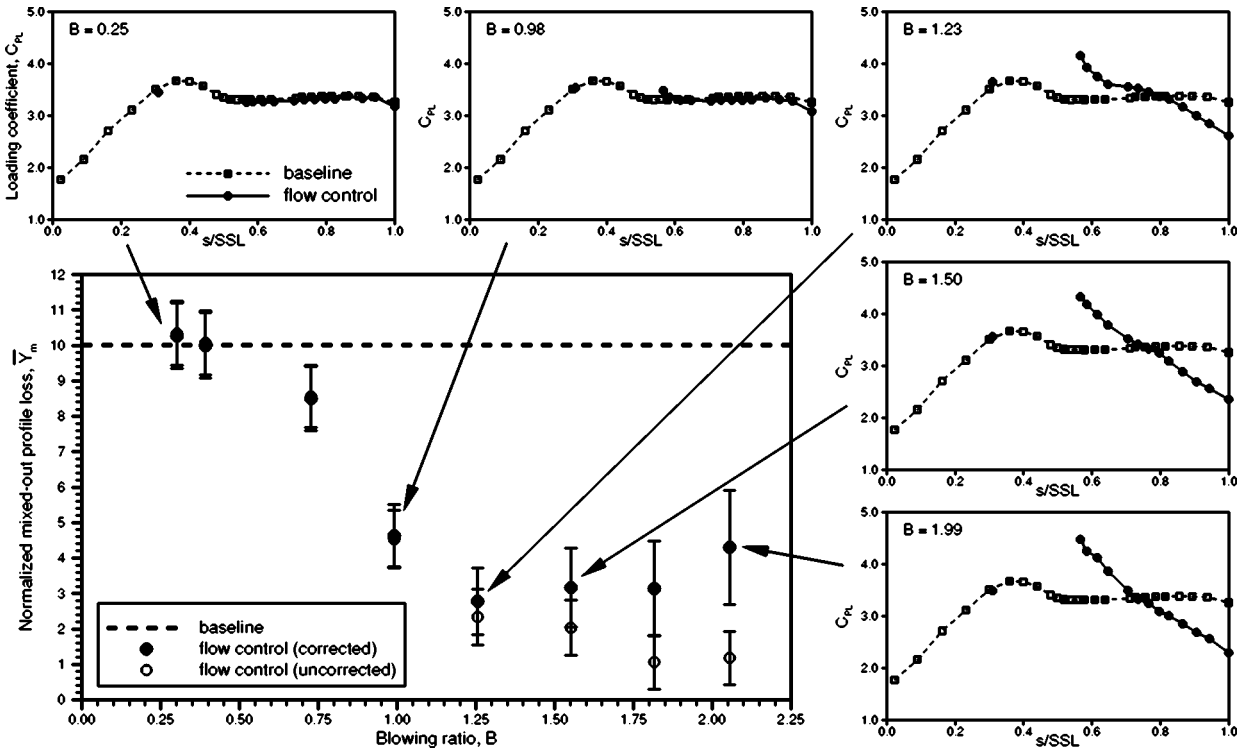


**Fig. 3 Surface static pressure distributions and losses for Re=25,000 and FSTI=0.4%**

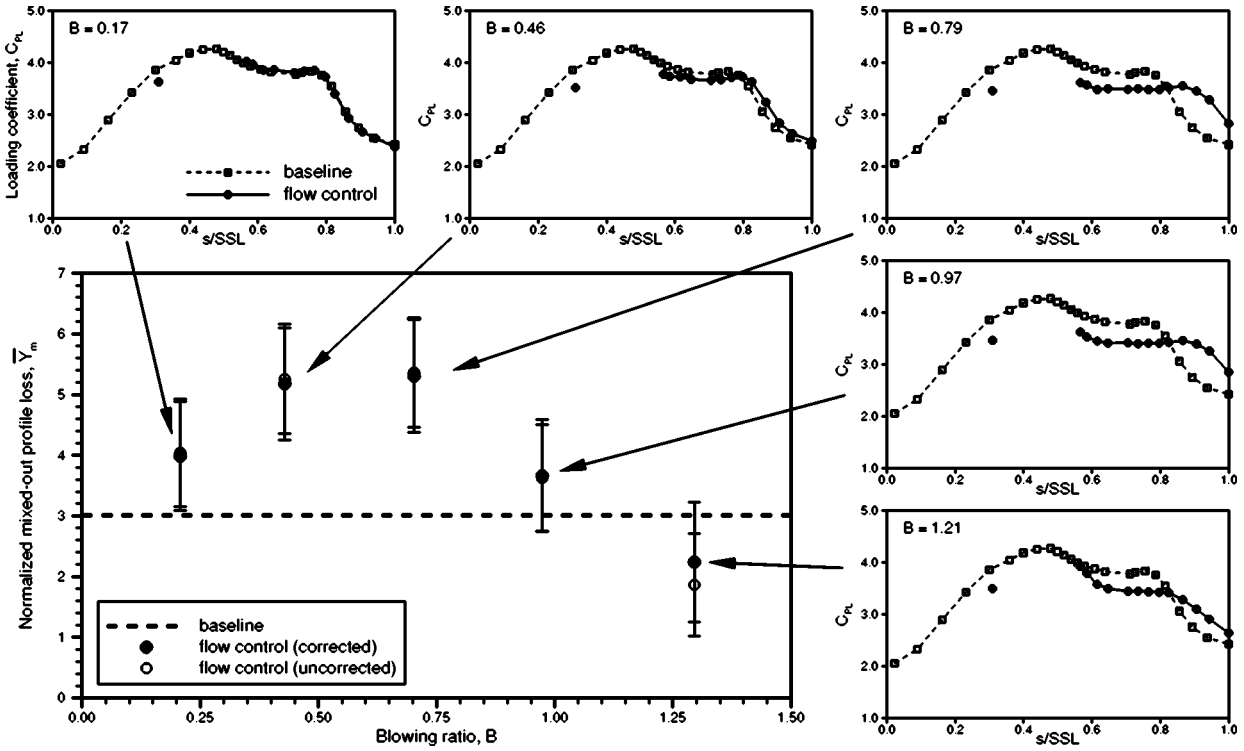


**Fig. 4 Surface static pressure distributions and losses for Re=25,000 and FSTI=4%**

1.23, the loading coefficient near the slot is increased and the separation point moves aft to approximately 65% SSL. At this blowing ratio, the separated shear layer appears reattached ahead of the trailing edge, but the reattachment point is difficult to locate. The ''corrected'' profile losses are also a minimum at a blowing ratio of around 1.25. For blowing ratios above 1.25, the boundary layer appears attached over the entire aft suction surface and the ''corrected'' losses remain relatively constant between blowing ratios of 1.25 and 1.80, above which the losses increase.

For low blowing ratios at a Reynolds number of 25,000, there is evidently insufficient momentum in the injected wall jet to re-energize the boundary layer and the blade remains stalled. As the blowing ratio is increased, the injected flow re-energizes the boundary layer which is then able to overcome the strong adverse pressure gradient, resulting in an attached suction surface boundary layer. The increased losses at high blowing ratios are assumed to be due to increased mixing losses between the jet and the blade passage flow.

*Re=25,000, FSTI=4%.* The surface static pressure distribution and profile losses at a Reynolds number of 25,000 and an FSTI of 4% are shown in Fig. 4.

The increased level of freestream turbulence apparently promotes earlier transition in the separated shear layer resulting in a closed separation bubble over the baseline Pak-B airfoil. At this Reynolds number, the baseline Pak-B profile losses are reduced compared to the low-FSTI case.

For the lowest blowing ratio of approximately 0.20, there is no difference in the aft suction surface pressure distribution between the baseline and flow control airfoils, but the flow control losses are approximately 30% higher. At a blowing ratio of 0.46, the separation bubble over the flow control airfoil appears slightly longer than that over the baseline airfoil and the losses are approximately 70% higher. Above a blowing ratio of 0.50, the separation bubble length increases and at a blowing ratio of around 1.20, the bubble length appears to be decreasing. The flow control profile losses decrease above a blowing ratio of approximately 0.7 and at a blowing ratio of 1.3, the losses are lower than that for the baseline airfoil. Thus, for an elevated level of freestream turbulence at a Reynolds number of 25,000, the current flow control configuration results in a larger separation bubble and higher losses for blowing ratios below 1.00.

*Re=50,000, FSTI=0.4%.* At a Reynolds number of 50,000 with low-FSTI, the baseline airfoil again stalls and profile losses are high. Fig. 5 presents the suction surface pressure distributions and profile losses for this operating condition.

At the lowest blowing ratio examined, stall is prevented and the profile losses are greatly reduced as compared to the baseline airfoil loss. For blowing ratios between 0.25 and 0.50, separation occurs at about 60% of the suction surface length (SSL) with a longer separation bubble at a blowing ratio of approximately 0.50. This increased bubble size is accompanied by an increase in the profile losses. At a blowing ratio of 0.76, the separation point moves downstream slightly but the reattachment point appears to be the same as at a blowing ratio of 0.48. The maximum flow-control losses for this operating condition are at a blowing ratio of approximately 0.50, above which the losses decrease. For a blowing ratio of 1.00 and higher, the boundary layer appears attached over the entire aft suction surface. The ''corrected'' profile losses plateau between blowing ratios of 1.00 and 1.50, above which they increase. At blowing ratios of 1.75 and 2.00, a jet flow was found to be present on the suction surface side of the downstream wake (not shown), and is the reason for the negative ''uncorrected'' losses observed at a blowing ratio of 2.00. In general, at a Reynolds number of 50,000 and an FSTI of 0.4%, low momentum injection ($B=0.25$) results in significantly reduced losses as compared to the baseline airfoil.

*Re=50,000, FSTI=4%.* Finally, the surface static pressure distributions and profile losses for a Reynolds number of 50,000 and an FSTI of 4% are shown in Fig. 6. The loss measurements and the surface pressure measurements were taken at different times, therefore the values of the blowing ratio do not always match.

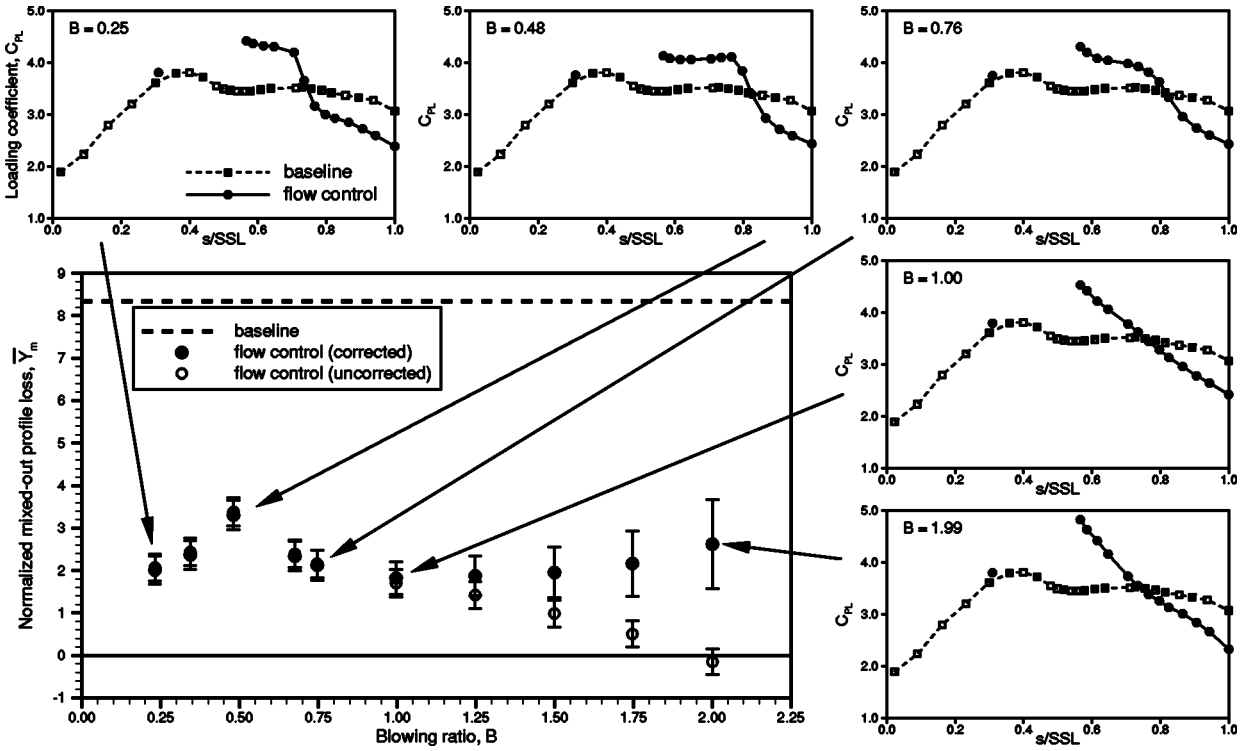


**Fig. 5 Surface static pressure distributions and losses for Re=50,000 and FSTI=0.4%**

The increased level of freestream turbulence promotes transition and a closed separation bubble over the baseline Pak-B airfoil, similar to the lower Reynolds number case.

At this Reynolds number, the separation bubble characteristics with blowing ratio are similar to those at a Reynolds number of 25,000, except that the separated shear layer reattaches well ahead of the trailing edge in all cases. For blowing ratios of 1.00 and higher, the injected momentum appears to suppress separation, resulting in a smooth deceleration up to the trailing edge. The profile losses reach a maximum near a blowing ratio of 0.50, as also seen for the corresponding low-FSTI condition. As the blowing ratio is increased to approximately 0.85, the losses decrease to

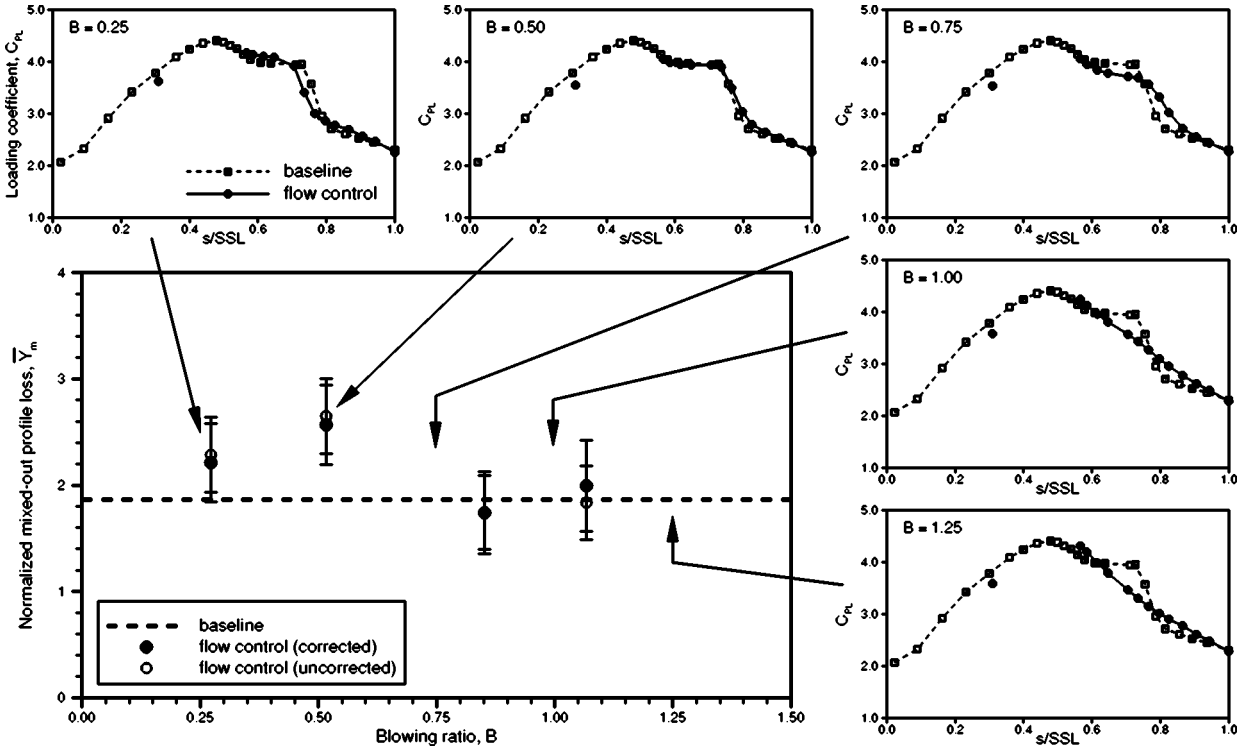


**Fig. 6 Surface static pressure distributions and losses for Re=50,000 and FSTI=4%**

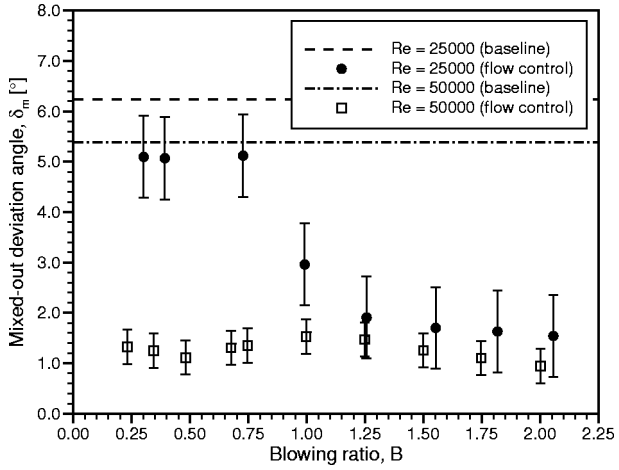


**Fig. 7 Deviation angles for FSTI=0.4%**

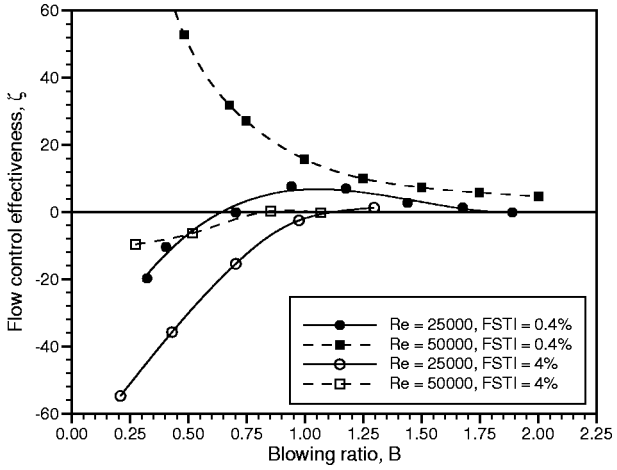


**Fig. 9 Active flow control effectiveness**

a value similar to that for the baseline airfoil, above which a slight increase in losses is observed. There appears to be no significant benefit from flow control at this operating condition.

**Mixed-Out Deviation Angles.** The mixed-out deviation angles for the low-FSTI measurements are presented in Fig. 7. High deviation angles are observed for the baseline airfoil at low-FSTI due to the fully separated suction surface boundary layer. At a Reynolds number of 25,000, the mixed-out deviation angles remain high for low blowing ratios ($B<1.00$), indicating decreased flow turning due to the fully-separated suction surface boundary layer. At a blowing ratio of 1.00, the deviation angle decreases and for blowing ratios greater than 1.00, the flow turning increases to values expected for this airfoil ($\delta_m=1.3$ deg based on the correlation of Islam and Sjolander [19]). At a Reynolds number of 50,000, deviation for the flow-control airfoil is much lower than for the baseline airfoil at all blowing ratios examined, indicating increased flow turning.

The mixed-out deviation angles for the high-FSTI measurements are presented in Fig. 8. At a Reynolds number of 25,000, the flow-control deviation angle is similar to that of the baseline airfoil for the lowest blowing ratios examined ($B=0.20$ and 0.40). At this Reynolds number, deviation reaches a maximum at a blowing ratio of approximately 0.70, above which it returns to a value similar to the baseline airfoil. The increased deviation is due to the larger separation bubble that forms on the suction surface in the presence of blowing, as seen in the surface pressure distributions (Fig. 4). At a Reynolds number of 50,000, the flow-control deviation angle remains relatively constant for all blowing ratios examined, and similar to the baseline airfoil.

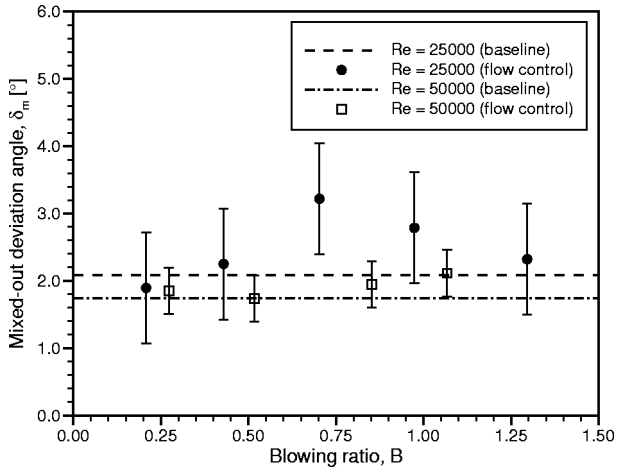


**Fig. 8 Deviation angles for FSTI=4%**

**Flow Control Effectiveness.** An effectiveness coefficient, $\zeta$, has been proposed [Eq. (3)] which relates the flow-control airfoil loss reduction, as compared to the baseline airfoil, to the momentum input of the flow control device. Based on the definition of $\zeta$, a negative value signifies an increase in losses from the baseline case. A maximum positive value of $\zeta$ signifies an optimum condition in which the use of the jet momentum is maximized in reducing the losses.

Figure 9 presents the effectiveness coefficients for all the flow control measurements presented thus far. At a Reynolds number of 25,000 and an FSTI of 0.4%, the effectiveness is negative for low-blowing ratios ($B<0.5$), indicating higher losses than the baseline airfoil. A maximum effectiveness occurs at a blowing ratio of approximately 1.00, which signifies an optimum blowing ratio. At a Reynolds number of 50,000 and an FSTI of 0.4%, the effectiveness tends to infinity as blowing ratio tends to zero, indicating that the blowing is effective at reducing losses even at very low blowing ratios. At an FSTI of 4%, the current active flow control method is not effective at low blowing ratios, where the profile losses are higher than those for the baseline airfoil. The cases where flow control reduces losses at high-FSTI show very small positive values of the effectiveness coefficient, much smaller than those achieved for the low-FSTI cases.

**Hot-Wire Traverse Measurements.** The measurements presented thus far show the effects of flow control on the airfoil pressure distribution and performance, but do not directly indicate the ways in which this flow control method affects the flow field. To examine this, hot-wire traverse measurements have been made in the region of the flow control slot. The traverse planes for the low-FSTI flow control cases were shown in Fig. 2. Hot-wire traverse measurements have been made at blowing ratios of 0.5, 1.0, and 2.0 at a Reynolds number of 50,000 and an FSTI of 0.4%, and at blowing ratios of 0.5 and 1.0 at a Reynolds number of 50,000 and an FSTI of 4%. These measurements are compared with hot-wire traverse measurements made over the baseline airfoil.

The development of the suction surface shear layer is presented in the form of profiles of mean velocity, $U$, and root-mean-square (RMS) of the velocity fluctuation level, $u'$. Both mean and fluctuation quantities are normalized by the local edge-of-the boundary layer velocity, $U_e$. One limitation of the current measurements is the inclination of the traverse planes to the blade surface, which is on the order of 45°, as seen from Fig. 2. To account for this inclination, the positions of the measurement points have been

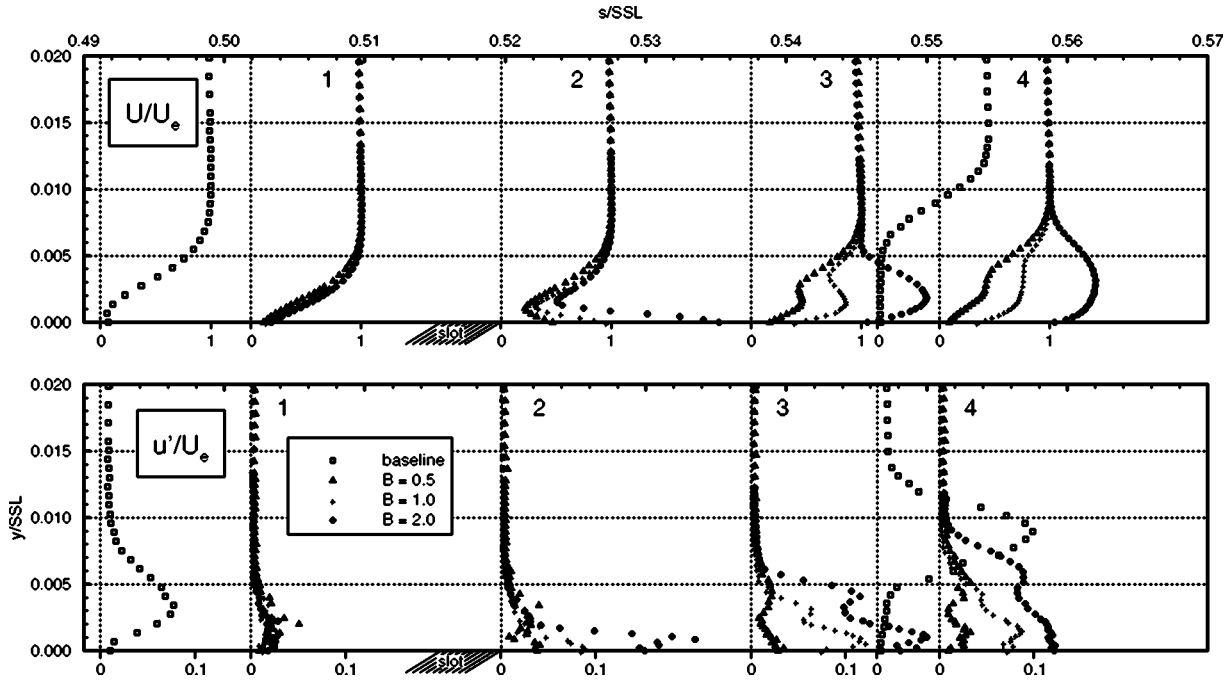


**Fig. 10 Hot-wire traverse measurements for FSTI=0.4%**

corrected, using the equation $y_{\text{normal}}=y_{\text{traverse}}\sin(\phi)$, where $\phi$ is the inclination angle of the traverse plane to the surface. Although the boundary layer profiles presented in this form do not represent the profile at a specific surface location, they are representative of the profiles in the region of the quoted surface location.

*FSTI=0.4%.* The velocity profiles for the low-FSTI measurements are shown in Fig. 10. The flow control slot is located between 51.5% and 52% SSL. Two sets of hot-wire traverse measurements for the baseline airfoil are also shown, but do not correspond to exactly the same traverse locations as the flow control measurements. It is apparent in the baseline airfoil measurements that separation occurs near 49% SSL and is fully established at 55% SSL. At Station 1 of the flow control measurements, there are slight differences in the mean velocity profiles for all values of blowing ratio examined. This is due to the effects of the downstream separation on the overall flow field. There is a visible inflection point in the profile for a blowing ratio of 0.5. All fluctuation profiles at Station 1 show low-level fluctuations within the boundary layer, which is therefore interpreted as laminar. At Station 2, which is located at the downstream edge of the slot, there

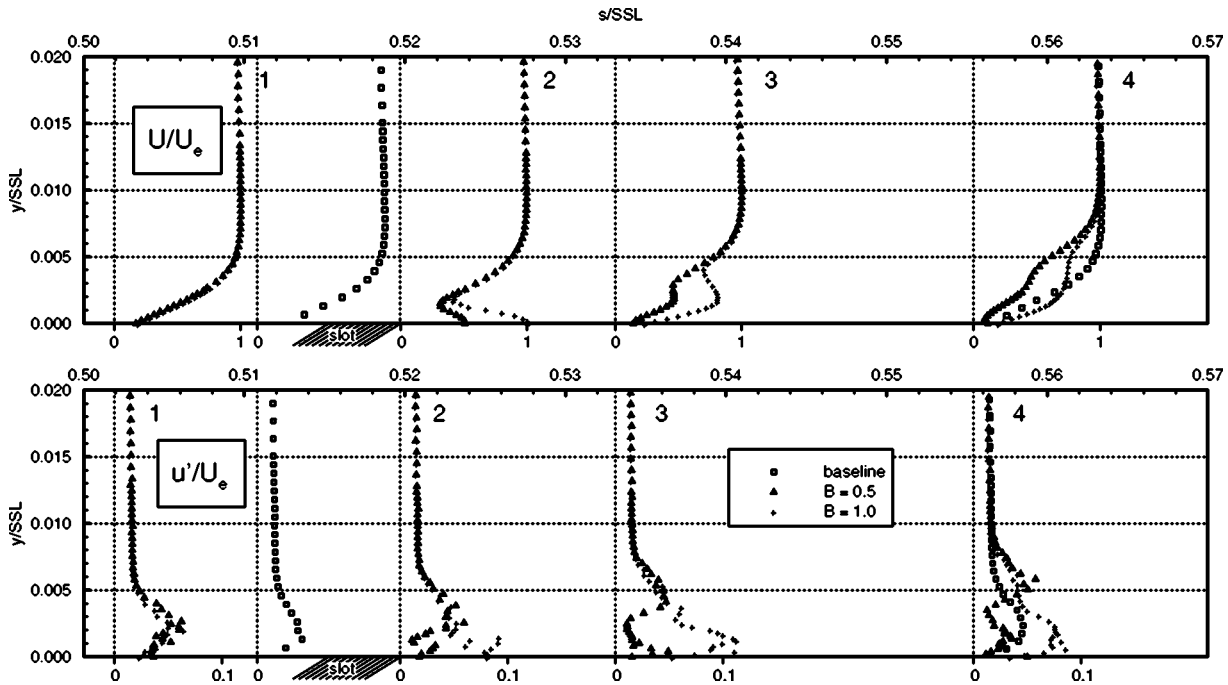


**Fig. 11 Hot-wire traverse measurements for FSTI=4%**

is a distinct shift of the laminar shear layer away from the surface due to the injected mass. This is the region where mixing between the wall jet and the laminar shear layer begins. High fluctuations near the surface indicate a turbulent wall jet. The velocity profiles at Stations 3 and 4 show the effects of mixing between the wall jet and the laminar free shear layer. At a blowing ratio of 0.5, the mean velocity profiles show the reason for an increased downstream separation bubble. The wall jet lifts the laminar free shear layer away from the surface, but contains insufficient momentum to entrain high-energy fluid towards the wall, resulting in a thick shear layer with a high momentum deficit and a near-wall inflection point. The mean velocity profiles for blowing ratios of 1.0 and 2.0 show a fuller near-wall profile, which results in a boundary layer less prone to separation. At a blowing ratio of 2.0, the high-momentum jet entrains boundary layer and freestream fluid resulting in a thick wall jet profile with minimal momentum deficit between the jet and the freestream. This strong wall jet is present over the entire aft suction surface and is apparent in the downstream wake profiles (not presented here). The fluctuation profiles at Stations 3 and 4 show a double peak. The peak nearest the wall is a result of turbulence in the wall jet flow. The second peak is in the region of highest shear in the outer mixing layer and may be interpreted as the onset of transition.

*FSTI=4%.* The velocity profiles for the high-FSTI measurements are shown in Fig. 11. Two hot-wire traverses were made over the baseline airfoil and are also shown in Fig. 11, but only the downstream baseline traverse plane corresponds with one of the flow control traverse planes (55.5% SSL). The baseline airfoil measurements show a laminar boundary layer with a visible inflection point at 55.5% SSL. At Station 1, located ahead of the slot, the mean velocity profiles for the two blowing ratios examined are very similar, as are the fluctuation profiles. The mean velocity profiles at Station 2 show the lifting effect of the wall jet on the laminar boundary layer. The profiles outside the jet region are very similar. For a blowing ratio of 0.5 at Station 2, the turbulent fluctuation level in the jet is in fact lower than the laminar fluctuations generated within the upstream laminar boundary layer. The high near-wall fluctuations at a blowing ratio of 1.0 indicate a turbulent wall jet flow. At Station 3, a thick low-momentum boundary layer is apparent at a blowing ratio of 0.5, similar to the low-FSTI case discussed in the previous section. At a blowing ratio of 1.0, high near-wall momentum and high near-wall fluctuations are observed at Station 3, indicating a boundary layer that is less susceptible to separation. The mean and fluctuation profiles at Station 4 are similar to those at Station 3, but a near-wall inflection point is visible at a blowing ratio of 0.5.

## Conclusions

Results from a study of separation control for the Pak-B low-pressure turbine airfoil have been presented. Active flow control, consisting of an inclined plane wall jet, has been used to inject momentum in the near-wall region of the suction surface boundary layer with the goal of reducing or suppressing separation.

It has been found that the use of active flow control is only useful when the baseline (nonflow control) airfoil is stalled. Stall occurs at low-Reynolds numbers (25,000 and 50,000) and low-freestream turbulence intensity (0.4%). At a Reynolds number of 25,000 and freestream turbulence intensity of 0.4%, a blowing ratio greater than 1.0 is required to suppress stall and reduce profile losses to an acceptable level. At a Reynolds number of 50,000 and freestream turbulence intensity of 0.4%, active flow control is effective at preventing stall and reducing losses for a low level of fluid injection (blowing ratio as low as 0.25). For high-freestream turbulence conditions, where the baseline airfoil has a reattached separation bubble, blowing does not significantly improve performance. For both Reynolds numbers examined at a freestream turbulence intensity of 4%, the current method of active flow control increases the profile losses of the Pak-B airfoil at low blowing ratios.

To examine the interaction between the jet and the surface shear layer, hot-wire traverse measurements made over the suction surface in the region of the flow control slot have been presented. At high blowing ratios ($B=1.0$ and 2.0), separation is prevented by injection of high-momentum turbulent fluid in the near-wall region, which ''fills-up'' the boundary layer and promotes transition in the outer shear layer. At low-blowing ratio ($B=0.5$), the low-momentum addition, coupled with the lifting effect of the injected fluid on the laminar boundary layer, results in a velocity profile with a high momentum deficit which promotes earlier separation and a larger separation bubble.

The current study has demonstrated that active flow control can prevent stall of the Pak-B airfoil for low freestream turbulence intensity (0.4%), a level much lower than would be expected in an engine. For high turbulence intensity (4%), more typical of engine conditions, the injection of fluid through the flow control slot promotes earlier separation and higher profile losses for low levels of blowing. Although the examined method of flow control does not benefit the Pak-B airfoil for engine conditions, the results suggest that a more highly loaded airfoil that stalls at high freestream turbulence levels may benefit from this flow control technique. One advantage of active flow control is that the control scheme can be activated only when required, and the disadvantages of the current control technique for un-stalled conditions could be avoided.

## Acknowledgment

Financial support for this study, as well as permission to publish this manuscript, has been provided by Pratt & Whitney, East Hartford, CT, and is gratefully acknowledged. The first author would also like to thank the Natural Sciences and Engineering Research Council of Canada for financial support through a postgraduate scholarship. We would like to acknowledge Ashish Nedungadi and Greg Tillman of the United Technologies Research Center (UTRC) for designing the slot and plenum arrangement for the flow control airfoil, and also Dr. Tom Praisner of Pratt & Whitney for the enlightening discussions regarding the results. Finally, we would like to thank Dr. Junqiang Zhu, who helped with performing the experiments.

## Nomenclature

$AR$ = airfoil aspect ratio ($=h/C$)
$b$ = flow control slot width
$B$ = jet blowing ratio ($=U_{j\,\max}/U_e$)
$C$ = airfoil true chord
$C_x$ = airfoil axial chord
$C_{PL}$ = surface static pressure coefficient $[=(P_{0i}-P_S)/q_i]$
FSTI = freestream turbulence intensity $(=\sqrt{\overline{u_i'^2}}/U_i)$
$h$ = airfoil span
$h_s$ = flow control slot length
$P_0$ = total pressure
$\overline{P}_0$ = mass averaged total pressure
$P_S$ = surface static pressure
$q$ = dynamic pressure ($=1/2\rho U^2$)
Re = Reynolds number ($=U_iC_x/\nu$)
$s$ = suction surface distance from leading edge
$S$ = airfoil pitch
SSL = suction surface length
$U$ = mean velocity
$\overline{U}_j$ = mean jet velocity $[=\int_0^1 U_j d(y/b)]$
$u'$ = fluctuating component of velocity
$y$ = distance from airfoil surface
$Y_m$ = mixed-out profile loss coefficient $[=(\overline{P}_{0i}-P_{0m})/q_m]$
$\overline{Y}_m$ = normalized profile loss coefficient ($=Y_m/Y_{m\mathrm{ref}}$)

$Z$ = Zweifel coefficient
$[=2(S/C_x)\cos^2\alpha_m|\tan\alpha_i-\tan\alpha_m|]$
$\alpha$ = flow angle from axial direction
$\beta$ = blade angle from axial direction
$\gamma$ = airfoil stagger angle
$\delta$ = deviation angle
$\phi$ = inclination of hot-wire traverse plane from surface
$\Lambda$ = integral length scale
$(=U\int_0^\infty[\overline{u'(t)u'(t+\Delta t)}/\overline{u'^2}]\,d\Delta t)$
$\nu$ = kinematic viscosity
$\theta$ = slot inclination angle from surface
$\rho$ = density
$\sigma$ = cascade solidity $(=C_x/S)$
$\zeta$ = effectiveness coefficient
$(=[(q_mY_m)_{\mathrm{BAS}}-(q_mY_m)_{\mathrm{AFC}}]S/\rho\overline{U_j^2}b)$

### Subscripts

AFC = flow control airfoil
BAS = baseline airfoil
$e$ = edge of shear layer
$i$ = cascade inlet
$j$ = jet
$m$ = mixed-out
$o$ = cascade outlet
ref = reference
$s$ = flow control slot

## References


[1] Hourmouziadis, J., 1989, ''Aerodynamic Design of Low Pressure Turbines,'' AGARD Lecture Series 167, pp. 1–40.
[2] Mayle, R. E., 1991, ''The Role of Laminar–Turbulent Transition in Gas Turbine Engines,'' ASME J. Turbomach., **113**, pp. 509–537.
[3] Hatman, A., and Wang, T., 1999, ''A Prediction Model for Separated-Flow Transition,'' ASME J. Turbomach., **121**, pp. 594–602.
[4] Malkiel, E., and Mayle, 1996, ''Transition in a Separation Bubble,'' ASME J. Turbomach., **118**, pp. 752–759.
[5] Yaras, M. I., 2001, ''Measurements of the Effects of Pressure-Gradient History on Separation-Bubble Transition,'' ASME Paper No. 2001-GT-0193, New Orleans, Louisiana.
[6] Yaras, M. I., 2002, ''Measurements of the Effects of Freestream Turbulence on Separation-Bubble Transition,'' ASME Paper No. GT-2002-30232, Amsterdam, The Netherlands.
[7] Mahallati, A., McAuliffe, B. R., Sjolander, S. A., and Praisner, T. J., 2004. ''Aerodynamics of a Low-Pressure Turbine Airfoil at Low-Reynolds Numbers, Part 1: Steady Flow Measurements,'' AIAA Paper No. 2004-3931, Fort Lauderdale, FL.
[8] Murawski, C. G., and Vafai, K., 2000, ''An Experimental Investigation of the Effect of Freestream Turbulence on the Wake of a Separated Low Pressure Turbine Blade at Low Reynolds Numbers,'' ASME J. Fluids Eng., **122**, pp. 431–433.
[9] Dorney, D. J., Lake, J. P., King, P. I., and Ashpis, D. E., 2000, ''Experimental and Numerical Investigation of Losses in Low-Pressure Turbine Blade Rows,'' AIAA Paper No. 2000-0737, Reno, NV.
[10] Bons, J. P., Sondergaard, R., and Rivir, R. B., 1999, ''Control of Low-Pressure Turbine Separation Using Vortex Generator Jets,'' AIAA Paper No. 99-0367, Reno, Nevada.
[11] Bons, J. P., Sondergaard, R., and Rivir, R. B., 2001, ''Turbine Separation Control Using Pulsed Vortex Generator Jets,'' ASME J. Turbomach., **123**, pp. 198–206.
[12] Gad-el-Hak, M., 2000, *Flow Control: Passive, Active, and Reactive Flow Management*, Cambridge University Press, Cambridge, UK.
[13] Volino, R. J., 2003, ''Passive Flow Control on Low-Pressure Turbine Airfoils,'' ASME Paper No. GT2003-38728, Atlanta, Georgia.
[14] Lake, J. P., King, P. I., and Rivir, R. B., 2000, ''Low Reynolds Number Loss Reduction on Turbine Blades with Dimples and V-Grooves,'' AIAA Paper No. 00–0738, Reno, NV.
[15] Fottner, L., 1979, ''Theoretical and Experimental Investigations on Aerodynamically Highly-Loaded Compressor Bladings with Boundary Layer Control,'' AIAA Paper No. 79-7032, Lake Buena Vista.
[16] Sturm, W., Scheugenpflug, H., and Fottner, L., 1992, ''Performance Improvements of Compressor Cascades by Controlling the Profile and Sidewall Boundary Layers,'' ASME J. Turbomach., **114**, pp. 477–486.
[17] Culley, D. E., Bright, M. M., Prahst, P. S., and Strazisar, A. J., 2003, ''Active Flow Separation Control of a Stator Vane Using Surface Injection in a Multistage Compressor Experiment,'' ASME Paper No. GT2003-38863, Atlanta, Georgia.
[18] Mahallati, A., 2003, ''Aerodynamics of a Low-Pressure Turbine Airfoil Under Steady and Periodically Unsteady Conditions,'' Ph.D. thesis, Carleton University, Ottawa, Canada.
[19] Islam, A. M. T., and Sjolander, S. A., 1999, ''Deviation in Axial Turbines at Subsonic Conditions,'' ASME Paper No. 99-GT-026, Indianapolis, IN.

# Time-Averaged and Time-Resolved Heat Flux Measurements on a Turbine Stator Blade Using Two-Layered Thin-Film Gauges

**V. Iliopoulou**
e-mail: iliopoul@vki.ac.be

**R. Dénos**

**N. Billiard**

**T. Arts**

von Karman Institute for Fluid Dynamics,
Turbomachinery & Propulsion Department,
Chaussée de Waterloo, 72
1640 Rhode Saint Genèse, Belgium

*This paper describes the steps undertaken to measure heat flux in a turbine tested in a blowdown windtunnel when using a two-layered thin film gauge array. The sensor consists of a nickel thermoresistor deposited onto a flexible polyamide sheet that can be easily bounded on a substrate using double sided adhesive. The assembly constitutes a two-layered system. First, a numerical algorithm is proposed to extract the wall heat flux from the surface temperature history measured by the thin film gauge. It is very flexible and handles multilayered systems. Then, an original procedure is proposed to determine the thermal properties and the thickness of the different layers. It uses the above numerical algorithm coupled with a minimization routine. The repeatability of the procedure is assessed. Finally, tests are processed according to the proposed method. The results are successfully compared with measurements performed with single-layered thin film gauges.*
[DOI: 10.1115/1.1791647]

## 1 Introduction

The design of a blade cooling scheme for a turbine stage requires the knowledge of the heat transfer coefficient around the considered airfoil. Not only the mean levels of heat fluxes should be known but also the variations due to blade passage events in order to assess their impact on high cycle fatigue.

The technique under investigation consists in measuring the wall temperature history of a test piece during a blowdown test. This information is used as boundary conditions together with the thermal properties of the substrate to solve the unsteady heat conduction equation and allows extracting the wall heat flux. The sensor considered here consists of a nickel thin-film deposited onto a flexible Upilex sheet. The sheet is bonded on a metallic turbine stator blade and constitutes thus a two-layered system from a heat transfer point of view.

The two-layered thin film gauge technique was intensively developed at Massachusettes Institute of Technology (MIT), Boston, MA (Epstein et al. [1]) and at the University of Oxford, Oxford England (Doorly and Oldfield [2]). The two-layered gauge proposed by Epstein et al. [1] consists of two temperature sensors (thin-films) on either side of the first insulating substrate and it is applied to the blade surface (Abhari et al. [3]). More recently, Piccini et al. [4] proposed to place a thermocouple between the first insulating layer and the metallic model. In both cases, the boundary conditions on each side of the instrumented sheet are known and only the thermal properties of the first layer are required.

An analytical solution of the unsteady heat conduction equation is proposed by Doorly and Oldfield [5] for a semi-infinite substrate submitted to a step in heat flux. The thermal properties of the successive layers are calibrated by the use of the electrical discharge method, extended for the determination of the thickness of the first layer, and the thermal properties of the second layer. Alternative methods consist in a step test using a laser [1] or a heated jet [4].

For the derivation of the wall heat flux from the wall temperature history, one can use electrical analogy (Doorly and Oldfield [2,5]) or numerical solutions of the unsteady heat conduction equation (Schultz and Jones [6]).

Steady heat transfer measurements are performed on metal turbine blades of an annular cascade by Guo et al. [7] and compared with liquid crystal results. Although the trends are identical for the two techniques, the liquid crystal measurements report higher mean values. This was attributed to the roughness of the liquid crystals compared to the smooth polyamide film.

Up to now, at van Karmen Institute (VKI), Belgium, platinum thin-film gauges fired onto a single-layered machinable glass ceramic substrate are used. The entire blade can be made of ceramic for cascade testing (Arts et al. [8]) or inserts can be fitted into metallic blades in the case of measurement on the rotor of a turbine stage (Didier et al. [9] and Dénos [10]). The main advantage of the two-layered technique with respect to the single-layered technique is the possibility of instrumenting existing metallic hardware in a cost-effective and quick manner.

In this paper, original calibration and data reduction techniques are proposed and validated. First, the operating principle of multilayered thin-film gauges is reminded. The computations of the heat flux from the wall surface temperature are performed thanks to a one-dimensional (1D) numerical solution of the unsteady conduction using a Crank-Nicholson scheme that can deal with multiple substrate thermal properties. Then, the technique for the determination of the thermal product of the two substrates and the thickness of the instrumented sheet is described. It uses an optimization technique coupled with the previously mentioned numerical solution. The repeatability of the calibration is assessed. Finally, the determined thermal properties and the data reduction technique are used to process experimental data acquired on the second stator of a one and a half stage turbine. Both time-

Contributed by the International Gas Turbine Institute (IGTI) of THE AMERICAN SOCIETY OF MECHANICAL ENGINEERS for publication in the ASME JOURNAL OF TURBOMACHINERY. Paper presented at the International Gas Turbine and Aeroengine Congress and Exhibition, Vienna, Austria, June 13–17, 2004, Paper No. 2004-GT-53437. Manuscript received by IGTI, October 1, 2003; final revision, March 1, 2004. IGTI Review Chair: A. J. Strazisar.

  

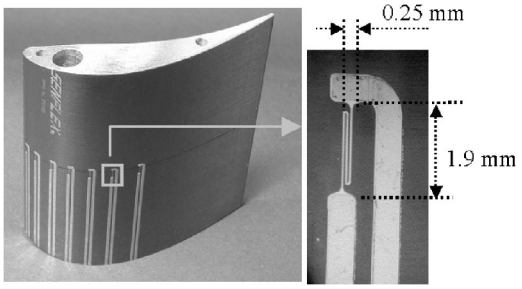


**Fig. 1 "Senflex" two-layered substrate thin-film gauge**

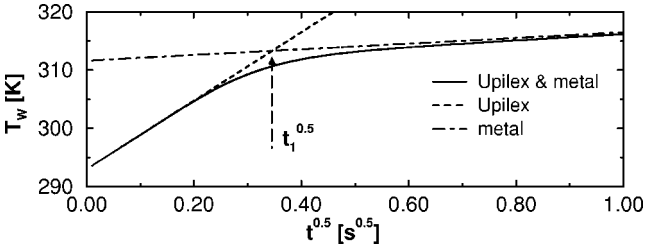


**Fig. 2 Linearization of the wall temperature evolution for a gauge submitted to a constant wall heat flux**

averaged and time-resolved (due to rotor blade passing events) components of the signal are processed. They are successfully compared with measurements performed with the single-layered gauges.

## 2 Operating Principle

The determination of the heat transfer coefficient $h$ by convection [Eq. (1)] requires the knowledge of (1) the gas temperature, (2) the wall temperature, and (3) the heat flux at the wall.

$$h=\frac{\dot{Q}_{\mathrm{WALL}}(t)}{T_{\mathrm{GAS}}-T_{\mathrm{WALL}}(t)} \tag{1}$$

1. The gas temperature is measured with a 25 $\mu$m thermocouple designed for measurements under transient conditions (Paniagua et al. [11]).
2. The surface temperature is monitored by the thin-film gauge. It consists of a serpentine nickel thin-film (0.25 mm wide and 1.9 mm long, see Fig. 1) with a resistance of 60 $\Omega$ deposited on a 50 $\mu$m thick Upilex-S polyamide sheet that can be glued on the blade surface with a 75 $\mu$m thick double-sided adhesive sheet. The sensing element of the thin-film acts as a variable resistance thermometer [Eq. (2)], whose change of resistance is monitored in a Wheatstone bridge. The use of copper paths allows performing connections with a negligible resistance.

$$R=R_0[1+a_0(T-T_0)] \tag{2}$$

3. The heat flux is derived from the wall surface temperature history during a blowdown test: Hot gas is suddenly released on the cold-instrumented test body and the surface temperature rises as a function of time. The 1D unsteady conduction equation for a multilayered substrate system can be written as

$$\frac{\partial^2 T(x,t)}{\partial x^2}=\frac{1}{\alpha(x)}\frac{\partial T(x,t)}{\partial t} \tag{3}$$

The thermal properties are obviously depending on the considered location $x$ inside the substrate. The thermal properties of the adhesive sheet are similar to the Upilex-S sheet, thus both are considered as a unique first layer. The second layer is the blade material itself.

The necessary boundary conditions to solve Eq. (3) are

1. The total depth of the substrates is such that at a given depth $x$, the temperature can be considered as constant during the short testing time (semi-infinite substrate hypothesis),
2. The wall temperature increase or the wall heat flux,
3. At the substrates interface $x=L$, the values of heat flux and temperature for the two substrates are the same

$$-k_1\left(\frac{\partial T_1(t)}{\partial x}\right)_{x=L-}=-k_2\left(\frac{\partial T_2(t)}{\partial x}\right)_{x=L+} \tag{4}$$

$$T_1(x=L^-,t)=T_2(x=L^+,t) \tag{5}$$

Finally, the heat flux at the wall is computed thanks to the Fourier law

$$\dot{Q}_{\mathrm{WALL}}(t)=-k_1\left(\frac{\partial T_1(t)}{\partial x}\right)_{x=0} \tag{6}$$

The sensing element of the gauge is so thin and conductive that it can be neglected in the modeling (Schultz and Jones [6]). The first layer of the substrate must be an electrical insulator because of the sensing element and the connections painted onto its surface. It should be a thermal insulator (low thermal diffusivity) in order to magnify the surface temperature increase, and to minimize lateral conduction (1D hypothesis).

The value of the heat flux at the wall will depend only on $k/\sqrt{\alpha}=\sqrt{\rho Ck}$, i.e., the so-called thermal product. For this reason, the accuracy on the heat flux is directly linked to the accuracy on the two thermal products of the two substrates. Additionally, the thickness of the first layer $L$ is the third parameter that determines the accuracy of the heat flux calculations [Eqs. (4) and (5)].

## 3 Determination of Surface Heat Flux

As far as the two-layered thin-film gauges are concerned, an analytical solution for Eq. (3) exists only for the case of a step in heat flux (see Doorly and Oldfield [2])

$$T_{\mathrm{WALL}}(t)=\frac{2\dot{Q}_{\mathrm{WALL}}}{\sqrt{\rho Ck_1}}\cdot\left\{\sqrt{\frac{t}{\pi}}+2\sum_{n=1}^{\infty}A^n\left[\left(\frac{t}{\pi}\right)^{1/2}\exp\left(-\frac{n^2L^2}{\alpha_1 t}\right)-\frac{nL}{\sqrt{\alpha_1}}\mathrm{erfc}\left(\frac{nL}{(\alpha_1 t)^{0.5}}\right)\right]\right\}$$

$$\text{where: } A=\frac{1-\sigma}{1+\sigma},\quad \sigma=\frac{\sqrt{\rho Ck_2}}{\sqrt{\rho Ck_1}} \tag{7}$$

When the surface temperature rise is plotted as a function of $t^{0.5}$, the response of the successive substrates can be approximated by straight lines [Eq. (8), see Fig. 2].

$$\Delta T_{\mathrm{WALL}}(t)=\frac{2\dot{Q}_{\mathrm{WALL}}}{\sqrt{\pi}\sqrt{\rho Ck_2}}\sqrt{t}+\dot{Q}_{\mathrm{WALL}}\frac{L}{k_1}\left(1-\frac{\rho Ck_1}{\rho Ck_2}\right) \tag{8}$$

The first slope is inversely proportional to the thermal product of the first layer. Similarly, the second slope can be related to the thermal product of the second layer. The time at which the two lines intersect allows the determination of the sheet thickness [Eq. (9)].

$$\frac{L}{k_1}=\frac{2}{\sqrt{\pi}}\sqrt{t_1}\frac{(\sqrt{\rho Ck_1})^{-1}-(\sqrt{\rho Ck_2})^{-1}}{1-\sigma^{-2}} \tag{9}$$

Note that even if the test consists of a step in gas temperature, the gauge response can be corrected with a superposition technique so that the solution for constant heat flux can be used (Piccini et al. [4], Billiard et al. [12]). For these reasons, this analyti-

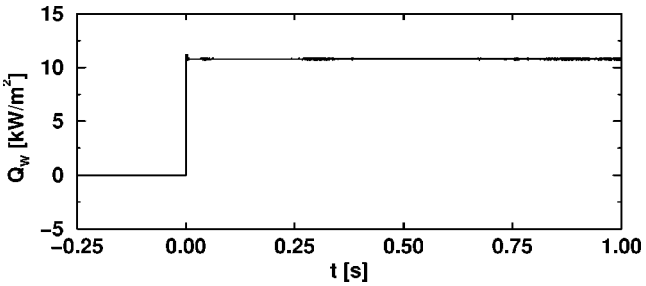


**Fig. 3 Calculated surface heat flux (10 800 W/m$^2$) with the Crank-Nicholson scheme**

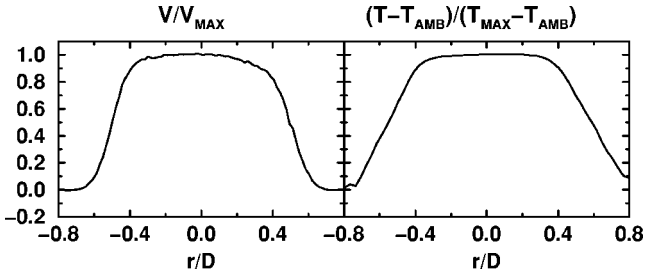


**Fig. 4 Aerothermal conditions of the jet**

cal solution [Eq. (7)] and its approximation [Eqs. (8) and (9)] are often used to determine the thermal properties of the substrate and the thickness of the sheet.

Although the analytical solution is very didactic, it cannot be used for the data reduction of a real test. The resolution proposed here uses a finite difference Crank-Nicholson scheme. It consists of an arithmetic average of the explicit and implicit formulation of the space derivative of Eq. (3). Note that $j$ is the index for space and $m$ is the index for time. The numerical parameter $\eta$ controls the stability of the scheme. This stability is ensured unconditionally if $\eta$ is larger than 0.5, i.e., time step and space step are completely decoupled. Note that the scheme with $\eta=0$ is explicit (Hirsch [13]). If the unknowns at time $m+1$ are expressed as a function of the computed solution at time $m$, a tridiagonal system is obtained that can be efficiently solved with existing algorithms. The solution provides the distribution of temperature in the gauge substrate at time step $m+1$.

$$\frac{T_j^{m+1}-T_j^m}{\Delta t} = \eta\left[\frac{\left(\frac{\alpha_j}{\Delta x_j}(T_{j+1}^{m+1}-T_j^{m+1})\right)-\left(\frac{\alpha_{j-1}}{\Delta x_{j-1}}(T_j^{m+1}-T_{j-1}^{m+1})\right)}{\frac{\Delta x_{j-1}}{2}+\frac{\Delta x_j}{2}}\right] + (1-\eta)\left[\frac{\left(\frac{\alpha_j}{\Delta x_j}(T_{j+1}^{m}-T_j^{m})\right)-\left(\frac{\alpha_{j-1}}{\Delta x_{j-1}}(T_j^{m}-T_{j-1}^{m})\right)}{\frac{\Delta x_{j-1}}{2}+\frac{\Delta x_j}{2}}\right] \tag{10}$$

The time step is obviously the sampling frequency. The space step can be variable. Clustering can be used close to the wall where the heat flux will be calculated as the derivative of the temperature profile. Low-pass filtering is applied to avoid the large amplification of high frequencies that is inherent to the transfer function that links the surface temperature to the heat flux. The numerical solution was validated using the analytic solution of Eq. (7) as an input. The computed response is shown in Fig. 3 and provides to the expected shape (a step) and magnitude. The technique is very fast and flexible and is routinely used for data reduction.

## 4 Calibration Procedure

The calibration procedure aims at determining the two thermal products and the thickness of the first layer (the thermal properties of the glue are supposed to be very close to the one of the polyamide sheet). This requires submitting the gauge to a source of heat flux of well-known magnitude.

**A Heat Flux Source Characterization.** The accurate determination of the magnitude of the heat flux is the most delicate task (see Diller [14]). Many techniques (calorimeters, thin-film gauges, etc.) are based on the thermal property of a reference material (copper, quartz, etc.). However, if manufacturers can guarantee a high level of purity of the selected reference material and provide values for the thermal properties ($\rho$, $C$, and $k$), they never provide the associated uncertainty, i.e., it is difficult to provide an uncertainty associated with the mean values of heat fluxes.

The electrical heating technique consists in submitting the gauge to a step of current with a well-known intensity (see Dénos [10]). In principle, the technique only requires the knowledge of the flux dissipated by Joule effect ($RI^2$) and the area. In practice, it is very difficult to determine the area of the gauge with accuracy. In addition, only the gauge area is heated and lateral conduction takes place very quickly. For these reasons, the technique requires two tests: one under vacuum and one in a liquid of well-known thermal properties. Consequently, the technique also relies on the thermal properties of a reference material.

Laser heating technique requires the accurate knowledge of the incident heat flux. Considering the different reflections on the substrate and on the gauge, it is also very difficult to guarantee a reasonable accuracy.

The approach used here consists in determining the thermal properties of several types of substrates [ceramic (Macor), quartz, polyamide (Upilex) and steel] and in comparing the values with manufacturer data. The repeatability of the measurements is then assessed to check if it is better than the uncertainty.

The source of heat flux is a 15 mm diameter heated jet (~340 K). The value of $T_{GAS}$ [Eq. (1)] is provided by a thermocouple that monitors the gas temperature inside the nozzle. The tested gauge ($0.25\times1.9$ mm$^2$, shown in Fig. 1) is placed on a flat plate ($50\times50$ mm$^2$, 5 mm thick) on which the jet impinges perpendicularly. A step function in gas temperature is applied to the gauge thanks to a fast opening shutter placed between the gauge and the nozzle. At an axial distance of 15 mm downstream of the nozzle, the aerothermal conditions are constant over 80% of the diameter (see Fig. 4). Measurements performed by Buchlin and Laperches [15] using infrared thermography ensure that the heat flux is also uniform on this portion of the jet. The semi-infinite assumption is satisfied by using a limited duration of the surface temperature history. This duration is estimated from the criterion proposed by Schultz and Jones [6] for one-layered substrate [depth $>3.648\,(\alpha t)^{0.5}$]. For example, this duration is of the order of 2.2 s for a 5 mm thick Macor substrate. Note that diameter of the jet (15 mm) is such that lateral conduction will also be negligible over this duration.

The heat exchange coefficient is determined using a reference gauge based on a ceramic (Macor). The thermal properties of the ceramic are evaluated by the electrical heating technique that provides a value of 2073 J/(m$^2$ Ks$^{0.5}$). The unsteady heat conduction equation is solved using the above-mentioned numerical methods. A correlation for Nusselt number as a function of Reynolds number is then produced. The results are plotted in Fig. 5. Note the test-to-test repeatability is better than 1%.

**B Thermal Product Calibration.** The two-layered substrate thin film gauges are implemented on three types of sub-

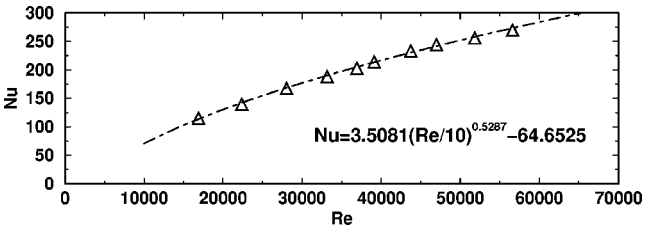


**Fig. 5 Nusselt-Reynolds correlation obtained with single-layered thin-film gauge**

strates: ceramic, quartz, and steel. Concerning the ceramic test piece, two layers of glue and Upilex are used. The purpose is to check if the glue layer can be distinguished from the Upilex and to enlarge the portion of the time history where only the influence of the Upilex/glue assembly is tested.

Steps in gas temperature were applied to the different samples. The correlation determined previously is used to provide the value of $h$. Since the gas temperature and the wall temperature are also measured, a reference wall heat flux history can be determined [Eq. (1)].

A second wall heat flux history can be evaluated using the measured wall temperature increase, the numerical algorithm presented earlier and a first guess of the thermal properties and of the sheet thickness.

The difference between the two heat flux histories is then computed point by point. The differences are squared and summed to provide a unique number indicating how close the heat flux computed with the first guess is from the reference one. A minimization routine based on a quasi-Newton algorithm (available from a mathematic library Nag) updates iteratively the thermal product and the sheet thickness until the difference between the two heat flux histories is minimum. More information about this technique is reported by Billiard et al. [12]. The results are presented in Table 1 together with the manufacturer and the test-to-test repeatability.

The tests with two successive layers of glue and polyamide did not reveal any inflexion point in the surface temperature history confirming thus that the thermal properties of the glue and the polyamide are very similar.

Regarding the thermal properties of Upilex, the differences with respect to the manufacturer values are +5.6%, +8.7%, and +1% for the samples based on Macor, quartz, and steel respectively. The value obtained for Macor [2117 J/(m$^2$ Ks$^{0.5}$)] is naturally close to the one determined by electrical heating [2073 J/(m$^2$ Ks$^{0.5}$)], which is the value used for the thermal product of the reference gauge that provides the Nusselt/Reynolds correlation. The large overestimation with respect to the manufacturer data (+19%) was also observed by Miller [16] with the electrical heating technique. The thermal product of quartz differs by +13% from the manufacturer data. For steel, a good agreement is obtained (less than 1% difference). These numbers show that a high accuracy on the absolute values of thermal products (and thus heat fluxes) is not expected.

**Table 1 Calibration results**

| | $\sqrt{\rho Ck}$ Upilex [J/m$^2$ Ks$^{0.5}$] | Upilex Thickness [$\mu$m] | $\sqrt{\rho Ck}$ 2nd layer [J/m$^2$ Ks$^{0.5}$] |
|---|---|---|---|
| on *Macor* (8 tests) | 731 | 305 | 2117 |
| Manufacturer value | 692 | 250 | 1780 |
| on *quartz* (9 tests) | 752 | 167 | 1726 |
| Manufacturer value | 692 | 125 | 1521 |
| on *steel* (5 tests) | 699 | 175 | 8147 |
| Manufacturer value | 692 | 125 | 8088 |
| | Dispersion (20:1) [±%] | | |
| on *Macor* (8 tests) | 2.3 | 3.9 | 5.9 |
| on *quartz* (9 tests) | 3.9 | 3.9 | 4.9 |
| on *steel* (5 tests) | 8.8 | 8.7 | 9.0 |

Note: Manufacturer data: Macor: Dow Corning, quartz: GE Silice product, Upilex: ICI films.

**Table 2 Turbine operating condition**

| | $P_{01}$ [bar] | $T_{01}$ [K] | $T_{03}/T_{01}$ | $P_{03}/P_{01}$ | $T_{04}/T_{01}$ |
|---|---|---|---|---|---|
| Mean | 2.231 | 472.4 | 0.769 | 0.362 | 0.741 |
| Disp (20:1) | | 6.1% | 2.3% | 1.9% | 2.1% |

Note: 01: total condition upstream of the stage, 03: total condition downstream of the stage/upstream of the second stator, 04: total condition downstream of the second stator.

The repeatability obtained for the thermal product of Upilex is satisfactory upon Macor (±2.3%) and upon quartz (±3.9%). The repeatability obtained for the thermal products of Macor and of quartz (±5.9% and ±4.9%) is reasonable. For the tests upon steel, the repeatability is larger. Steel is a highly conductive material. As a consequence, once the heat flux has traversed the insulating layer, the surface temperature increase is moderate. This means that a large variation of the thermal product of steel during the minimization process will not cause a large change of surface temperature. With a parametric study of the analytical solution for constant heat flux, it can also be shown that the accuracy on the thermal product of steel is less important than that of the Upilex layer. The low number of tests included calls for a new calibration with more tests.

In general, the repeatability on the tests is much better than the uncertainty on the mean value of the thermal product.

Another interesting point for performing a number of tests is to increase the confidence on the calculated mean value. If $\sigma$ is the confidence on a single test, the confidence on the mean is $\sigma/\sqrt{n}$.

The repeatability on the results obtained by this technique is much better than that obtained by the analytical solution for constant heat flux [Eq. (7)]. In the later case, the time zero ($t=0$) at which the step starts (see Fig. 2) must be defined with accuracy. This is not obvious since the experiment is never a perfect step. In addition, the lines plotted in Fig. 2 correspond to the evolution that the gauge reaches asymptotically. Particularly for the second layer, it is not easy to define two limits to perform a linear regression that will provide a slope value close to the one obtained asymptotically. In the following, the thermal properties obtained by the tests on steel are used. Although the dispersion is larger for this case, it is representative of the blade that will be tested.

## 5 Measurements

Heat flux measurements were carried out on the second stator of a turbine stage at 50% of the blade height with a 12-element thin film gauge array.

The turbine stage was tested with dry air in the VKI short duration compression tube facility CT3. This blowdown facility is capable of simulating Reynolds and Mach numbers, gas/wall and gas/coolant temperature ratios of modern aeroengine (HP) turbines (Sieverding and Arts [17]). The turbine operating total conditions are summarized in Table 2. The inlet and outlet Reynolds number (based on chord) to the second stator are equal to 520 000 and 480 000, respectively. The heat transfer distributions around the second stator profile are reported under the form of a Nusselt number:

$$Nu = \frac{hc}{k_{GAS}} = \frac{\dot{Q}_{WALL}(t)c}{k_{GAS}[T_{GAS} - T_{WALL}(t)]} \tag{11}$$

where $T_{GAS}$ is the total temperature of the gas upstream of the second stator indicated as $T_{03}$ in Table II, measured by a fast response thermocouple.

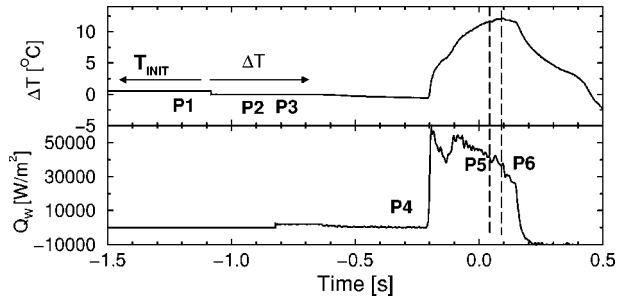


**Fig. 6 Surface temperature and heat flux for the time-averaged component**

**A Time-Averaged Component.** The relationship between the temperature and the resistance of the gauge is expressed in Eq. (2).

The resistance change of the gauge is recorded into two steps (Fig. 6):

1. Before the test, the overall resistance of each gauge is monitored (mode $T_0$, $R_0 \sim 60\,\Omega$) in order to know the initial temperature,
2. Just before the blowdown takes place (point P4), an automatic procedure (mode $\Delta T$) balances the Wheatstone bridge and changes the gain of the amplifier so that the small variation of the resistance ($\sim 1.5\ \Omega$) can be translated into a significant variation of voltage.

For the calculation of the Nusselt number [Eq. (11)], average values of gas temperature, wall temperature and wall heat flux (second graph) are evaluated between points P5 and P6.

Prior to the blowdown, the rotor is spun almost up to the design speed (6500 RPM) in such a way that the rotational speed takes the desired value when the blowdown takes place. Although the pressure level in the test section is low ($\sim$50 mbar absolute), the rotor is a source of ventilation losses and creates a non-uniform temperature profile around the second stator. In Fig. 7, the average initial temperature distributions obtained with the single and two-layered gauges are shown. The agreement between the two measurements is satisfactory. The gauge, with the highest initial temperature is the most exposed to the rotor ventilation and it is located on the suction side, close to the leading edge ($S/S_{\mathrm{MAX}}$ equal to 0.0516).

Figure 8 reports the averaged values of the blade wall temperature between the points $P_5$ and $P_6$ in Fig. 6. The corresponding wall heat fluxes and Nusselt numbers are given, for four tests (52–55). The scale of the graph hides the fact that the levels of temperature reached during the blowdown may change significantly from test to test. This is due to different initial temperature distribution (the test section gets hotter and hotter from test to test) and some variations of the gas inlet temperature. Note that

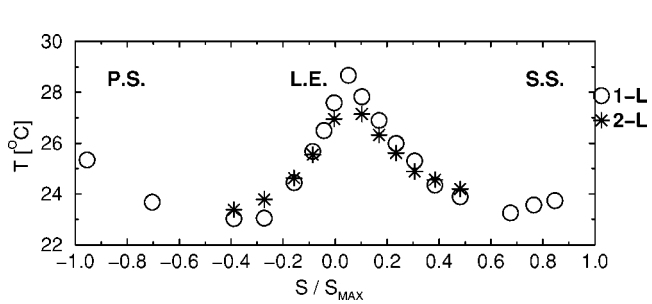


**Fig. 7 Blade initial temperature distributions prior to blowdown from single and two-layered gauges**

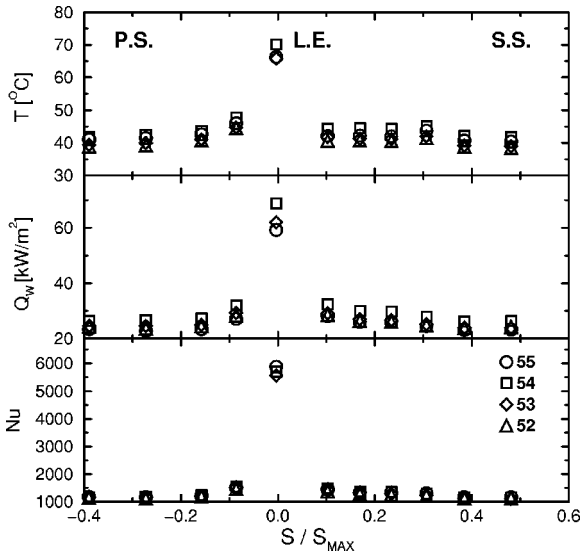


**Fig. 8 Surface temperature, heat flux, and Nusselt distribution for the two-layered gauges during the blowdown**

although one can have significant test-to-test variation on $T_{\mathrm{GAS}}$, $T_{\mathrm{WALL}}$ and thus $\dot{Q}_{\mathrm{WALL}}$, this does not mean that a large dispersion will be obtained on the heat transfer coefficient or the Nusselt number. Indeed, if for example $T_{\mathrm{GAS}}$ increases, the $T_{\mathrm{WALL}}$ history and the corresponding heat flux will change accordingly in such a way that the heat transfer coefficient or Nusselt number keep constant.

As expected, the highest heat flux is observed at the stagnation point owing to the absence of boundary layer. The Nusselt value of 6000 obtained with the two-layered gauge is most probably excessive. A similar plot is presented in Fig. 9 for measurements obtained with the single-layered gauges. In general, the surface temperature increase is higher with the two-layered gauges compared to the single-layered gauges. This effect is due to the lower thermal product of Upilex [699 J/(m$^2$ Ks$^{0.5}$)] (i.e., thermal insulation) compared to the one of Macor [2073 J/(m$^2$ Ks$^{0.5}$)].

Figure 10 compares the Nusselt distribution obtained with the two types of gauge. The bars illustrate the range in which 95%

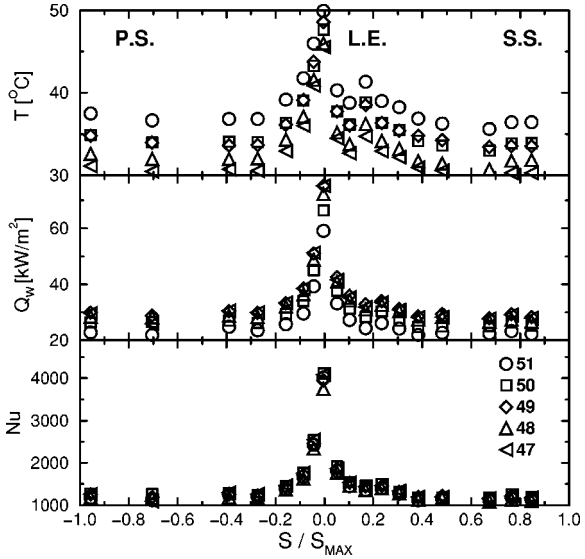


**Fig. 9 Surface temperature, heat flux, and Nusselt distribution for the single-layered gauges during the blowdown**

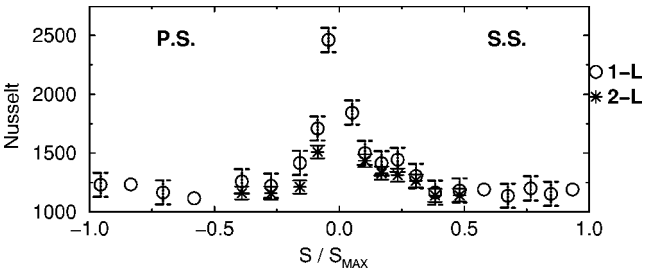


**Fig. 10 Comparison of the repeatability of the Nusselt distribution between the single- and two-layered gauges**

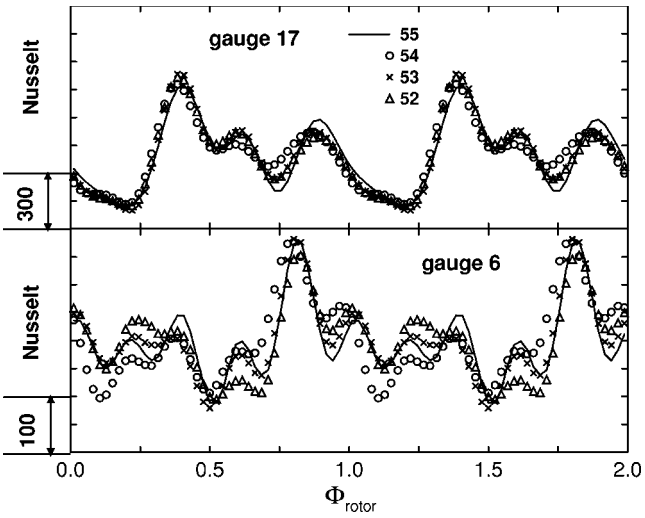


**Fig. 11 Unsteady Nusselt number traces of two gauges of four different measurements for the two-layered gauges**

(20:1) of the measurements are contained and it is evaluated from a set of 40 values in the case of the two-layered system and 85 values for the single-layered gauges. The corresponding values are $\pm 55$ and $\pm 103$, respectively, i.e., for a typical mean value of Nusselt number of 1250, percentages of $\pm 4.4\%$ and $\pm 8.2\%$. This better repeatability for the two-layered gauges is attributed to the larger surface temperature increase. Since the computation of the Nusselt number requires the evaluation of $T_{GAS}$, $T_{WALL}$, and thus $\dot{Q}_{WALL}$, the uncertainty on each of these quantities will affect the repeatability of the Nusselt number.

The gauges at the stagnation region are not included in the repeatability estimation due to the large dispersion observed. Note that in this region, the values can change by significant amounts with very small changes of incidence, error in the positioning of the gauge, distance from the real stagnation point, etc. Approximating the leading edge of the blade by a 3.5 mm diameter cylinder and using heat transfer correlations for cylinders provided by Kestin and Wood [18], a mispositioning of 0.9 mm with respect to the stagnation point would result in an underestimation of the Nusselt number of 10%.

The only two-layered gauge that does not follow the values of the correspondent single one is the leading edge gauge. It overestimates the Nusselt by about 50%. Since the leading edge area is highly curved and the layer of Upilex quite thin, it is possible that the one-dimensional heat conduction equation is not valid anymore. In addition, the second layer (steel) is highly conductive and lateral conduction will take place much sooner inside the substrate than inside the polyamide sheet.

**B Time-Resolved Component.** According to the transfer function that links the surface temperature to the heat flux in the Laplace domain for single-layered gauge [Eq. (12), Schultz and Jones [6]], a heat flux fluctuation of a given amplitude will cause a larger surface temperature increase at low frequency than at high frequency. For example, the ratio of this amplitude for sinusoidal heat flux fluctuations at 1 Hz (time scale of the blowdown) and 7 kHz (rotor blade passing frequency) is $\sqrt{7000}/\sqrt{1}=83.7$. For this reason, an analog circuit is used to amplify the variations at high frequency (see also Ainsworth et al. [19]). The transfer function of the circuit has a constant amplification up to 100 Hz and amplifies according to $\sqrt{j\omega}$ between 100 Hz and 20 kHz. Above 20 kHz, the gain decreases. Hence, a correct resolution of the fluctuations is allowed on the 12-bit data acquisition system. Before the post processing, the signal is demodulated using numerical systems that have a transfer function inverse to that of the analog circuit (sums of first orders or *N*th order linear systems).

$$\overline{T}_{WALL}(p)=\frac{\overline{\dot{Q}}_{WALL}(p)}{\sqrt{\rho Ck}\sqrt{p}} \tag{12}$$

In order to assess the repeatability of the time-resolved component of the measurements, the Nusselt traces of gauges 17 and 6 (gauge locations are indicated in Fig. 13) are reported in Fig. 11. These time-resolved traces represent the variation of the Nusselt number as a function of rotor blade passing events. The origin of the abscissa corresponds to the alignment of the stacking axis of the rotor with the one of the second stator. The traces are obtained with a phase-locked averaging technique that integrates 192 rotor passing events (three rotor revolutions). The technique does not use any interpolation and also permits the derivation of the random unsteadiness as a function of the rotor position (not shown here). The several fluctuations result from a complex rotor-stator interaction in which the wake and the potential field of the rotor affect the second stator flow field as the rotor traverses the second stator inlet passage. Gauge 17 is located on the suction side of the second stator (see Fig. 13) and reports the largest periodic fluctuations of Nusselt number (750 peak to peak) while gauge 6 is located on the pressure side and reports periodic fluctuations of small amplitude (250 peak to peak).

Owing to the moderate amplitude of the fluctuations, the obtained repeatability is satisfactory. The minimum-maximum envelope of the phase locked average (min-max Nu), the mean level of random unsteadiness averaged over one rotor blade passing event and the correlation coefficient of the single- and two-layered gauges are reported in Fig. 12. The agreement of the min-max envelopes obtained with the two techniques is satisfactory. The correlation coefficient is obtained by performing a linear regression between the ordinate of the original signal and the ordinate of the phase-locked average. It tells how close the raw signal resembles the phase locked average. If this coefficient is 1, then the raw signal is equal to the phase locked average, i.e., there is no random unsteadiness. As it gets away from 1, the amount of random unsteadiness increases with respect to the periodic part. In this case, random unsteadiness has two sources: electronic noise due to very high levels of amplification and heat transfer fluctuations from the flow field. In general, the correlation coefficient is higher for the two-layered gauges. This is attributed to the better signal to noise ratio that results from the larger surface temperature change (lower thermal product). Consequently, the mean level of random unsteadiness (RMS), that contains also the noise of the signal, is lower.

Figure 13 compares the time-resolved Nusselt traces from the single-layered gauges (gray long dashed lines) and two-layered gauges (black solid lines). The agreement between the two measurement techniques is satisfactory. The gray arrow indicates a perturbation linked to the rotor that propagates from the crown of the stator toward the leading edge as the rotor traverses a stator

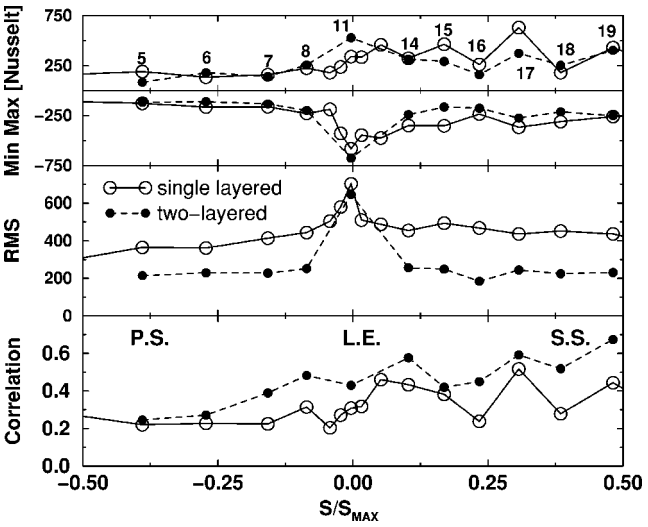


**Fig. 12 Min-max envelope, mean RMS, and correlation coefficient of the Nusselt number obtained with single and two-layered gauges**

passage. This event disappears on the pressure side of the stator blade, where the high unsteadiness of the flow is the dominant factor on the heat flux traces.

The minimum-maximum envelope (Fig. 12) indicates a region on the suction side where the amplitude of the Nusselt number fluctuations is large. In this region the correlation coefficient is high, which attests clear the above-mentioned periodic phenomenon.

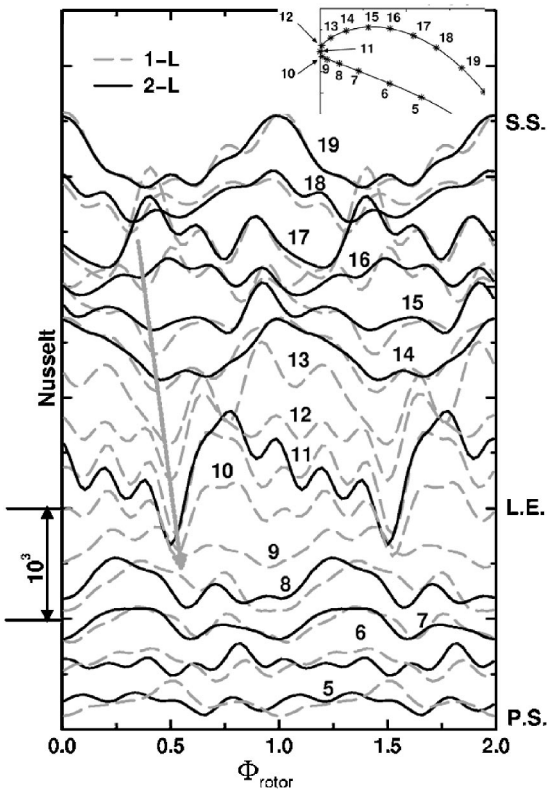


**Fig. 13 Comparison of the unsteady Nusselt traces between the single- (in grey) and the two-layered gauges (in black)**

## 6 Conclusions

A fast and flexible numerical technique that allows converting a surface temperature rise measured by a two-layered thin-film gauge into a heat flux is proposed and validated. It solves the unsteady 1D conduction equation using a Crank-Nicholson scheme, can handle multilayered substrates and can use wall heat flux or wall temperature as a boundary condition. Apart from the 1D hypothesis, there is no particular restriction.

A procedure is then proposed to determine the thermal properties and the thickness of the polyamide/glue layer. The heat flux source is a heated jet that impinges on a flat plate. The magnitude of the heat flux is measured thanks to a reference gauge. The size and the uniformity of the heated area guarantee both 1D and semi-infinite hypothesis. An accurate Nusselt/Reynolds correlation is derived. The heat flux source is used to perform step in gas temperature to a number of samples instrumented with two-layered thin film gauges. The numerical technique described above is used to predict the wall heat flux using a first guess of the thermal product of the two layers and the thickness of the first layer. A minimization algorithm compares the difference between this heat flux and the one computed with the Nusselt/Reynolds correlation and updates the values of thermal properties and thickness until the difference becomes minimum. As expected, differences exceeding 10% can be found when comparing the obtained absolute values of the thermal products with the manufacturer data. However, the repeatability of the proposed technique is better than the uncertainty. The estimated ranges in the case of the polyamide sheet are between $\pm 2.3\%$ and $\pm 3.9\%$, of the Macor ceramic is $\pm 5.9\%$ and of the quartz is $\pm 4.9\%$.

Finally, the numerical data reduction technique and the determined thermal products are used to perform measurements on a stator blade with a thin-film array based on a Upilex substrate as the first layer and steel as the second layer. The time-averaged and time-resolved component (rotor blade passing events) are processed and successfully compared with single-layered gauges measurements. The repeatability obtained with the two-layered gauges on the time-averaged values ($\pm 4.4\%$) is satisfactory and better than that of the single-layered gauges ($\pm 8.2\%$). The time-resolved component requires electronic frequency compensation before being acquired with high resolution on the 12-bit data acquisition system. Numerical demodulation is applied before applying a phase locked averaging technique. The repeatability obtained with the two-layered gauges on the time-resolved component is satisfactory. The signal-to-noise ratio of the two-layered gauges is better than that of the single-layered gauges.

## Nomenclature

**Roman**

$a_0$ = temperature-resistance coefficient [$\Omega$/K]
$c$ = blade chord [m]
$C$ = specific heat at constant pressure [J/(kg K)]
$D$ = diameter of the nozzle [m]
$h$ = convective heat transfer coefficient [W/(m$^2$ K)]
$I$ = current intensity [A]
$k$ = thermal conductivity [W/(m K)]
$L$ = substrate interface [m]
$L/k_l$ = thermal thickness parameter [m$^2$ K/W]
Nu = Nusselt number [hD/$k_{AIR}$]
$p$ = Laplace variable
$Q$ = heat flux [W/m$^2$]
$r$ = axis parallel to the gauges surface [m]
$R$ = resistance [$\Omega$]
Re = Reynolds number [UD/$\nu_{AIR}$]
S = curvilinear coordinate
$T$ = temperature [K]
$t$ = time [s]
$U$ = velocity of the jet [m/s]
$x$ = axis perpendicular to the gauges surface [m]

### Greek

$\alpha$ = thermal diffusivity [$m^2/s$]
$\eta$ = numerical parameter
$\nu$ = kinematic viscosity [$m^2/s$]
$\rho$ = density [$kg/m^3$]
$\omega$ = frequency [Hz]

### Subscripts

$i$ = index for the substrate layers
$j$ = index for space
$m$ = index for time
0 = reference
1,2 = first or second layer, respectively

## References


[1] Epstein, A. H., Guenette, G. R., Norton, R. J. G., and Yuzhang, C., 1986, ''High-Frequency Response Heat-Flux Gauge,'' Rev. Sci. Instrum., **57**(4), pp. 639–649.

[2] Doorly, J. E., and Oldfield, M. L. G., 1986, ''New Heat Transfer Gages for Use on Multilayered Substrates,'' ASME J. Turbomach., **108**, pp. 153–160.

[3] Abhari, R. S., Guenette, G. R., Epstein, A. H., and Giles, M. B., 1992, ''Comparison of Time-Resolved Turbine Rotor Blade Heat Transfer Measurements and Numerical Calculations,'' ASME J. Turbomach., **114**, pp. 818–827.

[4] Piccini, E., Guo, S. M., and Jones, T. V., 2000, ''The Development of a New Direct-Heat-Flux Gauge for Heat-Transfer Facilities,'' Meas. Sci. Technol., **11**, pp. 342–349.

[5] Doorly, J. E., and Oldfield, M. L. G., 1987, ''The Theory of Advanced Multi-Layer Thin Film Heat Transfer Gauges,'' J. Heat Mass Transfer, **30**(6), pp. 1159–1168.

[6] Schultz, D. L., and Jones, T. V., 1973, ''Heat Transfer Measurements in Short Duration Facilities,'' AGARDograph no. 165.

[7] Guo, S. M., Spencer, M. C., Lock, G. D., Jones, T. V., and Harvey, N. W., 1995, ''The Applications of Thin Film Gauges on Flexible Plastic Substrates to the Gas Turbine Situation,'' ASME paper No. 95-GT-357.

[8] Arts, T., Lambert de Rouvroit, M., and Rutherford, A. W., 1990, ''Aero-Thermal Investigation of a Highly Loaded Transonic Linear Turbine Guide Vane Cascade (A Test Case for Inviscid and Viscous Flow Computations),'' VKI TN 174.

[9] Didier, F., Dénos, R., and Arts, T., 2002, ''Unsteady Rotor Heat Transfer in a Transonic Turbine Stage,'' ASME J. Turbomach., **124(4)**, pp. 614–622.

[10] Dénos, R., 1996, ''Aerothermal Investigation of the Unsteady Flow in the Rotor of a Transonic Turbine Stage,'' Ph.D. thesis, University of Poitiers, France, December 1996.

[11] Paniagua, G., Dénos, R., and Oropesa, M., 2002, ''Thermocouple Probes for Accurate Temperature Measurements in Short Duration Facilities,'' Proceedings, ASME 2002, Amsterdam, GT-2002-30043.

[12] Billiard, N., Iliopoulou, V., Ferrara, F., and Dénos, R., 2002, ''Data Reduction and Thermal Product Determination for Single and Multilayered Substrates Thin-Film Gauges,'' Proceedings, 16th Symposium on Measuring Techniques, Cambridge University, Cambridge, UK.

[13] Hirsch, C., 1988, ''Fundamentals of Numerical Discretization,'' *Numerical Computation of Internal and External Flows*, Wiley, Great Britain, pp. 425–431.

[14] Diller, T. E., 1993, ''Advances in Heat Flux Measurements,'' Adv. Heat Transfer, **23**, pp. 279–368.

[15] Buchlin, J. M., and Laperches, M., 1998, ''Detailed Investigation of Aerothermal Behavior of Confined Impinging Jet,'' *Quantitative Infrared Themography QIRT 98*, D. Balageas, G. Busse, and G. M. Carlomagno, eds., S. A. Lodart, Lodz, Poland, pp. 258–264.

[16] Miller, C. G., 1981, ''Comparison of Thin-Film Resistance Heat Transfer Gauges With Thin-Skin Transient Calorimeter Gages in Conventional Hypersonic Wind Tunnels,'' NASA Technical Memorandum 83197.

[17] Sieverding, C. H., and Arts, T., 1992, ''The VKI Compression Tube Annular Cascade Facility CT3,'' ASME paper No. 92-GT-336.

[18] Kestin, J., and Wood, R., 1971, ''The Influence of Turbulence on Mass Transfer From Cylinders,'' J. Heat Transfer, **93C**, pp. 321–327.

[19] Ainsworth, R. W., Allen, J. L., Davies, M. R. D., Doorly, J. E., Forth, C. J. P., Hilditch, M. A., Oldfield, M. L. G., and Sheard, A. G., 1989, ''Developments in Instrumentation and Processing for Transient Heat Transfer Measurement in a Full-Stage Model Turbine,'' ASME J. Turbomach., **111**, pp. 20–27.

# Effect of the Hub Endwall Cavity Flow on the Flow-Field of a Transonic High-Pressure Turbine

**G. Paniagua**

**R. Dénos**

**S. Almeida**

Turbomachinery and Propulsion Department,
von Karman Institute for Fluid Dynamics,
Chaussée de Waterloo 72,
B1640—Rhode Saint Genèse, Belgium

*In high-pressure turbines, a small amount of cold flow is ejected at the hub from the cavity that exists between the stator and the rotor disk. This prevents the ingestion of hot gases into the wheel-space cavity, thus avoiding possible damage. This paper analyzes the interaction between the hub-endwall cavity flow and the mainstream in a high-pressure transonic turbine stage. Several cooling flow ratios are investigated under engine representative conditions. Both time-averaged and time-resolved data are presented. The experimental data is successfully compared with the results of a three-dimensional steady Navier-Stokes computation. Despite the small amount of gas ejected, the hub-endwall cavity flow has a significant influence on the mainstream flow. The Navier-Stokes predictions show how the ejected cold flow is entrained by the rotor hub vortex. The time-resolved static pressure field around the rotor is greatly affected when traversing the non-uniform vane exit flow field. When the cavity flow rate is increased, the unsteady forces on the rotor airfoil are reduced. This is linked to the decrease of vane exit Mach number caused by the blockage of the ejected flow.* [DOI: 10.1115/1.1791644]

## 1 Introduction

The high pressure in the main gas path forces hot gas to leak into the wheel-space cavity between the stator and the rotating disc. The ingress of hot gas into the turbine wheel-spaces can cause overheating, unwanted thermal fatigue, and uncontrolled dilatation rates of the rotor discs and bearings. The hot gas ingestion is prevented by continuously expelling cold air into the disc cavities to oppose the inward flow of hot gas and to cool down the disk. Furthermore, in the past some engines used this air to cool not only the disk but also the rotor blades, which were not internally cooled [1]. It is important to take into account these cavity flows during the design phase since they are supposed to maintain the working temperature of the disk at an acceptable level and to ensure a reasonable design life [2]. The flow rate of this purge air is controlled with interstage seals and preswirl nozzles. Steinetz and Hendricks [3] provide further details on advanced seal technologies.

Detailed investigations have been carried out on the discharge coefficient and the minimum flow rate to prevent ingress for various seal configurations. Campbell [4] noted the importance of the nonaxysimmetric external flow concerning flow ingestion into the cavity. Kobayashi et al. [5], Pahdke and Owen [6], Chew et al. [7], Dadkah et al. [8], and Daniels et al. [9] have performed investigations on the effect of a pitch-wise pressure gradient, including the effects of the mainstream swirl. Another concern is to ensure proper cooling in order to prevent disk thermal stress. Ko and Rhode [10], Bohn et al. [11], Ko et al. [12], and Laroche et al. [13] presented studies on the cavity thermal field showing the influence of the seal gap recirculation zone and giving practical information regarding the hot spots that affect the disc life.

Numerical studies have made a significant contribution to the current state of the art. Wilson et al. [14] performed direct Navier-Stokes (DNS) calculations of the highly unsteady flow within a rotating cavity with stationary casing. Hah [15] has been studying for several years the interaction between the turbine main-passage and the wheel-space cavity seal flow, using steady and unsteady three-dimensional (3D) Navier-Stokes (N-S) solvers. Hunter and Manwaring [16] evaluated the effect of various seal configurations on turbine performance using a steady 3D N-S solver. Förster et al. [17] performed 3D N-S simulations of the internal flow and seal leakage rate in a rotor-stator cavity including the seal lips and the rotor shank pockets with various external circumferential pressure gradients.

In recent years several experimental programs have been carried out on the cavity-mainstream interaction. Lindqvist et al. [18] addressed the span-wise mixing of the temperature in a cold turbine test rig ($M_2=0.48$) using the gas concentration analogy. They predicted a temperature minimum between 20% and 30% span at the rotor trailing edge plane. Gallier et al. [19] investigated the seal flow interaction in a two-stage turbine at low speed ($M_{2\,\max}\approx 0.28$) using particle image velocimetry (PIV). They noticed an increase of the horseshoe vortex intensity when cavity flow is ejected. McLean et al. [20] studied the effect on performance of two different types of wheel-space cooling, also at low speed ($M_2=0.23$). They observed that even 1% cooling air has significant effects on the turbine performance due to the modification of the secondary flows. Girgis et al. [21] presented the experimental and numerical results on the efficiency improvement in a transonic turbine ($M_2=1.22$) at low Reynolds (Re=97 000) due to the optimization of the ejected upstream cavity cooling flow. Cavity flows with a large tangential component allow an improvement of +0.3% efficiency compared to the case of flow injected radially, owing to the lower disturbance to the main flow field. Several authors have performed steady and unsteady pressure measurements, but they observed very weak effects on the vane outlet pressure, e.g., Roy et al. [22] at low speed ($M_2\approx 0.20$), and Gentilhomme et al. [23] at high subsonic conditions ($M_2\approx 0.96$).

Nevertheless, the literature on the mixing process between the wheel-space cooling flow and the mainstream flow is scarce especially on high speed flows. In addition, in a real engine environment, the interaction is highly unsteady. The hot gas ingress mechanism is affected by both the circumferential pressure field imposed by the vane and the unsteady pressure variations associated with the movement of the rotor blade.

In this work, a transonic high-pressure (HP) turbine stage ($M_2=1.16$) is tested under engine representative conditions for

Contributed by the International Gas Turbine Institute (IGTI) of THE AMERICAN SOCIETY OF MECHANICAL ENGINEERS for publication in the ASME JOURNAL OF TURBOMACHINERY. Paper presented at the International Gas Turbine and Aeroengine Congress and Exhibition, Vienna, Austria, June 13–17, 2004, Paper No. 2004-GT-53458. Manuscript received by IGTI, October 1, 2003; final revision, March 1, 2004. IGTI Review Chair: A. J. Strazisar.

  

three mass-flow rates across the wheel-space cavity. 3D N-S simulations support the experiments. First the vane exit time-averaged static pressure is investigated. Then the flow field on the cavity and rotor hub platform is described. The effect of the cavity flows on the rotor static pressure distribution is analyzed. Calculations show how the cold cavity flow interacts with the mainstream and alters the secondary flows. Additionally, the influence of hub disk leakage on the unsteady rotor blade and disk force is derived from experimental pressure data. Finally, the turbine exit flow field are discussed.

## 2 Generalities

**A HP Transonic Turbine Stage.** This transonic turbine has 43 cylindrical stator airfoils and 64 rotor blades (see Fig. 1). The nominal conditions are a stage pressure ratio $P_{01}/P_{s3}=3.0$, a stage loading coefficient $\Delta H/U^2=1.7$, and Reynolds numbers for the vane and the rotor: $\mathrm{Re}_{2,Cs}=1\times10^6$, $\mathrm{Re}_{3,Cr}=0.5\times10^6$. The stator airfoil is internally cooled, with a coolant ejection through a slot along the rear pressure side.

The channel height along the stator passage is constant, while across the rotor it increases by 10% on the rotor hub platform to limit the rotor exit Mach number. The stator and rotor axial chords at mid-span are respectively $C_{s\ \mathrm{ax}}=43.07$ mm and $C_{r\ \mathrm{ax}}=39.59$ mm. The spacing between the stator trailing edge and the rotor leading edge is $0.35\times C_{s\ \mathrm{ax}}$. Under running conditions, the rotor tip clearance is 0.6% of the mean rotor channel height, measured with wear gauges.

**B Experimental Test Facility.** The turbine stage is tested in the von Karman Institute (VKI) compression tube facility [24] that provides full similarity with engine operating conditions in a cost-effective way. After a short transient, nearly constant flow conditions are maintained for 300 ms. Due to the absence of any brake the net power of the turbine is converted into acceleration of the rotor. Typically, the rotational speed varies about 1.2% of its nominal rotational speed ($\omega$=6500 RPM).

Figure 2 shows a schematic of the coolant supply, which is independent of the vane cooling air supply. The mass flow ingested or ejected in the cavity slot is computed as the difference between the flow rates measured through the supply pipes and the mass flow leaking into the inner cavity through the lower labyrinth seal. The mass flow across the supply pipes is measured by means of choked orifices. The flow rate entering the inner cavity is estimated from the pressure evolution during the test. Note that prior to the blowdown, the pressure in this inner cavity is very low ($\sim$50 mbar absolute pressure). For the investigated conditions, the mass flow into the inner cavity was about 0.5% of the mainstream mass flow. Consequently, hot gas ingress occurs (at a rate of 0.5%) in the absence of cavity coolant flow ejection.

**C Test Conditions.** The stage inlet pressure and temperature ($P_{01}=1.62$ bar, $T_{01}=440$ K) ensure engine representative Reynolds numbers and temperature ratios $T_{01}/T_{\mathrm{wall}}=T_{01}/T_{\mathrm{coolant}}=1.5$. The stage mass flow is 10.5 kg/s. The vane cooling mass flow represents 3%. At midspan the Mach numbers at the exit of the vane and rotor are $M_2=1.03$ and $M_{3,r}=0.89$, respectively. For all the tests the slot width was kept constant with a gap ratio $G=0.0032\pm0.0003$.

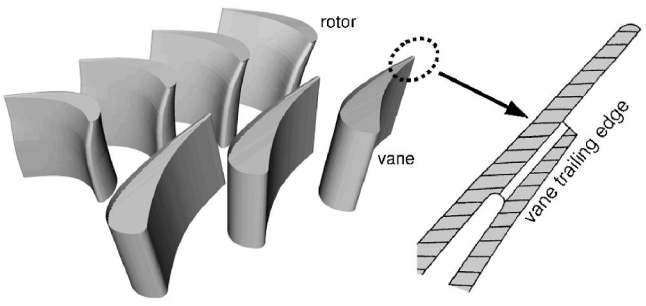


**Fig. 1 Three-dimensional view of the turbine stage**

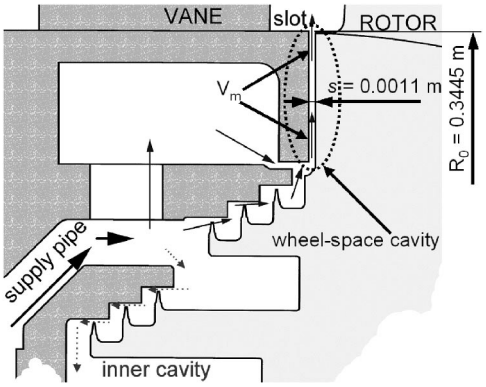


**Fig. 2 Turbine stage cross section with the disk cooling setup**

The three different testing conditions are summarized in Table 1. In the following, they will be referred to using the notation in the first column, namely, the cavity mass flow as a percentage of the mainstream flow. The $-0.5\%$ condition simulates the case in which hot gases are ingested through the labyrinth seals. The $+0.6\%$ and $+1.5\%$ represents the actual engine conditions in which cold flow is ejected radially at ambient temperature 290 K to prevent hot gas ingress. The nondimensional cooling mass flow rates, rotational, and axial Reynolds numbers are similar to real engine conditions. The pressure ratio ($P_{01}/P_{s3}$) reduces slightly from 3.03 to 2.96 (i.e., $-2.6\%$) when going from the $-0.5\%$ to the $+1.5\%$ condition.

**D Measurements and Instrumentation.** The measurement planes are represented in Fig. 3. Due to the supersonic nature of the vane exit flow field probes are not inserted there. The static pressure at the vane exit (plane 2) is measured in ten points at the hub endwall, covering one stator pitch. Five locations are instrumented with pneumatic taps and the other half are fitted with subsurface mounted fast response transducers. The vertical wall of

**Table 1 $C_w$, Reynolds numbers and turbine pressure ratio**

| Condition | $C_w$ | $\mathrm{Re}_\theta$ | $\mathrm{Re}_{\mathrm{ax}}$ | $P_{01}/P_{s3}$ |
|---|---|---|---|---|
| Ingestion$-0.5\%$ | $-7.3\times10^3$ | $2.68\times10^6$ | $1.49\times10^6$ | 3.03 |
| Ejection$+0.6\%$ | $9.7\times10^3$ | $3.88\times10^6$ | $1.49\times10^6$ | 3.00 |
| Ejection$+1.5\%$ | $25.4\times10^3$ | $4.09\times10^6$ | $1.48\times10^6$ | 2.95 |

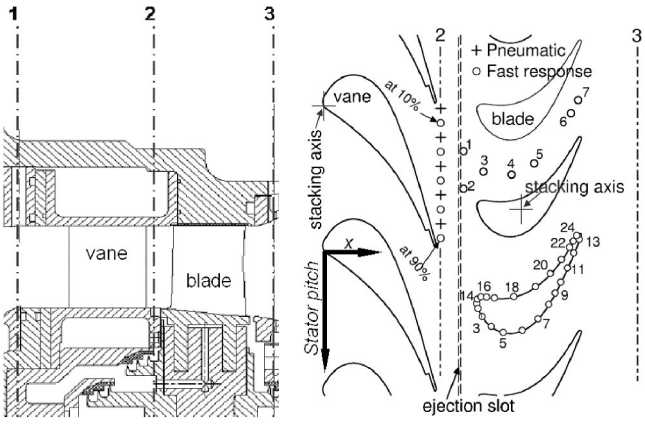


**Fig. 3 Measurement planes**

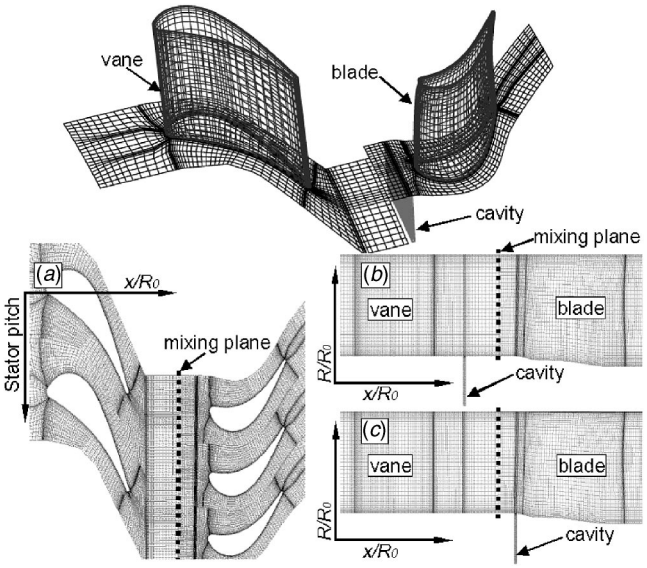


**Fig. 4 Three-dimensional view of the turbine stage grid: (*a*) blade-to-blade cut; (*b*) meridional plane cut, cavity upstream of the mixing plane; and (*c*) downstream**

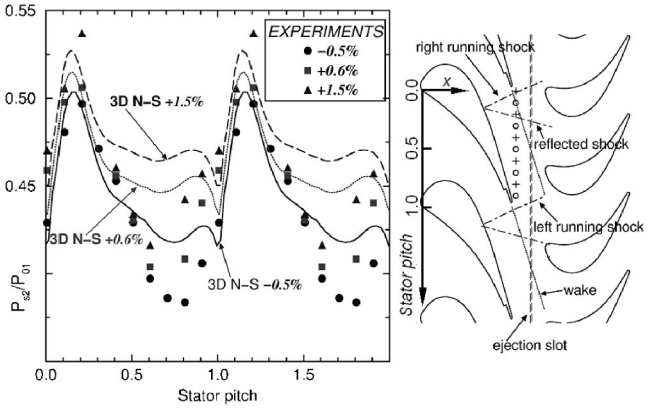


**Fig. 5 Time-averaged distribution of the pitch-wise static pressure at the vane exit hub**

the cavity on the stator side is instrumented with five pneumatic taps distributed over one vane pitch at constant $R/R_0=0.946$. The centerline of the rotor blade platform is instrumented with seven subsurface mounted fast response sensors. The rotor blade static pressure around the airfoil is measured at 15%, 50%, and 85% span with 24 flush-mounted fast response chips for each section. The stage downstream total pressure and flow angles are measured with a pneumatic five-hole probe $0.5\times C_{r\ \mathrm{ax}}$ downstream of the rotor trailing edge. Pneumatic taps monitor the stage exit static pressure at hub and tip in the same plane 3.

Typical uncertainty levels for single measurements (20:1) are $\pm 5$ mbar for pneumatic probes, $\pm 15$ mbar for fast response pressure probes, 2.5% for the coolant mass flows, $\pm 1°$ for the yaw and pitch angles, not considering the error due to the lack of response of the probe in unsteady flows. Note that these levels of uncertainties refer to the determination of absolute values. Higher accuracies can be reached when measuring variations or averaging several measurements.

**E Numerical Simulations.** The time-averaged results at the stage exit are compared with the results of the 3D Navier-Stokes stage computation performed with the CFX-TASCFLOW3D integrated software package. The grid generator allows local refinement of a coarse structured grid and to merge together two dissimilar structured grids. For both stator and rotor, the H-type mesh includes 129 nodes in the stream-wise direction, 43 in the circumferential direction, and 45 span-wise. The rotor tip clearance is meshed with 7 nodes in the radial direction. The cavity mesh has 10 nodes in the axial direction, 43 in circumferential, and 35 in the radial direction. Therefore the grid includes about half million points. A 3D view of the grid is displayed in Fig. 4.

The Navier-Stokes equations are modelled with the *mass-weighted averaging* procedure. The solver uses a finite element based implicit finite volume method for spatial discretisation. The time discretisation is implicit, utilizing a first-order accurate backward Euler approximation. The turbulence model used in all calculations is the *high Reynolds number k-ε model*, with logarithmic wall functions, widely used in industrial applications. In all the calculations, a fully turbulent flow was prescribed.

The coupling between the vane row and the rotor row is implemented by means of a mixing plane [see Fig. 4(*a*)] where all quantities are pitch-wise averaged. Therefore, wakes and shocks are not transferred downstream; only unsteady simulations would be able to accurately model the flow field. To circumvent this problem, two different configurations were investigated. In the first one, the cavity grid is located upstream of the mixing plane [see Fig. 4(*b*)]. This grid was used to study the interaction between the cavity and the vane, with the experimental distance from vane trailing edge to the cavity. The second configuration, with the cavity downstream of the mixing plane [see Fig. 4(*c*)], was used to investigate the effects on the rotor. The second model matches the experimental distance from the cavity to the blade leading edge. Following some previous guidelines [25], the stator-rotor axial distance was increased to $0.98\times C_{s\ \mathrm{ax}}$ in order to avoid problems of shock reflections in the mixing plane, which would cause large errors in the mass flow.

All the solid walls are considered adiabatic. The other boundary conditions include the measured turbine inlet pressure, temperature and exit pressure at hub. Table 2 summarizes the boundary conditions for the various calculations. For the *ingestion* −0.5% case the pressure at the bottom of the cavity is imposed, for the other cases the flow rate. There is a good agreement with the experimental data, except for *ingestion* −0.5% for which the ingested mass flow is a bit higher than the experimental one.

## 3 Results and Discussion

**A Time-Averaged Vane Exit Static Pressure.** At nominal conditions the vane outlet flow reaches transonic velocity causing the appearance of vane trailing edge shocks. In this section the computational results were obtained with the cavity mesh located upstream of the mixing plane, displayed in Fig. 4(*b*).

Figure 5-left shows the time-averaged static pressure distribution at hub, $0.035\times C_{s\ \mathrm{ax}}$ downstream of the vane. The static pressure variation across a pitch, for the −0.5% case, is of the order of

**Table 2 3D N-S boundary conditions, predicted inflow and pressure in the cavity**

| | $P_{01}$ | $T_{01}$ | $P_{01}/P_{s3}$ | Imposed in cavity | Computed in cavity |
|---|---|---|---|---|---|
| −0.5% | 1.62 | 440 K | 3.00 | $P_{\mathrm{hub\ slot}}/P_{01}=0.41$ | $C_w=-10.0\times 10^3$ |
| +0.6% | 1.62 | 440 K | 3.00 | $C_w=9.7\times 10^3$ | $P_{\mathrm{hub\ slot}}/P_{01}=0.47$ |
| +1.5% | 1.62 | 440 K | 3.00 | $C_w=25.4\times 10^3$ | $P_{\mathrm{hub\ slot}}/P_{01}=0.50$ |

**Table 3 Experimental and computed pitch-wise averaged static pressure at hub, mean, and max-min**

| | Experiments at hub | | | 3D N-S at hub | | |
|---|---|---|---|---|---|---|
| | $P_{s2\ \mathrm{mean}}/P_{01}$ | $\Delta P/P_{s2\ \mathrm{mean}}$ | $M_{2,is}$ | $P_{s2\ \mathrm{mean}}/P_{01}$ | $\Delta P/P_{s2\ \mathrm{mean}}$ | $M_{2,is}$ |
| −0.5% | 0.433 | 26% | 1.16 | 0.444 | 20% | 1.14 |
| +0.6% | 0.449 | 23% | 1.14 | 0.463 | 18% | 1.11 |
| +1.5% | 0.466 | 25% | 1.11 | 0.478 | 16% | 1.09 |

26% of its mean value. The large gradient of static pressure from pitch 1 to 1.15, is produced by the left running vane trailing edge shock, see Fig. 5-right. The simulation accurately predicts the location of the shock. The shock intensity is slightly lower in the computations owing to a lower vane exit Mach number. The most important feature is that the 3D N-S also reports the rise of averaged static pressure when increasing the ejection rate. This is probably due to the blockage effect caused by the ejection of flow perpendicular to the transonic mainstream flow.

Table 3 shows the static pressure and isentropic Mach number at the vane exit. The ejection of cold air from the cavity at +1.5% rate results in an increase of nearly 8% of the mean pressure at hub and 3% at tip. While the experiments do not show any attenuation on the large pitch-wise variations, which are of the order of 25% for all conditions, the 3D N-S shows a slight reduction from 20% to 16%. Since the vane exit pressure increases with the ejection rate, the degree of reaction of the turbine is altered. For the −0.5% case the degree of reaction at midspan in the experiments and 3D N-S is $r=0.314$ and $r=0.328$, respectively. When flow is injected in the cavity at +1.5% rate, the degree of reaction increases by about 10% in the experiments and 11% in the simulations at midspan. Therefore even in the preliminary design of transonic turbines it is necessary to consider the cavity flow to predict the rotor flow.

**B Cavity Flow Field.** Due to the proximity of the rotating rotor disc and the fixed stator rim, the cavity flow is submitted to high shear and swirl in its path toward the mainstream. Figure 6(*a*) shows the flow-field in the hub cavity for the −0.5% ingestion, at *stator pitch* 1.1. Flow is being ejected close to the stator rim, although there is net flow ingress. The recirculation observed at the entrance of the cavity is similar to what is found in a lid-driven cavity. The flow pattern results from the competition of several effects: the lid-driven cavity effect, the rotor disc that tends to pump flow outward, and the pressure difference imposed between the cavity and the external flow. Note that the balance between these three effects changes across a pitch since there is a large pitch-wise variation of pressure in the external flow. This results in a complex 3D flow with recirculating zones.

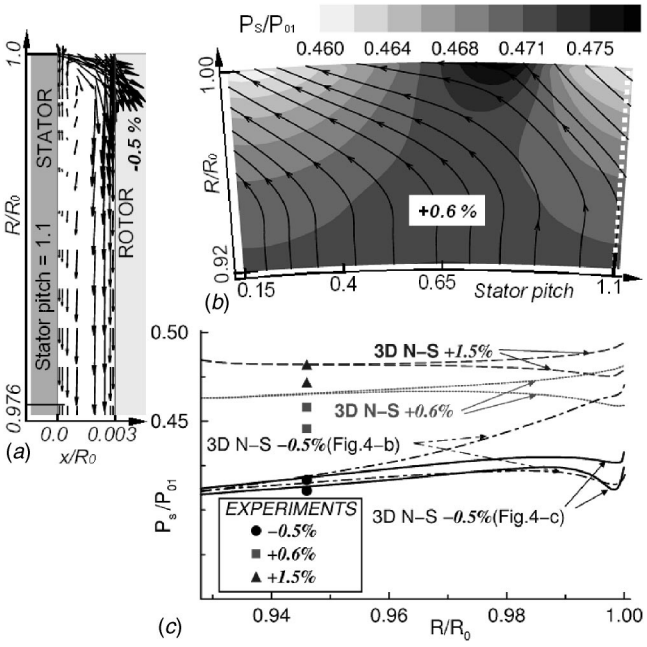


**Fig. 6 Flow field within the cavity: (*a*) Velocity vectors for −0.5% *ingestion* (at *Stator pitch*=1.1); (*b*) time averaged stream traces and static pressure contours across a vane pitch (at $x/R_0=0.0016$); and (*c*) maximum and minimum static pressure as a function of the radius**

Figure 6(*b*) displays the static pressure field within the cavity for the +0.6% case, at midgap $x/R_0=0.0016$. A comparison of the vane exit static pressure (Fig. 5) with the cavity static pressure [Fig. 6(*b*)] shows that the large pitch-wise vane exit static pressure variation dies out very rapidly in the cavity. Förster et al. [17] using a steady 3D N-S solver report similar results.

Figure 6(*c*) shows the static pressure maximum and minimum as a function of the radius for all the configurations. The largest pitch-wise variation of static pressure occurs for the −0.5% case. The experimental data at $R/R_0=0.946$ show a maximum scatter in the data of ±1%, while the 3D N-S at the same radius shows a lower dispersion. For the −0.5% case there is a noticeable difference in the static pressure results obtained with the two computational fluid dynamics (CFD) models [Figs. 4(*b*) and 4(*c*)]. For the +0.6% and +1.5% cases the difference between both models is negligible in the cavity static pressure. When the cavity is placed upstream of the mixing plane [Fig. 4(*b*)] the pitch-wise variation of pressure is three times larger than when the cavity is placed downstream of the mixing plane [Fig. 4(*c*)]. In the latter case, no pitch-wise effect of the vane is considered, only the effect of the rotor blades.

Table 4 shows the mean velocity through the cavity, the velocity ratio $V_m/V_{2\ \mathrm{ax}}$, and the cavity swirl ratio ($\beta=V_\theta/U$), which is the ratio between the tangential component of the cavity flow and the disk peripheral velocity. The velocity ratio is a common parameter to express the sealing effectiveness, which increases with it. The cavity swirl was obtained at $R_0$ using the experimental correlation of Pincombe and Oun [23] based on the flow parameter $C_w\cdot \mathrm{Re}_\theta^{-0.8}\cdot(R/R_0)^{-2.6}$. Increasing the dimensionless cavity mass flow ($C_w$) causes the flow within the cavity to become more radial. From +0.6% to the +1.5% condition $C_w$ is increased by 60%, which explains the large reduction of $\beta$.

**C Time-Resolved Static Pressure Upstream and Downstream of the Cavity.** The fluctuation measured by a gauge located at *stator pitch* 0.9 is reported in Fig. 7(*a*) together with the value of the pressure measured on the vertical wall of the cavity. The abscissa of the graph is the time made dimensionless with the

**Table 4 Velocity ratio and calculated cavity swirl**

| Condition | $V_m$ [m/s] | $V_m/V_{2\ \mathrm{ax}}$ | $\beta$ |
|---|---|---|---|
| Ingestion−0.5% | −31.6 | −0.25 | — |
| Ejection+0.6% | 29.3 | 0.23 | 0.3 |
| Ejection+1.5% | 72.6 | 0.58 | 0.2 |

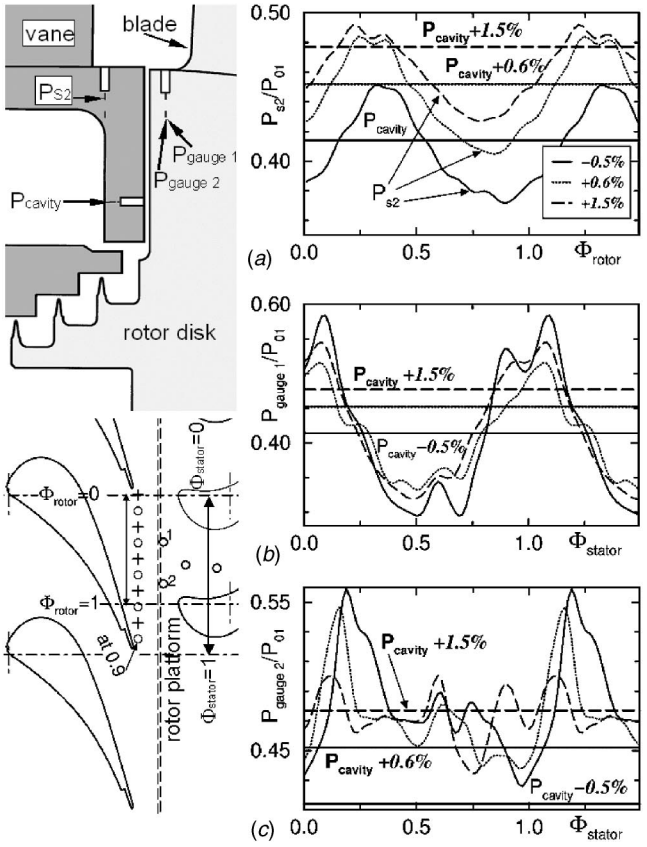


**Fig. 7 Time-resolved static pressure outside of the cavity: (*a*) at the vane exit, gauge at stator pitch=0.9; (*b*) gauge 1 on the rotor platform; and (*c*) gauge 2**

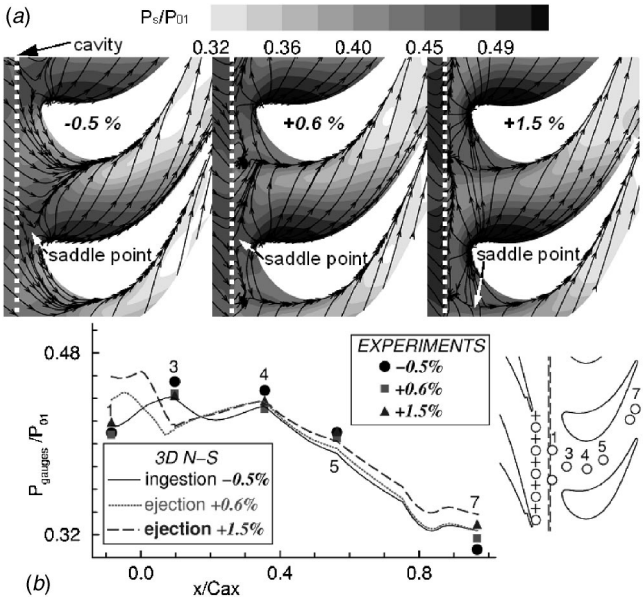


**Fig. 8 (*a*) Time-averaged stream traces and static pressure contours at the rotor platform; (*b*) measured static pressure**

rotor passing period (1/6900 s). The rotor is at position 0 ($\Phi_{rotor}=0$) when the vane and blade stacking axes are aligned. $\Phi_{rotor}=1$ when the rotor has completed one rotor pitch displacement. The amplitude of the time-resolved fluctuation [Fig. 7(*a*)] is of the same order as the variation of the time-averaged pressure across one pitch (Fig. 5). This suggests that the origin and inclination of the left running shock changes depending on the relative position of the rotor. When cold flow is ejected from the wheel-space, the amplitude of the pressure fluctuation related to the rotor blade displacement is strongly reduced for the +1.5% case. This can be explained by the blockage created by the leakage flow into the mainstream, which causes a reduction in the vane exit Mach number. The static pressure variation across the shock decreases accordingly as well as the intensity of the interaction. For the −0.5% condition the pressure at the vane exit (at *stator pitch* 0.9) is below the cavity pressure during the period $\Phi_{rotor}=0.5$ to 1.1, therefore flow ejection occurs. Conversely, for the +0.6% case, flow ingress exists during a small period of time $\Phi_{rotor}=0.1$ to 0.5. For the +1.5% flow ingress might not happen.

The fluctuations measured by two gauges located on the rotor platform are presented in Figs. 7(*b*) and 7(*c*). The abscissa is the time made dimensionless with the stator passing period (1/4600 s). Hereafter, the rotor is at position 0 ($\Phi_{stator}=0$) when the rotor blade-stacking axis is aligned with the vane stacking axis (see Fig. 3). $\Phi_{stator}=1$ when the rotor has completed an angular displacement equal to one stator pitch. The two gauges are at the same axial position, gauge 1 is located at midpitch, whereas gauge 2 is ahead of the blade leading edge. For the −0.5% case, the pressure at gauge 2 is always above the pressure in the cavity so there is flow ingress at any instant. However, for gauge 1 it depends on the position of the rotor with respect to the vane. For the +0.6% case flow ingress occurs in gauge 2 during most of the rotor displacement. For the +1.5% case flow ingress may appear during a short time.

Consequently, for a given leakage rate, the flow ingress or ejection does not only depend on the observed position along the vane pitch but also on the circumferential position of the rotor. Note that at low speed ($M_2=0.56$) Cao et al. [26] measured low amplitude pressure fluctuations in the cavity at a frequency independent of blade passing events.

**D Rotor Platform.** The numerical results computed for the rotor flow field are performed with the cavity mesh located downstream of the mixing plane [see Fig. 4(*c*)]. Figure 8(*a*) represents the stream traces and static pressure contours, three grid lines away from the platform, i.e., 0.45 mm. The pressure levels compare well with the experimental data available from the seven fast response pressure transducers that instrument the rotor platform along the midpassage line [Fig. 8(*b*)].

On the stator platform upstream of the cavity, the flow ejection causes an increase of static pressure (blockage-effect). By contrast, on the rotor platform downstream of the cavity, the static pressure decreases. Therefore, the streamlines from the front pressure side move toward this region of low pressure. The separation line is displaced upstream, the wall streamlines angle becomes more perpendicular to the suction side. Simultaneously the position of the saddle point is remarkably shifted toward the suction side and away from the blade surface, and this could be an indication of the strengthening of the suction side of the horseshoe vortex, counter-rotating with the main passage vortex. Additionally, the stagnation point moves towards the suction side, enlarging the area exposed to high pressure on the front pressure side.

**E Flow Field Around the Rotor Blade.** Figure 9-left shows the rotor static pressure at 15% span. The agreement between experiments and the 3D N-S is good. In both experiments and computations, the ejection of cold air into the main flow causes a noticeable increase of static pressure on the rotor front suction side between the leading edge and 40% of the axial chord. This can be explained by the decrease of the vane exit Mach number when the leakage flow rate increases. This reduction causes a negative incidence of the flow to the rotor as sketched in Fig. 9-right. For the +1.5% *ejection* case, the change of incidence

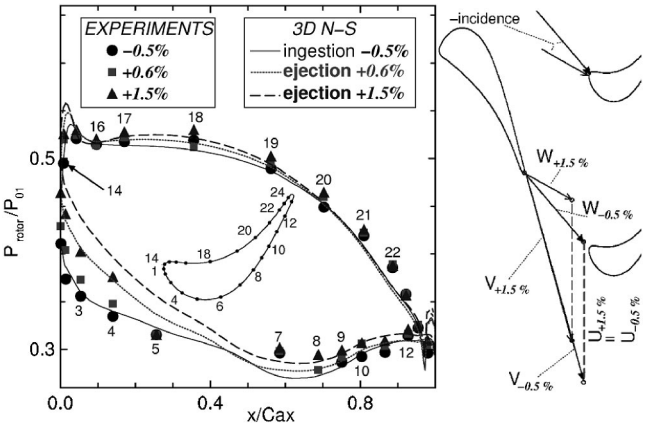


**Fig. 9 Time-averaged rotor static pressure distribution at 15% span**

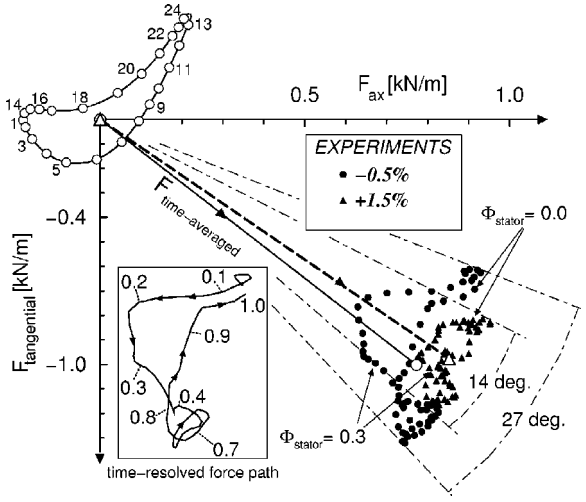


**Fig. 11 Time-resolved blade force at 15% of the span for −0.5% and +1.5%**

is estimated to 1.7°. Due to the increase of degree of reaction, the rotor is unloaded and this is reflected in the increase of pressure along the suction side.

At 50% of the span the effect of the cavity is still visible but less important. The agreement between simulations and experimental data is good.

A number of 3D stage N-S calculations were performed by various researchers (e.g., [27,28]) without modeling the cavity. In all cases, the Mach number distribution on the front suction side is under predicted all along the span. Of course, small changes in the stator exit angle [29] or on the rotor stagger [30] allow to match the experimental data. From the present results, it seems that the presence of this cavity is responsible for this mismatch.

Figures 10(*a*) and 10(*b*) show the computed iso-surfaces of constant rothalpy ($C_p[T_{0r}-U^2/(2\times C_p)]$) for the −0.5% and +1.5% cases. Figures 10(*c*) and 10(*d*) show the corresponding rothalpy field at the rotor trailing edge plane. The term $U^2/(2\times C_p)$ varies from 27 K at hub to 35 K at tip. The development and the migration of the hub and tip passage vortices can be observed. When cold flow is ejected from the cavity [see the +1.5% case on Fig. 10(*b*)], it is entrained by the hub passage vortex. As a consequence, the vortex core is cooler by about 30° [Fig. 10(*d*)]. The cavity flow is driven within the secondary flows from the pressure side toward the suction side. This may explain the significant reduction of heat fluxes on the front suction side observed by Dénos and Paniagua, [31] while only weak effects where noticed on the pressure side. Since the cold flow is lifted by secondary flows, its impact on the platform is limited. Therefore the radial ejection, i.e., coolant flow with no, or little axial velocity component, investigated here is not well suited for platform cooling. For this purpose, a different seal geometry would be adopted where the platforms overlap and the air is ejected almost parallel to the mainstream. Another visible feature is the migration of the hub passage vortex core to 25% of the span, which suggests that the cavity flow increases the strength of this vortex.

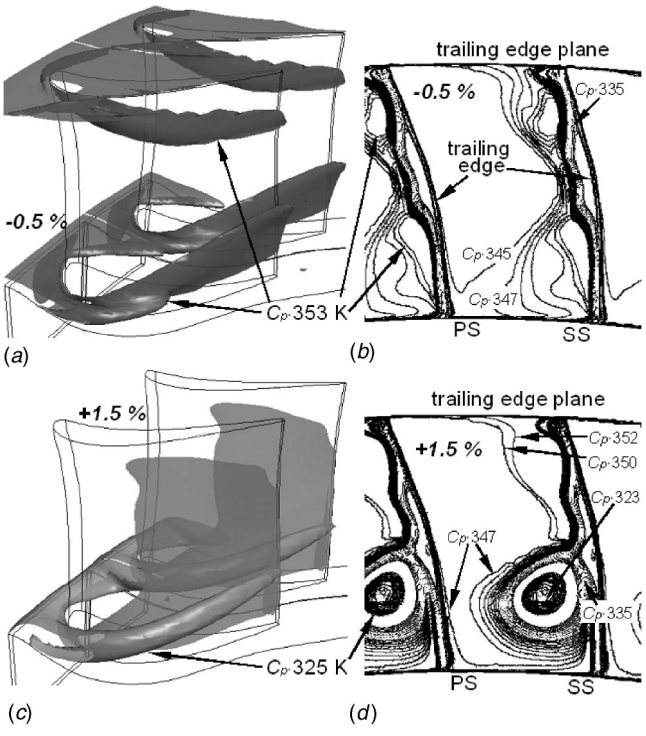


**Fig. 10 Isosurface of rothalpy (*a*- at $C_p\times 353$ K, *b*- at $C_p\times 325$ K) and contour plots of at the rotor trailing edge plane (*c*- for −0.5%, *d*- for +1.5%)**

The unsteady blade force around each section was computed by integrating the measured time-resolved pressure distributions reported by Dénos and Paniagua [31] around the blade profile. A linear distribution of static pressure is assumed between the consecutive gauges. The time-resolved data is presented in function of the relative position of the rotor respect to the vane (Fig. 7). The largest fluctuations of the blade force are located close to the hub, due to the higher intensity of the vane trailing edge shocks. Indeed, the radial equilibrium of the flow implies higher Mach numbers at hub than at tip.

Figure 11 shows the time-resolved force vector exerted on the blade at 15% of the span for the −0.5% and +1.5% conditions. The black solid line represents the time-averaged value for the −0.5% condition, while the black circles represent the successive instantaneous position of the force vector. The trajectory of the force vector is shown on the left indicating also the relative rotor position; note the large change of force direction over the blade of about 27°. Between $\Phi_{stator}=0.4$ and $\Phi_{stator}=0.8$ the force remains nearly constant, but from $\Phi_{stator}=0.8$ to $\Phi_{stator}=1.0$ the blade is submitted to a large change of force intensity and direction. This corresponds to the passage of the vane trailing edge shock sweeping the front suction side of the rotor blade. For the +1.5% ejection case, the fluctuations of tangential forces are reduced by 50%, and the angle variation diminishes to 14°. The axial force is re-

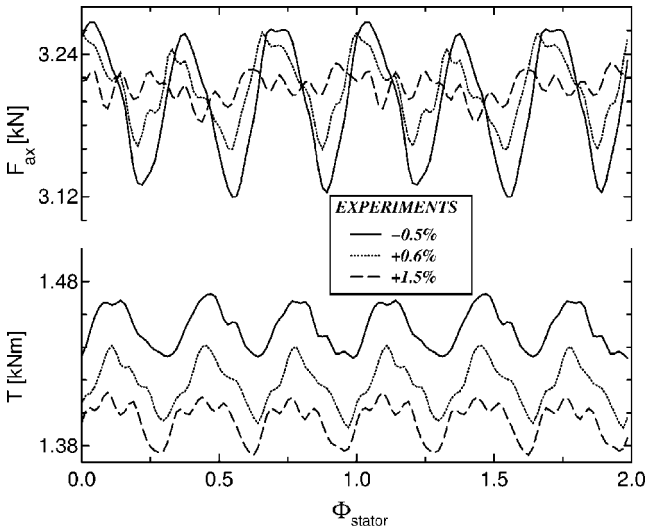


**Fig. 12 Time-resolved axial force and torque on the rotor disk**

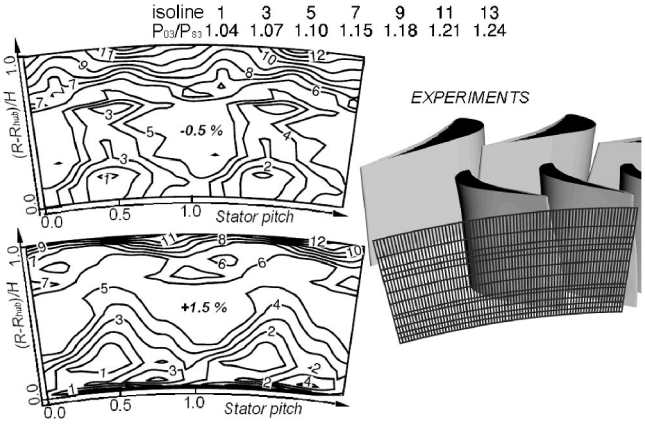


**Fig. 13 Measured time-averaged total pressure contours at the turbine exit**

duced linearly with respect to the increase of ejection rate in the wheel-space cavity: at −0.5% the variation is 39%, at +0.6%, 26%, and at +1.5% only 20%.

At 50% of the span, the effects of the flow ejections are similar but of smaller intensity. Due to the ejection of cold air the unsteady axial force is lowered from 30% to 24% and the tangential force from 13% to 11%. The variation of load distribution along the blade span causes a time-dependent torsional moment and a complex unsteady flexional moment.

Figure 12 shows the axial force and the torque over the disk, computed by integrating the force over the 64 blades. The pressure measured at 15% of the span is applied on the portion from hub to 20% of the blade height. In a similar way, the pressure measured at 50% and 85% of the span was applied to strips covering 20% to 80% span and 80% span to the tip, respectively. When flow is ingested into the wheel-space, the fluctuation of the axial force on the disk amounts to 4.6% of its mean level, i.e., about 150 N. The ejection of air gradually reduces the amplitude of the fluctuations to about 1.5% of its mean level for the +1.5% case. By contrast, the time-resolved torque of the disk is little affected by the ejection of cold air, the fluctuation around its mean value remains around 3%.

Table 5 presents the results of the global forces and torque on the blade and the disk. $F_{\text{radial}}$ is the centrifugal force on a single blade. The mechanical torque is computed from the rotor acceleration Torque$=I\cdot$accel. The moment of inertia ($I=17.70\,\text{kg m}^2$) is determined experimentally. It is remarkable that the two experimental methods to estimate the torque, pressure measurements on the blade, and the rate of acceleration, yield very similar results. Note that the uncertainty in the estimation of the power from acceleration and pressure measurements is 0.6% and 2.1%, respectively. There is a bias error of around 1% that may be attributed to the mechanical loss. The 3D N-S results are also in very good agreement with the values derived from the acceleration with an error of less than 1.2%.

**F Turbine Exit Flow Field.** Figure 13 shows the measured total pressure downstream of the stage from pitch-wise traverses at constant radius. The pressure is nondimensionalized by the static pressure at the turbine exit. It is clear that downstream of the rotor the flow is reminiscent of the stator secondary flows. The high pressure regions near the tip are attributed to the rotor tip clearance. The intensity of the hub passage vortex increases noticeably when cavity flow is ejected.

Figure 14 shows the measured and computed yaw angle, pitch angle and total pressure $0.5\times C_{r\,\text{ax}}$ downstream of the rotor trailing edge for −0.5% and +1.5% ejection. All the results are pitch-wise averaged. The 3D N-S predicts the general trends observed in the experiments. The injection of cold flow increases slightly the mean total pressure. The effect of the rotor hub passage vortex is much larger in the computations than in the experiment. In reality, the secondary flows of the vane and of the rotor are contra-rotating. This probably tends to attenuate the secondary flows of the rotor. In the calculations, the mixing plane removes pitch-wise nonuniformities. Consequently, there is no interaction between rotor and stator vortices.

The computed radial profiles confirm the trend observed when commenting on the rothalpy iso-surfaces. The injection of the cold cavity flow tends to increase the intensity of the hub secondary

**Table 5 Total force over the blade, torque on the disk, turbine power, from experimental pressure distribution, acceleration, and 3D N-S**

| | | Ingestion −0.5% | Ejection +0.6% | Ejection +1.5% |
|---|---|---|---|---|
| Blade | $F_{\text{axial}}$ [N] | 50.0 | 50.2 | 50.2 |
| AERO. | $F_{\text{tangential}}$ [N] | −61.4 | −60.0 | −59.0 |
| | $F_{\text{radial}}$ [N] | 63 403.2 | 63 403.2 | 63 403.2 |
| Disk | $F_{\text{axial}}$ [N] | 3199 | 3213 | 3212 |
| AERO. | Torque [N m] | 1452 | 1417 | 1395 |
| | Power [kW] | 988 | 964 | 950 |
| Disk | accel [RPM/s] | 791.2 | 789.7 | 768.9 |
| MECH. | Torque [N m] | 1467 | 1464 | 1426 |
| | Power [kW] | 998 | 996 | 970 |
| 3D N-S | Power [kW] | 984 | × | 961 |
| ΔPower (aero—mech) | | −1.0% | −3.2% | −2.1% |
| ΔPower (3D N-S—mech) | | −1.4% | × | −0.9% |

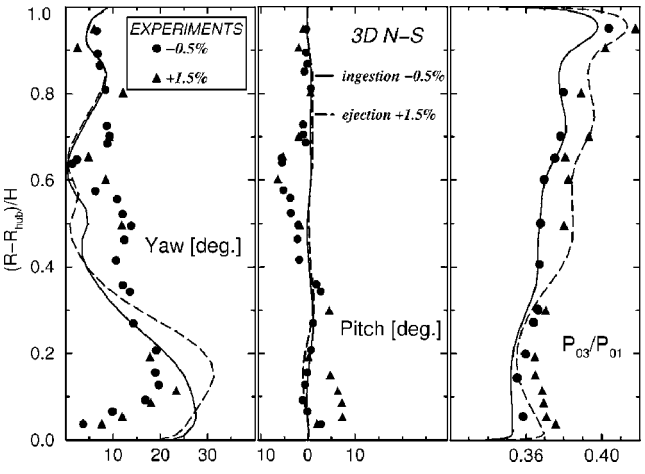


**Fig. 14 Radial profiles pitch-wise averaged**

flows and enhance its migration towards midspan. This is seen in the yaw angle distribution at hub with an increase of the overturning and the migration of the maximum to the center of the channel. Similarly, the total pressure minimum is more pronounced with ejection than without ejection.

Note that the cavity flow seems to affect a region between 10% and 15% span but at the hub both testing conditions come back to the same value. This can be understood since the cavity flow is driven within the hub rotor vortices. In the region 5% to 30% of the span it is evident a higher deficit of total pressure attributed to the hub vortex. Although McLean et al. [20] observed a similar displacement in the vortex location they indicated that the strength was unaltered.

## 4 Conclusions

The effect of the hub endwall cavity flow ejection on the mainstream is investigated with the time-averaged and time-resolved measurements in a transonic turbine stage. 3D N-S calculations complement the research work. Computational results show a good overall agreement with the experimental results for both the shapes of the curves and the effect of cavity flow ejection.

The ejection of wheel-space cold flow causes a large blockage to the transonic vane exit flow. For the +1.5% *ejection*, the static pressure is increased by 6% with respect to the −0.5% *ingestion* case, which causes a change of 11% in the degree of reaction at midspan. For this reason, such cavity flows should be taken into account during the design phase. Surprisingly, the large pitch-wise static pressure gradient measured in the mainstream is smoothed out inside the cavity. The time-resolved static pressure fluctuations at vane exit are also reduced with the cavity ejection due to the lower exit Mach number and associated weaker pressure discontinuity.

The flow at the entrance of the cavity results from the competition between the lid driven cavity flow pattern, the radial pumping of the rotor disc and the pressure imposed at the hub of the cavity. Due to the pitch-wise variation of the static pressure in the mainstream, the balance between these three phenomena depends on the location considered. In addition, the ingestion/ejection of the cavity flow is unsteady and depends, at a given point, on the position of the rotor with respect to the stator.

The reduction of the vane exit Mach number, due to leakage flow ejection, modifies the velocity triangles and the rotor relative incidence. This causes a decrease of the rotor isentropic Mach number in the front part of the suction side at 15% span.

The 3D N-S simulations clearly show the entrainment of the cold cavity flow into the rotor hub vortex. This cold flow is transported towards the suction side and is lifted up. Therefore, the effect of the cavity flow on the rotor platform is restrained to the front part. The cold flow reinforces the intensity of the rotor hub vortex and enhances its migration towards mid-span.

The time-resolved rotor blade force was obtained by integrating the time-resolved static pressure around a single rotor blade. For the −0.5% the axial force varies by 39% at hub to 47% at tip. The tangential force fluctuation is minimum at mid-span (only 13% variation), but at 15% span it amounts to 70%. When cold cavity flow is ejected at a rate of +1.5% the tangential force is notably reduced to 35% of its mean level. Moreover, the variation of the force vector is reduced from 27° to 15°. The time-resolved axial force and torque on the rotor disk were evaluated considering the forces exerted over the 64 rotor blades. The maximum amplitude of the axial force fluctuations was 4% for −0.5% case, by ejecting cold flow these fluctuations are attenuated to only 1.5%. This data provide boundary conditions for forced response calculations.

Larger secondary flow intensity and faster migration towards midspan in presence of leakage flow is also identified in the stage downstream flow field.


## Acknowledgments

The authors would like to thank J. Prinsier for his assistance regarding the 3D N-S calculations. The authors would like also to acknowledge the financial support of the European Commission and European manufacturers that participated in the BRITE-EuRAM III BE97-4440 Project ''Turbine Aero-Thermal External Flows.''


## Nomenclature

$C_P$ = specific heat at constant pressure [J/(kg K)]
$C_s$ = stator chord, $C_r$ rotor chord [m]
$C_w = \dot{m}_{\text{coolant}}/\mu \cdot R_0$ = nondimensional cooling flow rate
$F$ = force [N]
$G = s/R_0$ = cavity gap ratio
$H$ = blade height [m]
$M$ = Mach number
$\dot{m}$ = mass flow rate [kg/s]
$P$ = pressure [bar]
$r$ = degree of reaction
$R$ = radius [m]
$R_0$ = cavity outer radius, vane hub radius [m]
$\text{Re}_\theta = \rho \cdot \omega \cdot R_0^2/\mu$ = disk rotational Reynolds number
$\text{Re}_{2\ or\ 3} = \rho \cdot V_{2\ or\ 3} \cdot C_{s\ or\ r}/\mu$ = mainstream Reynolds number
$\text{Re}_{\text{ax}} = \rho \cdot V_{\text{ax}} \cdot R_0/\mu$ = main flow axial Reynolds number
$s$ = cavity axial clearance [m]
$T$ = temperature [K]
$U = \omega \cdot R$ = peripheral speed [m/s]
$V$ = velocity [m/s]
$V_\theta$ = swirl or tangential velocity in the cavity [m/s]
$V_m = \dot{m}_{\text{coolant}}/2\pi \cdot \rho \cdot R_0 \cdot s$ = average velocity through cavity
$\Delta H$ = turbine enthalpy drop [J/kg]
$x$ = axial distance along the machine axis [m]

### Greek

$\beta = V_\theta/U$ = core cavity swirl ratio
$\omega$ = rotational speed [rad/s or RPM]
$\mu$ = dynamic viscosity [kg/(m s)]
$\rho$ = density [kg/m$^3$]
$\Phi$ = phase in sense of rotation, relative to the rotor/stator
$\gamma$ = specific heat ratio

### Subscripts

0 = total conditions
1 = stator inlet
2 = stator outlet, rotor inlet
3 = rotor outlet
ax = axial direction, aligned with the machine axis
is = isentropic conditions
$r$ = frame of reference relative to rotor
$s$ = static conditions

## References


[1] Gunston, B., 1993, ''Jane's all the World's Aircraft 1992-93,'' *Jane's Data Division*, ed., Lambert M. Surrey, United Kingdom.

[2] Dunn, M. G., 2001, ''Heat Transfer and Aerodynamics in Axial Flow Turbines,'' ASME J. Turbomach., **123**, pp. 637–686.

[3] Steinetz, B. M., and Hendricks, R. C., 1996, ''Engine Seal Technology Requirements to Meet NASA's Advanced Subsonic Technology Program Goals,'' J. Propulsion and Power, **12**(4), pp. 786–793.

[4] Campbell, D. A., 1978, ''Gas Turbine Disc Sealing System Design,'' *Proceedings of the Conference on Seal Technology in Gas Turbine Engines*, Apr., London AGARD-CP-237.

[5] Kobayashi, N., Matsumato, M., and Shizuya, M., 1984, ''An Experimental Investigation of a Gas Turbine Disc Cooling System,'' ASME J. Eng. Gas Turbines Power, **106**, pp. 136–141.

[6] Phadke, U. P., and Owen, J. M., 1988, ''Aerodynamic Aspects of the Sealing of Gas-Turbine Rotor-Stator Systems. Part 1: The Behavior of Simple Shrouded Rotating-Disk Systems in a Quiescent Environment. Part 2: The Performance of Simple Seals in a Quasi-Axisymmetric External Flow. Part 3: The Effect of Non-Axisymmetric External Flow on Seal Performance,'' Int. J. Heat Fluid Flow, **9**(2), pp. 98–117.

[7] Chew, J. W., Dadkhah, S., and Turner, A. B., 1992, ''Rim Sealing of Rotor-Stator Wheelspaces in the Absence of External Flow,'' ASME J. Turbomach., **114**, pp. 433–438.

[8] Dadkhah, S., Turner, A. B., and Chew, J. W., 1992, ''Performance of Radial Clearance Rim Seals in Upstream and Downstream Rotor-Stator Wheelspaces,'' ASME J. Turbomach., **114**, pp. 439–445.

[9] Daniels, W. A., Johnson, B. V., Graber, D. J., and Martin, R. J., 1992, ''Rim Seal Experiments and Analysis for Turbine Applications,'' ASME J. Turbomach., **114**, pp. 426–432.

[10] Ko, S. H., and Rhode, D. L., 1992, ''Thermal Details in a Rotor-Stator Cavity at Engine Conditions With a Mainstream,'' ASME J. Turbomach., **114**, pp. 446–453.

[11] Bohn, D., Deuker, E., Emunds, R., and Gorzelitz, V., 1995, ''Experimental and Theoretical Investigations of Heat Transfer in Closed Gas-Filled Rotating Annuli,'' ASME J. Turbomach., **117**, pp. 175–183.

[12] Ko, S. H., Rhode, D. L., and Guo, Z., 1997, ''Circumferentially Smeared Computed Effects of Rim Seal Clearance on Wheelspace Thermal Distribution,'' ASME J. Turbomach., **119**, pp. 157–159.

[13] Laroche, E., Desportes de la Fosse, S., Djaoui, M., Debuchy, R., and Paté, L., 1999, ''A Combined Experimental and Numerical Investigation of the Flow in a Heated Rotor/Stator Cavity With a Centripetal Injection,'' ASME paper no. 99-GT-170.

[14] Wilson, M., Arnold, P. D., Lewis, T. W., Mirzaee, I., Rees, D. A. S., and Owen, J. M., 1997, ''Instability of Flow and Heat Transfer in a Rotating Cavity With a Stationary Outer Casing,'' *Proceedings of Eurotherm 55 ''Heat Transfer in Single Phase Flow,''* Santorini, Greece, September.

[15] Hah, C., 1997, ''Turbine Blade Tip, Outer Airseal, Platform Analysis,'' *VKI Lecture Series: ''Secondary and Tip Clearance Flows in Axial Turbines,''* Von Karman Institute for Fluid Dynamics, Rhode-Saint-Genese, Belgium, February.

[16] Hunter, S. D., and Manwaring, S. R., 2000, ''Endwall Cavity Flow Effects on Gaspath Aerodynamics in an Axial Flow Turbine: Part 1: Experimental and Numerical Investigation,'' ASME paper no. 2000-GT-651.

[17] Förster, I., Martens, E., Friedl, W.-H., and Peitsch, D., 2001, ''Numerical Study of Hot Gas Ingestion into an Engine Type High-Pressure Turbine Rotor-Stator Cavity,'' ASME paper no. 2001-GT-0114.

[18] Lindqvist, L. O., Wickholm, J. E., Fransson, T. H., and Torisson, T., 2000, ''Investigation of the Spanwise Transport of the Rotor-Stator Slot Flow in a Test Turbine,'' ASME paper no. 2000-GT-0485.

[19] Gallier, K. D., Lawless, P. B., and Fleeter, S., 2001, ''Particle Image Velocimetry Characterization of Secondary Flow Effects in Turbine Stage Including the Effects of Unsteady Forcing Functions,'' AIAA paper no. ISOABE-2001-1082.

[20] McLean, C., Camci, G., and Glezer, B., 2001, ''Mainstream Aerodynamic Effects due to Wheelspace Coolant Injection in a High Pressure Turbine Stage. Part 1: Aerodynamic Measurements in the Stationary Frame. Part 2: Aerodynamic Measurements in the Rotational Frame,'' ASME J. Turbomach., **123**(4), pp. 687–696 and 697–703.

[21] Girgis, S., Vlasic E., Lavoie, J.-P., and Moustapha, S. H., 2002, ''The Effect of Secondary Air Injection on the Performance of a Transonic Turbine Stage,'' ASME paper no. GT-2002-30340.

[22] Roy, R. P., Xu, G., Feng, J., and Kang, S., 2001, ''Pressure Field and Main-Stream Gas Ingestion in a Rotor-Stator Disk Cavity,'' ASME Paper no. 2001-GT-0564.

[23] Gentilhomme, O., Hills, N. J., Turner, A. B., and Chew, J. W., 2003, ''Measurement and Analysis of Ingestion Through a Turbine Rim Seal,'' ASME J. Turbomach., **125**(3), pp. 505–512.

[24] Sieverding, C. H., and Arts, T., 1992, ''The VKI Compression Tube Annular Cascade Facility CT3,'' ASME paper no. 92-GT-336.

[25] Arnone, A., and Benvenuti, E., 1994, ''Three-Dimensional Navier-Stokes Analysis of a Two-Stage Gas Turbine,'' ASME paper no. 94-GT-88.

[26] Cao, C., Chew, J. W., Millington, P. R., and Hogg, S. I., 2003, ''Interaction of Rim Seal and Annulus Flows in an Axial Flow Turbine,'' ASME paper no. GT2003-38368.

[27] Michelassi, V., Giangiacomo, P., Martelli, F., Dénos, R., and Paniagua, G., 2001, ''Steady Three-Dimensional Simulation of Transonic Axial Turbine Stage,'' ASME Paper no. 2001-GT-0174.

[28] Laumert, B., Mårtensson, H., and Fransson, T. H., 2000, ''Investigation of the Flowfield in the Transonic VKI Brite Euram Turbine Stage With 3D Steady and Unsteady N-S Computations,'' ASME paper no. 2000-GT-0433.

[29] Martelli, F., Adami, P., and Belardini, E., 2001, ''Heat Transfer Modelling in Gas Turbine Stage,'' *Presented at the RTO AVT Symposium on Advanced Flow Management*, RTO-MP-069, SYB 33, pp. 1–17. Loen, Norway, May.

[30] de la Calzada, P., and Fernández-Castañeda, J., 2003, ''Investigation of Numerical and Physical Modelling Effects on the CFD Simulation of the Unsteady Flow in an HPT Stage,'' ASME paper no. GT2003-38796.

[31] Dénos, R., and Paniagua, G., 2002, ''Influence of the Hub Endwall Cavity Flow on the Time-Averaged and Time-Resolved Aero-Thermics of an Axial HP Turbine Stage,'' ASME paper no. GT-2002-30185.

**Abd Rahim Abu Talib**[1]
Department of Aerospace Engineering,
Faculty of Engineering,
Universiti Putra Malaysia, Serdang,
43400 Selangor, Malaysia
e-mail: abrahim@eng.upm.edu.my

**Andrew J. Neely**[1]
School of Aerospace and Mechanical Engineering,
University of New South Wales,
Australian Defense Force Academy,
Northcott Drive,
Canberra ACT 2600, Australia
e-mail: a.neely@adfa.edu.au

**Peter T. Ireland**
Department of Engineering Science,
University of Oxford,
Parks Road,
Oxford OX1 3PJ, UK
e-mail: peter.Ireland@eng.ox.ac.uk

**Andrew J. Mullender**
Fire Precautions Group,
Rolls-Royce plc.,
P.O. Box 31,
Derby DE24 8BJ, UK
e-mail: andy.mullender@rolls-royce.com

# A Novel Liquid Crystal Image Processing Technique Using Multiple Gas Temperature Steps to Determine Heat Transfer Coefficient Distribution and Adiabatic Wall Temperature

*This paper presents a novel experimental technique, which combines thermochromic liquid crystals with multiple steps in gas temperature, to determine heat transfer coefficient and adiabatic wall temperature distributions. The transient heat transfer experiments have been conducted on a flat plate using the low-temperature analogue of an ISO standard propane-air burner commonly used in aero-engine fire certification. The technique involves the measurement of the surface temperature response of an insulating model to a change in gas temperature. A coating comprising more than one thermochromic liquid crystal material is used to increase the range of the surface measurement and this is combined with multiple step changes in gas temperature. These measures induce several peaks in liquid crystal intensity throughout the transient experiment and these are shown to improve the accuracy. The current technique employs useful data from both the heating and cooling phases in the heat transfer test. To the authors' knowledge, this has not been investigated before and it is likely to be very useful for other applications of the liquid crystal transient heat transfer experiment. The uncertainties in all measurements have been quantified and are presented in this paper.* [DOI: 10.1115/1.1776585]

## 1 Introduction

Temperature-sensitive liquid crystal has been used extensively in a wide variety of applications. The thermochromic liquid crystal (TLC) experimental techniques (Jones et al. [1], Ireland et al. [2] and Baughn [3]), image processing techniques (Wilson et al. [4] and Wang et al. [5]), liquid crystal calibration techniques (Camci et al. [6], Hay and Hollingsworth [7], and Chan et al. [8]), and data reduction techniques (Chen et al. [9]) have been greatly improved since the introduction of the method in order to obtain more accurate thermal results. Wang et al. [10] were the first to use the full-intensity history of a mixture of two TLCs together with a least-squares regression method to obtain heat transfer coefficient distributions. A review of liquid crystal measurements of heat transfer and surface shear stress is given in Ireland and Jones [11].

Unlike the earlier improvements by the other researchers, this paper will concentrate on the advantages of using multiple gas temperature steps in transient heat transfer experiments to determine two thermal parameters, especially heat transfer coefficients ($h$) and adiabatic wall temperature ($T_{aw}$). To the authors' knowledge, this has not been investigated before and it is likely to be very useful for other applications of TLCs to transient heat transfer experiments. The method is related to that used by Turnbull and Oosthuizen [12] who pulsed the heat supplied to a surface heater and to the method used by Baughn et al. [13] to determine $h$ by changing the fluid temperature.

## 2 Test Facilities and Instrumentation

To demonstrate this technique, transient heat transfer experiments were conducted using the compact low-temperature analogue of an aero-engine fire-certification burner described by Abu Talib et al. [14]. This low-temperature analogue burner simulates the flow field of the flame from a large ISO2685 [15] propane-air fire-certification burner. The development and validation of the low-temperature analogue technique are discussed in detail by Neely et al. [16,17]. The compact analogue burner consists of a square cross-section (86 mm×86 mm internal dimension) transparent perspex plenum chamber that is 260 mm long, a fast response stainless steel mesh heater (Gillespie et al. [18,19]); a square to circular contraction section and a perspex burner nozzle with a 0.13 mm thick Mylar burner face. The mesh heater is powered from a 240V AC transformer.

A 96:4 mixture by mass of helium and air are supplied to the plenum chamber with each gas stream measured with a BS1042, [20], orifice plate flow meter. The flow passes through a 40 mm length of honeycomb flow straightener and a wake dissipation screen 30 mm upstream from the mesh heater to give uniform flow through the fast response mesh heater. Gas thermocouples woven into an adiabatic nylon mesh, just upstream of the faceplate, are used to measure the exit gas temperature. The faceplate was shown not to influence the exit gas temperature (Abu Talib [21]). A small camera may be mounted in the plenum chamber to visualise the crystal color play on the surface of the model closest to the burner. The open area of the stainless steel heater mesh is sufficient to allow the surface to be viewed by the camera looking through the mesh. Video cameras and low-temperature fluorescent lights are positioned around the model to enable full observation of the extent of the model surface.

[1]Formerly at the Department of Engineering Science, University of Oxford.

Contributed by the International Gas Turbine Institute and presented at the International Gas Turbine and Aeroengine Congress and Exhibition, Atlanta, GA, June 16–19, 2003. Manuscript received by the IGTI December 2002; final revision March 2003. Paper No. 2003-GT-38198. Review Chair: H. R. Simmons.

  

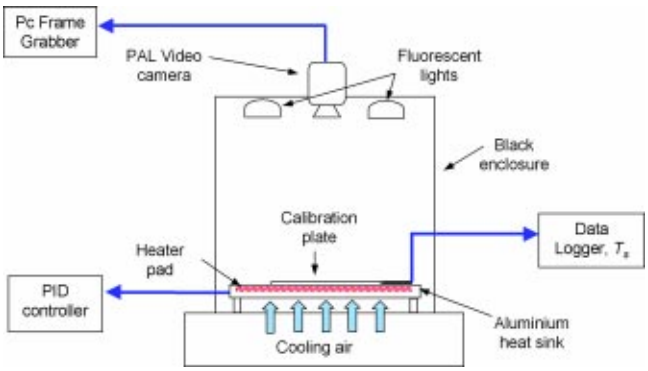


**Fig. 1 Schematic of calibration rig setup**

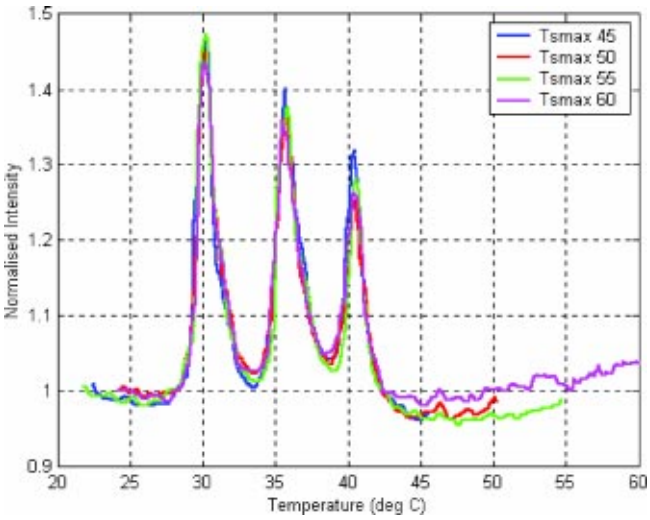


**Fig. 2 Heating phase of the calibration of a mix of three narrow-band liquid crystals**

## 3 Liquid Crystal Calibration

The behavior of coatings of mixtures of multiple encapsulated thermochromic liquid crystals must be characterized to enable accurate measurements of surface temperature and heat transfer coefficients in heat transfer experiments. In practice, the response of the encapsulated liquid crystals can differ between nominally the same coatings compositions and this is thought to be due to marginally different proportions of binder, which is mixed with the crystal before application to bond it to the surface. Ireland and Jones [22] have investigated in detail the response time of an encapsulated thermochromic liquid crystal, which they found to be typically 3 milliseconds. The response time is governed by the thermal conduction lag between the surface temperature changing and the thermometer indicating the change.

A rig was built to calibrate the thermochromic liquid crystal under controlled conditions. The calibration rig is designed to provide a uniform and controlled temperature distribution on a calibration plate coated with the liquid crystal mixture of interest. A schematic of the calibration set-up is shown in **Fig. 1**. A foil surface thermocouple is mounted on the center of the calibration plate to monitor the surface temperature. Good thermal contact is ensured between the foil thermocouple and the calibration plate. A thin layer of black paint is used to coat the top of the test plate followed by several layers of liquid crystal mixture. The instrumented plate is then clamped to the top of the calibration rig, ensuring good thermal contact. The calibration rig consists of an assembly of two aluminum plates within which is a machined cavity. A silicon rubber heater[2] pad is embedded within this cavity. When the two aluminum plates are clamped together there is no clearance between the plates and the heater pad ensuring good thermal contact between them.

A PID (proportional-integral-derivative) controller is used to control the rise of the temperature during the calibration. A vortex cooling tube is used to separate hot air and cold air from a compressed air supply, with the cold stream then used to cool down the aluminum plate from beneath, thus reducing the temperature of the calibration plate during the cooling phase. Plate temperature uniformity was tested, using an IR thermal imaging camera, during the heating and cooling phases and was found to be uniform across the surface of the test plate.

Two 11 W fluorescent lamps are used to illuminate the liquid crystal coated surface without significant radiative heating. It has been well established in the literature that the narrow-band liquid crystals used in this calibration are less sensitive to the illumination and viewing angle (Baughn [3]). A video camera is mounted above the rig to capture the crystal color play on the test plate. The entire rig is enclosed within black curtains to shield the calibration from extraneous light.

In order to be able to use the liquid crystal coating over a temperature range of about 20°C the authors conducted a simple calibration study. The aim was to investigate the effect of hysteresis of liquid crystals heated to a range of peak temperatures and thus establish a temperature versus intensity calibration for the crystal mixture. Previous researchers have investigated hysteresis in liquid crystals by studying hue-temperature curves (Kenning and Yan [23], Birrell and Eaton [24], and Baughn et al. [25]). However, the current study concentrates on the intensity-temperature calibration of liquid crystals. Dixon and Scala [26] reported that for several liquid crystal mixtures hysteresis was characterized by a shift in the peak wavelength at a particular temperature when cooled rather than heated.

A mixture of three narrow-band liquid crystals[3] (BW/R30C1W/S-40, BW/R35C1W/S-40, and BW/R40C1W/S-40) was used in the calibration, applied in thin layers to the plate (approximately of 10 microns). The calibration plate was heated up to a required uniform surface temperature and then slowly cooled back to the initial temperature. As the liquid crystal passed through its active range, images were acquired until the crystal color play was no longer visible. Four sets of calibrations were conducted. The surface temperature was raised to 45°C, 50°C, 55°C, and 60°C. The surface temperature was logged using a PC connected to a data acquisition card at a sample rate of 2 Hz. The intensity history from the liquid crystal color play was extracted from the captured video images. Only the green signal was used throughout the experiment to increase the selectivity of the sensor. The intensity and surface temperature history were then interpolated to obtain the intensity versus temperature calibration curve. The intensity was then normalized by the intensity level before color play, see **Fig. 2**.

**Figures 2 and 3** show the normalized intensity-temperature calibration curves for the heating and cooling phases, respectively. These results confirm that there is no shift in intensity peak in liquid crystals but the hysteresis behavior can clearly be seen in **Fig. 3** when cooling occurs from different peak temperatures. Hysteresis is thought to only occur if the crystal is heated above its useful color-play range (Baughn et al. [25]). The first clearing point (or cholestreric to isotropic transition) that the coating encounters on heating is that for the lowest temperature crystal. For this case the BW/R30C1W/S-40 crystal has a clearing point of 45°C to 46°C. Norman [27] reported that the calibrated clearing

[2]Watlow Metric silicon Rubber Heater, 100W—Watlow Ltd., Robey Close, Linby Industrial Estate, Linby, Nottingham NG15 8AA, U.K.

[3]TLC—Hallcrest Ltd., 8-9 Stepnell Reach, 541 Blanford Rd, Poole, Dorset BH16 5BW, U.K.

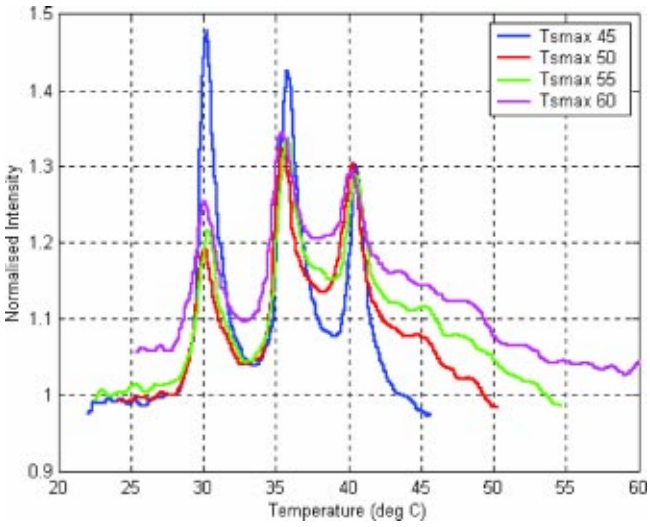


**Fig. 3 Cooling phase of the calibration of a mix of three narrow-band liquid crystals**

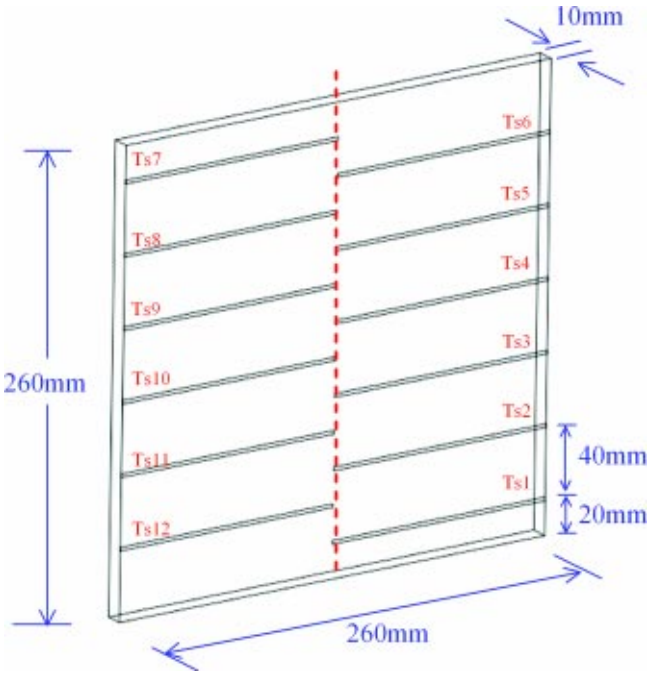


**Fig. 4 Schematic of the surface thermocouples arrangements**

point value is 45.5°C. This phenomenon was also observed during liquid crystal impingement heat transfer tests on a flat plate model using the low-temperature analogue burner (Abu Talib et al. [14]). The regression procedure to be described in Section 5 employs a prediction of the surface temperature variation for which the peak temperature is known at each pixel. It would be possible to use different cooling curves depending on the peak temperature achieved. In practice, it was possible to keep the perspex surface temperature to less than the lowest clearing point temperature and hence avoid the need to account for hysteresis.

## 4 Transient Heat Transfer Test

Since the 1980s, transient experiments using liquid crystal have been used to measure heat transfer and the technique is now well established. For this current work transient heat transfer tests have been conducted using the low-temperature analogue burner developed at the University of Oxford. A square perspex flat plate ($260\times260\times10$ mm) was subjected to the impingement of a helium-air plume preheated to a temperature of 80°C. Neely et al. [16] reported that the jet velocity is approximately 1.4 $m.s^{-1}$. The flat plate was instrumented with a centrally located vertical linear array of 12 equi-spaced foil thermocouples to monitor the surface temperature change on the plate as shown in **Fig. 4**.

The transparent perspex test plate was coated with the same liquid crystal mixture used in the calibration. The liquid crystal coating was then covered with a layer of black ink so that the color play of the crystal could be illuminated and viewed through the plate by lights and a camera located behind the plate (**Fig. 5**). The flat plate was subjected to a step change in gas temperature. For simple geometries, such as the flat plate, one-dimensional semi-infinite heat transfer can be assumed (Schultz and Jones [28]). At any point on the model surface $h$ is thus a function only of the driving gas temperature difference $(T_{aw}-T_i)$, the crystal change temperature $(T_c)$, the material properties of the substrate $(\rho ck)$ and the time at which the contour appears $(t)$.

$$h=\frac{\beta\sqrt{\rho ck}}{\sqrt{t}} \tag{1}$$

where

$$\frac{T_c-T_i}{T_{aw}-T_i}=1-\exp(\beta^2)\mathrm{erfc}(\beta). \tag{2}$$

Only liquid crystals with color change temperatures that are well placed between the initial surface temperature and the driving gas temperature are chosen.

The flow is initiated with unheated helium-air mixture, and then the mesh heater is activated to begin the test. Abu Talib et al. [14] reported that the time constant associated by the mesh heater is found to be 0.17 s. The used of a thin Mylar faceplate on the low-temperature analogue burner, which has a time constant of approximately 0.27 second, is sufficiently small to enable the use of the step change assumptions in the transient thermal analysis. The crystal color play on the plate was viewed through the rear of the transparent perspex plate and captured using a single video camera (**Fig. 5**).

To demonstrate the use of multiple temperature steps in a transient heat transfer experiment, two sets of tests were conducted, (a) one gas temperature step only and (b) two gas temperature

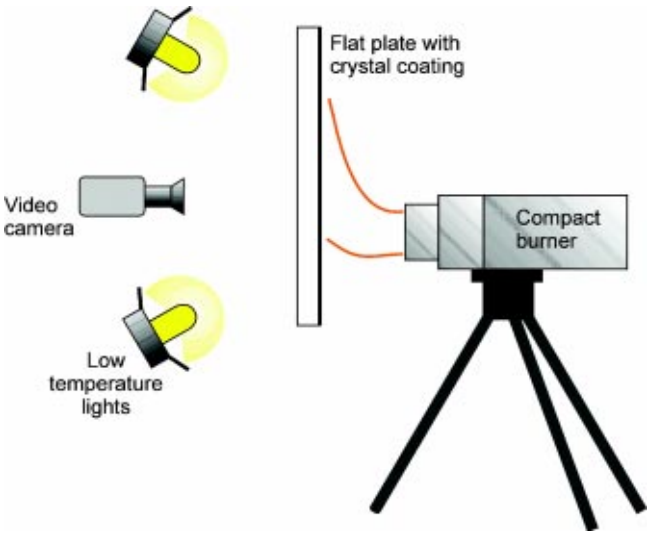


**Fig. 5 Schematic of perspex flat-plate test**

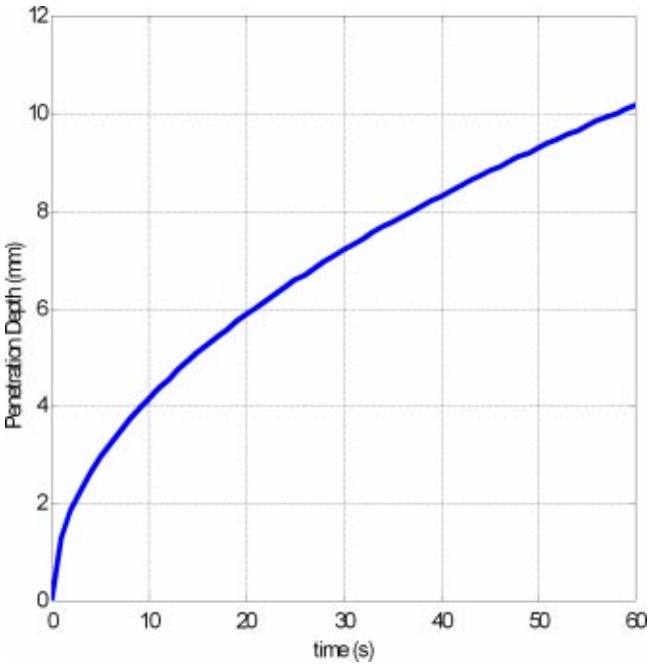


**Fig. 6 Penetration depth of heat pulse into perspex**

steps. The duration of test can only be conducted for less than 60 seconds for the assumption of one-dimensional semi-infinite analysis to remain valid. The calculation for the time for the heat pulse to penetrate into the substrate is shown in **Fig. 6** and is taken from Schultz and Jones [29];

$$d = 4\sqrt{t\alpha} \tag{3}$$

where $d$ is the penetration depth, $t$ is the time, and $\alpha$ is the thermal diffusivity of perspex, which is $1.08\times10^{-7}$ $m^2.s^{-1}$.

## 5 Data Reduction Technique

The basis of the current method of analysis builds on a technique developed for combustor cooling experiments reported by Ling et al. [29]. The entire calibration curve (normalized intensity versus temperature) is employed to process the data from the transient heat transfer tests. This intensity history matching method uses the complete profile of the measured data, which improves accuracy relative to versions of the method which use a single surface temperature to determine the heat transfer coefficient, $h$. In practice, all of the measured intensity data, not just the peaks are used to determine the heat transfer coefficient. The image processing technique can deduce distributions of both $T_{aw}$ and $h$ simultaneously in a single test (**Fig. 7**).

As stated, the well-established technique of crystal intensity peak-picking uses only a fraction of the available experimental data. In the new technique the full intensity history at each pixel is used in the analysis. A range of possible combinations of $T_{aw}$ and $h$ are used to generate a lookup table of ideal intensity history, which is then compared with the experimental intensity history from the observed crystal color play on the model. For ease of manipulation, $T_{aw}$ is normalized to $T_{\text{bar}}$ as follows:

$$T_{\text{bar}} = \frac{T_{aw} - T_i}{T_g - T_i} \tag{4}$$

where $T_i$ and $T_g$ are the initial substrate temperature and the peak exit gas temperature, respectively. The multicrystal image processing technique enables the experimental intensity history for each pixel to be matched to an ideal intensity history generated from the most appropriate combination of $h$ and $T_{\text{bar}}$.

A range of possible combinations of heat transfer coefficient ($h$) and adiabatic wall temperature ($T_{aw}$) are used to generate surface temperature histories, and from the crystal calibrations, ideal intensity histories. Comparison of each ideal intensity history with experimental intensity history allows the selection of the best fitting combination of $h$ and $T_{aw}$ at each pixel via residue minimization. The exit flow temperature of the burner will directly follow the mesh-heater temperature. This enables the use of temperature stepping by simply energising and de-energizing the mesh heater, to increase the accuracy of the image processing technique. The $T_{aw}$ is varied in a series of steps to induce multiple crystal transitions to increase the dataset from which $h$ and $T_{aw}$ are deduced.

## 6 Experimental Results

While the automated routines which carryout the data analysis for the complete camera view are complex and CPU intensive, a simple checking routine has been implemented using Matlab[4] software to enable the user to check the quality of the data being processed at a single position. First, the software loads the precalculated lookup table, which consists of the ideal intensity history, generated using a range of combinations of possible heat transfer coefficients, $h$ and adiabatic wall temperatures, $T_{aw}$. The

[4]Matlab, 2001, "The Language of Technical Computing," Version 6.1.0.450 Release 12.1, Math Works, Inc.

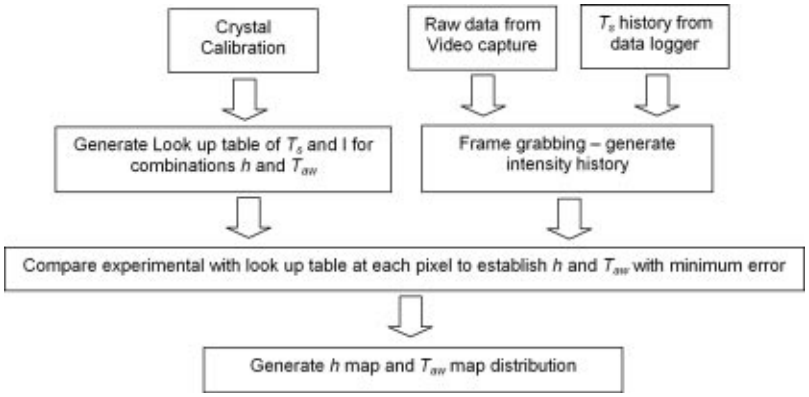


**Fig. 7 Image processing sequence**

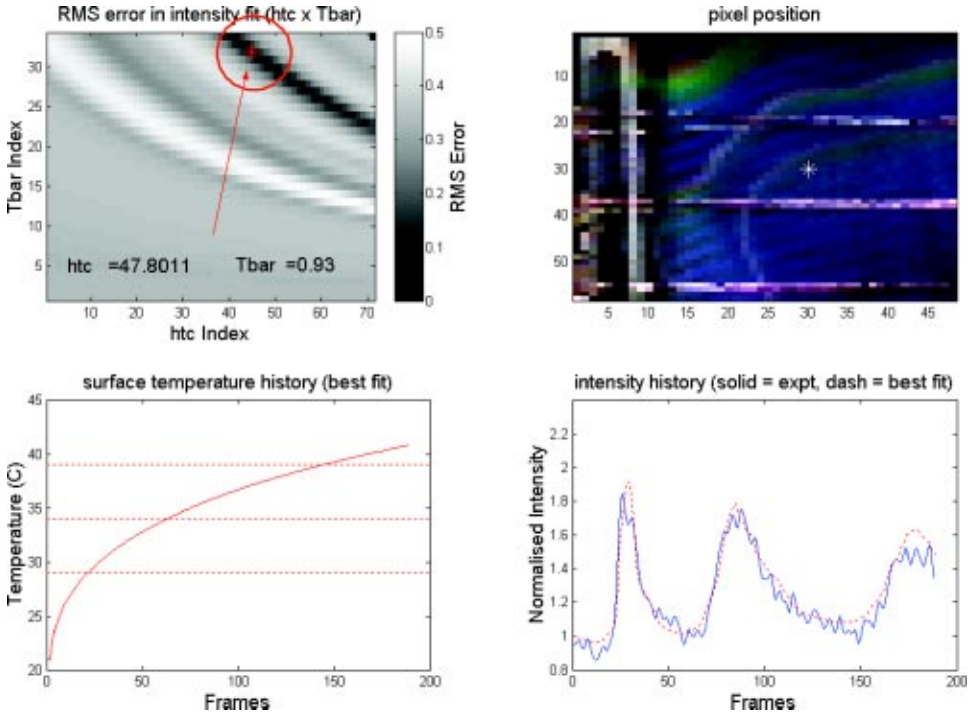


**Fig. 8 Result from a one gas-temperature step test**

user is then able to select a pixel position in the recorded camera view, such as shown in top right image in **Fig. 8**. The software then reads the corresponding intensity history at that pixel and compares it, via residue minimization, to the ideal intensity histories contained in the previously generated lookup table. $T_{\text{bar}}$ index and $h$ index in **Fig. 8** correspond to the range of $T_{\text{bar}}$ and $h$ values used in the lookup table to generate the ideal intensity history.

**Figures 8 and 9** shows the results for both one gas-temperature step and for two gas-temperature steps, respectively. It can be clearly seen in **Fig. 9** that more peaks can be induced when there are more gas-temperature steps. The intensity matching in both **Figs. 8 and 9** looks very good. As expected the minimum error trough (indicated by the dark region in the RMS error map) is larger in **Fig. 8** compared in **Fig. 9** which has two gas-temperature steps. Large areas of minimum error will reduce the accuracy of the selection of $h$ and $T_{aw}$ indicated by cross hairs on the figure.

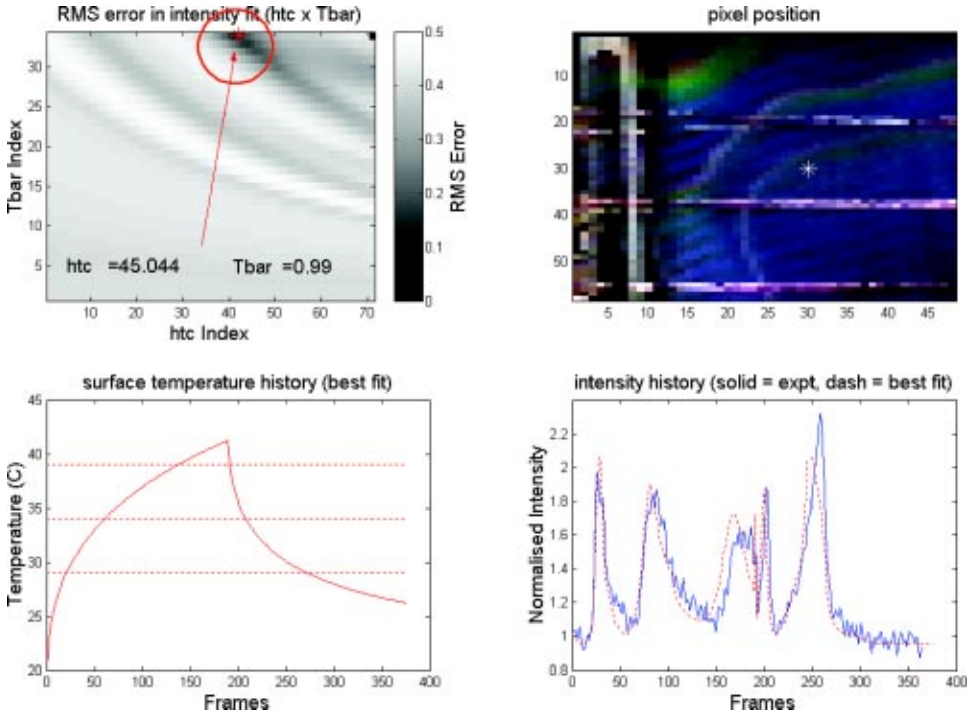


**Fig. 9 Result from a two gas-temperature steps test**

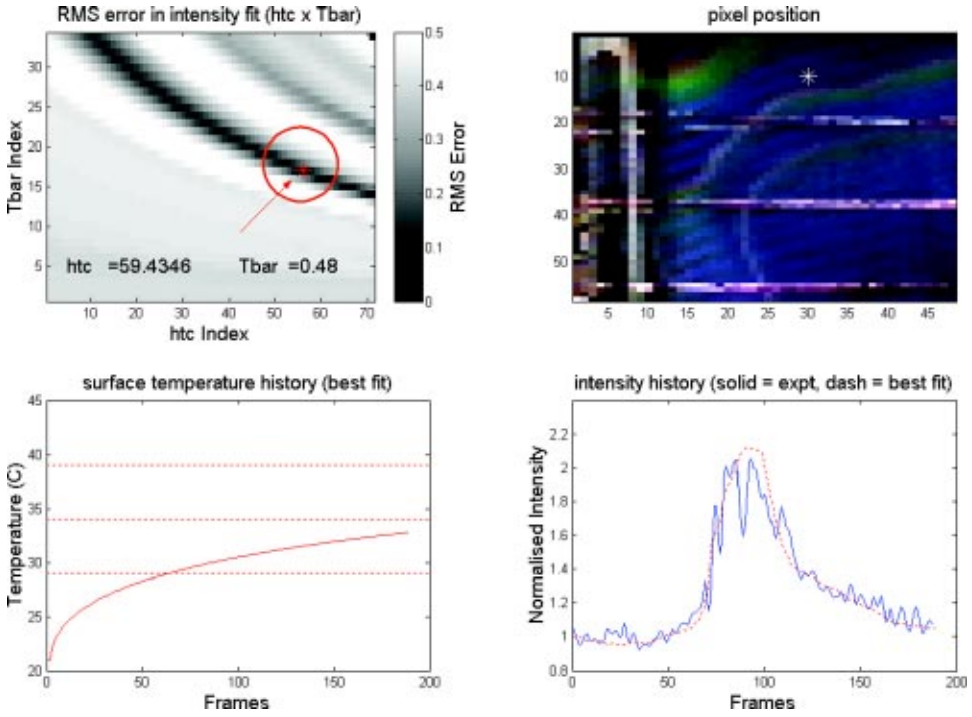


**Fig. 10 Result from a one gas-temperature step test**

However, there are only small differences between the values of $h$ and $T_{bar}$ deduced from the two experiments. The advantage of the two gas-temperature steps test over the one gas-temperature step test is more obvious when there are fewer crystal peaks in the area of interest as discussed below.

**Figures 10 and 11** show another example of the advantages of using more gas-temperature steps. In areas of either low $h$ or $T_{aw}$, where there are fewer crystal peaks, the software selects a more accurate result from the two gas-temperature steps test compared to one gas-temperature step. The $T_{bar}$ value of 0.48 in **Fig. 10** is far from the correct value of 0.99 shown in **Fig. 11**. The $T_{bar}$ value near the top edge of the plate was expected to be approximately near to 1. The RMS error trough in **Fig. 10** was darker than the error trough in **Fig. 11** indicating a small error. The full distribution of $h$ and $T_{aw}$ on the flat plate was presented and discussed by Abu Talib et al. [14]. The effect of the hysteresis in the multiple

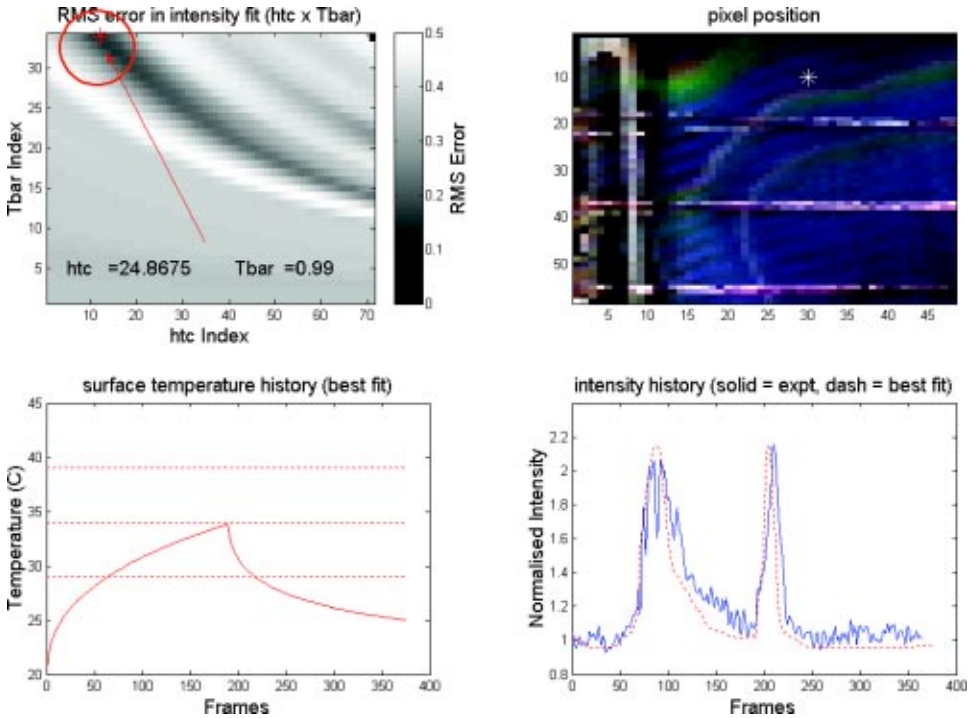


**Fig. 11 Result from a two gas-temperature steps test**

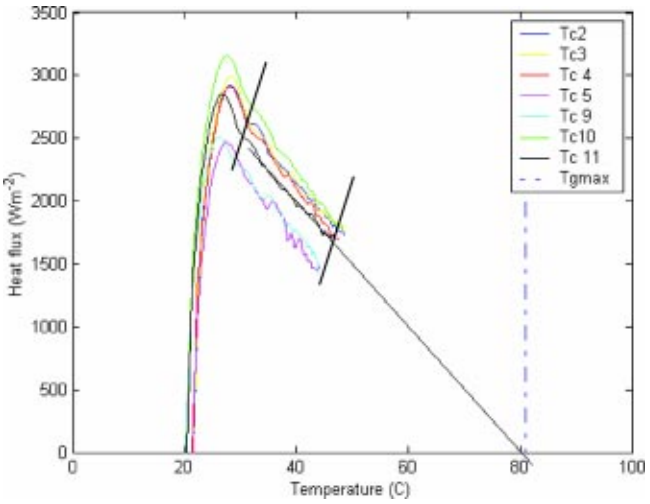


**Fig. 12 Plot of heat flux against temperature**

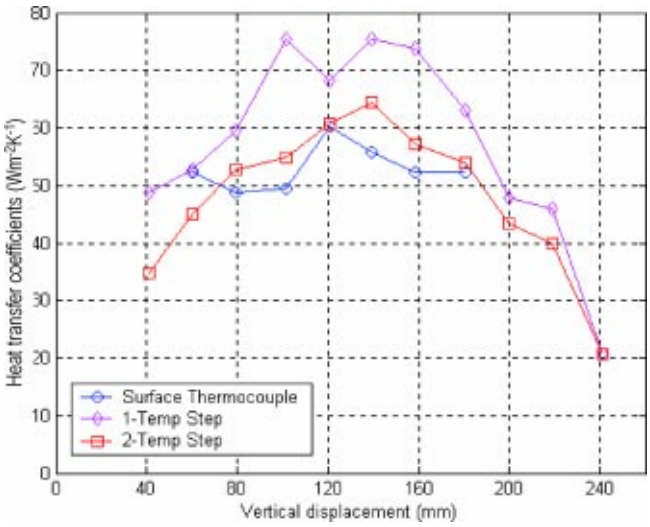


**Fig. 13 Plot of *h* against vertical displacement on the flat plate**

temperature stepping technique when using the low-temperature analogue burner could be ignored since the maximum surface temperature in all tests was lower than the lowest crystal clearing temperature.

The $h$ and $T_{\text{bar}}$ values obtained from the one gas-temperature step and two gas-temperature steps can also be compared to the $h$ and $T_{\text{bar}}$ measured from the surface thermocouples array as shown in **Fig. 4**. The surface temperature histories can be used to evaluate the surface heat flux histories using the following equation by Schultz and Jones [29].

$$q_n(t) = \frac{2\sqrt{\rho c k}}{\sqrt{\pi}} \left[ \sum_{i=1}^{n} \frac{T_s(t_i) - T_s(t_{i-1})}{(t_n - t_i)^{1/2} + (t_n - t_{i-1})^{1/2}} \right] \tag{5}$$

where $q$ is the surface heat flux and $T_s$ is the surface temperature. The heat fluxes generated from Eq. (5) were plotted against surface temperatures as shown in **Fig. 12**. Note that only readings from thermocouples number $T_s2$, $T_s3$, $T_s4$, $T_s5$, $T_s9$, $T_s10$, and $T_s11$ were used in the analysis. Due to the buoyant behavior of the plume from the low-temperature burner, the flow bends immediately upward before it impinges onto the flat plate surface. Therefore the surface thermocouple number $T_s1$ only experienced a low level of heat flux, which is not sufficient to obtain a reasonable extrapolation. Thermocouples $T_s6$, $T_s7$, and $T_s12$ were situated in the mixing region of the plume and cold air and yield noisy heat flux data. The slope from the $q$ versus $T$ plot correspond the $h$ and the intercept with the temperature axis is the $T_{aw}$. The best slope from the curve is chosen for every thermocouple signal (except $T_s1$, $T_s6$, $T_s7$, $T_s8$, and $T_s12$) as shown in **Fig. 12**.

Uncertainty is caused by the fact that the temperature change is small compared to the driving temperature difference. A slight change in the slope angle will result in large changes of adiabatic wall temperature. Therefore due to this error in the technique especially when choosing the best intercept to the temperature axis from the graph, the data obtained can only be used as a rough guide to the levels of $h$ and $T_{aw}$. **Figure 13** gives a comparison of $h$ in the central vertical displacement on the flat plate. The average $h$ and $T_{\text{bar}}$ values for both temperature step test were taken from the central vertical location on the flat plate as shown by the red dotted line in **Fig. 4**. The $h$ values from the two gas-temperature steps are much closer to the values generated from the surface thermocouple than the $h$ values from the one gas-temperature step.

**Figure 14** shows a comparison of $T_{\text{bar}}$ along a central vertical line. Due to the error mentioned earlier in the technique when trying to deduce the intercept on the temperature axis in **Fig. 12**, some of the $T_{\text{bar}}$ values from one gas-temperature step are closer to the values generated from the surface thermocouple (**Fig. 14**). However it would be expected that values of $T_{\text{bar}}$ would be near to 1 in the core of the plume where no dilution of hot plume has occurred.

## 7 Numerical Analysis

In order to demonstrate the application of multiple temperatures stepping with a greater number of steps, a simple Matlab routine has been developed by the authors. This enables the investigation of the effect on the maximum error of increasing the number of gas-temperature steps. First, a set of surface temperature predictions for a range of multiple gas-temperature step histories was constructed for sequences of gas temperature stepped up and down from one to three times.

These temperature histories were then converted to intensity histories via typical crystal calibration data. To simulate experimental intensity data, random noise with amplitude typical of the experiments was superimposed onto the intensity histories. These simulated intensity histories were then analyzed using the techniques described above to determine to most representative combinations of $h$ and $T_{aw}$ for each. The RMS error maps for each of

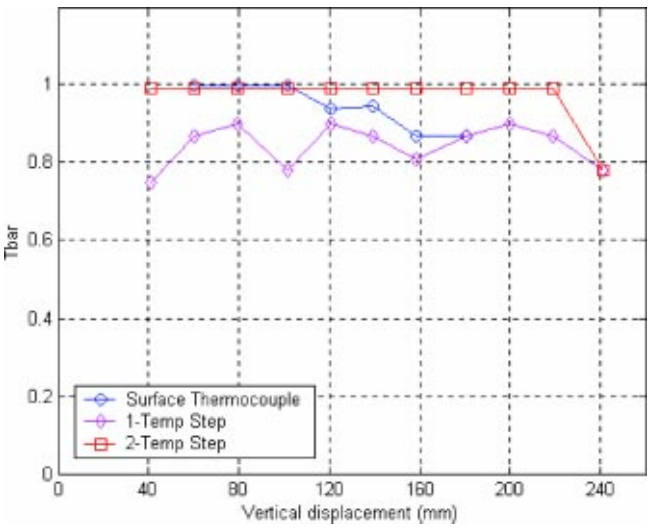


**Fig. 14 Plot of $T_{\text{bar}}$ against vertical displacement on the flat plate**

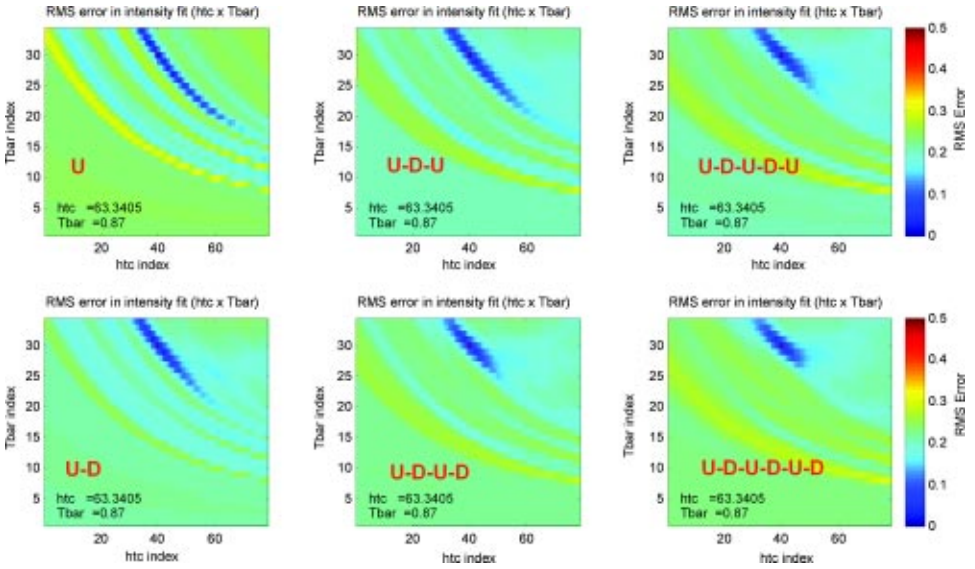


**Fig. 15 RMS error in intensity fit for multiple temperature steps ($U = T_g$ steps up, $D = T_g$ steps down)**

the sequences are displayed in **Fig. 15**. From **Fig. 15** the intensity-fit error is lowest when a six-step measurement is made. This can be judged by the extent of the trough (dark blue region) along by the $T_{\text{bar}}$ and $h$-axes. The trend is illustrated schematically in **Fig. 16**. It is clear that the region of maximum error in $h$ and $T_{aw}$ space will be reduced by increasing the number of gas temperature steps. The possibility that the software will pick the wrong combination of $h$ and $T_{aw}$ is very small when using more than one gas-temperature step.

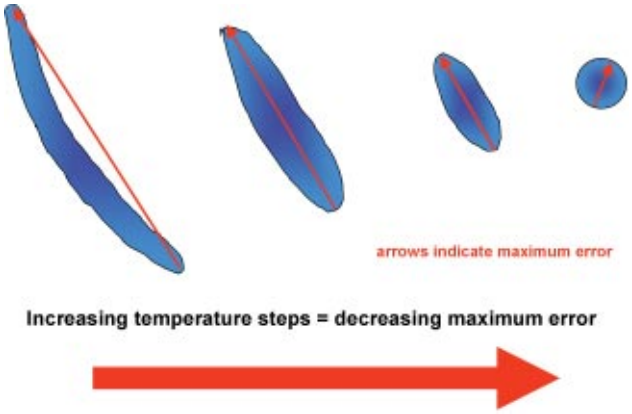


**Fig. 16 Effect of increasing the number of steps**

## 8 Estimations of Experimental Error

Estimates of the experimental uncertainties have been made using the method of small perturbations described by Moffat [30]. Calculations were performed to determine the effect of uncertainties in experimental parameters at test conditions typical to those found in the flat plate test for the low-temperature analogue burner. The error analyses were conducted using a typical experimental intensity data generated using a fix $h$ of 60 $\text{W.m}^{-2}\text{.K}^{-1}$ and $T_{\text{bar}}$ of 0.8. The steps in $h$ and $T_{\text{bar}}$ used to generate the lookup table were reduced to 2% for $h$ and 0.005 for $T_{\text{bar}}$. The uncertainty level in $h$ and $T_{aw}$ depending on the uncertainties in the initial temperature ($T_i$), gas temperature ($T_g$), surface temperature ($T_s$) during the calibration process, time to synchronize the LED appearance in the video image ($t$) and also the thermal product ($\sqrt{\rho ck}$) of perspex used. The $T_s$ values were perturbed from during the crystal calibration data procedure (intensity versus temperature data). The noise added in the numerical simulation is not accounted for in the uncertainty analysis since the actual experimental data also has the same noise level from the camera CCDs.

The experimental uncertainty has been estimated by calculating the RSS (root sum square) of the components error, which gives statistically appropriate total uncertainty. The worst-case error is defined by the maximum error and calculated as the sum of the components error. The summary of the uncertainties in $h$ and $T_{aw}$ for both one gas-temperature step test ($U$) and two gas-temperature steps ($U$-$D$) test are shown in **Table 1**. It is clearly shown that the error generated in $h$ and $T_{aw}$ for two gas-

**Table 1 Comparison of uncertainties in $h$ and $T_{aw}$**

| Test Conditions | Typical Value | Typical Error | 1 $T_g$ step (U) % Error | | 2 $T_g$ steps (U-D) % Error | | 3 $T_g$ steps (U-D-U) % Error | | 4 $T_g$ steps (U-D-U-D) % Error | |
|---|---|---|---|---|---|---|---|---|---|---|
| | | | $h$ | $T_{aw}$ | $h$ | $T_{aw}$ | $h$ | $T_{aw}$ | $h$ | $T_{aw}$ |
| $T_i$ (°C) | 21 | ± 0.5 | 13.036 | 6.418 | 1.000 | 2.778 | 1.980 | 3.086 | 1.000 | 2.469 |
| $T_g$ (°C) | 81 | ± 0.5 | 1.980 | 0.617 | 2.000 | 0.926 | 1.000 | 1.852 | 0.000 | 0.926 |
| $T_s$ (°C) | - | ± 0.3 | 7.005 | 3.086 | 3.000 | 3.704 | 3.000 | 3.704 | 1.980 | 3.086 |
| $t$ (s) | 10 | ± 0.04 | 1.980 | 1.235 | 1.000 | 0.617 | 0.000 | 1.235 | 0.000 | 1.235 |
| $\sqrt{\rho ck}$ | 569 | ± 29 | 5.944 | 0.617 | 5.002 | 0.617 | 5.002 | 1.852 | 5.002 | 1.543 |
| RSS Error | | | 16.192 | 7.336 | 6.326 | 4.801 | 6.240 | 5.624 | 5.472 | 4.515 |
| Maximum Error | | | 27.966 | 12.037 | 12.002 | 8.642 | 10.983 | 11.728 | 7.982 | 9.259 |

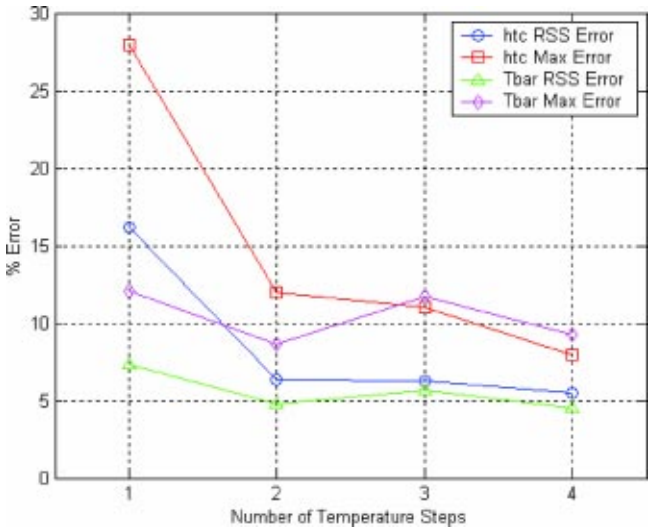


**Fig. 17 Plot of RSS error and maximum error against number of temperature steps**

temperature steps test is far less than the error from the one gas-temperature step test. It is found that the error introduced by changing $T_i$ by $\pm 0.5°C$ reduced significantly from 13% to 1% for one gas-temperature step to two gas-temperature steps. However the error will be insignificant with the increasing number of steps such as reported by Baughn et al. [13]. For infinite number of steps, the $T_s$ will be at the mean of the gas temperature and will be independent of the $T_i$. (Baughn et al. [13]). It can be seen that the value of $T_i$ is less important for more gas temperature step since new steps are more responsible to temperature change.

For further validation of the technique, the uncertainty analysis has been extended to three gas-temperature steps ($U$-$D$-$U$) and four gas-temperature steps ($U$-$D$-$U$-$D$). It can be seen that both RSS error and maximum error for $h$ and $T_{\text{bar}}$ reduce with an increase in the number of gas-temperature steps as shown in **Fig. 17**. It has been reported by previous researchers (Wang et al. [5] and Byerley [31]) that the local measurement of $h$ using the narrow band liquid crystal technique has an uncertainty of 7.5–8.5%. Furthermore Chambers et al. [32] reported that the total uncertainty of local $h$ is 8.85% for three test strategy and 13.68% for two crystals technique. It may be concluded that the local $h$ distributions presented here are of similar accuracy.

## 9 Conclusion

A novel experimental technique to simultaneously determine heat transfer coefficient and adiabatic wall temperature distributions from a single experiment, which combines thermochromic liquid crystals with multiple steps in gas temperature has been demonstrated. These measures induce several peaks in liquid crystal intensity throughout the transient experiment and these are shown to improve the accuracy. Both experimental results and numerical analysis of the multiple gas temperature technique demonstrate the potential decrease in the experimental uncertainty in measurements of $h$ and $T_{aw}$. Increasing the number of steps will decrease the maximum uncertainty. This paper also introduced a new liquid crystal calibration rig. The rig is able to calibrate any mixture of thermochromic liquid crystals, produce repeatable calibrations in an efficient manner, and which can control the temperature rise and temperature decrease and reproduce lighting representative of experiments. Hysteresis behavior in thermochromic liquid crystal is also been shown in the calibration studies. Nevertheless the effect of the hysteresis in the multiple temperature stepping technique when using the low-temperature analogue burner can be ignored since the maximum surface temperature in all tests is lower than the lowest crystal clearing temperature.

## Acknowledgments

The authors wish to thank Rolls-Royce plc for permission to publish this paper. Thanks are also due to the UK Ministry of Defense (MoD) and the UK Departmental of Trade and Industry (DTI) for their financial support for this work through the Defense Evaluation and Research Agency (DERA), Pyestock. The first author thanks the Malaysian Government and the University Putra Malaysia for their financial support.

## Nomenclature

$c$ = specific heat capacity ($J.kg^{-1}.K^{-1}$)
$d$ = penetration depth (m)
erfc = error function
$h$ = heat transfer coefficient ($W.m^{-2}.K^{-1}$)
$k$ = thermal conductivity ($W.m^{-1}.K^{-1}$)
$q$ = heat flux ($W.m^{-2}$)
RMS = root mean square
RSS = root sum square
$t$ = time (s)
$T_{aw}$ = adiabatic wall temperature (°C)
$T_{\text{bar}}$ = normalized temperature (°C)
$T_c$ = crystal temperature (°C)
$T_g$ = gas temperature (°C)
$T_i$ = initial temperature (°C)
$T_s$ = surface temperature (°C)

### Greek

$\rho$ = density ($kg.m^{-3}$)
$\beta$ = heat transfer parameter, $\beta = h\sqrt{t}/\sqrt{\rho ck}$
$\alpha$ = thermal diffusivity ($m^2.s^{-1}$)

## References

[1] Jones, T. V., Wang, Z., and Ireland, P. T., 1992, "Liquid Crystals in Aerodynamic and Heat Transfer Testing," *Proceedings, IMechE Conference-Optical Methods and Data Processing in Heat and Fluid Flow*, ImechE, London, UK.
[2] Ireland, P. T., Wang, Z., and Jones, T. V., 1995, "Liquid Crystal Heat Transfer Measurement," *Measurement Techniques Lecture Series*, von Karman Institute for Fluid Dynamics.
[3] Baughn, J. W., 1995, "Liquid Crystal Methods for Studying Turbulent Heat Transfer," Int. J. Heat Fluid Flow, **16**(5), pp. 365–375.
[4] Wilson, M., Syson, B. J., and Owen, J. M., 1993, "Image Processing Techniques Applied to Wide-Band Thermochromic Liquid Crystals," *Proceedings, Eurotherm*, **32**, pp. 41–49.
[5] Wang, Z., Ireland, P. T., Jones, T. V., and Davenport, R., 1994, "A Color Image Processing System for Transient Liquid Crystal Heat Transfer Experiments," ASME Paper No. 94-GT-290.
[6] Camci, C., Kim, K., Hippensteele, S. A., and Poinsatte, P. E., 1993, "Evaluation of Hue Capturing Based Transient Liquid Crystal Method for High-Resolution Mapping of Convective Heat Transfer on Curved Surfaces," ASME J. Heat Transfer, **115**, pp. 311–318.
[7] Hay, J. L., and Hollingsworth, D. K., 1998, "Calibration of Micro-Encapsulated Liquid Crystal Using Hue Angle and a Dimensionless Temperature," Exp. Therm. Fluid Sci., **18**, pp. 251–257.
[8] Chan, T. L., Ashforth-Frost, S., and Jambunathan, K., 2001, "Calibrating for Viewing Angle Effect During Heat Transfer Measurements on a Curved Surface," Int. J. Heat Mass Transfer, **44**, pp. 2209–2223.
[9] Chen, P. H., Ding, P. P., and Ai, D., 2001, "An Improved Data Reduction Method for Transient Liquid Crystal Thermography on Film Cooling Measurements," Int. J. Heat Mass Transfer, **44**, pp. 1379–1387.
[10] Wang, Z., Ireland, P. T., and Jones, T. V., 1995, "An Advanced Method of Processing Liquid Crystal Video Signals From Transient Heat transfer Experiments," ASME J. Turbomach., **117**, pp. 184–189.
[11] Ireland, P. T., and Jones, T. V., 2000, "Liquid Crystal Measurements of Heat Transfer and Surface Shear Stress," Meas. Sci. Technol., **11**, pp. 969–986.
[12] Turnbull, W. N. O., and Oosthuizen, P. H., 1999, "A New Experimental Technique for Measuring Surface Heat Transfer Coefficients Using Uncalibrated Liquid Crystals," Proceedings, ASME Winter Conference, Nashville, TN.
[13] Baughn, J. W., Mayhew, J. E., Anderson, M. R., and Butler, R. J., 1998, "A Periodic Transient Method Using Liquid Crystals for the Measurement of Local Heat Transfer Coefficients," ASME J. Heat Transfer, **120**, pp. 772–776.
[14] Abu Talib, A. R., Neely, A. J., Ireland, P. T., and Mullender, A. J., 2001, "Compact Low-Temperature Analogue of Aero Engine Fire-Certification Burner," ASME Paper No. 2001-GT-0364.
[15] The International Organisation for Standardisation (ISO), 1992, "Aircraft—Environmental Conditions and Test Procedures for Airborne Equipment-Resistance to Fire in Designated Fire Zones," ISO2685:1992(E).
[16] Neely, A. J., Ireland, P. T., and Mullender, A. J., 1999, "Pilot Study to Inves-

tigate Novel Experimental and Theoretical Fire-Event Modelling Techniques,'' Paper No. AIAA-99-09-0326.
[17] Neely, A. J., Abu Talib, A. R., Ireland, P. T., and Mullender, A. J., 2000, ''Development of Low-Temperature Fire-Event Modelling Technique,'' *Proceedings, 22nd International Congress of Aeronautical Science (ICAS) Conference*, Harrogate, UK.
[18] Gillespie, D. R., Wang, Z., and Ireland, P. T., 1995, ''Heating Element,'' PCT/GB96/02017.
[19] Gillespie, D. R., Wang, Z., Ireland, P. T., and Kohler, S. T., 1996, ''Full Surface Local Heat Transfer Coefficient Measurements in an Integrally Cast Impingement Cooling Geometry,'' ASME Paper No. 96-GT-200.
[20] British Standard, 1992, ''Fluid Flow in Closed Conduits,'' BS-1042.
[21] Abu Talib, A. R., 2003, ''Detail Investigation of the Low-Temperature Analogy of an Aircraft Engine Standard Fire-Test,'' Ph.D. thesis, Department of Engineering Science, University of Oxford, Oxford, UK.
[22] Ireland, P. T., and Jones, T. V., 1987, ''The Response Time of a Surface Thermometer Employing Encapsulated Thermochromic Liquid Crystals,'' J. Phys. Exp. Sci. Instru., **20**, pp. 1195–1199.
[23] Kenning, D. B. R., and Yan, Y., 1996, ''Pool Boiling Heat transfer on a Thin Plate: Features Revealed by Liquid Crystal Thermography,'' Int. J. Heat Mass Transfer, **39**, pp. 3117–3137.
[24] Birrell, D. C., and Eaton, J. K., 1998, ''Liquid Crystal Temperature Measurement for Real-Time Control,'' *Proceedings, SPIE Conference on Applications of Digital Image Processing XXI*, **3460**, pp. 58–66.
[25] Baughn, J. W., Anderson, M. R., Mayhew, J. E., and Wolf, J. D., 1999, ''Hysteresis of Thermochromic Liquid Crystal Temperature Measurement Based on Hue,'' ASME J. Heat Transfer, **121**, pp. 1067–1071.
[26] Dixon, G. D., and Scala, L. C., 1970, ''Thermal Hysteresis in Cholesteric Color Responses, Molecular Crystal and Liquid Crystals,'' Mol. Cryst. Liq. Cryst., **10**, pp. 317–325.
[27] Norman, M., 2003, personal communication, Business Development Manager, Hallcrest Ltd.
[28] Schultz, D. L., and Jones, T. V., 1973, ''Heat Transfer Measurements in Short Duration Hypersonic Facilities,'' AGARD-AG-165, Advisory Group for Aerospace Research & Development (AGARD).
[29] Ling, J. P. C. W., Ireland, P. T., and Turner, L., 2002, ''Full Coverage Film Cooling for Combustor Transition Sections,'' ASME Paper No. 2002-GT-30528.
[30] Moffat, R. J., 1982, ''Contributions to the Theory of Single Sample Uncertainty Analysis,'' J. Fluid Mech., **104**, p. 250.
[31] Byerley, A. R., 1989, ''Heat Transfer Near The Entrance to a Film Cooling Hole in a Gas Turbine Blade,'' Ph.D. thesis, Department of Engineering Science, University of Oxford, Oxford, UK.
[32] Chambers, A. C., Gillespie, D. R. H., Ireland, P. T., and Dailey, G. M., 2002, ''A Novel Transient Liquid Crystal Technique to Determine Heat Transfer Coefficient Distributions and Adibatic Wall Temperature in a Three Temperature Problem,'' ASME Paper No. GT-2002-30532.

# A Transient Infrared Thermography Method for Simultaneous Film Cooling Effectiveness and Heat Transfer Coefficient Measurements From a Single Test

**Srinath V. Ekkad**
e-mail address: ekkad@me.lsu.edu
Mechanical Engineering Department,
Louisiana State University,
Baton Rouge, LA 70803

**Shichuan Ou**

**Richard B. Rivir**

U.S. Air Force Research Laboratory,
Wright Patterson AFB, OH 45433

*In film cooling situations, there is a need to determine both local adiabatic wall temperature and heat transfer coefficient to fully assess the local heat flux into the surface. Typical film cooling situations are termed three temperature problems where the complex interaction between the jets and mainstream dictates the surface temperature. The coolant temperature is much cooler than the mainstream resulting in a mixed temperature in the film region downstream of injection. An infrared thermography technique using a transient surface temperature acquisition is described which determines both the heat transfer coefficient and film effectiveness (nondimensional adiabatic wall temperature) from a single test. Hot mainstream and cooler air injected through discrete holes are imposed suddenly on an ambient temperature surface and the wall temperature response is captured using infrared thermography. The wall temperature and the known mainstream and coolant temperatures are used to determine the two unknowns (the heat transfer coefficient and film effectiveness) at every point on the test surface. The advantage of this technique over existing techniques is the ability to obtain the information using a single transient test. Transient liquid crystal techniques have been one of the standard techniques for determining h and $\eta$ for turbine film cooling for several years. Liquid crystal techniques do not account for nonuniform initial model temperatures while the transient IR technique measures the entire initial model distribution. The transient liquid crystal technique is very sensitive to the angle of illumination and view while the IR technique is not. The IR technique is more robust in being able to take measurements over a wider temperature range which improves the accuracy of h and $\eta$. The IR requires less intensive calibration than liquid crystal techniques. Results are presented for film cooling downstream of a single hole on a turbine blade leading edge model.* [DOI: 10.1115/1.1791283]

## Introduction

''Film cooling is the introduction of secondary fluid (coolant) at one or more discrete locations along a surface exposed to a high temperature environment to protect that surface not only in the immediate region of injection but also in the downstream region'' [1]. Film cooling protects the surface directly and reduces the heat load to the turbine surface. There is a need to know both the local wall temperature and the associated convective heat transfer coefficient underneath the injected film to determine the levels of heat load reduction. Typically, in convection situations, local surface heat flux is represented as:

$$q'' = h(T_\infty - T_w) \tag{1}$$

where $T_w$ is the local surface temperature and $T_\infty$ is the mainstream temperature that drives the heat transfer from the fluid to the surface. Most convective heat transfer problems are two temperature problems indicating that the mainstream temperature and the wall temperature are the two driving temperatures for the heat transfer. However, in the case of film cooling or heating and jet impingement in cross-flow, there are two streams with different temperatures resulting in three temperature problems. The degree of mixing between the two interacting streams results in a new temperature, which is the driver for the heat transfer into the surface. The film temperature depends on the local mixing between the two streams. In this case, the alternate way of representing the heat flux into the surface is

$$q_f'' = h_f(T_f - T_w) \tag{2}$$

where the subscript $f$ indicates film conditions. For an adiabatic surface, the film temperature will be equal to the adiabatic wall temperature. There are two unknowns in the above equation, the heat transfer coefficient ($h_f$) and film temperature ($T_f$).

Detailed measurements of both adiabatic wall temperature and heat transfer coefficient distributions are required to assess film cooling performance accurately. Several techniques have been used to obtain both measurements for film cooling situations. Metzger and Mitchell [2] showed that the three-temperature convection problems could be shown in a graphical interpretation wherein a straight line represents the three temperature performance. The line is plotted between the ratio of heat transfer coefficient $h_f/h$ versus a nondimensional temperature ($\theta$). This heat transfer coefficient ratio is greater than 1.0 as the heat transfer coefficient for film injection is normally higher than without film injection due to enhanced turbulence from the mixing of the

Contributed by the International Gas Turbine Institute (IGTI) of THE AMERICAN SOCIETY OF MECHANICAL ENGINEERS for publication in the ASME JOURNAL OF TURBOMACHINERY. Paper presented at the International Gas Turbine and Aeroengine Congress and Exhibition, Vienna, Austria, June 13–17, 2004. Paper No. 2004-GT-54236. Manuscript received by IGTI, October 1, 2003; final revision, March 1, 2004. IGTI Review Chair: A. J. Strazisar.

  

streams downstream of injection. The nondimensional temperature ($\theta$) is defined as as $(T_c-T_\infty)/(T_w-T_\infty)$, where $T_c$ is coolant temperature, $T_\infty$ is mainstream temperature, and $T_w$ is local wall temperature. This representation is applicable for every location on the test surface. Each surface will have its own signature depending on the local mixing of the two streams. The heat transfer coefficient can be obtained from the condition where both streams have equal temperatures. The film effectiveness can be obtained when the temperatures between the streams are significantly different. To determine both these quantities, two points are needed on the line and the determination of the intercepts will result in the solution for heat transfer coefficient and film effectiveness at every point on the surface. Heater foil thermocouple techniques have been used to obtain local discrete measurements [3–5]. Vedula and Metzger [6] presented a transient test where the test surface is exposed to two different steady streams and the transient temperature response of the test surface was obtained from the color display of a thin coating of thermochromic liquid crystals. This test was based on a technique developed for two temperature situations as described by Metzger and Larson [7]. The test surface was modeled as a semi-infinite solid medium with transient heat conduction. A convection wall boundary condition was imposed by the sudden transient heating. The entire wall material was at a uniform initial temperature before the test. During the transient heating test, each point on the surface will produce a different transient response due to different convective heat transfer coefficient. A faster time of color change of the liquid crystal during the transient test to the prescribed color will produce higher heat transfer coefficients and vice versa. The basic equations defining the system are shown as:

$$k\frac{\partial^2 T}{\partial y^2}=\rho C_p\frac{\partial T}{\partial t} \tag{3a}$$

$$-k\left.\frac{\partial T}{\partial y}\right|_{y=0}=h(T_r-T_w) \tag{3b}$$

$$T|_{y=\infty}=T_i \tag{3c}$$

$$T|_{t=0}=T_i \tag{3d}$$

where $T_r$ is the reference temperature or the main flow temperature, $T_w$ is the prescribed wall condition (color-change) temperature, and $T_i$ is the initial temperature of the test surface before the transient. Applying the prescribed boundary conditions and initial conditions to the problem and solving for the wall temperature response with time at $y=0$ produces a solution of the form:

$$\frac{T_w-T_i}{T_\infty-T_i}=1-\exp\left(\frac{h^2\alpha t}{k^2}\right)\operatorname{erfc}\left(\frac{h\sqrt{\alpha t}}{k}\right) \tag{4}$$

where $h$ is the unknown quantity in the equation with $T_w$ is the wall temperature at time $t$ after the initiation of the transient test. The material properties, $\alpha$ $(0.1076\times e^{-6}\ m^2/s)$ and $k(0.187\ W/m\ K)$ dictate the applicability of the semi-infinite solid solution. From the liquid crystal color response, the time of color change to a particular color is measured at every point on the test surface and the above equation is used to calculate the local heat transfer coefficient. The above equation assumes that the oncoming mainstream flow imposes a step change in air temperature on the surface, which is not true in the transient experiment. Therefore, the above equation was modified to represent the response of the changing mainstream temperature. The mainstream temperature rise is simulated as a superposed set of elemental steps using the Duhamel's superposition theorem. Metzger and Larson [7] showed that the wall temperature response can be represented as

$$T_w-T_i=\sum_{j=1}^{N}U(t-\tau_j)\Delta T_\infty \tag{5}$$

where

$$U(t-\tau_j)=1-\exp\left[\frac{h^2}{k^2}\alpha(t-\tau_j)\right]\operatorname{erfc}\left[\frac{h}{k}\sqrt{\alpha(t-\tau_j)}\right] \tag{6}$$

The superposition is imposed by measuring the mainstream temperature ($T_\infty$) variation with time ($\tau$) during the transient test. The step changes are then input into the above solution to obtain the unknown heat transfer coefficient.

In film cooling situations, Eq. (4) is modified to include the film temperature based on the definition of the local heat flux as shown in Eq. (2). The equation becomes:

$$\frac{T_w-T_i}{T_f-T_i}=1-\exp\left(\frac{h_f^2\alpha t}{k^2}\right)\operatorname{erfc}\left(\frac{h_f\sqrt{\alpha t}}{k}\right) \tag{7}$$

where $T_f$ is the local film temperature and is a function of the local mixing between the mainstream and coolant jet near the surface.

Vedula and Metzger [6] presented a method wherein two color change times can be obtained from a single transient test at every location. If during the transient, the liquid crystal coating indicates one surface temperature ($T_{w1}$) at time, $t_1$ and another surface temperature ($T_{w2}$) at time, $t_2$. Basically, two events are measured at every point leading to the solution of both $h$ and $T_f$ from the simultaneous solution of the two equations:

$$\frac{T_{w1}-T_i}{T_f-T_i}=1-\exp\left(\frac{h_f^2\alpha t_1}{k^2}\right)\operatorname{erfc}\left(\frac{h_f\sqrt{\alpha t_1}}{k}\right)$$

$$\frac{T_{w2}-T_i}{T_f-T_i}=1-\exp\left(\frac{h_f^2\alpha t_1}{k^2}\right)\operatorname{erfc}\left(\frac{h_f\sqrt{\alpha t_2}}{k}\right) \tag{8}$$

In the proposed transient test, the mainstream will be heated and the coolant supply will be cold or similar to room temperature. The Duhamel's superposition theorem will be applied to the mainstream temperature response as the coolant will be at a constant temperature through the experiment. However, due to inherent difficulties of determining two events far apart so that the uncertainty can be reduced, this technique has never been applied to solve for both the unknowns from a single transient test. To avoid the difficulties associated with the single transient test, Vedula and Metzger [6] suggested two different tests with the same flow conditions but different coolant temperatures measuring the indication of the same color change temperature. They ran two tests with one that had mainstream and coolant running at about the same temperatures and another test that had the mainstream hot and the coolant at room temperature. Since they did not have a true step change in air temperatures for both mainstream and coolant, they applied the superposition integration for both temperatures. Also, they defined film effectiveness ($\eta$) as

$$\eta=\frac{T_f-T_\infty}{T_c-T_\infty} \tag{9}$$

where $T_f$ represents the film temperature which is the same as adiabatic wall temperature as there is no heat transfer into the wall during the transient test. Several studies have used this technique [8–10] to obtain film cooling measurements for different surface geometries. Ekkad et al. [11] and Du et al. [12] used a transient cooling technique to eliminate the use of superposition integration for the mainstream and coolant temperatures but they still needed two different tests to obtain both heat transfer coefficient and film effectiveness at every point on the surface.

The transient HSI technique for liquid crystals uses the real-time conversion of RGB color attribute to the Hue_Saturation_Intensity (HSI) attribute [13–15]. In this case, the entire wall temperature is measured at a certain instant using a wide band liquid crystal coating or a mixture of several different bands of liquid crystals. The surface temperature distribution is mapped from the measured Hue and Intensity of the color scheme on the surface. Using Eq. (4), the local heat transfer coefficient is determined at every surface point from the surface temperature

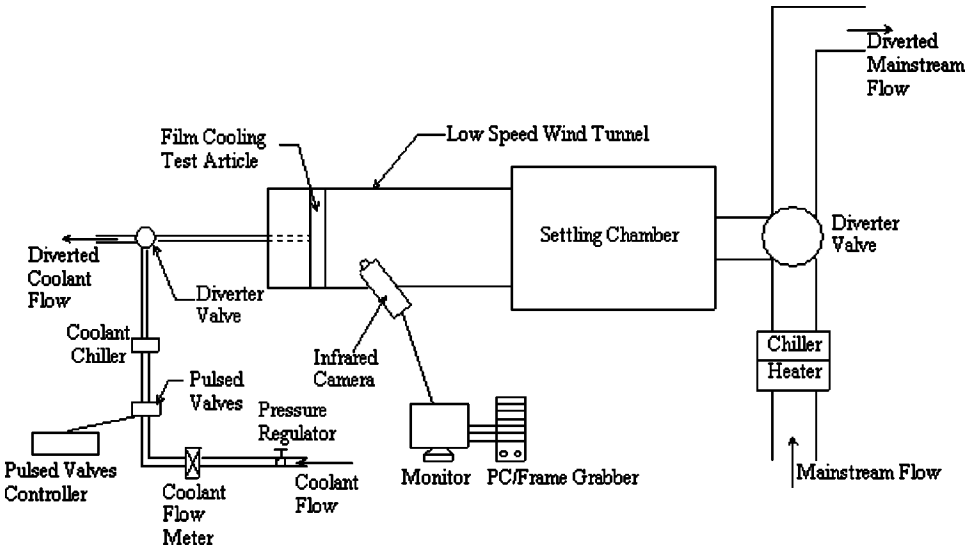


**Fig. 1 Schematic of test facility**

distribution at that particular time. If the temperature distribution is determined at another instant of time, then the two-equation scheme as shown in Eq. (8) can be used to determine heat transfer coefficient and film effectiveness for film cooling situations.

In the present study, a transient infrared thermography technique is described for obtaining both heat transfer coefficient and film effectiveness from a single test. The transient IR technique is based on the two-equation, single test proposed by Vedula and Metzger [6]. In this test, two images with surface temperature distributions are captured at two different times during the transient test. The two temperatures at two different instants are used in the two equations [Eq. (8)] shown above to calculate both heat the transfer coefficient and the film temperature. The test is typical of a transient liquid crystal technique experiment wherein the test surface at ambient is suddenly exposed to a hot mainstream and cold coolant jet. The surface temperature response is captured by the IR camera at different time instants during the transient test.

There have been several studies in the recent years that have used IR thermography techniques for heat transfer coefficient and film effectiveness measurements. Most of these studies either measured film effectiveness with adiabatic wall with steady state conditions [16–17] or a measured heat transfer coefficient with steady state conditions and a constant wall heat flux surface [18–19]. There are no studies that have used the IR technique for the simultaneous determination of film effectiveness and heat transfer coefficients in the transient mode. This is the first study to use the advantages of the IR technique for film cooling measurements.

It is also important to note that although this is the first study to provide both the heat transfer coefficient and film effectiveness from a single test using IR thermography, there have been other studies that have attempted to obtain both values from a single test. Chyu and Hsing [20] used a thermogrpahic phosphor flourescence technique to measure both the heat transfer coefficient and film effectiveness. Licu et al. [21] used a wide band liquid crystal on a constant heat flux wall and a transient test to determine both a heat transfer coefficient and film effectiveness. However, both techniques require significant surface preparation and lighting to obtain quality results.

Advantages. There are many advantages of this new technique.

1. There is no need for spraying expensive liquid crystals on the surface. Typical surface preparation requires only black paint.
2. The technique requires a single transient test thus reducing run time and also uncertainties relating to running two different tests at two different times.
3. The test is not limited by the operating point of the liquid crystals. Liquid crystals cannot operate beyond 100°C whereas the present technique has no such limits as long as the test plate material is made of low conductivity.
4. The IR camera also provides initial temperature distribution on the surface, which is very difficult to obtain from liquid crystals.
5. The coolant does not require to be heated as in the case of two test techniques resulting in reduced capital costs and time savings.

The IR system is relatively more expensive than the liquid crystal image processing system and also provides lower resolution than RGB-CCD cameras.

## Test Facility

The experimental setup is shown in Fig. 1. The facility consists of a low speed wind tunnel with a 76.2 cm diameter, settling chamber and a 30.5 cm diameter solenoid valve to switch the primary temperature controlled flow from a bypass loop to the test section. A temperature controlled coolant loop is designed to provide the coolant flow to the film hole. The coolant flow passes through a heat exchanger and a rotameter to measure the flowrate and finally through a 0.635 cm solenoid valve to switch the flow from bypass to the film hole. There is no heater for the coolant as the test is run with only cold flow. The test surface is a full half cylinder with a diameter of 8.89 cm and height of 36.4 cm joined by a flat afterbody. The film hole is located at $\pm 21.5$ deg from the stagnation line. The hole is 4.76 mm in diameter and is angled 20 deg and 90 deg to the surface in the spanwise and streamwise directions. The hole is located at the midpoint of the test channel. The hole to leading edge diameter $(d/D)$ is 0.054 and the hole length to hole diameter ratio $(L/d)$ is 11.69.

The infrared thermography system used is a FLIR system ThermaCAM SC 3000. The camera offers a high quality, nonintrusive method for obtaining thermal data through a commercially available software package for data analysis. The camera has several temperature ranges between $-20$°C and 1500°C and can be extended up to 2000°C with optional filters. The stated camera accuracy is $\pm 2\%$ of the chosen measurement range or $\pm 2$°C

($\pm 2$°K) whichever is larger. A temperature range of $-20$°C to 80°C with an accuracy of ($\pm 2$°C or $\pm 2$°K) is used for the present study. A thermocouple was placed on the black painted test surface to act as a reference for camera calibration. The thermocouple was used to estimate the emissivity of the surface. The emissivity of the black painted test when viewed through a calcium fluoride window was 0.96. The camera houses a Quantum Well Focal Plane Array (QWIP), which receives and records the thermal electromagnetic radiation between 8–9 $\mu$m in a 320 $\times$240 pixel field. The internal components were cooled using a Stirling cooler to 70 K.

To begin the procedure for obtaining measurements, the test surface is painted black and the IR camera is focused on the test surface region (typically downstream of the hole). The preparation for the actual tests requires pre-processing steps that are basically to calibrate the entire thermography system and the IR signal. The camera was focused on the hole and the surface was painted using flat black paint. Thermocouples were attached to the surface using aluminum tape. The surface was then heated using hot air from the blower. The thermocouples are monitored during the heat up and subsequent achievement of steady state. The IR camera is focused on the test surface. The parameters required for an accurate IR measurement to compensate for the effects of a number of different radiation sources are background temperatures, the relative humidity, and the distance between the test surface and the camera. A number of temperatures are used to establish the correct value of emissivity. Multiple temperatures compensate for all other emitting sources within view of the test article. To calibrate the surface emissivity, the IR temperature of the thermocouple bead is measured and compared to the indicated thermocouple temperature. The emissivity of the surface is then adjusted and determined until the IR temperature matches the thermocouple temperature within 0.1°C. The emissivity with flat black coating on the surface was typically in the range of 0.93–0.97. The mainstream airflow is routed away from the test section and heated to a required temperature. The coolant flow is maintained at ambient temperature and also routed away from the test section. Once the mainstream reaches the required temperature, the camera is triggered to take images at the same time the mainstream and the coolant flows are routed into the test section. Thermocouples are placed in the mainstream and upstream of the coolant hole to measure the transient responses of the air temperature during the transient heating test. The images are stored in the computer and the air temperatures are digitized through an A/D system. The image files from the IR camera are converted to temperature files at different instants of time. Figure 2 shows IR images at three times during the transient test. The temperatures range from 25 to 50°C (Blue is 25°C and Bright yellow is 50°C). All the other holes on the showerhead array are blocked off and only one hole is flowing.

The mainstream temperature increases from the initial temperature to the set temperature during the first 10–15 seconds and then steadies. Figure 3 shows the typical mainstream temperature rise during the transient test. Mainstream temperature increases from initial temperature to the set temperature of the heater. The coolant temperature is maintained at the initial temperature. The wall temperature on the mainstream side is monitored and rises as the surface gets heated during the transient test at a more gradual rate than the mainstream temperature. The inside wall temperature is unaffected by the heating on the opposite side during the test confirming the usage of the semi-infinite solid assumption.

The mainstream temperature, the coolant temperature, and the surface temperature distributions from the IR images are used to calculate the local heat transfer coefficient and film effectiveness at each pixel of the IR image. To calculate heat transfer coefficient and film effectiveness distributions, two images are required. The first image is typically around 15–20 seconds after the initiation of the test and the second image around 60–70 seconds after the test initiation as shown in Fig. 2.

Uncertainty in the calculation comes from the measurement of initial, mainstream, and coolant temperatures. Estimated uncertainty in initial and wall temperature ($\Delta T_i$) is $\pm 1.1$°C, mainstream temperature ($\Delta T_\infty$) is $\pm 1.1$°C, and coolant temperature ($\Delta T_c$) is $\pm 1.1$°C. The camera frame rate is 60 Hz resulting in a time error of $\pm 1.6\%$ and the test surface property uncertainty is estimated at $\pm 3\%$. The resulting average uncertainty using the methodology proposed by Kline and McClintock [22] for a heat transfer coefficient and film effectiveness is $\pm 4.5\%$ and $\pm 7.0\%$,

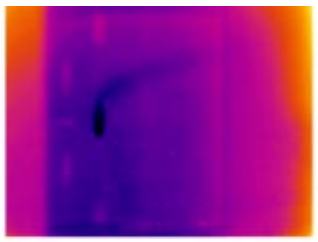

(a) Initial Image (Time = 0 seconds)

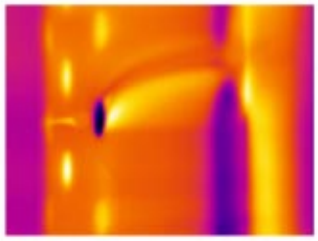

(b) Intermediate time (Time =25 seconds)

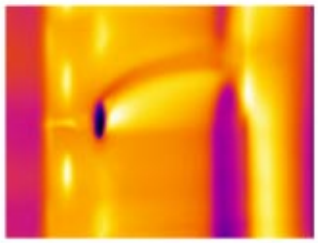

(c) Final Time (Time =70 seconds)

**Fig. 2 IR images from camera with single hole blowing**

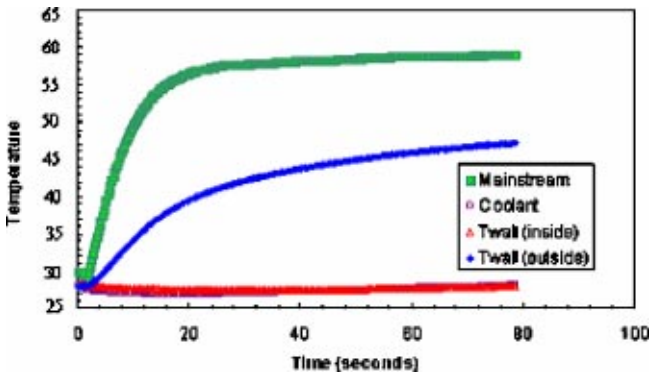


**Fig. 3 Temperature response of different thermocouples in °C.**

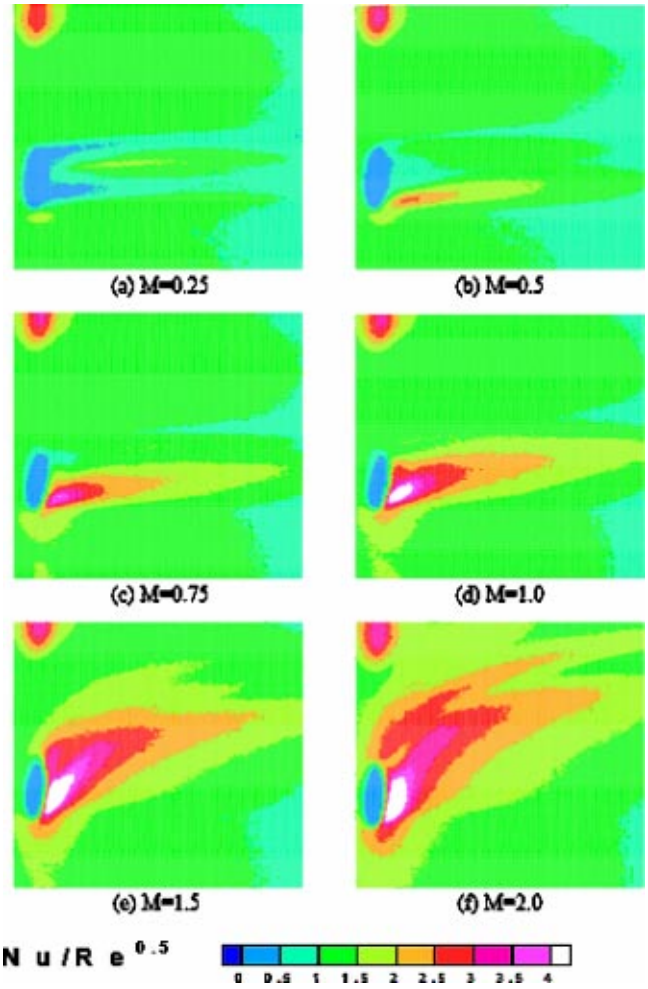


**Fig. 4 Detailed Nusselt number distributions downstream of the injection hole**

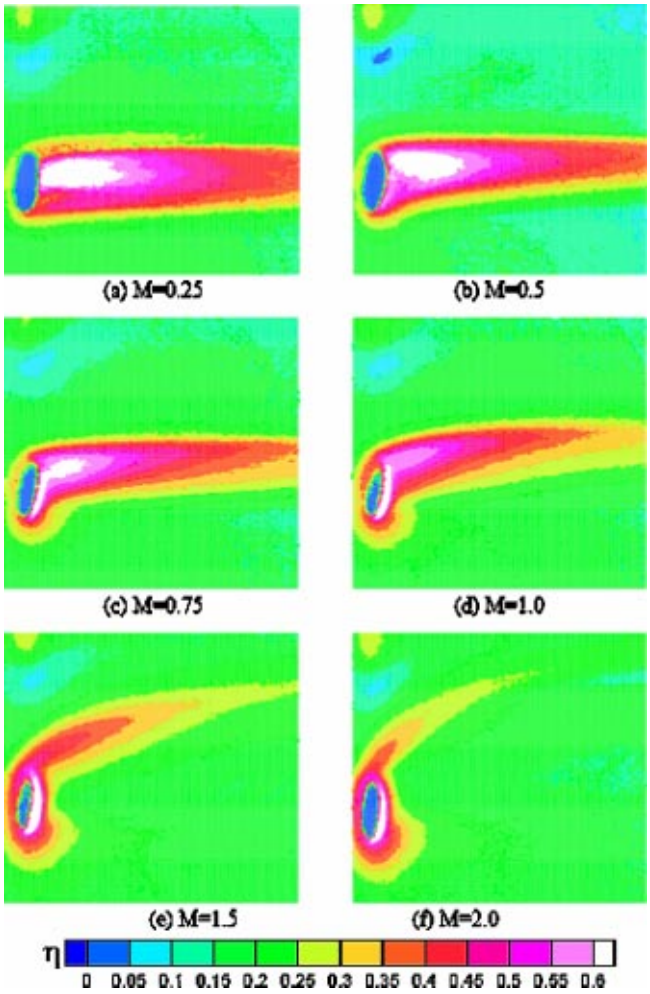


**Fig. 5 Detailed film effectiveness distributions downstream of the injection hole**

respectively. However, uncertainty for local film effectiveness depends on the local value. Uncertainty for effectiveness measurements is $\pm 0.05$.

## Results and Discussion

Experiments were performed at a mainstream velocity of 12.63 m/s, which represents a flow Reynolds number of 60,000 based on leading edge diameter. Six different coolant-to-mainstream blowing ratios were studied ranging from 0.25 to 2.0 for a single hole on the leading edge surface to evaluate the experimental technique.

Detailed heat transfer coefficient distributions on the leading edge region downstream of the film hole are presented as Frossling numbers ($Nu/Re^{0.5}$) in Fig. 4. For a circular leading edge with low free-stream turbulence, Frossling numbers at the stagnation point are around 1.0 and decrease downstream until about 80° from the stagnation point during which transition occurs. The film hole is located at 21.5 deg from the leading edge stagnation point which is well within the laminar boundary layer region. Film injection is orthogonal to the mainstream region resulting in a strong lateral velocity. As the film injection rate (or blowing rate) increases, the jet tends to resist the mainstream strongly and pushes upward. The jet-mainstream interaction also increases with increasing blowing ratio resulting in local turbulence behind the hole as shown by the high heat transfer region for higher blowing ratios. The Frossling numbers are around 1.0 for $M=0.25$ and as high as 4.0 for $M=2.0$.

Figure 5 presents the detailed film effectiveness distributions for each of the tested blowing ratios. The film effectiveness distributions clearly show the jet trajectory. For low blowing ratios, the jet does not possess a strong lateral momentum along the hole direction and gets pushed to the downstream edge resulting in high effectiveness values just downstream of the hole. The jet effect begins to decrease downstream due to reduced coverage. As the blowing ratio increases, the lateral momentum of the jet becomes stronger and the high film effectiveness region moves to the top of the hole location in the direction of the hole exit. Also for the higher blowing ratio, jet lift-off occurs resulting in lower effectiveness just downstream. Highest effectiveness coverage appears to occur between blowing ratios of 0.5 and 1.0.

First, the effect of increasing the blowing ratio on both the spanwise averaged heat transfer coefficient and film effectiveness has been explored. As expected, a higher blowing ratio provides higher heat transfer coefficients due to increase jet mixing and turbulence. Figure 6 shows the effect of blowing ratio on Frossling number distributions. At low blowing ratios, there is no enhancement downstream of injection due to low mixing and attached jets. The Frossling numbers are around 1.2 downstream of the hole for $M=0.25$. As the blowing ratio increases, the region downstream of the hole sees the highest enhancement due to jet–mainstream interactions. Farther downstream, the values decreases as the jet dissipates into the mainstream. The Frossling [23] solution for a cylinder in cross-flow is shown for comparison. This result is for a cylinder without film holes.

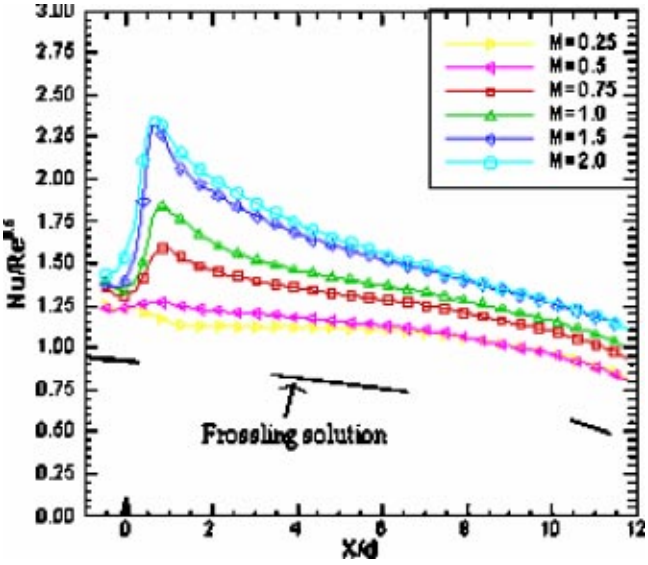


**Fig. 6 Effect of blowing ratio on spanwise averaged Nusselt number distribution**

Figure 7 shows the effect of blowing ratio on film effectiveness distributions. Lower blowing ratios produced attached jets downstream of the hole creating very high effectiveness and subsequently reducing downstream. Higher blowing ratios produce stronger jets that tend to lift off along the hole direction. The higher effectiveness region is along the hole direction and decreases downstream. This is the reason spanwise averaging shows higher effectiveness downstream of the hole for low blowing ratios. The jets get pushed downstream for low velocity jets whereas higher velocity jets mover farther laterally before losing the momentum and get pushed downstream. Higher effectiveness is seen at hole locations for higher blowing ratios as indicated in Fig. 5.

## Conclusions

A transient infrared thermography technique has been presented for a detailed heat transfer coefficient and film effectiveness measurements downstream of a single film hole. The technique is similar to the transient liquid crystal technique with some improvements. The IR technique does not require a thermochromic liquid crystal coating to show the temperature patterns on the surface during the transient test. Both the heat transfer coefficient and film effectiveness are obtained from a single test which greatly reduces the uncertainty associated with running two similar transient tests for the liquid crystal technique. The calibration is simple and the surface temperature measurements are obtained directly from the IR measurement of surface temperature. The major sources in uncertainty are dependent on the initial temperature distribution and the accurate measurement of color in the liquid crystal technique. In the IR technique, initial temperature distribution on the test surface can be easily measured before the initiation of the transient test resulting in better accuracy in calculating the heat transfer coefficient and film effectiveness.

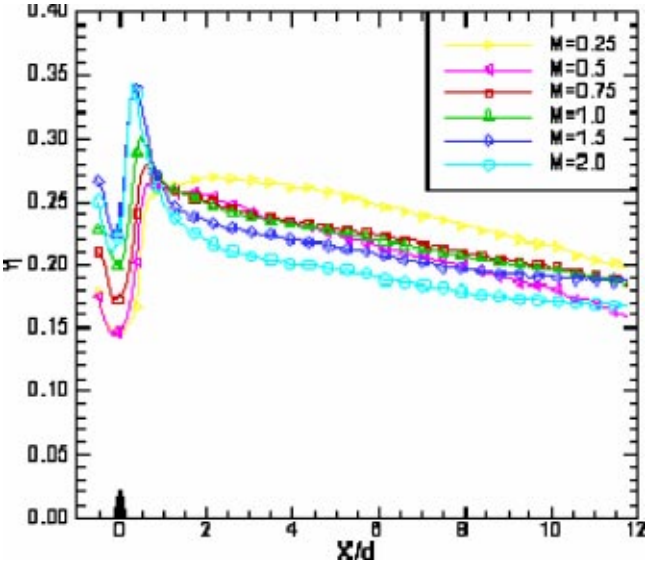


**Fig. 7 Effect of blowing ratio on spanwise averaged film effectiveness distribution**

## Nomenclature

$c_p$ = specific heat (kJ/kg K)
$d$ = cylinder diameter (m)
$h$ = local heat transfer coefficient without film injection ($W/m^2$ K)
$h_f$ = local heat transfer coefficient with film injection ($W/m^2$ K)
$k$ = thermal conductivity of test surface (W/m K)
$L$ = length of film hole (m)
$M$ = blowing ratio $=\rho_c V_c/\rho_\infty V_\infty$
Nu = Nusselt number based on leading edge diameter, $d$ ($=h_f d/k$)
$q''$ = surface heat flux ($W/m^2$)
Re = free-stream Reynolds number ($V_\infty d/\nu$)
$\rho$ = density of test surface
$\rho_c$ = coolant density ($kg/m^3$)
$\rho_\infty$ = mainstream density ($kg/m^3$)
$t$ = time (sec)
$T_c$ = coolant temperature (K)
$T_f$ = film temperature (K)
$T_i$ = test surface initial temperature (K)
$T_r$ = reference temperature (K)
$T_\infty$ = mainstream temperature (K)
Tu = free-stream mean turbulence intensity (%)
$T_w$ = local wall temperature (K)
$V_c$ = coolant velocity (m/s)
$V_\infty$ = mainstream velocity (m/s)
$x$ = streamwise distance from leading edge to trailing edge (m)
$y$ = coordinate normal to surface (m)
$\eta$ = film cooling effectiveness
$\theta$ = non-dimensional temperature $=(T_c-T_\infty)/(T_w-T_\infty)$
$\nu$ = kinematic viscosity of mainstream ($m^2/s$)
$\alpha$ = thermal diffusivity ($m^2/s$)
$\tau$ = time (sec)

## References

[1] Goldstein, R. J., 1971, "Film Cooling," Adv. Heat Transfer, **7**, pp. 321–329.
[2] Metzger, D. E., and Mitchell, J. W., 1966, "Heat Transfer from a Shrouded Rotating Disk with Film Cooling," ASME J. Heat Transfer, **88**, pp. 56–63.
[3] Eriksen, V. L., and Goldstein, R. J., 1974, "Heat Transfer and Film Cooling Following Injection Through Inclined Circular Holes," ASME J. Heat Transfer, **96**, pp. 239–245.
[4] Mick, W. J., and Mayle, R. E., 1988, "Stagnation Film Cooling and Heat Transfer, Including its Effect within the Hole Pattern," ASME J. Turbomach., **110**, pp. 66–72.
[5] Mehendale, A. B., and Han, J. C., 1992, "Influence of High Mainstream Turbulence on Leading Edge Film Cooling Heat Transfer," ASME J. Turbomach., **114**, pp. 707–715.
[6] Vedula, R. P., and Metzger, D. E., 1991, "A Method for the Simultaneous Determination of Local Effectiveness and Heat Transfer Distributions in a Three Temperature Convective Situations," ASME Paper No. 91-GT-345.
[7] Metzger, D. E., and Larson, D. E., 1986, "Use of Melting Point Surface Coatings for Local Convective Heat Transfer Measurements in Rectangular Channel Flows with 90-Deg. Turns," ASME J. Heat Transfer, **108**, pp. 48–54.

[8] Ekkad, S. V., Zapata, D., and Han, J. C., 1997, ''Heat Transfer Coefficients Over a Flat Surface with Air and $CO_2$ Injection Through Compound Angle Holes Using a Transient Liquid Crystal Image Method,'' ASME J. Turbomach., **119**, pp. 580–586.
[9] Ekkad, S. V., Zapata, D., and Han, J. C., 1997, ''Film Effectiveness Over a Flat Surface with Air and $CO_2$ Injection Through Compound Angle Holes Using a Transient Liquid Crystal Image Method,'' ASME J. Turbomach., **119**, pp. 587–593.
[10] Yu, Y., and Chyu, M. K., 1998, ''Influence of Gap Leakage Downstream of the Injection Holes on Film Cooling Performance,'' ASME J. Turbomach., **120**, pp. 541–548.
[11] Ekkad, S. V., Du, H., and Han, J. C., 1998, ''Detailed Film Cooling Measurements on a Cylindrical Leading Edge Model: Effect of Free-stream Turbulence and Density Ratio,'' ASME J. Turbomach., **120**, pp. 779–807.
[12] Du, H., Han, J. C., and Ekkad, S. V., 1998, ''Effect of Unsteady Wake on Detailed Heat Transfer Coefficient and Film Effectiveness Distributions for a Gas Turbine Blade,'' ASME J. Turbomach., **120**, pp. 808–817.
[13] Camci, C., Kim, K., and Poinsatte, P. E., 1993, ''Evaluation of a Hue Capturing Based Transient Liquid Crystal Method for High-Resolution Mapping of Convective Heat Transfer on Curved Surfaces,'' ASME J. Turbomach., **115**, pp. 311–318.
[14] Wang, Z., Ireland, P. T., and Jones, T. V., 1993, ''An Advanced Method for Processing Liquid Crystal Video Signals from Transient Heat Transfer Experiments,'' ASME Paper No. 93-GT-282.
[15] Van Treuren, K. W., Wang, Z., Ireland, P. T., and Jones, T. V., 1994, ''Detailed Measurements of Local Heat Transfer Coefficient and Adiabatic Wall Temperature Beneath an Array of Impingement Jets,'' ASME J. Turbomach., **116**, pp. 369–374.
[16] Bons, J. P., and Kerrebrock, J. L., 1998, ''Complementary Velocity and Heat Transfer Measurements in Rotating Cooling Passage with Smooth Walls,'' ASME Paper No. 98-GT-464.
[17] Mahmood, G. I., and Ligrani, P. M., 2002, ''Heat Transfer in a Dimpled Channel: Combined Influences of Aspect Ratio, Temperature Ratio, Reynolds Number, and Flow Structure,'' Int. J. Heat Mass Transfer, **45**, pp. 2011–2020.
[18] Colban, W. F., Lethander, A. T., Thole, K. A., and Zess, G., 2002, ''Combustor–Turbine Interface Studies: Part 2: Flow and Thermal Field Measurements,'' ASME J. Turbomach., **125**, pp. 203–209.
[19] Cutbirth, J. M., and Bogard, D. G., 2002, ''Evaluation of Pressure Side Film Cooling with Flow and Thermal Field Measurements, Part I: Showerhead Effects,'' ASME Paper No. No. GT-2002-30174.
[20] Chyu, M. K., and Hsing, Y. C., 1996, ''Use of Thermographic Phosphor Fluorescence Imaging System for Simultaneous Measurement of Film Cooling Effectiveness and Heat Transfer Coefficient,'' ASME Paper No. 96-GT-430.
[21] Licu, D. N., Findlay, M. J., Gartshore, I. S., and Salcudean, M., 2000, ''Transient Heat Transfer Measurements Using a Single Wide-Band Liquid Crystal Test,'' ASME J. Turbomach., **122**, pp. 546–552.
[22] Kline, S. J., and McClintock, F. A., 1953, ''Describing Uncertainties in Single Sample Experiments,'' Mech. Eng. (Am. Soc. Mech. Eng.), **75**, pp. 3–8.
[23] Frossling, N., 1958, ''Evaporation and Velocity Distribution in Two-Dimensional and Rotationally Symmetric Boundary Layer,'' NACA, TM-1432.

# Thermal Performance of Angled, V-Shaped, and W-Shaped Rib Turbulators in Rotating Rectangular Cooling Channels (AR=4:1)

**Lesley M. Wright**

**Wen-Lung Fu**

**Je-Chin Han**
e-mail: jchan@mengr.tamu.edu

Department of Mechanical Engineering,
Texas A&M University,
College Station, TX 77843-3123

*An experimental study was performed to measure the heat transfer distributions and frictional losses in rotating ribbed channels with an aspect ratio of 4:1. Angled, discrete angled, V-shaped, and discrete V-shaped ribs were investigated, as well as the newly proposed W-shaped and discrete W-shaped ribs. In all cases, the ribs are placed on both the leading and trailing surfaces of the channel, and they are oriented 45 deg to the mainstream flow. The rib height-to-hydraulic diameter ratio ($e/D$) is 0.078, and the rib pitch-to-height ratio ($P/e$) is 10. The channel orientation with respect to the direction of rotation is 135 deg. The range of flow parameters includes Reynolds number ($Re=10{,}000–40{,}000$), rotation number ($Ro=0.0–0.15$), and inlet coolant-to-wall density ratio ($\Delta\rho/\rho=0.12$). Both heat transfer and pressure measurements were taken, so the overall performance of each rib configuration could be evaluated. It was determined that the W-shaped and discrete W-shaped ribs had the superior heat transfer performance in both nonrotating and rotating channels. However, these two configurations also incurred the greatest frictional losses while the discrete V-shaped and discrete angled ribs resulted in the lowest pressure drop. Based on the heat transfer enhancement and the pressure drop penalty, the discrete V-shaped ribs and the discrete W-shaped ribs exhibit the best overall thermal performance in both rotating and nonrotating channels. These configurations are followed closely by the W-shaped ribs. The angled rib configuration resulted in the worst performance of the six configurations of the present study.*
[DOI: 10.1115/1.1791286]

## Introduction

To achieve higher thermal efficiency and power output in advanced gas turbines, the rotor inlet temperatures can exceed the melting point of the blade material. Therefore, it is necessary to cool the blades for safe and long operation of the turbine. Internal cooling is one method to cool the turbine blade. With internal cooling, pressurized cooling air is extracted from the compressor and injected into the turbine blade. The coolant circulates through cooling passages to remove heat from the blade. Pin-fin cooling is commonly used in the trailing edge. These pinfins not only enhance the heat transfer but also provide the structural support to the thin blade. Jet impingement cooling is the most effective technique to enhance the heat transfer, but these holes weaken the structural strength. Thus, jet impingement cooling is used in the leading edge where the thermal loads are high. Rib turbulators are often used to cool the mid portion of the blade. As the turbine blade rotates, Coriolis and rotational buoyancy forces alter the flow field of the cooling air through the cooling channels, which cause significantly different heat transfer distributions between the leading and trailing surfaces of the channel. These Coriolis and rotational buoyancy forces shift the coolant toward the trailing surface for the radially outward flow; thus heat transfer increases from the trailing surface, and decreases from the leading surface.

Figure 1 shows the orientation of a rectangular cooling channel in a gas turbine blade. As the blade becomes thinner toward the trailing edge, the cooling channels become narrower, and the orientation angle ($\beta$) of the channel increases. The knowledge of the flow field induced by rotation in channels with smaller aspect ratios (AR~1:1) cannot simply be applied to large aspect ratio channels. However, the availability of literature is limited concerning the heat transfer distribution for large aspect ratio channels. Therefore, it is necessary to investigate the heat transfer distribution for these narrow channels in the trailing edge portion of the blade.

A comprehensive review of turbine blade internal cooling can be seen in *Gas Turbine Heat Transfer and Cooling Technology* by Han et al. [1]. The book includes numerous studies that have been conducted over the years on a wide range of rib configurations in various size cooling channels using many experimental techniques. Early studies investigated cooling channels with orthogonal ribs (Han [2]). It was then determined that placing the ribs at an angle to the mainstream flow will result in greater heat transfer enhancement than ribs positioned at 90 deg to the mainstream flow. Studies by Han and Park [3] and Park et al. [4] investigated the thermal performance of angled ribs compared to orthogonal ribs. The results showed the heat transfer enhancement in angled rib channels is significantly greater than the heat transfer enhancement due to normal ribs.

The focus of rib turbulators began to shift to the investigation of ''high performance'' ribs. Han, Zhang, and Lee [5] studied a square channel with V, Λ, parallel (angled), and crossed ribs. They showed the V-shaped ribs (45 and 60 deg) perform better than the parallel ribs (45 and 60 deg).

Using the mass transfer technique, Lau, Kukreja, and McMillin [6] found the V-shaped ribs create the greatest heat transfer en-

Contributed by the International Gas Turbine Institute (IGTI) of THE AMERICAN SOCIETY OF MECHANICAL ENGINEERS for publication in the ASME JOURNAL OF TURBOMACHINERY. Paper presented at the International Gas Turbine and Aeroengine Congress and Exhibition, Vienna, Austria, June 13–17, 2004, Paper No. 2004-GT-54073. Manuscript received by IGTI, October 1, 2003; final revision, March 1, 2004. IGTI Review Chair: A. J. Strazisar.

  

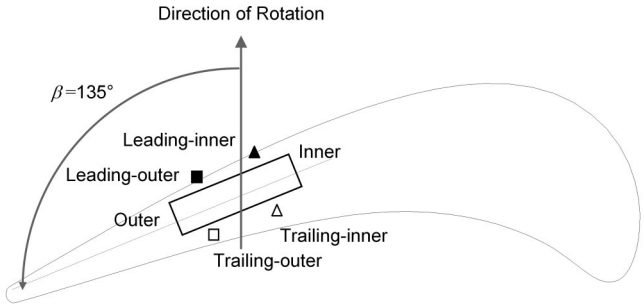


**Fig. 1 Orientation of a narrow Rectangular channel in a gas turbine blade**

hancement; however, they also create the greatest pressure drop. Their results showed that the V-shaped ribs and the full (angled) ribs had comparable thermal performances.

Han and Zhang [7] then completed a study of a square channel with various angled and V-shaped rib configurations. They concluded that broken ribs (similar to discrete ribs) create heat transfer enhancement levels of 2.5–4, while the enhancement created by the continuous ribs is only 2–3. Both the broken and continuous ribs incur a pressure penalty of 7–8 times.

Taslim, Li, and Kercher [8] studied various configurations of angled and V-shaped ribs using a liquid crystal technique. They also concluded that V-shaped ribs result in the greatest heat transfer enhancement while having the greatest pressure loss. Ekkad and Han [9] also used a liquid crystal technique to obtain detailed heat transfer distributions in a two-pass channel with parallel (angled), V-shaped, and broken V-shaped (discrete V-shaped) ribs. They concluded that the parallel, V-shaped, and broken V-shaped ribs produce similar heat transfer enhancement in the first pass, with the broken V-shaped ribs giving slightly higher enhancement.

Cho, Wu, and Kwon [10] recently investigated angled and discrete angled ribs using mass transfer. They concluded that the heat transfer performance of the discrete ribs is similar to that of the angled ribs in a rectangular channel with an aspect ratio of 2.04:1. A very narrow channel (AR=8:1) with V-shaped, Λ-shaped, and angled ribs was studied by Gao and Suden [11]. Using a liquid crystal technique, they too confirmed that V-shaped ribs result in the highest heat transfer enhancement and the highest frictional losses. They concluded that the V-shaped ribs yield the best overall thermal performance. Rhee et al. [12] also investigated rectangular channels (AR=3:1, 5:1, and 6.82:1). They studied the thermal performance of V-shaped and discrete V-shaped ribs. Based on their configurations, they concluded the thermal performance of the two configurations was comparable.

All of the above studies focus on the performance of various configurations of ribs in nonrotating channels. Many studies have been performed that investigate the effect of rotation on cooling channels. Johnson et al. [13] experimentally investigated the heat transfer in multi-pass rotating channels with angled ribs. Johnson et al. [14] performed additional tests with this four-pass test duct to determine the effect of channel orientation on the heat transfer enhancement. From these studies it was concluded that the heat transfer from both the leading and trailing surfaces of the ribbed channel was different from that of a nonrotating channel.

Parsons et al. [15,16] also studied the influence of channel orientation and wall heating condition on the regionally averaged heat transfer coefficients in a rotating, two-pass square channel with 60 and 90 deg ribbed walls. This study showed the heat transfer coefficients are greater in channels that are maintained at a constant wall temperature. They found this difference is greater for the channel oriented at 45 deg than the channel oriented perpendicular to the direction of rotation.

Dutta and Han [17] conducted an experimental study of regionally averaged heat transfer coefficients in rotating smooth and ribbed two-pass channels with three channel orientations. They found the effect of rotation is reduced for nonorthogonal alignment of the heat transfer surfaces with respect to the plane of rotation. They also concluded that the staggered half V-shaped ribs (comparable to the discrete V-shaped ribs of the present study) have better heat transfer performance than the 90 deg ribs and the 60 deg angled ribs.

Park, Lau, and Kukreja [18,19] conducted naphthalene sublimation experiments to examine the effects of rotation on the local heat and mass transfer distribution in a two-pass ribbed square channel. They also found that the overall heat and mass transfer in a rotating channel with ribbed surfaces was not affected by the Coriolis force as much as that in a rotating channel with smooth surfaces.

Due to the curved shape of a turbine blade, cooling channels near the trailing edge are rectangular and the orientation angle of the channel increases. The heat transfer trends in a square channel cannot simply be applied to rectangular channels. The effect of the Coriolis and rotational buoyancy forces is altered by the larger aspect ratios and orientation angles. Recently, more studies have focused on these rectangular channels.

Taslim et al. [20,21] investigated the heat transfer distribution in rotating square and rectangular rib-roughened channels using a liquid crystal technique. They found that the effects of rotation were more apparent in rib-roughened channels with a larger channel aspect ratio and a lower rib blockage ratio.

Kiml, Mochizuki, and Murata [22] examined the heat transfer and pressure drop in a ribbed rectangular channel (AR=2:1) for four rib configurations. (90, 75, 60, and 45 deg angled ribs). They revealed that 60 deg ribs produce the highest heat transfer enhancement due to the strong rotational momentum of the rib induced secondary flow. Kiml, Mochizuki, and Murata [23] also investigated heat transfer enhancement mechanisms in rectangular channels with V- and Λ-shaped ribs using a flow visualization technique to examine the secondary flow behaviors created by the V-shaped ribs.

Azad et al. [24] conducted an experimental study to determine heat transfer enhancement in a rotating two-pass ribbed rectangular channel with an aspect ratio of 2:1. They showed that the heat transfer decreases from the leading surface and increases from the trailing surface for the first passage. They also found the 90 deg channel orientation produces a greater rotation effect than the 135 deg channel orientation.

Al-Hadhrami, Han, and Griffith [25,26] studied the effect of rotation on heat transfer in rotating, two-pass square and rectangular channels (AR=2:1) with rib turbulators for two channel orientations. They found that the parallel and V-shaped ribs produce better heat transfer enhancement than the crossed and inverted V-shaped ribs. They also found that parallel angled ribs produce better heat transfer enhancement than the crossed angled ribs. Furthermore, the 90 deg channel orientation produces a greater rotation effect on the heat transfer than a 135 deg channel orientation.

Griffith, Al-Hadhrami, and Han [27] investigated the effect of rotation on heat transfer in a rib-roughened rectangular channel (AR=4:1). They found that the narrow rectangular passage exhibits much higher heat transfer enhancement for the ribbed surfaces than the ribbed surfaces in a smaller aspect ratio channel. They also found span wise heat transfer distributions exist across the leading and trailing surfaces, and the variation is accentuated by the use of angled ribs. Also, they showed the orientation of the channel significantly effects the heat transfer distribution.

Lee, Wright, and Han [28] also investigated the heat transfer performance of various rib configurations in a rotating rectangular duct with an aspect ratio of 4:1. They concluded that V-shaped ribs have superior heat transfer performance to the angled rib configurations. This is true for both nonrotating and rotating channels.

More recent studies have begun to focus on the leading edge of

the blade. Cho et al. [29] used mass transfer to study the effect of rotation in a rotating two-pass rectangular channel (AR=1:2) with 70 deg angled ribs. Agarwal, Acharya, and Nikitopoulos [30] used mass transfer to study a two-pass 1:4 rotating channel. In both channels with smooth walls and 90 deg angled ribs, they found that the heat/mass transfer in the 1:4 channel is less than that of a square channel.

The past studies have shown that V-shaped ribs perform better than angled ribs. However, the knowledge base for angled and V-shaped ribs is incomplete. Extensive studies have been performed for nonrotating channels; both heat transfer and pressure measurements have been taken in order to determine the overall thermal performance. The studies involving angled and V-shaped ribs in rotating channels are limited to heat transfer data. Therefore, the overall thermal performance of the rib configurations in rotating channels has not been considered. The majority of rotating heat transfer data presently available are limited to square (AR=1:1) channels or channels with an aspect ratio of 2:1. The rotating heat transfer data available for very narrow rib-roughened channels are scarce. The previous studies have also shown that discrete ribs perform better than complete ribs. However, the studies comparing the heat transfer enhancement and pressure penalty of complete and discrete ribs are limited to only nonrotating cases.

Therefore, it is necessary to provide designers with complete heat transfer and pressure data for narrow, rectangular channels. Heat transfer and pressure drop data are needed for the angled and V-shaped rib configurations under both rotating and nonrotating conditions. When considering narrow channels, the very wide leading and trailing surfaces make it possible for more complicated configurations to be cast into the cooling channel. Therefore, a W-shaped rib configuration is proposed for the internal cooling channels; this configuration could have better performance than the V-shaped ribs. In nonrotating channels, the discrete ribs outperform the complete ribs; therefore, it is necessary to investigate the performance of discrete angled, discrete V-shaped, and discrete W-shaped ribs in rotating channels.

In this study the thermal performance of the traditional angled ribs is compared with V-shaped ribs and the newly proposed W-shaped ribs; the thermal performance of discrete angled ribs, discrete V-shaped ribs, and the newly proposed discrete W-shaped ribs is also compared. This study systematically investigates the thermal performance of the six rib turbulator configurations in both nonrotating and rotating channels. The regionally averaged heat transfer distributions in rotating rectangular channels with an aspect ratio of 4:1 are experimentally investigated. The overall pressure drop is also measured, so the thermal performance of each configuration can be evaluated.

## Experimental Facility

**Rotating Test Facility.** The experimental rotating test rig used for this study was previously used by Wright, Lee, and Han [31] and is shown in Fig. 2. A gear attached to the shaft of a variable frequency motor is connected to a gear located at the base of a hollow shaft via a timing belt, so the variable frequency motor is used to rotate the hollow shaft. The hollow shaft extends from the base of the test rig to the work platform. A hollow rotating arm is attached orthogonal to the rotating shaft; the test section is inserted into this rotating arm. Thermocouple and heater wires are connected to a 100-channel slip ring assembly that is mounted to the rotating shaft. Power is supplied through the slip ring to the heaters using variable transformers. Cooling air is pumped to the test rig using a steady flow air compressor. The air flows through an ASME square-edge orifice meter, upward through the hollow rotating shaft, around a 90 deg bend, through two mesh screens, and into the rotating arm and test section. After flowing through the test section, the air is expelled to the atmosphere.

Minor modifications were made to the rotating test rig to incorporate the instrumentation required for recording pressure measurements. A 48-channel Scani-valve pressure transducer was fixed at the top of the slip ring to the rotating shaft. Flexible tubing from the Scani-valve runs through the hollow shaft to the base of the slip ring, where it exits the slip ring in the same locations as the slip ring lead wires. The tubing is then attached to the pressure taps of the test section. The signal of the pressure transducer is transmitted through the slip ring to the data acquisition system.

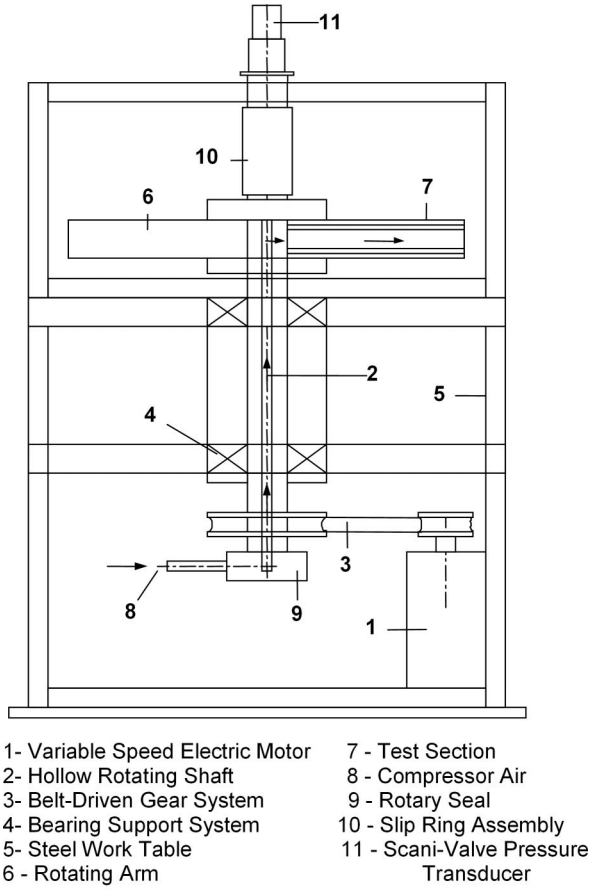


**Fig. 2 Rotating test facility**

**Experimental Test Section.** The test section is a one-pass rectangular channel. The ratio of mean rotating arm radius-to-channel hydraulic diameter ($R/D_h$) is 33.0 for the 4:1 channel. Likewise, the heated channel length-to-hydraulic diameter ratio ($L/D_h$) is 7.5. The air flows radially outward from the axis of rotation through the test section.

Figure 3 shows a schematic of the test section used in the present study. The test section consists of the leading, trailing, inner, and outer surfaces. The inner and outer surfaces each consist of six plates in the streamwise direction. The leading and trailing surfaces each consist of 12 plates. The cross section of the test section contains two plates for the leading surface to capture the spanwise variation on the leading surface, two plates for the trailing surface (spanwise variation), one plate for the inner surface, and one plate for the outer surface. A total of 36 copper plates make up the entire test section. Each plate is 0.9375 in. $\times$0.9375 in. (2.38 cm$\times$2.38 cm) and is surrounded by a 0.0625 in. (0.159 cm) strip of nylon to prevent conduction between the plates. This method provides a grid for analysis of the spanwise as well as the streamwise variation in the regionally averaged heat transfer coefficients. In order to maintain approximately the same circumferential wall temperature the power supplied to the heaters is varied. While maintaining the same temperature at two adjacent

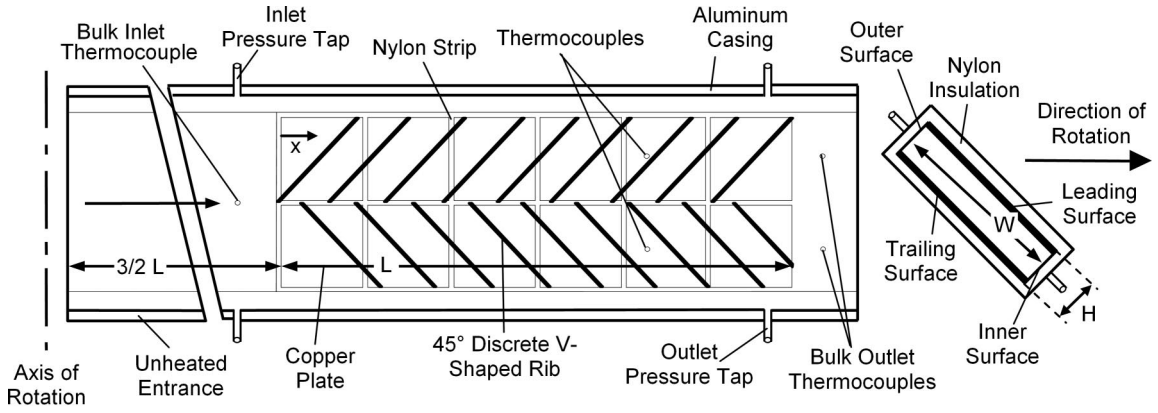


**Fig. 3 Schematic of the heated portion of the 4:1 test section**

copper plates, the net heat flux can vary by 45%. Therefore, the nylon strip is effectively limiting the conduction between adjacent copper plates.

Each 0.125 in. (0.318 cm) thick copper plate has a 0.0625 in. (0.159 cm) deep blind hole drilled in its backside. The temperature of each copper plate is measured using a 36 gauge, type T thermocouple. The thermocouple is secured in the blind hole using thermally conductive epoxy. With this setup, the thermocouple junction is located 0.0625 in. (0.159 cm) from the surface of the copper plate. The thermocouple output is monitored using commercially available software. The temperature data are displayed using the virtual instrument format, and the data are written to a data file specified by the user.

A nylon substrate serves as the support for the test section; each of the copper plates is mounted into this substrate. The nylon substrate forms a 3.25 in. (8.26 cm) diameter cylinder, and this test section is placed inside the aluminum, rotating arm of the test rig. Flexible heaters are installed beneath the leading and trailing surfaces, two for each surface. Thermal conducting paste is applied between the heater and copper plates to minimize contact resistance and promote heat transfer from the heater to the plates. The outer and inner walls (or sidewalls) are smooth, and they are unheated.

Static pressure taps are used to measure the pressure at the inlet and outlet of the heated portion of the test section. At the inlet, one pressure tap is located on the inner surface and one tap is located on the outer surface (the smooth walls), and two corresponding taps are located at the exit of the heated test section. Four channels of a 48-channel Scani-valve pressure transducer are used to measure the static pressure at each of the taps. The voltage output of the transducer is read using a multimeter. The Scani-valve transducer was calibrated prior to the tests using an inclined manometer. The pressure measurements are taken under adiabatic conditions (test section is not heated).

The test section is oriented at 135 deg from the direction of rotation. The experiments are conducted at Reynolds numbers (based on the hydraulic diameter) of 10,000, 20,000, and 40,000. In the heat transfer experiments, constant heat flux is supplied to the test section by each of the heaters. The maximum wall temperature is maintained approximately 38°C above the inlet coolant temperature to yield an inlet coolant-to-wall density ratio ($\Delta\rho/\rho$) of approximately 0.12 for all cases. The rotation speed remained constant at 550 rpm, resulting in a range of rotation number ($Ro$) from 0.038 to 0.150.

**Rib Configurations.** The six rib configurations investigated in this study are shown in Fig. 4. The geometry of the six rib configurations of the present study is similar. The ribs for each case are parallel, i.e., the ribs on the leading surface are aligned with the ribs on the trailing surface. In each case, the ribs are oriented at 45 deg to the mainstream flow. One-sixteenth inch square ribs are used in all cases with a pitch-to-rib height ($P/e$) of 10 and a rib height-to-hydraulic diameter ratio ($e/D_h$) of 0.078. The ribs are made of brass, and they are glued to the copper plates of the leading and trailing surfaces. The thickness of the glue is less than 0.01 cm and creates negligible thermal resistance between the ribs and the copper plates.

## Data Reduction

**Heat Transfer Enhancement.** This study investigates the regionally averaged heat transfer coefficient at various locations within the narrow rotating ducts with ribs. The heat transfer coefficient is determined by the net heat transferred from the heated plate, the surface area of the plate, the regionally averaged temperature of the plate, and the local bulk mean temperature in the channel. Therefore, the heat transfer coefficient is given as

$$h = (Q_{\text{net}}/A)/(T_w - T_{bx}) \tag{1}$$

The net heat transfer is calculated using the measured voltage and current supplied to each heater from the variac transformers multiplied by the area fraction of the heater exposed to the respective plate minus the external heat losses escaping from the test section. The heat losses are predetermined by performing a heat loss calibration for both the rotational and stationary experiments. The heat loss calibration is performed by inserting insulation into the channel to eliminate natural convection. During the calibration, the heat transfer (in the form of power from the variac transformers) and wall temperature of each plate is measured; therefore, from the conservation of energy principle it is possible to know how much heat is being lost to the environment. At a Reynolds number of 10,000, heat losses account for 17% of the heat put into the test section. However, at the highest Reynolds number of 40,000, just less than 8% of the heat input is lost by conduction through the test section.

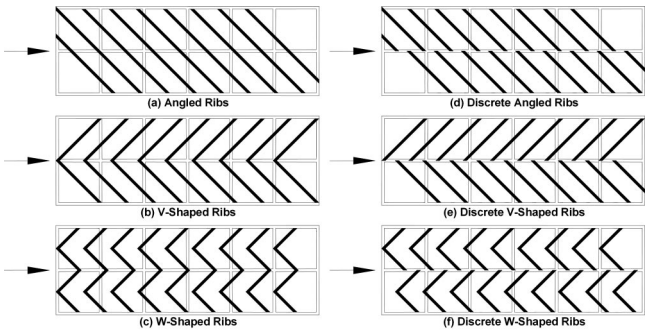


**Fig. 4 Top view of the six rib configurations**

**Table 1 Additional surface area created by the rib turbulators**

| Rib Configuration | Additional Area Increase due to Ribs |
|---|---|
| Angled | 24.4% |
| V-Shaped | 25.7% |
| W-Shaped | 25.7% |
| Discrete Angled | 24.0% |
| Discrete V-Shaped | 25.3% |
| Discrete W-Shaped | 25.7% |

The surface area used in this study is the projected surface area of the channel; in other words, the surface area of a smooth channel (the area increase due to the ribs is neglected). Table 1 shows the area increase for each configuration of ribs; the 1%–2% difference is the result of modifications to the ribs at the inlet and outlet of the heated test section. The regionally averaged wall temperature ($T_w$) is directly measured using the thermocouple installed in the blind hole on the backside of each copper plate. Because the plates are made of copper, which has a high thermal conductivity, the temperature of each plate is assumed uniform. One thermocouple at the inlet and two thermocouples at the outlet of the test section measure the inlet and outlet bulk temperatures, respectively. Therefore, the bulk temperature at any location in the test section can be calculated using linear interpolation. The results presented from this study are based on the linear interpolation method. However, the local bulk temperature can also be calculated using the conservation of energy principle. For the present study, both methods compare very well. The energy balance equation is

$$T_{bx} = T_{bi} + \sum_i (Q - Q_{\text{loss}})/mc_p \quad x = 1,2,\ldots,6 \tag{2}$$

The Dittus–Boelter/McAdams [32] correlation for heating ($T_w > T_{bx}$) is used in this study to provide a basis of comparison. The Dittus–Boelter/McAdams correlation is used to calculate the Nusselt number for fully developed turbulent flow through a smooth stationary circular tube. Therefore, the Nusselt number ratio is given as

$$\text{Nu}/\text{Nu}_0 = (hD_h/k)/(0.023\,\text{Re}^{0.8}\,\text{Pr}^{0.4}) \tag{3}$$

All air properties are taken based on the bulk air temperature with a Prandtl number (Pr) for air of 0.71.

The experimental uncertainty for the presented results was calculated using the method developed and published by Kline and McClintock [33]. The estimated uncertainty in the temperature measurements is 0.5°C for all cases. At the Reynolds number of 10,000, the overall uncertainty in the Nusselt number ratio is approximately 15% of the presented values. At this lowest Reynolds number, a greater percentage of the heat input is lost. Due to the estimation of these heat losses, the experimental uncertainty increases. However, at the higher Reynolds numbers, the percent uncertainty of the individual measurements decreases and the percentage of heat losses decreases. Therefore, the overall uncertainty in the Nusselt number ratio decreases to approximately 7% of the calculated value at the highest Reynolds number of 40,000.

**Frictional Losses.** The frictional losses in the cooling channel are determined by measuring the pressure drop from the inlet to the outlet of the heated test section. The friction factor is calculated using the measured inlet and outlet pressures as shown in Eq. (4)

$$f = (P_i - P_e)/(4(L/D_h)(1/2\rho V^2)). \tag{4}$$

The inlet pressure, $P_i$, is taken as the average of the two pressure measurements at the channel entrance, and the outlet pressure, $P_e$, is average of the two outlet pressure measurements.

The frictional losses can then be calculated by dividing the fiction factor by the turbulent friction factor in a smooth tube as given by the Blasius equation [34]. This ratio is shown in Eq. (5)

$$f/f_0 = f/(0.079\,\text{Re}^{-1/4}) \tag{5}$$

The experimental uncertainty for the frictional losses was also calculated using the method developed by Kline and McClintock [33]. At the Reynolds number of 10,000, where the most uncertainty exists in the measured quantities, the overall uncertainty in the friction factor ratio is approximately 16% of the presented values. However, at the higher Reynolds numbers, the percent uncertainty of the individual measurements decreases. Therefore, the overall uncertainty in the friction factor ratio decreases to approximately 6.5% of the calculated value at the highest Reynolds number of 40,000.

**Thermal Performance.** Based on the heat transfer enhancement ($\text{Nu}/\text{Nu}_0$) and the frictional loss penalty ($f/f_0$), the thermal performance, $\eta$, of each rib configuration can be calculated. Equation (6) shows the thermal performance based on the constant pumping power condition as used by Han, Pank, and Lei [35]

$$\eta = (\text{Nu}/\text{Nu}_0)/(f/f_0)^{1/3} \tag{6}$$

## Results and Discussion

The legend for the present channel is shown in Fig. 1. The inner surface is the surface located closest to the midchord of the blade, and the outer surface is the surface located closest to the trailing edge of the blade. The leading and trailing surfaces are each subdivided into two surfaces. The leading surface is divided into the leading-inner surface and the leading-outer surface, and the same is done for the trailing surface. With the narrow channels used in the trailing edge of the blade, the heat transfer from the inner and outer surfaces is much less than the contribution of the leading and trailing surfaces, so for the present study, the inner and outer surfaces were left unheated.

**Secondary Flow Behavior.** Figure 5 shows conceptual views of the rib induced secondary flow within the cooling channels with angled ribs [Fig. 5(a)], V-shaped ribs [Fig. 5(b)], and W-shaped ribs [Fig. 5(c)]. The secondary flow induced by angled ribs and V-shaped ribs has been verified by the numerical predictions of Al-Qahtani et al. [36] and Su et al. [37], respectively. As shown in Fig. 5(a), the secondary flow induced by the 45 deg angled ribs moves parallel to the ribs from the outer surface to the inner surface and returns back to the outer surface. Thus, the angled ribs create two counter rotating vortices rotating parallel to the angled ribs in the cross section of the channel. As the coolant travels along the rib, it gradually becomes warmer and the boundary layer continues to grow thicker. Therefore, the heat transfer enhancement for the leading and trailing-outer surfaces is expected to be greater than the leading and trailing-inner surfaces (enhancement is much greater on the upstream portion of the rib than the downstream portion).

As shown in Fig. 5(b), the secondary flow induced by the V-shaped ribs creates four vortices. Near the wall, the coolant splits into two streams, each stream following the V away from the center of the channel to the sidewalls. The coolant is forced to circulate to the center of the channel after impinging on the sidewalls. Therefore, two vortices are created on the leading surface, and two vortices are created on the trailing surface. Because the V-shaped ribs are symmetrical about the center of the channel, it is expected the leading-inner, leading-outer, trailing-inner, and trailing-outer surfaces will all experience the same level of heat transfer enhancement (unlike the cooling channel with angled ribs). The rib induced flow of the W-shaped ribs is shown in Fig. 5(c). Conceptually it is shown that eight vortices are created in the

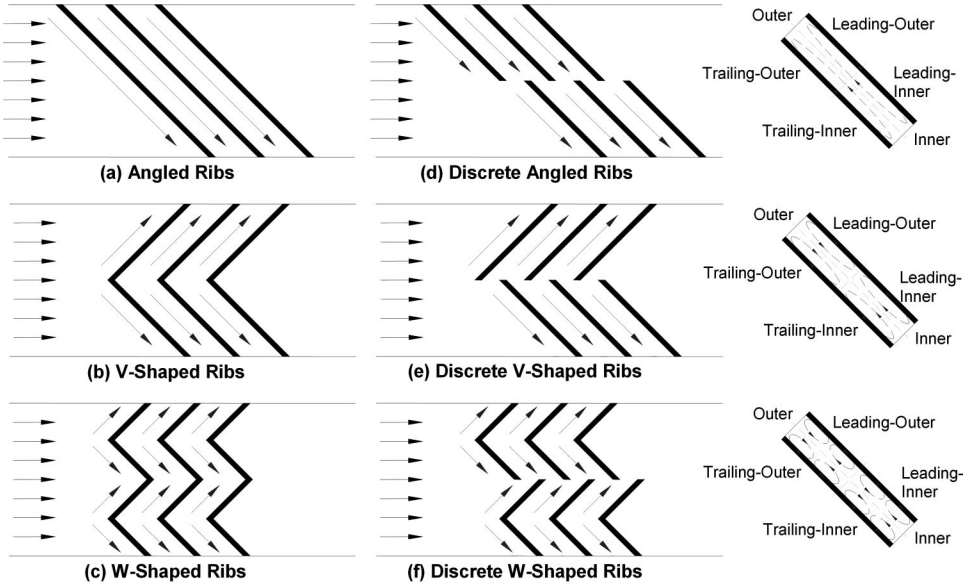


**Fig. 5 Rib induced secondary flow**

cooling channel. These W-shaped ribs are essentially two V-shaped ribs joined at the center of the channel. As with the V-shaped ribs, the W-shaped ribs are expected to produce uniform spanwise heat transfer.

The rib induced flow of the discrete rib configurations is expected to be similar to that induced by the complete rib configurations [Figs. 5(d), 5(e), and 5(f)]. The coolant near the wall will follow the rib resulting in the formation of counter rotating vortices as the coolant impinges on the sidewalls. The primary difference in the secondary flow behavior will occur near the centerline of the channel. As Ekkad and Han [9] showed with detailed liquid crystal measurements, the broken ribs create serpentine secondary flows. This flow behavior results in the highest heat transfer occurring immediately downstream of the rib.

In the discrete angled rib channel, the discrete ribs will result in the creation of a second set of vortices (on the leading and trailing inner surfaces). This will also result in the redevelopment of the boundary layer on the inner surfaces. This thin boundary layer will result in much higher heat transfer enhancement when compared to the complete angled ribs.

The Coriolis and buoyancy forces, induced by the rotation, affect the flow through a rotating channel. Two counter-rotating vortices are created in a rotating channel, as shown in Fig. 6. The vortices are created as a result of the coolant being forced from the leading-inner corner to the trailing-outer corner. The trailing surfaces experience enhanced heat transfer as the coolant is forced to the trailing side of the channel, and the trailing-outer surface typically experiences the greatest enhancement. However, due to the rectangular channel and orientation angle, the leading surface should also experience heat transfer enhancement.

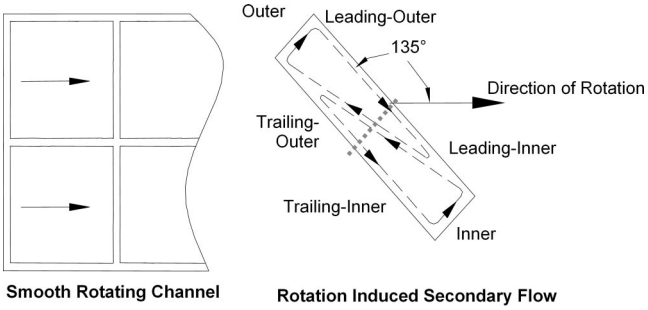


**Fig. 6 Rotation induced secondary flow**

**Regional Heat Transfer Enhancement.** Figures 7 and 8 contain a sample of the regionally averaged Nusselt number ratio results for the six rib configurations. Each figure contains results for the six rib configurations at Re=20,000. For the rotating cases, this Reynolds number corresponds to Ro=0.075.

Figure 7(a) shows the regionally averaged heat transfer distributions in the nonrotating channel with angled ribs. It can be seen that the heat transfer enhancement along the leading-outer and trailing-outer surfaces is significantly higher than the enhancement along the leading-inner and trailing-inner surfaces. The ribs are angled, so the coolant is forced from the outer surface to the inner surface [see Fig. 5(a)]. Therefore, the leading edge of the rib undergoes more enhancement, and as the coolant continues along the rib, the enhancement decreases as the boundary layer thickens. Moving in the streamwise direction, the Nusselt number ratio gradually increases as the rib induced vortices are gaining strength. As the Reynolds number increases, the difference between the enhancement on the inner (leading and trailing) and outer (leading and trailing) surfaces decreases.

The heat transfer enhancement in the cooling channel with V-shaped ribs is shown in Fig. 7(b). Unlike in the angled rib channel, all surfaces within the V-shaped rib channel undergo the same level of heat transfer enhancement. The strength of the vortices continues to grow as the coolant travels streamwise through the channel. Therefore, the Nusselt number ratio continues to increase until the flow becomes fully developed; at this point the Nusselt number ratio remains constant.

The Nusselt number ratios in the cooling channel with W-shaped ribs are shown in Fig. 7(c). Like the V-shaped rib channel, the symmetry of the rib configuration results in all surfaces undergoing the same level of enhancement. The magnitude of the Nusselt numbers for these W-shaped ribs is greater than the magnitude of that in the V-shaped channel. This configuration is essentially two V-shaped ribs which meet at the center of the channel. Therefore, two areas of high heat transfer are created at the tip of each V. In addition, because the ribs in this configuration are shorter than the ribs of V-shaped configuration, the boundary layer along these shorter ribs is thinner than the boundary layer along the V-shaped ribs [see Fig. 5(b)]. The result is more enhancement in the W-shaped rib channel than in the V-shaped rib channel.

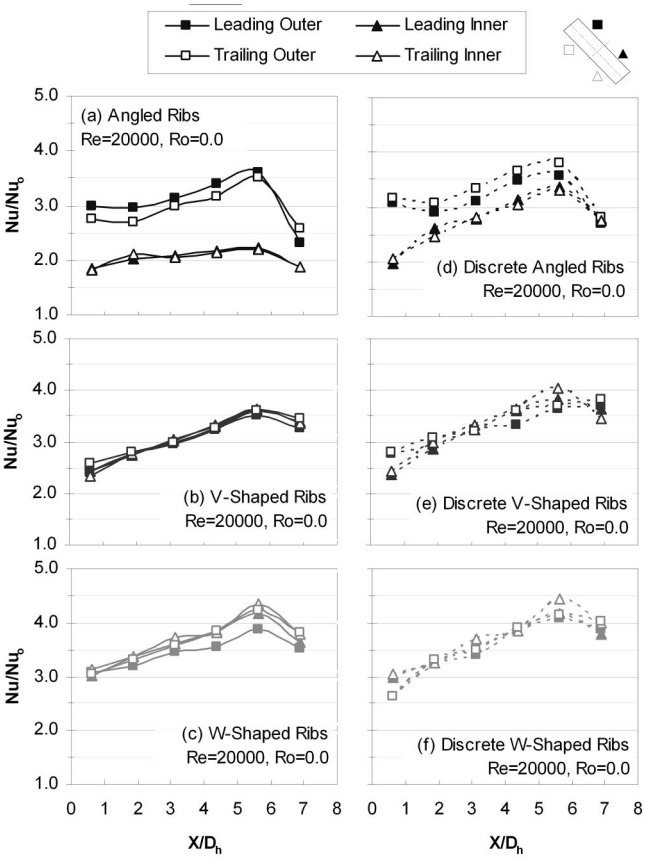


**Fig. 7 Nusselt number ratios in nonrotating channels**

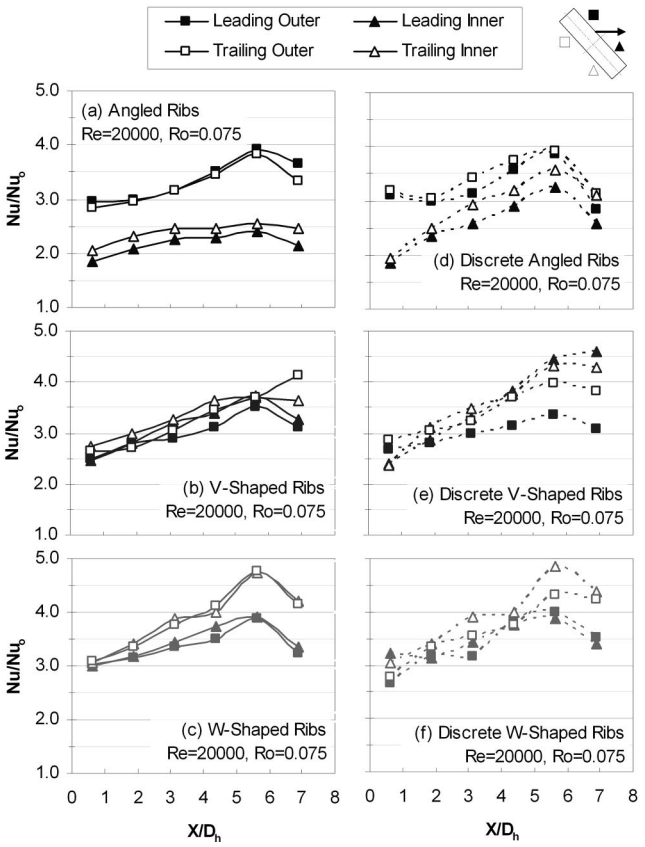


**Fig. 8 Nusselt number ratios in rotating channels**

The heat transfer distribution for the nonrotating channel with discrete angled ribs is shown in Fig. 7(d). Comparing the discrete angled ribs to the complete angled ribs [Fig. 7(a)], it is clearly seen the difference between the inner (leading and trailing) and outer (leading and trailing) surfaces decreases. The difference is the result of significant enhancement on the leading-inner and trailing-inner surfaces. As shown in Fig. 5, the long angled rib has been broken; therefore, the continuous growth of the boundary layer from the outer surface to the inner surface does not exist. Instead, the boundary layer forms at the leading edge of the rib near the outer surface and has only half the channel to grow (as opposed to the entire channel). Similarly, on the leading and trailing inner surfaces, the boundary layer forms at the center of the channel and grows as the coolant is forced to the inner wall. Therefore, the boundary layer on the leading and trailing inner surfaces is much thinner than in the angled rib channel, and the result is significantly more enhancement along these surfaces.

Figure 7(e) shows the regionally averaged heat transfer distributions in the channel with discrete V-shaped ribs. The trends within this channel are similar to those in the complete V-shaped rib channel [Fig. 7(b)]. The secondary flow induced by the ribs is not altered significantly when compared to the complete V-shaped ribs. The ribs create four rotating vortices; however, in this case, the vortices on the leading and trailing inner surfaces have been shifted downstream, as the V-shaped rib was broken. The advantage of this configuration over the complete V-shaped ribs is the enhancement that occurs just downstream of the V-shaped rib. As the coolant passes over the ribs, flow separation occurs, and immediately behind the ribs in the area of separation, there is relatively low heat transfer enhancement. When the V is broken, the area of low heat transfer immediately downstream of the point is reduced. Ekkad and Han [9] showed that the broken V-shaped ribs created a serpentine-like secondary flow in the center of the channel. This secondary flow behavior results in more enhancement than the complete V-shaped ribs.

The Nusselt number ratios in the cooling channel with discrete W-shaped ribs are shown in Fig. 7(f). As the V-shaped and discrete V-shaped ribs, the trends of the W-shaped and discrete W-shaped ribs are similar. However, only a negligible difference exists between Nusselt number ratios of the W-shaped and discrete W-shaped rib channels. This discrete W configuration does not help the areas of relatively low heat transfer. In other words, the discrete V-shaped ribs reduced the area of low heat transfer behind the point of the complete V. With the discrete W-shaped ribs, the point associated with the V's is still present, the difference occurs at the center of the channel where the legs of the V's meet. As the coolant travels along these legs of the V's to the center of the channel, the heat transfer is decreasing. By shifting the V's on the inner surfaces to create this discrete W-shaped configuration, the heat transfer near the center of the channel is not increased. The rib induced flow of the discrete W-shaped ribs is similar to that of the W-shaped ribs. Therefore, as the coolant travels along the ribs, the heat transfer enhancement decreases in both configurations. Breaking the ribs at the centerline does nothing to increase the heat transfer in this area of relatively low heat transfer enhancement. Therefore, the level of heat transfer enhancement in the discrete W-shaped rib is the same as that in the complete W-shaped rib channel.

The regional heat transfer for the rotating channels is shown in Fig. 8. For the given Reynolds number of 20,000, the corresponding rotation number is 0.075. Figure 8(a) shows the regionally averaged heat transfer distributions in the rotating channel with angled ribs. All surfaces in the angled rib channel experience heat transfer enhancement with rotation. Although it is not shown, as the rotation number increases (Reynolds number decreases), the variation between the leading-outer and trailing-outer surfaces in-

creases, and the same is true for the leading and trailing inner surfaces. Due to the nature of the rotation induced vortices, the trailing-outer surface undergoes greater heat transfer enhancement than the leading-outer surface because the rotation induced vortices are forcing the coolant from the leading-inner surface toward the trailing-outer surface (see Fig. 6). Likewise the trailing-inner surface experiences greater enhancement than the leading-inner surface.

The heat transfer enhancement in the rotating cooling channel with V-shaped ribs is shown in Fig. 8(b). It can be seen that the trailing-inner surface undergoes slightly higher heat transfer enhancement than the trailing-outer surface. This is due to the fact that the rib and rotation induced secondary flows move in opposite directions, and the combined effect of these secondary flows is weakened [see Figs. 5(b) and 6]. However, along the leading and trailing-inner surfaces, both the rib and rotation induced secondary flows move into the same direction, and the combined effect of these secondary flows is strengthened [see Figs. 5(b) and 6]. As the rotation number decreases, the spanwise variation of the surfaces diminishes.

The Nusselt number ratios in the rotating cooling channel with W-shaped ribs are shown in Fig. 8(c). The effect of rotation is obviously seen at this intermediate rotation number of 0.075 (Re $=$20,000). The trailing surfaces undergo significantly more enhancement than the leading surfaces, due to the rotation induced secondary flow. As the coolant travels through the channel, the difference between the enhancement of the trailing and leading surfaces increases, as the vortices induced by rotation gain strength. The variation in this channel is much greater than was seen in the V-shaped rib channel. This is a result of the interaction of the vortices induced by the ribs and the vortices induced by rotation. Rhee et al. [12] showed the vortices induced by their discrete V-shaped ribs (similar to the W-shaped ribs of the present study) were much weaker than the vortices induced by the complete V-shaped ribs. Therefore, in the present study, rotation has a more dominant effect in the W-shaped rib channel than the V-shaped rib channel. As one would anticipate, as the Reynolds number increases (rotation number decreases), the variation between the trailing and leading surfaces decreases.

The heat transfer distribution for the rotating channel with discrete angled ribs is shown in Fig. 8(d). The difference between the rotating complete angled ribs [Fig. 8(a)] and these discrete angled ribs is similar to the differences of the nonrotating configurations [Figs. 7(a) and 7(d), respectively]; the spanwise variation between the leading and trailing outer surfaces and the leading and trailing inner surfaces is dramatically reduced. The effect of rotation is also seen as the heat transfer on trailing-outer surface is enhanced more than the heat transfer on the leading-outer surface. The trailing-inner surface also undergoes more enhancement than the leading-inner surface. As the Reynolds number increases (rotation number decreases), the spanwise variation created by the ribs decreases, as well as the variation due to rotation.

The heat transfer trends of the rotating channel with discrete V-shaped ribs are shown in Fig. 8(e). The general trend is similar to the rotating channel with V-shaped ribs [Fig. 8(b)]; the additional enhancement of the trailing surfaces due to rotation can be seen. The Nusselt number ratios in the rotating cooling channel with discrete W-shaped ribs is shown in Fig. 8(f). The regional heat transfer trends of this configuration are similar to the complete W-shaped ribs [Fig. 8(c)].

**Channel Averaged Heat Transfer Enhancement.** The channel averaged heat transfer for the nonrotating and rotating channels is shown in Figs. 9 and 10, respectively. A comparison of the channel averaged values shown in Fig. 9 for the stationary channels indicates the W-shaped and discrete W-shaped ribs have the best heat transfer performance. These are followed by the discrete V-shaped ribs, the V-shaped and discrete angled offering approximately the same level of enhancement, and the least enhancement is present in the nonrotating channel with angled ribs. For all

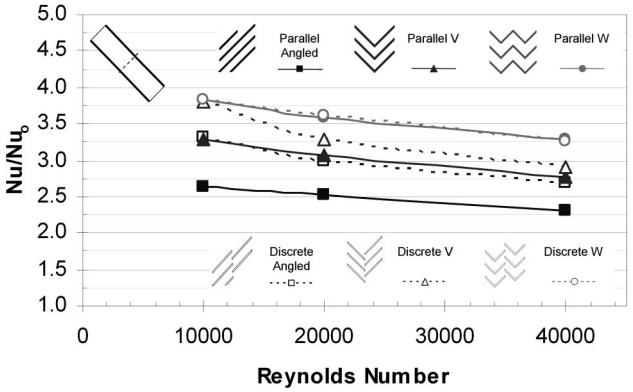


**Fig. 9 Channel averaged Nusselt number ratio in nonrotating channels**

cases, as the Reynolds number increases, the Nusselt number ratio decreases, and this should be anticipated as the Nusselt number for the smooth tube is increasing with Reynolds number. Figure 10 shows similar results for the rotating channel: the W shaped and discrete W shaped offer the greatest heat transfer enhancement.

**Channel Frictional Losses.** In an effort to determine which rib configuration has the best thermal performance, it is critical to investigate the pressure drop penalty, as well as the heat transfer enhancement. The measured pressure drop is presented in the form of the friction factor ratio in Figs. 11 and 12 for the nonrotating and rotating channels, respectively. As shown in Fig. 11, the greatest frictional losses are incurred in the channel with the W-shaped ribs. The discrete W-shaped ribs and the V-shaped ribs follow this channel. The lowest frictional losses are in the channels with the angled ribs, discrete V-shaped ribs, and the discrete angled ribs. Similar results are shown in Fig. 12, for the rotating channels. The W-shaped ribs and the discrete W-shaped ribs have the greatest pressure drop penalty.

It is important to address the accuracy of both the heat transfer enhancement measurements and the frictional loss measurements before continuing. The Nusselt number ratios and friction factor ratios of the stationary angled, discrete angled, V-shaped, and discrete V-shaped ribbed channels are compared to previous studies. Due to the infinite combinations of channel geometry and rib configurations, comparisons of the nature are generally difficult. However, previous studies involving rectangular channels with angled ribs [4,10], discrete angled ribs [10], V-shaped ribs [12], and discrete V-shaped ribs [12] are considered in Figs. 13 and 14. The channel dimensions and rib parameters for each study are

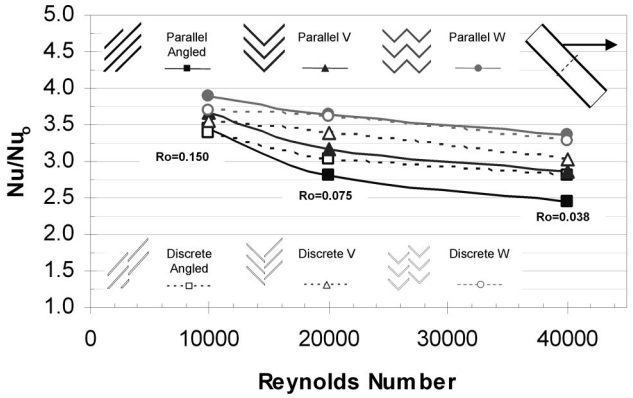


**Fig. 10 Channel averaged Nusselt number ratio in rotating channels**

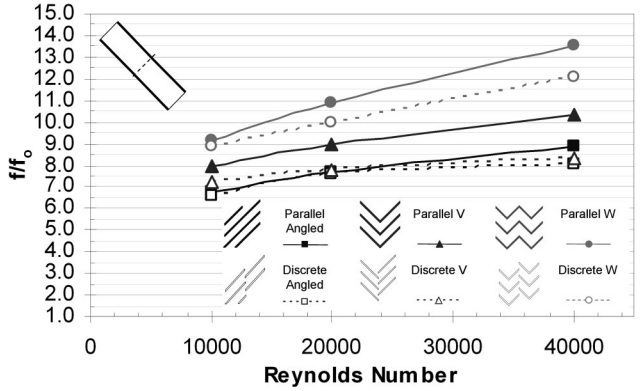


**Fig. 11 Friction factor ratio in nonrotating channels**

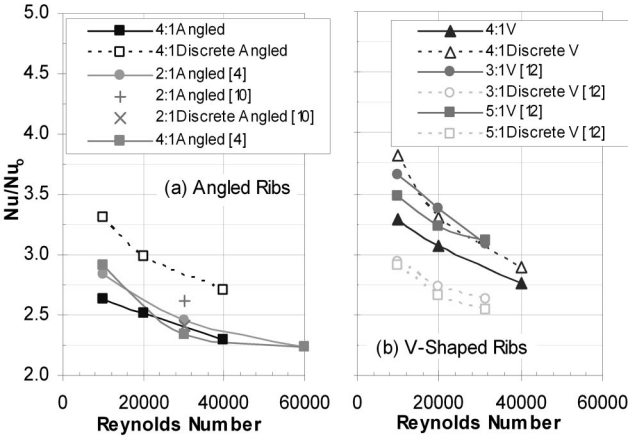


**Fig. 13 Nusselt number ratio comparison with previous studies**

shown in Table 2. As shown in Fig. 13, the Nusselt number ratios in the 4:1 channel with angled ribs are comparable to previous studies. Decreasing the aspect ratio to 2:1 increases the enhancement. The heat transfer enhancement of the 4:1 channel with V-shaped ribs is slightly lower than the enhancement in both the 3:1 and 5:1 channel of Rhee et al. [12]. With this comparison, not only is the aspect ratio changing, the rib height-to-channel height ratio is changing. The discrete V-shaped rib results of Rhee et al. [12] are significantly lower than the present study due to very different rib configurations.

Figure 14 compares the friction factor ratio of the current studies to the previous studies. As shown in Fig. 14(a), the friction factor ratios of the current 4:1 angle ribbed channels are less than those of the previous 4:1 study [4]. There is also significant difference between the previous 2:1 studies of Cho, Wu, and Kwon [10] and the previous 2:1 study of Park et al. [4]. However, because the nondimensional rib and channel parameters are identical for the 4:1 channels, closer agreement between the two investigations is expected. When the actual dimensions of the channels are compared, one can see the 4:1 channel of Park et al. [4] is twice as large as the one of the current study. Also, the ribs of the previous study are twice as large as the ribs of the current study. Although the nondimensional parameters are identical, the channels are actually very different. The situation is similar when comparing the V-shaped ribs of the present study with those of Rhee et al. [12]. With the large channel and ribs of the previous study, form drag becomes an issue. Form drag is primarily a function of the size and shape of an object. A large object creates an area of very low pressure immediately behind the object. Therefore, the smaller ribs of the present study create less pressure drop than the much larger ribs of the previous studies ([4] and [12]), resulting in a lower friction factor ratio.

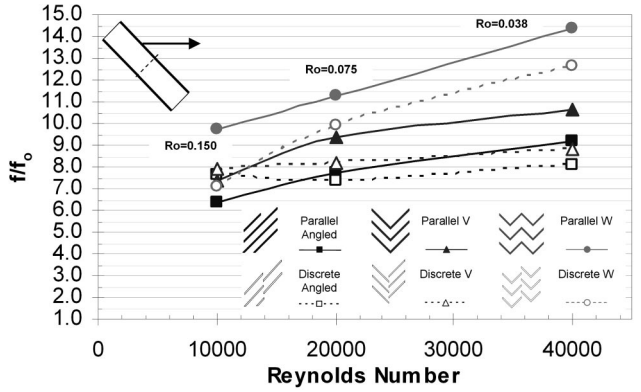


**Fig. 12 Friction factor ratio in rotating channels**

**Thermal Performance.** When the frictional losses are coupled with the heat transfer enhancement, the thermal performance of each rib configuration can be evaluated. Figure 15 shows the thermal performance of the rib configurations in the nonrotating channels. As shown previously, the W-shaped and discrete W-shaped ribs offered the greatest heat transfer enhancement; however, they also incurred the greatest frictional losses. From the overall performance point of view, the discrete V-shaped and discrete W-shaped ribs yield the greatest thermal performance. The discrete V-shaped ribs showed increased heat transfer enhancement and decreased frictional losses over the complete V-shaped ribs. Although the heat transfer enhancement for this configuration is lower than the W-shaped ribs, the frictional losses are significantly lower. The discrete V-shaped and discrete

**Table 2 Cooling channel and rib parameter comparison (units:cm)**

| | Configuration | AR | *e/H* | *P/e* | $\alpha$ |
|---|---|---|---|---|---|
| Present Study | Angled<br>Discrete Angled<br>V-Shaped<br>Discrete V-Shaped | 5.08 x 1.27 = 4:1 | 0.16 / 1.27 = 0.125 | 1.60 / 0.16 = 10 | 45° |
| Park et al. [4] | Angled | 10.16 x 5.08 = 2:1 | 0.32 / 5.08 = 0.063 | 3.2 / 0.32 = 10 | 45° |
| | | 10.16 x 2.54 = 4:1 | 0.32 / 2.54 = 0.125 | 3.2 / 0.32 = 10 | 45° |
| Cho et al. [10] | Angled<br>Discrete Angled | 10.16 x 5.08 = 2:1 | 0.50 / 5.08 = 0.098 | 5 / 0.5 = 10 | 45° |
| Rhee et al. [12] | V-Shaped | 15 x 5 = 3:1 | 0.30 / 5 = 0.06 | 3 / 0.3 = 10 | 60° |
| | | 15 x 3 = 5:1 | 0.30 / 3 = 0.10 | 3 / 0.3 = 10 | 60° |
| | Discrete V-Shaped | 15 x 5 = 3:1 | 0.30 / 5 = 0.06 | 3 / 0.3 = 10 | 45° |
| | | 15 x 3 = 5:1 | 0.30 / 3 = 0.10 | 3 / 0.3 = 10 | 45° |

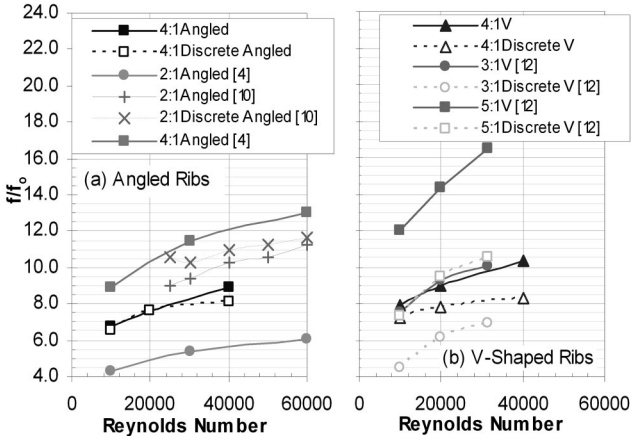


**Fig. 14 Friction factor ratio comparison with previous studies**

W-shaped configurations are followed closely by the complete W-shaped ribs. It is interesting to note the comparison between the angled and V-shaped ribs which are more commonly used in modern engines. The performance of the discrete angled rib is comparable to the performance of the complete V-shaped rib; a slight modification to the traditional angled rib design results in a significant increase in the overall thermal performance.

Figure 16 shows the thermal performance of the six rib configurations in the rotating channels. For the rotating channels, the discrete V-shaped ribs, the W-shaped ribs, and the discrete W-shaped ribs perform equally. The difference in the performance

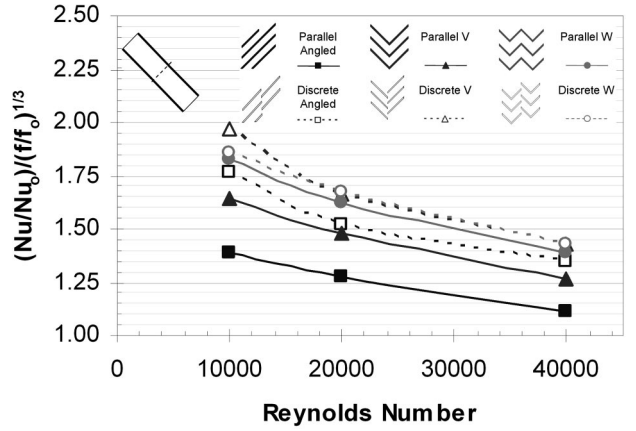


**Fig. 15 Thermal performance in nonrotating channels**

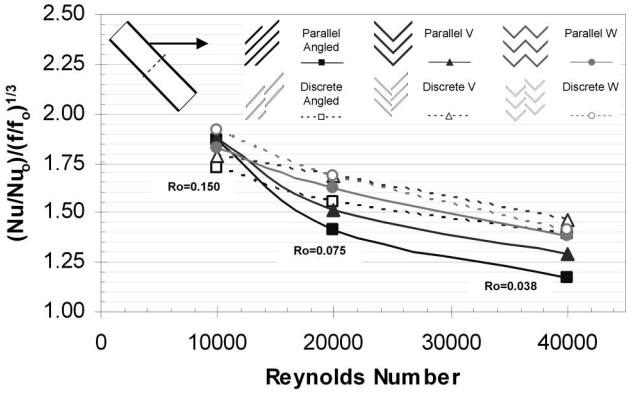


**Fig. 16 Thermal performance in rotating channels**

of each configuration is much less than was shown for the nonrotating channels. Again the performance of the discrete angled ribs is comparable to the V-shaped ribs, and the traditional angled ribs have the poorest performance of the six configurations under investigation.

## Conclusions

1. The discrete V-shaped and discrete W-shaped ribs have the best thermal performance in both rotating and nonrotating channels. These configurations are followed closely by the W-shaped configuration.
2. For the nonrotating and rotating rectangular channels, the W-shaped and discrete W-shaped ribs yield the best heat transfer enhancement. This comes at the cost of the greatest pressure drop.
3. The performance of the V-shaped ribs is better than the performance of the angled ribs. Furthermore, the performance of the discrete angled ribs is comparable to that of the V-shaped ribs in both nonrotating and rotating channels.
4. For narrow, rotating, rectangular channels (AR=4:1) with various rib configurations, the heat transfer enhancement on both the leading and trailing surfaces increases with rotation. This provides positive information for the cooling designers.
5. Significant span-wise variation of heat transfer enhancement exists on both the leading and trailing surfaces in narrow rectangular channels (AR=4:1) with angled ribs. However, the span-wise heat transfer in the channels with V-shaped and W-shaped ribs is significantly reduced.

## Acknowledgments

This publication was prepared with the support of the U.S. Department of Energy, Office of Fossil Energy, National Energy Technology Laboratory. However, any opinions, findings, conclusions, or recommendations expressed herein are those of the authors and do not necessarily reflect the views of the DOE.

## Nomenclature

$A$ = surface area of copper plate (m$^2$)
AR = channel aspect ratio, $W/H$
$c_p$ = specific heat of coolant [kJ/(kgK)]
$D_h$ = hydraulic diameter (m)
$e$ = rib height (m)
$f$ = friction factor
$f_0$ = Blasius fully developed friction factor in nonrotating smooth tube
$H$ = channel height (0.5 in., 1.27 cm)
$h$ = heat transfer coefficient (W/m$^2$ K)
$k$ = thermal conductivity of coolant (W/mK)
$L$ = heated length of duct (6 in., 15.24 cm)
$\dot{m}$ = mass flow rate of coolant (kg/s)
Nu = regionally averaged Nusselt number, $hD_h/k$
Nu$_0$ = Nusselt number for flow in fully developed turbulent nonrotating smooth tube
$P$ = rib pitch (m)
$P_i$ = pressure at the inlet of the heated test section (Pa)
$P_e$ = pressure at the outlet of the heated test section (Pa)
Pr = Prandtl number
$Q$ = rate of heat transfer (W)
$Q_{\text{net}}$ = net rate of heat transfer (W)
$q''_{\text{net}}$ = net heat flux at wall (W/m$^2$)
$R$ = mean rotating arm radius (m)
Re = Reynolds number based on hydraulic diameter, $\rho VD_h/\mu$
$Ro$ = Rotation number, $\Omega D_h/V$
$T_{bx}$ = local coolant bulk temperature (K)
$T_{bi}$ = inlet coolant bulk temperature (K)
$T_w$ = wall temperature (K)
$V$ = bulk velocity in streamwise direction (m/s)
$W$ = channel width (2 in., 5.08 cm)

$x$ = streamwise location (m)
$\alpha$ = rib angle
$\beta$ = angle of channel orientation
$\eta$ = thermal performance, $(\mathrm{Nu}/\mathrm{Nu}_0)/(f/f_0)^{(1/3)}$
$\rho$ = density of coolant (kg/m$^3$)
$\rho_{bi}$ = density of inlet coolant (kg/m$^3$)
$\rho_w$ = density of coolant near the wall (kg/m$^3$)
$\Delta\rho/\rho$ = inlet coolant-to-wall density ratio, $(\rho_{bi}-\rho_w)/\rho_{bi}$ $=(T_w-T_{bi})/T_w$
$\Omega$ = rotational speed (rad/s)

## References


[1] Han, J. C., Dutta, S., and Ekkad, S. V., 2000, *Gas Turbine Heat Transfer and Cooling Technology*, Taylor and Francis, New York.
[2] Han, J. C., 1988, ''Heat Transfer and Friction Characteristics in Rectangular Channels With Rib Turbulators,'' ASME J. Heat Transfer, , **110**, pp. 321–328.
[3] Han, J. C., and Park, J. S., 1988, ''Developing Heat Transfer in Rectangular Channels With Rib Turbulators,'' Int. J. Heat Mass Transfer, **31**, No. 1, pp. 183–195.
[4] Park, J. S., Han, J. C., Huang, Y., Ou, S., and Boyle, R. J., 1992, ''Heat Transfer Performance Comparisons of Five Different Rectangular Channels With Parallel Angled Ribs,'' Int. J. Heat Mass Transfer, **35**, No. 11, pp. 2891–2903.
[5] Han, J. C., Zhang, Y. M., and Lee, C. P., 1991, ''Augmented Heat Transfer in Square Channels With Parallel, Crossed, and V-Shaped Angled Ribs,'' ASME J. Heat Transfer, **113**, pp. 590–596.
[6] Lau, S. C., Kukreja, R. T., and McMillin, R. D., 1991, ''Effects of V-Shaped Rib Arrays on Turbulent Heat Transfer and Friction of Fully Developed Flow in a Square Channel,'' Int. J. Heat Mass Transfer, **34**, No. 7, pp. 1605–1616.
[7] Han, J. C., and Zhang, Y. M., 1992, ''High Performance Heat Transfer Ducts With Parallel Broken and V-Shaped Broken Ribs,'' Int. J. Heat Mass Transfer, **35**, No. 2, pp. 513–523.
[8] Taslim, M. E., Li, T., and Kercher, D. M., 1996, ''Experimental Heat Transfer and Friction in Channels Roughened With Angled, V-Shaped, and Discrete Ribs on Two Opposite Walls,'' ASME J. Turbomach., **118**, pp. 20–28.
[9] Ekkad, S. V., and Han, J. C., 1997, ''Detailed Heat Transfer Distribution in Two-Pass Square Channels With Rib Turbulators,'' Int. J. Heat Mass Transfer, **40**, No. 11, pp. 2525–2537.
[10] Cho, H. H., Wu, S. J., and Kwon, H. J., 2000, ''Local Heat/Mass Transfer Measurements in a Rectangular Duct With Discrete Ribs,'' ASME J. Turbomach., **122**, pp. 579–586.
[11] Gao, X., and Suden, B., 2001, ''Heat Transfer and Pressure Drop Measurements in Rib-Roughened Rectangular Ducts,'' Exp. Therm. Fluid Sci., **24**, pp. 25–34.
[12] Rhee, D. H., Lee, D. H., Cho, H. H., and Moon, H. K., 2003, ''Effects of Duct Aspect Ratios on Heat/Mass Transfer With Discrete V-Shaped Ribs,'' ASME Paper no. GT2003-38622.
[13] Johnson, B. V., Wagner, J. H., Steuber, G. D., and Yeh, F. C., 1994, ''Heat Transfer in Rotating Serpentine Passages With Trips Skewed to the Flow,'' ASME J. Turbomach., **116**, pp. 113–123.
[14] Johnson, B. V., Wagner, J. H., Steuber, G. D., and Yeh, F. C., 1994, ''Heat Transfer in Rotating Serpentine Passages With Selected Model Orientations for Smooth or Skewed Trip Walls,'' ASME J. Turbomach., **116**, pp. 738–744.
[15] Parsons, J. A., Han, J. C., and Zhang, Y. M., 1994, ''Wall Heating Effect on Local Heat Transfer in a Rotating Two-Pass Square Channel With 90° Rib Turbulators,'' Int. J. Heat Mass Transfer, **37**, No. 9, pp. 1141–1420.
[16] Parsons, J. A., Han, J. C., and Zhang, Y. M., 1995, ''Effects of Model Orientation and Wall Heating Condition on Local Heat Transfer in a Rotating Two-Pass Square Channel With Rib Turbulators,'' Int. J. Heat Mass Transfer, **38**, No. 7, pp. 1151–1159.
[17] Dutta, S., and Han, J. C., 1996, ''Local Heat Transfer in Rotating Smooth and Ribbed Two-Pass Square Channels With Three Channel Orientations,'' ASME J. Heat Transfer, **118**, pp. 578–584.
[18] Park, C. W., Lau, S. C., and Kukreja, R. T., 1998, ''Heat/Mass Transfer in a Rotating Two-Pass Square Channel With Transverse Ribs,'' AIAA J. Thermophys. Heat Transfer, **12**, No. 1. pp. 80–86.
[19] Park, C. W., Yoon, C., and Lau, S. C., 2000, ''Heat (Mass) Transfer in a Diagonally Oriented Rotating Two-Pass Channels With Rib-Roughened Walls,'' ASME J. Heat Transfer, **122**, pp. 208–211.
[20] Taslim, M. E., Rahman, A., and Spring, S. D., 1991a, ''An Experimental Investigation of Heat Transfer Coefficients in a Span-Wise Rotating Channel With Two Opposite Rib-Roughened Walls,'' ASME J. Turbomach., **113**, pp. 75–82.
[21] Taslim, M. E., Bondi, L. A., and Kercher, D. M., 1991b, ''An Experimental Investigation of Heat Transfer in an Orthogonally Rotating Channel Roughened With 45° Criss-Cross Ribs on Two Opposite Walls,'' ASME J. Turbomach., **113**, pp. 346–353.
[22] Kiml, R., Mochizuki, S., and Murata, A., 2001, ''Effects of Rib Arrangements on Heat Transfer and Flow Behavior in a Rectangular Rib-Roughened Passage: Application to Cooling of Gas Turbine Blade Trailing Edge,'' ASME J. Heat Transfer, **123**, pp. 675–681.
[23] Kiml, R., Mochizuki, S., and Murata, A., 2001, ''Heat Transfer Enhancement Mechanism in a Rectangular Passage With $\tilde{\mathrm{V}}$ and $\tilde{\Lambda}$ Shaped Ribs,'' J. Flow Visualization Image Process., **8**, pp. 51–68.
[24] Azad, G. S., Uddin, M. J., Han, J. C., Moon, H. K., and Glezer, B., 2002, ''Heat Transfer in a Two-Pass Rectangular Rotating Channel With 45-deg Angled Rib Turbulators,'' ASME J. Turbomach., **124**, pp. 251–259.
[25] Al-Hadhrami, L., and Han, J. C., 2003, ''Effect of Rotation in Two-Pass Square Channels With Five Different Orientations of 45° Angled Rib Turbulator,'' Int. J. Heat Mass Transfer, **46**, pp. 653–669.
[26] Al-Hadhrami, L., Griffith, T. S., and Han, J. C., 2003, ''Heat Transfer in Two-Pass Rotating Rectangular Channels (AR=2) With Five Different Orientations of 45° V-Shaped Rib Turbulators,'' ASME J. Heat Transfer, **125**, pp. 232–242.
[27] Griffith, T. S., Al-Hadhrami, L., and Han, J. C., 2002, ''Heat Transfer in Rotating Rectangular Channels (AR=4) With Angled Ribs,'' ASME J. Heat Transfer, **124**, pp. 617–625.
[28] Lee, E., Wright, L. M., and Han, J. C., 2003, ''Heat Transfer in Rotating Rectangular Channels (AR=4:1) With V-Shaped and Angled Rib Turbulators With and Without Gaps,'' ASME Paper no. GT2003-38900.
[29] Cho, H. H., Kim, Y. Y., Kim, K. M., and Rhee, D. H., 2003, ''Effects of Rib Arrangements and Rotation Speed on Heat Transfer in a Two-Pass Duct,'' ASME Paper no. GT2003-38609.
[30] Agarwal, P., Acharya, S., and Nikitopoulos, D. E., 2003, ''Heat/Mass Transfer in 1:4 Rectangular Passages With Rotation,'' ASME Paper no. GT2003-38615.
[31] Wright, L. M., Lee, E., and Han, J. C., 2003, ''Influence of Entrance Geometry on Heat Transfer in Rotating Rectangular Cooling Channels (AR=4:1) With Angled Ribs,'' ASME Paper no. IMECE2003-42572.
[32] Rohsenow, W. M., and Choi, H., 1961, *Heat, Mass, and Momentum Transfer*, Prentice–Hall, Englewood Cliffs, NJ, pp. 192–193.
[33] Kline, S. J., and McClintock, F. A., 1953, ''Describing Uncertainties in Single-Sample Experiments,'' Mech. Eng. (Am. Soc. Mech. Eng.), **75**, pp. 3–8.
[34] Kays, W. M., and Crawford, M. E., 1993, *Convective Heat and Mass Transfer*, 3rd ed., McGraw–Hill, New York, pp. 249.
[35] Han, J. C., Park, J. S., and Lei, C. K., 1985, ''Heat Transfer Enhancement in Channels With Turbulence Promoters,'' ASME J. Eng. Gas Turbines Power, **107**, pp. 628–635.
[36] Al-Qahtani, M., Jang, Y. J., Chen, H. C., and Han, J. C., 2002, ''Prediction of Flow and Heat Transfer in Rotating Two-Pass Rectangular Channels With 45-deg Rib Turbulators,'' ASME J. Turbomach., **124**, pp. 242–250.
[37] Su, G., Teng, S., Chen, H. C., and Han, J. C., 2003, ''Computation of Flow and Heat Transfer in Rotating Rectangular Channels (AR=4) With V-Shaped Ribs by a Reynolds Stress Turbulence Model,'' ASME Paper no. GT2003-38348.

# Local Heat/Mass Transfer With Various Rib Arrangements in Impingement/Effusion Cooling System With Crossflow

**Dong Ho Rhee**

**Yong Woo Nam**

**Hyung Hee Cho**
e-mail: hhcho@yonsei.ac.kr

Department of Mechanical Engineering,
Yonsei University,
Seoul 120-749, Korea

*The present study has been conducted to investigate the effect of rib arrangements on flow and heat/mass transfer characteristics for an impingement/effusion cooling system with initial crossflow. Two perforated plates of square hole array are placed in parallel and staggered arrangements with a gap distance of 2d and the crossflow passes between the injection and effusion plates. Both the injection and effusion hole diameters (d) are 10 mm and Reynolds number based on the hole diameter and hole-to-hole pitch are fixed at 10,000 and 6d, respectively. Square ribs of various rib arrangements and attack angles are installed on the effusion plate. With the initial crossflow, locally low transfer regions are formed and the level of heat transfer rate become lower as flow rate of the crossflow increases because wall jets are swept and the stagnation regions are affected by crossflow. With rib turbulators, the flow and heat transfer patterns are changed because the ribs protect near-wall flows including wall jets and generate secondary flow in a duct. For $M \geqslant 1.0$, the overall heat transfer is promoted when ribs are installed on the effusion surface, and higher values are obtained with smaller pitch of ribs. But, the attack angle of the rib has little influence on the average heat/mass transfer. For low blowing ratio of $M = 0.5$, the ribs have adverse effects on heat/mass transfer. Pressure drop between the inlet and exit of the channel increases up to 20% of total loss when ribs are installed while it is only 5% of total pressure loss across the perforated plates without ribs.*
[DOI: 10.1115/1.1791287]

## Introduction

Impingement/effusion cooling method is one of the advanced cooling techniques for combustor liner or turbine parts cooling in gas turbine engine. This technique combines two cooling schemes, array jet impingement and film cooling; hence the inner surfaces of hot components, such as combustor wall or blade surface, are cooled by the impingement of cooling air and outer surfaces which contact with hot gases are protected by effusion film cooling. The impingement/effusion cooling technique has been investigated and developed by some researchers since 1980's.

Hollwarth and Dagan [1] and Hollwarth et al. [2] measured average and local heat transfer coefficients on the effusion surface, and reported that arrays with staggered vents consistently yield higher heat transfer rates than do the impinging jets on the solid plates. Nazari and Andrews [3] studied film cooling performance with the effects of number of holes for impingement/effusion cooling. Cho and Goldstein [4] investigated the effect of hole arrangements on local heat/mass transfer characteristics inside the effusion plate. They found that the high transfer rate is induced by strong secondary vortices and flow acceleration, and the overall transfer rate is approximately 45%–55% higher than that for the impingement cooling alone. Cho and Rhee [5] and Rhee et al. [6] also investigated heat/mass transfer and flow characteristics of an impingement/effusion cooling system with various experimental conditions, such as gap distance, Reynolds number, hole arrangement and size.

In actual situations, a crossflow is formed in the internal passages, and this crossflow has significant effects on heat transfer in the passages. Therefore, the investigation of effects of crossflow is essential for estimate of cooling performance. However, most of the studies of crossflow effects have been concerned with array jet impingement cooling. Metzger and Korstad [7], Behbahani and Goldstein [8], Florschuetz et al. [9], Haiping et al. [10] and Rhee et al. [11] made examinations of the effects of crossflow on array jet impingements with various conditions, and reported that the crossflow has an adverse effects on jet impingement cooling. Recently, Bailey and Bunker [12] and Gao et al. [13] investigated heat transfer characteristics for array impinging jets with crossflow.

For the impingement/effusion cooling system, the effects of the crossflow on heat transfer were examined by Rhee et al. [14]. They reported that the overall heat/mass transfer rates on the effusion (target) plate decrease as the velocity of crossflow increases, which is a similar trend to array jet impingement. Also, they found that locally low transfer regions are formed between the adjacent effusion holes. These low heat/mass transfer regions can be considered potential hot spots and the nonuniform heat transfer causes thermal stresses.

In general, since it is not easy to control the amount of crossflow in the cooling system, how much one can reduce low heat transfer regions is a main key to enhance the cooling performance in the cooling system with crossflow at fixed operating condition. Installing the rib turbulators on the target or effusion surface is a possible method of increasing the performance with small change of geometry.

Researches on applying rib turbulators to cooling system except internal passage cooling have been confined to the jet impingement cooling. Haiping et al. [15,16] performed the experiments with various test conditions for jet impingement cooling on rib-roughened surface. Recently, Andrews et al. [17] investigated the effects of the direction of transverse rib with respect to the cross-

Contributed by the International Gas Turbine Institute (IGTI) of THE AMERICAN SOCIETY OF MECHANICAL ENGINEERS for publication in the ASME JOURNAL OF TURBOMACHINERY. Paper presented at the International Gas Turbine and Aeroengine Congress and Exhibition, Vienna, Austria, June 13–17, 2004. Paper No. 2004-GT-53686. Manuscript received by IGTI, October 1, 2003; final revision, March 1, 2004. IGTI Review Chair: A. J. Strazisar.

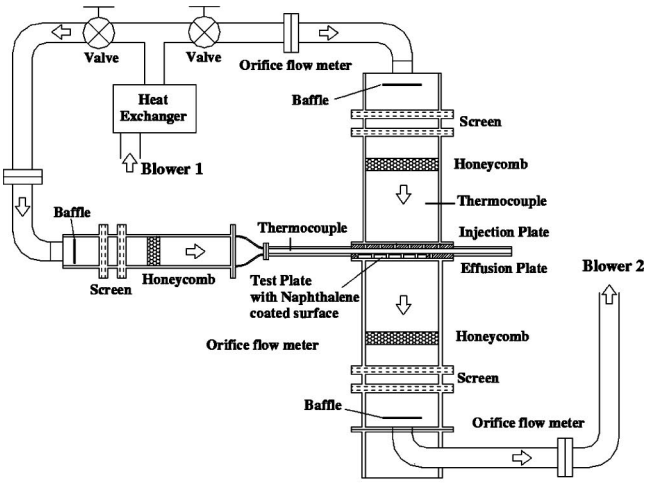


(a) experimental apparatus

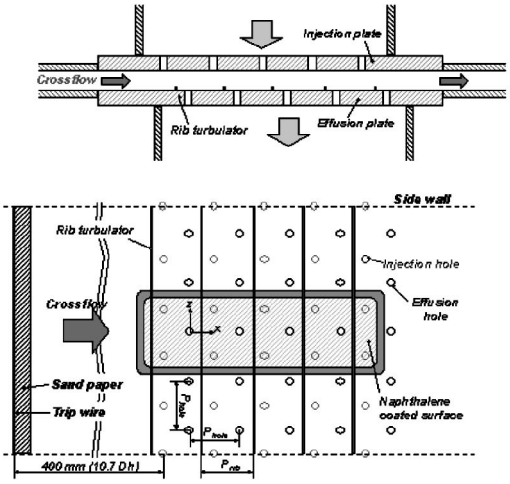


(b) test section

**Fig. 1 Schematic view of experimental facility: (*a*) experimental apparatus, (*b*) test section**

flow for impingement cooling, and reported that the rib turbulator changes the effects of crossflow and the enhancement of heat transfer is achieved with ribs, especially with ribs normal to the crossflow.

In the present study, flow patterns and local heat/mass transfer characteristics have been investigated for the impingement/effusion cooling with various rib arrangements and two different attack angles when initial crossflow is applied and the results are compared with the cases without rib turbulators and array jet impingement cooling with rib turbulator. Also, the effects of blowing ratio have been examined.

## Experimental Apparatus and Conditions

**1 Experimental Apparatus.** The experiments are conducted in the apparatus shown in Fig. 1($a$). The experimental apparatus is composed of three parts; impinging jet, flow effusion and crossflow supply parts. One blower (Blower 1) supplies the crossflow and impinging jet flow and the other blower (Blower 2) makes effusion flow through the effusion plate. The flow rates of the air supplied to each part are measured by orifice flow meters and controlled. The details are described in Ref. [14].

The schematics of test section and effusion plate are presented in Fig. 1($b$). The crossflow channel is located between the injection and the effusion plenum chambers and jets from injection holes impinge on the effusion plate and then are discharged through the effusion holes to simulate the impingement/effusion cooling. Cho and Goldstein [18] reported that heat/mass transfer coefficients on the inside surface of the effusion plate are the same with and without mainstream in film cooling. Therefore, in the present study, the effect of mainstream, in other words, the crossflow passing outer surface of effusion plate, is not considered.

The air supplied from a blower makes channel flow and impinging jet flow. By another blower, flow is drawn through the effusion holes. Turbulent flow in the channel is ensured by installing sand paper and trip wire at the inlet of channel after the contraction. The distance between the inlet of duct and the first row of injection holes is set to be 400 mm ($10.7\,D_h$). The cross section of the channel is 300 mm ($W$)$\times$20 mm ($H$), and the hydraulic diameter of the channel ($D_h$) is 37.5 mm.

The diameters of the injection and the effusion holes are 10 mm, and the thickness of plates is 20 mm ($t/d=2.0$). Each plate has 25 ($5\times5$) holes of square array, and the ratio of hole spacing to the diameter ($P_{\text{hole}}/d$) is 6.0. A staggered hole arrangement between the injection and the effusion plates is used in this study. The gap distance between the injection and the effusion plate is fixed at $H/d=2.0$ for all the tested cases.

The naphthalene coated test plate is installed on the effusion plate for local mass transfer measurements. Four effusion holes are located in the test plate and these holes are protected with the aluminum rim to maintain the circular hole shapes. The naphthalene-coated area in the test plate is $8.4d\times28d$ and a T-type thermocouple is installed in the test plate to measure the naphthalene surface temperature, which is needed to obtain naphthalene vapor density on the surface.

To measure pressure drop through crossflow channel, six static pressure taps are made at the sidewalls. Also, the static pressure at the injection and effusion plenum chambers is measured to get the pressure drop information across the perforated plates. Micromanometer (Microtector Model 1430, Dwyer) was used to measure differential static pressure.

**2 Rib Configurations.** As shown in Fig. 1($b$), the rib turbulators are installed on the effusion plate. The ribs have a square cross section of 3 mm$\times$3 mm, and the rib height-to-hydraulic diameter ratio ($e/D_h$) and the rib height-to-channel height ratio are 0.08 and 0.15, respectively. The rib-to-rib pitch ($P_{\text{rib}}$) is 60 mm so that $P_{\text{rib}}/e$ is 20 ($P_{\text{rib}}=30$ mm and $P_{\text{rib}}/e=10$ for the case of 90DU, which is mentioned below).

As illustrated in Fig. 2, five configurations of the rib turbulators (90D, 90U, 90DU, 45V and 45A) have been used. In the rib configurations, the numerals of rib configurations (90 and 45) and characters (D, U, V and A) represent the attack angle of the ribs and rib arrangement, respectively.

For 90 deg rib configurations, the ribs are installed between the effusion and injection holes as shown in Figs. 2($a$)–2($c$). ''D'' and ''U'' mean that the ribs are installed ''downstream'' and ''upstream'' positions of the effusion hole, respectively. Thus, the rib-to-rib spacing ($P_{\text{rib}}/e$) is 20. Note that the ribs are positioned at both sides of effusion holes, and corresponding rib-to-rib spacing is 10 for 90DU. For 45 deg rib configurations, ''V'' and ''A'' mean concave and convex toward the downstream direction ($x$ direction) at the centerline of the effusion holes, respectively. Thus, two different rib attack angles and rib-to-rib spacings are tested in the present study.

For each rib arrangement, the inactive ribs made of aluminum or acrylic are used. Therefore, the distortion of boundary condition in measuring domain could affect the heat/mass transfer on the surface. Cho et al. [19] reviewed some studies [20,21,22], and found that the deviations between the average heat transfer coef-

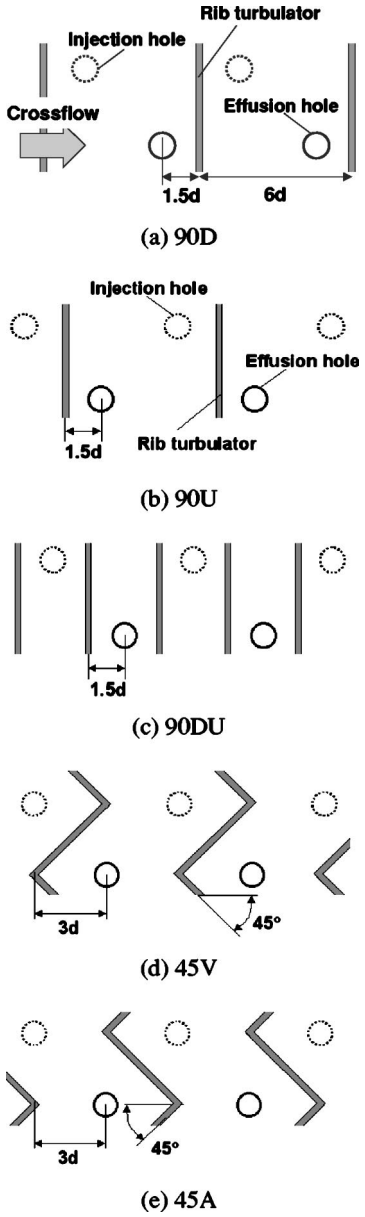


**Fig. 2 Schematic view of various rib configurations: (*a*) 90D, (*b*) 90U, (*c*) 90DU, (*d*) 45V, (*e*) 45A**

ficients from inactive rib experiments and those from active rib ones were less than 10% in subsection. In addition, Liou and Hwang [23] showed that the average heat transfer coefficients on the inter-rib regions with inactive ribs are not significantly different from those on the total area including active ribs. Therefore, the effects of rib boundary condition are not considered in this study.

**3 Operating Conditions.** To investigate the effect of the crossflow on the cooling system, the flow rate (velocity) of the crossflow through the channel is changed with fixed flow rate of impinging jets. In the present study, blowing ratio has been used to represent the influence of crossflow on the cooling system. Blowing ratio is a ratio of total flow rate of crossflow to the impinging jets and defined as Eq. (1)

$$M = Q_c / Q_i \tag{1}$$

The experiments had been performed for the blowing ratio from 0.5 to 1.5, and the desired conditions were obtained by changing the flow rate of the crossflow with fixed flow rate of impinging jets. For the impingement/effusion cooling, the flow rate of air through the effusion holes is set to be the same as that through the injection holes to catch the effects of crossflow precisely. The operating conditions are summarized in Table 1.

From a different point of view, the mass flux ratio of crossflow to jet flow ($MR$) or momentum ratio ($I$) may be a more important parameter than the blowing ratio (i.e., a ratio of total flow rate) to design the cooling system. These values corresponding to a given value of blowing ratio are also presented in Table 1.

**4 Data Reduction.** Mass transfer coefficients are calculated from sublimation depth, naphthalene vapor density, and solid naphthalene density. The details of the measuring system are described in Ref. [14]. Sherwood number, a dimensionless form of mass transfer coefficient, is used to present the heat/mass transfer results and can be expressed as

$$\mathrm{Sh} = h_m d / D_{\mathrm{naph}} \tag{2}$$

Note that for the channel flow cases (the simple channel cooling), the hydraulic diameter of channel was used as a characteristic length ($\mathrm{Sh}_{Dh} = h_m D_h / D_{\mathrm{naph}}$). $D_{\mathrm{naph}}$ is based on the discussion of naphthalene properties given by Goldstein and Cho [24].

The mass transfer coefficients can be converted to the heat transfer coefficients using the heat and mass transfer analogy per Eckert [25]. Prandtl number is 0.71 for air and the Schmidt number is 2.28 for the naphthalene vapor in air at 25°C. The experiments are conducted at room temperature, and the Lewis number (Pr/Sc) for this study is about 0.31

$$\mathrm{Nu/Sh} = (\mathrm{Pr/Sc})^{0.4}, \quad \mathrm{Nu} = 0.624 \ \mathrm{Sh} \tag{3}$$

The comparison between heat transfer and mass transfer results is presented by Rhee et al. [14].

Uncertainty of the Sherwood numbers using the method of Kline and McClintock [26] for single sample experiments, considering the measured surface temperature, depth, position and correlation equations, is within ±7.1% in the entire operating range of the measurement, based on a 95% confidence interval.

To estimate the pressure drop in the impingement/effusion cooling system, a ratio of pressure drop through the channel to that across the perforated plates ($\Delta P_{\mathrm{cross}} / \Delta P_{\mathrm{jet}}$) was measured. From these results, one can assess the additional pressure loss with rib turbulators and predict its effects on the operation of the cooling system.

**Table 1 Operating conditions and test parameters**

| $d$ (mm) | $D_h$ (mm) | $H/d$ | $e/D_h$ | $e/H$ | $P_{\mathrm{hole}}/d$ | $P_{\mathrm{rib}}/e$ |
|---|---|---|---|---|---|---|
| 10 | 37.5 | 2.0 | 0.08 | 0.15 | 6.0 | 20<br>10 for 90DU |

| $M$ | $MR$ | $I$ | $\mathrm{Re}_d$ | $\mathrm{Re}_{\mathrm{Dh}}$ |
|---|---|---|---|---|
| 0.5 | 0.164 | 0.027 | | 6130 |
| 1.0 | 0.327 | 0.107 | 10,000 | 12,270 |
| 1.5 | 0.491 | 0.241 | | 18,400 |

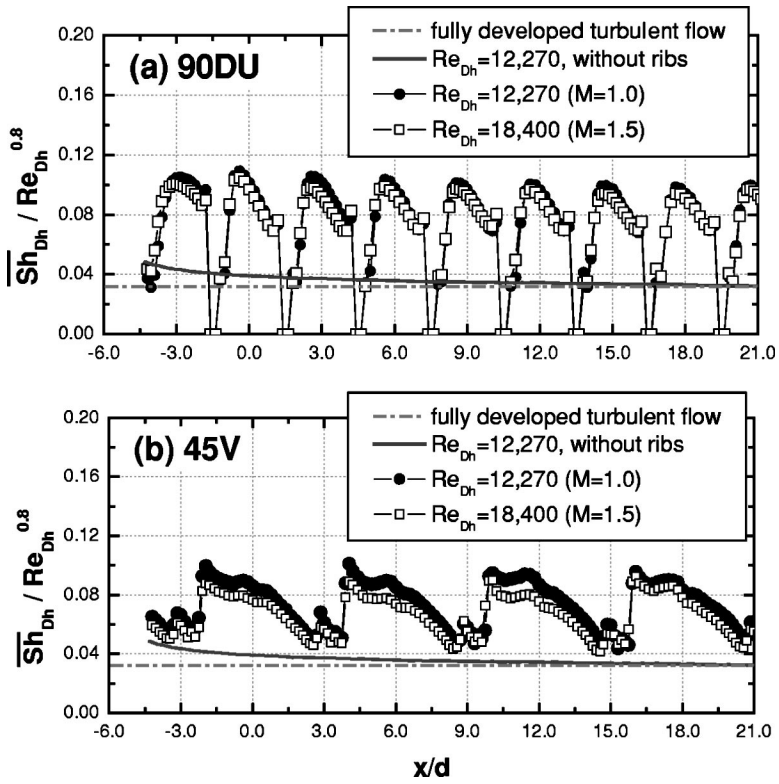


**Fig. 3 Streamwise distributions of span-wise averaged Sh on the rib-roughened surface for channel with different rib arrangements: (*a*) 90DU, (*b*) 45V**

## Numerical Simulation

In the present study, numerical simulations have been performed for the impingement/effusion cooling with different rib arrangements (without ribs, 90DU and 45V) and blowing ratios at $\mathrm{Re}_d=10{,}000$ and $H/d=2.0$ which are the same conditions to the experiments.

A commercial code, FLUENT 6.1 was used to calculate flow fields and computation domain grids were created using GAMBIT solid modeling. The computation domain is modeled by the geometry used in the experimental study. To observe the flow and heat transfer patterns for a fully developed flow, one pitch, including an injection hole, an effusion hole and ribs, was modeled with the periodic boundary conditions on the inlet and outlet boundaries. To simulate the flow fields at given conditions ($\mathrm{Re}_d=10{,}000$, $M=0.5-1.5$), uniform flow with the flow velocity of 0.3272 m/s, the turbulence intensity of 10% and the constant static temperature of 300 K is imposed on the inlet of the injection chamber. A fixed mass flow rate is applied to the periodic inlet/outlet planes (for example, 0.003 534 kg/s at $M=1.0$). The symmetric boundary conditions were imposed on the injection/effusion planes to reduce grid size and calculation time. Different grids with 400,000–1.5 million cells were tested to verify the grid independence of the solution, and the results for the grid with 800,000–900,000 cells were presented in the present study.

The steady solutions for turbulent flow field were calculated using a RNG $k$-$\varepsilon$ model with the enhanced wall treatment (two layer model), which is served in Fluent 6.1, for the near wall region. Enhanced wall treatment is a near-wall modeling that combines ''two layer model'' with ''enhanced wall function'' [27]. As suggested, the mesh near the wall was resolved to $y^+$ values less than 2. To calculate the heat transfer on the effusion surface, the constant temperature boundary condition is imposed on the effusion surface while other wall boundaries are set to be adiabatic. To solve the equations, second order of discretization was used on all the equations. The convergence of residuals for continuity, momentum, $k$ and $\varepsilon$ were resolved to levels of $10^{-5}$ for all entities and the energy equation was set to be a level of $10^{-7}$.

## Results and Discussion

In this study, the flow patterns and local heat/mass transfer characteristics are investigated for the impingement/effusion cooling with an initial crossflow and the rib turbulators attached on the effusion surface. The results are compared with the heat/mass transfer patterns for the simple channel cooling (crossflow only) and the impingement cooling of jet array which are also tested for base line data.

**1 Simple Channel Cooling With Rib Turbulator.** For the base line data and the qualification test, the simple channel flow with 90DU and 45V rib configurations is tested at different channel Reynolds numbers, which correspond to $M=1.0$ and 1.5 for the array jet impingement or the impingement/effusion cooling.

Figure 3 shows the stream-wise distributions of span-wise averaged Sh on the rib-roughened surface for different rib arrangements. The characteristics length of Sh is based on channel hydraulic diameter ($D_h$) and Sh values are normalized by $\mathrm{Re}_{\mathrm{Dh}}^{0.8}$ because heat transfer of turbulent channel flow is proportional to that value. In the figure, the case without rib is the result by Rhee et al. [14] and a red dash-dot line means the value for fully developed turbulent flow ($\mathrm{Sh}/\mathrm{Re}^{0.8}=0.023\,\mathrm{Sc}^{0.4}$; the Dittus–Boelter correlation [28]). Also, it is noted that zero values of Sh mean the position of rib turbulator and the rib-to-rib spacing ($P_{\mathrm{rib}}/e$) is 10 for 90DU and 20 for 45V as mentioned above.

For the 90DU configuration, as shown in Fig. 3($a$), the results of different Reynolds numbers are in good agreement and the distributions and the levels of Sh are fairly periodic in the overall region except the inlet, which means that the channel flow becomes fully developed after passing one or two transverse ribs. As

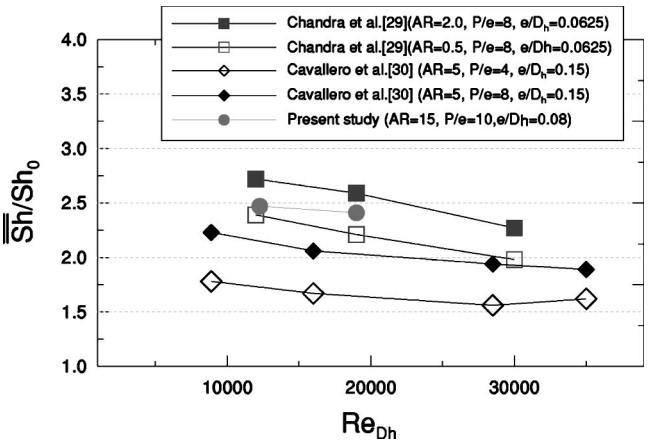


**Fig. 4 Comparison of average $Sh/Sh_0$ on the rib-roughened surface for channel with 90 deg rib arrangement**

expected, Sh values for the channel with transverse ribs are approximately 2.5 times higher than those without ribs, and these results are in accordance with other results [29,30] as shown in Fig. 4.

For the 45V case, the counter-rotating secondary flow affects heat/mass transfer in the channel. Angled ribs induce a pair of counter-rotating secondary flows; downward flow enhances heat/mass transfer coefficients on the surface, while upward flow lowers heat/mass transfer coefficients on the surface. Therefore, as shown in Fig. 3(*b*), local peaks are formed at downward flow regions ($x/d \cong -2$, 4, 10 and 16) while Sh values are low at upward flow regions ($x/d \cong -3$, 3, 9, and 15). Note that the slight discrepancy in normalized values for two cases of the different Reynolds numbers is because the secondary flow cells are not fully developed and the values become coincident as $x/d$ increases.

**2 Array Jet Cooling With Initial Crossflow.** Figure 5 shows the contour plots of Sh on the target surface for array jet impingement without effusion holes at $M=1.0$. The white dotted circles mean the projected positions of the injection holes in the contour plots. For an array jet impingement cooling, since the spent air from impinging jets is added to the crossflow, the effects of crossflow become stronger as flow moves downstream. Therefore, as shown in Fig. 5(*a*), the stagnation points of the impinging jets move downstream and the level of peak values becomes lower with increasing $x/d$ for the array jet impingement without rib turbulator. In addition, because the wall jets are swept by crossflow and the thermal boundary layer develops at the midway region (along $z/d \cong 0.0$), the heat/mass transfer coefficients at this region are much lower than stagnation regions.

When the ribs are attached on the target surface, the effects of crossflow are reduced significantly because the flow near the surface is disturbed by ribs and then spreads toward upstream and lateral directions as shown in Figs. 5(*b*) and 5(*c*).

For 90DU, the jet impinges on the region around the ribs and then two peak regions are formed in front of and behind the transverse ribs. Although the positions of the stagnation points are almost the same as those for the case without ribs, the levels of peak Sh behind the ribs are higher than those for the case without ribs. The reason is that the effects of crossflow at the near-wall region are weakened by ribs and flow passing over the ribs disturbs the jet flow and then enhances local turbulence of jet.

The remarkable feature with the installing transverse ribs is the uniformity enhancement of the heat/mass transfer, which is achieved because the wall jets near the surface are protected by the ribs and then reattach after passing over the ribs along $z/d = 3.0$. For the same reason, additional peaks of Sh due to flow reattachment are formed behind the ribs which are positioned in front of the impinging jets, i.e., at $x/d \cong 2$, 8 and 14 along $z/d = 3.0$ in Fig. 5(*b*). Although the magnitude is relatively lower than other peaks, the heat/mass transfer coefficients at the midway region are higher than those for the case without ribs because of the flow reattachment mentioned above.

For the 45 V case [Fig. 5(*c*)], the levels of Sh at the stagnation points are almost the same in the whole region and local peak values due to downward flow are observed along the ribs. However, the regions affected by the wall jets are reduced because the wall jets are lifted off. In addition, locally low heat/mass transfer regions are formed in front of the ribs along $z/d = 0.0$. Therefore, the increase of heat/mass transfer is not as high as that for 90DU. However, locally very high heat/mass transfer is generated for the 45 deg rib case because the secondary flow induced by ribs impinges on the target surface. These peak values are even higher than the values at the stagnation points. The reason is as follows. When the jet impinges on the surface, the jet flow disturbs the crossflow and acts as a blockage against the crossflow in the channel. Then the effective cross-sectional area of the channel is reduced and this causes the increase of the strength of secondary flow motion with increasing local Reynolds number (flow velocity).

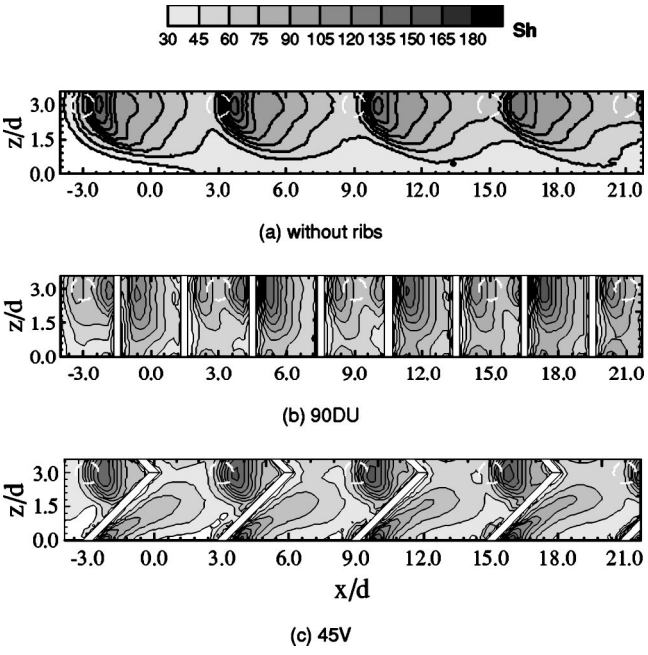


**Fig. 5 Contour plots of Sh for array jet cooling with initial crossflow at $M=1.0$: (*a*) without ribs, (*b*) 90DU, (*c*) 45V**

### 3 Impingement/Effusion Cooling With Crossflow

*3.1 Flow Characteristics.* Figure 6 shows the velocity vector plots on the injection and effusion planes ($z/d = 3.0$ and 0.0) for the case without ribs and with two different rib arrangements at $M=1.0$. As reported by Rhee et al. [14], for the impingement/effusion cooling with initial crossflow, the flow pattern on the injection plane shows that impinging jet is approximately $0.5d$ shifted toward downstream side, and channel flow and spent air are entrained into jet stream at the downstream side of the jet, hence weak downward flow is formed. Near the wall of the effusion plate, a small vortex is formed at the upstream region of stagnation point and most of the wall jets are swept toward the downstream region. On the effusion plane, the overall flow pattern is similar to the channel flow, but weak upward flow is formed upstream the effusion holes due to the interaction of the wall jets drawn into the effusion holes. Thus, the effusion surface is not

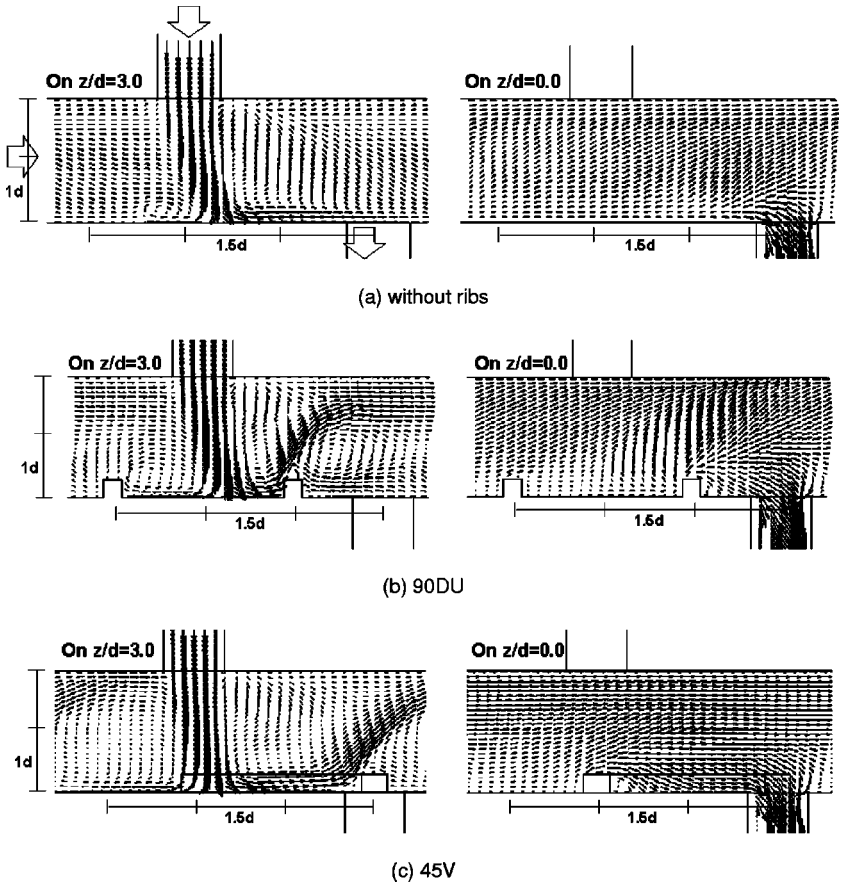


**Fig. 6 Velocity vector on the stagnation and effusion planes ($z/d=3.0$ and 0.0) at $M=1.0$: (*a*) without ribs, (*b*) 90DU, (*c*) 45V**

cooled effectively by the wall jets, except the region near the effusion holes where the flow is accelerated into the effusion hole.

When the transverse ribs are attached on the effusion surface, the flow pattern changes significantly. As shown in Fig. 6(*b*), the wall jets at the upstream of the stagnation point reach the transverse rib and then make a recirculating flow. Also, the wall jets at the downstream side of stagnation point make a strong upward flow after the flow goes over the rib. Thus, the transverse rib induces strong recirculating flow and helps wall jets cover the upstream and midway regions. As a result, the channel flow is partially blocked up by these strong recirculating flows. Although the rib height is only 15% of the channel height, an actual blockage ratio is up to 50% of the channel height due to the strong flow recirculation. Therefore, the crossflow is accelerated at the upper portion of channel, and then affects significantly impinging jets at this region. That is the possible reason why the position of stagnation point is almost the same as that for the case without ribs although there are no crossflow effects near the surface.

On the effusion plane, a strong upward flow is generated in front of the rib because of increased effects of the interaction between the wall jets. In addition, the flow passing over the rib reattaches on the surface in front of the effusion hole due to the flow suction. However, the stagnant flow pattern is observed near the surface in the inter-rib region where the impinging jet is located.

For 45 V, some different flow features are found in flow fields because the counter-rotating secondary vortices are generated by the angled rib. On the injection plane, the overall flow pattern is similar to that for 90DU. However, the effects of secondary flow induced by the angled rib are added in this case. Therefore, the upward flow is stronger and even impinges on the upper wall of the channel because the additional upward flow generated by the angled rib has favorable influence on upward flow. However, on the effusion plane, the flow pattern is similar to a channel flow and the flow passing over the rib reattaches quickly because downward flow induced by the angled ribs is dominant in this plane.

### *3.2 Heat/Mass Transfer Characteristics*

*3.2.1 Effects of rib configurations.* **Local heat/mass transfer**. Figure 7(*a*) presents the contour plot of Sh for the impingement/effusion cooling with initial crossflow at $M=1.0$. White dotted circles and the small half circles in the contour plot represent the projected positions of injection holes and the effusion holes with the aluminum rim between two circles, respectively. When initial crossflow is imposed, the distributions are nonuniform and asymmetric. Especially, the upstream regions of the stagnation points are not covered by the wall jets and the heart-shaped low transfer regions are formed at the upstream of the effusion holes as expected in flow patterns. These trends become more obvious as blowing ratio increases as reported in Ref. [14].

Figures 7(*b*), 7(*c*) and 7(*d*) show the contour plots of Sh on the rib-roughened surface for the 90 deg rib configurations at $M=1.0$. For all cases, the positions of the stagnation points are almost the same as those for the case without ribs. However, the overall distributions of Sh are more uniform and locally low transfer regions are reduced or disappear although the effects of jet impingement are dominant in whole domain. This is because the rib acts as a block against near-wall crossflow making a large circulating flow so that the wall jet spreads more widely toward upstream and lateral directions and covers those regions effectively. Also, additional heat/mass transfer enhancement is obtained due to the flow reattachment.

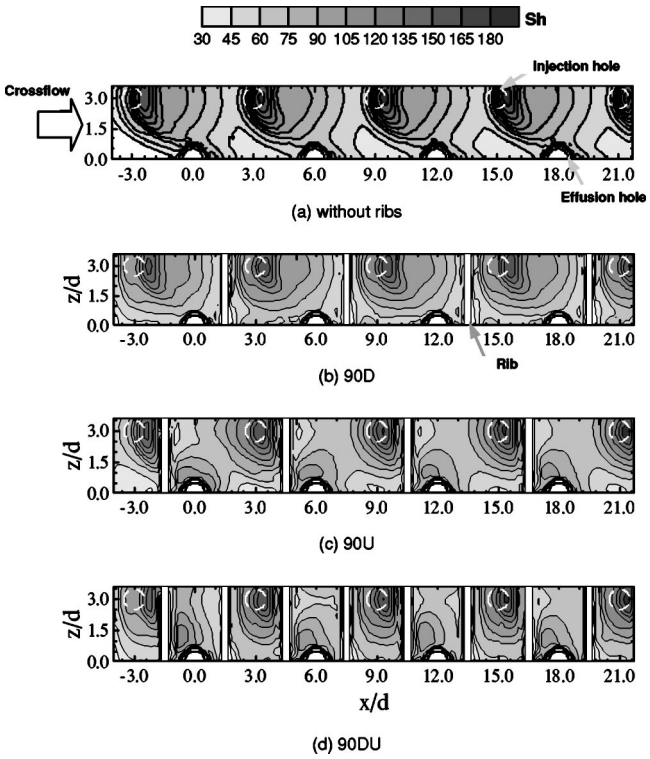


**Fig. 7 Contour plots of Sh for impingement/effusion cooling with 90 deg rib configurations at $M=1.0$: (*a*) without ribs, (*b*) 90D, (*c*) 90U, (*d*) 90DU**

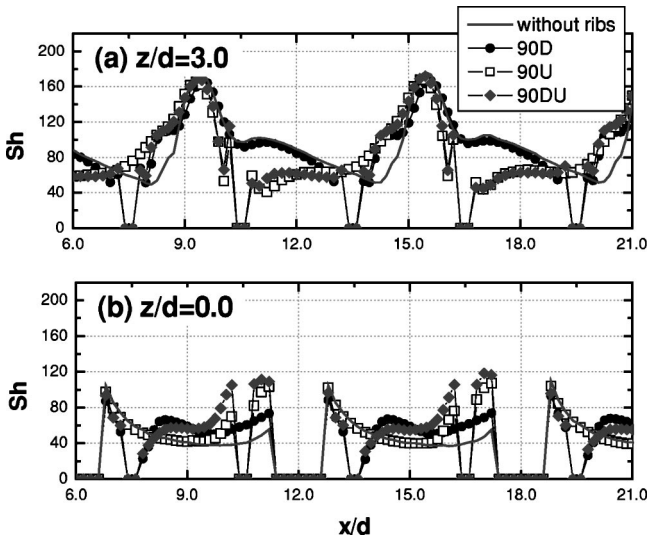


**Fig. 8 Local distributions of Sh for impingement/effusion cooling with 90 deg rib configurations at $M=1.0$: (*a*) $z/d=3.0$, (*b*) $z/d=0.0$**

When the transverse ribs are attached behind the effusion holes [90D, Fig. 7(*b*)], the wall jet spreads more laterally and in the upstream direction on the effusion surface and low transfer regions between the effusion holes are hardly seen due to the ribs. This is because the rib makes upward flows near the surface in the channel and then weakens the effect of crossflow while it helps the wall jets spread laterally and toward upstream region. However, the upward flows around the rib do not always have favorable influence on local heat/mass transfer because these flows can also generate low transfer region behind the rib, which will be shown in the results for 90U and 90DU. Slight heat/mass transfer enhancement is observed behind the ribs and around the effusion holes.

For the 90U case [Fig. 7(*c*)], the wall jet spreads more widely toward the upstream region due to the different position of rib while Sh distributions around the stagnation regions are similar to those for 90D. Locally high heat/mass transfer regions are formed around the effusion holes ($z/d \cong 1.0$), because the flow suction through the effusion holes promotes the reattachment over the ribs and accelerates local flow. However, the regions of low heat/mass transfer are formed behind the ribs along $z/d=3.0$ due to a strong upward flow as mentioned before and in front of the ribs along $z/d=0.0$ because of stagnant flow pattern at those regions.

The 90DU rib configuration [Fig. 7(*d*)] has combined features in the 90D and 90U configurations. Because its rib spacing is a half of that of 90D or 90U, 90DU has more uniform distribution and higher values of heat/mass transfer coefficients than other rib configurations. At the inter-rib regions of the stagnation points (for example, $1.5<x/d<4.5$), the wall jets spread more widely in the lateral direction than other cases and small peaks, which are not shown clearly in the case of 90U, appear in front of the ribs. At the inter-rib regions where effusion holes are positioned (for example, $4.5<x/d<7.5$), high heat/mass transfer coefficients are observed around the effusion holes like the 90U case because of the flow reattachment and acceleration, but these regions are slightly larger than those for 90U. In spite of its small rib spacing, the adverse effect of upward flow around the rib remains, and then small regions of the low heat/mass transfer are shown behind the ribs along the stagnation line ($z/d=3.0$) because of a strong upward flow with recirculation flow.

Local distributions of Sh for the 90 deg rib configurations are presented in Fig. 8. As shown in the contour plots, the heat/mass transfer at the inlet region is lower than that at the downstream region while the distributions are fairly periodic in the downstream region. Therefore, to observe the effects of rib on local heat transfer more clearly, the data in the range of $6.0 \leqslant x/d \leqslant 21.0$ are presented.

It is clearly shown in Fig. 8(*a*) that heat/mass transfer at the upstream regions of the stagnation points is enhanced while the positions of the stagnation points are almost the same for all cases. However, for 90U and 90DU, relatively low Sh values are obtained behind the ribs and the levels of these values are only 40%–60% of those for 90D or the cases without ribs due to the strong upward flow with ribs as mentioned.

Along the centerline of the effusion holes [Fig. 8(*b*)], the 90D and 90DU cases have about 50% higher values around the ribs due to the wall jet spreading, the flow disturbance and reattachment by the ribs. For the 90U case, the regions of low heat/mass transfer coefficients are formed behind the effusion holes because a certain amount of flow is discharged and the flow momentum is relatively low at those regions. That is a similar pattern to the case without ribs. However, like other cases, a significant enhancement of heat/mass transfer is obtained around the ribs for the 90U case by installing ribs in front of the effusion holes. Thus, small ribs can control wall jets and near-wall flow resulting in more uniform performances.

Contour plots of Sh for the 45 deg angled rib configurations are presented in Fig. 9. The features of the overall heat/mass transfer on the effusion surface are a little different from those for the 90 deg rib configurations because the effects of jet impingement and flow effusion are dominant in this cooling system. The positions and levels of the stagnation points are almost the same as the 90 deg rib cases and relatively high heat/mass transfer is achieved around the effusion hole because the flow at those regions is accelerated and disturbed. However, some different characteristics in local distributions are observed because the secondary flow is induced by angled ribs in the channel.

Small peak values in downward flow regions are formed along $z/d=0.0$ and 3.0 for 45V and 45A rib configurations, respectively.

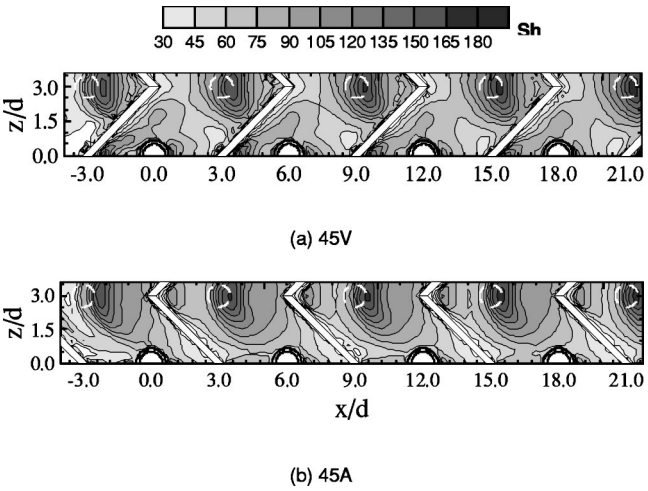


**Fig. 9 Contour plots of Sh for impingement/effusion cooling with 45 deg rib configurations at $M=1.0$: (*a*) 45V, (*b*) 45A**

Therefore, an additional heat transfer enhancement is obtained with the angled rib configurations. However, the angled rib configurations have also negative effects related to the secondary flows. After the flow reattaches to the surface in the downward flow region, it moves along the rib and boundary layer develops, and then the flow near the surface is lifted off by the upward secondary flow. Because of these flow characteristics, the regions of low heat/mass transfer are formed along the ribs and at the upward flow regions. For 45A, however, slightly high heat/mass transfer coefficients are observed in front of the effusion holes along $z/d=0.0$ in which the upward flow is formed if there are no effusion holes. The reason is that the effusion hole attracts the flow and makes flow reattachment in front of the hole while it weakens the strength of upward flow.

Local distributions of Sh are compared in Fig. 10. As mentioned, the position and levels of Sh at the stagnation points are almost the same, and the heat/mass transfer at the upstream regions of the stagnation points increases. It is similar pattern to that for the 90 deg ribbed cases. Local peaks due to downward secondary flow are observed for both cases (at $z/d=0.0$ and 3.0 for 45V and 45A, respectively), but the peak values for 45V are 30%

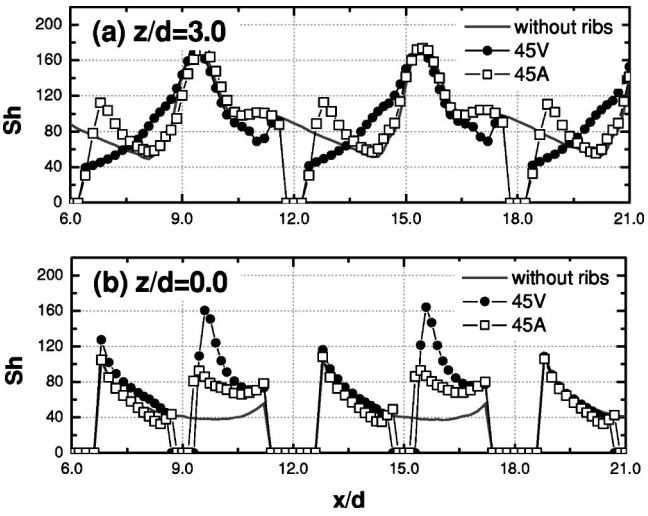


**Fig. 10 Local distributions of Sh for impingement/effusion cooling with 45 deg rib configurations at $M=1.0$: (*a*) $z/d=3.0$, (*b*) $z/d=0.0$**

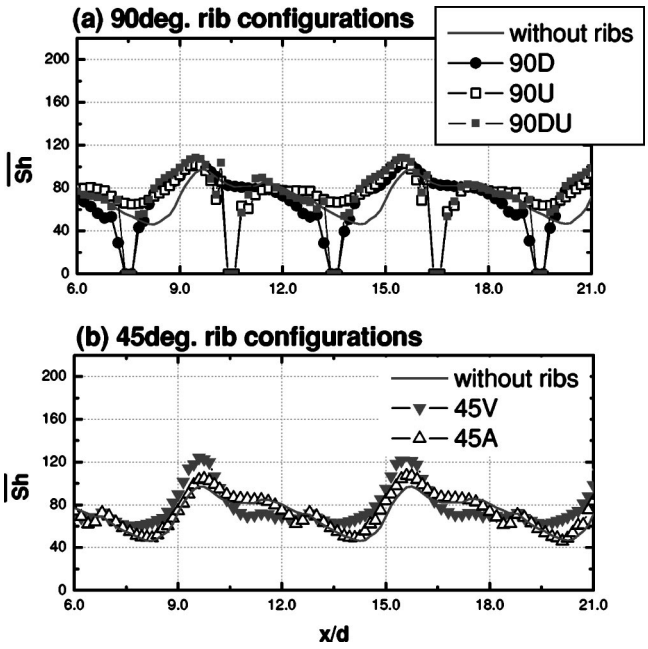


**Fig. 11 Span-wise averaged Sh for impingement/effusion cooling with various rib configurations at $M=1.0$: (*a*) 90 deg rib configurations, (*b*) 45 deg rib configurations**

higher than those for 45A because the wall jets form upward flow in front of the ribs and then this upward flow weakens the strength of the downward flow for 45A.

**Average heat/mass transfer**. Span-wise averaged Sh distributions for various rib configurations are presented in Fig. 11. The span-wise averaged Sh is calculated by averaging local data in the range of $0.0 \leqslant z/d \leqslant 3.0$ excluding the data in the region where the ribs are installed.

For the 90 deg rib configurations, the heat/mass transfer at the upstream region of the stagnation point is enhanced by installing rib turbulators while overall distributions are similar. This is due to the protection of wall jet by the rib turbulators. The 45 deg rib configurations have similar trends but some local peaks related to the secondary flows are shown as expected from the local data.

The area-averaged Sh values for impingement/effusion cooling with various rib configurations at $M=1.0$ are listed in Table 2. The averaged values are calculated by averaging local data in the range of $-3.0 \leqslant x/d \leqslant 21.0$ and $0 \leqslant z/d \leqslant 3.0$. It is noted that the averaged values at the inlet region ($-3.0 \leqslant x/d \leqslant 3.0$) are about 5% lower than those from other regions.

As expected in the local Sh distributions, the cases with rib turbulators have 4%–15% higher value than the case without ribs. The 90DU shows the highest heat/mass transfer coefficients among the cases with ribs. This is mainly related to the shorter rib spacing with better protection of wall jets. However, the average values are similar for the cases with rib spacing of 20 (90D, 90U, 45V and 45A). It means that the attack angle of rib is not a

**Table 2 Overall averaged Sh for various rib configurations at $M=1.0$**

| Rib configuration | Array impinging jet | Impingement/effusion cooling |
|---|---|---|
| Without ribs | 60.8 | 71.0 |
| 90D | ··· | 77.4 |
| 90U | ··· | 78.3 |
| 90DU | 72.7 | 81.4 |
| 45V | 63.5 | 78.5 |
| 45A | ··· | 76.5 |

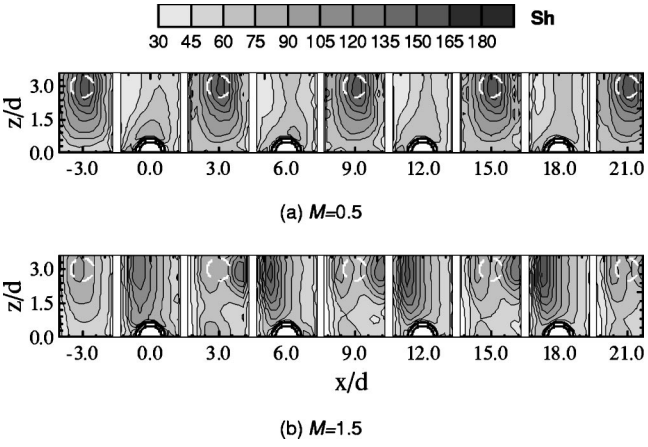


**Fig. 12 Contour plots of Sh for impingement/effusion cooling with 90DU rib configuration at different blowing ratios: (*a*) $M=0.5$, (*b*) $M=1.5$**

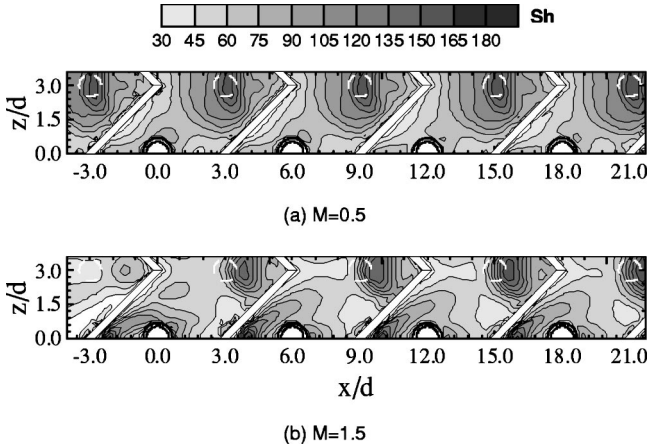


**Fig. 13 Contour plots of Sh for impingement/effusion cooling with 45V rib configuration at different blowing ratios: (*a*) $M=0.5$, (*b*) $M=1.5$**

significant parameter in an average heat/mass transfer for the impingement/effusion cooling system with initial crossflow.

For array jet impingement cooling, as expected, the rib-roughened cases have better performances. Especially, 90DU has almost 20% higher value than the smooth case. Small enhancement for 45V results from undeveloped secondary flow and reduction of stagnation region.

*3.2.2 Effects of blowing ratio.* To investigate the effects of blowing ratio, a set of experiments was conducted with various blowing ratios from 0.5 to 1.5 for 90DU and 45V rib configurations, and the contour plots of Sh are presented in Figs. 12 and 13.

For the cases without rib turbulators, which are presented in [14], the levels of Sh at stagnation region become lower as blowing ratio increases. Also, the regions of low heat/mass transfer between effusion holes become larger. However, some different characteristics are observed with the 90DU cases. At a low blowing ratio of $M=0.5$ [Fig. 12($a$)], the inter-rib regions where the stagnation points exist (for example, $7.5 \leqslant x/d \leqslant 10.5$) have high values, but the inter-rib regions where the effusion holes are located have very low heat/mass transfer coefficients. The reason is that rib turbulator acts as an obstacle to the wall jet with low velocity of the crossflow. Most of the near wall flow does not reattach on the surface after passing over the ribs but is discharged through the effusion holes. For those reasons, the heat/mass transfer coefficients are very low just behind the ribs because those regions are not covered by the wall jet flow or the channel crossflow. Therefore, the distributions of heat/mass transfer coefficients are nonuniform in a whole region.

At $M=1.5$ [Fig. 12($b$)], the stagnation regions are shifted and formed just around the ribs because the impinging jets are affected significantly by the crossflow. This is the same pattern of an array jet impingement cooling without effusion holes at $M=1.0$. Therefore, the heat/mass transfer coefficients on the inter-rib regions with the effusion holes increase considerably, and the local peak values due to jet impingement are observed in front of the ribs in other inter-rib regions. Furthermore, additional peaks behind the ribs ($x/d=2$, 8, 14 and 20) are shown at the midway region mainly due to the flow reattachment. However, the regions of relatively low heat/mass transfer coefficients are formed in front of ribs along the midway.

As shown in Fig. 13, the trend for 45V with blowing ratio is similar to that for 90DU. At the low blowing ratio, low heat/mass transfer coefficients appear along the ribs while the stagnation regions are not affected significantly by the crossflow. Moreover, there are no additional peaks along the centerline of effusion holes because of the low channel Reynolds number. At the higher blowing ratio of $M=1.5$, the stagnation regions shrink remarkably. Also, the regions of low heat/mass transfer rate are formed behind the ribs along $z/d=3.0$ and in front of the ribs at the midway. However, locally very high heat/mass transfer rate is achieved just behind the ribs along the midway due to the downward secondary flow induced by the angled ribs, and these peak values are even higher than those at the stagnation points. The high heat/mass transfer regions due to the secondary flow are limited to the region around the effusion holes; hence the overall heat/mass transfer rate is lower than those at the lower blowing ratios.

The overall averaged Sh with various blowing ratios are presented in Fig. 14. It is noted that the averaged values at the inlet region ($-3.0 \leqslant x/d \leqslant 3.0$) are about 5–25% lower than those from other regions for all cases.

For the cases without ribs, the average value decreases monotonically in the impingement/effusion cooling scheme as the blowing ratio increases. For example, the average Sh value at $M=1.5$ is only 70% of that at $M=0.5$. On the contrary, for the 90DU cases, the average value for the low blowing ratio of $M=0.5$ is even approximately 10% lower than that without ribs, which is due to the blocking up of the wall jets with ribs as mentioned above. However, for the blowing ratios of $M \geqslant 1.0$, the 90DU configuration has 10–15% higher values than the cases without ribs. The same trend is found for the 45V case. Therefore, it is concluded that one should pay much attention to the operating conditions when rib turbulators are considered as a solution to enhance heat/mass transfer for the impingement/ effusion cooling system. Note that 45V has slightly higher value than 90DU at

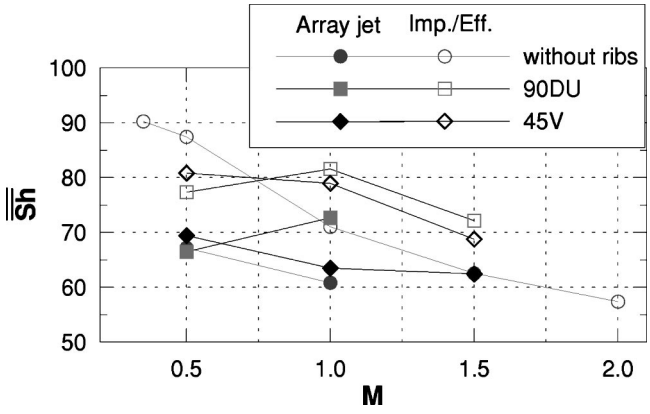


**Fig. 14 Overall averaged Sh for different cooling schemes with various rib arrangements**

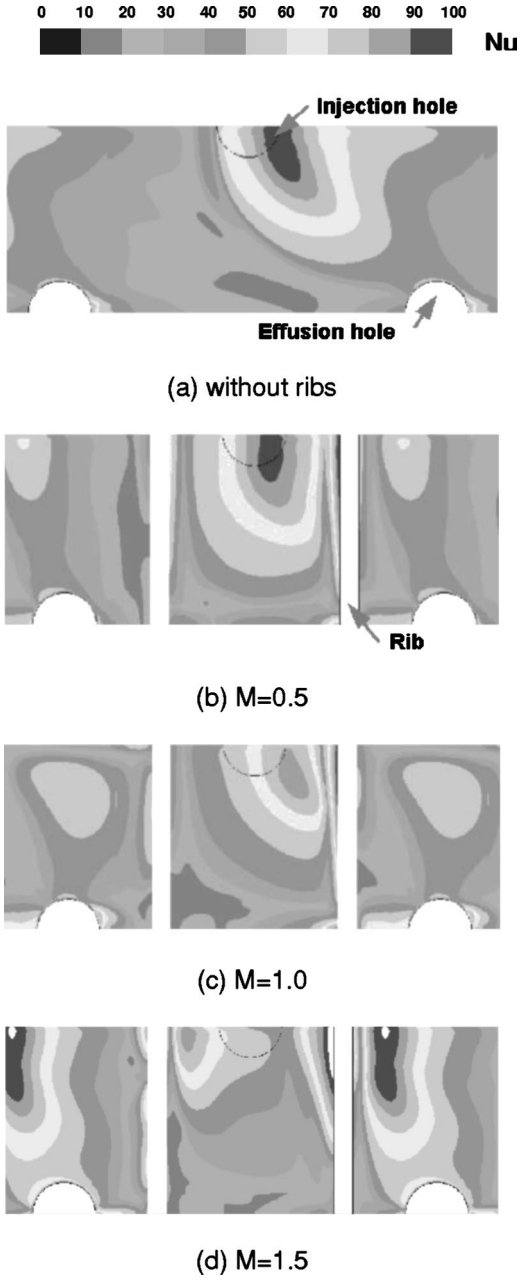


**Fig. 15 Contour plots of calculated Nusselt number for impingement/effusion cooling with 90DU at various blowing ratios: (*a*) without ribs, $M=1.0$, (*b*) $M=0.5$, (*c*) $M=1.0$, (*d*) $M=1.5$**

$M=0.5$ possibly because the adverse effect of rib, such as blocking the wall jets, is reduced with the larger rib-to-rib spacing.

For the array jet impingement with initial crossflow, the averaged values are similar at the low blowing ratio. However, 20% enhanced heat/mass transfer coefficient is obtained with 90DU at $M=1.0$, while approximately 4% enhancement is achieved with the angled rib configuration.

When the results for two different cooling schemes are compared, the average values for the impingement/effusion cooling have more than 10% higher values than those for the array jet impingement cooling because of the reduced effects of crossflow with the discharge of crossflow or spent air through the effusion holes. However, if the blowing ratio increases more than 1.5, the difference of values between two cooling schemes will decrease because heat transfer enhancement due to the rib will increase while the effect of jet impingement decreases.

*3.2.3 Comparison with numerical results.* Figures 15 and 16 show the contour plots and comparison of local distributions of calculated Nusselt number for the case without ribs at $M=1.0$ and for 90DU and the average values are listed in Table 3. In the local distributions, the experimental data are the converted Nusselt numbers from the Sherwood numbers using the heat and mass transfer analogy. On the whole, the calculated results are in quite good agreement qualitatively with experimental results. However, some discrepancies of values are observed particularly at the stagnation region and near the effusion hole, and the difference between the experimental and calculated results is more evident for ribbed cases as shown in Fig. 16. These are mainly related to the complex flow patterns such as jet impingement, flow recirculation behind the ribs, separation and reattachment due to the ribs. Therefore, proper near wall modeling with mesh generation is required to improve the accuracy of heat transfer calculation. As reported and suggested by Hermanson et al. [31,32], the V2F model can be one of the possible models and further works will be conducted.

*3.2.4 Pressure loss.* Pressure drop in the crossflow channel was measured and the results are presented in Fig. 17. The pressure drop through the channel is normalized by the pressure difference between injection and effusion plenum chambers. For all cases, the pressure drop increases as the blowing ratio increases; in other words, the Reynolds number of the channel flow increases. For the case without ribs, the pressure drop through the channel is less than 10% of that across the perforated plates. With the rib turbulators, the pressure drop through the channel increases as expected. For the 90DU cases, the pressure drop is approximately two times that without ribs but less than 20% of pressure drop across the injection/effusion plates. However, with the 45 deg rib turbulators, the pressure drop at $M=1.5$ is about 28% of total pressure drop across the plates, which means that the angled rib turbulators in the impingement/effusion cooling system may cause the problem related with insufficient cooling flow on the outer wall of liner (i.e., film cooling).

The numerical simulations predict fairly well the pressure drop ratio for all cases except 45V at $M=1.0$. This problem may be related to the secondary flow motion with periodic conditions and further studies should proceed.

## Conclusions

In the present study, the effects of rib configurations on local heat/mass transfer characteristics for the impingement/effusion cooling system are investigated with initial crossflow and are compared with the cases without ribs. The results are summarized as follows:

1. When 90 deg rib turbulators are installed on the surface, it induces a strong upward flow and then this upward flow prevents the channel crossflow from sweeping wall jets. In addition, the rib turbulators increases flow mixing and disturbance and flow suction to the effusion holes promotes flow reattachment behind the ribs. Hence, locally more uniform and higher heat/mass transfer coefficients are obtained with the rib turbulators although the effect of jet impingement on overall heat transfer is dominant. These characteristics are also observed for the array jet impingement cooling with crossflow.
2. The 45 deg rib configurations have similar heat/mass transfer characteristics to the 90 deg rib configurations in the overall region. However, additional local peaks of Sh and low transfer regions are formed due to the secondary flow motion induced by the angled ribs.
3. Using the rib turbulators, the average heat/mass transfer increases 4%–11%. The 90DU rib configuration has the highest

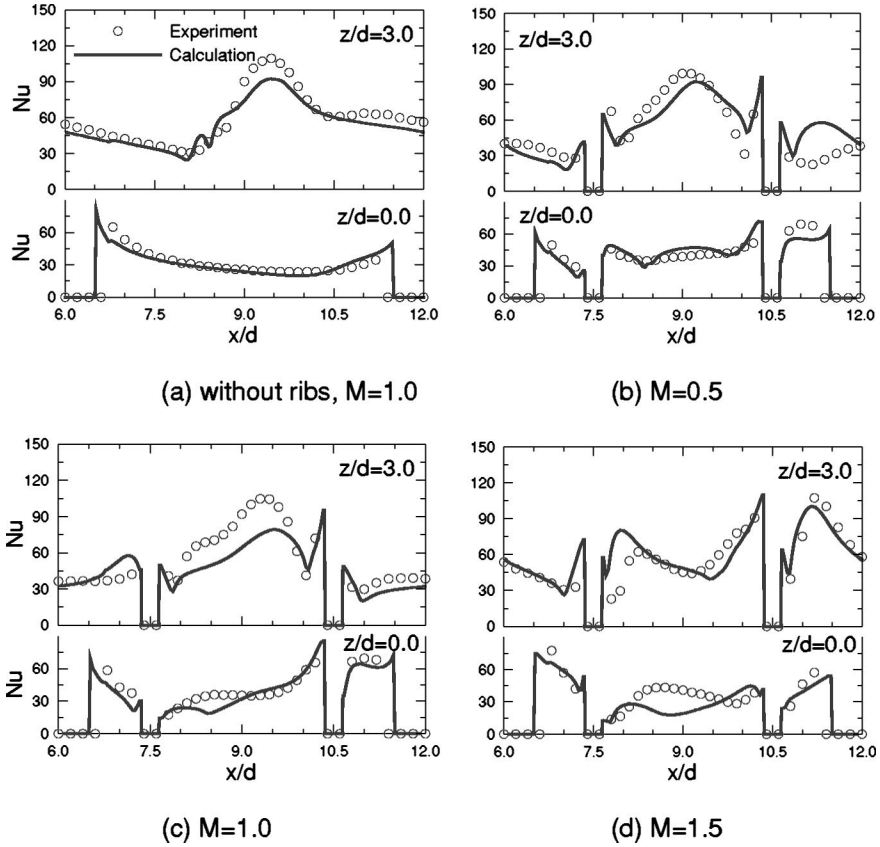


**Fig. 16 Comparison of calculated Nusselt number with experimental data for impingement/effusion cooling: (*a*) without ribs, $M=1.0$, (*b*) $M=0.5$, (*c*) $M=1.0$ (*d*) $M=1.5$**

average heat/mass transfer coefficient due to its smallest rib spacing among various rib configurations. However, the attack angle of rib has minor influence on the average heat/mass transfer for the fixed rib spacing.

**Table 3 Comparison of area-averaged Nusselt number for various configurations**

| | Without ribs | | 90DU | | 45V | |
|---|---|---|---|---|---|---|
| M | Exp. | Cal. | Exp. | Cal. | Exp. | Cal. |
| 0.5 | 54.0 | ··· | 48.2 | 45.5 | 50.3 | ··· |
| 1.0 | 44.3 | 43.5 | 50.9 | 43.0 | 49.2 | 47.6 |
| 1.5 | 39.5 | ··· | 45.0 | 47.5 | 42.1 | ··· |

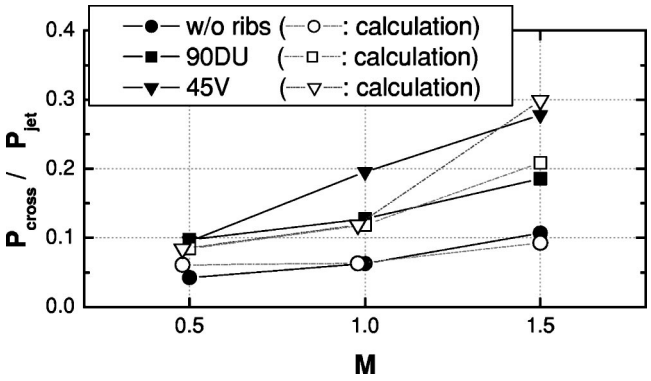


**Fig. 17 Pressure drop ratios for the impingement/effusion cooling with different rib arrangements**

4. For the lower blowing ratio of $M=0.5$, the transverse rib prevents the wall jets from spreading and confines to the inter-rib regions of stagnation points. Therefore, lower and nonuniform heat/mass transfer coefficients are obtained in the overall region. Moreover, the overall average value is approximately 10% lower than that for the case without ribs. As the blowing ratio increases, the ribs compensate the adverse effects of crossflow on heat transfer by preserving wall jets and generating flow disturbance and reattachment. As a result, the overall heat/mass transfer increases 10%–15% with rib turbulators for higher blowing ratios.

5. The calculated results are in quite good agreement qualitatively with the experimental results. However, some discrepancies of values are observed, and these discrepancies are more evident for the ribbed case. These are mainly related to the complex flow patterns due to jet impingement and rib installation, separation and reattachment with the ribs.

6. Pressure drop through the channel increases as the blowing ratio increases for all cases. While the pressure loss through the channel is less than 10% of that across the perforated plates for the case without ribs, the pressure loss increases up to 20% of that across the plates for 90DU. With the angled rib, the loss increases more than 25% of the total loss due to the secondary flow generation in the channel; hence the pressure loss should be considered with rib turbulators, especially angled rib turbulators, in the impingement/ effusion cooling system.

## Acknowledgments

The authors wish to acknowledge support for this study by the Korean Ministry of Science and Technology through the National Research Laboratory program.

## Nomenclature

$d$ = injection and effusion hole diameter
$D_h$ = hydraulic diameter of test duct
$D_{\text{naph}}$ = mass diffusion coefficient of naphthalene vapor in air
$H$ = gap distance between injection and effusion plates
$h_m$ = local mass transfer coefficient
$I$ = local momentum flux ratio of crossflow and impinging jets, $\rho_c V_c^2/\rho_i V_i^2$
$M$ = blowing ratio (total mass flow ratio of crossflow and impinging jets), $Q_c/Q_i$, Eq. (1)
$MR$ = local mass flux ratio of crossflow and impinging jets, $\rho_c V_c/\rho_i V_i$
Nu = Nusselt number based on the hole diameter, $hd/k$
Pr = Prandtl number
$P_{\text{hole}}$ = pitch of array holes
$P_{\text{rib}}$ = rib-to-rib spacing
$Q_c$ = flow rate of crossflow
$Q_i$ = flow rate of injected jet or effused flow
$\text{Re}_d$ = Reynolds number based on hole diameter and the average velocity in the hole
$\text{Re}_{\text{Dh}}$ = Reynolds number based on hydraulic diameter of duct and average velocity of crossflow
Sc = Schmidt number
Sh = Sherwood number based on the hole diameter, Eq. (2)
$\text{Sh}_0$ = Sherwood number for fully developed flow in a smooth pipe, $\text{Sh}_0 = 0.023\,\text{Re}_{\text{Dh}}^{0.8}\text{Sc}^{0.4}$
$\text{Sh}_{Dh}$ = Sherwood number based on the channel hydraulic diameter and average flow velocity in the channel
$\overline{\text{Sh}}$ = span-wise averaged Sherwood number
$\overline{\overline{\text{Sh}}}$ = overall averaged Sherwood number
$t$ = thickness of injection and effusion plates
$V_c$ = mean velocity of crossflow
$V_i$ = mean velocity of impinging jet
x, z = distance from the center of a effusion hole (Fig. 2)

### Greek symbols

$\Delta P_{\text{channel}}$ = differential pressure between the inlet and the exit of the channel
$\Delta P_{\text{jet}}$ = differential static pressure between the injection and effusion plenum chambers
$\rho_c$ = density of crossflow
$\rho_i$ = density of impinging jet flow

## References


[1] Hollwarth, B. R., and Dagan, L., 1980, ''Arrays of Impinging Jets with Spent Fluid Removal Through Vent Holes on the Target Surface. Part 1: Average Heat Transfer,'' J. Eng. Power, **102**, pp. 994–999.
[2] Hollwarth, B. R., and Lehmann, G., and Rosiczkowski, J., 1983, ''Arrays of Impinging Jets with Spent Fluid Removal through Vent Holes on the Target Surface. Part 2: Local Heat Transfer,'' J. Eng. Power, **105**, pp. 393–402.
[3] Nazari, A., and Andrews, G. E., 1999, ''Impingement/Effusion Cooling: Influence of Number of the Holes and Pressure Loss on Film and Heat Transfer Coefficient,'' Proc. 7th IGTC, **2**, 1999, pp. 638–648.
[4] Cho, H. H., and Goldstein, R. J., 1996, ''Effect of Hole Arrangements on Impingement/Effusion Cooling,'' *Proc. 3rd KSME-JSME Thermal Engineering Conf.*, pp. 71–76.
[5] Cho, H. H., and Rhee, D. H., 2001, ''Local Heat/Mass Transfer Measurement on the Effusion Plate in Impingement/Effusion Cooling System,'' J. Turbomach., **123**, pp. 601–608.
[6] Rhee, D. H., Choi, D. H., and Cho, H. H., 2003, ''Heat (Mass) transfer on Effusion Plate in Impingement/Effusion Cooling Systems,'' J. Thermophys. Heat Transfer, **17**, No. 1, pp. 95–102.
[7] Metzger, D. E., and Korstad, R. J., 1992, ''Effects of Crossflow in Impingement Heat Transfer,'' J. Eng. Power, **94**, pp. 35–41.
[8] Behbahani, A. I., and Goldstein, R. J., 1983, ''Local Heat Transfer to Staggered Arrays of Impinging Circular Air Jets,'' J. Eng. Power, **105**, pp. 354–360.
[9] Florschuetz, L. W., Metzger, D. E., and Su, C. C., 1984, ''Heat Transfer Characteristics for Jet Array Impingement With Initial Crossflow,'' J. Heat Transfer, **106**, pp. 34–41.
[10] Haiping, C., Wanbing, C., and Taiping, H., 1999, ''3-D Numerical Simulation of Impinging Jet Cooling with Initial Crossflow,'' ASME paper no. 99-GT-256.
[11] Rhee, D. H., Yoon, P. H., and Cho, H. H., 2003, ''Local Heat/Mass Transfer and Flow Characteristics of Array Impinging Jets with Effusion Holes Ejecting Spent Air,'' Int. J. Heat Mass Transfer, **46**, pp. 1049–1061.
[12] Bailey, J. C., and Bunker, R. S., 2002, ''Local Heat Transfer and Flow Distributions for Impinging Jet Arrays of Dense and Sparse Extent,'' ASME paper no. GT-2002-30473.
[13] Gao, L., Ekkad, S. V., and Bunker, R. S., 2003, ''Impingement Heat Transfer Under Linearly Stretched Arrays of Holes,'' ASME paper no. GT-2003-38178.
[14] Rhee, D. H., Choi, J. H., and Cho, H. H., 2003, ''Flow and Heat (Mass) Transfer Characteristics in an Impingement/Effusion Cooling System with Crossflow,'' J. Turbomach., **125**, pp. 74–82.
[15] Haiping, C., Dalin, Z., and Taiping, H., 1997, ''Impingement Heat Transfer from Rib Roughened Surface within Arrays of Circular Jets: The Effects of the Relative Position of the Jet Hole to the Ribs,'' ASME paper no. 97-GT-331.
[16] Haiping, C., Jingyu, Z., and Taiping, H., 1998, ''Experimental Investigation on Impingement Heat Transfer from Rib Roughened Surface within Arrays of Circular Jets: Effect of Geometric Parameters,'' ASME paper no. 98-GT-208.
[17] Andrews, G. E., Abdul Hussain, R. A. A., and Mkpadi, M. C., 2003, ''Enhanced Impingement Heat Transfer: Comparison of Co-flow and Cross-flow with Rib Turbulators,'' *Proc. IGTC2003, Paper No. IGTC2003*, Tokyo TS-075.
[18] Cho, H. H., and Goldstein, R. J., 1995, ''Heat (Mass) Transfer and Film Cooling Effectiveness with Injection through Discrete Holes—Part I: Within Holes and on the Back Surface,'' J. Turbomach., **117**, pp. 440–450.
[19] Cho, H. H., Wu, S. J., and Kwon, H. J., 2000, ''Local Heat/Mass Transfer Measurements in a Rectangular Duct with Discrete Ribs,'' ASME J. Turbomach., **122**, pp. 579–586.
[20] Han, J. C., Chandra, P. R., and Lau, S. C., 1988, ''Local Heat/Mass Transfer Distributions around 180 deg. Turns in Two-pass Smooth and Rib-Roughened Channels,'' J. Heat Transfer, **110**, pp. 91–98.
[21] Chandra, P. R., Han, J. C., and Lau, S. C., 1988, ''Effect of Rib Angle on Local Heat/Mass Transfer Distribution in a Two-pass Rib-Roughened Channel,'' J. Turbomach., **110**, pp. 233–241.
[22] Ekkad, S. K., and Han, J. C., 1997, ''Detailed Heat Transfer Distributions in Two-pass Square Channels with Rib Turbulators,'' Int. J. Heat Mass Transfer, **40**, No. 11, pp. 2525–2537.
[23] Liou, T. M., and Hwang, J. J., 1993, ''Effect of Ridge Shapes on Turbulent Heat Transfer and Friction in a Rectangular Channel,'' Int. J. Heat Mass Transfer, **36**, No. 4, pp. 931–940.
[24] Goldstein, R. J., and Cho, H. H., 1995, ''A Review of Mass Transfer Measurement Using Naphthalene Sublimation,'' Exp. Therm. Fluid Sci., **10**, pp. 416–434.
[25] Eckert, E. R. G., Analogies to Heat Transfer Processes, in *Measurements in Heat Transfer*, edited by Eckert, E. R. G., and Goldstein, R. J., 1976, pp. 397–423, Hemisphere Pub., New York.
[26] Kline, S. J., and McClintock, F., 1953, ''Describing Uncertainty in Single Sample Experiments,'' Mech. Eng. (Am. Soc. Mech. Eng.), **75**, pp. 3–8.
[27] Fluent 6.1 User's Guide Volume 2 (Chaps. 8–19), 2003.
[28] Dittus, P. W., and Boelter, L. M. K., 1930, Univ. Calif. Publ. Eng., **2**, No. 13, pp. 443–461; reprinted in 1985 Int. Commun. Heat Mass Transfer, **12**, pp. 3–22.
[29] Chandra, P. R., Niland, M. E., and Han, J. C., 1995, ''Turbulent Flow Heat Transfer and Friction in a Rectangular Channel with Varying Number of Ribbed Walls,'' ASME J. Turbomach., **119**, pp. 374–380.
[30] Cavellero, D., and Tanda, G., 2002, ''An Experimental Investigation of Forced Convection Heat Transfer in Channels with Rib Turbulators by means of Liquid Crystal Thermography,'' Exp. Therm. Fluid Sci., **26**, pp. 115–121.
[31] Hermanson, K., Parneix, S., Von Wolfersdorf, J., and Semmler, K., 2001, ''Prediction of Pressure Loss and Heat Transfer in Internal Cooling Passages,'' Heat Transfer in Gas Turbine Systems, Annals of the New York Academy of Sciences, **932**, pp. 448–455.
[32] Hermanson, K., Kern, S., Picker, G., and Parneix, S., 2003, ''Predictions of External Heat Transfer for Turbine Vanes and Blades With Secondary Flowfields,'' J. Turbomach., **125**, pp. 107–113.

# Large Eddy Simulation of Flow and Heat Transfer in a 90 deg Ribbed Duct With Rotation: Effect of Coriolis and Centrifugal Buoyancy Forces

**Samer Abdel-Wahab**

**Danesh K. Tafti**
e-mail: dtafti@vt.edu

Mechanical Engineering Department,
Virginia Tech,
Blacksburg, Virginia 24061 USA

*Results from large eddy simulations (LES) of fully developed flow in a 90 deg ribbed duct are presented with rib pitch-to-height ratio $P/e=10$ and a rib height-to-hydraulic-diameter ratio $e/D_h=0.1$. Three rotation numbers $Ro=0.18$, 0.36, and 0.68 are studied at a nominal Reynolds number based on bulk velocity of 20 000. Centrifugal buoyancy effects are included at two Richardson numbers of $Ri=12$, 28 (Buoyancy parameter, $Bo=0.12$ and 0.30) for each rotation case. Heat transfer augmentation on the trailing side of the duct due to the action of Coriolis forces alone asymptotes to a value of $3.7\pm5\%$ by $Ro=0.2$. On the other hand, augmentation ratios on the leading surface keep decreasing with an increase in rotation number with values ranging from 1.7 at $Ro=0.18$ to 1.2 at $Ro=0.67$. Secondary flow cells augment the heat transfer coefficient on the smooth walls by 20% to 30% over a stationary duct. Centrifugal buoyancy further strengthens the secondary flow cells in the duct cross-section which leads to an additional increase of 10% to 15%. Buoyancy also accentuates the augmentation of turbulence near the trailing wall of the duct and increases the heat transfer augmentation ratio 10% to 20% over the action of Coriolis forces alone. However, it does not have any significant effect at the leading side of the duct. The overall effect of buoyancy on heat transfer augmentation for the ribbed duct is found to be less than 10% over the effect of Coriolis forces alone. Friction on the other hand is augmented 15% to 20% at the highest buoyancy number studied. Comparison with available experiments in the literature show excellent agreement.* [DOI: 10.1115/1.1791648]

## 1 Introduction

Since their introduction shortly before World War II, gas turbine engines have replaced reciprocating engines in nearly all civilian and military aircraft. The increase in use of gas turbines for power generation is also remarkable. As consumer demand for more performance and efficiency grew, so did the challenge for turbine blade designers. Turbine inlet temperatures of modern gas turbine engines are well above the blade melting point temperatures. This requires aggressive cooling techniques with the use of bleed air from the compressor. Understanding the physics of internal cooling passages is crucial to making full use of such bleed air and continuing the progress of gas turbine design.

One of the benefits of accurate prediction of surface temperatures of turbine blades is the ability to predict blade life and time between engine overhauls. Numerous industry sources report that turbine blade life is very sensitive to turbine surface temperatures. However, accurate prediction is not trivial because of the complexities introduced by turbulent promoters and blade rotation. The vast majority of published work in the numerical prediction of internal duct heat transfer uses Reynolds averaged Navier-Stokes (RANS) models. These models, while computationally cheap are not always reliable over the range of physical conditions encountered in internal cooling flows. In large eddy simulation (LES), the time-dependent evolution of Navier-Stokes equations are solved for the majority of the relevant scales of turbulence. Only the smallest scales are modeled using subgrid scale models. The most popular subgrid scale model is the eddy-viscosity model proposed by Smagorinsky [1]. Later, Germano et al. [2] proposed a modification to the Smagorinsky model which allowed for dynamically calculating the Smagorinsky constant $C_s$ based on local flow conditions. LES in general is more accurate and repeatable than RANS. A drawback of LES is computational expense, however, the exponential increase in computational performance and the continuous drop in hardware price is removing this limitation.

**A Previous Numerical Studies.** LES was performed by Watanabe and Takahashi [3] for fully developed nonrotating ribbed duct flow. The Reynolds number based on the bulk velocity was 107,000. Results from their analysis agreed well with their experimental results. Murata et al. [4–6] considered the effects of centrifugal buoyancy on rotating ribbed duct flow. The parameters $e/D_h$ and $P/e$ were 0.1 and 10, respectively. The aspect ratio varied from 0.25 to 4, and the rotation numbers varied between 0 and 0.2. The Reynolds number ranged from 480 to 12,000. LES was performed with the Lagrangian dynamic subgrid scale model and results from these studies agreed fairly well with experimental results.

Iacovides and Launder [7] performed a numerical study of fully developed flow in a rotating rectangular duct. The standard high Reynolds number $k$-$\varepsilon$ model was used for the bulk of the flow. Near the wall, a low Reynolds number one-equation model was used. Secondary flow was correctly predicted, however, there was only qualitative agreement between predicted and experimental heat transfer results.

Developing flow in an orthogonally rotating square duct was

Contributed by the International Gas Turbine Institute (IGTI) of THE AMERICAN SOCIETY OF MECHANICAL ENGINEERS for publication in the ASME JOURNAL OF TURBOMACHINERY. Paper presented at the International Gas Turbine and Aeroengine Congress and Exhibition, Vienna, Austria, June 13–17, 2004, Paper No. 2004-GT-53799. Manuscript received by IGTI, October 1, 2003; final revision, March 1, 2004. IGTI Review Chair: A. J. Strazisar.

  

studied by Bo et al. [8] for two rotation numbers. Three turbulence models were used in the analysis: a $k$-$\varepsilon$ eddy viscosity model (EVM) with a low Reynolds number one-equation EVM near the wall, a low Reynolds number algebraic stress model, and a low Reynolds number $k$-$\varepsilon$ EVM. The first model gave very poor results. The second model performed well, but only for low rotation. The third model performed best of all, when buoyancy effects were considered. For all the models, results deviated significantly from experimental data for $x/D_h$ greater than 5.

Prakash and Zerkle [9] used the standard $k$-$\varepsilon$ model to simulate outward flow and heat transfer in a smooth square duct with radial rotation. Coriolis and buoyancy forces were included only in the mean equations. The Reynolds number was kept at 25,000 and the rotation numbers were 0.24 and 0.48. Simulations were done for buoyancy parameters of 0.01 and 0.13. The low buoyancy parameter simulations did not match trends from experimental data. However, results from the high buoyancy parameter simulations were in qualitative agreement with experimental data. The authors attributed the quantitative disagreement to the need for including rotation and buoyancy effects in the $k$-$\varepsilon$ model, among other things. The same authors [10] used the $k$-$\varepsilon$ model with wall functions in a ribbed duct with and without rotation. As in the smooth duct, their predictions showed good qualitative agreement. Ooi et al. [11] used RANS simulations to study heat transfer in a ribbed duct. Three turbulence models were used: the low-Re $k$-$\varepsilon$, the $v^2$-$f$ model, and the Spalart-Allmaras model. The first model was found to be inadequate. The $v^2$-$f$ model captured more of the physics of the flow but was still lacking in some respects. The $v^2$-$f$ model failed to capture secondary flow, which is responsible for sidewall impingement, and the result was a large discrepancy between experimental data and numerical predictions for heat transfer on the side walls.

An eddy-viscosity and an algebraic stress model were used to predict heat transfer in a ribbed duct with no rotation by Saidi and Sunden [12]. The parameters $e/D_h$ and $P$/e were 0.1 and 9, respectively. Although the averaged Nusselt numbers were in reasonable agreement with data, there were some errors in the trends of the data. For example, both models significantly underpredicted heat transfer enhancement on the side wall near the ribs and significantly overpredicted heat transfer on the center side wall locations. The authors recommended that current RANS models were perhaps insufficient for predicting detailed local heat transfer in internal ribbed duct cooling. They suggested that new RANS models be developed based on experimental data.

**B Previous Experimental Studies.** Experimental work in the area of internal duct cooling is challenging because of the general difficulty of measuring detailed surface heat transfer and flow data inside a duct. This is especially true for a rotating duct. As a result, there are few published papers with detailed surface heat transfer data and mean flow data. One of the most prolific groups in the area of internal cooling duct research has been Han's group at Texas A&M, College Station, TX. Parsons et al. [13] showed the results of different wall heating conditions on heat transfer in a two-pass 90 deg ribbed duct. Reynolds numbers varied from 2500 to 25 000, and rotation numbers were in the range 0–0.352. Three different heating conditions were tested: constant heat flux, constant temperature, and trailing wall hotter than leading wall. Generally, heat transfer on the ribbed walls was two to three times higher than those for a smooth wall with the same rotation number.

Ekkad and Han [14] studied the effects of ribs of various arrangements. Experiments were performed on a two-pass smooth duct and on ducts with 90 deg, 60 deg, 60 deg V, and 60 deg broken V ribs. Reynolds numbers were in the range 12,000–60,000. The 60 deg V and the 60 deg broken V produced the highest heat transfer enhancement. The high heat transfer on top of the ribs was attributed to flow impingement. They found that low heat transfer immediately behind the ribs was related to the counter-rotating vortex.

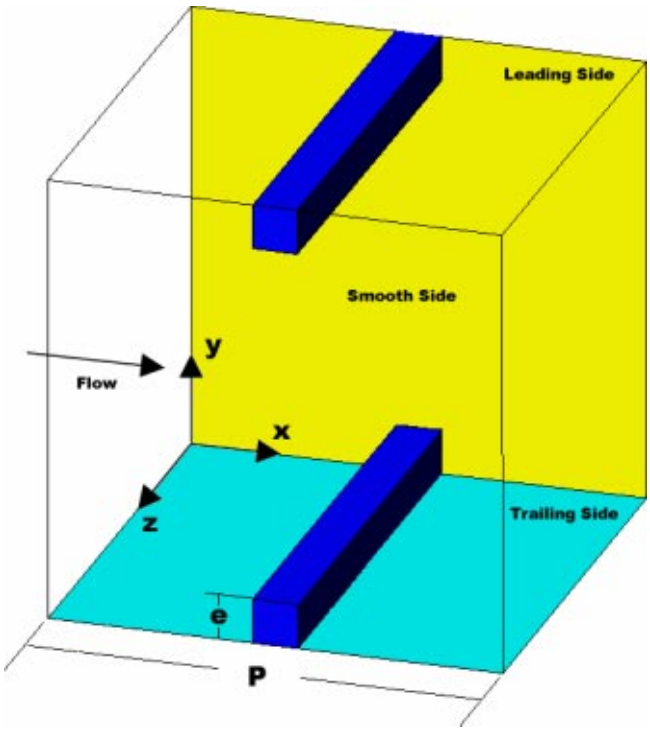


**Fig. 1 Streamwise periodic computational domain. Flow is in the $x$ direction and rotation vector is along the $+ve$ $z$-axis.**

Wagner et al. [15] studied rotating duct flow with rounded 90 deg ribs. The rotation number varied from 0 to 0.35 and the density ratio ranged from 0 to 0.23. For all of the experiments, the Reynolds number was kept constant at 25 000. Changes in rotation were found to contribute significantly to overall heat transfer for radially inward and radially outward flow. It was found that heat transfer on the trailing side was strongly affected by buoyancy for radially outward flow but was relatively unaffected by buoyancy for radially inward flow. Increasing buoyancy parameter for high rotation numbers caused an increase in overall heat transfer but more so for inward flows than for outward flows.

Due to advances in experimental instrumentation, researchers have been able to gather more detailed turbulence and heat transfer data from experiments. For example, Liou et al. [16] studied heat transfer and fluid flow in a rotating two-pass duct with 90 deg ribs. Laser Doppler velocimetry and transient thermochromic liquid crystal measurements were used to acquire the flow and heat transfer data. The parameters $P/e$ and $e/D_h$ were 10 and 0.136, respectively. The Reynolds number was kept at 10,000, and the rotation number was in the range 0–0.2. Heat transfer on the trailing side of the first pass (outward flow) systematically increased with an increase of rotation number, while heat transfer on the leading side of the first pass was systematically reduced.

Previous experiments have indicated that centrifugal buoyancy has a substantial effect on heat transfer at high rotation numbers. Our objective in this study is to evaluate LES in rotating duct flows at relatively high Reynolds numbers and rotation numbers and to quantify the role played by buoyancy forces over the above the action of Coriolis forces. No such detailed comprehensive validated study exists in the literature at the conditions presented here. Three rotation numbers, Ro=0.18, 0.35, and 0.67 and two nominal Richardson numbers, Ri=12 and 28 at Re=20,000 are calculated.

## 2 Computational Model and Governing Equations

The computational model assumes fully developed flow and heat transfer and simulates a periodically repeating spatial unit consisting of two ribs (one on either side of the duct) as shown in **Fig. 1**. The procedures used to solve the governing equations are

identical to that given in Abdel-Wahab and Tafti [17] with the inclusion of the centrifugal buoyancy term in the momentum equation. The duct walls as well as all six faces of the two ribs exposed to the main flow are heated by imposing a constant heat flux ($q''$) boundary condition. The duct is subjected to orthogonal rotation with axis along the positive $z$ direction at an angular velocity $\omega_z$ rad/s. The governing flow and energy equations are non-dimensionalized by a characteristic length scale which is chosen to be the hydraulic diameter of the channel ($D_h$), a characteristic velocity scale given by the friction velocity $u_\tau = \sqrt{\Delta P_x/\rho}$, and a characteristic temperature scale given by $q''D_h/k$. The assumed periodicity of the domain in the streamwise or $x$ direction requires that the mean gradients of pressure and temperature be isolated from the fluctuating periodic components as follows:

$$P(\vec{x},t) = P_{\text{in}} - \beta x + p(\vec{x},t)$$
$$T(\vec{x},t) = T_{\text{in}} + \gamma x + \theta(\vec{x},t) \tag{1}$$

On substitution into the Navier-Stokes and energy equations, the *nondimensional* time-dependent equations in transformed coordinates $\vec{\xi} = \vec{\xi}(\vec{x})$ take the following conservative form:[1]

Continuity:

$$\frac{\partial}{\partial \xi_j}(\sqrt{g}\overline{U^j}) = 0 \tag{2}$$

Momentum:

$$\frac{\partial}{\partial t}(\sqrt{g}\overline{u_i}) + \frac{\partial}{\partial \xi_j}(\sqrt{g}\overline{U^j}\overline{u_i}) = -\frac{\partial}{\partial \xi_j}(\sqrt{g}(\vec{a}^j)_i\overline{p}) + \frac{\partial}{\partial \xi_j}\left[\left(\frac{1}{\text{Re}_\tau} + \frac{1}{\text{Re}_{t_\tau}}\right)\sqrt{g}g^{jk}\frac{\partial \overline{u_i}}{\partial \xi_k}\right] + \sqrt{g}\beta\delta_{i1} - 2\sqrt{g}(Ro_\tau)\overline{u}_m \in_{i3m} - \sqrt{g}Ri_\tau(\overline{\theta} - \overline{\theta}_{ref})\delta_{i1} \tag{3}$$

Energy:

$$\frac{\partial}{\partial t}(\sqrt{g}\overline{\theta}) + \frac{\partial}{\partial \xi_j}(\sqrt{g}\overline{U^j}\overline{\theta}) = \frac{\partial}{\partial \xi_j}\left[\left(\frac{1}{\text{Pr}\,\text{Re}_\tau} + \frac{1}{\text{Pr}_t\,\text{Re}_{t_\tau}}\right)\sqrt{g}g^{jk}\frac{\partial \overline{\theta}}{\partial \xi_k}\right] - \sqrt{g}\gamma\overline{u_1} \tag{4}$$

where $\vec{a}^i$ are the contravariant basis vectors, $\sqrt{g}$ is the Jacobian of the transformation, $g^{ij}$ are the elements of the contravariant metric tensor, $\sqrt{g}U^j = \sqrt{g}(\vec{a}^j)_i u_i$ is the contravariant flux vector, $u_i$ is the Cartesian velocity vector, $\text{Ro}_\tau$ is the rotation number, $\text{Ri}_\tau$ is the Richardson number, and $\theta$ is the modified temperature. $\text{Re}_{t_\tau}$ is the inverse of the nondimensional subgrid eddy-viscosity and is modeled by the dynamic Smagorinsky model. Details of this procedure are given in Abdel-Wahab and Tafti [17].

In Eq. (3), both the rotational Coriolis forces and the centrifugal buoyancy forces are included in the formulation. In the context of a periodic fully developed flow, buoyancy number does not change with the radial or streamwise location. In a developing flow, the effect of centrifugal buoyancy is strongest at the inlet to the duct and gets weaker as the temperature approaches the wall temperature in the streamwise direction. The fully developed calculations assume that the same buoyancy number is acting over the periodic pitch and represents one $x$ location (or a pitch surrounding one $x$ location) in a corresponding developing flow.

In formulating Eq. (3) the following assumptions are made: the mean centrifugal force is combined with the mean pressure gradient term; the effect of variable density due to temperature differences only manifests itself through the centrifugal force term; centrifugal buoyancy is only consequential in the balance of $x$ momentum, its contribution to the balance of $y$ momentum is deemed to be negligible (the radial vector has a small component in the $y$ direction); and for compatibility with the fully developed formulation, the Richardson number represents a fixed radial location and is constant.

The mean pressure gradient $\beta$ is assumed to be unity, whereas $\gamma$ is calculated from a global energy balance as $\gamma = q''\Omega/\text{Re}_\tau \text{Pr} Q_x L_x$. The boundary conditions imposed on the duct walls and the ribs are as follows:

$$\vec{u} = 0$$
$$\vec{\nabla} p \cdot \vec{n} = 0 \tag{5}$$
$$\vec{\nabla}\theta \cdot \vec{n} = 1 - \gamma \vec{e}_x \cdot \vec{n}$$

and in the streamwise direction as

$$\phi(x + L_x) = \phi(x), \quad \phi = \vec{u},\ p \text{ and } \theta. \tag{6}$$

The governing equations for momentum and energy are discretized with a conservative finite-volume formulation using a second-order central difference scheme on a non-staggered grid topology. The Cartesian velocities, pressure, and temperature are calculated and stored at the cell center, whereas contravariant fluxes are stored and calculated at the cell faces. For the time integration of the discretized continuity and momentum equations, a projection method is used. The temporal advancement is performed in two steps, a predictor step, which calculates an intermediate velocity field, and a corrector step, which calculates the updated velocity at the new time step by satisfying discrete continuity. The energy equation is advanced in time by the predictor step. Details about the algorithm, functionality, and capabilities of the computer program GENIDLEST (generalized incompressible direct and large-eddy simulations of turbulence) can be found in Tafti [18].

## 3 Computational Details

In this paper, calculations for three nominal rotation numbers Ro=0.18, 0.35, and 0.67 and two Richardson numbers, Ri=12 and 28, at a nominal bulk Reynolds number of 20,000 are presented. The Richardson numbers correspond to buoyancy parameters, Bo=0.12 and 0.3. For each case, the dynamic Smagorinsky subgrid stress model is used on a $128^3$ mesh. **Table 1** summarizes all the calculations. Also shown in Table 1 are the results of Abdel-Wahab and Tafti [17] considering only the effects of Coriolis forces. The mesh distribution is exactly the same as used in earlier studies (Tafti [19]; Abdel-Wahab and Tafti [17]) and which have yielded reliable and accurate predictions for stationary as well as rotating ducts. At Ro=0.74 and Ri=27, a posteriori evaluation of the mesh in wall units based on local friction shows that $\Delta_\perp^+ \ll 1.0$ over the majority of the duct and rib surfaces, with streamwise $\Delta_{\|1}^+$, and spanwise $\Delta_{\|2}^+$ varying between 10 to 70 wall units.

Initial conditions are obtained from previous calculations. The flow and heat transfer is then allowed to reach a stationary state for approximately five nondimensional time units. Once stationary conditions are established, statistical sampling of the data is initiated for approximately 5.5 nondimensional time units. The sample size is doubled by using $z$-directional symmetry of the flow and presenting the mean and turbulent quantities in half of the duct cross section.

The local Nusselt number is calculated as

$$\text{Nu} = \frac{1}{\theta_s - \theta_{\text{ref}}} \tag{7}$$

where $\theta_s$ is the surface temperature and $\theta_{\text{ref}}$ is the reference temperature defined as[2]

[1] Henceforth, all usage is in terms of nondimensionalized values.

[2] For time-averaged Nusselt number $\theta_s$ and $\theta_{ref}$ are calculated from the time averaged temperature field.

**Table 1 Summary of heat transfer and friction results for three rotation cases and three buoyancy cases**

| | Rotation 1 | | | Rotation 2 | | | Rotation 3 | | |
|---|---|---|---|---|---|---|---|---|---|
| | Buoy 1 | Buoy 2 | Buoy 3 | Buoy 1 | Buoy 2 | Buoy 3 | Buoy 1 | Buoy 2 | Buoy 3 |
| $Re_\tau$ | 6660 | 6660 | 6660 | 6660 | 6660 | 6660 | 6660 | 6660 | 6660 |
| Re | 18 821 | 19 008 | 17 516 | 18 981 | 18 268 | 17 269 | 19 980 | 19 454 | 18 095 |
| $Ro_\tau$ | 0.5 | 0.5 | 0.5 | 1 | 1 | 1 | 2 | 2 | 2 |
| Ro | 0.18 | 0.18 | 0.19 | 0.35 | 0.36 | 0.39 | 0.67 | 0.68 | 0.74 |
| $Ri_\tau$ | 0 | 100 | 200 | 0 | 100 | 200 | 0 | 100 | 200 |
| Ri | 0 | 12.3 | 28.9 | 0 | 13.3 | 29.7 | 0 | 11.7 | 27.1 |
| Bo | 0 | 0.12 | 0.29 | 0 | 0.13 | 0.31 | 0 | 0.12 | 0.29 |
| | $\overline{Nu}/Nu_0$ | | | $(Nu_0 = 0.023 \times Re_b^{0.8} \cdot Pr^{0.4})$ | | | | | |
| Ribs | 3.38 | 3.26 | 3.52 | 2.97 | 3.37 | 3.40 | 2.78 | 3.09 | 3.08 |
| Leading | 1.71 | 1.43 | 1.43 | 1.36 | 1.37 | 1.27 | 1.18 | 1.12 | 1.11 |
| Trailing | 3.70 | 3.69 | 4.13 | 3.63 | 4.18 | 4.41 | 3.76 | 4.17 | 4.33 |
| Smooth | 2.32 | 2.31 | 2.47 | 2.32 | 2.62 | 2.67 | 2.45 | 2.66 | 2.62 |
| Overall with ribs | 2.62 | 2.54 | 2.74 | 2.48 | 2.79 | 2.84 | 2.50 | 2.71 | 2.72 |
| | $f/f_0$ | | | $(f_0 = 0.046 \times Re_b^{-0.2})$ | | | | | |
| Overall | 9.75 | 9.57 | 11.09 | 9.6 | 10.28 | 11.38 | 8.75 | 9.18 | 10.46 |

$$\theta_{\text{ref}} = \frac{\int\int |u_1| \theta dA_x}{\int\int |u_1| dA_x}. \tag{8}$$

The surface-averaged Nusselt number is obtained by averaging the local Nusselt number as

$$\langle \text{Nu} \rangle = \frac{1}{\int\int_\Omega dS} \left[ \int \int_\Omega \frac{1}{\theta_s - \theta_{\text{ref}}} dS \right] \tag{9}$$

where $S$ denotes the surface under consideration. Based on the applied nondimensional pressure gradient of unity, the Fanning friction factor is calculated as

$$f = \frac{1}{2 \times \overline{u_b^2}}. \tag{10}$$

To calculate the augmentation ratio, reference values for Nusselt number and friction factor for a smooth duct are obtained from the Dittus-Boelter and Blasius correlation, respectively [20].

$$\text{Nu}_0 = 0.023 \times \text{Re}_b^{0.8} \times \text{Pr}^{0.4} \tag{11}$$

and

$$f_0 = 0.046 \times \text{Re}_b^{-0.2} \tag{12}$$

The predicted heat transfer results are compared with data of Liou et al. [16], Wagner et al. [15], and Parsons et al. [13]. The Buoyancy number (Bo) is commonly used to quantify the effect of centrifugal buoyancy. In the present context, the Buoyancy parameter (Bo) is related to the Richardson number ($\text{Ri}_\tau$) by the following expression:

$$\text{Bo} = \frac{\Delta\rho}{\rho_0} \frac{r}{D_h} \text{Ro}^2 \approx \frac{\text{Ri}_\tau \overline{(\theta_s - \theta_{\text{ref}})}}{\overline{u_b^2}} \tag{13}$$

where the quantity under the bar is area averaged over all heat transfer surfaces in the duct. The equivalent Buoyancy numbers for the different calculations are presented in **Table 1**. They have nominal values of 0.12 and 0.3, respectively, for the two Richardson numbers.

## 4 Results and Discussion

Rotation induced Coriolis forces have two significant effects on the flow and heat transfer [17]. The first effect is the destabilization and augmentation of turbulence at the trailing side of the duct together with stabilization and attenuation on the leading side. Another effect of Coriolis forces is the generation of secondary flow cells in the cross section of the duct, which develop strong upwash and/or downwash regions. The direct effect on turbulent structure has a large effect on the heat transfer at the trailing and leading ribbed walls of the duct. The heat transfer coefficient on the trailing wall of the duct increases 50% to 60% over a nonrotating duct, whereas at the leading wall, the heat transfer coefficient decreases 30% to 50% for Ro=0.18 to 0.67. The most obvious effect of the secondary flow is the augmentation of heat transfer at the side walls of the duct caused by the strong movement of fluid from the trailing to the leading wall along the smooth wall. This results in augmentations of 20% to 30% over a stationary duct.

Centrifugal buoyancy can either complement or oppose the effect of Coriolis forces. Through the action of Coriolis forces, fluid in the vicinity of the trailing duct wall is cooler than at the leading wall for radially outward flow. The higher density exposes the fluid at the trailing wall to a larger centrifugal force than at the leading side of the duct and complements the effect of Coriolis forces. If the flow is radially inward, the leading wall of the duct will have cooler fluid temperatures in its vicinity than the trailing wall by the action of Coriolis forces. In this case, the centrifugal buoyancy body force is larger at the leading wall but opposes the action of Coriolis forces because of its outward direction.

**Table 1** summarizes all the major results of this study. In all cases, centrifugal buoyancy complements the effect of Coriolis forces. A total of six cases are presented, for three Rotation numbers and two Richardson numbers. The exclusive effect of Coriolis forces have been presented in Ref. [17].

Coriolis forces have the effect of shrinking the recirculation bubble behind the rib from its stationary value. The reattachment length on the trailing side decreases with rotation and asymptotes to a value between $3.6-3.8e$ by Ro=0.18, versus $4-4.25e$ without rotation. Centrifugal buoyancy forces do not have any noticeable effect on the extent of the recirculation region on the trailing side of the duct. However, they add considerably to the Coriolis force effect on the leading side of the duct. **Figure 2** shows the mean streamlines at the leading wall in the center of the duct at $z=0.5$ for three Richardson numbers and two rotation numbers. At both rotation numbers, Ro=0.35 and 0.68, there is a substantial increase in the reattachment length with increasing Richardson number, till eventually the recirculation bubble extends the full length of the rib pitch. The increase in the extent of the separation zone has a slight effect on the heat transfer coefficient, which is already attenuated substantially from its stationary value by the action of Coriolis forces.

**Figure 3(*a*)** shows the distribution of mean cross-stream velocity ($v_b$) and mean spanwise velocity ($w_b$) in different halves of the duct cross section at the rib for Ro=0.35, where it is assumed that the flow is symmetric about the center $z$ plane. Two secondary flow cells can be identified in each half of the cross section. The strong cross-stream velocity in the vicinity of the smooth wall and the center of the duct represents the upwash regions of two struc-

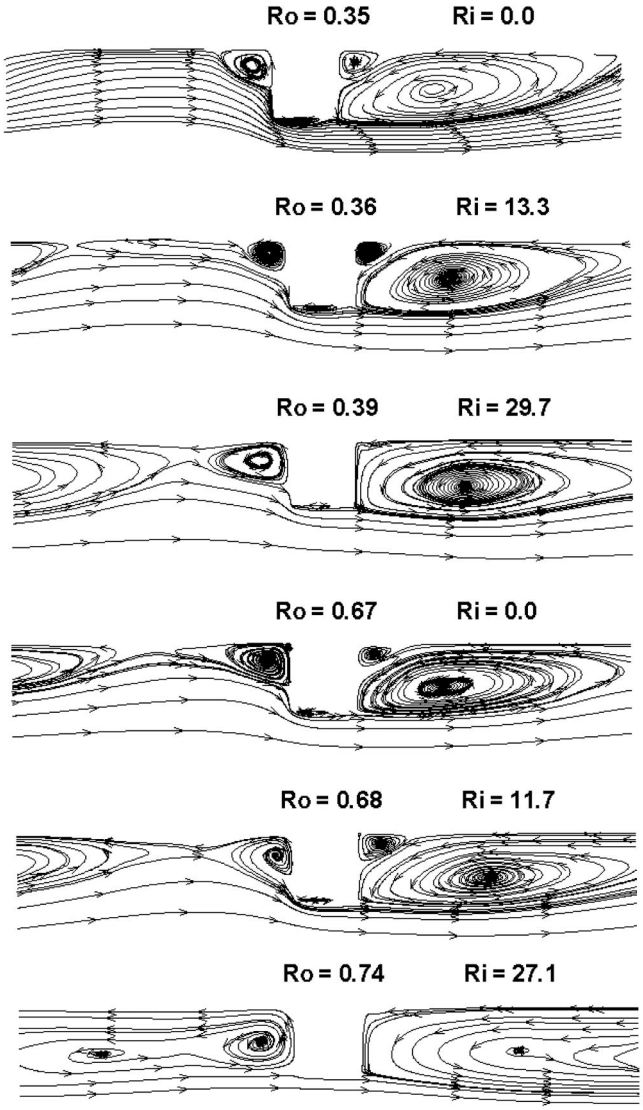


**Fig. 2 Mean streamlines on the leading side of the center plane $z=0.5$ for two rotation numbers and increasing Richardson number. The large separation region behind the rib grows on the leading side, while remaining constant on the trailing side (not shown).**

tures which originate at the trailing side. The structures are dominant near the trailing side but do not quite extend all the way to the leading side of the duct. The high velocities induced by the secondary flow in the vicinity of the smooth wall lead to augmentation of heat transfer coefficients. The high lateral velocities that impinge on the smooth wall at the trailing side on the rib are also present for a nonrotating duct but are largely localized unlike the organized motion seen here throughout the length of the duct. Similar flow structures were found to exist for the other rotation numbers as well. **Figures 3(*b*)–3(*c*)** shows the effect of centrifugal buoyancy on the secondary flow cells for Ro=0.35 at the two Richardson numbers. At Ri=13, the overall strength of the cell near the smooth wall increases. Vertical velocities as high as 0.75 (versus 0.55 at Ri=0) of the bulk mean velocity are observed in the vicinity of the smooth wall and transverse impingement velocities on top of the rib increase to 0.36 (versus 0.31 at Ri=0). As the Richardson number increases, the two cells tend to merge into one coherent cell in each half of the cross section. The magnitude or strength of the induced velocities near the smooth wall does not increase when Richardson number increases from 13 to 30. This trend is reflected in the heat transfer augmentation on the smooth walls in **Table 1**. The augmentation ratio increases from 2.32 to 2.62 at Ri=13, but does not increase any further at the higher Richardson number.

**Figure 4(*a*)** shows the effect of Coriolis forces on tke plotted midway between the ribs ($x=0$) at the centerplane ($z=0$). The effect of Coriolis forces on turbulent kinetic energy (tke) is complicated by the fact that they do not make a direct contribution to the production of tke but act through their contributions to the production of streamwise and cross-stream turbulent fluctuations. These in turn affect the production of turbulent shear stress, which feeds back into the production of the streamwise fluctuations and into tke. The interaction between different stress components, and the added effect of secondary flow on the transport of stresses results in very complicated interactions. The net effect of Coriolis forces is to reduce tke at the leading side and augment it on the trailing side, at least at low to moderate rotation numbers. There is a sharp increase in tke at the trailing side at Ro=0.18 in the shear layer and in the near wall region compared to that without rotation. A further increase is seen as the rotation number increases to 0.35 after which there is a marked decrease in the tke. The decrease in the peak value of tke with an increase in rotation number has been alluded to in previous studies in turbulent channel flow. Johnston et al. [21] found that for Ro>0.2 the wall friction on the unstable side reached an asymptotic state and did not increase further with rotation number. They hypothesized that the secondary roll cells in the cross section were responsible for this by interfering with the production of turbulence near the trailing wall. This trend also bears out quite well in the prediction of heat transfer coefficients in the present study. For the three rotation numbers, Ro=0.18, 0.35, and 0.67, the heat transfer augmentation ratio on the trailing side remains fairly constant between 3.6–3.75.

The effect of buoyancy forces on turbulent kinetic energy (tke) is presented in **Figs. 4(*b*)–4(*c*)** at Ro=0.18 and Ro=0.7. At both rotation numbers, there is a steady increase in peak tke in the vicinity of the trailing side wall and a subsequent decrease at the leading side wall. At Ro=0.18, the peak in the boundary layer at the trailing wall varies between 9% at Ri=0 to 15% at Ri=29. At the higher rotation number, Ro=0.7, the peak values vary between 11% at Ri=0 to 18% at Ri=27.

**Figure 5** shows the distribution of resolved turbulent shear stress $\overline{u'v'}$ at the same location as in **Fig. 4** at two rotation numbers, Ro=0.18 and Ro=0.7. At Ro=0.18, as the Richardson number increases from 0 to 12, there is a slight increase in the magnitude of $\overline{u'v'}$ in the trailing side shear layer with little or no change at the leading side. However, at Ri=29, there is a large increase in the magnitude of $\overline{u'v'}$ in the shear layer at the trailing side. Contours of $\overline{u'v'}$ in a plane through the duct center (not shown) indicate a highly energetic separated shear layer with turbulence intensities much higher than normal. A similar pattern can be seen at the highest rotation number Ro=0.7. At Ri=12, there is a slight increase in the magnitude of $\overline{u'v'}$ at the trailing wall with a decrease at the leading wall. Increasing the Richardson number further to 27, increases the magnitude of the shear stress to over 10% at the trailing wall, while damping it to about 1% at the leading wall.

Heat transfer augmentation on the trailing and leading walls correlate directly with the level of tke in the vicinty of the wall. In **Table 1**, at Ro=0.18, there is no overall increase in the augmentation on the trailing wall at Ri=12. A closer look at contours of tke suggests that over the whole trailing surface, the levels of tke are quite similar to those at Ri=0, while there is a noticeable increase as the Richardson number increases to Ri=29. This trend is reflected in the augmentation ratio which increases from 3.7 at Ri=0 and 12 to 4.13 at Ri=29. At the higher rotation number Ro=0.68, there is a steady increase in the augmentation ratio at the trailing wall from 3.76 to 4.17 at Ri=12, to 4.33 at Ri=27. A

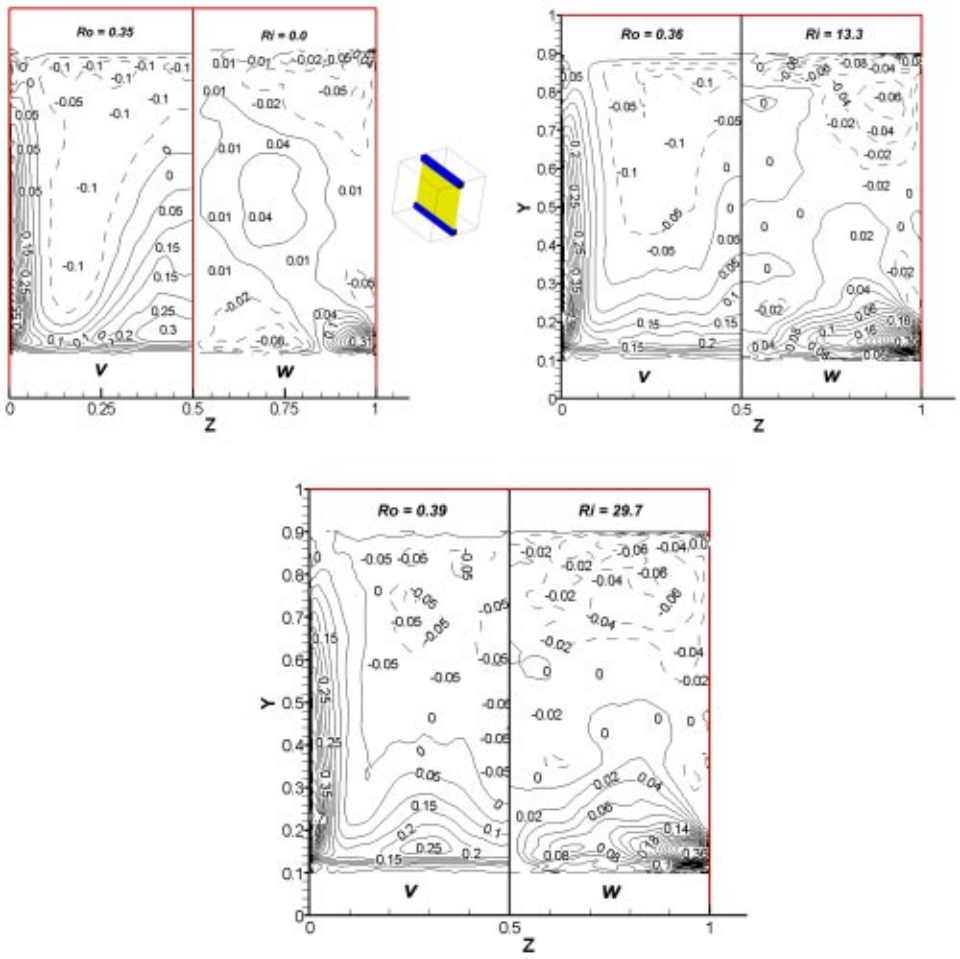


**Fig. 3 Contours of mean velocity at $x=0.5$ at the midrotation number with increasing Richardson number. Illustrated is the strong impingement of flow onto the smooth sidewall which is enhanced by centrifugal buoyancy forces. The left and right sides of the figures show averaged vertical and lateral velocities, respectively. A positive lateral velocity implies impingement on the side wall.**

similar trend is found at the intermediate rotation number Ro $=0.35$. At the leading wall, an increasing Richardson number has minimal effect on the augmentation ratio which is less than $-10\%$ at Ro$=0.35$ and Ro$=0.68$. At lower rotation Ro$=0.18$, the decrease is $-17\%$ at Ri$=12$. The general trends observed are consistent with previous experimental results of Wagner et al. [15] which have suggested that centrifugal buoyancy does not have a large effect on heat transfer augmentation at the leading edge, but augment the heat transfer on the trailing wall as rotation number increases.

**Figure 6** shows the typical surface distribution of heat transfer augmentation ratios at the trailing, leading, and the smooth side wall at Ro$=0.39$ and Ri$=30$. The general pattern of augmentation does not change at the trailing side with an increase in Richardson number. High augmentation ratios occur at the leading edge of the rib which is a result of the highly unsteady eddies which form in this region. This is followed by a region of low augmentation immediately behind the rib in the recirculating region. These values progressively increase to reach their maximums near the region of reattachment, followed by a steady decrease. Compared to the high augmentation ratios on the trailing side, low augmentation ratios between 0.5 and 1.8, dominate the leading side of the duct. On the smooth walls of the duct, once again the pattern of augmentation near the trailing side rib does not vary. As Richardson number increases, the secondary flow gains additional strength as seen in **Fig. 3**, and increases the augmentation ratio in the region where the cross-flow impinges on the smooth wall directly above the rib. Near the leading wall, however, the secondary flow is weakened considerably and augmentation is weak.

Averaged Nusselt number results on the leading and trailing faces for the three rotation numbers and for three buoyancy numbers (including Ri$=0$) are compared with the experiments of Liou et al. [16], Parsons et al. [13], and Wagner et al. [15] in **Fig. 7**. The experimental data of Ref. [16] is at Re$=10\,000$ for $e/D_h=0.136$ and $P/e=10$ and the data of [13] is obtained at Re$=5000$ for $e/D_h=0.125$ and $P/e=10$. The data of Ref. [15] include the effects of buoyancy. The experiments were conducted for a staggered rib arrangement with $e/D_h=0.1$ and $P/e=10$ at Re $=25\,000$. In all cases, fully developed data is extracted for comparison.

The augmentation ratios from Wagner et al. [15] is extracted from their Fig. 9($a$) at $x/d=8.5$ for three inlet density ratios ($\Delta\rho/\rho=0.07$, 0.13, and 0.23). To make meaningful comparisons, the corresponding *local* Buoyancy numbers at $x/d=12$ are obtained from their Fig. 10. Hence each symbol plotted in **Fig. 7** from Wagner's data has a different local buoyancy number associated with it. The buoyancy number associated with each data point is tabulated in **Fig. 7**. At Ro$=0.125$, the local buoyancy numbers range from 0.04 to 0.112, at Ro$=0.25$, from 0.16 to 0.43, and at Ro$=0.35$, from 0.34 to 0.78. Since the augmentation ratios are obtained at $x/D=8.5$, the actual local buoyancy numbers will be slightly higher than these values.

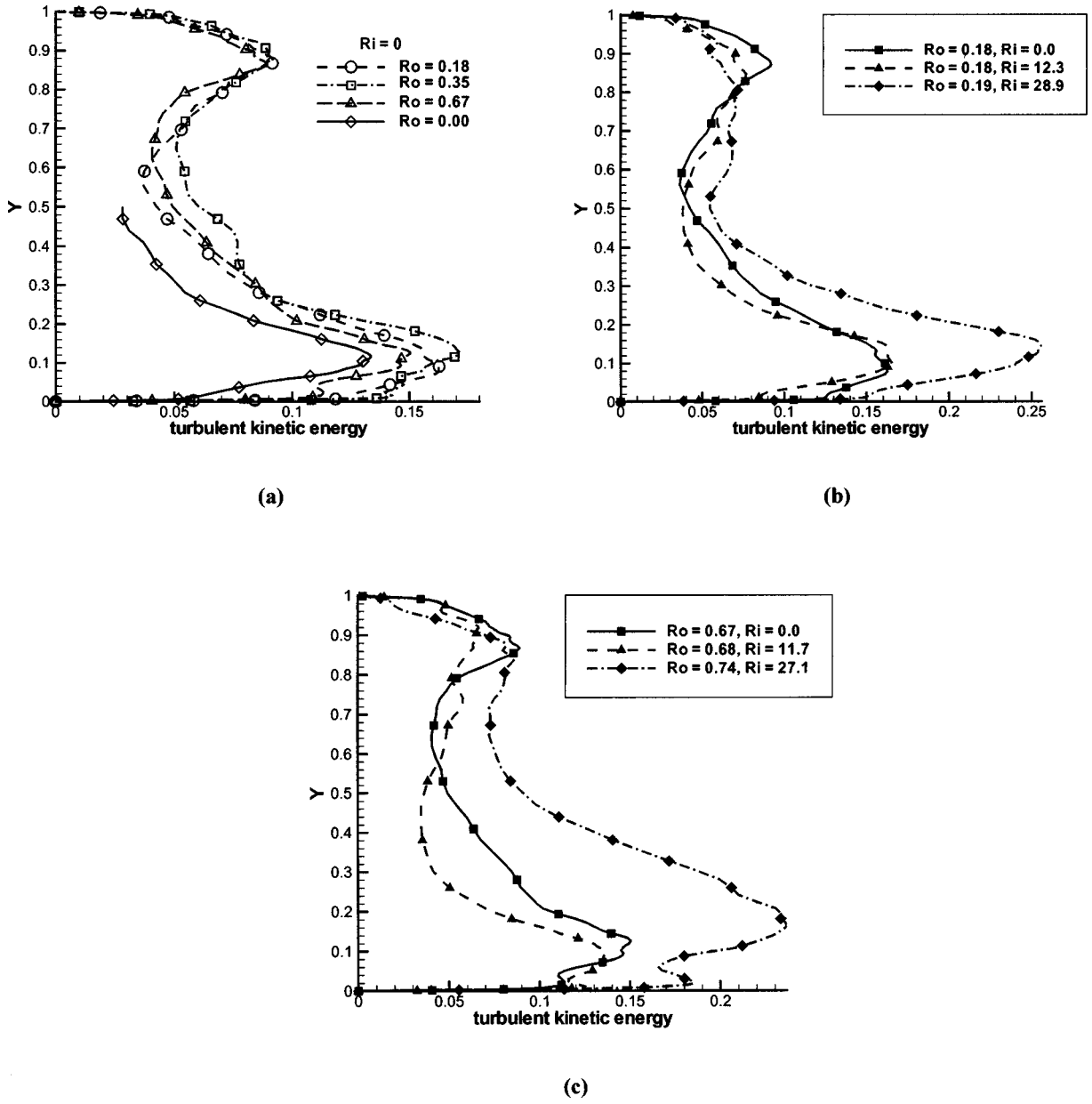


**Fig. 4 Turbulent kinetic energy at the center of the duct and midway between ribs ($x=0$, $z=0.5$). (*a*) Effect of Coriolis forces at different rotation numbers; distribution is symmetric about $y=0.5$ for Ro=0. (*b*) Effect of centrifugal buoyancy at Ro=0.18. (*c*) Effect of buoyancy at Ro=0.68. Generally, tke is increased near the trailing side (bottom) and decreases near the leading side (top). The effect of centrifugal buoyancy on tke is similar to that of Coriolis forces.**

At Ro=0.18, there is good agreement with the results of Parsons et al. [13] and Liou et al. [16] for the case of Ri=0. In general there is excellent agreement with the data of Wagner et al. At the leading side of the duct, the experimental data does not show a strong dependence on the buoyancy number at Ro=0.12 and 0.25. At Ro=0.35, the experimental augmentation ratio shows an initial decrease at Bo=0.34, and then subsequent increases at Bo=0.57 and 0.78. The calculations which have equivalent buoyancy numbers of 0.12 and 0.3 still show a decrease in augmentation ratio with buoyancy consistent with the experiments at low buoyancy numbers. The quantitative agreement is also quite good. At the trailing side of the duct, at low rotation, Ro=0.125, buoyancy has very little effect on the experimental augmentation ratio. As rotation increases to 0.35, the augmentation ratio increases with an increase in buoyancy number from 0.26 to 0.43. These same trends are illustrated by the computations at Ro=0.18 when the buoyancy number increases from 0.12 to 0.3. With further increase in rotation to Ro=0.35, the augmentation ratios on the trailing side exhibit a higher sensitivity to the buoyancy number. Both experiments and computations clearly illustrate this effect. The experimental augmentations increase from 3.6 at Bo=0.34 to 4.6 at Bo=0.78, whereas the computational augmentation ratios increase from 3.6 at Bo=0 to 4.4 at Bo=0.3. At the highest rotation number computed Ro=0.7, there is no heat transfer data in the literature to the best of our knowledge. Current results show that heat transfer augmentation continues to drop on the leading side but is not significantly affected by buoyancy forces. On the trailing side, buoyancy does increase the augmentation ratio, but it is not significantly different than that at the lower rotation number of Ro=0.35.

The overall heat transfer augmentation for the ribbed duct provided by centrifugal buoyancy over and above the action of Co-

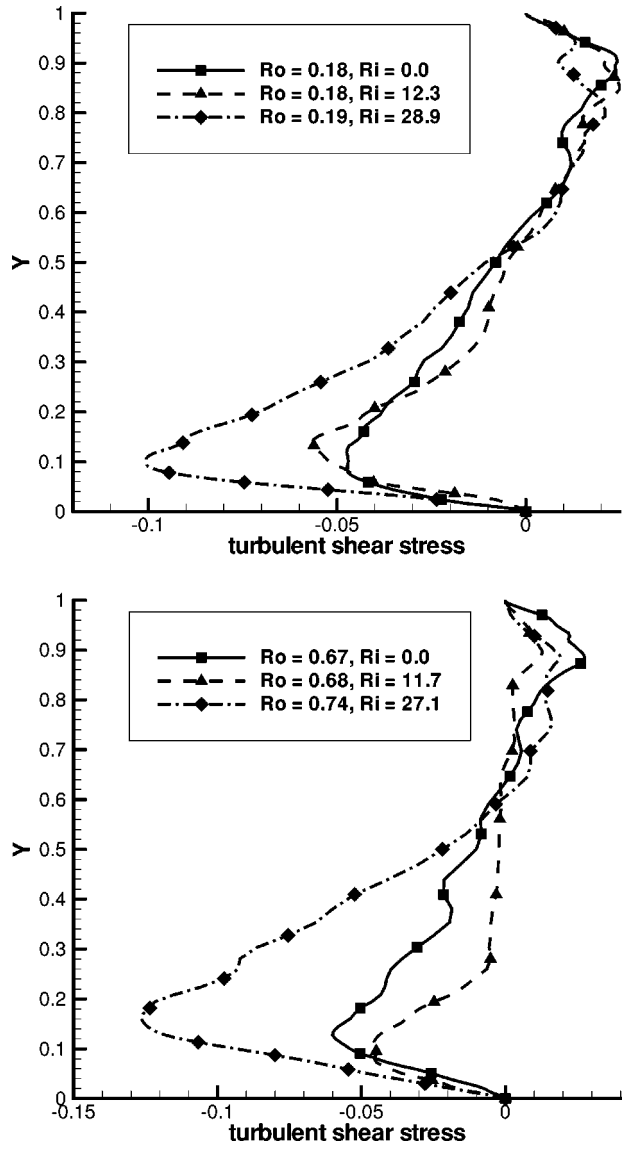


**Fig. 5 Turbulent shear stress at the center of the duct ($x=0$, $z=0.5$) for two different rotation numbers and for varying Richardson numbers. There is a large increase in turbulent shear stress on the trailing side (bottom) due to centrifugal buoyancy forces.**

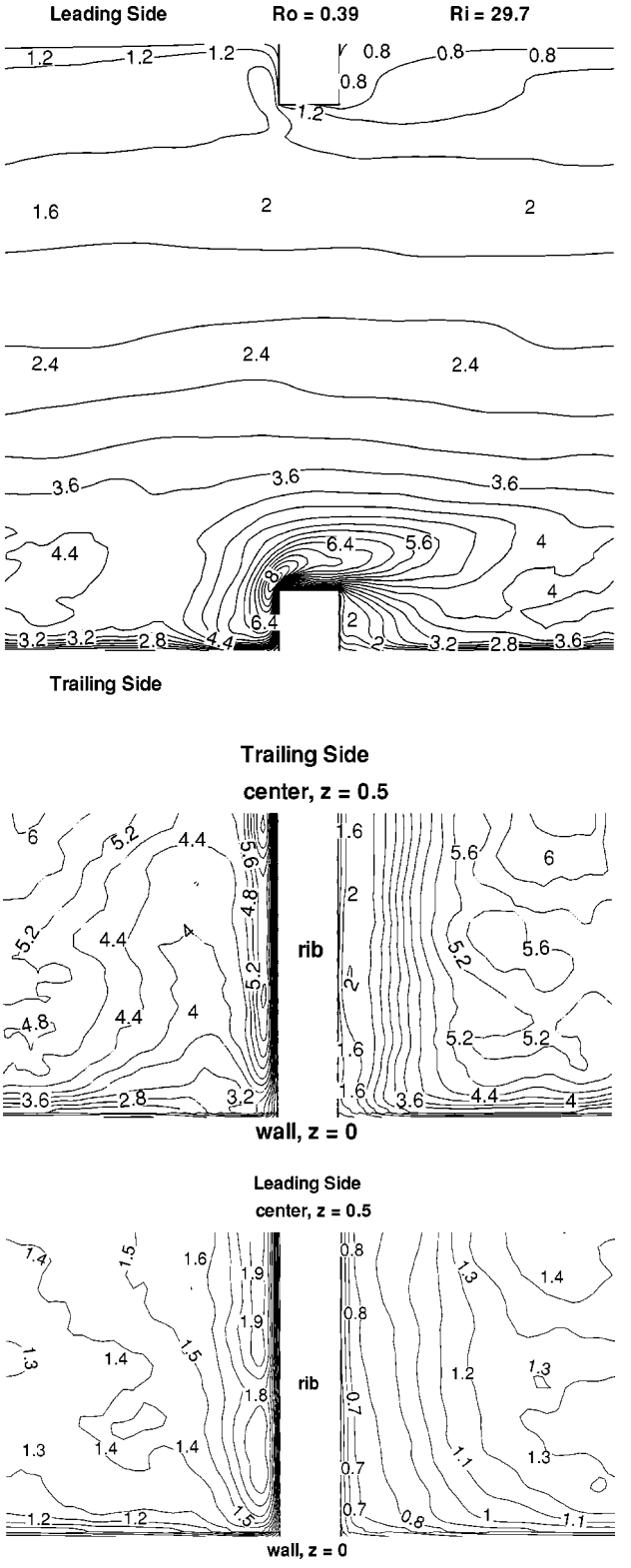


**Fig. 6 Contours of surface averaged Nusselt numbers for Ro =0.39 and Ri=29.7. Sidewall impingement on the trailing side of the smooth wall dominates heat transfer augmentation in that section. The reattachment region on the trailing side shows heat transfer augmentation of 6, which is a local maximum.**

riolis forces is found to be less than 10%. Friction on the other hand is augmented 15% to 20% at the highest buoyancy number studied.

## 5 Conclusions

Results from LES of 90 deg ribbed duct flow are presented for three nominal rotation numbers, Ro=0.18, 0.35, and 0.67, and three Richardson numbers Ri=0, 12, 29 (Bo=0,0.12,0.3) at a nominal Re=20 000 using the dynamic Smagorinsky model. The combined effects of Coriolis and centrifugal buoyancy forces on mean flow and turbulent quantities, together with heat transfer and friction augmentation data are presented.

Rotational Coriolis forces in the absence of centrifugal buoyancy increase the peak in turbulent kinetic energy by a factor of two over a nonrotating duct in the trailing wall boundary layer up to Ro=0.18, after which it increases slightly or even decreases with a further increase in rotation number. The heat transfer augmentation ratio on the trailing surface follows a somewhat similar pattern. The augmentation ratio asymptotes to a value of about 3.7%±5% and does not show any increasing trend as the rotation number increases beyond 0.18. On the other hand, augmentation ratios on the leading side keep decreasing with an increase in rotation number ranging from 1.7 at Ro=0.18 to 1.2 at Ro=0.67.

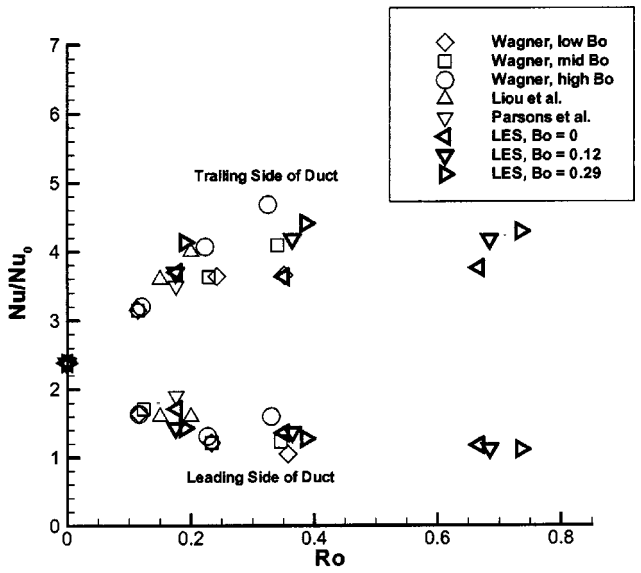


Buoyancy Information for Data of Wagner et al.[14]

| | Diamond | | |
|---|---|---|---|
| Ro | 0.12 | 0.25 | 0.35 |
| Bo | 0.04 | 0.16 | 0.34 |
| | **Box** | | |
| Ro | 0.12 | 0.25 | 0.35 |
| Bo | 0.07 | 0.26 | 0.57 |
| | **Circle** | | |
| Ro | 0.12 | 0.25 | 0.35 |
| Bo | 0.11 | 0.43 | 0.78 |

**Fig. 7 Comparison of average Nusselt number augmentation ratios at the leading and trailing sides with experiments. Liou et al. [16]: Re=10 000, $e/D_h$=0.136 and $P/e$=10; Parsons et al. [13]: Re=5000, $e/D_h$=0.125. $P/e$=10; Wagner et al. [15] Re =25 000, $e/D_h$=0.1, $P/e$=10, buoyancy information in table above.**

Smooth wall coefficients are increased by 20% to 30% over a stationary duct. The increase is primarily caused by the large cross-stream velocities in the vicinity of the wall by the cross-sectional secondary flow.

For the conditions simulated, centrifugal buoyancy forces complement the effect of Coriolis forces. They significantly affect the mean flow at the leading side of the duct by progressively increasing the reattachment length until finally at high rotation and high buoyancy, the separated shear layer extends all the way to the next rib. Conversely, buoyancy has little or no effect on the recirculating region at the trailing side over that of Coriolis forces alone. In the duct cross section, buoyancy strengthens the secondary flow cells and merges the two-cell structure observed with Coriolis forces alone into a single coherent cell in one half of the duct cross section. This leads to a further increase of 10% to 15% in heat transfer augmentation at the smooth walls.

Buoyancy accentuates the augmentation of turbulence near the trailing wall of the duct over and above the action of Coriolis forces alone. At the highest buoyancy (Ri=30, Bo=0.3), the separated shear layer at the trailing wall rib assumes a highly energetic state with large turbulence intensities. Turbulent shear stresses as high as 10% and turbulent kinetic energies at 28% are observed in the shear layer midway between the ribs.

Inclusion of centrifugal buoyancy does not have a large effect on leading side augmentation ratios for all rotation numbers. Only at the lowest rotation number of 0.18, does buoyancy reduce the leading side augmentation ratio by more than 10%. At the higher rotation numbers, the reduction is less than 10%. Conversely at the trailing side, buoyancy has a larger effect on heat transfer augmentation. At Ro=0.18, the increase is 10% for the large buoyancy number, which increases to 20% and 15% at Ro=0.35 and Ro=0.67, respectively. The overall effect of buoyancy on heat transfer augmentation for the ribbed duct is found to be less than 10% over the effect of Coriolis forces alone. Friction on the other hand is augmented 15% to 20% at the highest buoyancy number studied. Comparisons with available experiments show excellent agreement.

## Acknowledgments

This research was supported by the US DOE, Office of Fossil Energy, and National Energy Technology Laboratory. Any opinions, findings, conclusions, or recommendations expressed herein are those of the authors and do not necessarily reflect the views of the DOE. This work was also supported by the National Computational Science Alliance under MCA98N042N and used an IA64 Itanium Linux cluster at the National Center for Supercomputing Applications, University of Illinois, Urbana-Champaign.

## Nomenclature

- Bo = buoyancy parameter ($=\Delta\rho/\rho\times r/D_h\times Ro^2$)
- $D_h$ = hydraulic diameter
- $e$ = rib height
- $\vec{e}_x$ = unit vector in $x$ direction
- $f$ = Fanning friction factor
- $k$ = thermal conductivity (W/mK)
- $L_x$ = length of domain in $x$ direction
- $\vec{n}$ = surface normal vector
- Nu = local Nusselt number
- $\langle \mathrm{Nu} \rangle$ = spatially averaged Nusselt number
- $\overline{\mathrm{Nu}}$ = time-averaged Nusselt number
- $P$ = total pressure OR rib pitch
- $p$ = fluctuating, modified or homogenized pressure
- Pr = Prandtl number ($\mu C_p/k$)
- $Q_x$ = flow in $x$ direction
- $q''$ = constant heat flux boundary condition on duct walls and rib
- $r$ = outward radial distance from axis of rotation
- Re = Reynolds number based on bulk velocity ($\overline{u_b} D_h/\nu$)
- $\mathrm{Re}_\tau$ = Reynolds number based on friction velocity ($u_\tau D_h/\nu$)
- Ri = Richardson number based on bulk velocity ($\beta q'' r D_h^2 \omega_z^2 / k \overline{u_b^2}$)
- $\mathrm{Ri}_\tau$ = Richardson number based on friction velocity ($\beta q'' r D_h^2 \omega_z^2 / k u_\tau^2$)
- $\mathrm{Ro}_\tau$ = rotation number based on friction velocity ($=\omega_z D_h/u_\tau$)
- $\mathrm{Ro}_\tau$ = rotation number based on bulk velocity ($=\omega_z D_h/\overline{u_b}$)
- $t$ = temperature
- tke = turbulent kinetic energy
- $\vec{u}$ = Cartesian velocity vector
- $\overline{u_b}$ = mean bulk flow velocity
- $u_\tau$ = friction velocity
- $\vec{x}$ = physical coordinates
- $\beta$ = mean pressure gradient, also volumetric thermal expansion coefficient
- $\delta_{ij}$ = Kronecker delta
- $\gamma$ = mean temperature gradient
- $\theta$ = fluctuating, modified or homogenized temperature
- $\rho$ = density
- $\Omega$ = total heat transfer surface area
- $\omega_z$ = angular velocity of rotation (rad/s) about $z$-axis.
- $\vec{\xi}$ = computational coordinates

### Subscripts

$s$ = surface
$b$ = bulk
0 = smooth duct
rms = root mean square

## References


[1] Smagorinsky, J., 1963, ''General Circulation Experiments With the Primitive Equations. I. The Basic Experiment,'' Monthly Weather Review, **91**, pp. 99–164.
[2] Germano, M., Piomelli, U., Moin, P., and Cabot, W. H., 1991, ''A Dynamic Subgrid-Scale Eddy Viscosity Model,'' Phys. Fluids A, **3**, pp. 1760–1765.
[3] Watanabe, K., and Takahashi, T., 2002, ''LES Simulation and Experimental Measurement of Fully Developed Ribbed Channel Flow and Heat Transfer,'' ASME Paper No. 2002-GT-30203.
[4] Murata, A., and Mochizuki, S., 1999, ''Effect of Cross-Sectional Aspect Ratio on Turbulent Heat Transfer in an Orthogonally Rotating Rectangular Smooth Duct,'' Int. J. Heat Mass Transfer, **42**, pp. 3803–3814.
[5] Murata, A., and Mochizuki, S., 2000, ''Large, Eddy Simulation With a Dynamic Subgrid-Scale Model of Turbulent Heat Transfer in an Orthogonally Rotating Rectangular Duct With Transverse Rib Turbulators,'' Int. J. Heat Mass Transfer, **43**, pp. 1243–1259.
[6] Murata, A., and Mochizuki, S., 2001, ''Comparison Between Laminar and Turbulent Heat Transfer in a Stationary Square Duct With Transverse or Angled Rib Turbulators,'' Int. J. Heat Mass Transfer, **44**, pp. 1127–1141.
[7] Iacovides, H., and Launder, B. E., 1991, ''Parametric and Numerical Study of Fully Developed Flow and Heat Transfer in Rotating Rectangular Ducts,'' ASME J. Turbomach., **133**, pp. 331–338.
[8] Bo, T., Iacovides, H., and Launder, B. E., 1995, ''Developing Buoyancy-Modified Turbulent Flow in Ducts Rotating in Orthogonal Mode,'' ASME J. Turbomach., **177**, pp. 474–484.
[9] Prakash, C., and Zerkle, R., 1992, ''Prediction of Turbulent Flow and Heat Transfer in a Rotating Square Duct,'' ASME J. Turbomach., **114**, pp. 835–846.
[10] Prakash, C., and Zerkle, R., 1995, ''Prediction of Turbulent Flow and Heat Transfer in a Ribbed Rectangular Duct With and Without Rotation,'' ASME J. Turbomach., **117**, pp. 255–264.
[11] Ooi, A., Iaccarino, G., Durbin, P. A., and Behnia, M., 2002, ''Reynolds Averaged Simulation of Flow and Heat Transfer in Ribbed Ducts,'' Int. J. Heat Fluid Flow, **23**, pp. 750–757.
[12] Saidi, A., and Sunden, B., 2001, ''On Prediction of Thermal-Hydraulic Characteristics of Square-Sectioned Ribbed Cooling Ducts,'' ASME J. Turbomach., **123**, pp. 614–620.
[13] Parsons, J. A., Han, J. C., and Zang, Y. M., 1994, ''Wall Heating Effect on Local Heat Transfer in a Rotating Two-Pass Square Channel With 90° Rib Turbulators,'' Int. J. Heat Mass Transfer, **37**, pp. 1411–1420.
[14] Ekkad, S. V., and Han, J. C., 1997, ''Detailed Heat Transfer Distributions in Two-Pass Square Channels With Rib Turbulators,'' Int. J. Heat Mass Transfer, **40**, pp. 2525–2537.
[15] Wagner, J. H., Johnson, B. V., Graziani, R. A., and Yeh, F. C., 1992, ''Heat Transfer in Rotating Serpentine Passages With Trips Normal to the Flow,'' ASME J. Turbomach., **114**, pp. 847–857.
[16] Liou, T. M., Chen, M. Y., and Tsai, M. H., 2001, ''Fluid Flow and Heat Transfer in a Rotating Two-Pass Square Duct With In-Line 90° Ribs,'' ASME Paper No. 2001-GT-0185.
[17] Abdel-Wahab, S., and Tafti, D. K., 2004, ''Large Eddy Simulation of Flow and Heat Transfer in a 90° Ribbed Duct With Rotation—Effect of Coriolis Forces,'' ASME Paper No. 2004-GT-53796.
[18] Tafti, D. K., 2001, ''GENIDLEST—A Scalable Parallel Computational Tool for Simulating Complex Turbulent Flows,'' *Proceedings ASME Fluids Engineering Division, FED*—Vol. 256, ASME-IMECE, New York.
[19] Tafti, D. K., 2004, ''Evaluating the Role of Subgrid Stress Modeling in a Ribbed Duct for the Internal Cooling of Turbine Blades,'' Intl. J. Heat Fluid Flow, in press.
[20] Incropera, F. P., and Dewitt, D. P., 2002, *Fundamentals of Heat and Mass Transfer*, 5th ed., Wiley, New York.
[21] Johnston, J. P., Halleen, R. M., and Lezius, D. K., 1972, ''Effects of Spanwise Rotation on the Structure of Two-Dimensional Fully Developed Turbulent Channel Flow.'' J. Fluid Mech., **56**, pp. 533–557.

# Thermoacoustic Stability of Quasi-One-Dimensional Flows—Part I: Analytical and Numerical Formulation

**Dilip Prasad**

**Jinzhang Feng**

Aerodynamics Division,
Pratt & Whitney Aircraft Engines,
East Hartford, CT 06108

*A numerical method is developed for transient linear analysis of quasi-one-dimensional thermoacoustic systems, with emphasis on stability properties. This approach incorporates the effects of mean flow variation as well as self-excited sources such as the unsteady heat release across a flame. Working in the frequency domain, the perturbation field is represented as a superposition of local wave modes, which enables the linearized equations to be integrated in space. The problem formulation is completed by specifying appropriate boundary conditions. Here, we consider impedance boundary conditions as well as those relevant to choked and shocked flows. For choked flows, the boundary condition follows from the requirement that perturbations remain regular at the sonic point, while the boundary conditions applicable at a normal shock are obtained from the shock jump conditions. The numerical implementation of the proposed formulation is described for the system eigenvalue problem, where the natural modes are sought. The scheme is validated by comparison with analytical and numerical solutions.* [DOI: 10.1115/1.1791288]

## Introduction

The unsteady flows that are invariably present in fluid machinery frequently lead to the generation of performance-limiting instabilities. In gas turbine flows, the evolution of these instabilities can be influenced by the acoustic properties of the underlying system as in the case of flutter, surge, and rotating stall in compressors. Another example is that of combustion instability, wherein the transient interaction between pressure and heat release can give rise to violent oscillations, resulting in structural or thermal failure. Industrial gas turbines that employ lean premixed prevaporized combustors are susceptible to this type of instability as are aircraft engine afterburners. In the latter case, the instability is referred to as screech or rumble, depending on the type of acoustic mode involved.

Several approaches have been developed to predict the onset of combustion instabilities. These include Galerkin projection techniques [1], time-domain simulations [2,3], and linearized methods [4–8], which are usually formulated in the frequency domain. In developing the latter models, the background flow is often taken to be piecewise uniform so that small perturbations can be represented as a superposition of independent entropic and acoustic modes. With this simplification, analytical transmission (or transfer) matrices can be constructed, permitting the governing equations to be integrated spatially. Using this approach, mean flow variations with length scales much smaller than those of the unsteady flow are treated as flow discontinuities, across which matching conditions that follow from the conservation laws must be applied. This approach enables the development of reduced-order models which can be used to rapidly explore the design space. For perturbations with length scales comparable to that of the mean flow, it is possible in principle to discretize the flow path into several uniform segments connected by jump discontinuities. However, since this procedure is spatially only first-order accurate, it may be necessary to employ a large number of segments in order to arrive at a good estimate for the eigenvalue.

In the present investigation, we seek to incorporate in a more direct fashion the effects of mean flow variation on the perturbations. We shall be concerned with systems in which the spatial variation of the background flow occurs primarily along the streamwise direction; further, diffusive effects are assumed to be negligible so that the system can be described using the one-dimensional Euler equations. The effect of variations in the mean flow is to alter the local wave propagation speeds. More importantly, the modal disturbances are no longer independent and the standard transmission matrix approach cannot be used. One method of accounting for mean flow variations is to discretize the linearized frequency-domain equations using one of many different spatial differencing techniques. When appropriate inlet and exit boundary conditions are imposed, a matrix eigenvalue problem is obtained, which can be solved numerically. However, the true system eigenvalues are interspersed among a large number of nonphysical eigenvalues and algorithms for the detection of the former are not always reliable.

In the present study, we develop a general framework to examine the transient behavior of nonuniform one-dimensional thermoacoustic systems. This approach is well-suited for the study of both the system eigenproblem and its forced response. Here, we focus on the former type of problem, taking into account the presence of spatially and temporally lagged self-excited sources such as the unsteady heat release across a flame. The perturbations are represented in the frequency domain as a superposition of local wave modes that are modulated in the streamwise direction. This enables the linearized equations to be integrated efficiently to second-order spatial accuracy.

Upon applying the relevant boundary conditions at the flow inlet and exit, a global eigenvalue problem is derived. In this study, we describe the application of impedance-type boundary conditions and those corresponding to choked flows and flows with shocks. In the case of choked flows, the boundary condition follows from the requirement that perturbations remain well-behaved at the sonic point. The boundary conditions applicable at a normal shock are obtained by linearizing the Rankine–Hugoniot

Contributed by the International Gas Turbine Institute (IGTI) of THE AMERICAN SOCIETY OF MECHANICAL ENGINEERS for publication in the ASME JOURNAL OF TURBOMACHINERY. Paper presented at the International Gas Turbine and Aeroengine Congress and Exhibition, Vienna, Austria, June 13–17, 2004, Paper No. 2004-GT-53943. Manuscript received by IGTI, October 1, 2003; final revision March 1, 2004. IGTI Review Chair: A. J. Strazisar.

conditions. The eigenproblem solution procedure consists of a grid-search algorithm coupled with Newton–Raphson iteration, which circumvents the difficulties associated with identifying spurious eigenvalues. The method is validated by comparison with analytical and numerical solutions. We also discuss briefly the manner in which the present analysis can be modified to determine the forced response of a system.

## Problem Formulation

We assume a one-dimensional compressible unsteady inviscid flow of a perfect gas with constant specific heat ratio $\gamma$ through a device with cross-sectional area $A=A(x)$, where $x$ represents the streamwise coordinate. Denoting the density, velocity, and pressure by $\rho$, $u$, and $p$ respectively, the governing equations of mass, momentum, and energy conservation may be written as

$$\frac{\partial \rho}{\partial t}+u\frac{\partial \rho}{\partial x}+\frac{\rho}{A}\frac{\partial}{\partial x}(uA)=m, \tag{1}$$

$$\frac{\partial u}{\partial t}+u\frac{\partial u}{\partial x}+\frac{1}{\rho}\frac{\partial p}{\partial x}=f, \tag{2}$$

$$\frac{\partial p}{\partial t}+u\frac{\partial p}{\partial x}+\frac{\gamma p}{A}\frac{\partial}{\partial x}(uA)=(\gamma-1)q+mc^2, \tag{3}$$

where $m=m(x,t)$ and $q=q(x,t)$ are volumetric mass and heat sources, $f=f(x,t)$ represents an external body force per unit mass and $c=(\gamma p/\rho)^{1/2}$ is the sonic speed. The state vector $\mathbf{Q}=[\rho\ u\ p]^T$ is now written as the sum of a mean and time-harmonic perturbation

$$\mathbf{Q}=\overline{\mathbf{Q}}(x)+\tilde{\mathbf{Q}}(x;\omega)e^{i\omega t}. \tag{4}$$

Similarly, the quantities comprising the source terms on the right-hand sides of Eqs. (1)–(3) are written as

$$(m,f,q)=(\overline{m},\overline{f},\overline{q})+(\tilde{m},\tilde{f},\tilde{q})e^{i\omega t}.$$

Assuming further that the perturbations are small, $|\tilde{\mathbf{Q}}|\ll|\overline{\mathbf{Q}}|$, we find that $\overline{\mathbf{Q}}$ is a solution of the steady versions of Eqs. (1)–(3), while the perturbations are governed by the linearized frequency-domain Euler equations

$$B\frac{d\tilde{\mathbf{Q}}}{dx}+(i\omega I+G)\tilde{\mathbf{Q}}=\tilde{\mathbf{S}}, \tag{5}$$

where

$$B=\begin{bmatrix}\overline{u} & \overline{\rho} & 0\\ 0 & \overline{u} & \dfrac{1}{\overline{\rho}}\\ 0 & \gamma\overline{p} & \overline{u}\end{bmatrix}, \tag{6}$$

and $G$, which represents the effect of mean flow gradients is defined by

$$G=\begin{bmatrix}\dfrac{1}{A}\dfrac{d}{dx}(\overline{u}A) & \dfrac{1}{A}\dfrac{d}{dx}(\overline{\rho}A) & 0\\ \dfrac{\overline{u}}{\overline{\rho}}\dfrac{d\overline{u}}{dx} & \dfrac{d\overline{u}}{dx} & 0\\ 0 & \dfrac{d\overline{p}}{dx}+\dfrac{\gamma\overline{p}}{A}\dfrac{dA}{dx} & \dfrac{\gamma}{A}\dfrac{d}{dx}(\overline{u}A)\end{bmatrix}. \tag{7}$$

The vector $\tilde{\mathbf{S}}$ on the right-hand side of Eq. (5) represents the effects of mean source-perturbation interactions as well as transient sources and can be written as

$$\tilde{\mathbf{S}}=T\tilde{\mathbf{Q}}+\tilde{\mathbf{F}}, \tag{8}$$

where we have defined

$$T=\begin{bmatrix}0 & 0 & 0\\ \dfrac{\overline{f}}{\overline{\rho}} & 0 & 0\\ -\dfrac{\overline{mc^2}}{\overline{\rho}} & 0 & \dfrac{\overline{mc^2}}{\overline{p}}\end{bmatrix};\quad \tilde{\mathbf{F}}=\begin{bmatrix}\tilde{m}\\ \tilde{f}\\ (\gamma-1)\tilde{q}+\overline{c}^2\tilde{m}\end{bmatrix}.$$

The terms $\tilde{m},\tilde{f},\tilde{q}$ in the expression for $\tilde{\mathbf{F}}$ occur as a consequence of either external or self-excited forcing. This issue is discussed in more detail later.

**Local Wave Decomposition.** Introducing now a matrix $\mathcal{M}^{-1}$ which remains to be defined, we obtain from Eqs. (5) and (8)

$$\mathcal{M}\frac{d}{dx}(\mathcal{M}^{-1}\tilde{\mathbf{Q}})+\left[\frac{d\mathcal{M}}{dx}-C\mathcal{M}\right](\mathcal{M}^{-1}\tilde{\mathbf{Q}})=B^{-1}\tilde{\mathbf{F}}, \tag{9}$$

where

$$C=-B^{-1}(i\omega I+G-T). \tag{10}$$

We select $\mathcal{M}$ to be the solution of the eigenproblem

$$\frac{d\mathcal{M}}{dx}+\mathcal{M}\Lambda-C\mathcal{M}=0, \tag{11}$$

where the matrix of eigenvalues $\Lambda$ is diagonal and the columns of $\mathcal{M}$ are the eigenvectors. This choice of $\mathcal{M}$ diagonalizes Eq. (9), which assumes the form

$$\frac{d}{dx}(\mathcal{M}^{-1}\tilde{\mathbf{Q}})-\Lambda(\mathcal{M}^{-1}\tilde{\mathbf{Q}})=\mathcal{M}^{-1}B^{-1}\tilde{\mathbf{F}}. \tag{12}$$

When background flow is uniform, $\mathcal{M}$ becomes independent of $x$ and the solutions of Eq. (12) can be determined analytically: the eigenvectors consist of two isentropic pressure (acoustic) modes and one entropic mode that carries no pressure. The eigenvalues corresponding to these modes are given, respectively, by $-i\omega/(\overline{u}\pm\overline{c})$ and $-i\omega/\overline{u}$, indicating that the acoustic modes propagate at speeds $\overline{u}\pm\overline{c}$, while the entropic mode is of convected type and propagates at speed $\overline{u}$. When the mean flow is nonuniform, pure acoustic or entropic modes cease to exist. Moreover, in view of the fact that the wave speeds are dependent on the mean quantities, it is evident that local modes are refracted by the nonuniform flow.

We now assume that a mean flow, determined, for example, by numerical solution of the steady Euler equations, has been specified on a grid $x_j, j=1,\ldots,N$. Assuming further that the steady and time-dependent flow quantities are spatially smooth, we may represent the matrices $C,\mathcal{M}$, and $\Lambda$ by series expansions in the neighborhood of $x_j$

$$\Phi=\Phi^{(0)}+\Phi^{(1)}(x-x_j)+\Phi^{(2)}(x-x_j)^2+\ldots, \tag{13}$$

where $\Phi$ stands for one of $C$, $\Lambda$, or $\mathcal{M}$. Inserting these expansions into Eq. (11) yields at lowest order in $(x-x_j)$

$$\mathcal{M}^{(1)}+\mathcal{M}^{(0)}\Lambda^{(0)}-C^{(0)}\mathcal{M}^{(0)}=0. \tag{14}$$

If $\mathcal{M}^{(0)}$ and $\Lambda^{(0)}$ are taken to be solutions of the local zeroth-order eigenproblem

$$\mathcal{M}^{(0)}\Lambda^{(0)}-C^{(0)}\mathcal{M}^{(0)}=0, \tag{15}$$

it follows from Eqs. (13) and (14) that

$$\mathcal{M}=\mathcal{M}^{(0)}+O(x-x_j)^2, \tag{16}$$

indicating a locally second-order accurate representation of the eigenvector matrix $\mathcal{M}$. In what follows, the superscript (0) is dropped and the solution of Eq. (15) at the $j$-th node is denoted by $\mathcal{M}_j,\Lambda_j$.

Considering now the control volume contained between the grid nodes at $j$ and $j+1$, we define $x_{j+1/2}=(x_j+x_{j+1})1/2$. The preceding discussion shows that, to second-order in $\delta x_j=x_{j+1}$

$-x_j$, we may set $\mathcal{M}=\mathcal{M}_j$ and $\mathcal{M}=\mathcal{M}_{j+1}$ in the regions $x_j<x<x_{j+1/2}$ and $x_{j+1/2}<x<x_{j+1}$ respectively. Integrating Eq. (12) from $x_j$ to a point $x$ lying between $x_j$ and $x_{j+1/2}$, we obtain

$$\tilde{\mathbf{Q}}=\mathcal{M}\mathcal{E}\left[\mathcal{M}_j^{-1}\tilde{\mathbf{Q}}_j+\int_{x_j}^{x}(\mathcal{E}^{-1}\mathcal{M}^{-1}B^{-1}\tilde{\mathbf{F}})\mathrm{d}x\right], \tag{17}$$

where

$$\mathcal{E}=\exp\int_{x_j}^{x}\Lambda(x')\mathrm{d}x=\exp[\Lambda_j(x-x_j)]+O(x-x_j)^2; \tag{18}$$

the second equality in Eq. (18) is obtained by making use of the expansion in Eq. (13) for $\Lambda$. Making use of Eqs. (16)–(18), it is shown in the Appendix that the perturbation quantities at $j+1/2$ are given by

$$\tilde{\mathbf{Q}}_{j+1/2}=[\mathcal{M}_jE_{j,j}\mathcal{M}_j^{-1}]\left(\tilde{\mathbf{Q}}_j+\frac{1}{2}\delta x_jB_j^{-1}\tilde{\mathbf{F}}_j\right), \tag{19}$$

with $E_{j,j}=\exp[\Lambda_j\delta x_j/2]$. Following a similar procedure, integration of Eq. (12) between $x_{j+1}$ and $x_{j+1/2}$ yields

$$\tilde{\mathbf{Q}}_{j+1/2}=[\mathcal{M}_{j+1}E_{j+1,j}^{-1}\mathcal{M}_{j+1}^{-1}]\left(\tilde{\mathbf{Q}}_{j+1}-\frac{1}{2}\delta x_jB_{j+1}^{-1}\tilde{\mathbf{F}}_{j+1}\right), \tag{20}$$

with $E_{j+1,j}=\exp[\Lambda_{j+1}\delta x_j/2]$. Equating the right-hand sides of Eqs. (19) and (20), we have the relation

$$\tilde{\mathbf{Q}}_{j+1}=\mathcal{A}_{j+1,j}\tilde{\mathbf{Q}}_j+\frac{1}{2}\delta x_j(B_{j+1}^{-1}\tilde{\mathbf{F}}_{j+1}+\mathcal{A}_{j+1,j}B_j^{-1}\tilde{\mathbf{F}}_j), \tag{21}$$

where

$$\mathcal{A}_{j+1,j}=[\mathcal{M}_{j+1}E_{j+1,j}\mathcal{M}_{j+1}^{-1}][\mathcal{M}_jE_{j,j}\mathcal{M}_j^{-1}].$$

We note that in the case of a uniform flow without forcing, the above expression for $\mathcal{A}_{j+1,j}$ reduces to the standard acoustic transmission matrix.

**Self-Excited Forcing.** Although $\tilde{\mathbf{F}}$ incorporates the effects of both external and self-excited sources, the latter are usually of the greatest interest. Indeed, the unsteady heat release $\tilde{q}$ plays a central role in the occurrence of combustion instabilities. In this context, the connection between the self-excited source and perturbation field is generally rather complex and, with the exception of simple configurations, not readily derived from first principles. Instead, semiempirical models are usually employed. For example, the unsteady heat release in the case of the ducted premixed flame studied by Bloxsidge et al. [4] was shown to be given by

$$\frac{\tilde{q}}{\bar{q}}=\frac{\tilde{u}_f}{\bar{u}_f}\exp(-\mathrm{i}\omega\tau)F(\omega)H(x-x_f), \tag{22}$$

where $F$ is a function of the frequency and geometric parameters, $H$ is the Heaviside step function, $x_f$ denotes the coordinate of the flame anchor, and $\tau=(x-x_f)/\bar{u}_f$ represents a time delay. In what follows, we assume that external forcing does not occur. Furthermore, it is assumed that a single source exists at some interior point $x=x_f$ and that its effects may be written as a generalization of Eq. (22) in the form

$$\tilde{\mathbf{F}}=W(x;x_f,\omega)\tilde{\mathbf{Q}}(x_f). \tag{23}$$

The definition of $C$ in Eq. (10) must then be altered to read

$$C=\begin{cases}-B^{-1}(\mathrm{i}\omega I+G-T) & (x\neq x_f),\\ -B^{-1}(\mathrm{i}\omega I+G-T+W) & (x=x_f).\end{cases} \tag{24}$$

Upon substituting Eq. (23) into Eq. (21) and defining $D_{j+1,j}=(B_{j+1}^{-1}W_{j+1}+\mathcal{A}_{j+1,j}B_j^{-1}W_j)\delta x_j/2$, we obtain

$$\tilde{\mathbf{Q}}_{j+1}=\mathcal{A}_{j+1,j}\tilde{\mathbf{Q}}_j+D_{j+1,j}\tilde{\mathbf{Q}}_{j_f} \tag{25}$$

where $j_f$ denotes the index of the point with coordinate $x_f$. Equation (25) relates disturbance values at a given index $j$ to its successor $j+1$ and therefore provides a means of integrating the perturbation equations over the flow domain. Applying Eq. (25) recursively between $j=1$ and an intermediate point $j=n$, it is found that

$$\tilde{\mathbf{Q}}_n=P_n\tilde{\mathbf{Q}}_1+\mathcal{F}_n\tilde{\mathbf{Q}}_{j_f}, \tag{26}$$

where we have defined

$$P_n=\mathcal{A}_{n,n-1}\mathcal{A}_{n-1,n-2}\ldots\mathcal{A}_{2,1}$$

and $\mathcal{F}_n$ is given by

$$\mathcal{F}_n=\begin{cases}D_{n,n-1}+\sum_{j=2}^{n-1}P_nP_j^{-1}D_{j,j-1} & (n>2),\\ D_{n,n-1} & (n=2).\end{cases} \tag{27}$$

Next, upon setting $j=j_f$ in Eq. (26), we obtain

$$\tilde{\mathbf{Q}}_{j_f}=[I-\mathcal{F}_{j_f}]^{-1}P_{j_f}\tilde{\mathbf{Q}}_1. \tag{28}$$

Finally, making use of Eqs. (28) and (26) with $j=N$ gives

$$\tilde{\mathbf{Q}}_N=R\tilde{\mathbf{Q}}_1, \tag{29}$$

where the matrix $R$, which is given by

$$R=P_N+\mathcal{F}_N[I-\mathcal{F}_{j_f}]^{-1}P_{j_f},$$

is analogous to a transmission matrix across the entire flow domain. The problem specification is completed by setting appropriate boundary conditions at the inlet and exit, an issue that we take up next. It should be noted that although we have assumed a single source at $x=x_f$, the present formulation can be generalized to account for multiple sources at different spatial locations. Moreover, self-excited sources that are not spatially lagged but related to local values of the perturbation quantities can also be included by appropriately defining the matrix $T$ in Eq. (8).

## Boundary Conditions

The definition of an eigenproblem for the natural modes is only possible over regions where the flow is entirely subsonic. The spatial variations of the background flow and perturbations are then smooth so that the Taylor expansions in Eq. (13) hold. As we have observed previously, the perturbations are of acoustic or entropic type for a uniform subsonic background flow. This makes it necessary to specify the amplitudes of the downstream-propagating acoustic mode and entropic mode at the inflow boundary and that of the upstream-propagating acoustic mode at the outflow boundary. Hence, it follows that two conditions must be prescribed at the inlet ($j=1$) and one at the exit ($j=N$). In general, these conditions may be written in the form

$$L\tilde{\mathbf{Q}}_1=0, \tag{30}$$

$$X\tilde{\mathbf{Q}}_N=0, \tag{31}$$

where $L$ and $X$ are frequency-dependent matrices of size $2\times3$ and $1\times3$, respectively.

Combining Eq. (29) with the boundary conditions in Eqs. (30) and (31), we obtain

$$Z\tilde{\mathbf{Q}}_1=0, \tag{32}$$

where

$$Z=\begin{bmatrix}L_{11} & L_{12} & L_{13}\\ L_{21} & L_{22} & L_{23}\\ (XR)_1 & (XR)_2 & (XR)_3\end{bmatrix}.$$

In order for Eq. (32) to possess nontrivial solutions, we must demand that

$$\det(Z)=0,$$

the solution of which yields the values of $\omega$ corresponding to the natural modes of the system. The mode shapes can then be determined using these known values of $\omega$, together with Eq. (21) and the boundary conditions. We now examine specific boundary conditions that are required in applying the preceding method to common thermoacoustic systems.

**Acoustic Impedance Conditions.** In ordinary acoustics, the reflection and transmission properties of devices such as flow restrictors are characterized by their impedance $\zeta$, which relates the frequency-domain pressure and velocity perturbations according to the relation

$$\tilde{p}=\overline{\rho c}\zeta\,\tilde{\mathbf{u}}\cdot\hat{\mathbf{n}},$$

where $\hat{\mathbf{n}}$ is the outward-pointing unit normal vector and $\zeta$ is, in general, frequency-dependent. In conjunction with the assumption of isentropic flow for purely acoustic disturbances, the matrices $L$ and $X$ in Eqs. (30) and (31) therefore take the form

$$L=\begin{bmatrix}0 & \overline{\rho c}\zeta & 1\\ \overline{c}^2 & 0 & -1\end{bmatrix}_{\text{in}};\quad X=\begin{bmatrix}0 & \overline{\rho c}\zeta & -1\end{bmatrix}_{\text{ex}},$$

where the subscripts ''in'' and ''ex'' denote values at the inlet and exit respectively. A flow boundary that is acoustically ''open'' ($\tilde{p}=0$) corresponds to $\zeta=0$, while acoustically ''closed'' ($\tilde{u}=0$) inlet and exit conditions, for which $\zeta\to\infty$, are given by

$$L=\begin{bmatrix}0 & 1 & 0\\ \overline{c}_{\text{in}}^2 & 0 & -1\end{bmatrix};\quad X=[0\quad 1\quad 0].$$

**Choked Flow.** We turn now to the case of a subsonic flow that is accelerated through the sonic transition to a supersonic state. In a study of isentropic background flows of this kind, Marble and Candel [9] derived a compatibility relation between the perturbation quantities, which applies in the limit of a compact nozzle. The behavior of unsteady disturbances in a finite-length nozzle with a linear variation of the mean velocity was also examined. However, it becomes necessary to derive more general conditions to accommodate the arbitrary mean flows considered here.

From the definition of $B$ in Eq. (6), we obtain

$$B^{-1}=\begin{bmatrix}\dfrac{1}{\overline{u}} & \dfrac{-\gamma\overline{p}}{\overline{c}^4\beta} & \dfrac{1}{\overline{uc}^4\beta}\\ 0 & \dfrac{M}{\overline{c}\beta} & \dfrac{-1}{\gamma\overline{p}\beta}\\ 0 & \dfrac{-\gamma\overline{p}}{\overline{c}^2\beta} & \dfrac{M}{\overline{c}\beta}\end{bmatrix},\tag{33}$$

where $M=\overline{u}/\overline{c}$ is the Mach number and $\beta=M^2-1$. At the sonic location, $x=x_*$, we have $M=1$ so that $\beta=0$. It is then evident from Eqs. (33) and (10) that $B$ and $C$ become singular at this point. However, the perturbation variables $\tilde{\mathbf{Q}}$ must remain finite and this requirement leads to a boundary condition at $x=x_*$.

Assuming that $T$ and $\tilde{\mathbf{F}}$ are well-behaved throughout the domain and observing that, in addition to $\tilde{\mathbf{Q}}$, the matrices $B$ and $G$ are also regular at the sonic point, we may expand all quantities as Taylor series in the neighborhood of $x=x_*$

$$Y=Y_*+Y'_*(x-x_*)+\ldots,$$

where $Y$ stands for any flow variable and $Y_*=Y(x_*)$, $Y'_*=Y'(x_*)$. Inserting these expansions into Eq. (5), we find that

$$B_*\tilde{\mathbf{Q}}'_*+(\mathrm{i}\omega I+G_*-T_*)\tilde{\mathbf{Q}}_*=\tilde{\mathbf{F}}_*,\tag{34}$$

which can be diagonalized by introducing the eigensystem

$$B_*\mathcal{N}=\mathcal{N}K,$$

where $\mathcal{N}$ is the matrix of eigenvectors given by

$$\mathcal{N}=\begin{bmatrix}\overline{\rho} & \overline{\rho} & 1\\ -\overline{c} & \overline{c} & 0\\ \gamma\overline{p} & \gamma\overline{p} & 0\end{bmatrix},$$

and $K$ is the corresponding (diagonal) matrix of eigenvalues, the elements of which are $K_{11}=\overline{u}-\overline{c}$, $K_{22}=\overline{u}+\overline{c}$, $K_{33}=\overline{u}$. Inserting the expression into Eq. (23) for $\tilde{\mathbf{F}}$ into Eq. (34) and making use of Eqs. (28) and (29), we obtain

$$K\mathcal{N}^{-1}\tilde{\mathbf{Q}}'_*+H\tilde{\mathbf{Q}}_*=0,\tag{35}$$

where the matrix $H$, defined by

$$H=\mathcal{N}^{-1}(\mathrm{i}\omega I+G_*-T_*-W_*[I-\mathcal{F}_{j_f}]^{-1}P_{j_f}R^{-1})$$

is well-behaved at the sonic point. Since $K_{11}=0$ at $x=x_*$, it follows from Eq. (29) that

$$H_{11}\tilde{\rho}+H_{12}\tilde{u}+H_{13}\tilde{p}=0;\quad (x=x_*).\tag{36}$$

Equation (36) is the analog of the compatibility condition of Marble and Candel [9], who point out that a condition of this type, being applicable on both sides of the sonic point, represents an exit (inlet) boundary condition for the subsonic (supersonic) regions. Therefore, the subsonic region is decoupled from the supersonic part of the flow field. From the viewpoint of the system eigenproblem, this implies that the subsonic zone can be considered in isolation, with the exit boundary condition matrix $X$ in Eq. (31) given by $X=[H_{11}H_{12}H_{13}]$.

**Shock Jump Conditions.** We now consider flows with shocks, which in the present context of quasi-one-dimensional flow, are normal. Consequently, the background flow decelerates from a supersonic ($M>1$) to a subsonic ($M<1$) state across the shock. The response of a normal shock in a one-dimensional flow to acoustic excitations has been studied by Culick and Rogers [10], who considered isentropic steady flows on both sides of the shock. In the present investigation, we adapt their approach to examine mean flows and perturbations that are more general.

The shock location is time-dependent in an unsteady flow. In analogy with the frequency-domain representation for the state vector given by Eq. (4), we write the shock position $x_{\text{Sh}}$ as

$$x_{\text{Sh}}(t)=\overline{x}_{\text{Sh}}+\tilde{x}_{\text{Sh}}\mathrm{e}^{\mathrm{i}\omega t},\tag{37}$$

where $\overline{x}_{\text{Sh}}$ is the mean shock location and $\tilde{x}_{\text{Sh}}$ represents the amplitude of its oscillation, which we assume to be small. The steady flow states on either side of the shock are related by the Rankine–Hugoniot conditions [11]. Since the volume enclosed by the shock is infinitesimal, the unsteady flow across it is quasi-steady so that the flow relations for small disturbances are obtained by linearizing the steady shock jump conditions. The Rankine–Hugoniot conditions are most conveniently written in a frame in which the shock is stationary. We therefore adopt the following definitions: the unsteady states upstream and downstream of the shock in the reference frame fixed to it are denoted by the subscripts ''Sh,u'' and ''Sh,d,'' respectively, while the corresponding states in the frame of the flow device are denoted by the subscripts ''u'' and ''d.''

Observing that the supersonic flow upstream of the shock precludes transmission of upstream-propagating disturbances across it, we obtain upon making use of Eq. (37)

$$\tilde{u}_{\text{Sh,u}}=\left[\left.\frac{\mathrm{d}\overline{u}_{\text{u}}}{\mathrm{d}x}\right|_{\overline{x}_{\text{Sh}}}-\mathrm{i}\omega\right]\tilde{x}_{\text{Sh}}.\tag{38}$$

That is, the upstream velocity perturbation in the shock frame is a result of two distinct effects: the first is due to the motion of the shock through a nonuniform flow field and may be regarded as a convective phenomenon, while the second is a consequence of the

Galilean coordinate transformation corresponding to a translating reference frame. By similar reasoning, the downstream velocity perturbation is determined by the expression

$$\tilde{u}_{\mathrm{Sh,d}}=\tilde{u}_{\mathrm{d}}+\left[\left.\frac{\mathrm{d}\overline{u_{\mathrm{d}}}}{\mathrm{d}x}\right|_{\overline{x}_{\mathrm{Sh}}}-\mathrm{i}\omega\right]\tilde{x}_{\mathrm{Sh}}. \tag{39}$$

The disturbances in density and pressure at the shock upstream and downstream locations are caused only by the movement of the shock through the corresponding (nonuniform) mean fields so that we have

$$\tilde{\rho}_{\mathrm{Sh,u}}=\left.\frac{\mathrm{d}\overline{\rho_{\mathrm{u}}}}{\mathrm{d}x}\right|_{\overline{x}_{\mathrm{Sh}}}\tilde{x}_{\mathrm{Sh}};\quad \tilde{\rho}_{\mathrm{Sh,d}}=\tilde{\rho}_{\mathrm{d}}+\left.\frac{\mathrm{d}\overline{\rho_{\mathrm{u}}}}{\mathrm{d}x}\right|_{\overline{x}_{\mathrm{Sh}}}\tilde{x}_{\mathrm{Sh}}, \tag{40}$$

$$\tilde{p}_{\mathrm{Sh,u}}=\left.\frac{\mathrm{d}\overline{p_{\mathrm{u}}}}{\mathrm{d}x}\right|_{\overline{x}_{\mathrm{Sh}}}\tilde{x}_{\mathrm{Sh}};\quad \tilde{p}_{\mathrm{Sh,d}}=\tilde{p}_{\mathrm{d}}+\left.\frac{\mathrm{d}\overline{p_{\mathrm{u}}}}{\mathrm{d}x}\right|_{\overline{x}_{\mathrm{Sh}}}\tilde{x}_{\mathrm{Sh}}, \tag{41}$$

The jump (Rankine–Hugoniot) conditions for the steady flow are given by

$$\frac{\overline{\rho_{\mathrm{d}}}}{\overline{\rho_{\mathrm{u}}}}=\frac{\overline{u_{\mathrm{u}}}}{\overline{u_{\mathrm{d}}}}=\frac{(\gamma+1)M_{\mathrm{u}}^2}{2+(\gamma-1)M_{\mathrm{u}}^2};\quad \frac{\overline{p_{\mathrm{d}}}}{\overline{p_{\mathrm{u}}}}=\frac{2\gamma M_{\mathrm{u}}^2-(\gamma-1)}{\gamma+1}.$$

Upon linearizing these conditions and making use of Eqs. (38)–(41), we obtain, after some algebra

$$\left(\frac{\tilde{\rho}_{\mathrm{d}}}{\overline{\rho_{\mathrm{d}}}},\frac{\tilde{u}_{\mathrm{d}}}{\overline{u_{\mathrm{d}}}},\frac{\tilde{p}_{\mathrm{d}}}{\overline{p_{\mathrm{d}}}}\right)=(\mathcal{R},\mathcal{U},\mathcal{P})\tilde{x}_{\mathrm{Sh}}, \tag{42}$$

where the functions $\mathcal{R}$, $\mathcal{U}$, and $\mathcal{P}$ are given by

$$\mathcal{R}=\left[\frac{1}{\overline{\rho_{\mathrm{u}}}}\frac{\mathrm{d}\overline{\rho_{\mathrm{u}}}}{\mathrm{d}x}-\frac{1}{\overline{\rho_{\mathrm{d}}}}\frac{\mathrm{d}\overline{\rho_{\mathrm{d}}}}{\mathrm{d}x}+\frac{1}{M_{\mathrm{u}}^3}\frac{\overline{\rho_{\mathrm{d}}}}{\overline{\rho_{\mathrm{u}}}}\left(\frac{4}{\gamma+1}\right)\left(\frac{\mathrm{d}M_{\mathrm{u}}}{\mathrm{d}x}-\frac{\mathrm{i}\omega}{\overline{c_{\mathrm{u}}}}\right)\right]_{\overline{x}_{\mathrm{Sh}}},$$

$$\mathcal{U}=\left[\frac{1}{\overline{u_{\mathrm{u}}}}\frac{\mathrm{d}\overline{u_{\mathrm{u}}}}{\mathrm{d}x}-\frac{1}{\overline{u_{\mathrm{d}}}}\frac{\mathrm{d}\overline{u_{\mathrm{d}}}}{\mathrm{d}x}+\frac{1}{M_{\mathrm{u}}^3}\frac{\overline{u_{\mathrm{u}}}}{\overline{u_{\mathrm{d}}}}\left(\frac{4}{\gamma+1}\right)\times\left\{\frac{\mathrm{d}M_{\mathrm{u}}}{\mathrm{d}x}-\frac{\mathrm{i}\omega}{2\overline{c_{\mathrm{u}}}}(M_{\mathrm{u}}^2+1)\right\}\right]_{\overline{x}_{\mathrm{Sh}}},$$

$$\mathcal{P}=\left[\frac{1}{\overline{p_{\mathrm{u}}}}\frac{\mathrm{d}\overline{p_{\mathrm{u}}}}{\mathrm{d}x}-\frac{1}{\overline{p_{\mathrm{d}}}}\frac{\mathrm{d}\overline{u_{\mathrm{d}}}}{\mathrm{d}x}+M_{\mathrm{u}}\frac{\overline{p_{\mathrm{u}}}}{\overline{p_{\mathrm{d}}}}\left(\frac{4}{\gamma+1}\right)\left(\frac{\mathrm{d}M_{\mathrm{u}}}{\mathrm{d}x}-\frac{\mathrm{i}\omega}{\overline{c_{\mathrm{u}}}}\right)\right]_{\overline{x}_{\mathrm{Sh}}}.$$

The unsteady shock jump conditions are obtained by eliminating $\tilde{x}_{\mathrm{Sh}}$ from any two of Eq. (42). Thus, the matrix $L$ in Eq. (29) takes the form

$$L=\begin{bmatrix}\mathcal{U}\overline{u_{\mathrm{d}}} & -\mathcal{R}\overline{\rho_{\mathrm{d}}} & 0\\ \mathcal{P}\overline{p_{\mathrm{d}}} & 0 & -\mathcal{R}\overline{\rho_{\mathrm{d}}}\end{bmatrix}.$$

## Numerical Method

We now focus attention on the numerical implementation of the procedure described in the preceding sections. For a given mean flow $\overline{\mathbf{Q}}$, the matrices $B$, $G$, $T$, and $W$ are first computed. The gradients that appear in $G$ are calculated using centered second-order finite differences in shock-free regions, while one-sided second-order differences are employed in the neighborhood of a shock.

With $\omega$ set to any complex value, the local eigenproblem of Eq. (15) is solved at every station. Since the characteristic equation is cubic, its solutions can be determined analytically. Consequently, the matrix $R$ in Eq. (29), which relates the inlet and exit perturbation states can be computed. Next, the boundary condition matrices $L$ and $X$ are calculated, enabling the construction of $Z$ in Eq. (32) and the evaluation of its determinant.

The system eigenvalues, defined to be those values of $\omega=\omega_{\mathrm{r}}+\mathrm{i}\omega_{\mathrm{i}}$ for which $D(\omega)=D_{\mathrm{r}}+\mathrm{i}D_{\mathrm{i}}=\det(Z)$ vanishes, are determined using a grid-search method [12,13]. In this procedure, $D(\omega)$ is evaluated on a grid constructed using discrete values of $\omega_{\mathrm{r}}$ and $\omega_{\mathrm{i}}$. Regarding $D_{\mathrm{r}}$ and $D_{\mathrm{i}}$ as surfaces in the $\omega_{\mathrm{r}}-\omega_{\mathrm{i}}$ space, a standard contouring algorithm is employed to determine the curves corresponding to $D_{\mathrm{r}}=0$ and $D_{\mathrm{i}}=0$. The points that lie at the intersection of these two families of curves are the system eigenvalues. In practice, a coarse grid-search is employed to yield approximate eigenvalues, which are then used to initialize a Newton–Raphson iteration to obtain more accurate estimates by driving $D$ to zero.

The present technique of determining the eigenvalues is to be contrasted with the more conventional procedure of discretizing the governing equations using finite difference, finite element, or spectral methods and solving the resulting $3N\times 3N$ nonsparse matrix eigenproblem. This procedure yields $3N$ modes and eigenvalues, not all of which are physical. While algorithms have been developed to identify the spurious eigenvalues, they are not always reliable. This difficulty does arise in the present method since all roots found within the specified search window satisfy the condition $D=0$.

Once an eigenvalue has been determined, the mode shape corresponding to it is determined as follows. The value of one of the unsteady variables is set to an arbitrary value at the inlet. For example, if the inlet is ''open,'' one may set $\tilde{u}=1$. The remaining unsteady inlet variables are then determined by solving Eq. (32) for the specified (complex) value of $\omega$. Next, these values of inlet variables are used in conjunction with Eq. (21) to obtain the system mode shape at the node locations. We note that since the local eigenvalues and eigenmodes can be taken as constant (to second-order accuracy) between grid nodes, the mode shape can also be determined at intermediate points. In addition to the system mode shapes corresponding to $\tilde{\rho}$, $\tilde{u}$, and $\tilde{p}$, the shape of the entropy content of the mode is often of interest. The unsteady entropy $\tilde{s}(x)$ is constructed using the relation

$$\frac{\tilde{s}}{c_v}=\frac{\tilde{p}}{\overline{p}}-\gamma\frac{\tilde{\rho}}{\overline{\rho}},$$

where $c_v$ is specific heat at constant volume.

## Validation of Procedure

We will now demonstrate that the present method of determining the system modes and eigenvalues yields results in agreement with those obtained by other means. We begin by considering the unsteady flow through a duct with area variation

$$A(x)=A_0\left(\frac{x_0+x}{l}\right)^2;\quad 0\leqslant x\leqslant l,$$

where $A_0=0.1\ \mathrm{m}^2$, $x_0=1$ m, and $l=1$ m. The solution for a configuration of this type in the absence of a mean flow for ''open'' isentropic boundaries can be determined following the procedure described by Munjal [14], and yields the eigenvalues

$$\omega_n=\frac{n\pi c}{l};\quad n=1,2,3,\ldots, \tag{43}$$

which are identical to those for flow in a uniform channel. However, the mode shapes differ from those of a constant-area configuration; specifically, the structure of the pressure modes $\tilde{p}_n$, $n=1,2,3\ldots$, is given by

**Table 1 Comparison of numerical and analytical eigenfrequencies for low Mach number flow through a channel with quadratic area variation**

| $n$ | Numerical (Hz) | Analytical (Hz) |
|---|---|---|
| 1 | 170.184 | 170.131 |
| 2 | 340.337 | 340.263 |
| 3 | 510.466 | 510.394 |
| 4 | 680.578 | 680.525 |

**Table 2 Comparison of eigenfrequencies for a model combustor determined using the present analysis with the results of Lin [16]**

| | $\mathrm{Re}(\omega_n)$ | | $\mathrm{Im}(\omega_n)$ | |
|---|---|---|---|---|
| $n$ | Present | Lin [16] | Present | Lin [16] |
| 1 | 253.2 | 254.2 | 32.5 | 34.8 |
| 2 | 622.2 | 621.0 | −64.0 | −64.1 |
| 3 | 996.0 | 994.8 | 61.6 | 64.4 |
| 4 | 1502.0 | 1502.2 | 103.0 | 105.4 |

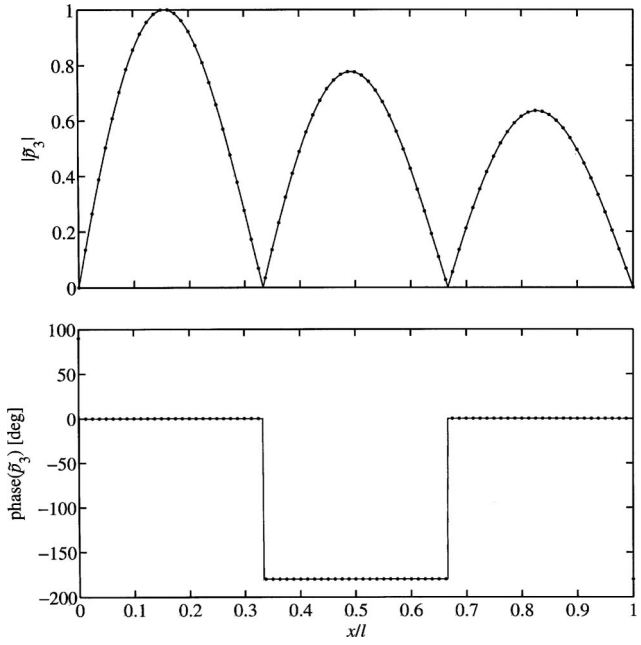


**Fig. 1 Numerical (•) and analytical (——) magnitude (top panel) and phase (bottom panel) of the pressure mode corresponding to the third eigenvalue in Table 1**

$$\tilde{p}_n(x) = \frac{1}{x+x_0}\exp\left(in\pi\frac{x_0}{l}\right)\sin\left[n\pi\frac{(x-x_0)}{l}\right]. \qquad (44)$$

Since the present formulation becomes singular for $M=0$, the effect of a stationary medium is simulated by setting the inlet Mach number to $5\times10^{-4}$. Using a grid comprised of $N=21$ points, the first four eigenfrequencies $f_n=\omega_h/2\pi$ as determined by the present numerical method are compared with those obtained from Eq. (43) in Table 1 and found to be in very good agreement. As is evident from Eq. (44), the area divergence attenuates the pressure mode from inlet to exit. This behavior is correctly predicted by the present method and both the magnitude and phase of the third pressure mode $\tilde{p}_3(x)$, shown in **Fig. 1**, are seen to be in excellent agreement with the analytical result. The numerical mode shapes in **Fig. 1** are determined at two equally spaced points between the grid nodes, in addition to the grid nodes themselves.

Next, we examine a configuration studied recently by Lin [16], which represents a simplified model of an industrial gas turbine combustor and consists of a flame tube of inlet area $1.267\times10^{-2}$ m$^2$, terminated by a converging-diverging nozzle. The overall length of the device is 1.543 m. Air at a total pressure of 2026.9 kPa and total temperature of 683.9 K enters the flame tube at a Mach number of 0.136. A flame, located at $x/l=0.18$, raises the total temperature by 712.4 K. The area distribution for the configuration is depicted in **Fig. 2(*a*)**; also shown are the mean flow parameters determined by numerical solution of the steady Euler equations using 194 nonuniformly spaced grid points. The inlet boundary conditions are set as $\tilde{p}=\tilde{s}=0$, while the condition in Eq. (36) for choked flow is applied at the exit.

Assuming that there are no self-excited sources, the complex frequencies for the first four modes are shown in Table 2. We observe that the second mode is unstable, while the remaining modes are damped. The real parts of the eigenvalues predicted by the present approach are generally in very good agreement with those obtained by Lin [16]. The growth rate of the unstable mode is also well predicted. However, the damping rates of the three stable modes obtained by the present method are observed to be slightly lower than those of Lin [16]. The shapes of the pressure and entropy modes corresponding to $\omega_2$ are illustrated in

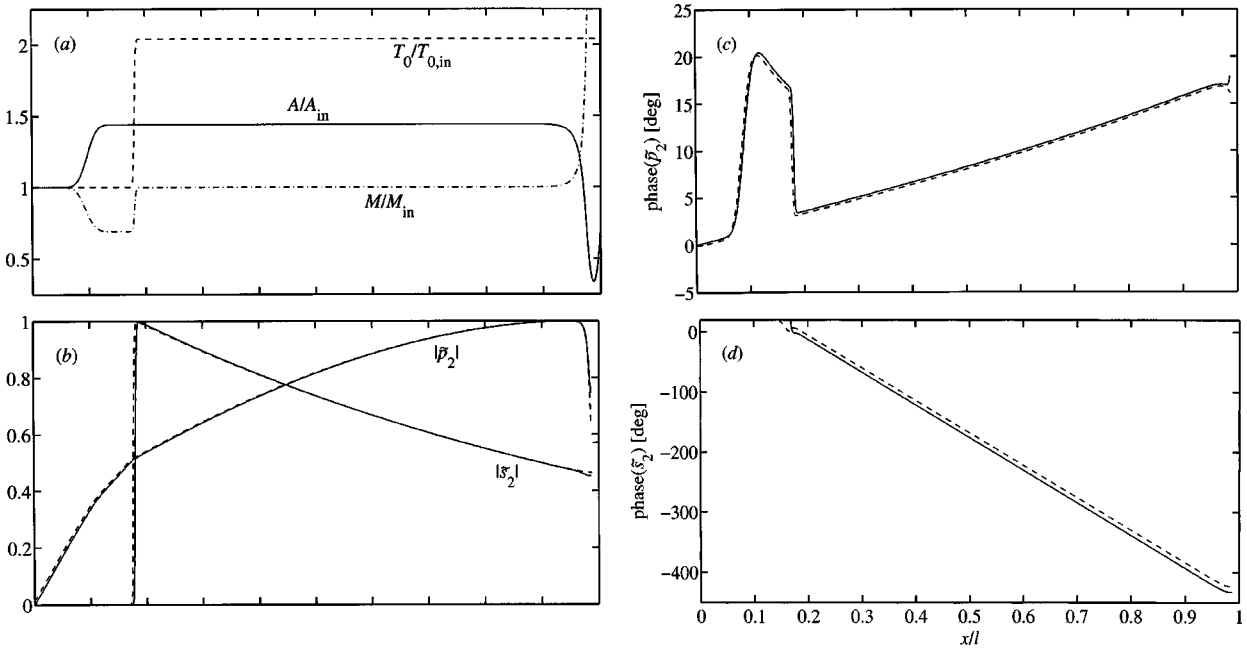


**Fig. 2 (*a*) Mean flow for the configuration of Lin [16]. (*b*),(*c*),(*d*) Pressure and entropy mode shapes corresponding to $\omega_2$ in Table 2 [16]: the present results (——) are compared with those of Lin [16] (— — —)**

**Figs. 2(*b*),(*c*),(*d*)** and the agreement is observed to be good in general. There are some differences evident near the sonic point in the nozzle, but these appear to be small and locally confined. It is interesting to observe that, owing to the inlet boundary condition, the amplitude of the entropy mode is zero upstream of the flame and that the interaction between the flame and the unsteady pressure results in entropy generation downstream. In fact, the unsteady pressure and entropy are coupled at the choked exit as shown in [9]. The acceleration of hot spots through the choked nozzle generates acoustic disturbances which in turn cause entropy perturbations, resulting in instability [5,6,16].

## Conclusion

A formulation has been developed for the stability analysis of spatially nonuniform thermoacoustic systems, accounting for self-excited sources. In this frequency-domain method, the unsteady disturbances are represented as a superposition of local wave modes, which are modulated in the flow direction. This enables the linearized Euler equations to be integrated across the flow domain with second-order spatial accuracy. The general development presented here is applicable both to forced problems and those in which the natural modes of the system are sought. The emphasis here is on the latter class of problems, where appropriate inlet and exit conditions are required to complete the problem specification. The formulation of impedance-type boundary conditions as well as those corresponding to shocks and choked flows was described. The global eigenproblem is solved using a grid-search algorithm in conjunction with Newton iteration. The scheme was validated by comparison with analytical and numerical solutions.

Although the focus in this study has been on the determination of the natural modes and frequencies of a thermoacoustic system, the calculation of the forced response readily follows from the general formulation. Specifically, repeated application of Eq. (21) between the nodes at $j=1$ and $j=N-1$ yields an expression of the form

$$\tilde{\mathbf{Q}}_N = P_N \tilde{\mathbf{Q}}_1 + \sum_{j=1}^{N} \mathcal{C}_j \tilde{\mathbf{F}}_j ,$$

where $\mathcal{C}_j, j=1,\ldots,N$ are $3\times 3$ matrices which depend only on the mean flow. Applying the boundary conditions in Eqs. (30) and (31), we find that

$$Z\tilde{\mathbf{Q}}_1 = \left[ 0 \quad 0 \quad -X\sum_{j=1}^{N} \mathcal{C}_j \tilde{\mathbf{F}}_j \right]^T . \tag{45}$$

Equation (45) can be inverted to determine $\tilde{\mathbf{Q}}_1$ provided $Z$ is nonsingular. This latter condition requires that the forcing not occur at a natural frequency of the system. Once $\tilde{\mathbf{Q}}_1$ is determined, the response at other points in the flow domain can be computed by marching using Eq. (21).

It is worth pointing out that the assumption of quasi-one-dimensional flow ignores an effect that can be significant when rapid area changes are present in the flow path. Under these conditions, a local three-dimensional distortion of the acoustic field will occur. This can affect the system eigenvalues in much the same manner as the end correction alters the natural frequency of a Helmholtz resonator. In addition, flow separation can occur at the the abrupt area change, which has a dissipative effect on the perturbation field.


## Acknowledgment

The authors are grateful to Pratt & Whitney for granting permission to publish the present work. The authors are also indebted to Dr. R.-S. Lin of United Technologies Research Center for making available the results of his calculations presented in the last section.


## Appendix

Here we illustrate the derivation of Eq. (19) which relates the perturbation vector at a point $j+1/2$ between the grid nodes at $j$ and $j+1$ to the flow quantities at the node $j$. In accordance with the approximation described in the main body of the paper, we set $\mathcal{M}=\mathcal{M}_j, \Lambda=\Lambda_j$ in the region $x_j<x<x_{j+1/2}$. Evaluating Eq. (17) at $x=x_{j+1/2}$ yields

$$\tilde{\mathbf{Q}}_{j+1/2} = \mathcal{M}_j E_{j,j} \left[ \mathcal{M}_j^{-1} \tilde{\mathbf{Q}}_j + \int_{x_j}^{x_{j+1/2}} (\mathcal{E}^{-1} \mathcal{M}_j^{-1} B^{-1} \tilde{\mathbf{F}}) \mathrm{d}x \right], \tag{A1}$$

where $E_{j,j}=\exp[\Lambda_j \delta x_j/2]$. The first term on the right-hand side of Eq. (*A*1) is readily determined in terms of $\tilde{\mathbf{Q}}_j$ and it then remains to evaluate the integral

$$\mathcal{J} = \int_0^{\delta x_j/2} \exp[-\Lambda_j \xi] \mathbf{P} \mathrm{d}\xi, \tag{A2}$$

where we have defined $\xi=x-x_j$ and

$$\mathbf{P} = \mathcal{M}_j^{-1} B^{-1} \tilde{\mathbf{F}}. \tag{A3}$$

Since $B$ is a nonsingular smooth function of $x$, we may expand $\mathbf{P}$ as a Taylor series in $\xi=x-x_j$:

$$\mathbf{P} = \mathbf{P}_0 + \mathbf{P}_0' \xi + O(\xi^2),$$

where $\mathbf{P}_0=\mathbf{P}(x_j)$, $\mathbf{P}_0'=\mathbf{P}'(x_j)$. Substituting Eq. (*A*3) into Eq. (*A*2) and integrating by parts yields, to second order in $\delta x_j$

$$\mathcal{J} = -\Lambda_j^{-1}[\mathrm{e}^{-\Lambda_j \delta x_j/2} - I]\mathbf{P}_0 - \Lambda_j^{-1}\left[ \left( \frac{1}{2}\delta x_j I + \Lambda_j^{-1} \right) \times \mathrm{e}^{-\Lambda_j \delta x_j/2} - \Lambda_j^{-1} \right] \mathbf{P}_0' . \tag{A4}$$

Using the Taylor expansion of the exponential function in Eq. (*A*4) and retaining only terms of order $\delta x_j$ gives the result

$$\mathcal{J} = \frac{1}{2}\delta x_j \mathbf{P}_0 + O(\delta x_j^2). \tag{A5}$$

Combination of Eqs. (*A*3), (*A*4), and (*A*5) then shows that

$$\tilde{\mathbf{Q}}_{j+1/2} = \mathcal{M}_j E_{j,j} \mathcal{M}_j^{-1} \left[ \tilde{\mathbf{Q}}_j + \frac{1}{2}\delta x_j B_j^{-1} \tilde{\mathbf{F}}_j \right].$$

## References


[1] Culick, F. E. C., 1994, "Some Recent Results for Nonlinear Acoustics in Combustion Chambers," AIAA J., **32**, pp. 146–269.
[2] Pankiewitz, C., and Sattelmayer, T., 2002, "Time Domain Simulation of Combustion Instabilities in Annular Combustors," ASME Paper GT-2002-30064.
[3] Cohen, J. M., Wake, B. E., and Choi, D., 2003, "Investigation of Instabilities in a Lean Premixed Step Combustor," J. Propul. Power, **19**, pp. 81–88.
[4] Bloxsidge, G. J., Dowling, A. P., and Langhorne, P. J., 1988, "Reheat buzz: An Acoustically Coupled Combustion Instability. Part 2. Theory," J. Fluid Mech., **193**, pp. 445–473.
[5] Dowling, A. P., 1995, "The Calculation of Thermoacoustic Oscillations," J. Sound Vib., **180**, pp. 557–581.
[6] Keller, J. J., 1995, "Thermoacoustic Oscillations in Combustion Chambers of Gas Turbines," AIAA J., **33**, pp. 2280–2287.
[7] Stow, S. R., and Dowling, A. P., 2001, "Thermoacoustic Oscillations in an Annular Combustor," ASME Paper 2001-GT-0037.
[8] Evesque, S., and Polifke, W., 2002, "Low-order Acoustic Modelling for Annular Combustors: Validation and Inclusion of Modal Coupling," ASME Paper GT-2002-30064.
[9] Marble, F. E., and Candel, S. M., 1977, "Acoustic Disturbance from Gas Non-uniformities Convected Through a Nozzle," J. Sound Vib., **55**, pp. 225–243.
[10] Culick, F. E. C., and Rogers, T., 1983, "The Response of Normal Shocks in Diffusers," AIAA J., **21**, pp. 1382–2390.

[11] Whitham, G. B., 1974, *Linear and Nonlinear Waves* (Wiley, New York).
[12] Tam, C. K. W., and Hu, F. Q., 1989, ''On the Three Families of Instability Waves of High-Speed Jets,'' J. Fluid Mech., **201**, pp. 447–483.
[13] Kuo, C.-Y., and Dowling, A. P., 1996, ''Oscillations of a Moderately Underexpanded Choked Jet Impinging Upon a Flat Plate,'' J. Fluid Mech., **315**, pp. 267–291.
[14] Munjal, M. L., 1987, *Acoustics of Ducts and Mufflers with Application to Exhaust and Ventilation System Design* (Wiley, New York).
[15] Prasad, D., and Feng, J., 2004, ''Thermoacoustic Stability of Quasi-One-Dimensional Flows. Part II Application to Basic Flows,'' J. Turbomach, **126**, pp. 644–652.
[16] Lin, R.-S., ''Entropy Driven Thermoacoustic Instability,'' (unpublished).

# Thermoacoustic Stability of Quasi-One-Dimensional Flows—Part II: Application to Basic Flows

**Dilip Prasad**

**Jinzhang Feng**

Aerodynamics Division,
Pratt & Whitney Aircraft Engines,
East Hartford, CT 06108

*In this paper, applications of a previously developed numerical formulation (Prasad, D., and Feng, J., 2004, "Thermoacoustic Stability of Quasi-One-Dimensional Flows—Part I: Analytical and Numerical Formulation," J. Turbomach.,* **126***, pp. 636–643. for the stability analysis of spatially varying one-dimensional flows are investigated. The results are interpreted with the aid of a generalized acoustic energy equation, which shows that the stability of a flow system depends not only on the nature of the unsteady heat, mass and momentum sources but also on the mean flow gradients and on the inlet and exit boundary conditions. Specifically, it is found that subsonic diffusing flows with strongly reflecting boundary conditions are unstable, whereas flows with a favorable pressure gradient are not. Transonic flows are also investigated, including those that feature acceleration through the sonic condition and those in which a normal shock is present. In both cases, it is found that the natural modes are stable. Finally, we study a simplified ducted flame configuration. It is found that the length scale of the mean heat addition affects system stability so that the thin-flame model commonly used in studies of combustion stability may not always be applicable.*
[DOI: 10.1115/1.1791289]

## Introduction

The stability of thermoacoustic systems plays a significant role in the development and operation of gas turbine power plants and other fluid machinery. In particular, the deleterious effects of compression and combustion system instabilities on the performance and operability of aircraft engines and industrial power generation units are well known. The ability to predict these instabilities during the development process is therefore of crucial importance since it enables the designer to adopt measures that minimize or eliminate their occurrence.

A class of methods for analyzing the stability of thermoacoustic systems that has found widespread acceptance is based on the frequency–domain linearized equations of motion, assuming that the background flow is piecewise uniform. A method applicable to one-dimensional flows with arbitrary spatial variations was recently developed by Prasad and Feng [1]. In this method, the unsteady flow is represented as a superposition of local wave modes, which enables the governing equations to be integrated across the domain. Together with the appropriate boundary conditions, a global eigenvalue problem can then be derived, which is solved numerically. While a large variety of flows can be studied using this method, we consider here several relatively simple configurations. Specifically, subsonic and transonic flows with adverse and favorable pressure gradients and a ducted flame with distributed heat release are examined. These configurations represent elements found in many thermoacoustic systems of engineering interest. Moreover, the study of these components in isolation, as is done here, leads to an improved understanding of their impact on the stability properties of the complex systems within which they are embedded.

In order to better interpret the stability aspects of the flow, we employ the acoustic energy equation of Dowling [2], which reveals the roles played by the mean flow and boundary conditions. We then examine subsonic diffusing flows with strongly reflecting boundary conditions such as that due to a pressure release and show that they are unstable. On the other hand, even with strongly reflecting boundary conditions, subsonic flows with favorable pressure gradients are found to only possess stable natural modes.

We also examine the stability of two types of transonic flows. In the first type, the flow accelerates from a subsonic state to a supersonic state through a converging–diverging nozzle while in the second, deceleration from supersonic to subsonic flow occurs across a normal shock. Both instances of transonic flow are found to be stable. For the accelerating case, it is found that the damping rate depends on the length scale of the area variation while that for the diffuser is controlled by the shock strength.

Finally, we examine a simplified model of a flame in a constant-area duct with a distributed heat release intended to simulate realistic combustor flows. The unsteady heat release across the flame is modeled using a time-lag model. The dependence of the system eigenvalues on the flame temperature is studied. When the distributed heat release is replaced with a concentrated one, the system eigenvalues and mode shapes are found to behave differently. These results suggest that the compact flame model commonly employed in reduced order models of thermoacoustic systems may not always be applicable.

## Generalized Acoustic Energy Equation

In interpreting the stability behavior of thermoacoustic systems, the use of an energy balance equation often provides insight into the mechanisms involved. An early instance is the celebrated Rayleigh [4] criterion for thermoacoustic stability in the absence of a mean flow, which has been examined in more mathematical terms by Chu [5]. More recently, Dowling [2] has derived a generalized acoustic energy equation which incorporates the effect of a mean flow as well as the generation of acoustic energy from vortical and entropic perturbations. Following the procedure in [2], a one-dimensional variant of this equation may be developed, taking

Contributed by the International Gas Turbine Institute (IGTI) of THE AMERICAN SOCIETY OF MECHANICAL ENGINEERS for publication in the ASME JOURNAL OF TURBOMACHINERY. Paper presented at the International Gas Turbine and Aeroengine Congress and Exhibition, Vienna, Austria, June 13–17, 2004. Paper No. 2004-GT-53945. Manuscript received by IGTI, October 1, 2003; final revision, March 1, 2004. IGTI Review Chair: A. J. Strazisar.

into account mass sources and body forces, in addition to heat sources. Adopting the nomenclature of [1] and denoting perturbation quantities by primes [e.g., $u'=\overline{u}(x)-u(x,t)$], the acoustic energy $\varepsilon$ and intensity $\mathcal{I}$ are defined according to

$$\varepsilon=\frac{1}{2}\overline{\rho}u'^2+\frac{1}{\overline{\rho c^2}}\left(\frac{1}{2}p'^2+\overline{\rho u}p'u'\right), \tag{1}$$

$$\mathcal{I}=\left(u'+\frac{\overline{u}}{\overline{\rho c^2}}p'\right)(p'+\overline{\rho u}u'), \tag{2}$$

The acoustic energy equation then takes the form

$$\frac{\partial}{\partial t}(\varepsilon A)+\frac{\partial}{\partial x}(\mathcal{I}A)=\mathcal{S}A, \tag{3}$$

where $\mathcal{S}$ is given by

$$\begin{aligned}\mathcal{S}=&\left[\frac{\gamma-1}{\gamma\overline{p}}q'-\frac{(\gamma-1)^2\overline{q}}{\gamma^2\overline{p}^2}p'\right](p'+\overline{\rho u}u')+\left[\frac{m'}{\overline{\rho}}+\frac{\overline{m}}{\overline{\rho}}\left(\frac{p'}{\gamma\overline{p}}-\frac{\rho'}{\overline{\rho}}\right)\right]\\&\times(p'+\overline{\rho u}u')+\overline{\rho}\left(u'+\frac{\overline{u}}{\overline{\rho c^2}}p'\right)f'+\frac{\mathcal{I}}{A}\frac{\mathrm{d}A}{\mathrm{d}x}\\&+\overline{\rho u}\left(\frac{1}{\overline{\rho}}\frac{\mathrm{d}\overline{\rho}}{\mathrm{d}x}-\frac{1}{\gamma\overline{p}}\frac{\mathrm{d}\overline{p}}{\mathrm{d}x}\right)\left(u'+\frac{\overline{u}}{\overline{\rho c^2}}p'\right)u'\\&+\frac{\mathrm{d}\overline{p}}{\mathrm{d}x}\left(u'+\frac{\overline{u}}{\overline{\rho c^2}}p'\right)\left(\frac{\rho'}{\overline{\rho}}-\frac{p'}{\gamma\overline{p}}\right)\end{aligned} \tag{4}$$

It then follows from Eq. (3) that

$$\frac{\mathrm{d}}{\mathrm{d}t}\int_0^l\langle\varepsilon\rangle A\,\mathrm{d}x=\langle\mathcal{I}\rangle A|_{x=0}-\langle\mathcal{I}\rangle A|_{x=l}+\int_0^l\langle\mathcal{S}\rangle A\,\mathrm{d}x, \tag{5}$$

where the notation $\langle\cdot\rangle$ denotes the average over one temporal cycle. Equation (5) shows that the rate of growth of the system acoustic energy is determined by the flux of the intensity through the flow boundaries and the volumetric "sources" that comprise $\mathcal{S}$. In the case of self-excited oscillations, the contributions due to the intensity fluxes are determined by the nature of the conditions imposed at the inlet and exit boundaries. Specifically, strongly reflecting conditions such as those corresponding to "open" or "closed" boundaries, which cause energy to become trapped within the device can lead to instability.

Turning now to the term $\mathcal{S}$, we observe from the right-hand side of Eq. (4) that the first component is associated with heat sources; in fact, as shown in [2], it reduces to the Rayleigh source term, $(\gamma-1)p'q'/\gamma\overline{p}$ for a constant-area configuration without mean flow. The second and third terms on the right-hand side of Eq. (4) illustrate the fact that mass sources and body forces, in addition to heat sources, have an impact on system stability. The effect of area changes and mean flow variations are incorporated in the last three terms; in particular, the fifth and sixth terms represent explicitly the effects of coupling between the perturbations and mean flow gradients.

The preceding discussion illustrates that the nature of instability even in one-dimensional flow systems can be quite complicated. The eventual fate of a disturbance is determined by several different, possibly competing mechanisms and, unlike the case examined by Rayleigh [4], it is difficult to arrive at a general criterion for stability. In what follows, we consider disturbances of the form

$$(\rho',u',p')=(\tilde{\rho}(x),\tilde{u}(x),\tilde{p}(x))\mathrm{e}^{\mathrm{i}\omega t},$$

and numerically solve an eigenproblem as described in [1] to determine the complex natural frequencies $\omega_n$ and system eigenmodes $(\tilde{\rho}_n,\tilde{u}_n,\tilde{p}_n)$ for mode orders $n=1,2,3,\ldots$ .

## Subsonic Flows

We focus attention now on flows in which the Mach number remains subsonic throughout the domain. It is assumed that there are no heat or mass sources and that no external forces act on the fluid. Flows with both adverse and favorable pressure gradients through ducts of length $l=0.5$ m are considered. The inlet area is $0.1\ \mathrm{m}^2$, while the inlet total pressure and total temperature are set to 101.3 kPa and 300 K, respectively. Then, assuming that the flow is isentropic, the mean quantities can be determined by enforcing conservation of mass and the stagnation quantities.

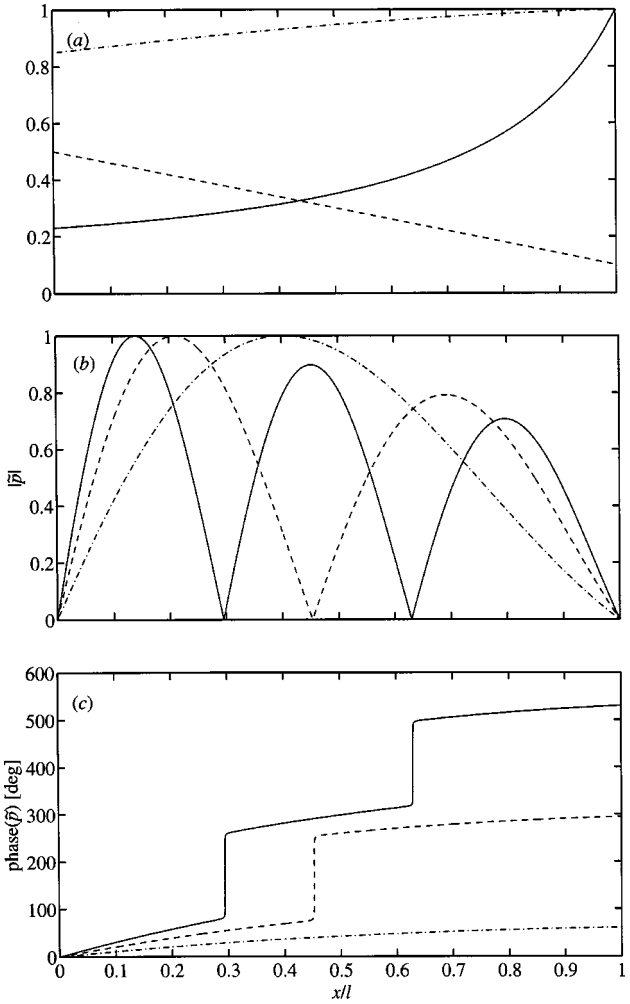


**Fig. 1** (***a***) **Mach number** (— — —)**, normalized area** [$\overline{A}/\overline{A}(l)$, ——] **and normalized pressure** [$\overline{p}/\overline{p}(l)$, —·—·—] **distributions for diffusing subsonic flow.** (***b***) **Magnitude and** (***c***) **phase of the first three pressure modes** $\tilde{p}_n(x)$**:** $n=1$ (—·—·—)**,** $n=2$ (— — —) **and** $n=3$ (——)**.**

**Diffusing Flows.** We examine first a diffusing flow in which the Mach number decreases linearly from 0.5 to 0.1. The area and pressure distributions (normalized by their exit values) and Mach number are shown in **Fig.** 1($a$). In this calculation, the diffuser is discretized using a grid consisting of 101 equally-spaced points. The boundary conditions are taken as $\tilde{p}=\tilde{s}=0$ at the inlet ($x=0$) and $\tilde{p}=0$ at $x=l$, where $s$ represents the entropy.

The spectrum is shown in **Fig.** 2, with the eigenvalues normalized by $\overline{u}_{\mathrm{in}}/l$, where the subscript "in" denotes inlet conditions. The most prominent feature of the eigenvalues is that $\mathrm{Im}(\omega)<0$, indicating that the natural modes are unstable. The shapes of the pressure modes $\tilde{p}_n(x)$, $n=1,2,3$ are illustrated in **Figs.** 1($b$) and 1($c$). The local peaks of $|\tilde{p}_1|$ and $|\tilde{p}_3|$ decrease in the direction of increasing area and their nodes are not evenly spaced. This lack of symmetry is a consequence of the fact that the local wave modes are refracted by the mean flow, as discussed in [1].

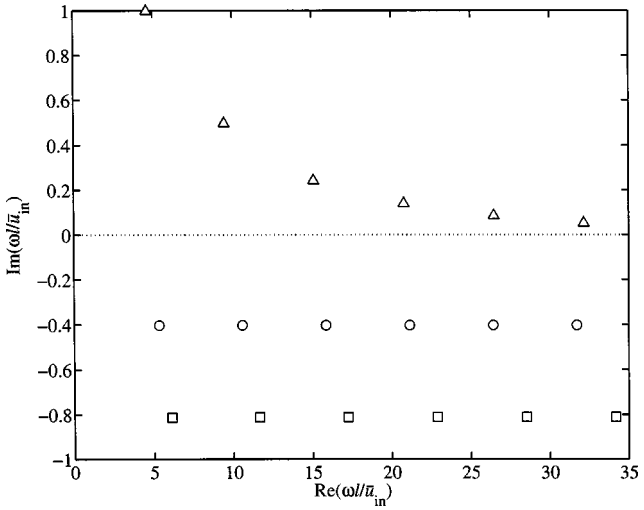


**Fig. 2 Spectra for subsonic diffuser flow with $M_{in}=0.5$ and "open" inlet condition: results are shown for $M_{ex}=0.1$ with "open" exit condition (□), $M_{ex}=0.1$ with $\zeta_{ex}=1+i$ (△) and $M_{ex}=0.3$ with "open" exit condition (○)**

We now examine the unstable nature of the system modes, a feature that has received only limited attention in the past. For the flow considered here, Eq. (5) reduces to

$$\frac{d}{dt}\int_0^l \langle\varepsilon\rangle A\,dx = \langle\mathcal{I}\rangle A|_{x=0} - \langle\mathcal{I}\rangle A|_{x=l} + \int_0^l \langle\mathcal{I}\rangle \frac{dA}{dx}\,dx. \quad (6)$$

It therefore appears that the overall growth or damping of a disturbance for this flow field is determined by the nature of the inlet and exit conditions and the mean flow and area distributions. In order to verify the first of these conjectures, we carry out an eigenanalysis for a flow with the same mean properties but with the "open" downstream boundary replaced with an acoustic impedance $\zeta_{ex}=1+i$. The spectrum obtained using this boundary condition, illustrated in **Fig.** 2, is observed to consist of damped modes. This is to be expected, for the downstream impedance with $\mathrm{Re}(\zeta_{ex})>0$ represents a dissipative element so that energy is no longer trapped within the device. We also note that the effect of the nonzero reactance $[\mathrm{Im}(\zeta_{ex})\neq 0]$ is to cause a shift in the frequencies of the resonant modes relative to the "open" case.

We now address the second conjecture, viz., the effect of the mean flow and area variations on system stability by considering a less diffusive mean flow, in which the Mach number decreases linearly from 0.5 to 0.3; the inlet and exit boundaries are taken to be "open" ($\tilde{p}=0$). The resulting spectrum is shown in **Fig.** 2; it is evident that the effect of the reduced diffusion is to move the eigenvalues in the direction of neutral stability. In the limiting case of no diffusion (uniform flow), the natural modes become neutrally stable so that the eigenvalues lie along the real axis.

Although the instability of diffuser flows has been studied previously, the focus has been restricted to low-speed configurations. Specifically, Kline [6] first demonstrated the existence of a "transitory stall" regime for diffusers with moderately large area divergence, where the flow is highly unsteady. Early attempts to collapse the oscillation frequency proved unsuccessful [7–9]. Recent experiments by Kwong and Dowling [10] have however revealed that in this regime, the unsteadiness is caused by oscillations in the upstream edge of the stall cell across the entire section of the diffuser, suggesting that the inception of the instability can be described using a one-dimensional analysis. An analysis of this type was carried out in [10] for a configuration consisting of a diffuser connected to a downstream plenum, assuming incompressible flow in the diffuser and treating the plenum as a Helmholtz resonator. Using a "steady stall" model, wherein the flow within the stall cell was taken to be incompressible, good agreement of the unstable frequency with experiment was obtained although the theoretical eigenvalue was damped.

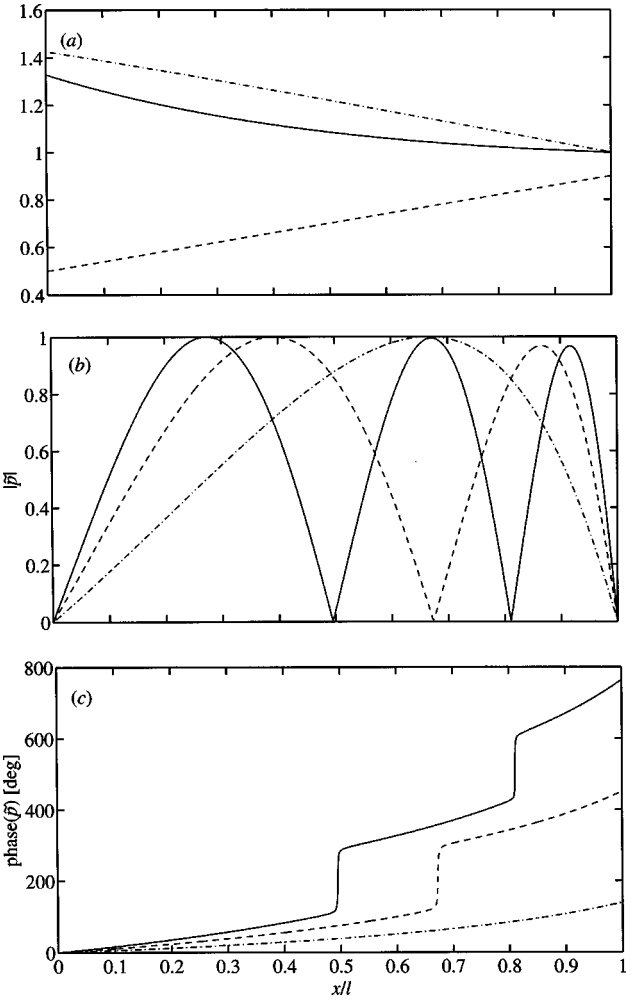


**Fig. 3 (*a*) Mach number (— — —), normalized area [$A/A(l)$, ——] and normalized pressure [$\bar{p}/\bar{p}(l)$, —·—·] distributions for accelerating subsonic flow. (*b*) Magnitude and (*c*) phase of the first three pressure modes $\tilde{p}_n(x)$: $n=1$ (—·—·), $n=2$ (— — —) and $n=3$ (——).**

Kwong and Dowling [10] have emphasized the necessity for an unsteady flow model of the diffuser to incorporate the acoustics of the duct (or plenum) to which the diffuser is connected. In their case, the compressibility of the plenum is decoupled from the inertia of the fluid in the diffuser. This separation of the compliance and inertia does not occur in the examples we have considered since the flow is compressible. As a consequence, a multitude of unstable modes is obtained, whereas the analysis of [10] predicts a single unstable frequency. This occurs because the assumption of incompressible flow in the diffuser precludes acoustic wave propagation there so that the only mode of oscillation results from a balance between the compliance of the plenum and the inertia of the fluid in the diffuser.

**Accelerating Flows.** Pursuing the previous line of reasoning further, it is natural to inquire whether the system modes are damped for an accelerating background flow. Thus we consider in **Fig.** 3(*a*) a subsonic flow with converging area such that the Mach number rises linearly from 0.5 at the inlet to 0.9 at the exit. Assuming $\tilde{p}=0$ at the inlet and exit boundaries and isentropic flow at the inlet, the spectrum obtained for this flow is illustrated in **Fig.** 4. We observe that the eigenvalues correspond to damped

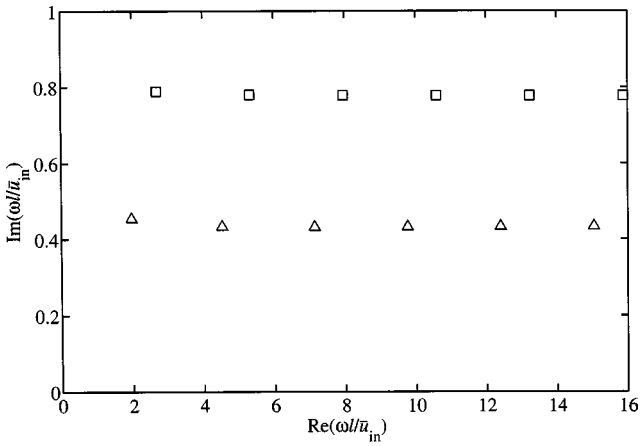


**Fig. 4 Spectra for subsonic nozzle flow with $M_{in}=0.5$, $M_{ex}=0.9$ and "open" inlet condition: results are shown for the "open" exit condition (□) and for $\zeta_{ex}=-1+i$ (△)**

natural modes. The shapes of the pressure modes corresponding to the first three eigenvalues are shown in **Figs.** 3(*b*) and 3(*c*). As in the case of the diffuser flow, we observe a marked lack of symmetry in the amplitudes; here, the refractive effect of the background flow variations on the local wavelength is even more pronounced, owing to the proximity of the Mach number to unity near the nozzle exit.

Next, we investigate the effect of the downstream boundary condition on system stability. In analogy with the approach adopted for the diffuser flow, we set the exit impedance to a value $\zeta_{ex}=-1+i$; this implies a negative acoustic resistance so that the energy is fed into the system at $x=l$. The effect of this impedance condition is to move the eigenvalues closer to the real axis, as shown in **Fig.** 4. However, the modes remain stable, illustrating the fact that the nature of the boundary conditions does not solely determine the stability of the system. Rather, the mean flow and area distributions also play an important role in this regard, in accord with Eq. (5).

## Transonic Flows

We now turn to flows in which the Mach number exceeds unity. However, since only inlet boundary conditions can be specified for a purely supersonic flow, it is evident that such a configuration does not possess eigensolutions. Thus, for natural modes to exist, the flow must be subsonic at one of the boundaries. We consider both possibilities here, the first configuration being a transonic nozzle in which the incoming flow is subsonic and undergoes isentropic acceleration to a supersonic state. The second configuration is a transonic diffuser, where a supersonic flow decelerates to subsonic speed across a normal shock.

**Transonic Nozzle.** A transonic nozzle of length $l=1$ m, and inlet total pressure and total temperature of 101.3 kPa and 300 K, respectively, is considered. The nozzle is designed for a Mach number variation given by

$$M(x)=0.2+0.8[1+\tanh 10(x-0.8)],$$

shown in **Fig.** 5(*a*). Setting the throat area to 0.1 $m^2$, the area distribution and mean flow parameters are determined by imposing conservation of mass and the total quantities. Here, we have employed a grid consisting of 101 equally-spaced points. The area and pressure, normalized by their inlet values, are shown in **Fig.** 5 (*a*). The flow variables are nearly constant over $0<x/l<0.6$; beyond $x/l\approx 0.6$ the flow accelerates rapidly and achieves the sonic state at $x/l=0.8$. The inlet boundary at $x=0$ is assumed to be "open" and isentropic ($\tilde{p}=\tilde{s}=0$) while the boundary condition derived in [1] for choked flow is applied at the sonic point.

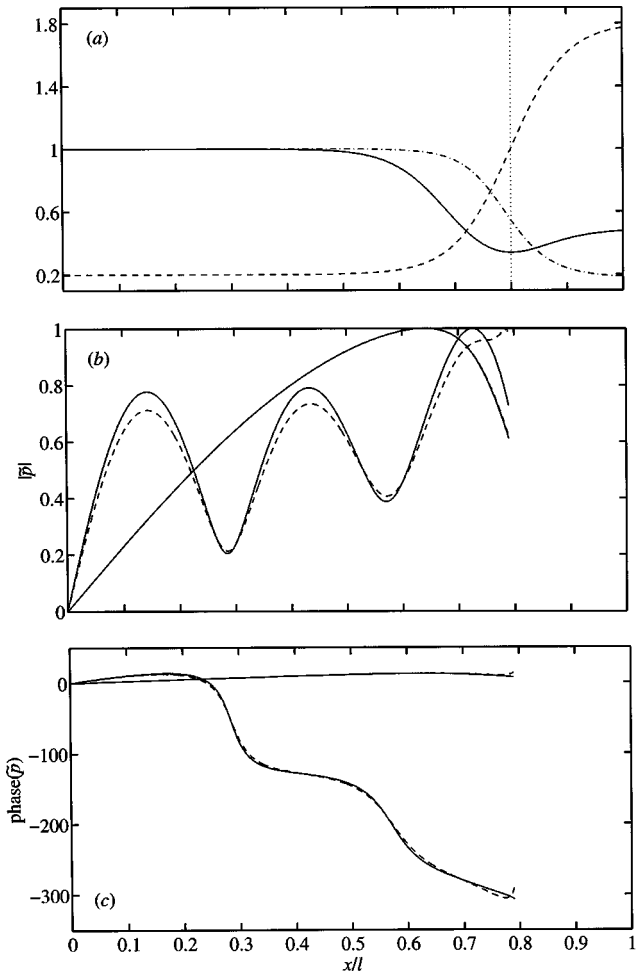


**Fig. 5 (*a*) Mach number (— — —), normalized area [$A/A(0)$, ——] and normalized pressure [$\bar{p}/\bar{p}(0)$, —·—·—·—] distributions for small length-scale transonic flow. (*b*) Magnitude and (*c*) phase of $\tilde{p}_1(x)$ and $\tilde{p}_3(x)$ determined using the exact (——) and compact-nozzle (— — —) boundary conditions.**

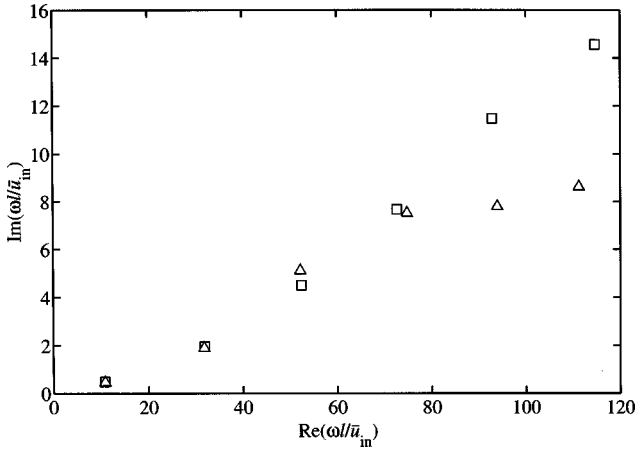


**Fig. 6 Spectrum for transonic flow through the nozzle of Fig. 5 (*a*). Eigenvalues determined using the exact (□) and compact-nozzle (△) boundary conditions are shown.**

The spectrum is shown in **Fig.** 6 and is seen to consist of damped natural modes. While the damping rate of the first ($n=1$) mode is small, it increases rapidly with the mode order $n$. In **Figs.** 5($b$) and 5($c$), we illustrate the structure of the $n=1$ and $n=3$ pressure modes. Neither the slope nor the value of $|\tilde{p}|$ is zero at the throat, indicating that its acoustic impedance is finite and nonzero.

In the limit of a compact nozzle, where the length scale of the nozzle is much larger than that of the perturbations, Marble and Candel [3] have shown that the matching condition between the subsonic and supersonic regions is given by

$$\frac{\tilde{\rho}}{\bar{\rho}}+\frac{2\tilde{u}}{\bar{u}}-\frac{\tilde{p}}{\bar{p}}=0. \tag{7}$$

For isentropic flow, it follows from Eq. (7) that the acoustic impedance at the throat is given by

$$\zeta=\frac{2}{\gamma-1},$$

illustrating that the compact choked nozzle represents a purely resistive element with positive damping. The simplicity of the analytical expression in Eq. (7) makes it attractive for use in reduced-order models for combustion instability. It is therefore of interest to investigate its applicability to the present flow. To this end, the spectrum obtained using the boundary condition in Eq. (7) is shown in **Fig.** 6. For modes with $n\leqslant 4$, the eigenvalues are seen to be in good agreement with those of the exact analysis. At larger values of $n$, increasingly large differences are observed in the damping rate although the frequency obtained using the asymptotic condition in Eq. (7) appears to be in reasonably good agreement with the exact boundary condition value. The shapes of the pressure modes $\tilde{p}_n(x)$ for $n=1,3$ obtained using the boundary condition of Eq. (17) are depicted in **Figs.** 5($b$) and 5($c$). The magnitude and phase of $\tilde{p}_1(x)$ are in excellent agreement with those of the exact analysis with small differences evident near the sonic point. In the case the third mode, we observe that the magnitude differs noticeably from the solution corresponding to the exact boundary condition although the phase variation is well captured.

Next, we consider a quite different transonic nozzle flow with the same end states. Thus the inlet quantities, nozzle length and sonic location are the same as in the previous case but the Mach number varies linearly, as shown in **Fig.** 7($a$); the corresponding area and pressure distributions (normalized by their inlet values) are also shown. In contrast with the nozzle examined previously, the area contraction occurs over an extended length scale. The spectrum of eigenvalues for this flow configuration, discretized on a grid comprised of 101 equally-spaced points, is depicted in **Fig.** 8. Since the nozzles in **Figs.** 5($a$) and 7($a$) possess the same length and inlet velocities, it is appropriate to compare the spectra of **Figs.** 8 and 6. The frequencies of the natural modes in **Fig.** 8 are observed to be smaller than those in **Fig.** 6; they are also more heavily damped, particularly at the lower mode orders.

The shapes of the pressure modes $\tilde{p}_n(x)$ for $n=1,3$ are shown in **Figs.** 7($b$) and 7($c$). In contrast with the previous case, the refractive effect of the mean flow is much stronger and both modes are seen to exhibit significant changes in the local wavelength between the inlet and sonic point. Observing, in particular, that even the lowest order mode features variations on the length scale of the area variation, it is evident that the asymptotic boundary condition of Eq. (7) cannot be expected to apply. Nevertheless, for completeness we examine its effect on the spectrum and mode shapes in **Figs.** 8 and 7($b$) and 7($c$), respectively. Although the frequencies are estimated to good approximation, the compact nozzle condition is seen to severely underpredict the damping rates. Similarly, we observe that the mode shapes differ significantly from those obtained using the more precise analysis.

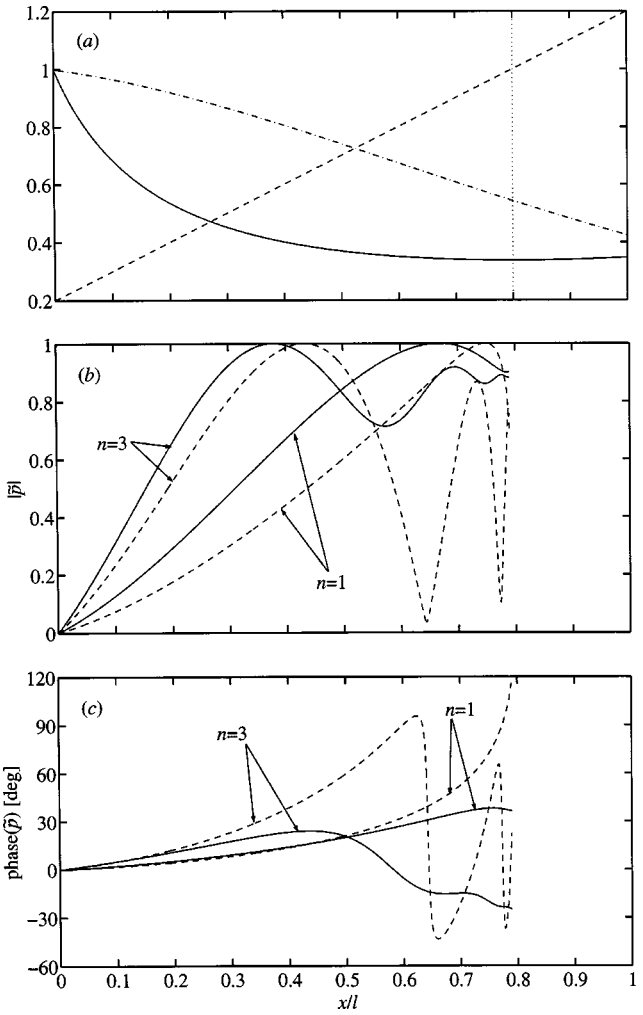


**Fig. 7 (*a*) Mach number (– – –), normalized area [$A/A(0)$, ——] and normalized pressure [$\bar{p}/\bar{p}(0)$, —·—·] distributions for large length-scale transonic flow. (*b*) Magnitude and (*c*) phase of $\tilde{p}_1$ and $\tilde{p}_3$ as determined using the exact (——) and compact-nozzle (– – –) boundary conditions.**

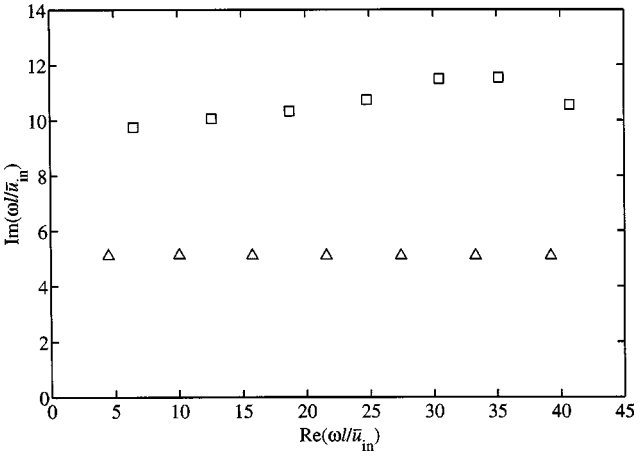


**Fig. 8 Spectrum for transonic flow through the nozzle of Fig. 7 (*a*). Eigenvalues determined using the exact (□) and compact-nozzle (△) boundary conditions are shown**

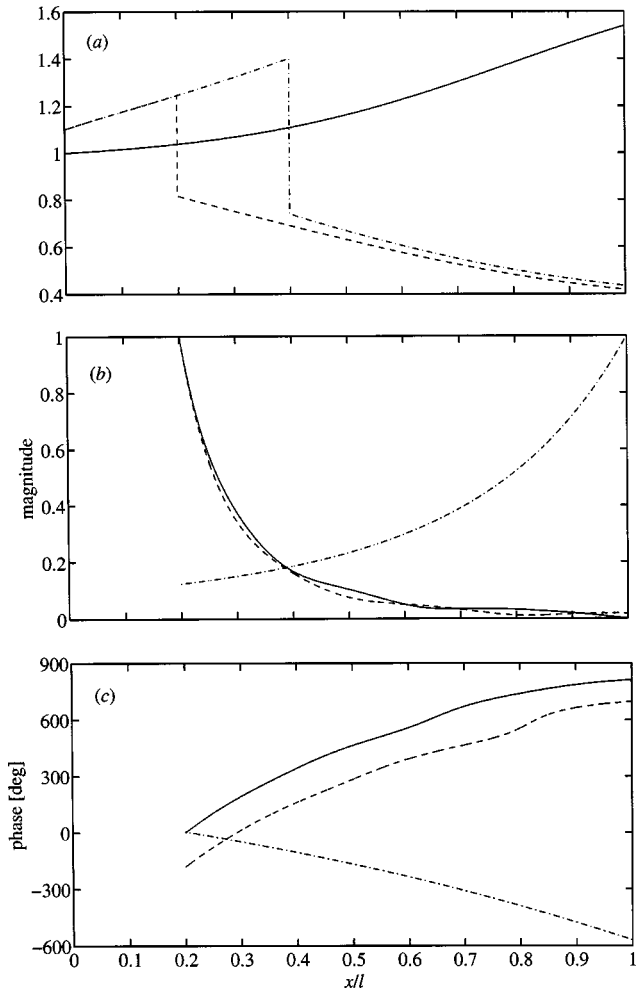


**Fig. 9 (*a*) Transonic diffuser flow, showing the normalized area [$A/A(0)$, ——] distribution and Mach number variations for a shock located at $x/l=0.2$ (– – –) and at $x/l=0.4$ (—·—·). (*b*) Magnitude and (*c*) phase of $\tilde{p}_3$ (——), $\tilde{u}_3$ (– – –) and $\tilde{s}_3$ (—·—·).**

**Transonic Diffuser.** We now consider flow through a transonic diffuser. Air at a total pressure of 101.3 kPa, a total temperature of 300 K and a Mach number of 1.1 enters a diffuser of length $l=1$ m with an area variation given by

$$A=0.1+0.03\tanh 2(x-0.8),$$

which is shown in **Fig.** 9($a$). Assuming that a shock exists at $x/l=0.2$, the mean flow is determined as follows. The flow quantities between the inlet and shock are determined by enforcing conservation of mass and the stagnation quantities. The Rankine–Hugoniot conditions applied across the shock are then used to compute the stagnation quantities downstream of the shock. Applying conservation of mass and these stagnation quantities between the shock and the flow exit, the mean flow variables in the downstream region are determined. In the present case, we use 101 points to discretize the mean flow. The boundary conditions derived in [1] are applied at the shock location while the exit boundary is assumed to be "open."

The spectrum for this flow, illustrated in **Fig.** 10, is observed to consist of stable natural modes with a nearly constant damping rate. We examine in **Figs.** 9($b$) and 9($c$) the shape of the third mode in terms of its unsteady pressure, velocity and entropy components. The magnitude of the normalized unsteady pressure and velocity are largest at the shock location and decrease downstream of it. The phase behavior shows that the pressure and velocity are

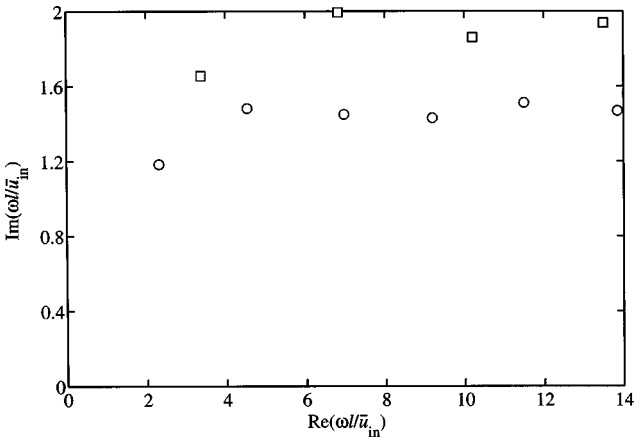


**Fig. 10 Spectrum for the transonic diffuser flow of Fig. 9(*a*) with a shock located at $x/l=0.2$ (○) and $x/l=0.4$ (□)**

almost completely out of phase at the shock and that this phase difference persists throughout the flow domain. An interesting feature of the present flow field is that although the mean flows upstream and downstream of the shock are isentropic, the perturbations that exist downstream are not. Thus we observe from **Fig.** 9($b$) that unsteady entropy is generated at the shock front, the magnitude of which grows downstream. This is in accord with the analysis of Stow et al. [11], who have shown that the previously employed boundary condition of zero mass flow perturbation at the shock neglects this entropy wave and is therefore erroneous. Returning to **Fig.** 9($c$), we also note that although the entropic field is approximately in phase with the pressure perturbation at the shock, the phases of the two quantities differ significantly downstream.

We now suppose that the shock is located at $x/l=0.4$, the inflow conditions being the same as before. The mean flow is determined using the same procedure as before. The shock is stronger than when it lies at $x/l=0.2$, as evidenced by the Mach number distribution shown in **Fig.** 9($a$). The spectrum obtained for this flow is shown in **Fig.** 10. In comparison with the case where the shock is located at $x/l=0.2$, the eigenvalues occur at higher frequencies and are seen to be somewhat more damped. The stable nature of the system modes predicted by the present analysis is entirely consistent with results obtained by Culick and Rogers [12] for the acoustic admittance of a normal shock in a diverging channel. In particular, it was shown in [12] that the shock acts to dissipate incident acoustic energy when the flow on both sides of it is isentropic, as is the case here.

## Stability of a Ducted Flame

The flow configurations examined thus far have not included sources of mass, momentum or energy. In this section, we examine a simple ducted flame model, which takes into account the effects of a transient heat release. We consider flow through a duct of constant area $A$ and length $l$ containing a flame. The flame is modeled by specifying the axial mean temperature distribution, $\bar{T}=\bar{T}(x)$. Assuming that mass addition in the form of fuel is negligible, the mean density field is given by

$$\bar{\rho}=\frac{\bar{m}}{\bar{u}A}, \tag{8}$$

where $\bar{m}$ is the mean mass flow rate. Making use of Eq. (8) and the ideal gas law, the momentum equation yields, after some manipulation

$$\frac{d\bar{u}}{dx} = -\mathcal{R}\frac{d}{dx}\left(\frac{\bar{T}}{\bar{u}}\right), \tag{9}$$

where $\mathcal{R}$ is the gas constant. Integrating Eq. (9), we obtain

$$\bar{u}^2 + \mathcal{R}\bar{T} - C\bar{u} = 0, \tag{10}$$

where the constant $C$ is given by

$$C = \left[\bar{u} + \frac{\mathcal{R}\bar{T}}{\bar{u}}\right]_{\text{in}},$$

the subscript "in" denoting evaluation at the inlet. Solving Eq. (10) then yields the velocity distribution

$$\bar{u} = \frac{1}{2}\left[C - (C^2 - 4\mathcal{R}\bar{T})^{1/2}\right]. \tag{11}$$

It is evident that specification of the inlet mass flow and velocity, in addition to the temperature distribution $\bar{T}(x)$, is sufficient to define the entire flow field. Specifically, the velocity distribution is obtained from Eq. (11), while the density and pressure distributions are determined using Eq. (8) and the ideal gas law. The mean heat release is obtained using

$$\bar{q} = \frac{\bar{m}c_p}{A}\frac{d\bar{T}_t}{dx}, \tag{12}$$

where $c_p$ is the specific heat at constant pressure and $\bar{T}_t$ is the total temperature.

In addition to the mean temperature distribution, it is also necessary to specify the manner in which the flame responds to flow perturbations. As was pointed out in [1], the flame response function cannot generally be derived from first principles. Consequently, many different models have been proposed, which depend, among other things, on the nature of the flame-holding mechanism. In the present study, we make use of the results of a pioneering study of a ducted premixed flame by Bloxsidge et al. [13], who determined that the unsteady heat release downstream of the flame holder, located at $x_f$, was given by

$$\frac{\tilde{q}}{\bar{q}} = \frac{\tilde{u}_f}{\bar{u}_f}\exp(-i\omega\tau)F(\omega)H(x-x_f), \tag{13}$$

where $H$ is the Heaviside step function and $\tau = (x-x_f)/\bar{u}_f$ represents a time delay. Here, we modify the definition of the time delay to account for mean flow spatial variations by setting

$$\tau = \int_{x_f}^{x} \bar{u}^{-1}dx.$$

The function $F$ is, in general, dependent on the frequency and flow configuration. In the present model, which is intended to be more illustrative than comprehensive, we assume that $F$ is constant. It should nevertheless be noted that this is in accord with the kinematic lean premixed flame model of Dowling and Hubbard [14], where it is shown that $F \approx 3$ at high frequencies for methane fuel at an equivalence ratio of 0.6.

We now define the mean temperature distribution as

$$\bar{T}(x) = \bar{T}_{\text{in}} + \delta\bar{T}[\tanh\beta(x-x_c) + \tanh\beta(x_c-x_f)] \times [\tanh\beta(l-x_c) + \tanh\beta(x_c-x_f)]^{-1}H(x-x_f), \tag{14}$$

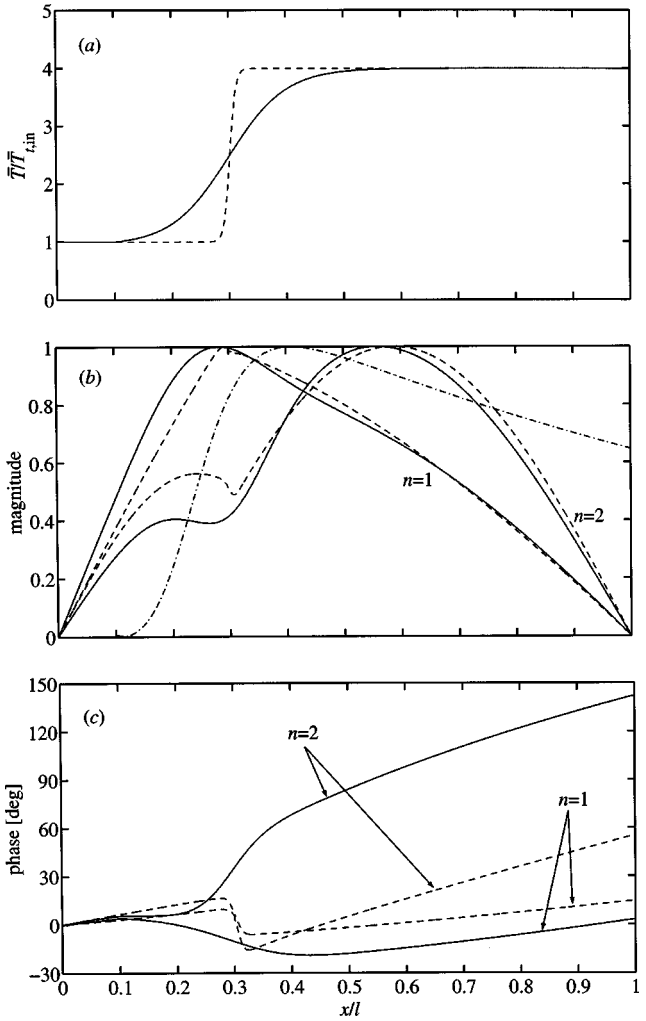


**Fig. 11 (*a*) Normalized static temperature distribution for a ducted flame with concentrated (——) and distributed heat (— — —) release and $\delta\bar{T}/\bar{T}_{t,\text{in}} = 3$. (*b*) Magnitude and (*c*) phase of the corresponding first and second pressure modes. Also shown in (*b*) is the magnitude of the first entropic mode, $\tilde{s}_1$ (— · — ·) for the distributed heat release.**

where $\delta\bar{T}$ is the temperature rise across the flame and the parameters $x_c$ and $\beta$ control the flame location and width. The inlet total pressure, total temperature and Mach number are taken as 200 kPa, 500 K and 0.18, respectively. The duct length $l$ is 1 m and the flame anchor is assumed to be located at $x_f = 0.1$ m. The boundary conditions for the perturbations are $\tilde{p} = \tilde{s} = 0$ at $x = 0$ and $\tilde{p} = 0$ at $x = l$. Following Dowling and Hubbard [14], we set $F = 3$ in Eq. (13).

We consider first a flame with spatially extended heat release by setting $\beta = 10\ \text{m}^{-1}$ and $x_c = 0.3$ m in Eq. (14). The temperature distribution (normalized by the inlet total temperature $\bar{T}_{t,\text{in}}$) is illustrated in Fig. 11(*a*) for $\delta\bar{T}/\bar{T}_{t,\text{in}} = 3$. The length scale of the flame is observed to be about 30% of the duct length. The spectrum of natural modes for this flow field is determined numerically using the unsteady heat release model of Eq. (13) and the procedure described in [1]. The behavior of the first three eigenvalues as the normalized flame temperature rise $\delta\bar{T}/\bar{T}_{t,\text{in}}$ varies between 1 and 4 is investigated in Fig. 12. At the lowest value of $\delta\bar{T}/\bar{T}_{t,\text{in}}$, the first mode is weakly unstable and the second and third modes are damped. As $\delta\bar{T}/\bar{T}_{t,\text{in}}$ rises, the eigenvalue corresponding to the first mode becomes increasingly unstable. The

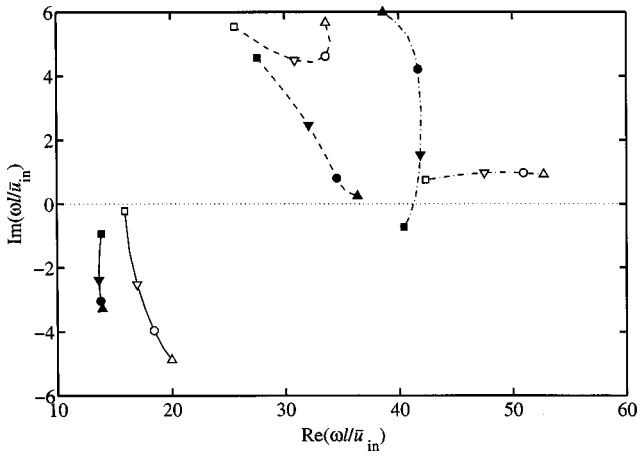


**Fig. 12 Spectra for the ducted flame model for $\beta=10$ (open symbols) and $\beta=100$ (filled symbols) with $x_c=0.3$ in Eq. (14). Results are shown over a range of flame temperature ratios for the $n=1$ (——), $n=2$ (– – –) and $n=3$ (— · — · —) modes. The symbols represent eigenvalues obtained with $\delta\bar{T}/\bar{T}_{t,\mathrm{in}}$ set to 1.0 (□), 2.0 (▽), 3.0 (○) and 4.0 (△).**

second and third modes remain stable over the range of $\delta\bar{T}/\bar{T}_{t,\mathrm{in}}$ considered. In general, the resonant frequencies of all three modes increase with $\delta\bar{T}/\bar{T}_{t,\mathrm{in}}$.

The amplitude and phase of the first and second pressure modes for $\delta\bar{T}/\bar{T}_{t,\mathrm{in}}=3$ are illustrated in **Figs.** 11($b$) and 11($c$). The spatial structure of the mode amplitudes suggests that that they are acoustic in origin rather than entropic [14]. The magnitude of the first entropic mode is shown in Fig. 11($b$). As a consequence of the isentropic inlet boundary condition, the magnitude is zero between the inlet and flame holder station but increases rapidly through the flame. The generation of unsteady entropy here is caused by the interaction of the unsteady pressure and mean temperature fields.

We consider next the effect of treating the flame as a compact element by setting $b=100\ \mathrm{m}^{-1}$ in Eq. (14), with $x_c=0.3$ m. The flame is then centered at the same location, as is evident from the normalized static temperature distribution for $\delta\bar{T}/\bar{T}_{t,\mathrm{in}}=3$ in Fig. 11($a$). Observing that the mean flow quantities are all functions only of $\bar{T}(x)$ and making use of the result

$$\int_0^l \bar{q}(x)\mathrm{d}x=\frac{\bar{m}c_p}{A}[\bar{T}_t(l)-\bar{T}_t(0)],$$

obtained from Eq. (12), it follows that the total mean heat added by the two flames in Fig. 11($a$) is the same. The loci of the first three eigenvalues as flame temperature rises is varied are illustrated in Fig. 12. The behavior of the first eigenvalue is qualitatively similar to that of the distributed flame case and remains unstable over the range of $\delta\bar{T}/\bar{T}_{t,\mathrm{in}}$ considered. The frequency and growth rate are however different from the distibuted case. The differences in the second and third eigenvalues obtained for the compact and distributed flames are more pronounced. Specifically, whereas the distributed model yields a strongly damped second mode, the corresponding compact flame mode approaches neutral stability for large $\delta\bar{T}/\bar{T}_{t,\mathrm{in}}$. Similarly, the third mode for the compact flame is highly damped for large $\delta\bar{T}/\bar{T}_{t,\mathrm{in}}$ but becomes unstable for $\delta\bar{T}/\bar{T}_{t,\mathrm{in}}<1.3$, unlike that for the distributed flame, which remains stable.

The shapes of the first and second pressure modes for the compact flame model are compared with their distributed flame counterparts in **Figs.** 11($b$) and 11($c$). Although the amplitudes appear to be reasonably well approximated by the compact model, the phases are seen to differ quite significantly, especially downstream of the flame. The steep mean flow gradients of the compact flame cause the rapid variations in the magnitude and phase close to the flame front. In the limit where the flame is assumed to be be infinitesimally thin, these spatial changes become discontinuous. This is the case when piecewise-continuous models for the mean flow are employed as in the study of Stow and Dowling [15], for example. While these models are appropriate when the wavelength of the disturbance far exceeds the length scale of the mean flow, the present, admittedly idealized study suggests that the instability behavior may be incorrectly predicted when the heat release occurs over even modestly large length scales. This issue assumes significance, however, in view of the fact that combustor flow fields can feature precisely this type of extended heat release distribution. Indeed, the measurements of Bloxsidge et al. [13] in a model combustor demonstrate that the temperature continues to rise far downstream of the flame initiation front. Similarly, recent numerical simulations by Kim et al. [16] of an afterburner-like flow configuration indicate that combustion occurs over a length scale between 3 and 8 times the transverse dimension of the flameholder, depending on the equivalence ratio.

## Summary

In the present investigation, we have applied a previously developed formulation [1] to analyze the stability of several quasi-one-dimensional flows. These configurations, while simple, form parts of many thermoacoustic systems. Their study here also serves to develop a better understanding of the stability behavior of more complex systems.

A one-dimensional version of the generalized acoustic energy equation of Dowling [2] was used to bring out the influence of the boundary conditions and mean flow gradients on system stability. An examination of the natural modes in subsonic diffusing flows shows that they are unstable when the inlet and exit conditions are strongly reflecting. In contrast, the natural modes of subsonic flow with favorable pressure gradients are found to be stable.

The stability behavior of transonic flows was studied next, including nozzle-like configurations where the flow accelerates through the sonic state and diffuser-like configurations, in which the flow decelerates across a normal shock. Both types of flows are found to be stable. In the case of the accelerating flow, the damping rate depends on the length scale of the area variation, while in the case of the diffuser, it is controlled by the shock strength.

As a final application of the formulation in [1], the stability properties of a ducted flame were studied using an unsteady heat release function based on the models of Bloxsidge et al. [13] and Dowling and Hubbard [14]. Mean flow temperature distributions representing both distributed and concentrated flames were considered. It was found that for a flame with even a moderate spatial length scale, the spectra and mode shapes differ from the concentrated case. This suggests that the approximation of the flame as a compact element, frequently employed in many reduced-order models, may not always be valid.

## Acknowledgments

The authors are grateful to Pratt & Whitney for granting permission to publish the present work. Discussions with William Proscia, Gavin Hendricks and Jeffrey Cohen on this topic are also greatly appreciated.

## References

[1] Prasad, D., and Feng, J., 2004, "Thermoacoustic stability of Quasi-One-Dimensional Flows. Part I—Analytical and Numerical Formulation," J. Turbomach., **126**, pp. 636–643.
[2] Dowling, A. P., 1996, "Acoustics of Unstable Flows," *Theoretical and Applied Mechanics*, T. Tatsumi, E. Watanabe, and T. Kambe eds., Elsevier, Amsterdam.
[3] Marble, F. E., and Candel, S. M., 1977, "Acoustic Disturbance From Gas

non-uniformities Convected Through a Nozzle,'' J. Sound Vib., **55**, pp. 225–243.
[4] Rayleigh, J. W. S., 1896, *The Theory of Sound*, Dover, New York.
[5] Chu, B. T., 1964, ''On the Energy Transfer to Small Disturbances in Fluid Flow. Part I,'' Acta Mech., **1**, pp. 215–324.
[6] Kline, S. J., 1959, ''On the Nature of Stall,'' J. Basic Eng., **81**, pp. 305–320.
[7] Smith, C. R., and Kline, S. J., 1974, ''An Experimental Investigation of the Transitory Stall Regime in Two-Dimensional Diffusers,'' J. Fluids Eng., **96**, pp. 11–15.
[8] Smith, C. R., 1978, ''Transitory Stall Time-Scales for Plane-Wall Air Diffusers,'' J. Fluids Eng., **100**, pp. 133–135.
[9] Smith, C. R., and Layne, J. L., 1979, ''An Experimental Investigation of Flow Unsteadiness Generated by Transitory Stall in Plane-Wall Diffusers,'' J. Fluids Eng., **101**, pp. 181–185.
[10] Kwong, A. H. M., and Dowling, A. P., 1994, ''Unsteady Flow in Diffusers,'' J. Fluids Eng., **116**, pp. 842–847.
[11] Slow, S. R., Dowling, A. P., and Hynes, T. R., 2002, ''Reflection of Circumferential Modes in a Choked Nozzle,'' J. Fluid Mech., **467**, pp. 215–239.
[12] Culick, F. E. C., and Rogers, T., 1983, ''The Response of Normal Shocks in Diffusers,'' AIAA J., **21**, pp. 1382–2390.
[13] Bloxsidge, G. J., Dowling, A. P., and Langhone, P. J., 1988, ''Reheat Buzz: An Acoustically Coupled Combustion Instability. Part 2. Theory,'' J. Fluid Mech., **193**, pp. 445–473.
[14] Dowling, A. P., and Hubbard, S., 2000, ''Instability in Lean Premixed Combustors,'' Proc. Inst. Mech. Eng., Part A, **214**, pp. 317–332.
[15] Stow, S. R., and Dowling, A. P., 2001 ''Thermoacoustic Oscillations in an Annular Combustor,'' ASME Paper 2001-GT-0037.
[16] Kim, W.-W., Lienau, J., van Slooten, P. R., Colket, M. B., Malecki, R. E., and Syed, S., 2004, ''Towards Modeling Lean Blowout in Gas Turbine Flameholder Applications,'' ASME Paper GT2004-53967.

# Method for Direct Parametric Analysis of Nonlinear Forced Response of Bladed Disks With Friction Contact Interfaces

**E. P. Petrov**
e-mail: y.petrov@ic.ac.uk
Mechanical Engineering Department,
Centre of Vibration Engineering,
Imperial College London,
South Kensington Campus,
London, SW7 2AZ, UK

*An effective method for direct parametric analysis of periodic nonlinear forced response of bladed disks with friction contact interfaces has been developed. The method allows, forced response levels to be calculated directly as a function of contact interface parameters such as the friction coefficient, contact surface stiffness (normal and tangential coefficients), clearances, interferences, and the normal stresses at the contact interfaces. The method is based on exact expressions for sensitivities of the multiharmonic interaction forces with respect to variation of all parameters of the friction contact interfaces. These novel expressions are derived in the paper for a friction contact model, accounting for the normal load variation and the possibility of separation-contact transitions. Numerical analysis of effects of the contact parameters on forced response levels has been performed using large-scale finite element models of a practical bladed turbine disk with underplatform dampers and with shroud contacts.* [DOI: 10.1115/1.1776588]

## Introduction

Bladed disk assemblies and blisks commonly contain friction and impact contact interfaces. Such contact interfaces are located at blade root-disk joints, at contact surfaces of friction dampers, at contact surfaces of blade shrouds, etc. Friction and other contact forces at these contact interfaces are usually dependent on displacements nonlinearly. Nonlinear forces significantly affect the properties of the forced response, making it necessary to develop special methods for analysis.

Analysis of the forced response of bladed disks with friction contact interfaces is usually performed in the frequency domain owing to the high computational efficiency of this approach. Transformation of the formulation of the problem into the frequency domain can be carried out by representing each steady-state displacement as a sum of harmonic components, or even as one harmonic only. After that, forced response is calculated customarily as a function of excitation frequency. The general scheme for solution of a nonlinear problem, using the multiharmonic balance method, is described in [1]. Some examples of the analysis of monoharmonic vibrations with friction damping in blade forced response analysis, can be found in papers [2–6], and multiharmonic vibrations are studied in papers [7–14]. In these papers, and in many others on the topic (see, e.g., survey in [15]), the dependency of forced response on excitation frequency is calculated.

In design practice there is usually a need to choose sets of contact interface parameters that provide minimum forced response or satisfy other design requirements. In order to do this, it is necessary to understand how forced response levels are dependent on the choice of contact interface parameter values and how the forced response is dependent on their variation, occurring, for example, when service conditions of a gas turbine engine changes, together with the rotor speed/excitation frequency variation. A simple calculation of a frequency-dependent forced response characteristics for a single set of contact parameters cannot provide such understanding.

The customary approach to date, which was applied in papers on forced response analysis of structures with friction interfaces, including the papers referenced above, has been generally this: to choose several sets of the contact parameters and to calculate the forced response as a function of the excitation frequency, in some frequency range, for each set. Yet, such multivariant calculations of the forced response calculated for discrete, a priori selected sets of the contact parameters values, require significant computation expense and still such calculations in many cases do not give all necessary information.

Forced response of bladed disks with friction contact interfaces is essentially nonlinear and is highly sensitive to contact parameter variation. Hence, when dependency of the forced response on a friction contact parameter is required for some fixed excitation frequency, this often cannot be calculated by seemingly apparent approach—simply by the multivariant calculations performed for this frequency. Such calculation cannot be performed due to a frequent inability to find a converged solution of the nonlinear problem when contact parameters are alternate from one discrete value to another.

Moreover, in all practical bladed disk problems the contact parameters are subjected to variation due to service condition change. For example, values of the normal stresses in underplatform dampers are proportional to the square of the rotation speed, clearances and interferences between blade shrouds or at blade-disk joints are dependent on rotation speed and temperature, friction coefficients and contact stiffness are dependent on temperature and wear, etc. Forced response characteristics of essentially nonlinear systems, which bladed disks with friction contact interfaces certainly are, can be significantly dependent on history and on the rates of these variations. Because of this, simple multivariant calculations may give significant errors in the forced response prediction, even for a specified set of parameters when simultaneous variation of the contact parameters under service conditions variation is not accounted for.

In this paper, for the first time, an effective method is developed for calculation of the forced response level directly as a function of contact interface parameters including the friction coefficient,

Contributed by the International Gas Turbine Institute (IGTI) of THE AMERICAN SOCIETY OF MECHANICAL ENGINEERS for publication in the ASME JOURNAL OF TURBOMACHINERY. Paper presented at the International Gas Turbine and Aeroengine Congress and Exhibition, Vienna, Austria, June 13–17, 2004, Paper No. 2004-GT-53894. Manuscript received by IGTI, October 1, 2003; final revision, March 1, 2004. IGTI Review Chair: A. J. Strazisar.

  

normal and tangential contact surface stiffness coefficients, clearances, interferences, and normal stresses at the contact interfaces. The problem of tracing of solutions of the nonlinear equations of motion is formulated. The equations of motion are obtained in the frequency domain using the multiharmonic balance method, allowing the forced response to be represented by as many harmonic components as required. Exact expressions for sensitivities of the multiharmonic interaction forces with respect to variation of all parameters of the friction contact interfaces are derived. These novel expressions are obtained for a friction model accounting for normal load variation and separation-contact transitions. The robustness and outstanding efficiency of the method is based essentially on this analytical derivation of the sensitivity coefficients. Application areas for the new capabilities, provided by this method of prediction of forced response levels, are discussed. Then, a numerical investigation of effects of contact parameters of underplatform dampers and shroud contact interfaces on forced response levels of a practical high-pressure turbine blade disk is performed using its detailed large-scale finite element model.

## Formulation of the Problem

**Multiharmonic Balance Equation of Motion.** A structure containing nonlinear contact interfaces between its different components and/or interfaces at boundaries of the structure is subjected to action of internal, linear and nonlinear forces and external, excitation forces. The linear forces usually comprise inertia forces, elastic deformation forces, and viscous damping or material damping forces. Nonlinear forces considered here are forces of nonlinear interaction at the contact interfaces. The linear forces are expressed in the finite element method linearly through displacements using corresponding matrices (e.g., mass, stiffness, or damping matrices). These matrices are constant and are independent of the displacements, for a linear system. Nonlinear forces in general cannot be represented in this form and are usually described by nonlinear equations depending on the displacements and on design parameters of the contact interfaces. The equation for motion for a structure with nonlinear interfaces can be written in the following form:

$$\mathbf{K}\mathbf{q}(t)+\mathbf{C}\dot{\mathbf{q}}(t)+\mathbf{M}\ddot{\mathbf{q}}(t)+\mathbf{f}(\mathbf{q}(t),\dot{\mathbf{q}}(t),\mathbf{b}(\lambda))-\mathbf{p}(t,\lambda)=\mathbf{0} \quad (1)$$

where $\mathbf{q}(t)$ $(N_S\times 1)$ is a vector comprising all degrees-of-freedom (DOFs) of the structure considered; $N_S$ is the total number of DOFs, $\mathbf{K}$, $\mathbf{C}$, and $\mathbf{M}$ are stiffness, viscous damping and mass matrices used for description of linear forces. For a bladed disk, which is usually analyzed in a non-inertial coordinate system fixed to the rotor, rotating with speed $\omega$, the stiffness matrix can comprise not only conventional elastic stiffness matrix $\mathbf{K}_e$, but can also include terms accounting for the rotations effects, i.e., $\mathbf{K}=\mathbf{K}_e+\mathbf{K}_g(\omega)-\omega^2\mathbf{M}_\omega$, where $\mathbf{K}_g$ is a so-called geometric stiffness matrix reflecting stiffening effects of the centrifugal forces; $\mathbf{M}_\omega$ is a spin-softening-matrix describing stiffness softening due to the changing direction of the centrifugal forces under vibration. $\mathbf{f}(\mathbf{q}(t),\dot{\mathbf{q}}(t),\mathbf{b}(\lambda))$ is a vector of non-linear interface forces, which is dependent on displacements and velocities of DOFs at interface nodes and also on a vector of parameters of the contact interfaces, $\mathbf{b}(\lambda)$. $\mathbf{p}(t,\lambda)$ is a vector of external excitation forces, which can also be dependent, together with the principal frequency of the excitation forces, $\omega(\lambda)$, on some parameter, $\lambda$.

This service condition parameter, $\lambda$, introduced here, reflects possible dependencies of the parameters of the contact interfaces on service conditions, for example their dependency on rotor rotation speed, $\omega$, (for this case $\lambda=\omega$), on temperature at the contact surfaces, $t^o$, (for this case $\lambda=t^o$), and on time although with a rate of variation much slower than the motion process, ($\lambda=\varepsilon t$, where $\varepsilon\ll 1$). Variation of the service conditions can change parameters of the contact interfaces, $\mathbf{b}(\lambda)$, excitation forces, $\mathbf{p}(t,\lambda)$, rotation speed, $\omega(\lambda)$, etc. The parameter $\lambda$ can also describe the summarized action of several condition parameters, i.e., $\omega(\lambda)$, $t^0(\lambda)$, and other factors on the contact parameters, as appropriate in practice. For this case the parameter, $\lambda$, is simply a tracing parameter which is used to describe simultaneous variation of all variable service condition parameters. Hence, it does not necessarily have to have a physical meaning, but allows interdependence of all the service parameters and contact interface parameters to be described. For each value of the tracing parameter, all service and contact interface parameters are easily calculated, as prescribed functions of the tracing parameter.

For a search of the periodic vibration response, the displacements' variation in time can be represented as a restricted Fourier series, which can contain whichever harmonic components are necessary to approximate the sought solution, i.e.,

$$\mathbf{q}(t)=\mathbf{Q}_0+\sum_{j=1}^{n}\left(\mathbf{Q}_j^{(c)}\cos m_j\omega t+\mathbf{Q}_j^{(s)}\sin m_j\omega t\right) \quad (2)$$

where $\mathbf{Q}_j^{(c)}$ and $\mathbf{Q}_j^{(s)}$ $(j=1\ldots n)$ are vectors of cosine and sine harmonic coefficients for system DOFs, marked by superscripts $^{(c)}$ and $^{(s)}$ accordingly; $\mathbf{Q}_0$ is a vector of constant components of the displacements; $m_j$ $(j=1\ldots n)$ are specific numbers of harmonics that are kept in the displacement expansion in addition to the constant component. The expansion from Eq. (2) is substituted into the equation of motion (1), which is then sequentially multiplied by $(\cos m_j\omega t)$ and $(\sin m_j\omega t)$ for all harmonics from 1 to $n$ of the expansion and integrals over the vibration period, $T=2\pi/\omega$, are calculated.

As a result, the following multiharmonic balance equation of motion which is nonlinear with respect to a vector of harmonic coefficients of displacements is obtained:

$$\mathbf{R}(\mathbf{Q},\lambda)=\mathbf{Z}(\omega(\lambda))\mathbf{Q}+\mathbf{F}(\mathbf{Q},\mathbf{b}(\lambda))-\mathbf{P}(\lambda)=\mathbf{0} \quad (3)$$

where $\mathbf{Q}=\{\mathbf{Q}_0,\mathbf{Q}_1^{(c)},\mathbf{Q}_1^{(s)},\ldots,\mathbf{Q}_n^{(s)}\}^T$ is the vector of harmonic coefficients of displacements comprising all $N=n\times N_S$ harmonic coefficients for displacements; $\mathbf{P}=\{\mathbf{P}_0,\mathbf{P}_1^{(c)},\mathbf{P}_1^{(s)},\ldots,\mathbf{P}_n^{(s)}\}^T$ is the vector of harmonic components of the excitation forces; $\mathbf{F}(\mathbf{Q},\mathbf{b}(\lambda))=\{\mathbf{F}_0,\mathbf{F}_1^{(c)},\mathbf{F}_1^{(s)},\ldots\mathbf{F}_n^{(s)}\}^T$ is the vector of harmonic components of nonlinear forces and $\mathbf{Z}(\omega)$ is the dynamic stiffness matrix of the linear part of the system, constructed for all harmonic components, i.e.,

$$\mathbf{Z}=\mathrm{diag}[\mathbf{Z}_0,\mathbf{Z}_1,\ldots,\mathbf{Z}_n] \quad (4)$$

$$\mathbf{Z}_0=\mathbf{K};\quad \text{and}\quad \mathbf{Z}_j=\begin{bmatrix}\mathbf{K}-(m_j\omega)^2\mathbf{M} & m_j\omega\mathbf{C}+\eta\mathbf{K}_e\\ -m_j\omega\mathbf{C}-\eta\mathbf{K}_e & \mathbf{K}-(m_j\omega)^2\mathbf{M}\end{bmatrix} \quad (5)$$

where $\eta$ is the material damping loss factor.

**Tracing of the Solution Under Parameter Variation.** It is evident that different choice of the parameters for the contact interfaces, $\mathbf{b}(\lambda)$, provides different solutions for Eq. (3). There is a wide range of practical design problems where there is a need to choose values for these parameters to satisfy special criteria such as, for example, to minimize level of amplitude for a bladed disc by increasing friction damping.

The predictor-corrector technique (see its major variants in papers [16–18]) allows solutions for a nonlinear equation to be traced when parameters of the nonlinear structure are varied. At the predictor stage of this technique, for a found solution, $\mathbf{Q}$, a prediction for the solution is calculated which corresponds to new parameter values. In order to make such a prediction, a vector, $\mathbf{t}=\{\mathbf{s},s_\lambda\}^T$, tangent to the trajectory of solutions, is calculated. The tangent direction can be determined from solution of the following equation:

$$\begin{bmatrix}\underset{N\times N}{\dfrac{\partial\mathbf{R}(\mathbf{Q},\lambda)}{\partial\mathbf{Q}}} & \underset{N\times 1}{\dfrac{\partial\mathbf{R}(\mathbf{Q},\lambda)}{\partial\lambda}}\end{bmatrix}\begin{Bmatrix}\underset{N\times 1}{\mathbf{s}}\\ s_\lambda\end{Bmatrix}=\mathbf{0}. \quad (6)$$

A good approximation for the next solution, located on the same trajectory of solutions can then be determined as

$$\mathbf{Q}^* = \mathbf{Q} + \ell \mathbf{s}; \quad \lambda^* = \lambda + \ell s_\lambda ; \tag{7}$$

where $\ell$ is a coefficient which determines the size of the predictor step.

It should be noted that Eq. (6) has a rank-deficient matrix and its solution vector is determined with accuracy of some arbitrary chosen scaling coefficient. A value of the step size coefficient, $\ell$, can be chosen in Eq. (7) to provide: (i) a small enough increment in order to give an approximation which is close enough to the trajectory of solutions (since too large a step can cause a jump to another trajectory of solution or loss of convergence of the iterative solution of the nonlinear equations), and (ii) a large enough increment to progress along the trajectory with sufficient rate (i.e., to avoid too small steps). A simple approach for the choice of the length for the predictor step, $\{\ell \mathbf{s}, \ell s_\lambda\}^T$, is to determine it by the number of iterations required at the corrector stage in order to find the solution with a required accuracy from the prediction given by Eq. (7). Moreover, direction of the predictor step should advance the tracing process along the trajectory of solutions without spurious turns back. This requirement can be satisfied, for example, by the following condition imposed over all predictor steps: $\text{sign}(\ell s_\lambda \det[\partial \mathbf{R}/\partial \mathbf{Q}]) = \text{const}$.

At the corrector stage a new solution is calculated using the iterative Newton-Raphson algorithm with the approximation determined at the predictor stage. In order to be able to trace the complex trajectories of solutions that are inherent for nonlinear systems, the tracing parameter, $\lambda$, is treated as an unknown and determined together with the vector of multiharmonic amplitudes, $\mathbf{Q}$. An additional equation is added to make the number of equations equal to the number of unknowns. In accordance with paper [18], Eq. (3) is supplemented by the condition that the solution should be orthogonal, at each iteration, to the tangent to the field of the solutions. The iterative solution process can then be performed using the following recurrence equation:

$$\begin{bmatrix} \dfrac{\partial \mathbf{R}^{(k)}}{\partial \mathbf{Q}} & \dfrac{\partial \mathbf{R}^{(k)}}{\partial \lambda} \\ (\mathbf{s}^{(k)})^T & s_\lambda^{(k)} \end{bmatrix} \begin{Bmatrix} \mathbf{Q}^{(k+1)} - \mathbf{Q}^{(k)} \\ \lambda^{(k+1)} - \lambda^{(k)} \end{Bmatrix} = - \begin{Bmatrix} \mathbf{R}(\mathbf{Q}^{(k)}, \lambda^{(k)}) \\ 0 \end{Bmatrix} \tag{8}$$

where superscript $k$ indicates the number of the previous iteration; and $\{\mathbf{s}^{(k)}, s_\lambda^{(k)}\}^T$ is the tangent direction corresponding to the approximated solution, $\mathbf{Q}^{(k)}$ and $\lambda^{(k)}$. For each iteration Eq. (8) is solved to find $\mathbf{Q}^{(k+1)}$ and $\lambda^{(k+1)}$; and for the first iteration the prediction from Eq. (7), i.e., $\mathbf{Q}^{(0)} = \mathbf{Q}^*$ and $\lambda^{(0)} = \lambda^*$ is used. The iterations are stopped when a prescribed accuracy, $\delta$, is achieved, i.e., when $\|\mathbf{R}(\mathbf{Q}, \lambda)\| < \delta$.

One can see that, for effective tracing of the solution under parameter variation, there is a need for efficient calculation of derivatives of the residual function, $\mathbf{R}(\mathbf{Q}, \mathbf{b}(\lambda))$ with respect to the vector of multiharmonic amplitudes, $\mathbf{Q}$, and with respect to the service condition parameter, $\lambda$. Taking the derivatives of Eq. (3) we can obtain

$$\frac{\partial \mathbf{R}(\mathbf{Q}, \lambda)}{\partial \mathbf{Q}} = \mathbf{Z}(\omega(\lambda)) + \frac{\partial \mathbf{F}(\mathbf{Q}, \mathbf{b}(\lambda))}{\partial \mathbf{Q}} \tag{9}$$

$$\frac{\partial \mathbf{R}(\mathbf{Q}, \lambda)}{\partial \lambda} = \frac{\partial \mathbf{Z}(\omega)}{\partial \omega} \frac{\partial \omega}{\partial \lambda} \mathbf{Q} - \frac{\partial \mathbf{P}}{\partial \lambda} + \frac{\partial \mathbf{F}(\mathbf{Q}, \mathbf{b}(\lambda))}{\partial \mathbf{b}} \frac{\partial \mathbf{b}}{\partial \lambda}. \tag{10}$$

Equation (9) contains the matrix of derivatives, $\mathbf{K}(\mathbf{Q}, \mathbf{b}(\lambda)) = \partial \mathbf{F}(\mathbf{Q}, \mathbf{b}(\lambda))/\partial \mathbf{Q}$, of the nonlinear forces, $\mathbf{F}$, with respect to the multiharmonic displacement vector, $\mathbf{Q}$. This matrix is called the tangent stiffness matrix of the contact interfaces. It is usually nonlinearly dependent on displacements, $\mathbf{Q}$, and characterizes the stiffness properties of the contact interface corresponding to the solution found. Friction contact interface elements are developed in paper [13], which provides a very fast and accurate calculation of the tangent stiffness matrix for each contact node, and hence for the whole structure. The total tangent matrix for a whole structure, $\mathbf{K}(\mathbf{Q}, \mathbf{b}(\lambda))$, is formed by summing the tangent matrices for all contact elements.

The vector of derivatives of the residual function with respect to the tracing parameter, $\partial \mathbf{R}(\mathbf{Q}, \lambda)/\partial \lambda$, defined by Eq. (10) comprises three major summands:

1. a vector of derivatives of the linear forced response with respect to the tracing parameter: $(\partial \mathbf{Z}(\omega)/\partial \omega)(\partial \omega/\partial \lambda)\mathbf{Q}$. The matrix of derivatives, $\partial \mathbf{Z}(\omega)/\partial \omega$, of the dynamic stiffness matrix with respect to the principal excitation frequency can be obtained by differentiating Eq. (5) with respect to $\omega$, to give the expression

$$\partial \mathbf{Z}/\partial \omega = \text{diag}[\partial \mathbf{Z}_0/\partial \omega, \partial \mathbf{Z}_1/\partial \omega, \ldots, \partial \mathbf{Z}_n/\partial \omega] \tag{11}$$

$$\frac{\partial \mathbf{Z}_0}{\partial \omega} = \frac{\partial \mathbf{K}}{\partial \omega}; \quad \frac{\partial \mathbf{Z}_j}{\partial \omega} = \begin{bmatrix} \dfrac{\partial \mathbf{K}}{\partial \omega} - 2 m_j^2 \omega \mathbf{M} & m_j \mathbf{C} \\ -m_j \mathbf{C} & \dfrac{\partial \mathbf{K}}{\partial \omega} - 2 m_j^2 \omega \mathbf{M} \end{bmatrix}. \tag{12}$$

2. a vector of derivatives of the excitation forces with respect to the tracing parameter: $\partial \mathbf{P}/\partial \lambda$. Since excitation loads are usually prescribed, calculation of such derivatives does not represent a difficulty. If the excitation loads are independent of the tracing parameter, as for example for the case of excitation with constant amplitudes of the multi or monoharmonic excitation, then $\partial \mathbf{P}/\partial \lambda = \mathbf{0}$.

3. a vector of derivatives of the nonlinear forces with respect to the tracing parameter: $\partial \mathbf{F}(\mathbf{Q}, \mathbf{b}(\lambda))/\partial \mathbf{b}$. To calculate this vector it is necessary to be able to determine a matrix of the derivatives of the nonlinear forces with respect to parameters of the friction contact interfaces $\partial \mathbf{F}(\mathbf{Q}, \mathbf{b}(\lambda))/\partial \mathbf{b}$ and to have a rate of variation of the contact interface parameter vector, $\mathbf{b}$, with respect to the tracing parameter, i.e., $\partial \mathbf{b}/\partial \lambda$. The latter vector is normally given to a designer or there are some dependencies $\mathbf{b}(\lambda)$ allowing its calculation. This parameter sensitivity matrix, $\partial \mathbf{F}(\mathbf{Q}, \mathbf{b}(\lambda))/\partial \mathbf{b}$, has never been determined before, for friction contact interfaces. Because of this, no direct parametric analysis for structures containing the friction contact interfaces has been available to date. In order to make such analysis feasible, exact expressions for these derivatives are derived for friction contact and gap interfaces as reported in the following section.

It should be noted that formulation of the multiharmonic nonlinear equations of motion can be performed not only using finite element matrices directly as shown in Eqs. (5) and (12) but also applying FRF matrices of structures. Such formulations for structures with cyclically symmetric properties are developed in paper [14]. A formulation which takes into account scatters of blade and friction interface characteristics resulting in mistuning is developed in paper [19].

## Sensitivity Coefficients With Respect to Contact Parameters for Nonlinear Forces

**Friction Contact Interface Elements.** Friction interface elements including the effects of normal load variation on the friction forces, have been developed in paper [13]. In accordance with the friction model developed a friction contact interface has the following parameters:

1. friction coefficient, $\mu$
2. static normal load due to prior deformation, $N_0$
3. normal contact stiffness coefficient, $k_n$
4. tangential contact stiffness coefficient, $k_t$.

Expressions for the multiharmonic force vectors of the contact interaction are obtained in paper [13] together with tangent stiffness matrix. In this section exact expressions for the sensitivity

**Table 1 Forces of the friction contact interaction**

| Status | Tangential Force, $f_x$ | Normal Force, $f_y$ |
|---|---|---|
| Contact | Stick: $k_t(x-x_0)-\xi\mu f_y^0$<br>Slip: $\xi\mu f_y$ | $N_0+k_n y$ |
| Separation | 0 | 0 |

coefficients for these forces with respect to these parameters, needed for the direct parametric analysis, are derived. The friction model used here describes macroslip friction forces at each contact point. Multitude of the friction elements applied over a contact surface takes into account for microslip friction interaction, variation of the contact patch over the vibration period and possibility of slip over all contact nodes of the contacting interfaces.

Forces occurring at the friction contact interface can be expressed in terms of the relative displacement along a direction tangential to the contact surface, $x(t)$, and a normal relative displacement, $y(t)$. There are several major possible states of the contact interaction and expressions for tangential and normal components of the interaction force are shown for each of these in **Table 1.**

Here $x^0$ and $f_y^0$ are values of the tangential displacement and of the normal component of the contact interaction force at the beginning of the current stick state. Equations that are used to determine time instants when contact state changes are:

- stick-to-slip transition:

$$f_x(\tau)=\pm\mu f_y(\tau) \tag{13}$$

- slip-to-stick transition:

$$\xi k_x\dot{x}(\tau)=\mu k_y\dot{y}(\tau) \tag{14}$$

- contact-separation transitions

$$N_0+k_y y(\tau)=0 \tag{15}$$

where $\tau=\omega t$ is nondimensional time, and $\xi=\pm 1$ is a sign function. Details of the friction model can be found in a paper [13].

Multiharmonic relative displacements at the contact node can be expressed in the form

$$x(\tau)=\mathbf{H}_-^T(\tau)\mathbf{X};\quad y(\tau)=\mathbf{H}_-^T(\tau)\mathbf{Y} \tag{16}$$

where $\mathbf{H}_-(\tau)=\{1,\cos m_1\tau,\sin m_1\tau,\ldots,\cos m_n\tau,\sin m_n\tau\}^T$; $\mathbf{X}$ and $\mathbf{Y}$ are vectors of harmonic coefficients of relative motion in the tangential and normal directions, respectively, which are selected from vector, $\mathbf{Q}$, of harmonic coefficients for the whole system.

Expanding the interaction forces given in **Table 1** in Fourier series and using Eq. (16) one can obtain vectors of multiharmonic components for tangential, $\mathbf{F}_x$, and normal, $\mathbf{F}_y$, forces in the form

$$\begin{Bmatrix}\mathbf{F}_x\\ \mathbf{F}_y\end{Bmatrix}=\frac{1}{\pi}\sum_{j=1}^{n_\tau}\int_{\tau_j}^{\tau_{j+1}}\begin{Bmatrix}\mathbf{H}_+(\tau)f_x\\ \mathbf{H}_+(\tau)f_y\end{Bmatrix}d\tau=\sum_{j=1}^{n_\tau}\begin{Bmatrix}\mathbf{J}_x^{(j)}\\ \mathbf{J}_y^{(j)}\end{Bmatrix} \tag{17}$$

where $\mathbf{H}_+(\tau)=\{1/2,\cos m_1\tau,\sin m_1\tau,\ldots,\cos m_n\tau,\sin m_n\tau\}^T$, $\tau_j$ are instants when contact state changes, and $n_\tau$ is the total number of these contact state changes over the period of vibrations. These instants are determined by Eqs. (13)–(15). Introduced here are vectors of integrals $\mathbf{J}_x^{(j)}$ and $\mathbf{J}_y^{(j)}$, which are expressed in the following form for each interval of stick, slip or separation:

$$\mathbf{J}_x^{(j)}=\begin{cases}k_t\mathbf{W}_j\mathbf{X}+c_j\mathbf{w}_j & \text{stick}\\ \xi\mu(N_0\mathbf{w}_j+k_n\mathbf{W}_j\mathbf{Y}) & \text{slip}\\ \mathbf{0} & \text{separation}\end{cases} \tag{18}$$

$$\mathbf{J}_y^{(j)}=\begin{cases}N_0\mathbf{w}_j+k_n\mathbf{W}_j\mathbf{Y} & \text{contact}\\ \mathbf{0} & \text{separation}\end{cases} \tag{19}$$

where

$$\underset{(n\times n)}{\mathbf{W}_j}=\frac{1}{\pi}\int_{\tau_j}^{\tau_{j+1}}\mathbf{H}_+(\tau)\mathbf{H}_-^T(\tau)d\tau;\qquad \underset{(n\times 1)}{\mathbf{w}_j}=\frac{1}{\pi}\int_{\tau_j}^{\tau_{j+1}}\mathbf{H}_+(\tau)d\tau \tag{20}$$

$$c_j=-\xi\mu(N_0+k_n y(\tau_j))-k_t x(\tau_j). \tag{21}$$

Integrals in Eq. (20) are products of sine and cosine functions of different orders and can therefore be easily calculated analytically. The analytical derivation provides an exact and very fast calculation for the vectors of multiharmonic coefficients of the interface forces.

The analytical derivation allows efficient determination of the sensitivity coefficients for the vector of multiharmonic coefficients of the interface forces, with respect to all parameters of the contact interfaces. These sensitivity coefficients are calculated by differentiation of Eq. (17). When all these parameters can be varied by variation of the tracing parameter, λ, the sensitivities of the multiharmonic forces are expressed in the form

$$\frac{\partial}{\partial\lambda}\begin{Bmatrix}\mathbf{F}_x\\ \mathbf{F}_y\end{Bmatrix}=\sum_{\gamma=\mu,N_0,k_t,k_n}\frac{\partial}{\partial\gamma}\begin{Bmatrix}\mathbf{F}_x\\ \mathbf{F}_y\end{Bmatrix}\frac{\partial\gamma}{\partial\lambda} \tag{22}$$

where $\partial\gamma/\partial\lambda$ are the rates of variation of the parameters of contact interfaces as a function of the tracing parameter, λ, and expressions for the sensitivities with respect to each of the of parameters, can be obtained from Eq. (17) in the form

$$\frac{\partial}{\partial\gamma}\begin{Bmatrix}\mathbf{F}_x\\ \mathbf{F}_y\end{Bmatrix}=\sum_{j=1}^{n_\tau}\frac{\partial}{\partial\gamma}\begin{Bmatrix}\mathbf{J}_x^{(j)}\\ \mathbf{J}_y^{(j)}\end{Bmatrix}\quad\text{for}\quad\gamma=\mu,N_0,k_t,k_n. \tag{23}$$

Exact expressions for all summands in Eq. (23) and for each of the four contact parameters considered are analytically derived in the following section.

*Sensitivity With Respect to Friction Coefficient.* Sensitivity coefficients with respect to the friction coefficient are obtained by differentiating Eqs. (18) and (19) with respect to $\mu$, which gives us the following expression:

$$\frac{\partial\mathbf{J}_x^{(j)}}{\partial\mu}=\begin{cases}\dfrac{\partial c_j}{\partial\mu}\mathbf{w}_j & \text{stick}\\ \xi(N_0\mathbf{w}_j+k_n\mathbf{W}_j\mathbf{Y}) & \text{slip}\end{cases};\quad\frac{\partial\mathbf{J}_y^{(j)}}{\partial\mu}=0. \tag{24}$$

The interaction forces in the separation interval are always equal to zero, together with their derivatives with respect to the contact parameters, and these trivial expressions are omitted here and further. The derivative, $\partial c_j/\partial\mu$, introduced here, is determined by differentiating Eq. (21)

$$\frac{\partial c_j}{\partial\mu}=-\xi(N_0+k_n y)-\xi\mu k_n\dot{y}\frac{\partial\tau_j}{\partial\mu}-k_t\dot{x}\frac{\partial\tau_j}{\partial\mu}$$

$$=-(\xi\mu k_n\dot{y}+k_t\dot{x})\frac{\partial\tau_j}{\partial\mu}-\xi(N_0+k_n y). \tag{25}$$

The above expression contains a derivative, $\partial\tau_j/\partial\mu$ of the time instant when stick begins with respect to the friction coefficient. This derivative is calculated by differentiating Eq. (14), which defines the time at which stick starts:

$$\xi k_t\ddot{x}(\tau_j)\frac{\partial\tau_j}{\partial\mu}=k_n\dot{y}(\tau)+\mu k_t\ddot{y}(\tau)\frac{\partial\tau_j}{\partial\mu} \tag{26}$$

and hence

$$\frac{\partial\tau_j}{\partial\mu}=\frac{k_n\dot{y}(\tau)}{\xi k_t\ddot{x}(\tau_j)-\mu k_n\ddot{y}(\tau)}. \tag{27}$$

For a case when there are separation-contact transitions, and if stick starts immediately after separation-contact transition the derivative for the time when stick starts with respect to the friction coefficient is obtained by differentiating Eq. (15), which results in the following expression:

$$\partial \tau_j / \partial \mu = 0. \tag{28}$$

*Sensitivity With Respect to Normal Load.* Sensitivity coefficients with respect to the normal load, $N_0$, take the following form:

$$\frac{\partial \mathbf{J}_x^{(j)}}{\partial N_0} = \begin{cases} \dfrac{\partial c_j}{\partial N_0}\mathbf{w}_j & \text{stick} \\ \xi\mu\mathbf{w}_j & \text{slip} \end{cases}; \quad \frac{\partial \mathbf{J}_y^{(j)}}{\partial N_0} = \mathbf{w}_j \tag{29}$$

where

$$\frac{\partial c_j}{\partial N_0} = -\xi\mu\left(1 + k_n\dot{y}\frac{\partial \tau_j}{\partial N_0}\right) - k_t\dot{x}\frac{\partial \tau_j}{\partial N_0}$$

$$= -(\xi\mu k_n\dot{y} + k_t\dot{x})\frac{\partial \tau_j}{\partial N_0} - \xi\mu \tag{30}$$

and the derivative for the stick start time is determined from Eq. (14)

$$\xi k_t\ddot{x}(\tau_j)\frac{\partial \tau_j}{\partial N_0} = \mu k_n\ddot{y}(\tau_j)\frac{\partial \tau_j}{\partial N_0} \tag{31}$$

which results in the following value for this derivative:

$$\partial \tau_j / \partial N_0 = 0. \tag{32}$$

For a case when stick starts immediately after a separation-contact transition the derivative $\partial \tau_j / \partial N_0$ is obtained by differentiating Eq. (15) with respect to the normal load, which gives the expression:

$$\partial \tau_j / \partial N_0 = -1/k_n\dot{y} \tag{33}$$

*Sensitivity With Respect to the Contact Stiffnesses.* Sensitivities of the vector of the multiharmonic friction contact forces with respect to the other contact parameters of the contact surface: the stiffness coefficients along normal, $k_n$, and tangential direction, $k_t$, are readily obtained analogously to the cases of the friction coefficient, $\mu$, and the normal load, $N_0$, derived above.

**Gap Interface Elements.** The gap interface element models unilateral interaction forces acting along a direction normal to the contact surface. The interaction force is expressed in the form

$$f_y = \begin{cases} k_n(y-g) & \text{for } y > g \quad \text{(contact)} \\ 0 & \text{for } y \leqslant g \quad \text{(separation)} \end{cases} \tag{34}$$

where $g$ is a gap value. Expansion of this force in Fourier series gives an expression for the vector of multiharmonic components

$$\mathbf{F}_y = \frac{1}{\pi}\sum_{j=1}^{n_\tau}\int_{\tau_j}^{\tau_{j+1}}\mathbf{H}_+(\tau)f_y d\tau = \sum_{j=1}^{n_\tau}\mathbf{J}_y^{(j)} \tag{35}$$

where integrals taken analytically have the form

$$\mathbf{J}_y^{(j)} = \begin{cases} k_n\mathbf{W}_j\mathbf{Y} - k_n g\mathbf{w}_j & \text{contact} \\ \mathbf{0} & \text{separation.} \end{cases} \tag{36}$$

There are two parameters for this interface element:

1. the normal stiffness coefficient, $k_n$,
2. and the gap value, $g$.

When both these parameters vary with the tracing parameter, $\lambda$, sensitivities of the multiharmonic forces are expressed in the form

$$\frac{\partial}{\partial \lambda}\mathbf{F}_y = \frac{\partial \mathbf{F}_y}{\partial k_n}\frac{\partial k_n}{\partial \lambda} + \frac{\partial \mathbf{F}_y}{\partial g}\frac{\partial g}{\partial \lambda}. \tag{37}$$

*Sensitivity With Respect to Normal Stiffness.* Sensitivity coefficients with respect to the normal stiffness coefficient of the contact surface, referenced in Eq. (37), are determined by differentiating Eq. (36) with respect to $k_n$:

$$\frac{\partial \mathbf{J}_y^{(j)}}{\partial k_n} = \begin{cases} \mathbf{W}_j\mathbf{Y} - g\mathbf{w}_j & \text{contact} \\ \mathbf{0} & \text{separation.} \end{cases} \tag{38}$$

*Sensitivity With Respect to Gap Value.* Analogously by differentiating Eq. (36) with respect to $g$ we obtain

$$\frac{\partial \mathbf{J}_y^{(j)}}{\partial g} = \begin{cases} -k_n\mathbf{w}_j & \text{contact} \\ \mathbf{0} & \text{separation.} \end{cases} \tag{39}$$

## Modes of Application of the Direct Parametric Analysis to Bladed Disks

The method developed allows the vector of multiharmonic amplitudes, **Q**, obtained as a result of solution Eq. (3) to be calculated as a function of many parameters, not only of excitation frequency as has been customary in the past. The dependencies of the vibration amplitudes can be calculated for each parameter of friction contact interface for a single contact node or for any group of contact nodes.

Moreover, in most previous investigations all parameters, of the structure were supposed to be constant, e.g., $\mathbf{b}(\omega)$=const, while rotation or excitation frequency was varied within some frequency range. The new approach allows us to take into account variation in all friction contact properties accompanying variation in rotation speed.

The new capabilities developed for direct parametric analysis can be used in analysis of nonlinear vibrations of bladed disks in different modes. Among these are the following:

1. determination of vibration amplitudes over some rotation speed range taking into account variation of all contact parameters, for example due to change of centrifugal forces, temperature, wear of the contact interfaces, etc. For this case the rotation speed, $\omega$, can be chosen as the tracing parameter, i.e., $\lambda = \omega$, and variation of all contact parameters for the whole bladed disk assembly included into a vector, **b**, described in terms of rotation speed: $\mathbf{b} = \mathbf{b}(\omega)$.
2. analysis of the influence of one chosen parameter on forced response. For this case the tracing parameter, $\lambda$ is the contact parameter analyzed, i.e., $\lambda = b_j$. Force response amplitudes are calculated when this $j$th contact parameter varied within a range of interest.
3. analysis of influence of a set of chosen parameters, dependent on service condition, on forced response. For this case, a set of all components of a vector of parameters, **b**, are considered as some prescribed functions of the tracing parameter, $\lambda$, i.e., $\mathbf{b} = \mathbf{b}(\lambda)$. The range of the contact parameter variation can be set as $[\mathbf{b}^-, \mathbf{b}^+]$. The tracing parameter is used here simply to describe parametrically the variation of many parameters when they are simultaneously varied. For example the range of variation can be selected for $\lambda$, as [0,1], then bound values for the parameters are defined as $\mathbf{b}(0) = \mathbf{b}^-$ and $\mathbf{b}(1) = \mathbf{b}^+$.

## Numerical Results

**A Model of a High-Pressure Turbine Bladed Disk.** As an example of a practical application of the method developed a tuned turbine high-pressure bladed disk with 92 shrouded blades is studied. A sector of the bladed disk is shown in **Fig. 1(*a*)**. Natural frequencies of the bladed disc, normalized with respect to the first blade-alone frequency, are shown in **Fig. 1(*b*)** for all possible nodal diameter numbers from 0 to 46. These frequencies were calculated for the case of a linear system where no contact interface elements were applied. Aerodynamic excitation forces are distributed uniformly over nodes located at the blade airfoil. A case of excitation by a forward travelling wave of 8th engine order is considered for the results reported here. Three harmonics are used in the multiharmonic expansion: 8, 24, and 40, which are correspond to 8th engine order multiplied by first three odd num-

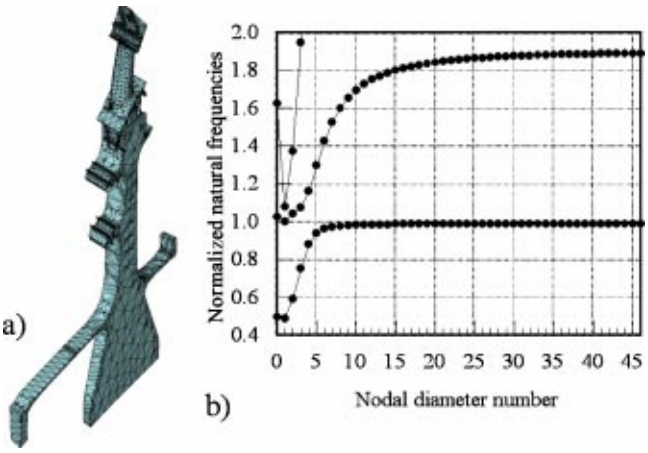


**Fig. 1 Bladed disk analyzed: (*a*) a sector of the bladed disk; (*b*) natural frequencies in the frequency range analyzed**

bers and which are dominant in the solution. The damping loss factor for the material of the blades and disc is assumed to be 0.003.

A full finite element model of the bladed disc comprises about 15 million DOFs and the finite element model for one sector contains 162,708 DOFs. In order to make nonlinear forced response calculations feasible, a method developed in paper [14] is applied. The method takes cyclic symmetry properties of the bladed disc into account for nonlinear vibrations and allows a nonlinear model for a whole bladed disk to be reduced to a single sector model without any loss of its accuracy.

The method developed here provides capability to analyze dependencies of displacement levels on parameter variation for each DOF. In the following figures the displacement levels are plotted for a representative node located at the blade tip, which is marked by letter ''A'' in **Fig. 2(*a*)**. The node was chosen to as having the maximum (compared with other nodes) displacement levels for the frequency ranges analyzed.

The forced response analyzed is multiharmonic and forced response level is determined by contribution of all harmonics included. To quantify the forced response level a maximum displacement reflecting contribution of all multiharmonic components is calculated for each excitation frequency. The maximum displacement, $d_{max}$, is defined as the maximum displacement over the period of vibration, i.e., $d_{max}=\max_{\tau\in[0,2\pi]}\sqrt{x^2(\tau)+y^2(\tau)+z^2(\tau)}$.

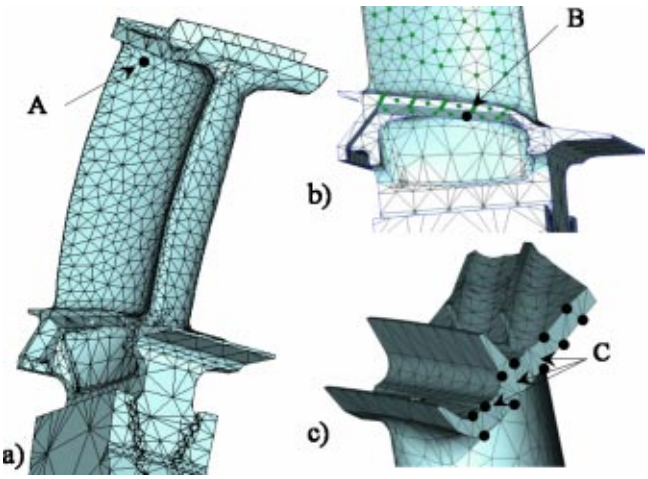


**Fig. 2 Finite element model: (*a*) a blade; (*b*) a blade damper contact node; (*c*) shroud contact nodes**

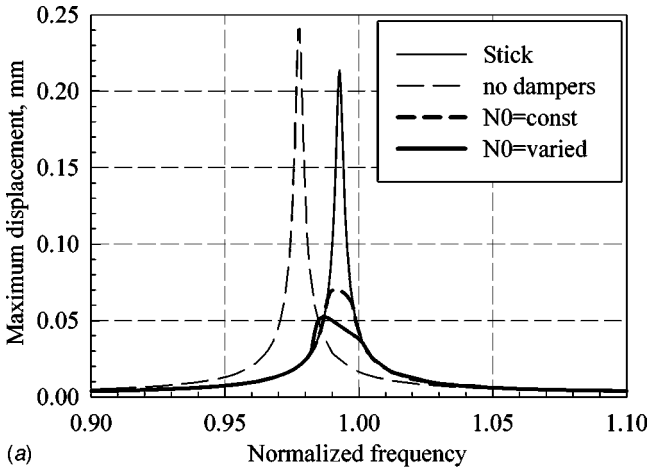


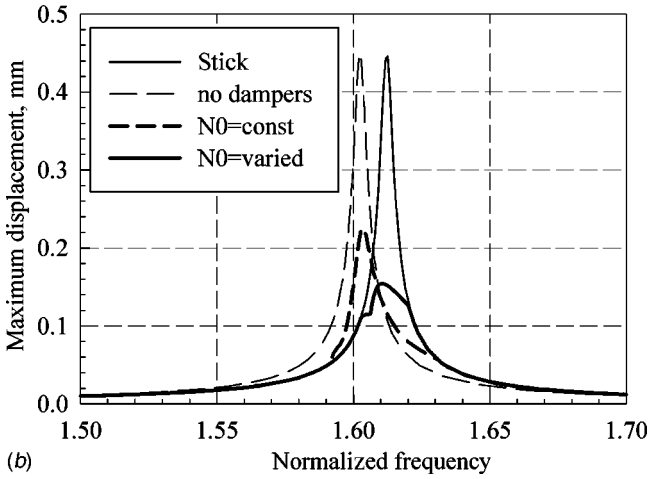


**Fig. 3 Forced response for the bladed disc with underplatform dampers: (*a*) in vicinity of 1st resonance (with 1F mode); (*b*) in vicinity of 2nd resonance (with 1E mode)**

Effects of two major sources of the nonlinear interaction forces on forced response levels are analyzed separately: (i) effects of blade underplatform dampers (UPD) producing friction damping forces when the dampers are slipping and (ii) effects of friction impacts of shrouds. Contact nodes at which the friction contact interface element are applied to model the nonlinear interaction are shown in **Fig. 2(*b,c*)** where they are marked by letters ''B'' (for underplatform dampers) and ''C'' (for friction contacts of shrouds).

**Effects of Parameters of the Underplatform Dampers.** The underplatform dampers are pressed by centrifugal forces to the contact surfaces and friction forces produced, when the dampers are slipping due to blade vibrations, dissipate the vibration energy. The normal load applied at the UPD is proportional to square of the rotor rotation speed, to distance from the rotation axis, $R_{UPD}$, and to mass of the damper, i.e., $N_0=c_{UPD}\omega^2 m_{UPD}R_{UPD}$, where a coefficient $c_{UPD}$ is mostly determined by shape of the damper. The method developed allows effective tracing of the solution with accounting for variation of the normal load due to speed variation. In **Fig. 3** results of calculation of the forced response with exact allowance for this variation is compared with the forced response determined with the forced response calculated with a normal load value fixed at the middle of the frequency range analyzed.

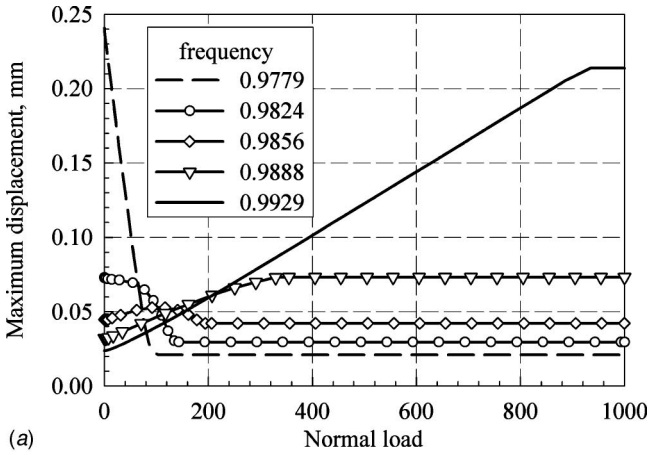


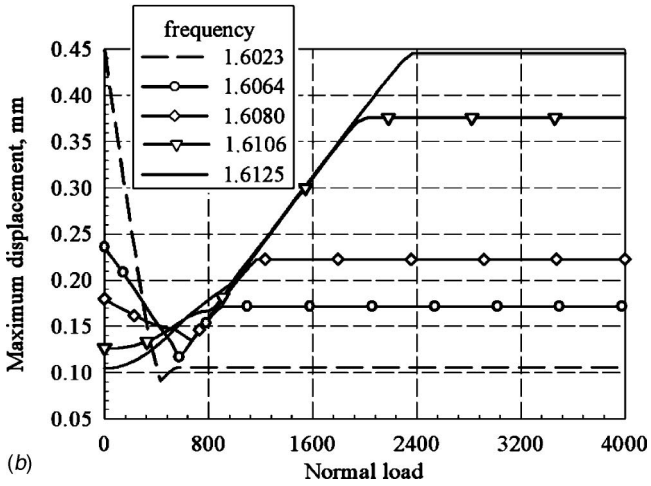


**Fig. 4 Forced response as a function of the normal load at UPD: (*a*) in vicinity of 1st resonance (with 1F mode); (*b*) in vicinity of 2nd resonance (with 1E mode)**

The fixed value for the normal load is $N_0 = 250$ N and the two other parameters of the friction damper are: $\mu = 0.3$ and $k_t = 4 * 10^4$ N/mm. Frequency ranges containing two first resonance frequencies are displayed. For comparison purposes, forced response is also plotted for two cases of linear vibration: (i) a bladed disk without the underplatform dampers; (ii) a bladed disk with

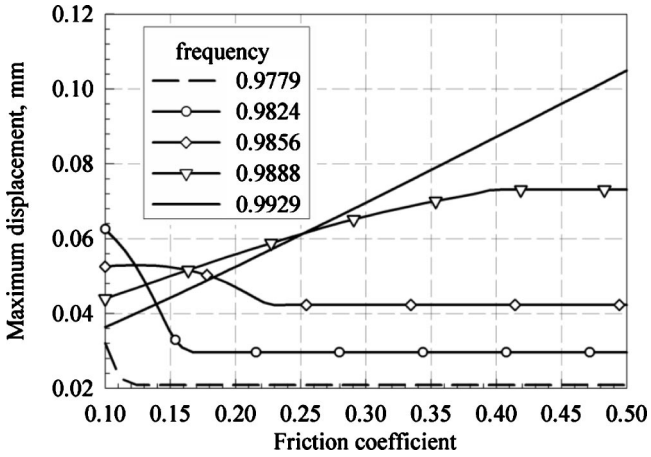


**Fig. 5 Forced response as a function of the UPD's friction coefficient in vicinity of 1st resonance (with 1F mode)**

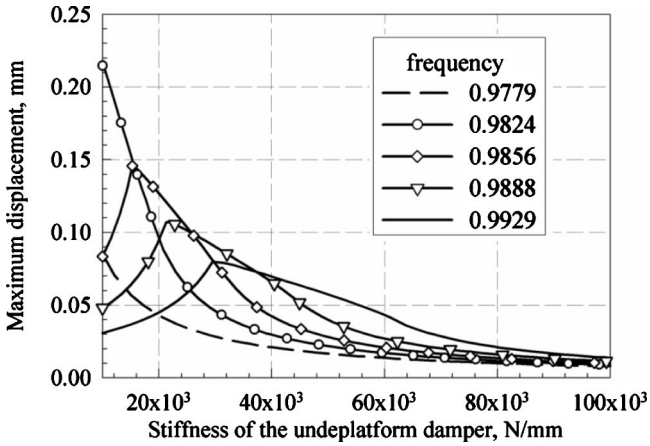


**Fig. 6 Forced response as a function of the stiffness of the UPD in vicinity of 1st resonance (with 1F mode)**

underplatform dampers that are always stuck (e.g., as a result of a large normal loads). Significant effects of the normal load variation on the forced response are observed. The method can, equally efficiently, find a solution when not only excitation frequency but also the normal load are varied as a function of the rotation speed.

In many cases there is a need to choose parameters of the UPD to optimize its damping capabilities. Variation of size of the UPD changes its mass and consequently the normal load and the stiffness of the damper. The friction coefficient value is affected by quality of finish and polishing of the contact surface, and by the temperature conditions. The new method provides powerful capabilities to calculate directly forced response levels as a function of the parameters of the underplatform dampers, which facilitates

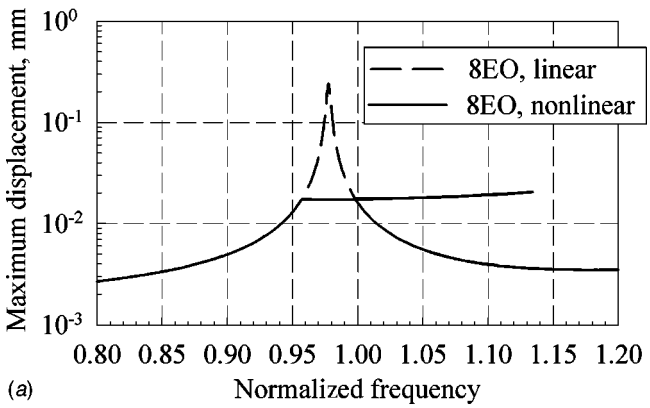


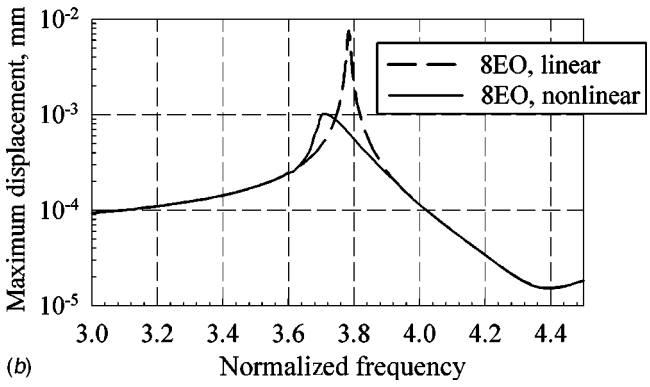


**Fig. 7 Forced response for shroud contacts: (*a*) a case with clearances; (*b*) a case with interferences**

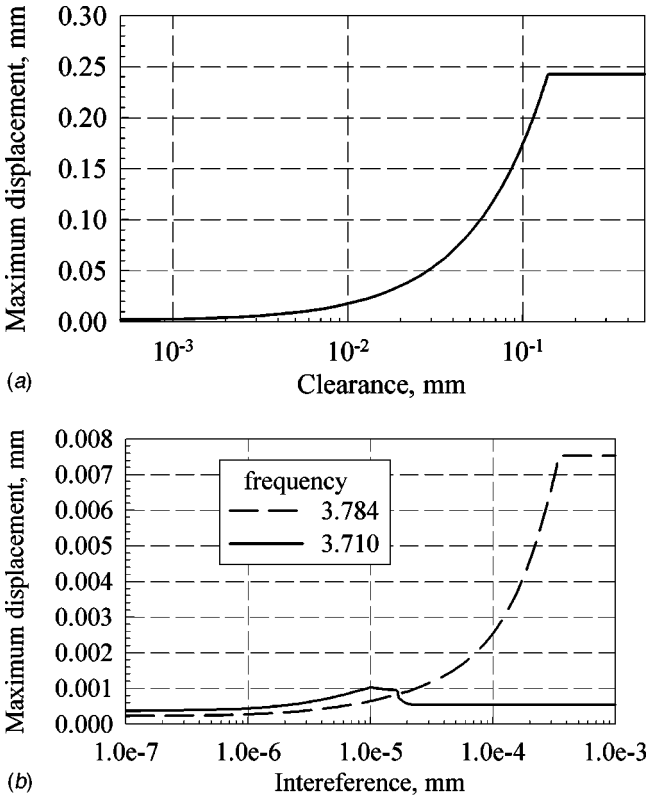


**Fig. 8 Forced response as a function of clearances (*a*) and interferences (*b*)**

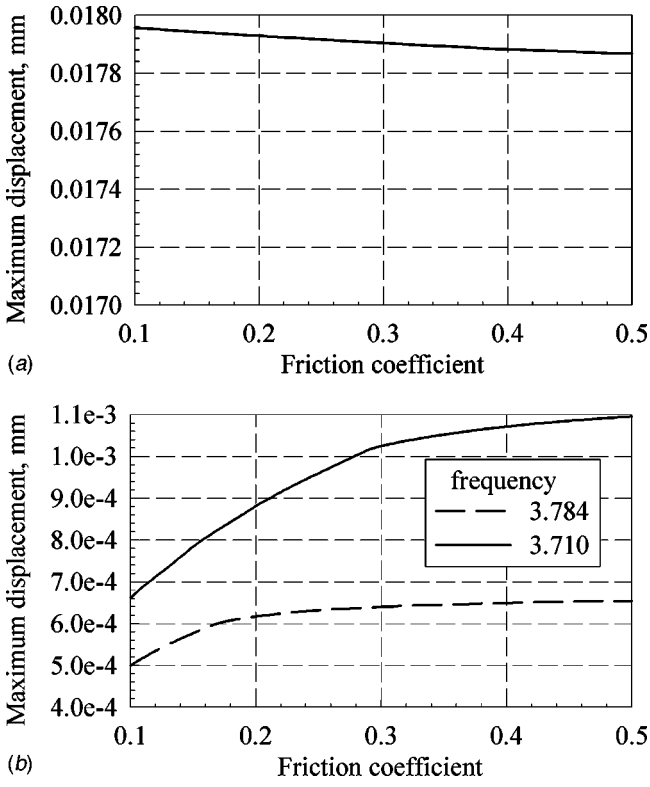


**Fig. 9 Forced response as a function of friction coefficient, $\mu$, for shrouds with clearances (*a*) and interferences (*b*)**

choice of the optimum set of the parameters for underplatform dampers. The maximum forced response was calculated as a function of the normal load for both resonance modes considered in **Fig. 3.**

This maximum forced response is plotted in vicinity of the first flap-wise resonance (**Fig. 4(*a*)**) and of the first edge-wise resonance (**Fig. 4(*b*)**) for several values of the excitation frequency. Curves without marks plotted in black were calculated for the assembly with UPDs but at resonance frequencies determined for two cases of linear vibration: (i) for a case when dampers are always stuck (a solid line), and for a case without underplatform dampers (a dashed line). The curves marked by circles, triangles, and squares in these figures correspond to frequency values between these two limiting resonance frequencies. One can see that a normal force of 120 N can provide the minimum forced response for the 1 F resonance mode, and a normal force of 480 N provides the minimum forced response for the 1 E resonance mode.

Dependencies of the forced response levels, for the 1 F mode resonance frequency range on the friction coefficient and on the stiffness of the UPD are shown in **Figs. 5 and 6**, respectively. One can see that the friction coefficient of 0.25 provides the minimum forced response level when all other parameters are fixed. Change of stiffness of the UPD affects the resonance frequency. In **Fig. 6** resonance level of amplitude corresponds to the peak value of the function of the response level with respect to the stiffness coefficient which can be achieved by its variation. A stiffness coefficient of $3.6*10^4$ for the UPD provides the minimum forced response while keeping the resonance frequency in the range between resonances for the two limiting linear cases, i.e., without dampers (dashed line) and with stuck dampers (solid line) without marks.

**Effects of Parameters of Shroud Contacts.** For the bladed disk with shroud contacts a set of friction contact interface elements was distributed over the shroud contact surfaces at the nodes shown in **Fig. 2(*c*)**. The contact interface elements describe friction forces occurring during time intervals when shrouds of the neighboring blades come into contact. Unilateral action of forces normal to the contact surface is allowed for also. They allow for the normal load variation and they also allow determination of all stick-slip and contact-separation transitions that occur during the vibrations.

Examples for two cases of shroud contact conditions are explored here: (i) a case when there are clearances between shrouds, and (ii) a case with interferences between shrouds. Examples of the forced responses calculated for a frequency range containing first resonance peak are shown in **Figs. 7(*a*) and 7(*b*)** for a clearance of $10^{-2}$ mm and for an interference of $10^{-5}$ mm, respectively. Abrupt change of stiffness properties of the system when the gap is closed is reflected in the shape of forced response characteristics, which is especially prominent in **Fig. 7(*a*)**. For comparison the forced responses of corresponding linear systems are plotted in these figures by dashed lines. These corresponding linear systems are: (i) a bladed disk with shrouds that never contact—for a case of shroud clearances; (ii) a bladed disk with shrouds that are always in contact—for a case of shroud interferences.

Dependencies of the resonance amplitudes on parameters of the shroud contact interfaces were calculated directly as functions of these parameters. Examples of such dependencies as a function of clearance and interference values are shown in **Fig. 8**. One can see that, for both cases, increase of these values increases amplitude levels up to the maximum value of the forced response level of the corresponding linear system. These levels are reached when clearance and interference values become large enough to guarantee contact absence (for a case of clearances) or full contact (for a case of interferences).

Dependencies of the response levels calculated as a function of friction coefficient at the shroud contact surface are plotted in **Fig. 9**. The plots indicate that, for the example of shrouds with clearances shown in **Fig. 9(*a*)**, variation of the friction coefficient does

**Table 2 Computational time for the parametric analysis**

| Parameter | Variation Range | CPU Time, sec |
|---|---|---|
| $\mu$ | 0.1–0.5 | 0.515 |
| $N_0$ | $0-10^3$ N | 0.719 |
| $k_t$ | $10^3-10^4$ N/mm | 1.047 |

not change forced response levels significantly, which is explained by the predominant effects of shroud impacts rather than friction forces. Yet, for the case of shrouds with interferences, effect of friction forces becomes significant which is reflected in significant influence of the friction coefficient on the forced response level, as seen from **Fig. 9(*b*)**.

**Efficiency of the Direct Parameter Analysis.** It should be noted that the new method developed for direct parametric analysis not only provides new capabilities for analysis of the forced response with respect to parameter variation, but it also provides very high speed of calculations for such analysis. The computational expense for solution tracing as a function of contact interface parameters, for the examples considered, was less by several orders of magnitudes than that required to calculate the forced response as a function of frequency for a single set of the contact parameters. Examples of computation time required to perform the parametric analysis of the bladed disk with UPD on a conventional PC are shown in **Table 2** together with the ranges of parameter variation that were analyzed.

## Conclusions

An effective method for direct parametric analysis of periodic, nonlinear forced response of bladed discs, with friction contact interfaces has been developed.

The method allows, for the first time, forced response levels to be calculated directly as a function of contact interface parameters such as friction coefficient, normal and tangential contact surface stiffness coefficients, clearances, interferences, and normal stresses at the contact interfaces.

Transformation of the equations of motion to the frequency domain is performed using the multiharmonic balance method. Contact interaction is described by specially-derived multiharmonic friction interface elements modelling contact forces and contact stiffness.

The method is based on exact expressions for sensitivities of the multiharmonic interaction forces with respect to variation of all parameters of the friction contact interfaces derived in the paper. These novel expressions are obtained for a friction model including normal load variation and separation-contact transitions.

Modes of application of the new capabilities in practical design are examined. Numerical analysis of effects of design parameters on forced response levels has been performed for large-scale finite element models of a practical bladed turbine disk with underplatform dampers and with shroud contacts between neighboring blades in the bladed disk. The direct parametric analysis allows optimum design parameters providing minimum forced response levels to be efficiently determined.

## Acknowledgments

The author is grateful to Rolls-Royce plc. for providing the financial support for this project and for giving permission to publish this work.

## References

[1] Cardona, A., Coune, T., Lerusse, A., and Geradin, M., 1994, ''A Multiharmonic Method for Non-Linear Vibration Analysis,'' Int. J. Numer. Methods Eng., **37**, pp. 1593–1608.
[2] Griffin, J. H., and Labelle R. F., 1996, ''A Rational Method for Optimizing Shroud Damping,'' ASME Paper 96-GT-402.
[3] Sanliturk, K. Y., Imregun, M., and Ewins, D. J., 1997, ''Harmonic Balance Vibration Analysis of Turbine Blades With Friction Dampers,'' ASME J. Vibr. Acoust., **119**, pp. 96–103.
[4] Yang, B.-D., and Menq, C.-H., 1997, ''Modelling of Friction Contact and Its Application to the Design of Shroud Contact,'' ASME J. Eng. Gas Turbines Power, **119**, pp. 958–963.
[5] Szwedowicz, J., Sextro, W., Visser, R., and Masserey, P., 2003, ''On Forced Vibration of Shrouded Turbine Blades,'' ASME Paper GT-2003-38808.
[6] Sanliturk, K. Y., Ewins, D. J., and Stanbridge, A. B., 2003, ''Underplatform Dampers for Turbine Blades: Theoretical Modeling, Analysis, and Comparison With Experimental Data,'' ASME J. Eng. Gas Turbines Power, **123**, pp. 919–929.
[7] Pierre, C., Ferri, A. A., and Dowell, E. H., 1985, ''Multi-Harmonic Analysis of Dry Friction Damped Systems Using an Incremental Harmonic Balance Method,'' ASME J. Appl. Mech., **52**, pp. 958–964.
[8] Cameron, T., and Griffin, J., 1989, ''An Alternating Frequency/Time Domain Method for Calculating the Steady-State Response of Nonlinear Dynamic Systems,'' ASME J. Appl. Mech., **56**, pp. 149–154.
[9] Nacivet, S., Pierre, C., Thouverez, F., and Jezequel, L., 2003, ''A Dynamic Lagrangian Frequency—Time Method for the Vibration of Dry-Friction-Damped Systems,'' J. Sound Vib., **265**, pp. 201–219.
[10] Wang, J. H., and Chen, W. K., 1993, ''Investigation of the Vibration of a Blade With Friction Damper by HBM,'' ASME J. Eng. Gas Turbines Power, **115**, pp. 294–299.
[11] Berthillier, M., Dupont, C., Mondal, R., and Barrau, R. R., 1998, ''Blades Forced Response Analysis With Friction Dampers,'' ASME J. Vibr. Acoust., **120**, pp. 468–474.
[12] Chen, J. J., and Menq, C. H., 1999, ''Prediction of Periodic Response of Blades Having 3D Nonlinear Shroud Constraints,'' ASME Paper 99-GT-289.
[13] Petrov, E. P., and Ewins, D. J., 2003, ''Analytical Formulation of Friction Interface Elements for Analysis of Nonlinear Multi-Harmonic Vibrations of Bladed Discs,'' ASME J. Turbomach., **125**, April, pp. 364–371.
[14] Petrov, E. P., 2004, ''A Method for Use of Cyclic Symmetry Properties in Analysis of Nonlinear Multiharmonic Vibrations of Bladed Discs,'' ASME J. Turbomach., **126**, January, pp. 175–183.
[15] Griffin, J. H., 1990, ''A Review of Friction Damping of Turbine Blade Vibration,'' International J. of Turbo and Jet Engines, **(7)**, pp. 297–307.
[16] Riks, E., 1979, ''An Incremental Approach to the Solution of the Snapping and Buckling Problems,'' Int. J. Solids Struct., **15**, pp. 529–551.
[17] Crisfield, M., 1981, ''A Fast Incremental/Iterative Solution Procedure That Handles Snap-Through,'' Comput. Struct., **13**, pp. 55–62.
[18] Fried, I., 1984, ''Orthogonal Trajectory Accession to the Nonlinear Equilibrium Curve,'' Comput. Methods Appl. Mech. Eng., **47**, pp. 283–297.
[19] Petrov, E. P., and Ewins, D. J., 2004, ''Method for Analysis of Nonlinear Multiharmonic Vibration of Bladed Discs Mistuned by Scatters in Characteristics of Friction Contact Interfaces and Blades,'' ASME Paper GT2004-53891.

# Experimental Study of the Effect of Periodic Unsteady Wake Flow on Boundary Layer Development, Separation, and Reattachment Along the Surface of a Low Pressure Turbine Blade

**M. T. Schobeiri**
e-mail: tschobeiri@mengr.tamu.edu

**B. Öztürk**

Turbomachinery Performance and Flow Research Laboratory,
Texas A&M University,
College Station, Texas 77843-3123

*The paper experimentally studies the effects of periodic unsteady wake flow on boundary layer development, separation and reattachment along the suction surface of a low pressure turbine blade. The experimental investigations were performed on a large scale, subsonic unsteady turbine cascade research facility at the Turbomachinery Performance and Flow Research Laboratory (TPFL), Texas A&M University. The experiments were carried out at a Reynolds number of 110,000 (based on suction surface length and exit velocity) with a free-stream turbulence intensity of 1.9%. One steady and two different unsteady inlet flow conditions with the corresponding passing frequencies, wake velocities, and turbulence intensities were investigated. The reduced frequencies cover the entire operating range of LP turbines. In addition to the unsteady boundary layer measurements, blade surface measurements were performed at the same Reynolds number. The surface pressure measurements were also carried out at one steady and two periodic unsteady inlet flow conditions. The results presented in ensemble-averaged, and the contour plot forms help to understand the physics of the separation phenomenon under periodic unsteady wake flow. It was found that the suction surface displayed a strong separation bubble for these three different reduced frequencies. For each condition, the locations and the heights defining the separation bubble were determined by carefully analyzing and examining the pressure and the mean velocity profile data. The location of boundary layer separation was independent of the reduced frequency level. However, the extent of the separation was strongly dependent on the reduced frequency level. Once the unsteady wake started to penetrate into the separation bubble, the turbulent spot produced in the wake paths caused a reduction of the separation bubble height.*
[DOI: 10.1115/1.1791646]

## Introduction

In recent years, gas turbine engine aerodynamicists have focused their attention on improving the efficiency and performance of the low pressure turbine (LPT) component. Research works from industry, research centers, and academia have shown that a reduction of the blade number can be achieved without substantially sacrificing the efficiency of the LPT blading. This reduction contributes to an increase in thrust/weight ratio, thus reducing the fuel consumption. Contrary to the high pressure turbine (HPT) stage group that operates in a relatively high Reynolds number environment, based on the operating conditions, the LPT experiences an adverse change in Reynolds number ranging from 50,000 to 250,000. Since the major portion of the boundary layer, particularly along the suction surface is laminar, the low Reynolds number in conjunction with the local adverse pressure gradient makes it susceptible to flow separation, thus increasing the complexity of the LPT boundary layer aerodynamics. The periodic unsteady nature of the incoming flow associated with wakes that originate from upstream blades substantially influences the boundary layer development including the onset of the laminar separation, the extent of the separation bubble, and its turbulent reattachment. Of particular relevance in the context of LPT aerodynamics is the interaction of the wake flow with the suction surface separation bubble. While the phenomenon of the unsteady boundary layer development and transition in the absence of the separation bubbles has been the subject of intensive research, that has led to better understanding the transition phenomenon, comprehending the multiple effects of mutually interacting parameters on the LPT boundary layer separation and their physics still requires more research.

The significance of the unsteady flow effect on efficiency and performance of compressor and turbine stages was recognized in the early seventies by several researchers. Fundamental studies by Pfeil and Herbst [1], Pfeil et al. [2], and Orth [3] studied and quantified the effect of unsteady wake flow on the boundary layer transition along flat plates. Schobeiri and his co-workers [4–7] experimentally investigated the effects of the periodic unsteady wake flow and pressure gradient on the boundary layer transition and heat transfer along the concave surface of a constant curvature plate. The measurements were systematically performed under different pressure gradients and unsteady wake frequencies using a squirrel cage type wake generator positioned upstream of the curved plate. Liu and Rodi [8] carried out the boundary layer and

Contributed by the International Gas Turbine Institute (IGTI) of THE AMERICAN SOCIETY OF MECHANICAL ENGINEERS for publication in the ASME JOURNAL OF TURBOMACHINERY. Paper presented at the International Gas Turbine and Aeroengine Congress and Exhibition, Vienna, Austria, June 13–17, 2004, Paper No. 2004-GT-53929. Manuscript received by IGTI, October 1, 2003; final revision, March 1, 2004. IGTI Review Chair: A. J. Strazisar.

  

heat transfer measurements on a turbine cascade, which was installed downstream of a squirrel cage type wake generator mentioned previously.

Analyzing the velocity and the turbulence structure of the impinging wakes and their interaction with the boundary layer, Chakka and Schobeiri [7] developed an intermittency based unsteady boundary layer transition model. The analysis revealed a universal pattern for the relative intermittency function for all the frequencies and pressure gradients investigated. However, the above investigations were not sufficient to draw any conclusion with regard to an eventual universal character of the relative intermittency function. Further detailed investigations of the unsteady boundary layer on a high Reynolds number turbine cascade by Schobeiri et al. [9,10] and its subsequent analysis [11] and [12] verified the universal character of the relative intermittency function. For this purpose, Schobeiri et al. [9] utilized a conceptually different type wake generator, which is also used for the investigation presented in this paper. Fottner and his coworkers [13,14] and Schulte and Hodson [15] used the same wake generating concept for the investigations on the influence of the unsteady wake flow on the LPT-boundary layer. Kaszeta, Simon, and Ashpis [16] experimentally investigated the laminar-turbulent transition aspect within a channel with the side walls resembling the suction and pressure surfaces of a LPT blade. Lou and Hourmouziadis [17] investigated the mechanism of separation, transition, and reattachment, and the effect of oscillating inlet flow conditions on laminar boundary layer separation along a flat plate under a strong negative pressure gradient which was similar to the LPT pressure gradient. This was simulated by contouring the top wall. They studied the Reynolds number effect on the transition region. Their results showed that the higher Reynolds numbers cause an earlier transition and reduction of the transition length, while the separation point does not change its location. Using the top wall contouring, Volino and Hultgren [18] performed an experimental study and measured the detailed velocity along a flat plate which was subjected to a similar pressure gradient as the suction side of a low pressure turbine blade. They also stated that the location of the boundary layer separation does not strongly depend on the Reynolds number or free-stream turbulence level, as long as the boundary layer remains nonturbulent before separation occurs. Furthermore, they showed that the extent of the transition is strongly dependent on the Reynolds number and turbulence intensity.

Using the surface mounted hot film measurement technique, Fottner and his coworkers [13] and [14], Schröder [19], and Haueisen, Hennecke, and Schröder [20] documented strong interaction between the wakes and the suction surface separation bubble on the LPT blades, both in the wind tunnel cascade tests and in a turbine rig. Furthermore, they investigated the boundary layer transition under the influence of the periodic wakes along the LPT surface and found that the interaction of the wake with the boundary layer greatly affects the loss generation. Shyne et al. [21] performed an experimental study on a simulated low pressure turbine. The experiments were carried out at Reynolds numbers of 100,000 and 250,000 with three levels of free-stream turbulence. They indicated that the transition onset and the length are strongly dependent on the free-stream turbulence. As the free-stream turbulence increases, the onset location and the length of the transition are decreased. Treuren et al. [22] performed an experimental study along a LPT surface at the very low Reynolds number of 25,000 and 50,000 with different free-stream turbulence levels. They showed that a massive separation at the very low Reynolds number of 25,000 is persistent, in spite of an elevated free stream turbulence intensity. However, at the higher Reynolds number of 50,000, there was a strong separation on the suction side for the low free-stream turbulence level. The separation bubble was eliminated for the higher free-stream turbulence level of 8–9%. The investigations by Halstead et al. [23] on a large scale LP turbine uses surface mounted hot films to acquire detailed information about the quasishear stress directly on the blade surface. Investigations by Cardamone et al. [14] and Schröder [19] indicate that the benefit of the wake-boundary layer interaction can be used for the design procedure of modern gas turbine engines with a reduced LPT blade number without altering the stage efficiency.

Most of the studies mentioned above on LP turbine cascade aerodynamics have largely concentrated on the measurement of the signals stemming from hot films mounted on the suction and pressure surfaces of the blades under investigation. Although this technique is qualitatively reflecting the interaction of the unsteady wake with the boundary layer, because of the lack of an appropriate calibration method, it is not capable of quantifying the surface properties such as the wall shear stress. The few boundary layer measurements are not comprehensive enough to provide any conclusive evidence for interpretation of the boundary layer transition and separation processes and their direct impact on profile loss, which is a critical parameter for blade design. Furthermore, the numerical simulation of the unsteady LPT blade aerodynamics using conventional turbulence and transition models fails if it is applied to low Reynolds number cases. Recent work presented by Cardamone et al. [14] shows that in the steady state case at Re $=60{,}000$, the separation is captured, however, for the unsteady case, the separation bubble is not reproduced.

A recent experimental study by Schobeiri and Öztürk [24] investigated the physics of the inception, onset and extent of the separation bubble along a low pressure turbine blade which was the first part of a series of investigations carried out at TPFL. A detailed experimental study on the behavior of the separation bubble on the suction surface of a highly loaded LPT blade under a periodic unsteady wake flow was presented in Ref. [24]. Surface pressure measurements were performed at Re=50,000, 75,000, 100,000, 125,000. Increasing the Reynolds number has resulted in no major changes to the surface pressure distribution. They concluded that the unsteady wake flow with its highly turbulent vortical core over the separation region caused a periodic contraction and expansion of the separation bubble. It was proposed that, in conjunction with the pressure gradient and periodic wakes, the temporal gradient of the turbulence fluctuation, or more precisely the fluctuation acceleration $\partial \nu_{rms}/\partial t$ provides a higher momentum and energy transfer into the boundary layer, energizing the separation bubble and causing it to partially or entirely disappear. They found that for $\partial \nu_{rms}/\partial t > 0$, the separation bubble starts to contract, whereas for $\partial \nu_{rms}/\partial t < 0$, it gradually assumes the shape before the contraction. They argued that not only the existence of higher turbulence fluctuations expressed in terms of higher turbulence intensity influences the flow separation, but also its gradient is of crucial importance in suppressing or preventing the onset and the extent of the separation bubble. They stated that the fluctuation gradient is an inherent feature of the incoming periodic wake flow and does not exist in a statistically steady flow that might have a high turbulence intensity.

The objective of the present study dealing with the specific issues of the LPT boundary layer aerodynamics is to provide detailed unsteady boundary flow information to understand the underlying physics of the inception, onset, and extension of the separation bubble. Furthermore, the unsteady boundary layer data from the present and planned experimental investigations will serve to extend the intermittency unsteady boundary layer transition model developed by Schobeiri and his coworkers [7,11,12] to the LPT cases, where a massive separation occurs on the suction surface at a low Reynolds number at the design and off-design incidence. Furthermore, the experimental results are intended to serve as benchmark data for a comparison with numerical computation using DNS or RANS-codes.

It is well known that the boundary layer measurement is one of the most time consuming aerodynamic measurements. Any attempt to increase the number of parameters to be studied would inevitably result in substantial increase of the measurement time. Considering this fact, the research facility described in Refs. [9]

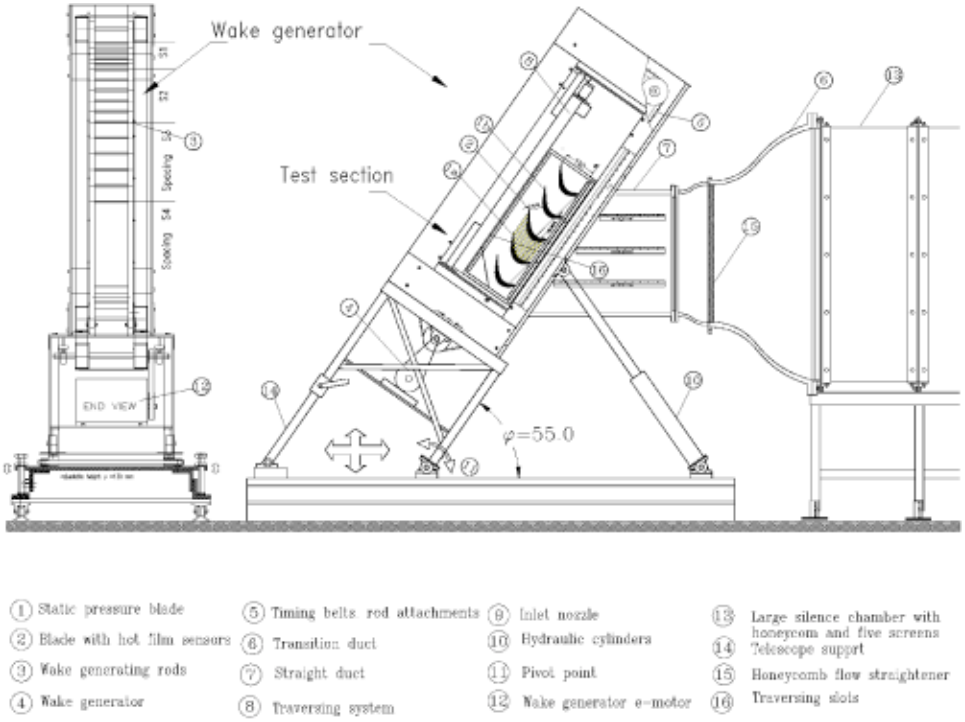


**Fig. 1 Turbine cascade research facility with the components and the adjustable test section**

and [10] with state-of-the-art instrumentation has been substantially modified to study systematically and efficiently the influence of the periodic unsteady and highly turbulent flow on the LPT cascade aerodynamics at the design and off-design incidence angles, where the Reynolds number, wake impingement frequency, free-stream turbulence, and the blade solidity can be varied independently.

## Experimental Research Facility

To investigate the effect of unsteady wake flow on turbine and compressor cascade aerodynamics, particularly on unsteady boundary layer transition, a multipurpose large-scale, subsonic research facility was designed and has been taken into operation since 1993. Since the facility in its original configuration is described in Refs. [9], [10] and [24] only a brief description of the modifications and the main components is given below. The research facility consists of a large centrifugal compressor, a diffuser, a settling chamber, a nozzle, an unsteady wake generator, and a turbine cascade test section as shown in Fig. 1. The compressor with a volumetric flow rate of 15 $m^3/s$ is capable of generating a maximum mean velocity of 100 m/s at the test section inlet. The settling chamber consists of five screens and one honeycomb flow straightener to control the uniformity of the flow.

Two-dimensional periodic unsteady inlet flow is simulated by the translational motion of a wake generator (see Fig. 1), with a series of cylindrical rods attached to two parallel operating timing belts driven by an electric motor. To simulate the wake width and spacing that stem from the trailing edge of rotor blades, the diameter and number of rods can be varied. The rod diameter, its distance from the LPT blade leading edge, the wake width and the corresponding drag coefficient are chosen according to the criteria outlined by Schobeiri et al. [25]. The belt-pulley system is driven by an electric motor and a frequency controller. The wake-passing frequency is monitored by a fiber optic sensor. The sensor also serves as the triggering mechanism for data transfer and its initialization, which is required for ensemble-averaging. This type of wake generator produces clean 2-dimensional wakes, whose turbulence structure, decay and development are, to a great extent, predictable [25]. The unsteady boundary layer transition and heat transfer investigations [9–12] performed on this facility serve as the benchmark data for validation of turbulence models, transition models, and general code assessments.

To account for a high flow deflection of the LPT cascade, the entire wake generator and test section unit including the traversing system was modified to allow a precise angle adjustment of the cascade relative to the incoming flow. This is done by a hydraulic platform, which simultaneously lifts and rotates the wake generator and test section unit. The unit is then attached to the tunnel exit nozzle with an angular accuracy less than 0.05 deg, which is measured electronically.

The special design of the facility and the length of the belts ($L_{belt}=5{,}000$ mm) enables a considerable reduction of the measurement time. For the present investigation, two clusters of rods with constant diameter of 2 mm are attached to the belts as shown in Fig. 1. The two clusters with spacings $S_R=160$ mm and $S_R=80$ are separated by a distance which does not have any rods, thus simulating the steady state case ($S_R=\infty$). Thus, it is possible to measure sequentially the effect of three different spacings at a single boundary layer point. To clearly define the influence domain of each individual cluster with the other one, the clusters are arranged with a certain distance between each other. Using the triggering system mentioned above and a continuous data acquisition, the buffer zones between the data clusters are clearly visible.

The data analysis program cuts the buffer zones and evaluates the data pertaining to each cluster. Comprehensive preliminary measurements were carried out to make sure that the data were exactly identical to those, when the entire belt length was attached with rods of constant spacing, which corresponded to each individual cluster spacing. The cascade test section shown in Fig. 1, located downstream of the wake generator, includes 5 LPT blades with a height of 200.0 mm and the chord of 203.44 mm, Fig. 2. For boundary layer investigations, five identical ''Pak B'' airfoils designed by Pratt & Whitney were implemented whose cascade geometry is given in Table 1. The blade geometry resembles the essential feature such as the laminar boundary layer separation

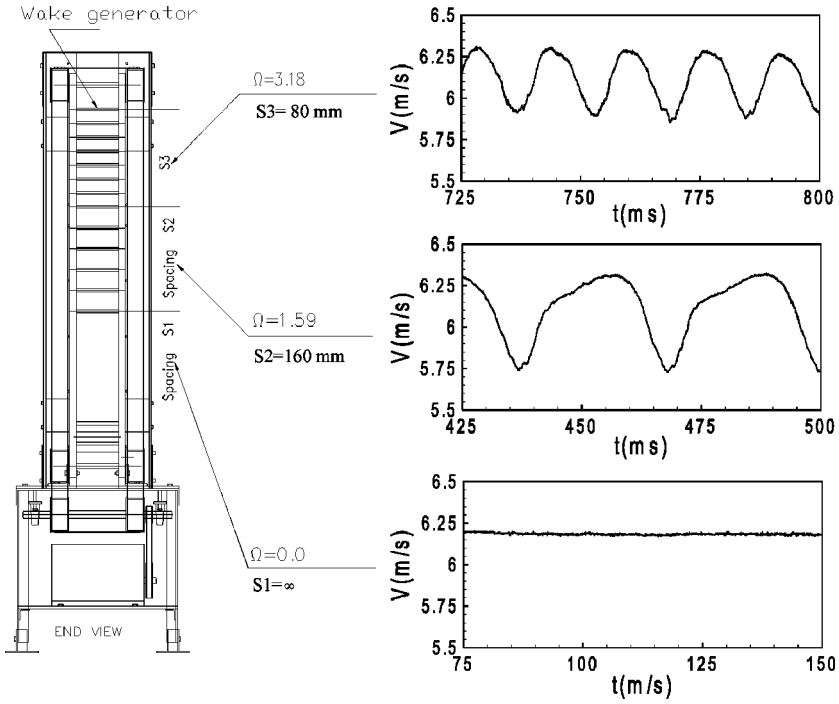


**Fig. 2 Wake Generator**

that is inherent to typical LPT blades. The blade geometry was made available to NASA researchers and academia to study the specific problems of LPT flow separation, its passive and active control and its prevention. As shown in Ref. [9], this blade number is necessary and sufficient to secure a spatial periodicity for the cascade flow. The periodicity is demonstrated by the pressure distributions of the blade numbers 2 and 4, shown in Fig. 1 as part 1(*a*) and 1(*b*). These blades were specially manufactured for measurement of pressure and showed identical pressure distributions. A computer controlled traversing system is used to measure the inlet velocities and turbulence intensities, as well as the boundary layers on suction and pressure surfaces. The traversing system is vertically mounted on the Plexiglas side wall. It consists of a slider and a lead screw that is connected to a DC-stepper motor with an encoder and decoder. The optical encoder provides a continuous feedback to the stepper motor for accurate positioning of the probes. The system is capable of traversing in small steps up to 2.5 $\mu$m, which is specifically required for boundary layer investigations where the measurement of the laminar sublayer is of particular interest.

## Instrumentation, Data Acquisition, and Data Reduction

The data acquisition system is controlled by a personal computer that includes a 16 channel, 12-bit analog-digital (A/D) board. Time dependent velocity signals are obtained by using a commercial 3-channel (TSI), constant temperature hot-wire anemometer system that has a signal conditioner with a variable low pass filter and adjustable gain. A Prandtl probe, placed upstream of the diffuser, monitors the reference velocity at a fixed location. The pneumatic probes are connected to high precision differential pressure transducers for digital readout. Several calibrated thermocouples are placed downstream of the test section to constantly monitor the flow temperature. The wake generator speed and the passing frequency signals of the rods are transmitted by a fiber-optic trigger sensor. The passage signals of the rods are detected by the sensor using a silver-coated reflective paint on one of the belts. This sensor gives an accurate readout of the speed of the wake generator and the passing frequency of the rods. The signals of the pressure transducers, thermocouples, and trigger sensors are transmitted to the A/D board and are sampled by the computer. To

**Table 1 Parameters of turbine cascade test section**

| Parameters | Values | Parameters | Values |
|---|---|---|---|
| Inlet velocity | $V_{in}=4$ m/s | Inlet turbulence intensity | $Tu_{in}=1.9\%$ |
| Rod translational speed | $U=5.0$ m/s | Blade Re-number | $Re=110{,}000$ |
| Nozzle width | $W=200.0$ mm | Blade height | $h_B=200$ mm |
| Blade chord | $c=203.44$ mm | Cascade solidity | $\sigma=1.248$ |
| Blade axial chord | $c_{ax}=182.85$ mm | Zweifel coefficient | $\psi_A=1.254$ |
| Blade suction surface length | $L_{SS}=270.32$ mm | Cascade angle | $\varphi=55°$ |
| Cascade flow coefficient | $\Phi=0.80$ | Cascade spacing | $S_B=163$ mm |
| Inlet air angle to the cascade | $\alpha_1=0°$ | Exit air angle from the cascade | $\alpha_2=90°$ |
| Rod diameter | $D_R=2.0$ mm | Rod distance to leading edge | $L_R=122$ mm |
| Cluster 1 (no rod, steady) | $S_R=\infty$ mm | $\Omega$—parameter steady case | $\Omega=0.0$ |
| Cluster 2 rod spacing | $S_R=160.0$ mm | $\Omega$—parameter for cluster 1 | $\Omega=1.59$ |
| Cluster 3 rod spacing | $S_R=80.0$ mm | $\Omega$—parameter for cluster 2 | $\Omega=3.18$ |

ensure the cascade periodicity, the second and fourth blades are instrumented each with 48 static pressure taps. Two adjacent blades are used for boundary layer measurement. The taps are connected to a scanivalve, which sequentially transferred the pressure signals to one of the transducers that was connected to the A/D board. Using the newest version of Labview, the data acquisition system including the computer and the A/D board was upgraded.

The unsteady data are taken by calibrated, custom designed miniature, single hot wire probes. At each boundary layer position, samples were taken at a rate of 20 kHz for each of 100 revolutions of the wake generator. The data were ensemble-averaged with respect to the rotational period of the wake generator. Before final data were taken, the number of samples per revolution and the total number of revolutions were varied to determine the optimum settings for convergence of the ensemble-average.

For the steady state case, the instantaneous velocity components are calculated from the temperature compensated instantaneous voltages by using the calibration coefficients. The instantaneous velocity can be represented in the following form:

$$V=\overline{V}+v \tag{1}$$

where $\overline{V}$ is the mean (time-averaged) velocity and v is the turbulent fluctuation component. The mean velocity, also known as the time-average, is given by:

$$\overline{V}=\frac{1}{M}\sum_{j=1}^{M} V_j \tag{2}$$

where $M$ is the total number of samples at one boundary layer location. The root mean square value of the turbulent velocity fluctuation is:

$$v=\sqrt{\frac{1}{M}\sum_{j=1}^{M}(V_j-\overline{V})^2} \tag{3}$$

and the local turbulence intensity is defined as:

$$Tu_{loc}=\frac{v}{\overline{V}}\times 100=\frac{1}{\overline{V}}\sqrt{\frac{1}{M}\sum_{j=1}^{M}(V_j-\overline{V})^2\times 100} \tag{4}$$

For unsteady cases, the ensemble-averaged velocity, fluctuation velocity, and the turbulence intensity were calculated from the instantaneous velocity samples by:

$$V_i(t_i)=\langle V_i(t_i)\rangle=\frac{1}{N}\sum_{j=1}^{N} V_{ij}(t_i) \tag{5}$$

$$v_i(t_i)=\langle v_i(t_i)\rangle=\sqrt{\frac{1}{N}\sum_{j=1}^{M}[V_{ij}(t_i)-\langle V_i(t_i)\rangle]^2} \tag{6}$$

$$Tu_i(t_i)=\langle Tu_i(t_i)\rangle=\frac{\langle v_i(t_i)\rangle}{\langle V_i(t_i)\rangle}\times 100 \tag{7}$$

where N=100 is the total number of wake generator periods and M the number of samples taken per period. $\langle V_i(t_i)\rangle$ is the reference ensemble averaged velocity for the particular boundary layer traverse. The ensemble-averaged boundary layer parameters such as displacement thickness $\langle\delta_1\rangle$, momentum thickness $\langle\delta_2\rangle$, and shape factor $\langle H_{12}\rangle$ are calculated as follows:

$$\delta_1\equiv\langle\delta_1\rangle=\int_0^{\langle\delta\rangle}\left(1-\frac{\langle V\rangle}{\langle V\rangle_e}\right)dy \tag{8}$$

$$\delta_2\equiv\langle\delta_2\rangle=\int_0^{\langle\delta\rangle}\frac{\langle V\rangle}{\langle V\rangle_e}\left(1-\frac{\langle V\rangle}{\langle V\rangle_e}\right)dy \tag{9}$$

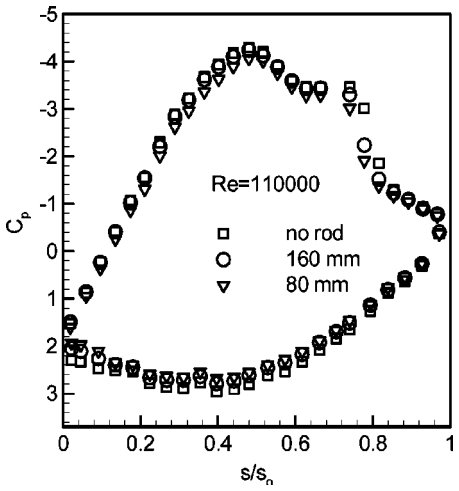


**Fig. 3 Static pressure distributions at Re=110,00 and reduced frequencies Ω=0, 1.59, 3.18 ($S_R$=:, $S_R$=160 mm, 80 mm)**

$$H_{12}\equiv\langle H_{12}\rangle=\frac{\langle\delta_1\rangle}{\langle\delta_2\rangle} \tag{10}$$

In the above equations the signs $\langle\ \rangle$ refer to ensemble averaged quantities. Since we are dealing with ensemble averaged data, for the sake of consistency, we will drop $\langle\ \rangle$ in the following discussions. Precise calculation of $\delta_1$, $\delta_2$, and $H_{12}$ requires accurate determination of the boundary layer thickness $\delta$ as given in Ref. [26].

## Experimental Results and Discussion

To investigate the influence of the unsteady wake flow on the boundary layer development along the suction and pressure surfaces of the LPT blade and, particularly, its impact on the inception and onset of the separation bubble, the detailed surface pressure and boundary layer measurements were performed at a Reynolds number of 110,000. This Reynolds number, which pertains to a typical cruise operation, exhibits a representative value within LPT operating range between 75,000 and 400,000 as discussed by Hourmouziadis [27]. Furthermore, it produces separation bubbles that can be accurately measured by miniature hot wire probes. For this Reynolds number, three different reduced frequencies were examined. For generation of the unsteady wakes, cylindrical rods with the diameter $d_R=2$ mm were chosen to fulfill the similar criterion that requires the generation of a drag coefficient $C_D$ that is approximately equal to the $C_D$ of the turbine blade with the chord and spacing given in Table 1 (for details we refer to the studies in [25] and [28]).

To accurately account for the unsteadiness caused by the frequency of the individual wakes and their spacings, the flow velocity, and the cascade parameters, we define a reduced frequency Ω that includes the cascade solidity $\sigma$, the flow coefficient $\varphi$, the blade spacing $S_B$, and the rod spacing $S_R$. Many researchers have used the Strouhal number as the unsteady flow parameter, which only includes the speed of the wake generator and the inlet velocity. However, the reduced frequency Ω is an extension of the Strouhal number in the sense that it incorporates the rod spacing $S_R$ and the blade spacing $S_B$ in addition to the inlet velocity and wake generator speed. For the surface pressure measurement, rods with uniform spacings as specified in Table 1 were attached over the entire belt length. For boundary layer measurement, however, the clusters of rods were attached, as mentioned previously.

**Surface Pressure Distributions.** Detailed pressure measurements were taken by a 48-port scanivalve at the Re-number of 110,000. Three different reduced frequencies of Ω=0, 1.59, 3.18 were applied. These reduced frequencies correspond to the rod

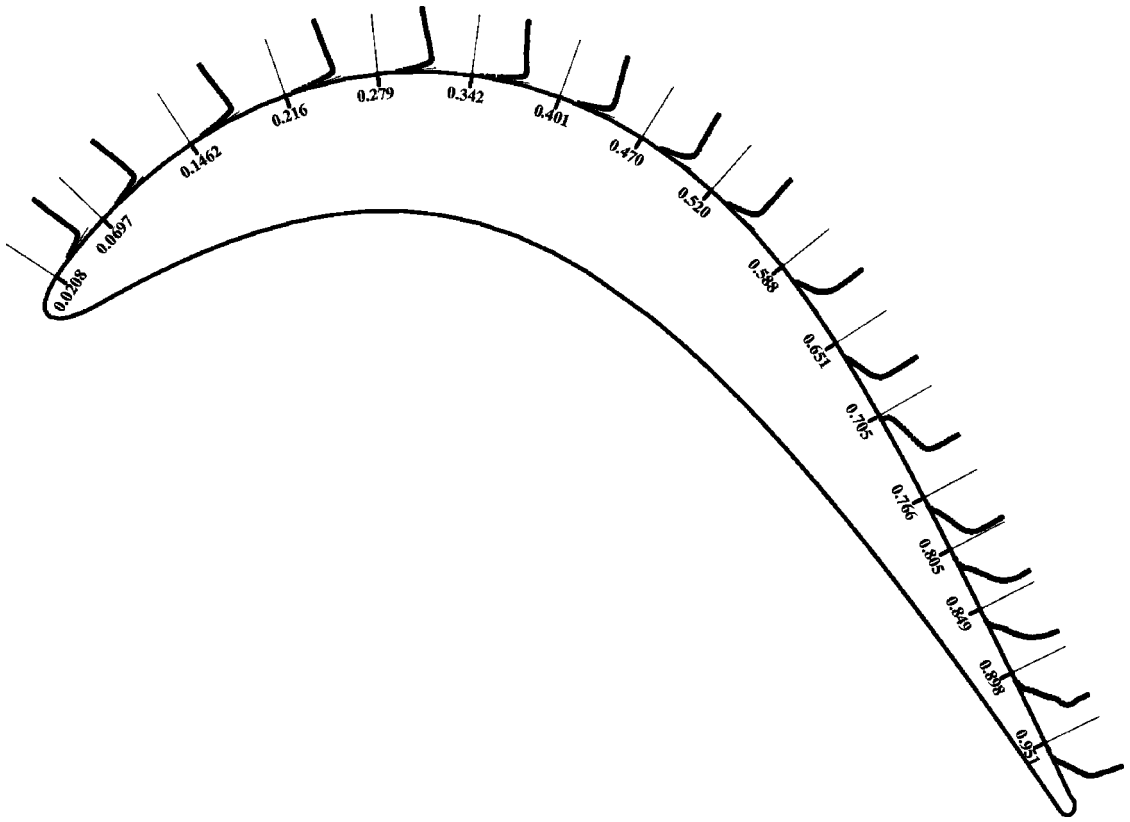


**Fig. 4 Time-averaged velocity profiles along the suction surface of the blade at $\Omega=1.59$ ($S_R=160$ mm), Re $=110{,}000$ (the numbers represent local $s/s_0$)**

spacings of $S_R=\infty$, 160 mm, and 80 mm respectively. The pressure distributions in Fig. 3 show the results of one steady and two unsteady cases. The pressure signals inherently signify the time-averaged pressure because of the internal pneumatic damping effect of the connecting pipes to the transducer. The noticeable differences in pressure distributions between steady and unsteady cases, especially on the suction surface, are due to the drag forces caused by moving rods. The drag forces cause a momentum deficiency that leads to a reduction of total and static pressure.

The time-averaged pressure coefficients along the pressure and suction surfaces are plotted in Fig. 3. The suction surface (upper portion), exhibits a strong negative pressure gradient. The flow accelerates at a relatively steep rate and reaches its maximum surface velocity that corresponds to the minimum $C_p=-4.0$ at $s/s_0=0.42$. Passing through the minimum pressure, the fluid particles within the boundary layer encounter a positive pressure gradient that causes a sharp deceleration to $s/s_0=0.55$ to be reached. This point signifies the beginning of the laminar boundary layer separation and the onset of a separation bubble. As seen in the subsequent boundary layer discussion, the separation bubble characterized by a constant $C_p$-plateau extends up to $s/s_0=0.746$, thus occupying more than 19% of the suction surface and constituting a massive separation. Passing the plateau, the flow first experiences a second sharp deceleration indicative of a process of reattachment followed by a further deceleration at a moderate rate. On the pressure surface, the flow accelerates at a very slow rate, reaches a minimum pressure coefficient at $s/s_0=0.42$ and continues to accelerate until the trailing edge has been reached. Unlike the suction surface, the pressure surface boundary layer does not encounter any adverse positive pressure gradient that triggers separation. However, close to the leading edge, a small plateau extending from $s/s_0=0.08$ to 0.16 indicates the existence of a small size separation bubble that might be attributed to a minor inlet flow incident angle.

Considering the unsteady case with the reduced frequency $\Omega=1.59$ corresponding to a rod spacing of $S_R=160$ mm, Fig. 3 exhibits a slight difference in the pressure distribution between the steady and unsteady cases. As mentioned above, this deviation is attributed to the momentum deficiency that leads to a reduction of the total and static pressure. Increasing the reduced frequency to $\Omega=3.18$ by reducing the rod spacing to $S_R=80$ mm causes a slight shift of the $C_p$-distribution compared with the $\Omega=1.59$ case. One should bear in mind that pneumatically measured surface pressure distribution represents a time integral of the pressure events only. Detailed information regarding the structure of the separation bubble is delivered by means of a detailed unsteady boundary layer or surface pressure measurement by fast response probes, as will be discussed in the subsequent sections.

**Time Averaged Velocity Distributions.** Consistent with the surface pressure distribution which is discussed above, the effect of the wake frequency on the time-averaged velocity profiles and turbulence intensity distribution is presented for the corresponding rod spacings of $S_R=80$ mm, and 160 mm at different longitudinal locations in Figs. 4–7. In the upstream region of the separation bubble, the flow is attached. Upstream of the separation bubble at $s/s_0=0.52$ and also at its immediate proximity $s/s_0=0.588$, the velocity distributions inside the boundary layer experience a slight decrease with increasing the reduced frequency. Inside the separation bubble at $s/s_0=0.705$, a substantial influence of the wake frequency is observed. The higher wake frequency introduces a fluctuation kinetic energy into the boundary layer trying to reverse the separation tendency. As can be seen from the velocity distribution profiles, the onset and the length of the separation bubble are not changed. However, there is a slight change of the bubble height. This shows that the flow does not have the capability to suppress the separation bubble. It only reduces the separation bubble height. In the downstream of the separation bubble, where the flow is fully reattached, $s/s_0=0.951$, the impact of the wake on

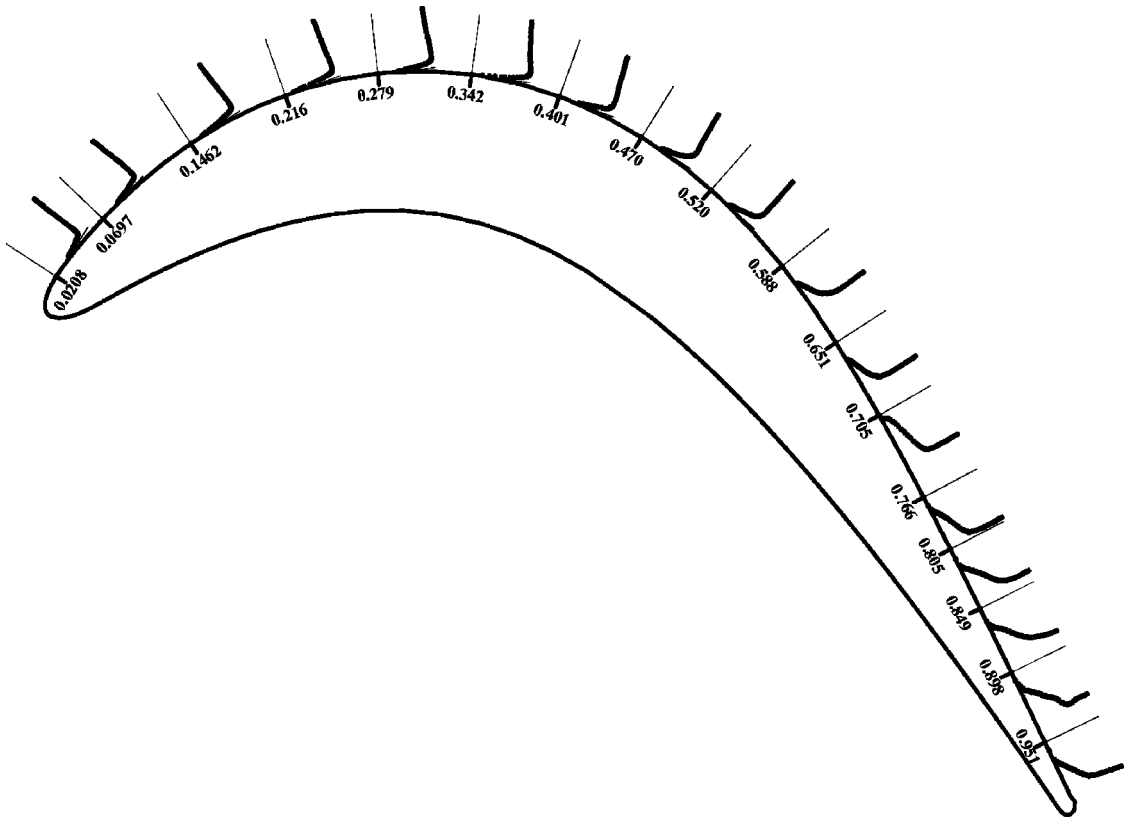


**Fig. 5 Time-averaged velocity profiles along the suction surface of the blade at $\Omega=3.18$ ($S_R=80$ mm), Re $=110{,}000$ (the numbers represent local $s/s_0$)**

the boundary layer is reduced. This effect is clearly shown in the velocity distribution at $s/s_0=0.951$. According to the previous investigations by Schobeiri et al. [10] on a HP-turbine cascade, an increased wake frequency causes turbulence fluctuations to rise inside and outside the boundary layer. However, in the LPT case with the boundary layer separation once the boundary layer is reattached and the velocity distribution assumes a fully turbulent profile, no major changes are observed neither in the velocity nor in the turbulence intensity distribution.

**Change of Separation Bubble Under Unsteady Wake Flow.** The shape of the bubble configuration can be identified from the time-averaged velocity distributions. The dividing streamline and the line of the inflection points are found by taking the second derivative of the velocity profiles and equating them to zero. A similar bubble formation is found for three different frequencies as shown in Fig. 8. The separation points, where the separation starts and ends, remain the same for the three different frequencies. The separation bubble height decreases with the increase of the reduced frequency. The separation bubble is exposed to a wake external flow being under the influence of relatively a lower turbulence followed by a periodic sequence of the wake impingements. When the wake passes over the blade introducing a high turbulence kinetic energy into the boundary layer, the boundary layer is energized causing the separation bubble to be partially reduced. Thus, this flow does not have the capability to completely suppress the separation bubble. The main parameters describing the separation bubble for the three test frequencies are the starting point of the separation bubble $s_s$, the location of the maximum separation bubble height $s_{md}$, reattachment of the separation bubble $s_r$, and the maximum separation bubble height $h_m$. These parameters are shown in dimensionless form in Table 2.

**Behavior of Separation Bubble Under Wake Flow.** The effect of the periodic unsteady wakes on the onset and extent of the separation bubble is shown in Figs. 9 and 10 for two different frequencies, namely $\Omega=1.59$ and $\Omega=3.18$. These figures display the full extent of the separation bubble and its behavior under a periodic wake flow impingement at different $t/\tau$. The wake propagation for $\Omega=1.59$ and $\Omega=3.18$ is analyzed, and the value of $t/\tau$ corresponds to the point in the cycle at which the data acquisition system is triggered. During a rod passing period, the wake flow and the separation bubble undergo a sequence of flow states which are not noticeably different when the unsteady data are time-averaged. To compare the temporal changes of the spatial position of the separation bubble, the time-averaged separation bubble is marked red. Starting with a reduced frequency of $\Omega=1.59$ at $t/\tau=0.25$, the separation bubble is under a full influence of the wake. The wake passing over the blade introduces a high turbulence kinetic energy into the boundary layer. The energized boundary layer bubble is partially reduced or disappeared compared to the time-averaged separation bubble size shown red in Fig. 9(*a*). As the wake passes, $t/\tau=0.50$, the height of the separation bubble reaches its maximum size at $s/s_0=0.705$. The contraction starts again that reduces the size of the separation bubble at $t/\tau=0.75$. At $s/s_0=0.705$ the core region has slightly moved towards to the leading edge. At $t/\tau=1$, the full effect of the wake on the boundary layer can be seen before another wake appears and the bubble moves back to the original position. Once the wake starts to penetrate into the separation bubble, the turbulent spot produced in the wake paths causes a total suppression at some streamwise positions. Similar results are observed when operating at a reduced frequency of $\Omega=3.18$. The wake frequency exerts no influence on the position of the separation bubble. However, doubling the reduced frequency is associated with the higher turbulence intensity that leads to stronger suppression of the separation bubble as shown in Fig. 10.

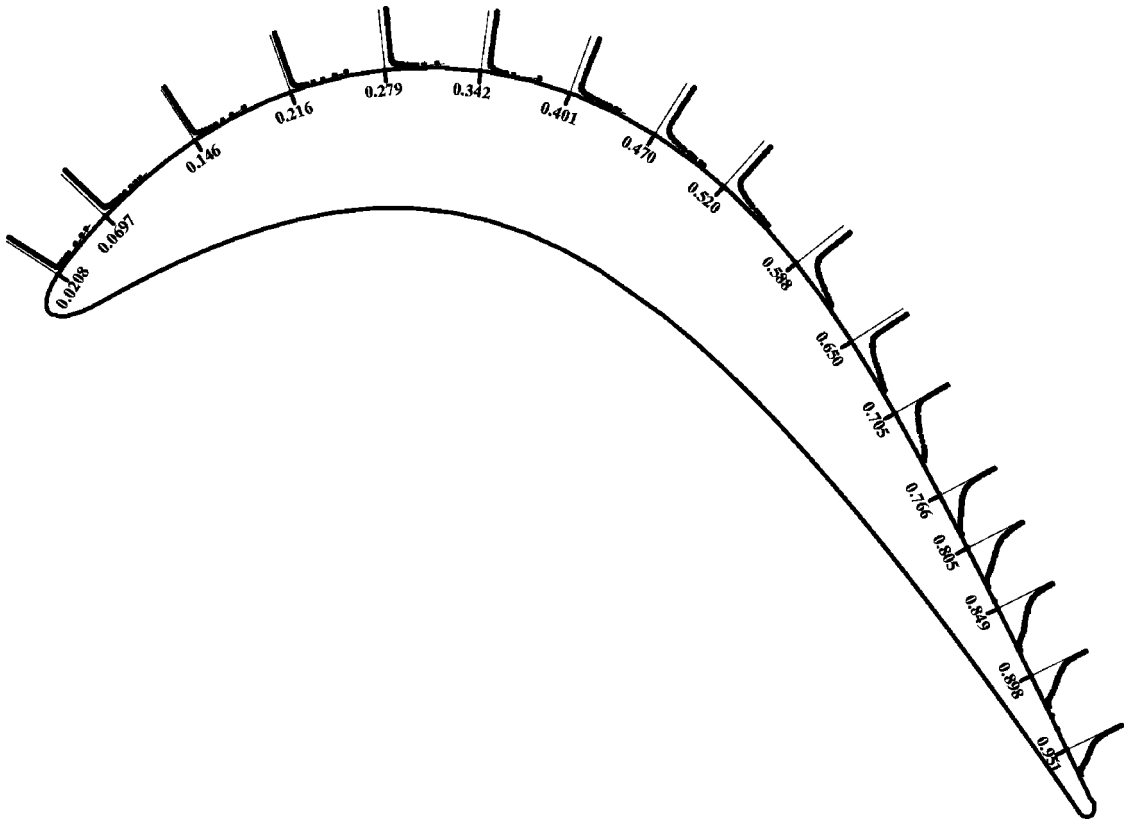


**Fig. 6 Time-averaged turbulent intensity profiles along the suction surface of the blade at $\Omega=1.59$ ($S_R=160$ mm), Re=110,000 (the numbers represent local $s/s_0$)**

**Ensemble-Averaged Fluctuation RMS Velocity Distribution.** The temporal-spatial contours of the ensemble-averaged fluctuation rms velocity at three different lateral positions for two reduced frequencies are presented in Fig. 11. As shown in Fig. 11, the wakes periodically disturb the boundary layer with the high turbulence intensity cores. As is seen in Fig. 11(*a*), three wake passes are visible for $\Omega=1.59$ at a normal distance from the wall of $y=1.065$ mm. At $s/s_0=0.52$, the visibility of the wake vanishes due to the separation bubble. As explained earlier, the separation bubble starts at $s/s_0=0.5$ and extends up to $s/s_0=0.746$, thus occupying more than 24% of the suction surface and forming a massive separation. It perfectly matches the results obtained from the static pressure measurements (Fig. 3). At $s/s_0=0.746$, the fluctuation rms velocity field in Fig. 11(*a*) shows the stagnant fluid region and the area of the rms maximum, which indicates the development of a transition and reattachment. Increasing $\Omega$ to 3.18 causes an earlier mixing of the impinging wakes, which leads to a complete degeneration of the deterministic periodic flow into a stochastic turbulent flow. As can be seen from Fig. 11(*b*), increasing the reduced frequency has not brought any major changes, regarding the structure of the separation bubble.

**Boundary Layer Time-Averaged Integral Quantities.** The time-averaged distribution of the boundary layer thickness, displacement thickness, momentum thickness and the shape factor for the suction surface are shown in Fig. 12. The momentum thickness value for three different reduced frequencies remains the same along the blade and does not demonstrate any unusual behavior within the separation bubble between the separation start point $s_s$ and the reattachment $s_r$ as shown in Fig. 12(*c*). The initial growth of the boundary layer displacement thickness and the shape factor is comparatively small up to the maximum displacement location. As is seen from the Figs. 12(*b*) and 12(*d*), both the boundary layer displacement thickness and the shape factor were decreased in the separation bubble and after the reattachment, as the reduced wake frequency was increased. These results clearly show the impact of the unsteady wake flow on the boundary layer parameters and hence on the profile loss coefficient and efficiency. The unsteady wake flow causes a reduction of the losses due to the suppressed or reduced separation bubble.

**Boundary Layer Ensemble Averaged Integral Quantities.** The integral parameters, such as the momentum thickness and shape factor, are of particular interest to a turbine designer, since they provide an accurate first estimation of the quality of the designed blade. The ensemble-averaged distributions of the momentum thickness and shape factor for the suction surface are shown in Figs. 13(*a*)–13(*d*) for $\Omega=1.59$ and $\Omega=3.18$ values discussed earlier. The momentum thickness values are nondimensionalized with respect to the value corresponding to the steady case with $\Omega=0$. The period $\tau$ represents the wake-passing period that is specific to the individual wake generating cluster, which is characterized by the $\Omega$—value under investigation. The periodic behavior of the ensemble-averaged momentum thickness over the entire suction surface as a result of the embedded periodic wake flow is clearly visible from Fig. 13. It represents the momentum thickness behavior at different $s/s_0$ locations upstream, within and outside the separation bubble. The relative momentum thickness distribution upstream of the separation bubble in Fig. 13(*a*) integrally exhibits a slight increase, whereas inside the zone shown in Fig. 13(*a*), a substantial decrease is apparent. At the immediate vicinity of the separation bubble trailing edge, $s/s_0=0.705$ close to reattachment, Fig. 13(*b*), the momentum thickness experiences a noticeable increase, which by convecting downstream decreases again and approaches the integral values that are close to the steady state case.

The ensemble averaged relative shape factor $H_{12}$-distributions on the suction surface at the same streamwise locations are plotted

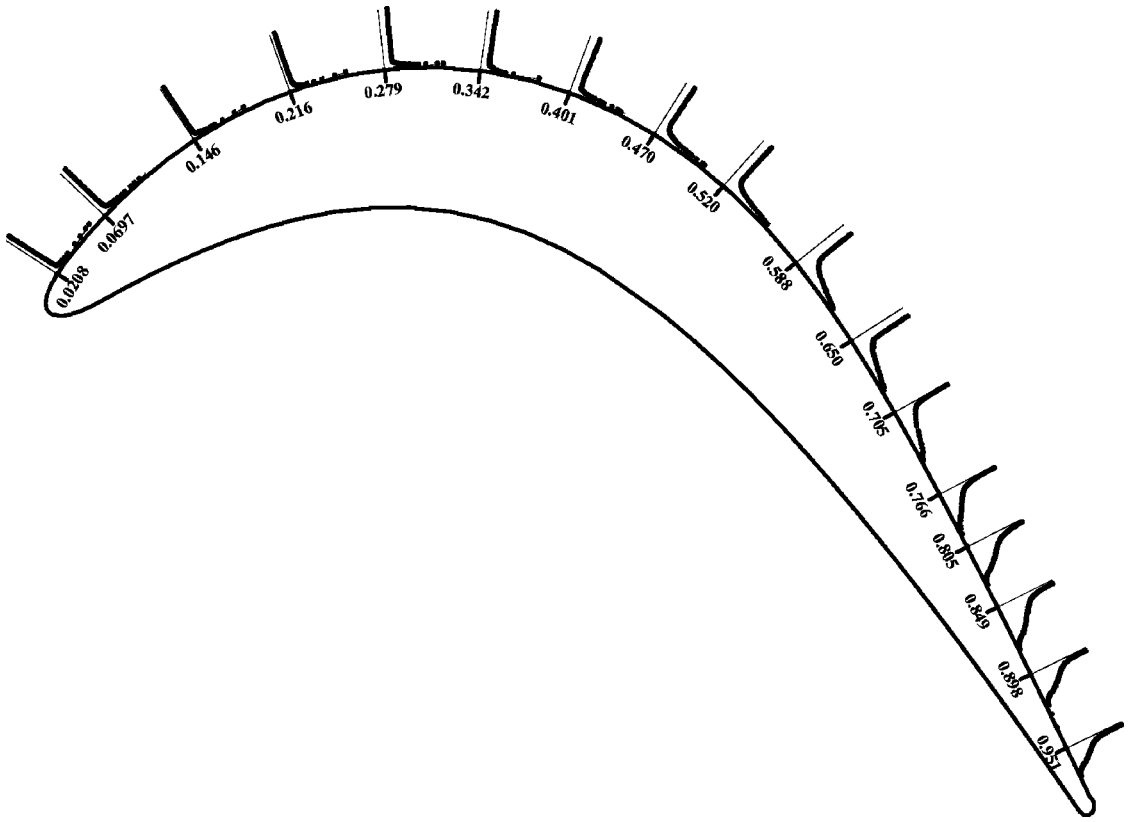


**Fig. 7 Time-averaged turbulent intensity profiles along the suction surface of the blade at $\Omega=3.18$ ($S_R=80$ mm), Re=110,000 (the numbers represent local $s/s_0$)**

in Figs. 14(*a*)–14(*d*). Upstream of the separation bubble, Fig. 14(*a*) they experience a similar periodic change with an average slightly close to the steady case. Moving into the separation bubble, Fig. 14(*b*), each streamwise location presents its own shape factor that is specific to the velocity distribution we discussed. Similar results are observed when operating at a reduced frequency of $\Omega=3.18$ which is shown in Figs. 13, and 14(*c*) and 14(*d*).

The ensemble averaged integral parameters discussed above are essential to calculate the ensemble averaged and time averaged profile loss coefficients at each streamwise position. Furthermore, the integration of the time averaged loss coefficient distribution over the entire blade surface provides the global profile loss coefficient. A simple procedure given in Ref. [26] describes how the loss coefficient can be calculated using the integral parameters.

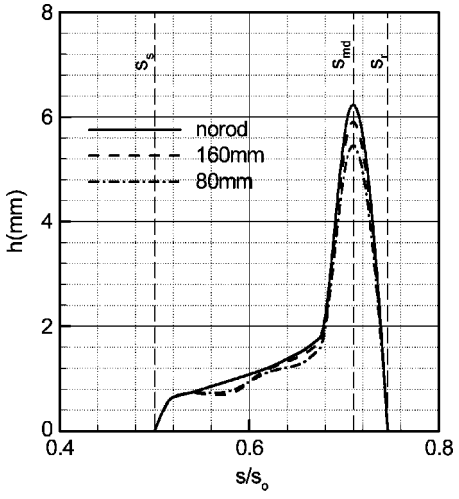


**Fig. 8 Change of separation bubble height under the influence of different reduced frequencies of $\Omega=0$, 1.59, 3.18 ($S_R=\infty$, $S_R=160$ mm, 80 mm)**

## Conclusions

A detailed experimental study on the behavior of the separation bubble on the suction surface of a highly loaded LPT blade under periodic unsteady wake flow was investigated. The measurements were carried out utilizing a custom designed hot-wire probe. One steady and two different unsteady inlet wake flow conditions with the corresponding passing frequencies, the wake velocity and the turbulence intensities, were investigated by utilizing a large-scale, subsonic research facility. Translational motion of the timing belt created the unsteady wake flow. It is found that the turbulent spots generated by the unsteady wake flow were effective in suppressing or reducing the size of the separation bubble. The results of the unsteady boundary layer measurements were presented in the ensemble-averaged and contour plot forms. Surface pressure measurements were performed at Re=110,000. Slight changes of the pressure distribution occurred, while operating at the unsteady flow conditions. Detailed unsteady boundary layer measurement

**Table 2 Parameters describing separation bubble for three different reduced frequencies**

| Parameters | $\Omega=0.0$ | $\Omega=1.59$ | $\Omega=3.18$ |
|---|---|---|---|
| $s_s/s_0$ | 0.5 | 0.5 | 0.5 |
| $s_{md}/s_0$ | 0.705 | 0.705 | 0.705 |
| $s_r/s_0$ | 0.746 | 0.746 | 0.746 |
| $h_m$ (mm) | 6.123 | 5.818 | 5.358 |

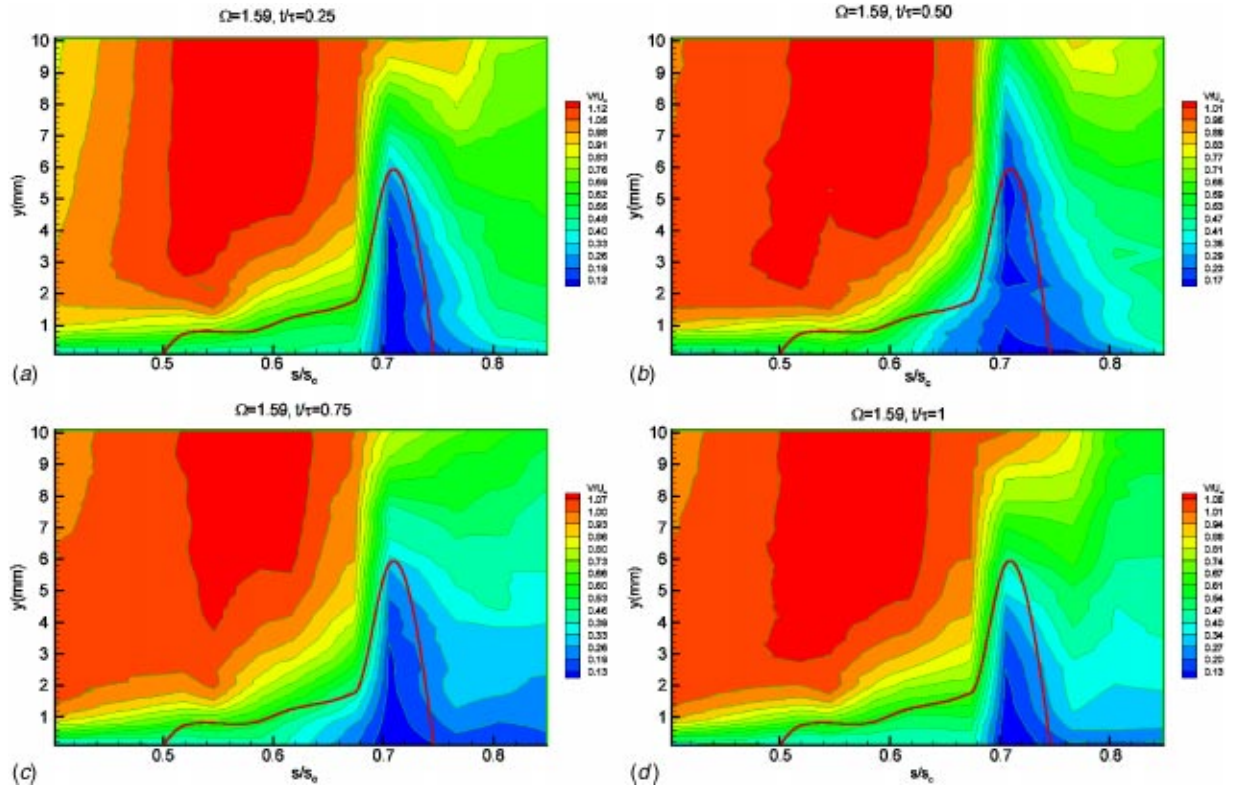


**Fig. 9 Ensemble-averaged velocity contours along the suction surface for different $s/s_0$ with time $t/\tau$ as parameter for $\Omega=1.59$ ($S_R=160$ mm), Re=110,000 (time-averaged separation bubble for $\Omega=1.59$ marked red)**

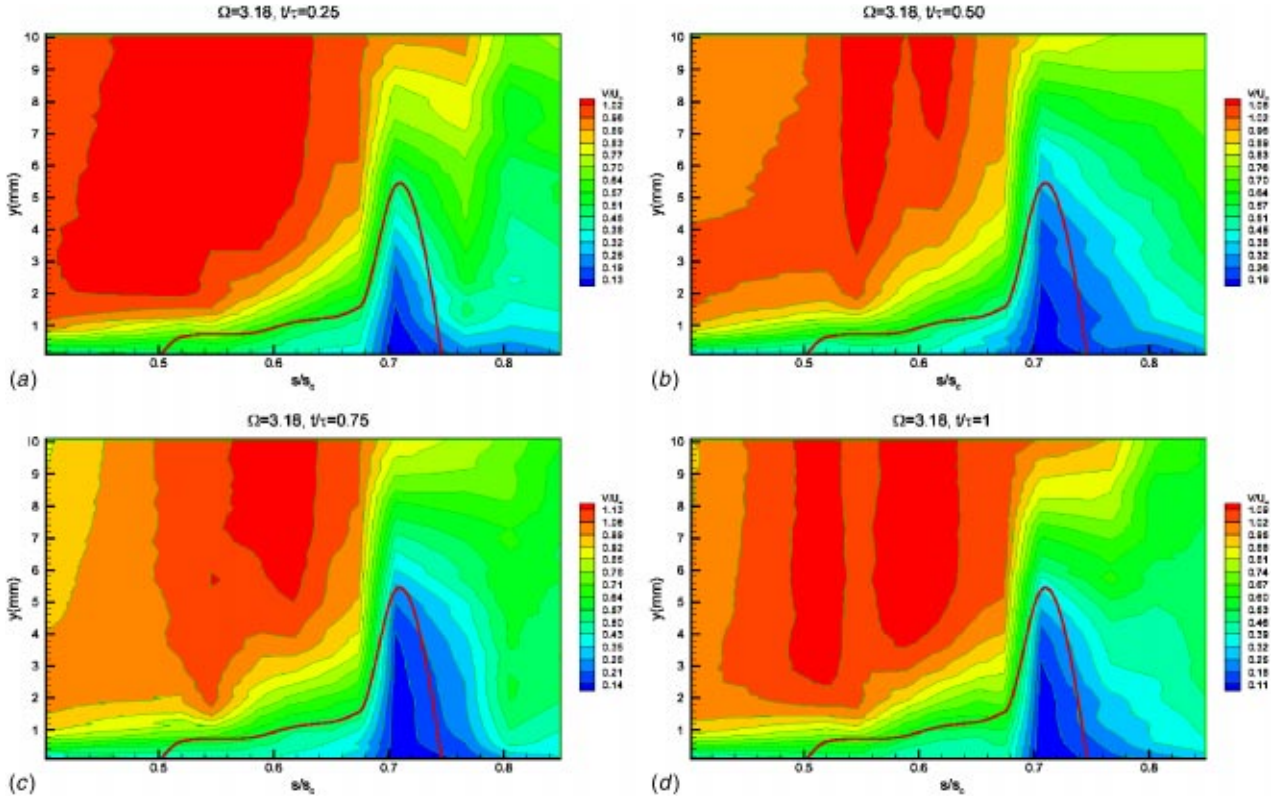


**Fig. 10 Ensemble-averaged velocity contours along the suction surface for different $s/s_0$ with time $t/\tau$ as parameter for $\Omega=3.18$ ($S_R=80$ mm), Re=110,000 (time-averaged separation bubble for $\Omega=3.18$ marked red)**

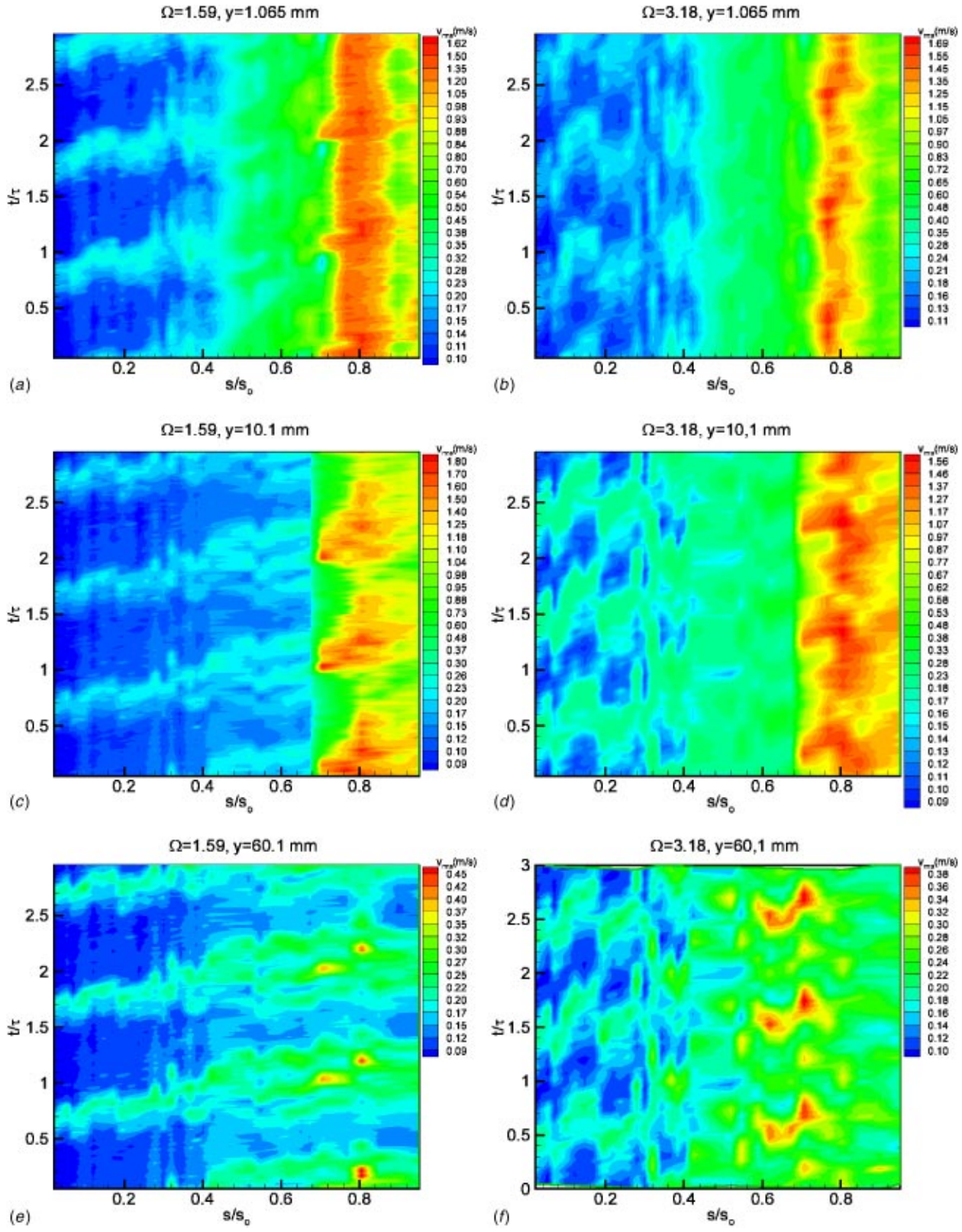


**Fig. 11 Ensemble-averaged rms fluctuation velocity in the temporal-spatial domain at different y positions for Ω=1.59 ($S_R$=160 mm), and Ω=3.18 ($S_R$=80 mm)**

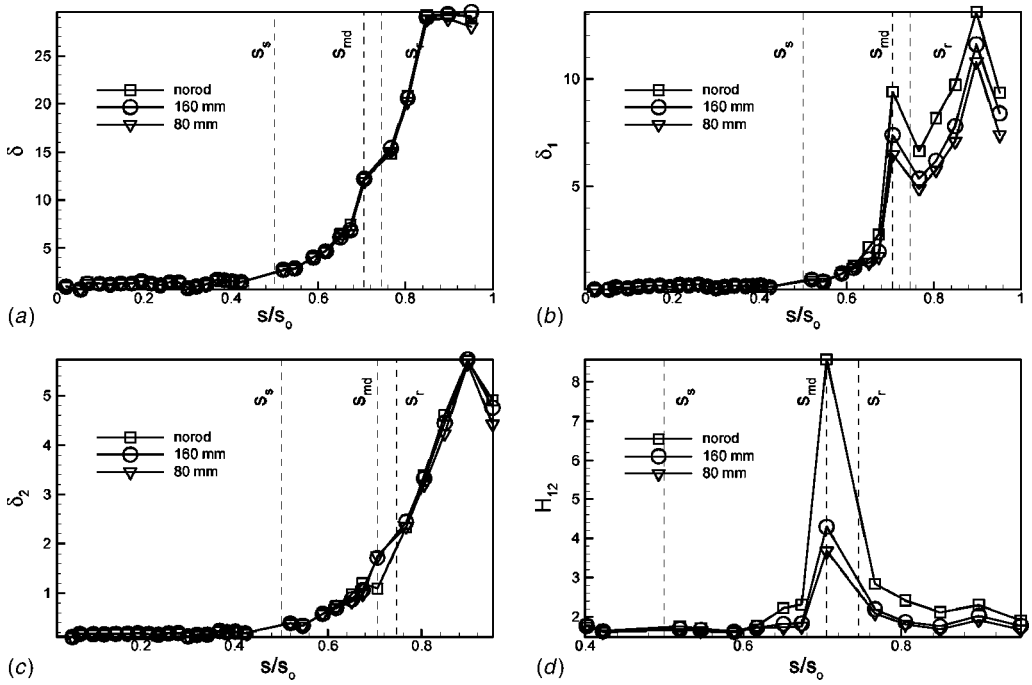


**Fig. 12 Time averaged (*a*) boundary layer thickness, (*b*) displacement thickness, (*c*) momentum deficiency thickness and (*d*) shape factor for three different reduced frequency of $\Omega$=0, 1.59, 3.18 ($S_R=\infty$, $S_R$=160 mm, 80 mm), Re=110,000, $s_s$=starting point of separation zone, $s_{md}$=location of maximum separation bubble height**

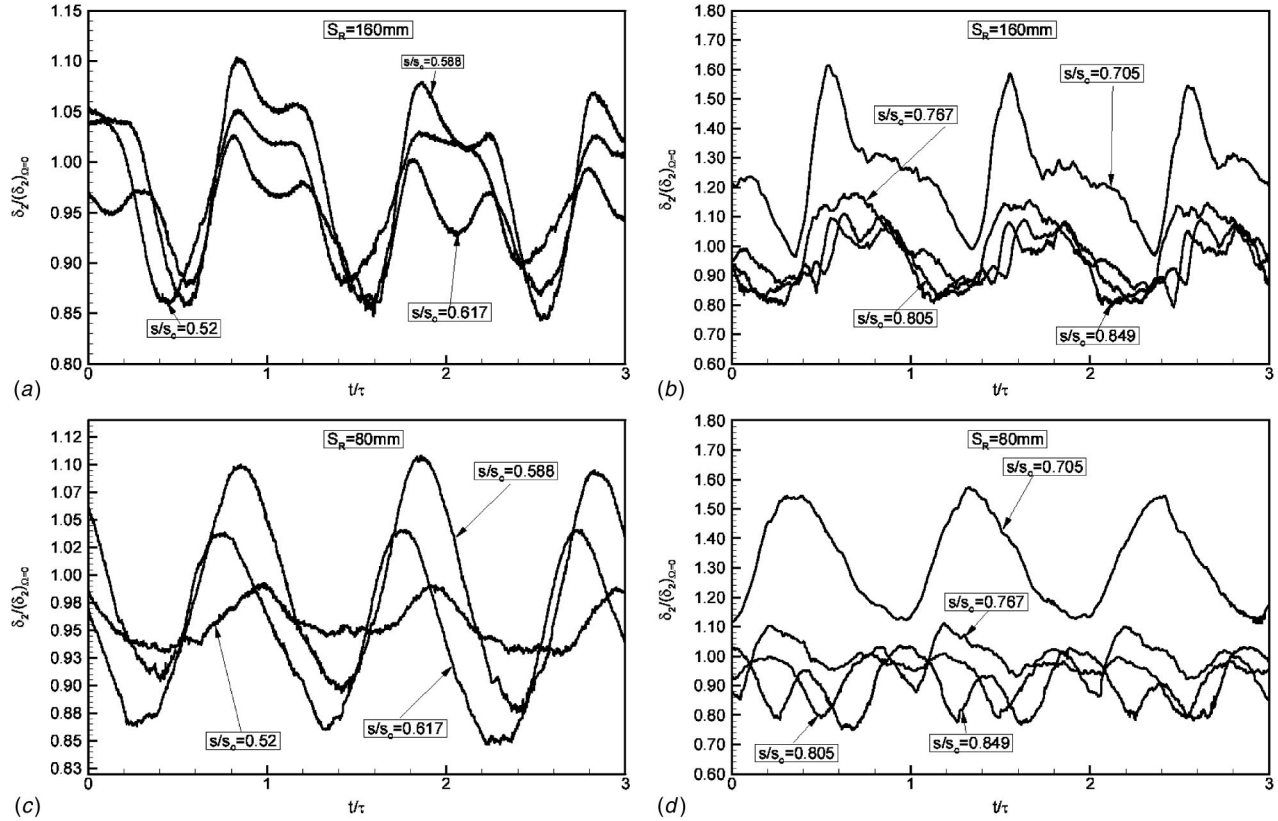


**Fig. 13 Ensemble-averaged relative momentum thickness distribution along the suction surface for different streamwise positions for (*a*) and (*b*) at $\Omega$=1.59 ($S_R$=160 mm), (*c*) and (*d*) at $\Omega$=3.18 ($S_R$=80 mm)**

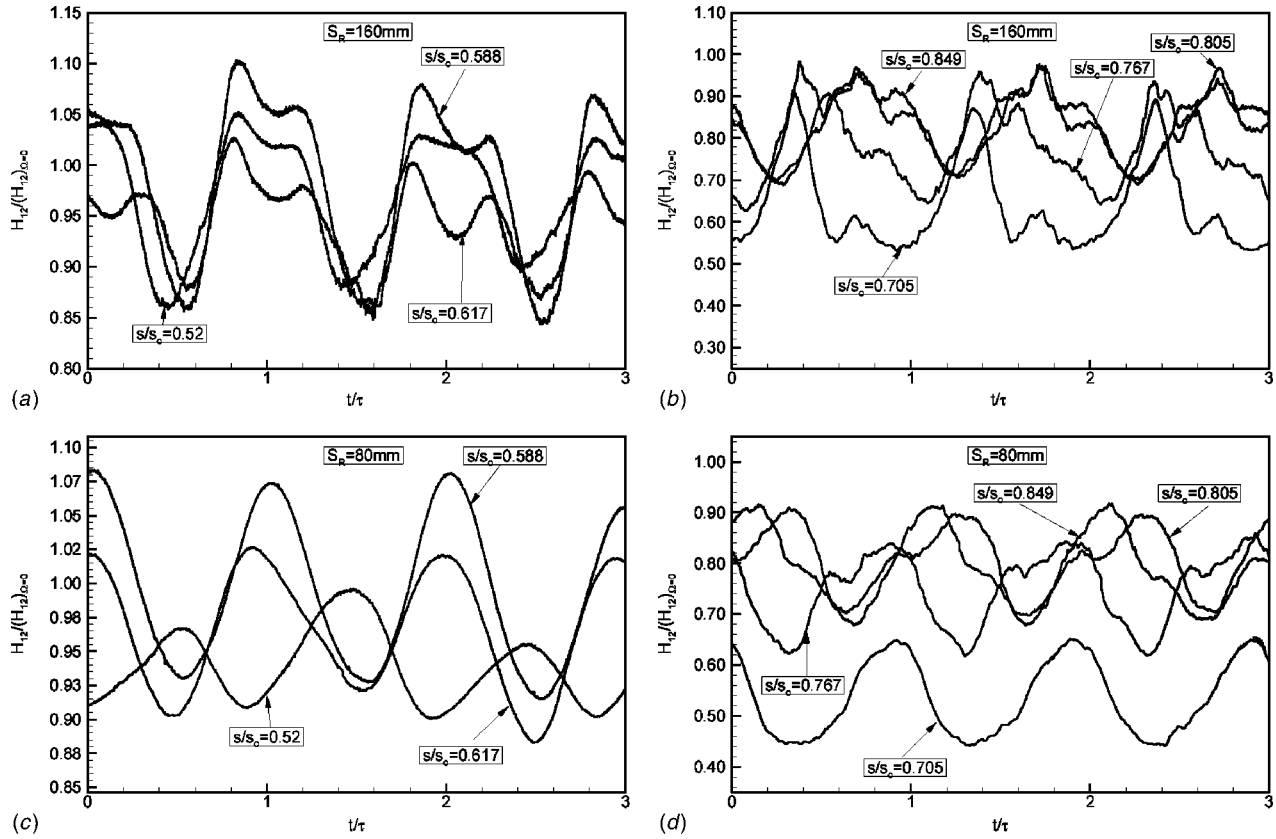


**Fig. 14 Ensemble-averaged relative shape factor distribution along the suction surface for different streamwise positions for (*a*) and (*b*) at Ω=1.59 ($S_R$=160 mm), (*c*) and (*d*) at Ω=3.18 ($S_R$=80 mm)**

identified the onset and extension of the separation bubble as well as its behavior under the unsteady wake flow. Passing the wake flow with its highly turbulent vortical core over the separation region caused a periodic contraction and expansion of the separation bubble and a reduction of the separation bubble height. Increasing the passing frequency associated with higher turbulence intensity further reduced the separation bubble height. The time averaged integral quantities showed the impact of the unsteady wake flow on the boundary layer parameters and, hence, on the profile loss coefficient and efficiency. Unsteady wake flow caused a reduction of the losses due to the suppressed or reduced separation boundary layer.

Future processing of the data, including different Reynolds numbers, different free-stream turbulence intensity level with different reduced frequencies will provide further insight into the nature of the separation bubble behavior in these cases.

## Uncertainty Analysis

The Kline and McClintock [29] uncertainty analysis method was used to determine the uncertainty in the velocity after calibration and data reduction for the single-wire probe. In addition, the uncertainty in the heat transfer measurements was also determined. The Kline and McClintock method determines the uncertainty with a 95% confidence level. The uncertainty in the velocity for the single-wire probe after the data reduction is given in Table 3. As shown, the uncertainty in the velocity increases as the flow velocity decreases. This is due to the pneumatic pressure transducer having a large uncertainty during calibration.

**Table 3 Uncertainty in velocity measurement for hot-wire probe**

| $\bar{U}$ (m/s) | 3 | 5 | 12 |
|---|---|---|---|
| $\omega\bar{U}/\bar{U}(\%)_{red}$ | 5.78 | 2.41 | 1.40 |

## Acknowledgments

The first author would like to dedicate this paper to the memory of Leonard Fottner; a dear friend, an outstanding engineer, scientist and educator. The presented study is a part of an ongoing LPT-aerodynamics project executed by the NASA Glenn Research Center. The authors were supported by NASA Cooperative Agreement NCC3-793 monitored by Dr. David Ashpis. The support and the permission for publication is gratefully acknowledged. The authors also gratefully acknowledge Pratt & Whitney for providing the research community with the blade coordinates.

## Nomenclature

- $c$ = blade chord
- $c_{ax}$ = axial chord
- $C_p$ = pressure coefficient, $C_p = P_i - P_s/(P_t - P_s)_{inl}$
- $d_R$ = rod diameter
- $H_{12}$ = shape factor, $H_{12} = \delta_1/\delta_2$
- $h_m$ = maximum separation bubble height
- $L_{SS}$ = suction surface length
- $M$ = number of samples
- $N$ = number of wake cycles
- $p_i$ = static pressure taps i=1, . . . ,48
- $p_s$, $p_t$ = static, total pressure
- $Re_{LSS}$ = Reynolds number based on suction surface length $Re_{LSS} = L_{ss}V_{exit}/\nu$
- $S_B$ = blade spacing
- $S_R$ = rod spacing

$s$ = streamwise distance from the leading edge of the blade
$s_0$ = streamwise distance from the leading edge to the trailing edge of the blade
$s_{md}$ = maximum separation bubble height at a streamwise distance from blade leading edge
$s_r$ = re-attachment point of the separation bubble at a streamwise distance from blade leading edge
$s_s$ = starting point of the separation bubble at a streamwise distance from blade leading edge
$t$ = time
$Tu$ = turbulence intensity
$U$ = belt translational velocity
$V_{ax}$ = axial velocity
$V_{exit}$ = exit velocity
$V$ = velocity
$v$ = fluctuation velocity
$\gamma$ = blade stagger angle
$\delta$ = boundary layer thickness
$\delta_1$ = boundary layer displacement thickness
$\delta_2$ = boundary layer momentum deficiency thickness
$\delta_3$ = boundary layer energy deficiency thickness
$\nu$ = kinematic viscosity
$\sigma$ = cascade solidity, $\sigma = c/S_B$
$\tau$ = one wake-passing period
$\varphi$ = flow coefficient, $\varphi = V_{ax}/U$
$\psi_A$ = Zweifel coefficient $\psi_A = 2\sin^2\alpha_2(\cot\alpha_2 - \cot\alpha_1)s_B/c_{ax}$
$\Omega$ = reduced frequency $\Omega = (c/S_R)U/V_{ax} = (\sigma/\varphi)(S_B/S_R)$

## References


[1] Pfeil, H., and Herbst R., 1979, ''Transition Procedure of Instationary Boundary Layers,'' ASME Paper No. 79_GT_128.
[2] Pfeil, H., Herbst, R., and Schröder, T., 1983, ''Investigation of the Laminar Turbulent Transition of Boundary Layers Disturbed by Wakes,'' ASME J. Eng. Power, **105**, pp. 130–137.
[3] Orth, U., 1993, ''Unsteady Boundary Layer Transition in Flow Periodically Disturbed by Wakes,'' ASME J. Turbomach., **115**, pp. 707–713.
[4] Schobeiri, M. T., and Radke, R. E., 1994, ''Effects of Periodic Unsteady Wake Flow and Pressure Gradient on Boundary Layer Transition Along the Concave Surface of a Curved Plate,'' ASME Paper 94-GT-327, presented at the International Gas Turbine and Aero-Engine Congress and Exposition, The Hague, Netherlands, June 13–16, 1994.
[5] Schobeiri, M. T., Read, K., and Lewalle, J., 2003, ''Effect of Unsteady Wake Passing Frequency on Boundary Layer Transition, Experimental Investigation and Wavelet Analysis,'' ASME J. Fluids Eng., **125**, pp. 251–266.
[6] Wright, L., and Schobeiri, M. T., 1999, ''The Effect of Periodic Unsteady Flow on Boundary Layer and Heat Transfer on a Curved Surface,'' ASME Trans. J. Heat Transfer, **120**, pp. 22–33.
[7] Chakka, P., and Schobeiri, M. T., 1999, ''Modeling of Unsteady Boundary Layer Transition on a Curved Plate Under Periodic Unsteady Flow Condition: Aerodynamic and Heat Transfer Investigations,'' ASME Trans. J. Turbomach., **121**, pp. 88–97.
[8] Liu, X., and Rodi, W., 1991, ''Experiments on Transitional Boundary Layers With Wake-Induced Unsteadiness,'' J. Fluid Mech., **231**, pp. 229–256.
[9] Schobeiri, M. T., Pappu, K., and Wright, L., 1995, ''Experimental Sturdy of the Unsteady Boundary Layer Behavior on a Turbine Cascade,'' ASME 95-GT-435, presented at the International Gas Turbine and Aero-Engine Congress and Exposition, Houston, Texas, June 5–8, 1995.
[10] Schobeiri, M. T., John, J., and Pappu, K., 1997, ''Experimental Study on the Effect of Unsteadiness on Boundary Layer Development on a Linear Turbine Cascade,'' J. Exp. Fluids, **23**, pp. 303–316.
[11] Schobeiri, M. T., and Wright, L., 2003, ''Advances in Unsteady Boundary Layer Transition Research,'' Int. J. Rotating Mach., **9**(1), pp. 1–22.
[12] Schobeiri, M. T., and Chakka, P., 2002, ''Prediction of Turbine Blade Heat Transfer and Aerodynamics Using Unsteady Boundary Layer Transition Model,'' Int. J. Heat Mass Transfer, **45**, pp. 815–829.
[13] Brunner, S., Fottner, L., and Schiffer, H.-P., 2000, ''Comparison of Two Highly Loaded Turbine Cascade Under the Influence of Wake-Induced Transition,'' ASME 2000-GT-268, presented at the International Gas Turbine and Aero-Engine Congress and Exposition, Munich, Germany, May 8–11, 2000.
[14] Cardamone, P., Stadtmüller P., Fottner, L., and Schiffer, H.-P., 2000, ''Numerical Investigation of the Wake-Boundary Layer Interaction on a Highly Loaded LP Turbine Cascade Blade,'' ASME 2002-GT-30367, presented at the International Gas Turbine and Aero-Engine Congress and Exposition, Amsterdam, Netherlands, June 3–6, 2002.
[15] Schulte, V., and Hodson, H. P., 1996, ''Unsteady Wake-Induced Boundary Layer Transition in High Lift LP Turbines,'' ASME Paper No. 96-GT-486.
[16] Kaszeta, R., Simon T. W., and Ashpis, D. E., 2001, ''Experimental Investigation of Transition to Turbulence as Affected by Passing Wakes,'' ASME Paper 2001-GT-0195.
[17] Lou, W., and Hourmouziadis, J., 2000, ''Separation Bubbles Under Steady and Periodic Unsteady Main Flow Conditions,'' ASME Paper 200-GT-270.
[18] Volino, R. J., and Hultgren, L. S., 2001, ''Measurements in Separated and Transitional Boundary Layers Under Low-Pressure Turbine Airfoil Conditions,'' ASME J. Turbomach., **123**, pp. 189–197.
[19] Schröder, Th., 1989, ''Measurements With Hot-Film Probes and Surface Mounted Hot Film Gages in a Multi-Stage Low Pressure Turbine,'' European Propulsion Forum, Bath, UK.
[20] Haueisen V., Hennecke D. K., and Schröder, T., 1997, ''Measurements With Surface Mounted Hot Film Sensors on Boundary Layer Transition in Wake Disturbed Flow,'' AGARD-CP-598.
[21] Shyne, R. J., Sohn, K. H., and De Witt, K. J., 2000, ''Experimental Investigation of Boundary Layer Behavior in a Simulated Low Pressure Turbine,'' ASME J. Fluids Eng., **122**, pp. 84–89.
[22] Treuren, K. W. V., Simon, T., Koller, M. V., Byerley, A. R., Baughn, J. W., and Rivir, R., 2002, ''Measurements in a Turbine Cascade Flow Under Ultra Low Reynolds Number Conditions,'' ASME J. Turbomach., **124**, pp. 100–106.
[23] Halstead, D. E., Wisler, D. C., Okiishi, T. H., Walker, G. J., Hodson, H. P., and Shin, H.-W., 1997, ''Boundary Layer Development in Axial Compressors and Turbines: Part 3 of 4,'' ASME J. Turbomach., **119**, pp. 225–237.
[24] Schobeiri, M. T., and Oztürk, B., 2003, ''On the Physics of the Flow Separation Along a Low Pressure Turbine Blade Under Unsteady Flow Conditions,'' ASME 2003-GT-38917, presented at International Gas Turbine and Aero-Engine Congress and Exposition, Atlanta, Georgia, June 16–19, 2003.
[25] Schobeiri, M. T., John, J., and Pappu, K., 1996, ''Development of Two-Dimensional Wakes Within Curved Channels, Theoretical Framework and Experimental Investigation,'' ASME Trans. J. Turbomach., **118**, pp. 506–518.
[26] Schobeiri, M. T., 2001, ''Experimental Determination of LPT-Profile Losses at Low Reynolds Numbers,'' Progress Report No 12, October 25, 2001, NASA GRC, Project Monitor: Dr. D. Ashpis.
[27] Hourmouziadis, J., 1989, ''Blading Design for Axial Turbomachines,'' AGARD, Lecture Series LS-167.
[28] Eifler, J., 1975, ''Zur Frage der freien turbulenten Strömungen, insbesondere hinter ruhenden und bewegten Zylindern,'' Dissertation D-17, Technische Hochschule Darmstadt, Germany.
[29] Kline, S. J., and McKlintock, F. A., 1953, ''Describing Uncertainties in Single-Sample Experiments,'' Mech. Eng. (Am. Soc. Mech. Eng.), **75**, pp. 3–8.

Journal of Turbomachinery

Technical Brief

# Flow Through a Repeating Stage in an Axial Compressor: A Reconsideration

**J. H. Horlock**
Whittle Laboratory, Cambridge University, Madingley Road, Cambridge CB3 0DY, UK

*A simple thermo-fluid-dynamic analysis is presented for the ultimate steady flow in a repeating stage of an axial-flow compressor.*
[DOI: 10.1115/1.1791282]

## 1 Introduction

Many papers in the literature have been devoted to study of the ''boundary layers'' on the annulus walls of axial flow turbomachines. But it is now generally agreed that conventional boundary layer theory is inappropriate for describing these flows, as they are three dimensional, often with areas of separation, and full CFD calculations of the whole flow are generally required. However the concept of the ''ultimate steady flow'' (USF) in a repeating stage, first described by Howell [1] and later by Smith [2]—that through an ''embedded'' stage in a multi-stage compressor or turbine where the flow changes little between entry and exit—has proved useful and enlightening.

Smith reported on the testing of a twelve-stage General Electric research compressor with high-aspect-ratio blading as follows:

> ''The flow does not actually deteriorate, but remains reasonably well behaved. Of course the flow details may be quite complex, particularly near the walls. Evidence that losses are larger near the walls than at mid-passage is given . . . . The excess total temperature near the blade ends is seen to increase as the flow proceeds through the compressor: the fluid near the walls is the receptacle of the energy dissipated by these losses.''

In a recent paper [3], Horlock and Denton reported CFD calculations of the flow through a Rolls Royce research compressor, and these were compared with experimental measurements obtained by Howard et al. [4] at Cranfield University. It was indeed shown that the axial velocity and stagnation pressure profiles repeated quite well from stage to stage, after the first. Further the work input per unit radius repeated, its magnitude increasing towards the walls, and Smith's observation that the difference between the stagnation temperature near the walls and that at midspan increased continually through the machine was partly confirmed.

In this Technical Brief, an attempt is made to present simply and analytically the thermo-fluid-dynamic implications of this phenomenon.

Contributed by the Turbomachinery Division of THE AMERICAN SOCIETY OF MECHANICAL ENGINEERS for publication in the JOURNAL OF TURBOMACHINERY. Manuscript received and accepted by the ASME Turbomachinery Division, May 6, 2004. Associate Editor: D. C. Wisler.

## 2 The Smith Theorem

The argument starts from a ''theorem'' originally stated by Smith [2]:

''As the flow passes through one (USF) stage all streamlines will experience the same increase in static pressure; this must be so because the same radial and circumferential distribution of velocities exist and hence radial and circumferential pressure gradients must be the same according to the momentum equation. Furthermore all streamlines experience the same increase in total pressure, which is the same as the static pressure because the dynamic pressure is the same at stage inlet and outlet from each streamline.''

## 3 Analysis

A statement of the Second Law in terms of radial gradients of stagnation enthalpy $H$, stagnation pressure $P$, stagnation temperature $T$ and entropy $s$ is

$$\frac{dH}{dr} - T\frac{ds}{dr} = \frac{1}{\rho}\frac{dP}{dr}. \tag{1}$$

We shall consider flow of a perfect gas (of constant specific heat $c_p$) at low Mach number through the repeating stage of a compressor; the flow then approaches one of constant density $\rho$, so that $P$ may be written as

$$P = p + 1/2\rho c^2, \tag{2}$$

where $c$ is the velocity. From Smith's theorem, the complete velocity distribution repeats from entry (station 1) to exit (station 3) of the stage under study. Thus for the component velocities in the $x$ (axial), $u$ (tangential) and $r$ (radial) directions: $c_{x1}[r] = c_{x3}[r]$; $c_{u1}[r] = c_{u3}[r]$; $c_{r1}[r] = c_{r3}[r]$; the flow angles also repeat. [Note however that the velocity profiles change from stator exit to rotor exit (state 2), i.e. $c_{x1}[r] \neq c_{x2}[r]$.] It follows then from the radial equation of motion that the static pressure gradient $\partial p_1/\partial r$ at stage entry is equal to $\partial p_3/\partial r$ at stage exit (but *not* equal to $\partial p_2/\partial r$ at the rotor exit).

Since both static pressure $p$ and kinetic energy $c^2/2$ repeat, the stagnation pressure $P$ must also repeat, i.e.,

$$\partial P_3/\partial r = \partial P_1/\partial r, \tag{3}$$

and

$$\partial(P_3 - P_1)/\partial r = \partial(\Delta P)/\partial r = 0. \tag{4}$$

Thus the stagnation pressure rise, $\Delta P = (P_3 - P_1)$, is constant through the end-wall region and equal to $\Delta P$ in the mainstream. $\Delta P$ is also equal to the (constant) static pressure rise $\Delta p$. But note again that $\partial P_2/\partial r \neq \partial P_1/\partial r$.

If it is now assumed that the flow is in radial equilibrium with $c_r = 0$, the partial differentials become full differentials. This assumption will be valid near the annulus walls in a stage with long blades, and indeed approximately true across the whole stream for a compressor of high hub-tip ratio.

  

As previously argued, the work transfer per unit mass flow, $\Delta w = \Delta H = c_p \Delta T$, repeats from stage to stage, since the velocity triangles will be the same in each stage. It then follows from Eqs. (1) and (3) that

$$\frac{d(\Delta w)}{dr} = \frac{dH_3}{dr} - \frac{dH_1}{dr} = \frac{d(\Delta H)}{dr} = T_3 \frac{ds_3}{dr} - T_1 \frac{ds_1}{dr} \approx \frac{dL}{dr}, \quad (5)$$

where $L \approx T_m \Delta s$ is the "loss" or "lost work," in which $T_m$ is a mean temperature. To summarize this discussion of the flow in a repeating stage, following from Smith's theorem:

(i) there are gradients in $H$ and $P$ with $r$;

(ii) there is a gradient in work input $w$ (and therefore in $\Delta H$) with $r$, usually an increase toward the annulus walls;

(iii) there is no gradient in $\Delta P$, the increase of stagnation pressure;

(iv) there is a gradient in "loss" $L \approx T_m \Delta s$, and it is equal to the gradient of the work input, $\Delta H$.

Analytically these results may be written as

$$\frac{d(\Delta H - \Delta P)}{dr} = \frac{d(\Delta H)}{dr} \approx \frac{dL}{dr}. \quad (6)$$

Hence if subscript $_{\mathrm{MS}}$ refers to the mainstream and subscript $_{\mathrm{EW}}$ to a location within the end-wall region, Eq. (6) may be integrated to give

$$\Delta H_{\mathrm{EW}} - \Delta H_{\mathrm{MS}} = L_{\mathrm{EW}} - L_{\mathrm{MS}} = X(r),$$

or

$$\Delta H_{\mathrm{EW}} = \Delta H_{\mathrm{MS}} + X(r), \quad (7)$$

$$L_{\mathrm{EW}} = L_{\mathrm{MS}} + X(r).$$

Thus the "extra" work input $X(r)$ at any radius in the end-wall regions is equal to the "extra" loss there. In the absence of any mixing the stagnation temperature will distort progressively through the compressor within the end-wall region, as will the entropy; both will go on rising. But mixing will spread the increases in these extensive properties into the main stream due to secondary flow and/or turbulent diffusion, as Adkins and Smith [5] and Gallimore and Cumpsty [6], Wisler et al. [7] have explained. Cumpsty [8] has given an excellent account of this phenomenon, together with an illustration of a calculation of the radial redistribution of the losses, without dissipation, in which the total stage loss remained unchanged.

## 4 The Stage Efficiency

Smith expressed the efficiency of the whole repeating stage $[\eta]$ in terms of the mainstream efficiency (or the efficiency of the stage running full, $\eta_{\mathrm{MS}}$), the end-wall displacement thicknesses and blade force deficit thicknesses. He used the fact that the pressure rise (static or stagnation) in the end-wall region was the same as that in the mainstream. Here we initially repeat Smith's approach and then examine it in the light of the analysis derived above.

**4.1 Smith's Analysis.** For simplicity here we assume that near the inner casing (at $r = r_{\mathrm{HUB}}$) there is just one thin end-wall region (of thickness $\delta$), through which the blade speed $U$ changes little. Smith's approach was simply to state the stage efficiency as

$$\eta = \int \rho c_x \Delta P \, dr \Big/ \int \rho c_x \Delta H \, dr$$

$$= \Delta P \int \rho c_x \, dr \Big/ \int F_u U \, dr, \quad (8)$$

where $F_u$ is the local tangential force on the blade, per unit length. The integrals refer to the total flow, but Smith restated them using the flow displacement thickness

$$\delta_x^* = \int_{r_{\mathrm{HUB}}}^{r_{\mathrm{HUB}}+\delta} [1 - (\rho c_x)/(\rho c_x)_{\mathrm{MS}}] dr \quad (9)$$

and the force deficit thickness

$$\upsilon = (1/F_{u\mathrm{MS}}) \int_{r_{\mathrm{HUB}}}^{r_{\mathrm{HUB}}+\delta} (F_{u\mathrm{MS}} - F_u) dr$$

$$\approx (1/F_{u\mathrm{MS}} U) \int_{r_{\mathrm{HUB}}}^{r_{\mathrm{HUB}}+\delta} (F_{u\mathrm{MS}} U - F_u U) dr. \quad (10)$$

It then followed that

$$\eta = [Q \, \Delta P (l - \delta^*)/[F_{u\mathrm{MS}} U [l - \upsilon)], \quad (11)$$

where $l$ is the blade length and $Q$ is the flow for the annulus running full, for which the stage efficiency would be

$$\eta_{\mathrm{MS}} = Q \, \Delta P / F_{u\mathrm{MS}} U l. \quad (12)$$

Thus the stage efficiency of the USF stage is given by

$$\eta = \eta_{\mathrm{MS}} \frac{[1 - (\delta^*/l)]}{[1 - (\upsilon/l)]}, \quad (13)$$

which is essentially Smith's final result. It can be elaborated to allow for end-wall regions on separate hub and casing walls, for lower hub-tip ratio stages, and variations in blade speed with radius. Smith gave experimental correlations of $(\delta^*/g)$ where $g$ is the staggered spacing of the blading, and of the ratio $(\upsilon/\delta^*)$; these correlations depended on the stage geometry, including tip clearance.

It is of interest that Smith's equation (13) does not involve the extra loss explicitly.

**4.2 Alternative Analysis.** Smith's approach has the virtue of simplicity but to some extent it hides the basic understanding of the flow that follows from the result derived in Sec. 3—that the "extra" work in the end-wall region is equal to the "extra" loss there. In an alternative approach, Smith's result can be derived using the analysis of Sec. 3, as follows.

It may be shown from Eq. (7) that

$$L_{\mathrm{EW,TOTAL}} = \int_{r_{\mathrm{HUB}}}^{r_{\mathrm{HUB}}+\delta} \rho c_x X \, dr = (\upsilon - \delta^*)(\rho c_x \Delta H)_{\mathrm{MS}}. \quad (14)$$

The total loss in the USF stage is

$$L_{\mathrm{STAGE}} = (\rho c_x L)_{\mathrm{MS}} (l - \delta) + \int_{r_{\mathrm{HUB}}}^{r_{\mathrm{HUB}}+\delta} \rho c_x (L_{\mathrm{MS}} + X) dr$$

$$= (\rho c_x L)_{\mathrm{MS}} (l - \delta^*) + \int_{r_{\mathrm{HUB}}}^{r_{\mathrm{HUB}}+\delta} \rho c_x X \, dr. \quad (15)$$

Similarly the total work input may be written as

$$\Delta W_{\mathrm{STAGE}} = (\rho c_x \Delta H)_{\mathrm{MS}} (l - \delta^*) + \int_{r_{\mathrm{HUB}}}^{r_{\mathrm{HUB}}+\delta} \rho c_x X \, dr, \quad (16)$$

so that

$$\eta = 1 - (L_{\mathrm{STAGE}} / \Delta W_{\mathrm{STAGE}})$$

$$= 1 - \frac{(\rho c_x L)_{\mathrm{MS}} (l - \delta) + \int_{r_{HUB}}^{r_{\mathrm{HUB}}+\delta} \rho c_x X \, dr}{(\rho c_x \Delta H)_{\mathrm{MS}} (l - \delta^*) + \int_{r_{\mathrm{HUB}}}^{r_{\mathrm{HUB}}+\delta} \rho c_x X \, dr}. \quad (17)$$

Using Eq. (14) for $L_{\mathrm{EW,TOTAL}}$, and

$$\eta_{\mathrm{MS}} = 1 - (L_{\mathrm{MS}} / \Delta H_{\mathrm{MS}}) \quad (18)$$

it follows from Eq. (17) that

$$\eta = 1 - \left[ \frac{[(1-\eta_{MS})(l-\delta)] + (\delta^* - \upsilon)}{(l-\delta^*) + (\delta^* - \upsilon)} \right] = \eta_{MS} \left[ \frac{1-(\delta^*/l)}{1-(\upsilon/l)} \right], \tag{19}$$

which is Smith's expression for the stage efficiency.

## 5 Discussion

This note has made reference to the "extra" loss and the "extra" work in the end-wall flows of repeating stages, and shown that these extra quantities are equal [to $X(r)$ in the notation of this paper]. This would imply that if the extra work could be determined then the (equal) extra loss would also be known.

Attention has already been drawn to the fact that Smith's expression for stage efficiency does not explicitly involve the "extra" losses in the end-wall regions. But Eq. (14) shows that if $\upsilon$ and $\delta^*$ can each be determined (for example from Smith's correlations) then the total extra loss across the end-wall region ($L_{EW,TOTAL}$) is indeed known. It *is* therefore included within the Smith efficiency expression, if in a hidden way.

An alternative way to enter this logistical circle is suggested from the analysis of this note. It would be to use Smith's correlation for the blockage ($\delta^*$) and to find the extra work from inviscid secondary flow analysis. Such an attempt to calculate the "ultimate" secondary flow in repeating stages was made earlier (Horlock [9]). The angle perturbations through the end-wall regions in Howard's compressor [4] were calculated from the mainstream deflections and the observed velocity distributions. With the effects of tip clearance also included, the general trend of the experimental data was confirmed.

Thus the prediction of the USF stage efficiency would involve the following steps:

(a) Find the displacement thicknesses ($\delta^*$) in the USF stage (from Smith's original results for stator exit, and from Horlock [10] for rotor exit) and make estimates of the corresponding velocity profiles;

(b) calculate the angle distributions and the velocity triangles in the end-wall region;

(c) either calculate the total "extra" work and the total "extra" loss, $L_{EW,TOTAL}$, and hence the force deficit thickness ($\upsilon$) from Eq. (14); or calculate the value of $\upsilon$ more directly from $F_u(r)$.

An earlier attempt to calculate $\upsilon$ in the latter way was made in the preparation of Ref. [9], but as the results did not correlate well with Smith's data for ($\upsilon/\delta^*$) this work was not included in the published paper. However, even had this method proved more successful, there would still be an inconsistency in this second approach, as in the Smith method of Sec. 4.1, in that no direct calculations would be made of the viscous effects.

## 6 Conclusion

Thus the conclusion must be drawn that the concept of the ultimate steady flow in a repeating stage is really not more than an experimental observation, and that the Smith efficiency expression is therefore essentially an ingenious development of this observed phenomenon.

## References


[1] Howell, A. R., 1947, "Fluid Dynamics of Axial Compressors," Inst. Mech. Engrs. War Emergency Issue 12; American Edition ASME January 1947, p. 450.

[2] Smith, L. H., 1969, "Casing Boundary Layers in Multi-Stage Axial-Flow Compressors, Flow Research in Blading," L. S. Dzung, ed., Elsevier Publishing Company, New York.

[3] Horlock, J. H., and Denton, J. D., 2003, "A Review of Early Design Practice Using Modern CFD," ASME Paper No. 2003 GT-38973.

[4] Howard, M. A., Ivey, P. C., Barton, J. P., and Young, K. F., 1994, "End Wall Effects at Two Tip Clearances in a Multi-Stage Axial Flow Compressor With Controlled Diffusion Blading," ASME J. Turbomach., **116**, pp. 635–647.

[5] Adkins, G. G., and Smith, L. H., 1982, "Span-Wise Mixing in Axial-Flow Turbomachines," ASME J. Eng. Power, **104**, pp. 97–100.

[6] Gallimore, S. J., and Cumpsty, N. A., 1986, "Span-Wise Mixing in Multi-Stage Axial-Flow Compressors," ASME J. Turbomach., **108**, pp. 2–16.

[7] Wisler, D. C., Bauer, R. C., and Okiishi, T. H., 1987, "Secondary Flow, Turbulent Diffusion and Mixing in Axial-Flow Compressors," ASME J. Turbomach., **109**, pp. 455–482.

[8] Cumpsty, N. A., 1989, *Compressor Aerodynamics*, Longman, UK.

[9] Horlock, J. H., 1995, "Secondary Flow in the Repeating Stages of Axial Turbomachines," Proc. Inst. Mech. Eng., **209**, pp. 101–110.

[10] Horlock, J. H., 2000, "The Determination of End-Wall Blockage in Axial Flow Compressors—A Comparison Between Various Approaches," ASME J. Turbomach., **122**, pp. 218–224.